

POLISH SOCIETY OF THEORETICAL AND APPLIED MECHANICS

**JOURNAL OF THEORETICAL
AND APPLIED MECHANICS**

No. 1 • Vol 56

Quarterly

WARSAW, JANUARY 2018

JOURNAL OF THEORETICAL AND APPLIED MECHANICS

(until 1997 Mechanika Teoretyczna i Stosowana, ISSN 0079-3701)

Beginning with Vol 45, No. 1, 2007, *Journal of Theoretical and Applied Mechanics* (JTAM) has been selected for coverage in Thomson Reuters products and custom information services. Now it is indexed and abstracted in the following:

- **Science Citation Index Expanded** (also known as SciSearch®)
- **Journal Citation Reports/Science Edition**

Advisory Board

MICHAŁ KLEIBER (Poland) – Chairman

JORGE A.C. AMBROSIO (Portugal) ★ ANGEL BALTOV (Bulgaria) ★ ROMESH C. BATRA (USA)
★ ALAIN COMBESURE (France) ★ JÜRI ENGELBRECHT (Estonia) ★ WITOLD GUTKOWSKI (Poland)
★ JÓZEF KUBIK (Poland) ★ ZENON MRÓZ (Poland) ★ RYSZARD PARKITNY (Poland)
★ EKKEHARD RAMM (Germany) ★ EUGENIUSZ ŚWITOŃSKI (Poland) ★ HISAAKI TOBUSHI (Japan)
★ ANDRZEJ TYLIKOWSKI (Poland) ★ DIETER WEICHERT (Germany) ★ JOSE E. WESFREID (France)
★ JÓZEF WOJNAROWSKI (Poland) ★ JOSEPH ZARKA (France)
★ VLADIMIR ZEMAN (Czech Republic)

Editorial Board

Editor-in-Chief – **WŁODZIMIERZ KURNIK**

Section Editors: IWONA ADAMIEC-WÓJCIK, PIOTR CUPIAŁ, KRZYSZTOF DEMS,
WITOLD ELSNER, ELŻBIETA JARZĘBOWSKA, OLEKSANDR JEWtusZENKO,
PIOTR KOWALCZYK, ZBIGNIEW KOWALEWSKI, TOMASZ KRZYŻYŃSKI, STANISŁAW KUKLA,
TOMASZ ŁODYGOWSKI, EWA MAJCHRZAK, WIESŁAW NAGÓRKO, JANUSZ NARKIEWICZ,
PIOTR PRZYBYŁOWICZ, BŁAŻEJ SKOCZEŃ, ANDRZEJ STYCZEK,
JACEK SZUMBARSKI, UTZ VON WAGNER (Germany), JERZY WARMIŃSKI

Language Editor – PIOTR PRZYBYŁOWICZ

Technical Editor – EWA KOISAR

Secretary – ELŻBIETA WILANOWSKA



Articles in JTAM are published under Creative Commons Attribution – Non-commercial 3.0. Unported License <http://creativecommons.org/licenses/by-nc/3.0/legalcode>. By submitting an article for publication, the authors consent to the grant of the said license.



The journal content is indexed in Similarity Check, the Crossref initiative to prevent plagiarism.

* * * * *

Editorial Office

Al. Armii Ludowej 16, room 650

00-637 Warszawa, Poland

phone (+48 22) 825 7180, (+48) 664 099 345, e-mail: biuro@ptmts.org.pl

www.ptmts.org.pl/jtam.html

* * * * *



Ministerstwo Nauki
i Szkolnictwa Wyższego

Publication supported by Ministry of Science and Higher Education of Poland

(Journal of Theoretical and Applied Mechanics: 1) digitalizacja publikacji i monografii naukowych w celu zapewnienia i utrzymania otwartego dostępu do nich przez sieć Internet, 2) stworzenie anglojęzycznych wersji wydawanych publikacji, 3) wdrożenie procedur zabezpieczających oryginalność publikacji naukowych oraz zastosowane techniki zabezpieczeń – są finansowane w ramach umowy 715/P-DUN/2017 ze środków Ministra Nauki i Szkolnictwa Wyższego przeznaczonych na działalność upowszechniającą naukę)

HYGROTHERMOELASTIC BUCKLING RESPONSE OF COMPOSITE LAMINATES BY USING MODIFIED SHEAR DEFORMATION THEORY

MASOUD KAZEMI

Environmental Sciences Research Center, Islamshahr Branch, Islamic Azad University, Islamshahr, Iran
e-mail: masoud_kazemi@hotmail.com; kazemii@iiu.ac.ir

In this study, a finite element based formulation is developed for analyzing the buckling and post-buckling of composite laminates subjected to mechanical and hygrothermal loads using Modified Hyperbolic Shear Deformation Theory (MHSDT). The changes in the critical buckling load are presented for different lamination schemes, thicknesses, material properties and plate aspect ratios. In addition, post buckling analysis is performed for a composite plate subjected to uniform in-plane thermal and moisture induced loadings by using MHSDT. Matlab software has been used for programming the analysis. The results obtained by Matlab codes are in a satisfactory consistence compared to the references. Thus, the developed MHSDT has been validated for buckling and post buckling analysis of laminated plates in hygrothermal environment.

Keywords: angle-ply laminate, buckling, composite plate, finite element method, shear deformation theory

1. Introduction

Compared to conventional metal structures, fibrous composite materials continue to experience increased application in aerospace, marine, automobile and other mechanical and civil structures due to their superior strength and stiffness to weight ratios; however, due to material anisotropy, analyzing and designing these materials are more complicated than metallic materials.

In order to prevent buckling and post-buckling effects in laminated plates, using an extra-strength is of great practical importance in the structural design of laminated plates.

Buckling is known as one of the most critical failure modes, often pre-generated or produced during service life. A significant reduction in weight of laminated plates can be achieved considering the post buckling behavior, which is an important factor in aerospace structures. The elastic buckling and post-buckling of fiber reinforced composite plates are investigated in several textbooks (Agarwal *et al.*, 2006; Reddy, 2004; Turvey and Marshall, 2012). Composite laminates are also susceptible to delamination buckling and exterior damage at stress free edges, which occurs when the properties mismatch at the ply interface. It can also be produced by external forces, elevated temperature and absorbed moisture. Stresses within laminates are redistributed to reduce the load carrying capacity, when delamination occurs. Composite laminates are subjected to changing environmental conditions like temperature and moisture. The effect of temperature and moisture is known as thermal and hygroscopic effect, respectively. The combined effect of these two parameters is called the hygrothermal effect. A hygrothermal environment reduces both strength and elastic properties, especially in the case of fibrous polymeric composites. Furthermore, associated hygrothermal expansion, either alone or in combination with mechanically produced deformation, can result in buckling, large deflections, and high stress levels. Consequently, examining the hygrothermal effects is essential in analyzing and designing laminated systems (Tauchert and Huang, 2012). Due to the fact that most applications are limited to purely thermal loadings, the majority of published researches lie in this field.

According to the similarities between mathematical formulations of the governing thermal and hygroscopic loadings, the given thermoelastic solutions could be generalized to elasto-hygrothermal cases. Similarly, it is not difficult to simplify the hygrothermal formulations and solution methods to include the isothermal effects. For predicting the real behavior of a structure, it is important to choose an adequate theory which is used in the expansion of different variables (Mantari *et al.*, 2012). In the 3D elasticity theory, heterogeneous laminated plates are modeled as 3D solid elements, so predicting transverse shear stresses can be significantly improved, however, by using this theory would lead to a complex procedure and multiplied computational cost.

In the literature, different models have been suggested for studying the composite laminated structures, including layerwise, quasi-layerwise and equivalent single layer models. Three principal equivalent theories have been proposed to reduce the 3D models to 2D ones; which are known as the Classical Laminated Plate Theory (CLPT), First-order Shear Deformation Theory (FSDT) and Higher-order Shear Deformation Plate Theory (HSDT) (Kharazi *et al.*, 2014).

In the CLPT, which relies on the Love-Kirchhoff assumptions, the transverse shear deformation is neglected and is only applicable for thin laminated plates, so, in order to consider the shear effect, the FSDT based on Reissner-Mindlin theory has been developed. The FSDT is simple to perform and can be applied for both thick and thin laminates; however, the accuracy of solutions strongly relies on the shear correction factors. In addition, the FSDT would not give satisfactory results in predicting the accurate and smooth variations of stresses, specifically for laminated plates with clamped or free edges, sharp corners and highly skewed geometry where high stress gradients occur. To overcome the limitation of the FSDT, a simple higher order theory was presented by Reddy (2004) for laminated plates, various types of HSDT, which include higher order terms in Taylor's expansion.

Many studies in the literature investigated the buckling and post-buckling in composite laminated thin plates subjected to mechanical or thermal loadings or both based on the classical plate theory, see for example (Kazemi and Verchery, 2016; Peković *et al.*, 2015; Ahmadi and Pourshahsavari, 2016; Muc and Chwał, 2016). In some other studies (Girish and Ramachandra, 2005; Mechab *et al.*, 2012; Dafedar and Desai, 2002), the application of shear deformation plate theories was developed for buckling and post-buckling analysis of laminated plates under combined mechanical and thermal loading. It should be noted that in all these investigations, the material properties are considered to be independent of temperature. Although comprehensive literature has been published in the field of pure mechanical or pure thermal loadings, few investigations have been devoted to the elastic buckling and post-buckling caused by coupled thermal and mechanical loads, which is encountered in real cases and operational life of composite structures.

A refined two-dimensional model was proposed by Brischetto (2013) for static hygrothermal analysis of laminated composites and sandwich shells neglecting the transverse shear deformation effects. Sreehari and Maiti (2015) introduced a finite element solution for handling buckling and post buckling analysis of laminated plates under mechanical and hygrothermal loads using a refined HSDT; however, the accuracy of the method was verified only for cross-ply laminates. Natarajan *et al.* (2014) considered the effect of moisture condensation and thermal variation on the vibration and buckling of laminates with cutouts within the formulation of the extended finite element method. Pandey *et al.* (2009) examined the influence of moisture concentration, temperature variation, plate parameters and fiber-volume fraction on the buckling and post buckling of the laminated plates based on HSDT and von Karman's nonlinear kinematics; however, the distribution of temperature and moisture on the surface was assumed to be uniform.

The aim of present work is to analyze the buckling and post buckling behavior of composite laminated plates in hygrothermal environment using the Finite Element Method (FEM) based on a new higher order formulation, in which the displacement of the middle surface is developed

as a trigonometric and exponential function of thickness, and the transverse displacement is assumed to be constant through the thickness. An appropriate distribution of the transverse shear strain is assumed across the plate thickness and, also, the stress-free boundary conditions are considered on the boundary surface, therefore, a shear modification factor is not needed.

2. Trigonometric shear displacement model (TSDM)

A laminated plate consisting of N orthotropic plies is considered. Length, width and thickness of the rectangular plate are a , b , and h , respectively. An 8-noded serendipity quadrilateral element, which is C^0 -continuous isoperimetric bi-quadratic, has been used for discretization of the laminated plate. In this work, the following new displacement model is proposed to satisfy the boundary conditions at the top and bottom of the laminated plate

$$\begin{aligned} u(x, y, z) &= u_0(x, y) - z \frac{\partial w}{\partial x} + \left[\sin \frac{\pi z}{h} \exp\left(m \cos \frac{\pi z}{h}\right) + \frac{\pi}{h} m z \right] \theta_x(x, y) \\ v(x, y, z) &= v_0(x, y) - z \frac{\partial w}{\partial y} + \left[\sin \frac{\pi z}{h} \exp\left(m \cos \frac{\pi z}{h}\right) + \frac{\pi}{h} m z \right] \theta_y(x, y) \\ w(x, y, z) &= w_0 \end{aligned} \quad (2.1)$$

where u , v , w represent displacement components in the x , y and z directions, respectively; and u_0 , v_0 , w_0 are displacement components in the middle surface of the plate. θ_x and θ_y are rotations about the y and x axes at the mid-plane, respectively. The first order derivatives of the transverse displacement can be formulated in terms of the in-plane displacement parameters as separate independent degrees of freedom as given below

$$\begin{aligned} u(x, y, z) &= u_0(x, y) - z \phi_x(x, y) + [g(z) + \Gamma z] \theta_x(x, y) \\ v(x, y, z) &= v_0(x, y) - z \phi_y(x, y) + [g(z) + \Gamma z] \theta_y(x, y) \\ w(x, y, z) &= w_0(x, y) \end{aligned} \quad (2.2)$$

where

$$\phi_x = \frac{\partial w}{\partial x} \quad \phi_y = \frac{\partial w}{\partial y} \quad g(z) = \sin \frac{\pi z}{h} \exp\left(m \cos \frac{\pi z}{h}\right) \quad \Gamma = \frac{\pi}{h} m$$

The linear displacement vector given in the above equation can be expressed in terms of the middle surface of the laminated plate as follows

$$\boldsymbol{\varepsilon}_{5 \times 1} = \mathbf{Z}_{5 \times 13} \bar{\boldsymbol{\varepsilon}}_{13 \times 1} \quad (2.3)$$

where

$$\begin{aligned} \bar{\boldsymbol{\varepsilon}} &= \left\{ \varepsilon_1^0 \quad \varepsilon_2^0 \quad \varepsilon_6^0 \quad \kappa_1^1 \quad \kappa_2^1 \quad \kappa_6^1 \quad \varepsilon_4^0 \quad \varepsilon_5^0 \quad \kappa_4^2 \quad \kappa_5^2 \right\}^T \\ \varepsilon_1^0 &= \frac{\partial u_0}{\partial x} \quad \varepsilon_2^0 = \frac{\partial v_0}{\partial y} \quad \varepsilon_6^0 = \frac{\partial u_0}{\partial y} + \frac{\partial v_0}{\partial x} \quad \varepsilon_4^0 = \frac{\partial w_0}{\partial y} - \phi_y \\ \varepsilon_5^0 &= \frac{\partial w_0}{\partial x} - \phi_x \quad \kappa_1^0 = \Gamma \frac{\partial \theta_x}{\partial x} - \frac{\partial \phi_x}{\partial x} \quad \kappa_2^0 = \Gamma \frac{\partial \theta_y}{\partial y} - \frac{\partial \phi_y}{\partial y} \\ \kappa_6^0 &= \Gamma \left(\frac{\partial \theta_x}{\partial y} + \frac{\partial \theta_y}{\partial x} \right) - \frac{\partial \phi_x}{\partial y} - \frac{\partial \phi_y}{\partial x} \quad \kappa_1^1 = \frac{\partial \theta_x}{\partial x} \quad \kappa_2^1 = \frac{\partial \theta_y}{\partial x} \\ \kappa_6^1 &= \frac{\partial \theta_y}{\partial x} + \frac{\partial \theta_x}{\partial y} \quad \kappa_4^2 = \theta_y \quad \kappa_5^2 = \theta_x \end{aligned}$$

$$\mathbf{Z} = \begin{bmatrix} 1 & 0 & 0 & z & 0 & 0 & g(z) & 0 & 0 & 0 & 0 & 0 & 0 \\ 0 & 1 & 0 & 0 & z & 0 & 0 & g(z) & 0 & 0 & 0 & 0 & 0 \\ 0 & 0 & 1 & 0 & 0 & z & 0 & 0 & 0 & g(z) & 0 & 0 & 0 \\ 0 & 0 & 0 & 0 & 0 & 0 & 0 & 0 & 0 & 1 & 0 & g(z) & 0 \\ 0 & 0 & 0 & 0 & 0 & 0 & 0 & 0 & 0 & 0 & 1 & 0 & g(z) \end{bmatrix}$$

and

$$\bar{\boldsymbol{\varepsilon}}_{13 \times 1} = \mathbf{L}_{13 \times 7} \boldsymbol{\Delta}_{7 \times 1} \quad \boldsymbol{\Delta} = \{u_0 \quad v_0 \quad w_0 \quad \theta_x \quad \theta_y \quad \phi_x \quad \phi_y\}^T$$

The following assumptions are considered in the derivation of the equations:

- Small elastic deformations are assumed (i.e. deformations and rotations are small and agree to the Hooke's law).
- The plies of the composite laminated structure are supposed to be well bonded.

The linear strain equations derived from the displacements of Eqs. (2.1), which are valid for thin as well as thick plates under consideration, are as follows

$$\begin{aligned} \varepsilon_{xx} &= \varepsilon_{xx}^0 + z\varepsilon_{xx}^1 + \sin \frac{\pi z}{h} \exp\left(m \cos \frac{\pi z}{h}\right) \varepsilon_{xx}^2 \\ \varepsilon_{yy} &= \varepsilon_{yy}^0 + z\varepsilon_{yy}^1 + \sin \frac{\pi z}{h} \exp\left(m \cos \frac{\pi z}{h}\right) \varepsilon_{yy}^2 \\ \varepsilon_{xy} &= \varepsilon_{xy}^0 + z\varepsilon_{xy}^1 + \sin \frac{\pi z}{h} \exp\left(m \cos \frac{\pi z}{h}\right) \varepsilon_{xy}^2 \\ \varepsilon_{xz} &= \varepsilon_{xz}^0 + \frac{\pi}{h} \left(\cos \frac{\pi z}{h} - m \sin^2 \frac{\pi z}{h} \right) \exp\left(m \cos \frac{\pi z}{h}\right) \varepsilon_{xz}^3 \\ \varepsilon_{yz} &= \varepsilon_{yz}^0 + \frac{\pi}{h} \left(\cos \frac{\pi z}{h} - m \sin^2 \frac{\pi z}{h} \right) \exp\left(m \cos \frac{\pi z}{h}\right) \varepsilon_{yz}^3 \end{aligned} \quad (2.4)$$

and

$$\begin{aligned} \varepsilon_{xx}^0 &= \frac{\partial u}{\partial x} & \varepsilon_{xx}^1 &= m \frac{\pi}{h} \frac{\partial \theta_x}{\partial x} - \frac{\partial^2 w}{\partial x^2} & \varepsilon_{xx}^2 &= \frac{\partial \theta_x}{\partial x} \\ \varepsilon_{yy}^0 &= \frac{\partial v}{\partial x} & \varepsilon_{yy}^1 &= m \frac{\pi}{h} \frac{\partial \theta_y}{\partial x} - \frac{\partial^2 w}{\partial x^2} & \varepsilon_{yy}^2 &= \frac{\partial \theta_y}{\partial x} \\ \varepsilon_{xy}^0 &= \frac{\partial v}{\partial x} + \frac{\partial u}{\partial y} & \varepsilon_{xy}^1 &= m \frac{\pi}{h} \frac{\partial \theta_y}{\partial x} + m \frac{\pi}{h} \frac{\partial \theta_x}{\partial y} - 2 \frac{\partial^2 w}{\partial x \partial y} & \varepsilon_{xy}^2 &= \frac{\partial \theta_y}{\partial x} + \frac{\partial \theta_x}{\partial y} \\ \varepsilon_{xz}^0 &= m \frac{\pi}{h} \theta_x & \varepsilon_{xz}^3 &= \theta_x & \varepsilon_{yz}^0 &= m \frac{\pi}{h} \theta_y & \varepsilon_{yz}^3 &= \theta_y \end{aligned} \quad (2.5)$$

3. Governing equations of the hygrothermal buckling and post-buckling

The laminated plate composed of elastic orthotropic plies and the stress-strain relations in the orthotropic local frame are as follows (Reddy, 2004)

$$\begin{Bmatrix} \sigma_1 \\ \sigma_2 \\ \tau_{12} \\ \tau_{13} \\ \tau_{23} \end{Bmatrix} = \begin{bmatrix} Q_{11} & Q_{12} & 0 & 0 & 0 \\ Q_{12} & Q_{22} & 0 & 0 & 0 \\ 0 & 0 & Q_{66} & 0 & 0 \\ 0 & 0 & 0 & Q_{55} & 0 \\ 0 & 0 & 0 & 0 & Q_{44} \end{bmatrix} \begin{Bmatrix} \varepsilon_1 \\ \varepsilon_2 \\ \gamma_{12} \\ \gamma_{13} \\ \gamma_{23} \end{Bmatrix} \quad (3.1)$$

where Q_{ij} are elastic stiffness coefficients relative to the plane-stress state that neglects the transversal stress. These coefficients are given below (Reddy, 2004) in terms of the engineering constants in the material coordinates

$$\begin{aligned}
Q_{11} &= \frac{E_1}{1 - \nu_{12}\nu_{21}} & Q_{22} &= \frac{E_2}{1 - \nu_{12}\nu_{21}} & Q_{12} &= \nu_{12}Q_{11} & Q_{33} &= G_{12} \\
Q_{44} &= G_{23} & Q_{55} &= G_{13} & \nu_{21} &= \nu_{12}\frac{E_2}{E_1}
\end{aligned} \tag{3.2}$$

In general, the laminates are in the plane stress state due to temperature or moisture changes; therefore, externally applied stresses would develop at the supports. These in-plane stresses can be evaluated using elasto-hygrothermal constitutive equation. When hygrothermal effects are considered, the stress tensor is usually expressed in the contracted notation as follows

$$\sigma_i = Q_{ij} \left(\varepsilon_j - \int_{T_0}^T \alpha_j(\tau, M) d\tau - \int_{M_0}^M \beta_j(T, m) dm \right) \quad i, j = 1, 2, 3 \tag{3.3}$$

where the elastic stiffness coefficients Q_{ij} , the thermal expansion coefficients α_j , and the moisture coefficients β_j depend upon the temperature T and moisture concentration M . For moderate temperature $\Delta T = T - T_0$ and moisture $\Delta M = M - M_0$ changes from the corresponding stress-free values T_0 and M_0 , if the elastic properties are considered independent from the hygrothermal, the stress-strain relations are simplified as follows

$$\sigma = Q_{ij}(\varepsilon_1 - \alpha_j \Delta T - \beta_j \Delta M)(\varepsilon_1 - \alpha_j \Delta T - \beta_j \Delta M) \quad i, j = 1, 2, 3 \tag{3.4}$$

Proper tensor transformations can be employed in transforming equation (3.4) from principal material coordinates x_1, x_2 and x_3 to the plate coordinates x, y and z . For a typical k -th ply of the laminate, the resulted expression can be written as

$$\begin{Bmatrix} \sigma_{xx} \\ \sigma_{yy} \\ \tau_{xy} \\ \tau_{xz} \\ \tau_{yz} \end{Bmatrix}_k = \begin{bmatrix} \overline{Q}_{11} & \overline{Q}_{12} & \overline{Q}_{16} & 0 & 0 \\ \overline{Q}_{12} & \overline{Q}_{22} & \overline{Q}_{26} & 0 & 0 \\ \overline{Q}_{16} & \overline{Q}_{26} & \overline{Q}_{66} & 0 & 0 \\ 0 & 0 & 0 & \overline{Q}_{55} & \overline{Q}_{54} \\ 0 & 0 & 0 & \overline{Q}_{45} & \overline{Q}_{44} \end{bmatrix}_k \begin{Bmatrix} \varepsilon_{xx} - \alpha_x \Delta T - \beta_x \Delta C \\ \varepsilon_{yy} - \alpha_y \Delta T - \beta_y \Delta C \\ \varepsilon_{xy} - \alpha_{xy} \Delta T - \beta_{xy} \Delta C \\ \varepsilon_{xz} \\ \varepsilon_{yz} \end{Bmatrix}_k \tag{3.5}$$

or in a condensed form

$$\sigma_k = \overline{\mathbf{Q}}_k \varepsilon_k \tag{3.6}$$

where \overline{Q}_{ij} , α_i , β_i ($i, j = x, y, xy$) denote the transformed material coefficients.

According to the potential energy theorem, the equilibrium state can be achieved when variation of the total potential energy equates to zero.

The potential energy theorem can be expressed for the typical i -th ply enclosing a space volume V as follows

$$\int_V (\sigma_{xx} \delta \varepsilon_{xx} + \sigma_{yy} \delta \varepsilon_{yy} + \tau_{xy} \delta \varepsilon_{xy} + \tau_{xz} \delta \varepsilon_{xz} + \tau_{yz} \delta \varepsilon_{yz}) dV_e - \int_A q \delta w dA_e = 0 \tag{3.7}$$

When the laminate is subjected to temperature or moisture changes, due to the restriction on freeing the hygrothermal loading, some stresses are developed at the supports. The governing equations on the pre-buckling can be obtained via the following formula

$$\mathbf{K} \Delta = \mathbf{F} \tag{3.8}$$

where \mathbf{K} is the linear stiffness matrix and \mathbf{F} represents the load vector associated with the temperature variation or hygroscopic effects. Equation (3.8) is solved under the specified boundary condition and in-plane loads. In the next step, the geometric stiffness matrix \mathbf{K}_G associated

with these in-plane loads is calculated. The critical hygrothermal buckling is calculated through solving the linear eigenvalue problem

$$(\mathbf{K} + \lambda_{cr}\mathbf{K}_G)\mathbf{\Delta} = \mathbf{0} \quad (3.9)$$

The smallest eigenvalue corresponds to the amplitude of the critical buckling load. In the post-buckling step, the nonlinear stiffness matrix \mathbf{K}_{nl} is incorporated as

$$(\mathbf{K} + \mathbf{K}_{nl} + \lambda_{cr}\mathbf{K}_G)\mathbf{\Delta} = \mathbf{0} \quad (3.10)$$

The geometric stiffness matrix can be expressed as

$$\mathbf{K}_G = \sigma_x^p \mathbf{K}_{G1} + \sigma_y^p \mathbf{K}_{G2} \quad (3.11)$$

where σ_x^p , σ_y^p denote externally applied stresses acting in the x and y directions. Subsequently, the critical buckling stresses can be calculated by the following formulas

$$\sigma_{xc}^p r = \lambda_{cr} \sigma_x^p \quad \sigma_{yc}^p r = \lambda_{cr} \sigma_y^p \quad (3.12)$$

4. Numerical results and discussion

In this Section, numerical examples are presented for buckling and post buckling of the laminated composite plates under mechanical and hygrothermal loads. The accuracy of the proposed TSDM model considering the transverse shear stresses is examined. A variety of problems are solved using the finite element formulation and the results are compared with 3D elasticity solution. It is important to note that the proposed displacement model can be applied to any lay-up of the laminated plates. The different mechanical properties examined in the numerical examples are given in Table 1.

Table 1. Material properties used in the numerical examples

Material No.	Elastic constants (Reddy and Liu, 1985; Dafedar and Desai, 2002)							
1	$E_1/E_2 = 25$, $G_{12} = G_{13} = 0.5E_2$, $G_{23} = 0.2E_2$, $\nu_{12} = 0.25$							
2	$E_1/E_2 = 3$ to 40 , $E_3 = E_2$, $G_{12}/E_2 = G_{13}/E_2 = 0.60$, $G_{23}/E_2 = 0.50$, $\nu_{12} = \nu_{23} = \nu_{13} = 0.25$							
3	$E_1/E_2 = 40$, $E_3 = E_2$, $G_{12}/E_2 = G_{13}/E_2 = 0.50$, $G_{23}/E_2 = 0.20$, $\nu_{12} = \nu_{23} = \nu_{13} = 0.25$							
4	$E_1/E_2 = 15$, $E_3 = E_2$, $G_{12}/E_2 = G_{13}/E_2 = 0.50$, $G_{23}/E_2 = 0.3356$, $\nu_{12} = \nu_{23} = \nu_{13} = 0.3$, $a_1/a_0 = 0.015$, $a_2/a_0 = a_3/a_0 = 1.00$							
5	Elastic moduli of graphite/epoxy ply at different moisture concentrations C [%], $E_1 = 130$ GPa, $G_{13} = G_{12} = 6.0$ GPa, $G_{23} = 0.5G_{12}$, $\nu_{12} = \nu_{23} = \nu_{13} = 0.3$, $\beta_1 = 0$ and $\beta_2 = \beta_3 = 0.44$ and							
	C [%]	0.00	0.25	0.50	0.75	1.00	1.25	1.50
	E_2 [GPa]	9.50	9.25	9.00	8.75	8.50	8.50	8.50

In order to simplify comparison, the critical buckling stresses have been transformed into dimensionless coefficients as follows

$$\lambda_{cr} = \frac{\sigma_{cr} b^2}{E_2 h^2} \quad (4.1)$$

4.1. Examples for validating the TSDM model

Three cases are examined to confirm TSDM formulation using finite element programming.

Case A

A symmetric four-layered (0/90/90/0) cross-ply laminated plate is considered under uniaxial compression loading. The critical buckling coefficients for various values of length-to-thickness ratios a/h are presented in Table 2. As it is demonstrated in Table 2, the HSDT overestimates the critical buckling loads in comparison with the results from the present formulation and those given by Pagano *et al.* (1994).

Table 2. Effect of length to thickness ratio on the critical buckling load

a/h	Present	3D (Pagano and Reddy, 1994)	HSDT (Reddy and Liu, 1985)
5	1.922	1.575	1.997
10	13.367	13.453	13.384
20	20.689	21.707	21.886
50	23.354	23.356	23.747
100	24.034	24.255	24.953

Case B

The effect of elastic moduli ratios on the buckling loads of a square plate under uniaxial loading is examined, and the results are presented in Table 3. According to the results obtained via the TSDM formulation are in excellent agreement with other references.

Table 3. Effect of elastic moduli ratios on critical buckling loads

E_1/E_2	Present	3D (Pagano and Reddy, 1994)	HSDT (Reddy and Liu, 1985)
3	5.396	5.399	5.114
10	9.952	9.967	13.384
20	15.327	15.352	15.297
30	19.703	19.758	19.968
40	23.564	23.451	23.344

Case C

Table 4 presents the comparison between the critical buckling coefficients obtained through the present model and the reference values for the square laminated plate under uniaxial compression loading. The analysis is carried out for two values of fiber orientation angles $\theta = 30^\circ$ and $\theta = 45^\circ$ for both of the two-ply and six-ply antisymmetric angle-ply laminates. The results are validated by comparing them with the HSDT model proposed by Reddy and Liu (1985).

4.2. Effect of the length-to-thickness ratio on the critical buckling load

A symmetric four-layered (0/90)s cross-ply laminated plate is considered under both uniaxial and biaxial compression loadings. The effect of the side-to-thickness ratio for the simply supported rectangular plate is examined using material No. 1, and the results are plotted in Fig.1. It is

Table 4. Critical buckling coefficients for angle-ply laminates

$\theta = 30^\circ$					$\theta = 45^\circ$				
a/h	2 ply		6 ply		a/h	2 ply		6 ply	
	Present	[10]	Present	[10]		Present	[10]	Present	[10]
5	10.694	11.543	13.404	13.536	5	10.084	10.782	12.169	12.172
10	16.108	17.123	29.046	33.624	10	16.734	18.051	30.648	32.504
20	18.234	18.764	41.023	46.231	20	19.234	19.764	48.230	52.132
50	19.748	19.863	49.963	51.643	50	20.746	20.863	58.963	59.643
100	20.308	30.603	53.079	54.896	100	21.267	21.664	59.431	61.021

[10] – Muc and Chwał (2016)

observed that the critical buckling loads are higher in the uniaxial loading case. Additionally, the buckling load coefficients increase considerably as the thickness ratio decreases. The variations of both curves for two loading conditions are very slow above the $a/h = 40$ ratio (are only a little above $a/h = 40$).

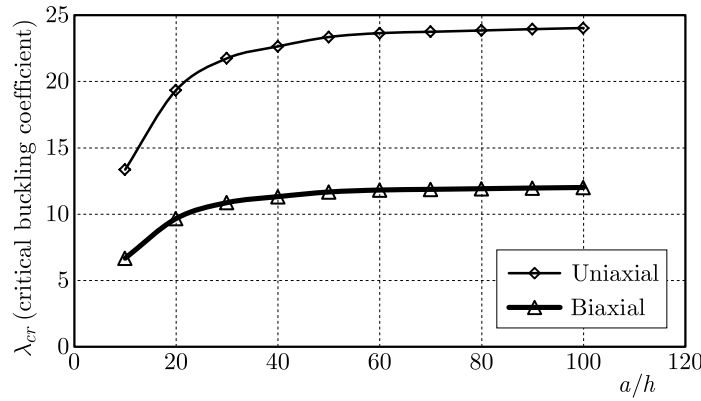


Fig. 1. Effect of the length-to-thickness ratio on the critical buckling load for cross-ply laminates

4.3. Effect of ply orientation on the critical buckling load

The buckling load coefficient for a square and antisymmetric angle-ply laminated plate is tested under uniaxial compressive loading; the effect of ply orientation for various numbers of layers of the angle-ply laminate is plotted in Fig. 2. All the edges are supposed to be simply supported, and material 5 of Table 1 is used in all cases. It is observed that in all cases, the

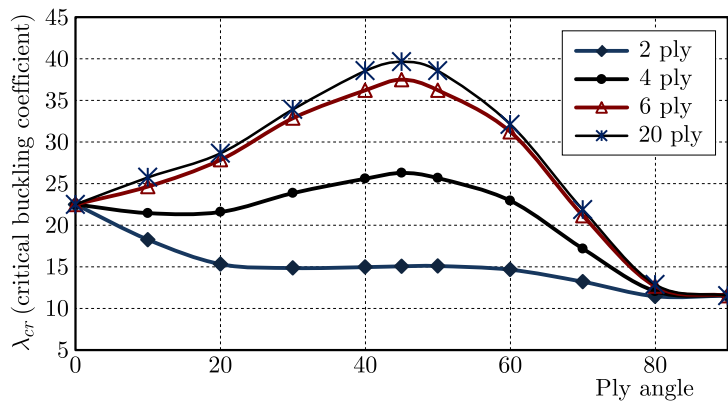


Fig. 2. Effect of the ply angle on the critical buckling load

critical buckling load increases at first but decreases then. By varying the fiber orientation angles from 0° to 90° , it is observed that the maximum critical buckling load occurs at 45° .

4.4. Effect of the elastic moduli ratio on the critical buckling load

The variations of critical buckling coefficients of antisymmetric cross-ply laminated plates under uniaxial and biaxial loadings are demonstrated in Figs. 3, respectively. The results are presented for $a/h = 10$. It is observed that as the elastic moduli ratio rises, the critical buckling load also increases in both uniaxial and biaxial loadings; however, in biaxial cases, the buckling loads are approximately half of the corresponding uniaxial values at all analyzed ratios.

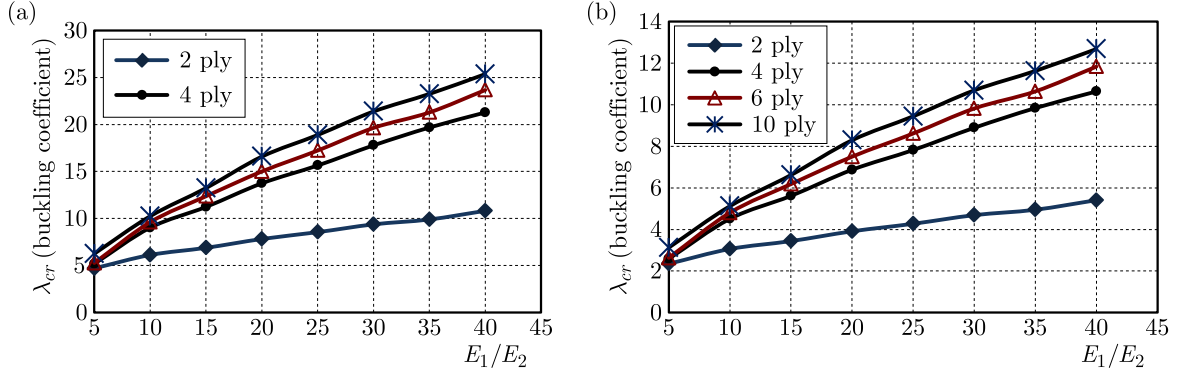


Fig. 3. Variation of the buckling load for square antisymmetric cross-ply laminate when $a/h = 10$; (a) uniaxial loading, (b) biaxial loading

4.5. Effect of thermal loads on the buckling of laminates

Buckling under thermal loads for a laminated plate consisting of 10 plies of material 4 is examined using TSDM model and compared with 3D elasticity solutions. The thermal buckling coefficients of $\lambda_T = \alpha_0 T_{cr}$ are provided in Table 5. The obtained results are in excellent agreement with the 3D elasticity results proposed by Noor and Burton (1992), for both the thin and thick laminated plates. In this case, the critical buckling loads correspond to the buckling modes of $m, n = 1, 2$, because the laminates under high temperature variations are mainly subjected to the biaxial loading condition. The results confirm that the buckling in the thick laminated plates occur at higher temperatures compared to the thin ones. In Fig. 4, the thermo-buckling curve is plotted for a simply supported square and $[\pm 45^\circ]$ antisymmetric angle-ply laminate. The obtained results by the present model are very close to the analytical solutions proposed by Singha *et al.* (2001).

Table 5. Thermal buckling coefficient $\lambda_T = \alpha_0 T_{cr}$ for a square angle-ply laminated plate

a/h	Present	3D solution (Noor and Burton, 1992)
100.0000	$0.7463 \cdot 10^{-3}$	$0.7458 \cdot 10^{-3}$
20.0000	$0.1739 \cdot 10^{-3}$	$0.1721 \cdot 10^{-3}$
10.0000	$0.5782 \cdot 10^{-3}$	$0.5820 \cdot 10^{-3}$
6.6667	0.1029	0.1034
5.0000	0.1436	0.1515
4.0000	0.1777	0.1886
3.3333	0.2057	0.2063

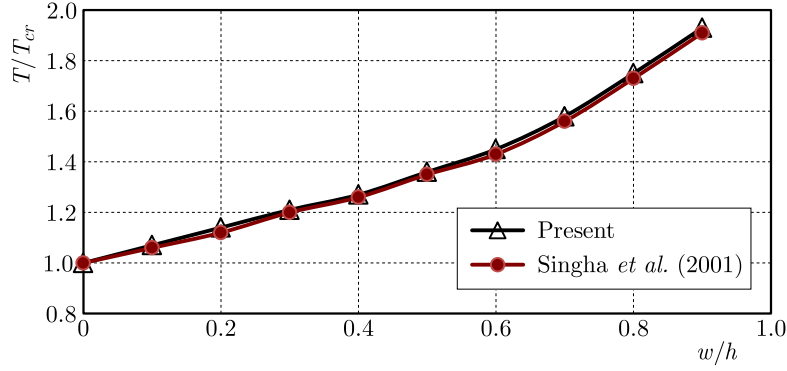


Fig. 4. Thermo-buckling path plotted for a simply supported square $[\pm 45^\circ]$ antisymmetric angle-ply laminate

4.6. Effect of change in moisture concentration on the buckling load

The effects of changes in moisture concentrations on the uniaxial buckling load coefficients λ_U of a cross-ply $[(0/90)_s]$ laminate using material 5 is presented in Table 6. The buckling loads are evaluated by reducing the material properties and increasing the moisture concentration. The parameter $(E_2)_{c=0\%}$ is used to calculate the buckling load coefficient λ_U using the TSDM model. In Fig. 6, the variation of the buckling load coefficient with respect to the moisture concentration is shown for different b/h ratios. As it is seen from this figure, in thin plates, the buckling coefficient decreases faster compared to the thick ones. However, the slope is almost linear for both thin and thick laminates, and the thin plates may buckle due to a little change in the moisture concentration, even in the absence of external loads.

Table 6. Effect of moisture concentration on the critical buckling load coefficient of a symmetric cross-ply laminated plate for various values of the thickness-to-length ratio

a/h	C [%]	Present	Dafedar and Desai (2002)
5	0.0	6.9932	7.1383
	0.5	6.8911	7.0365
	1.0	6.7963	6.9420
	1.5	6.7320	6.8776
10	0.0	11.3466	11.4275
	0.5	11.0183	11.0990
	1.0	10.7205	10.8009
	1.5	10.4631	10.5435
20	0.0	13.6835	13.7106
	0.5	12.5247	12.5517
	1.0	11.4879	11.5147
	1.5	10.4582	10.4851
40	0.0	14.4529	14.4602
	0.5	10.0180	10.0254
	1.0	6.0708	6.0781
	1.5	1.9523	1.9596

5. Conclusions

A new finite element formulation is developed using MHSMT for investigating the effects of elasto-hygrothermal loads in the buckling of composite laminated plates. The transverse stresses through thickness of a plate and the continuity of displacements are entirely satisfied in the proposed formulation. From the extensive numerical investigation, the results obtained using Trigonometric Shear Displacement Model (TSDM) is in excellent agreement with the three-dimensional elasticity solutions as well as other equivalent higher-order theories. The variations of the critical buckling load are presented for different lamination lay-ups, elastic constants and length-to-thickness plate ratios. The effect of thermally-induced loading and moisture concentration on the buckling and post-buckling of the laminated plates are investigated using TSDM formulation. The following conclusions are obtained:

- In the hygrothermal buckling analysis of composite plates, it is mandatory to exploit refined higher-order theories dealing with the transverse normal deformation.
- Increasing the moisture concentrations and temperatures would result in a reduction in the buckling and post-buckling strength. The results also confirm that the post-buckling characteristics are significantly affected by a rise in the temperature, moisture concentration, transverse shear deformation, plate geometry, total number of plies and fiber orientation.
- Increasing the length-to-thickness ratio, the number of layers and the orthotropic ratio (E_1/E_2) would lead to an increase in the buckling strength due to in-plane compressive loading.
- The critical buckling load is higher in the case of uniaxial loading compared to the biaxial one.

References

1. AGARWAL B.D., BROUTMAN L.J., CHANDRASHEKHARA K., 2006, *Analysis and Performance of Fiber Composites*, 3rd ed., Wiley, New York
2. AHMADI S.A., POURSHAHSAVARI H., 2016, Three-dimensional thermal buckling analysis of functionally graded cylindrical panels using differential quadrature method (DQM), *Journal of Theoretical and Applied Mechanics*, **54**, 1, 135-147
3. BRISCHETTO S., 2013, Hygrothermoelastic analysis of multilayered composite and sandwich shells, *Journal of Sandwich Structures and Materials*, **15**, 2, 168-202
4. DAFEDAR J.B., DESAI Y.M., 2002, Thermomechanical buckling of laminated composite plates using mixed, higher-order analytical formulation, *Journal of Applied Mechanics*, **69**, 6, 790-799
5. GIRISH J., RAMACHANDRA L.S., 2005, Thermomechanical post-buckling analysis of symmetric and antisymmetric composite plates with imperfections, *Composite Structures*, **67**, 4, 453-460
6. KAZEMI M., VERCHERY G., 2016, Design of composite laminated plates for maximum buckling load with stiffness and elastic modulus constraints, *Composite Structures*, **148**, 27-38
7. KHARAZI M., OVESY H.R., MOONEGHI M.A., 2014, Buckling analysis of delaminated composite plates using a novel layerwise theory, *Thin-Walled Structures*, **74**, 246-254
8. MANTARI J.L., OKTEM A.S., SOARES C.G., 2012, A new higher order shear deformation theory for sandwich and composite laminated plates, *Composites Part B: Engineering*, **43**, 3, 1489-1499
9. MECHAB B., MECHAB I., BENAÏSSA S., 2012, Analysis of thick orthotropic laminated composite plates based on higher order shear deformation theory by the new function under thermo-mechanical loading, *Composites Part B: Engineering*, **43**, 3, 1453-1458

10. MUC A., CHWAŁ M., 2016, Analytical discrete stacking sequence optimization of rectangular composite plates subjected to buckling and FPF constraints, *Journal of Theoretical and Applied Mechanics*, **54**, 2, 423-436
11. NATARAJAN S., DEOGEKAR P.S., MANICKAM G., BELOUETTAR S., 2014, Hygrothermal effects on the free vibration and buckling of laminated composites with cutouts, *Composite Structures*, **108**, 848-855
12. NOOR A.K., BURTON W.S., 1992, Three-dimensional solutions for thermal buckling of multilayered anisotropic plates, *Journal of Engineering Mechanics*, **118**, 4, 683-701
13. PAGANO N.J., REDDY J.N., 1994, *Mechanics of Composite Materials: Selected Works of Nicholas J. Pagano*, **34**, Springer Science & Business Media
14. PANDEY R., UPADHYAY A.K., SHUKLA K.K., 2009, Hygrothermoelastic postbuckling response of laminated composite plates, *Journal of Aerospace Engineering*, **23**, 1, 1-13
15. PEKOVIĆ O., STUPAR S., SIMONOVIĆ A., SVORCAN J., TRIVKOVIĆ S.A., 2015, Free vibration and buckling analysis of higher order laminated composite plates using the isogeometric approach, *Journal of Theoretical and Applied Mechanics*, **53**, 2, 453-466
16. REDDY J.N., LIU C.F., 1985, A higher-order shear deformation theory of laminated elastic shells, *International Journal of Engineering Science*, **23**, 3, 319-330
17. REDDY J.N., 2004, *Mechanics of Laminated Composite Plates and Shells*, 2nd ed., CRC Press
18. SINGHA M.K., RAMACHANDRA L.S., BANDYOPADHYAY J.N., 2001, Thermal post-buckling analysis of laminated composite plates, *Composite Structures*, **54**, 4, 453-458
19. SREEHARI V.M., MAITI D.K., 2015, Buckling and post buckling analysis of laminated composite plates in hygrothermal environment using an Inverse Hyperbolic Shear Deformation Theory, *Composite Structures*, **129**, 250-255
20. TAUCHERT T., HUANG N., 2012, Laminated Plates, *Composite Structures 4: Volume 1 Analysis and Design Studies*, 424
21. TURVEY G.J., MARSHALL I.H., EDS., 2012, *Buckling and Postbuckling of Composite Plates*, Springer Science & Business Media, Netherlands

Manuscript received March 30, 2017; accepted for print June 7, 2017

A GENERALIZED THERMOELASTIC DUAL-PHASE-LAGGING RESPONSE OF THICK BEAMS SUBJECTED TO HARMONICALLY VARYING HEAT AND PRESSURE

ASHRAF M. ZENKOUR

Department of Mathematics, Faculty of Science, King Abdulaziz University, Jeddah, Saudi Arabia and

Department of Mathematics, Faculty of Science, Kafrelsheikh University, Kafrelsheikh, Egypt

e-mail: zenkour@kau.edu.sa; zenkour@sci.kfs.edu.eg

The generalized thermoelastic problem of a thermo-mechanically loaded beam is studied. The upper surface of the beam is thermally isolated and subjected to a mechanical load while the bottom surface is traction free and subjected to a heating source. Based on the heat conduction equation containing the thermoelastic coupling term and the two-dimensional elasticity theory, thermoelastic coupling differential equations of motion are established. The generalized thermoelasticity theory with the dual-phase-lagging (DPLs) model is used to solve this problem. A closed-form analytical technique is used to calculate vibration of displacements and temperature. The effects of the phase-lagging (PLs), the intensity of the applied load and heat parameters on the field quantities of the beam are discussed. The variation along the axial direction and through-the-thickness distributions of all fields are investigated. Some comparisons have been also shown graphically to estimate the effects of the time on all the studied fields.

Keywords: thermoelasticity, dual-phase-lag model, two-dimensional elasticity solution

Nomenclature

C^e	–	specific heat per unit mass at constant strain
e	–	volumetric strain
E	–	Young's modulus
K	–	thermal conductivity
L, h	–	beam length and thickness, respectively
Q^*	–	heat source
\mathbf{q}	–	heat flux vector
$T(x, z, t)$	–	temperature distribution
T_0	–	environmental temperature
\mathbf{u}	–	displacement vector
u, w	–	axial and transverse displacements
u^*, w^*	–	amplitudes of axial and transverse displacements

Greek symbols

α	–	linear thermal expansion coefficient
δ	–	unification parameter
$\varepsilon_{ij}, \sigma_{ij}$	–	strain and stress tensor, respectively
γ	–	stress-temperature modulus, $\gamma = E\alpha/(1 - 2\nu)$
λ^*, μ^*	–	Lamé's constants
ν	–	Poisson's ratio
ω	–	angular frequency
ρ	–	material density of medium

σ_j^*	–	stress amplitudes
σ_0	–	intensity of applied load at upper face surface
τ_θ, τ_q	–	phase-lag of temperature gradient and of heat flux
$\theta = T - T_0$	–	temperature increment
θ^*	–	amplitude of temperature increment
θ_0	–	intensity of heat source
$\partial\theta/\partial z$	–	normal components of heat flux vector

1. Introduction

Many generalized theories of thermoelasticity have been developed in the literature to study the behavior of thermoelastic structures. These theories can be classified in different models, such as the theory of coupled thermoelasticity (CTE) (Biot, 1956), the Lord and Shulman (L-S) theory (Lord and Shulman, 1967), the Green and Lindsay (G-L) theory (Green and Lindsay, 1972), the Green and Naghdi (G-N) theory (Green and Naghdi, 1991, 1992, 1993) as well as the Tzou (1955a,b, 1006) dual-phase-lag (DPL) thermoelasticity theory (see also Chandrasekharaia (1998)). To the author's best knowledge, only a few authors have presented the exact two-dimensional solution to the generalized thermoelastic beam problem up to present time. Most authors used the classical theory for thin beams as well as one of the generalized thermoelasticity theories.

The investigation of harmonic plane wave propagations in an elastic medium have been attempted by several researchers. Prasad *et al.* (2010) investigated the propagation of harmonic plane waves with an assigned frequency by employing the thermoelasticity theory with dual-phase-lags. Mukhopadhyay (2004) presented thermoelastic interactions without energy dissipation in a spherical-cavity medium subjected to harmonically varying temperature. Kobzar' and Fil'shtinskii (2008) presented the plane dynamic problem of coupled thermoelasticity taking into account the harmonic form of the change of field quantities with time. Allam *et al.* (2009) presented the 2-D problem of electromagneto-thermoelasticity for a perfectly conducting thick plate subjected to a harmonically time-dependent heat source in the context of G-N theory. Ram *et al.* (2008) obtained a general solution to the field equations of a harmonically time-dependent generalized thermodiffusion in an elastic solid. Mukhopadhyay and Kumar (2008) studied thermoelastic interactions in a spherical-cavity medium subjected to a time-dependent-heating effect in the context of different thermoelasticity theories. Gue *et al.* (2012) analyzed thermoelastic damping of a micro-beam resonator by the dual-phase-lag thermal conduction model of the generalized thermoelasticity theory. Zenkour and Abouelregal (2014) presented nonlocal thermoelastic vibrations for variable thermal conductivity nanobeams due to harmonically varying heat. Recently, Zenkour (2015) presented a three-dimensional thermal shock plate problem within the framework of different thermoelasticity theories.

The present article is concerned with the two-dimensional transient generalized thermoelastic problem for a thick beam subjected to thermal and thermomechanical loads at its faces. Based on the dual-phase-lags model (Abouelregal and Zenkour, 2014; Abbas and Zenkour, 2014; Zenkour and Abouelregal, 2015; Zenkour *et al.*, 2013), the exact closed-form solution for the governing equations is established. The equations of the classical thermoelasticity theory, Lord and Shulman theory, and Green and Naghdi theory may be established as special cases of the DPLs theory. All expressions for temperature, displacements and stresses are presented. Numerical results showing the thermoelastic dynamic responses of the field quantities through the axial and thickness directions of the beam are presented. The effect of the time parameter is also investigated.

2. Thermoelastic basic equations

Let us consider a homogenous isotropic thermoelastic solid in the Cartesian coordinate system $Oxyz$ initially un-deformed and at a uniform temperature T_0 . The basic governing equations of motion, balance of the equilibrated force and heat conduction in the context of generalized (non-Fourier) thermoelasticity for the displacement vector $\mathbf{u}(x, y, z, t)$ in the absence of body forces should be considered.

The modified classical thermoelasticity model is given by the Tzou theory in which the Fourier law is replaced by an approximation of the equation

$$\mathbf{q}(x, t + \tau_q) = -K \nabla T(x, t + \tau_\theta) \quad (2.1)$$

The above equation may be approximated by

$$\left(1 + \tau_q \frac{\partial}{\partial t}\right) \mathbf{q} = -K \left(1 + \tau_\theta \frac{\partial}{\partial t}\right) \nabla T \quad (2.2)$$

where $0 < \tau_\theta \leq \tau_q$. Then the heat conduction equation corresponding to the dual-phase-lag model proposed by Tzou in this case takes the form

$$K \left(1 + \tau_\theta \frac{\partial}{\partial t}\right) \nabla^2 \theta + \left(1 + \tau_q \frac{\partial}{\partial t}\right) \rho Q^* = \left(\delta + \tau_q \frac{\partial}{\partial t}\right) \left(\rho C^e \frac{\partial \theta}{\partial t} + \gamma T_0 \frac{\partial e}{\partial t}\right) \quad (2.3)$$

Equation (2.3) describes the coupled dynamical thermoelasticity theory (CTE), the generalized thermoelasticity theories proposed by Lord and Shulman (L-S), Green and Naghdi (G-N) theory and dual-phase-lag (DPL) model for different sets of values of phase-lags parameters τ_q , τ_θ and the unification parameter δ as follows:

CTE: $\tau_\theta = \tau_q = 0$ and $\delta = 1$

L-S: $\tau_\theta = 0$, $\tau_q = \tau_0$ (τ_0 is the relaxation time) and $\delta = 1$

G-N: $\tau_\theta = 0$, $\delta = 0$, $\tau_q \neq 0$, and $K = K^*$ (the material constant characteristic)

DPL: $\delta = 1$ and $0 < \tau_\theta \leq \tau_q$

3. Governing equations

Let us consider small flexural deflections of an elastic beam with dimensions $(L \times b \times h)$ as shown in Fig. 1. The beam may be subjected to various thermal and mechanical loads according to the type of the problem used. Let u , $v = 0$ and w denote displacement components of a material point located at (x, y, z) in the present beam in the x , y , and z directions, respectively. The stress-strain relationships in the beam coordinates are written in the form

$$\begin{Bmatrix} \sigma_x \\ \sigma_z \end{Bmatrix} = \frac{E}{(1 + \nu)(1 - 2\nu)} \begin{bmatrix} 1 - \nu & \nu \\ \nu & 1 - \nu \end{bmatrix} \begin{Bmatrix} \varepsilon_x - \alpha\theta \\ \varepsilon_z - \alpha\theta \end{Bmatrix} \quad \sigma_{xz} = \frac{E}{2(1 + \nu)} \varepsilon_{xz} \quad (3.1)$$

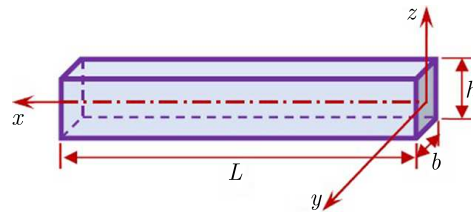


Fig. 1. Schematic diagram of the beam

The strain-displacement relations are taken in the linear form

$$\varepsilon_x = \frac{\partial u}{\partial x} \quad \varepsilon_z = \frac{\partial w}{\partial z} \quad \varepsilon_{xz} = \frac{\partial w}{\partial x} + \frac{\partial u}{\partial z} \quad (3.2)$$

The governing equations of motion $\sigma_{ij,j} = \rho \ddot{u}_i$ can be presented in an expanded form as

$$\begin{aligned} \frac{E(1-\nu)}{(1+\nu)(1-2\nu)} \frac{\partial^2 u}{\partial x^2} + \frac{E}{2(1+\nu)} \frac{\partial^2 u}{\partial z^2} + \frac{E}{2(1+\nu)(1-2\nu)} \frac{\partial^2 w}{\partial x \partial z} - \frac{E\alpha}{(1+\nu)(1-2\nu)} \frac{\partial \theta}{\partial x} &= \rho \frac{\partial^2 u}{\partial t^2} \\ \frac{E}{2(1+\nu)(1-2\nu)} \frac{\partial^2 u}{\partial x \partial z} + \frac{E}{2(1+\nu)} \frac{\partial^2 w}{\partial x^2} + \frac{E(1-\nu)}{(1+\nu)(1-2\nu)} \frac{\partial^2 w}{\partial z^2} - \frac{E\alpha}{(1+\nu)(1-2\nu)} \frac{\partial \theta}{\partial z} &= \rho \frac{\partial^2 w}{\partial t^2} \end{aligned} \quad (3.3)$$

In addition, the thermal conduction equation for the beam without a heat source ($Q^* = 0$) is given as

$$\left(1 + \tau_\theta \frac{\partial}{\partial t}\right) \left(\frac{\partial^2 \theta}{\partial x^2} + \frac{\partial^2 \theta}{\partial z^2}\right) = \left(\delta + \tau_q \frac{\partial}{\partial t}\right) \left[\eta \frac{\partial \theta}{\partial t} + \frac{\gamma T_0}{K} \frac{\partial}{\partial t} \left(\frac{\partial u}{\partial x} + \frac{\partial w}{\partial z}\right)\right] \quad (3.4)$$

where $\eta = \rho C^e / K$. Now, the following dimensionless definitions will be used for the variable quantities

$$\begin{aligned} \{\bar{x}, \bar{z}, \bar{L}, \bar{h}, \bar{u}, \bar{w}\} &= \eta c \{x, z, L, h, u, w\} & \{\bar{t}, \bar{\tau}_0, \bar{\tau}_\theta, \bar{\tau}_q\} &= \eta c^2 \{t, \tau_0, \tau_\theta, \tau_q\} \\ \bar{\theta} &= \frac{\theta}{T_0} & \{\bar{\sigma}_x, \bar{\sigma}_z\} &= \frac{(1+\nu)(1-2\nu)}{E} \{\sigma_x, \sigma_z\} \\ \bar{\sigma}_{xz} &= \frac{2(1+\nu)}{E} \sigma_{xz} & c^2 &= \frac{E}{\rho(1+\nu)(1-2\nu)} \end{aligned} \quad (3.5)$$

Therefore, the heat equation and equations of motion are given by (dropping the prime for convenience)

$$\begin{aligned} \left(1 + \tau_\theta \frac{\partial}{\partial t}\right) \left(\frac{\partial^2 \theta}{\partial x^2} + \frac{\partial^2 \theta}{\partial z^2}\right) &= \left(\delta + \tau_q \frac{\partial}{\partial t}\right) \left[\frac{\partial \theta}{\partial t} + \frac{\gamma}{\eta K} \frac{\partial}{\partial t} \left(\frac{\partial u}{\partial x} + \frac{\partial w}{\partial z}\right)\right] \\ (1-\nu) \frac{\partial^2 u}{\partial x^2} + \frac{1-2\nu}{2} \frac{\partial^2 u}{\partial z^2} + \frac{1}{2} \frac{\partial^2 w}{\partial x \partial z} - \alpha T_0 \frac{\partial \theta}{\partial x} &= \frac{\partial^2 u}{\partial t^2} \\ \frac{1}{2} \frac{\partial^2 u}{\partial x \partial z} + \frac{1-2\nu}{2} \frac{\partial^2 w}{\partial x^2} + (1-\nu) \frac{\partial^2 w}{\partial z^2} - \alpha T_0 \frac{\partial \theta}{\partial z} &= \frac{\partial^2 w}{\partial t^2} \end{aligned} \quad (3.6)$$

In addition, the stress components will be

$$\begin{aligned} \begin{Bmatrix} \sigma_x \\ \sigma_z \end{Bmatrix} &= \begin{bmatrix} 1-\nu & \nu \\ \nu & 1-\nu \end{bmatrix} \begin{Bmatrix} \frac{\partial u}{\partial x} - \alpha T_0 \theta \\ \frac{\partial w}{\partial z} - \alpha T_0 \theta \end{Bmatrix} & \sigma_{xz} &= \frac{\partial w}{\partial x} + \frac{\partial u}{\partial z} \end{aligned} \quad (3.7)$$

4. Solution of the problem

To obtain the displacements, temperature and stresses of the beam, thermal and mechanical boundary conditions must be satisfied. Firstly, the following simply-supported conditions are imposed at the edges of the beam

$$\sigma_x(x, z, t) = 0 \quad w(x, z, t) = 0 \quad \theta(x, z, t) = 0 \quad \text{at} \quad x = 0, L \quad (4.1)$$

The closed form solution of the governing and constitutive equations may be obtained by adapting the supported-normal mode analysis as

$$\{u, w, \theta\}(x, z, t) = \{u^*(z) \cos(\mu x), w^*(z) \sin(\mu x), \theta^*(z) \sin(\mu x)\} e^{\omega t} \quad (4.2)$$

where $\mu = \pi/L$. The displacement and temperature components given in Eq. (4.2) are satisfying the above boundary conditions on the edges of the beam. Then, Eqs. (3.6), after some elementary manipulations, become

$$\begin{aligned} \left(\frac{d^2}{dz^2} - c_1\right)u^* + c_2 \frac{dw^*}{dz} &= c_3 \theta^* & \left(\frac{d^2}{dz^2} - c_4\right)w^* + c_5 \frac{du^*}{dz} &= c_6 \frac{d\theta^*}{dz} \\ \left(\frac{d^2}{dz^2} - c_7\right)\theta^* &= c_8 u^* + c_9 \frac{dw^*}{dz} \end{aligned} \quad (4.3)$$

where the expressions c_k are given by

$$\begin{aligned} c_1 &= \frac{2[\omega^2 + \mu^2(1 - \nu)]}{1 - 2\nu} & c_2 &= \frac{\mu}{1 - 2\nu} & c_3 &= \frac{2\mu\alpha T_0}{1 - 2\nu} \\ c_4 &= \frac{2\omega^2 + \mu^2(1 - 2\nu)}{2(1 - \nu)} & c_5 &= -\frac{\mu}{2(1 - \nu)} & c_6 &= \frac{\alpha T_0}{1 - \nu} \\ c_7 &= \mu^2 + \frac{(\delta + \tau_q \omega)\omega}{1 + \tau_\theta \omega} & c_8 &= -\frac{(\delta + \tau_q \omega)\gamma \mu \omega}{(1 + \tau_\theta \omega)\eta K} & c_9 &= \frac{(\delta + \tau_q \omega)\gamma \omega}{(1 + \tau_\theta \omega)\eta K} \end{aligned} \quad (4.4)$$

In addition, the stresses are

$$\{\sigma_x, \sigma_z\} = \{\sigma_x^*(z), \sigma_z^*(z)\} e^{\omega t} \sin(\mu x) \quad \sigma_{xz} = \sigma_{xz}^*(z) e^{\omega t} \cos(\mu x) \quad (4.5)$$

They are given by

$$\begin{Bmatrix} \sigma_x^* \\ \sigma_z^* \end{Bmatrix} = \begin{bmatrix} 1 - \nu & \nu \\ \nu & 1 - \nu \end{bmatrix} \begin{Bmatrix} -\mu u^* - \alpha T_0 \theta^* \\ \frac{dw^*}{dz} - \alpha T_0 \theta^* \end{Bmatrix} \quad \sigma_{xz}^* = \mu w^* + \frac{du^*}{dz} \quad (4.6)$$

Eliminating $u^*(z)$ and $w^*(z)$ in Eqs. (4.3), one obtains

$$\left(\frac{d^6}{dz^6} - A_1 \frac{d^4}{dz^4} + A_2 \frac{d^2}{dz^2} - A_3\right) \theta^*(z) = 0 \quad (4.7)$$

where

$$\begin{aligned} A_1 &= c_1 + c_4 + c_7 + c_2 c_5 + c_6 c_9 \\ A_2 &= c_1(c_4 + c_7 + c_6 c_9) - c_3(c_8 - c_5 c_9) + c_5(c_2 c_7 + c_3 c_9) + c_4 c_7 \\ A_3 &= c_4(c_1 c_7 - c_3 c_8) \end{aligned} \quad (4.8)$$

Now, Eq. (4.7) may be factorized as

$$\left(\frac{d^2}{dz^2} - \lambda_1^2\right) \left(\frac{d^2}{dz^2} - \lambda_2^2\right) \left(\frac{d^2}{dz^2} - \lambda_3^2\right) \theta^*(z) = 0 \quad (4.9)$$

where λ_j^2 ($j = 1, 2, 3$) denote the roots of the characteristic equation

$$\lambda^6 - A_1 \lambda^4 + A_2 \lambda^2 - A_3 = 0 \quad (4.10)$$

They are given by

$$\begin{aligned}\lambda_{1,2} &= \mp \frac{\sqrt{i\sqrt[3]{A_0}[(1+i\sqrt{3})\sqrt[3]{A_0}-4A_1]+4(1-i\sqrt{3})(A_1^2-3A_2)}}{2\sqrt{3}\sqrt[6]{A_0}} \\ \lambda_{3,4} &= \mp \frac{\sqrt{\sqrt[3]{A_0}[4A_1-(1-i\sqrt{3})\sqrt[3]{A_0}]-4(1+i\sqrt{3})(A_1^2-3A_2)}}{2\sqrt{3}\sqrt[6]{A_0}} \\ \lambda_{5,6} &= \mp \frac{\sqrt{\sqrt[3]{A_0}(\sqrt[3]{A_0}+2A_1)+4(A_1^2-3A_2)}}{\sqrt{6}\sqrt[6]{A_0}}\end{aligned}\quad (4.11)$$

where $i = -1$ and

$$A_0 = 8A_1^3 - 36A_1A_2 + 108A_3 + \sqrt{3A_1^2(4A_1A_3 - A_2^2) - 6A_2(9A_1A_3 - 2A_2^2) + 81A_3^2} \quad (4.12)$$

The solution $\theta^*(z)$ of Eq. (4.7) is given by

$$\theta^*(z) = \sum_{j=1}^3 (B_{1j}e^{\lambda_j z} + B_{2j}e^{-\lambda_j z}) \quad (4.13)$$

where B_{kj} ($k = 1, 2$) are arbitrary unknown complex constants connected with the boundary conditions. In a similar manner, one gets

$$\{u^*(z), w^*(z)\} = \sum_{j=1}^3 (\{\hat{B}_{1j}, \check{B}_{1j}\}e^{\lambda_j z} + \{\hat{B}_{2j}, \check{B}_{2j}\}e^{-\lambda_j z}) \quad (4.14)$$

where \hat{B}_{kj} and \check{B}_{kj} are additional unknown constants. Substitution of Eqs. (4.13) and (4.14) into Eqs. (4.3)₁ and (4.3)₂ gives

$$\{\hat{B}_{1j}, \hat{B}_{2j}\} = U_{\lambda_j} \{B_{1j}, B_{2j}\} \quad \{\check{B}_{1j}, \check{B}_{2j}\} = W_{\lambda_j} \{B_{1j}, -B_{2j}\} \quad (4.15)$$

in which

$$U_{\lambda_j} = \frac{c_3(\lambda_j^2 - c_4) - c_2c_6\lambda_j^2}{(\lambda_j^2 - c_1)(\lambda_j^2 - c_4) - c_2c_5\lambda_j^2} \quad W_{\lambda_j} = \frac{\lambda_j[c_6(\lambda_j^2 - c_1) - c_3c_5]}{(\lambda_j^2 - c_1)(\lambda_j^2 - c_4) - c_2c_5\lambda_j^2} \quad (4.16)$$

Finally, the stress amplitudes are

$$\begin{aligned}\sigma_x^* &= \sum_{j=1}^3 \sigma_{\lambda_j}^x (B_{1j}e^{\lambda_j z} + B_{2j}e^{-\lambda_j z}) & \sigma_z^* &= \sum_{j=1}^3 \sigma_{\lambda_j}^z (B_{1j}e^{\lambda_j z} + B_{2j}e^{-\lambda_j z}) \\ \sigma_{xz}^* &= \sum_{j=1}^3 \sigma_{\lambda_j}^{xz} (B_{1j}e^{\lambda_j z} - B_{2j}e^{-\lambda_j z})\end{aligned}\quad (4.17)$$

where

$$\sigma_{\lambda_j}^x = -\mu(1-\nu)U_{\lambda_j} + \nu\lambda_j W_{\lambda_j} - \alpha T_0 \quad \sigma_{\lambda_j}^z = -\mu\nu U_{\lambda_j} + (1-\nu)\lambda_j W_{\lambda_j} - \alpha T_0 \quad (4.18)$$

Now, the upper surface of the beam is considered to be thermally insulated and subjected to a mechanical load while the bottom surface is traction free and subjected to a heating source (Zenkour and Abouelregal, 2016). So, the beam is subjected to the following boundary conditions

$$\begin{aligned}\theta\left(x, -\frac{h}{2}, t\right) &= \theta_0 \sin(\mu x) e^{\omega t} & \frac{\partial \theta}{\partial z} \Big|_{z=+\frac{h}{2}} &= 0 \\ \sigma_z\left(x, -\frac{h}{2}, t\right) &= \sigma_{xz}\left(x, \pm\frac{h}{2}, t\right) = 0 & \sigma_z\left(x, \frac{h}{2}, t\right) &= -\sigma_0 \sin(\mu x) e^{\omega t}\end{aligned}\quad (4.19)$$

Substituting Eqs. (4.13), (4.14) and (4.17) into the above boundary conditions, one obtains six linear equations in the following matrix form

$$\beta \mathbf{B} = \mathbf{G} \quad (4.20)$$

where $\mathbf{G} = \{\theta_0, 0, 0, -\sigma_0, 0, 0\}^T$ and $\mathbf{B} = \{B_{11}, B_{12}, B_{13}, B_{21}, B_{22}, B_{23}\}^T$ is the vector of constants. The elements β_{kj}^l ($l = 1, 2, \dots, 6$) of the matrix β are given by

$$\begin{aligned} \beta_{1j}^1 &= e^{-\lambda_j \frac{h}{2}} & \beta_{2j}^1 &= e^{\lambda_j \frac{h}{2}} & \beta_{1j}^2 &= \lambda_j \beta_{2j}^1 & \beta_{2j}^2 &= -\lambda_j \beta_{1j}^1 \\ \beta_{1j}^3 &= \beta_{2j}^4 = \sigma_{\lambda_j}^z e^{-\lambda_j \frac{h}{2}} & \beta_{2j}^3 &= \beta_{1j}^4 = \sigma_{\lambda_j}^z e^{\lambda_j \frac{h}{2}} \\ \beta_{1j}^5 &= -\beta_{2j}^6 = \sigma_{\lambda_j}^{xz} e^{-\lambda_j \frac{h}{2}} & \beta_{2j}^5 &= -\beta_{1j}^6 = -\sigma_{\lambda_j}^{xz} e^{\lambda_j \frac{h}{2}} \end{aligned} \quad (4.21)$$

Solving the system of above equations to get values of the constants B_{kj} . So, this completes the solution of the problem. Hence, one can easily obtain expressions for the dimensionless quantities of temperature θ , displacements u and w , and stresses $\sigma_1 = \sigma_x$, $\sigma_3 = \sigma_z$ and $\sigma_5 = \sigma_{xz}$ in the present beam.

5. Numerical results

The thermoelastic coupling effect is presented here to get the temperature, displacements and stresses. The material parameters used here are due to physical data of copper at $T_0 = 293$ K: $\lambda^* = 7.76 \cdot 10^{10}$ N/m², $\mu^* = 3.86 \cdot 10^{10}$ N/m², $\rho = 8954$ kg/m³, $C^e = 383.1$ J/(kg K), $K = 386$ N/(s K), $\alpha = 1.78 \cdot 10^{-5}$ K⁻¹).

It is to be noted that Young's modulus E and Poisson's ratio ν are given in terms of Lamé's constants λ^* and μ^* by

$$E = \frac{\mu^*(3\lambda^* + 2\mu^*)}{\lambda^* + \mu^*} \quad \nu = \frac{\lambda^*}{2(\lambda^* + \mu^*)} \quad (5.1)$$

The length-to-thickness ratio of the beam is fixed at $L/h = 5$ and the angular frequency $\omega = \omega_0 + i\zeta$. All plots are prepared by using the real values of the dimensionless variables defined in Eq. (3.5) for a wide range of the beam length and thickness. The computations are carried out for different values of time and delay time parameters τ_θ and τ_q . Once again, the directions of the beam are given in terms of the length and thickness of the beam, that is $\bar{x} = x/L$ and $\bar{z} = z/h$ (the prime is dropped in the figures for convenience). Figures 2-7 compare the results obtained for temperature, displacements and stresses against the x and z directions when $t = 0.3$. The variation of the field quantities versus the time parameter are also presented in Figs. 8-10. The graphs represent curves predicted by the CTE, L-S and G-N models of thermoelasticity obtained as special cases of the present general DPL model. The results of the CTE model ($\tau_\theta = \tau_q = 0, \delta = 1$), the L-S model ($\tau_\theta = 0, \tau_q = 0.05, \delta = 1$), the G-N model ($\tau_\theta = 0, \tau_q = 0.05, \delta = 0$), and the DPL model ($\tau_\theta = 0.02 < \tau_q = 0.05, \delta = 1$) are all presented. Also, other parameters are fixed at $\theta_0 = 0.5$, $\omega_0 = 2$, $\zeta = -1$, and two values are considered for the intensity of the applied load, namely $\sigma_0 = 0.5$ and $\sigma_0 = 1$.

Figure 2a shows the variation of the dimensionless temperature θ along the axial direction at the upper surface $z = 0.5$ of the beam. The behavior of all models may be the same with different amplitudes. The absolute maximum temperature occurs at the center of the beam. For the two load cases, the temperature of the L-S model is positive for $\sigma_0 = 0.5$ while it changes to negative for $\sigma_0 = 1$. The DPL model gives the largest temperatures while L-S model gives the smallest ones.

Figure 2b shows the variation of the dimensionless axial displacement u along the axial direction at the mid-plane $z = 0$ of the beam. The axial displacement, as expected, vanishes at the center of the beam for all models. The CTE model gives the smallest axial displacements at the first edge of the beam and the smallest ones at the second edge. However, the DPL model gives the largest axial displacements at the first edge of the beam and the smallest ones at the second edge. The behavior of the L-S model may be unchanged for the two cases of lateral loads.

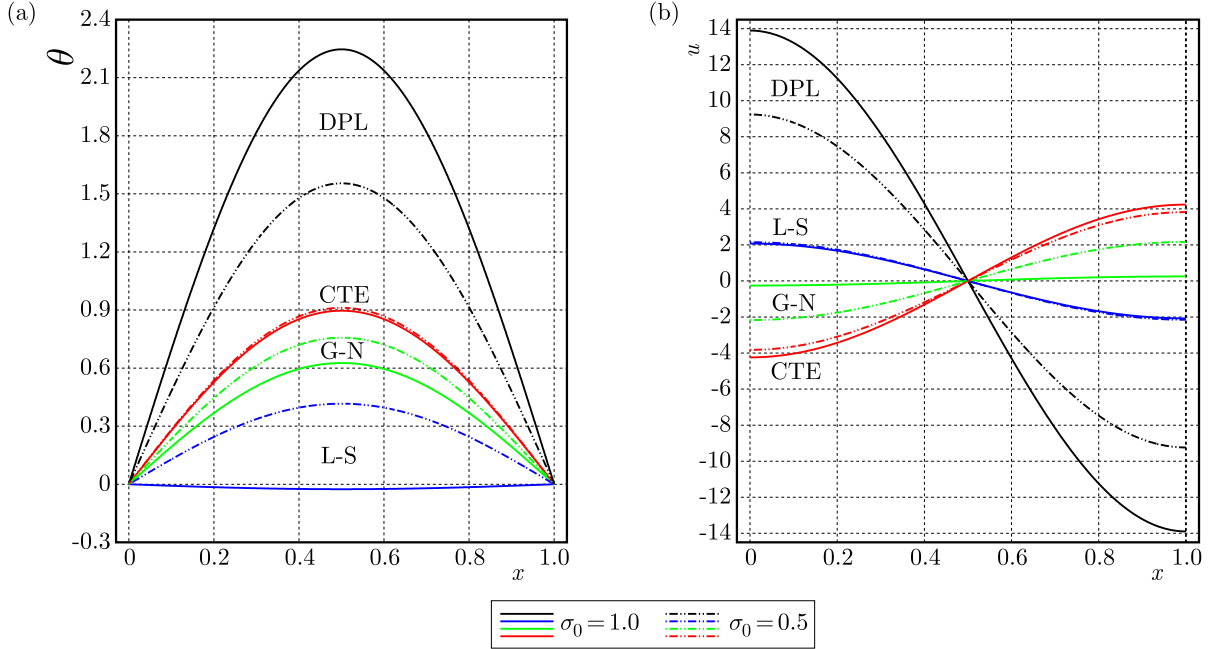


Fig. 2. Distribution of temperature θ (a) and of axial displacement u (b) in the axial direction for two load parameters

Figure 3a shows the variation of the transverse displacement w along the axial direction at the middle surface $z = 0$. Each model gives different behavior of w along the axial direction of the beam. The maximum (minimum) deflection occurs at the center of the beam for the L-S model (CTE model) in the two cases $\sigma_0 = 1$ and $\sigma_0 = 0.5$.

Figure 3b shows the variation of the dimensionless axial stress σ_1 along the axial direction at the upper surface $z = 0.5$ of the beam. The absolute maximum axial stress σ_1 occurs at the center of the beam ($x = 0.5$). For the first loaded beam ($\sigma_0 = 0.5$), the axial stress σ_1 of the G-N model only still positive while other models give negative axial stresses along the axial direction for the two loaded beams.

Figure 4a shows the variation of the dimensionless normal stress σ_3 along the axial direction at the upper surface $z = 0.5$ of the beam. All of the transverse normal stresses are compressive due to different models. The DPL model gives the smallest normal stress when $\sigma_0 = 1$ and the largest ones when $\sigma_0 = 0.5$.

Figure 4b shows the variation of the dimensionless transverse shear stress σ_5 along the axial direction at the mid-plane $z = 0$ of the beam. The shear stresses vanish at the center of the axial direction according to all models. The shear stresses for $\sigma_0 = 0.5$ are much smaller than those for $\sigma_0 = 1$. The DPL and L-S models give tensile shear stresses at the first edge and compressive shear stresses at the second edge of the beam for both $\sigma_0 = 0.5$ and $\sigma_0 = 1$. Also, the CTE model gives compressive shear stresses at the first edge and tensile shear stresses at the second edge of the beam for both $\sigma_0 = 0.5$ and $\sigma_0 = 1$. However, the G-N model gives compressive shear stress at the first edge and tensile shear stresses at the second edge of the beam for $\sigma_0 = 1$ and vice versa for $\sigma_0 = 0.5$.

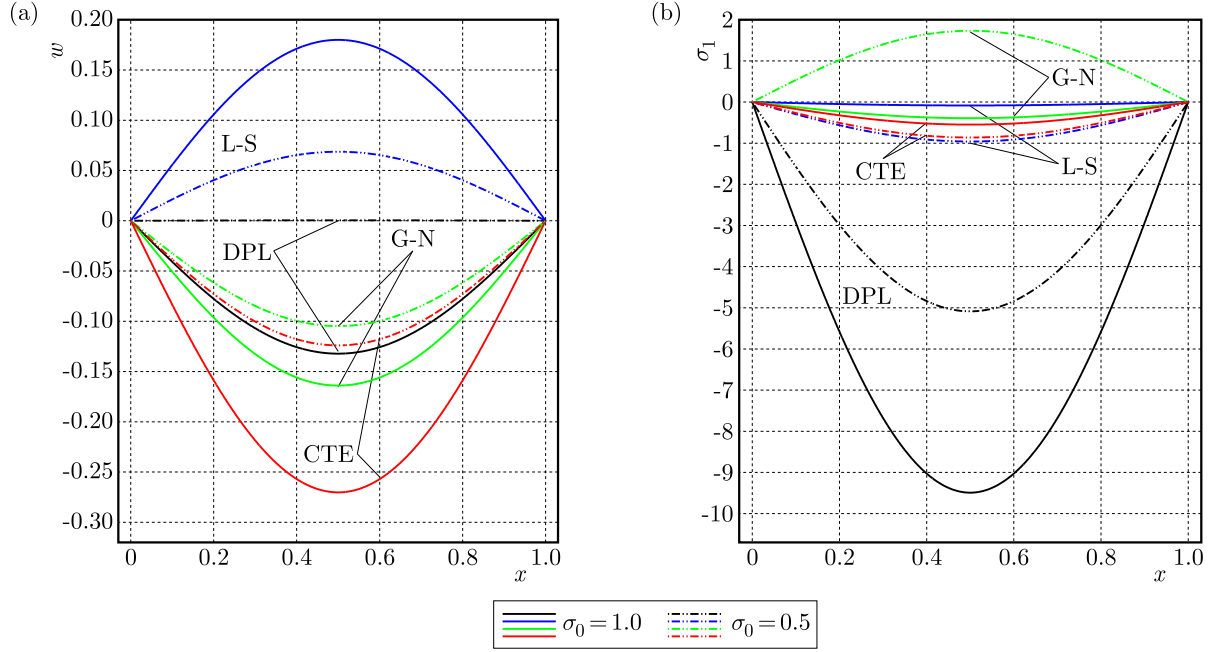


Fig. 3. Distribution of transverse deflection w (a) and of axial stress σ_1 (b) in the axial direction for two load parameters

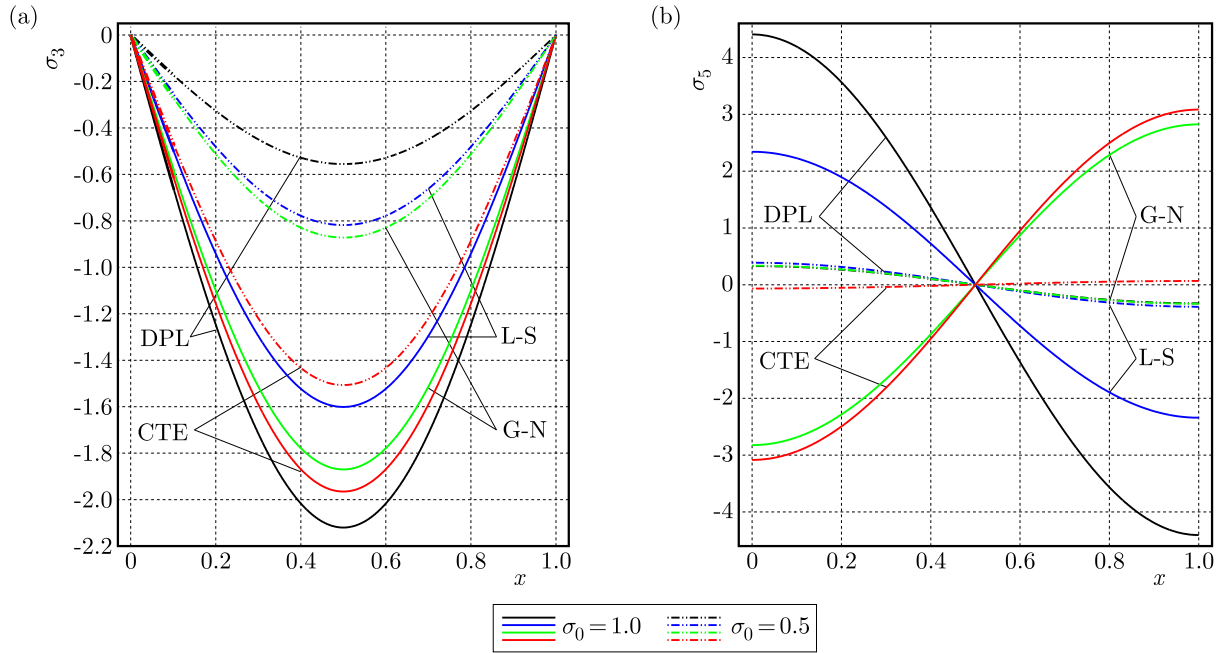


Fig. 4. Distribution of transverse normal stress σ_3 (a) and of transverse shear stress σ_5 in the axial direction for two load parameters

Figure 5a shows the through-the-thickness variation of the dimensionless temperature θ at the center $x = 0.5$ of the beam. The maximum temperature occurs at the upper face of the beam according to all models due to thermal conditions. The temperature for the CTE model may change through the beam thickness with a very small magnitude comparing to other models. All models, as expected, have the same temperature at the bottom surface of the beam. However, the DPL and L-S models give, respectively, the largest and smallest temperature at the upper surface of the beam.

Figure 5b shows the through-the-thickness variation of the axial displacement u at the first edge $x = 0$ of the beam under various loads. All models give different behavior of the axial displacements. The axial displacements for the DPL model are positive, and for the CTE and G-N models are negative.

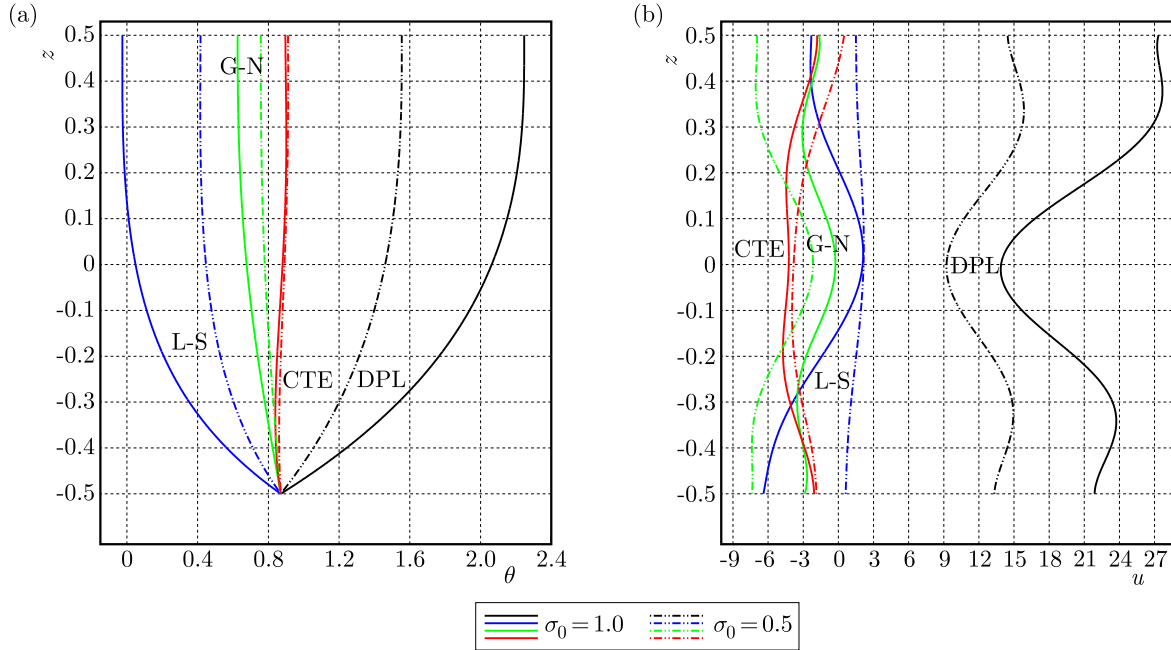


Fig. 5. Distribution of temperature θ (a) and of axial displacement u (b) in the thickness direction for two load parameters

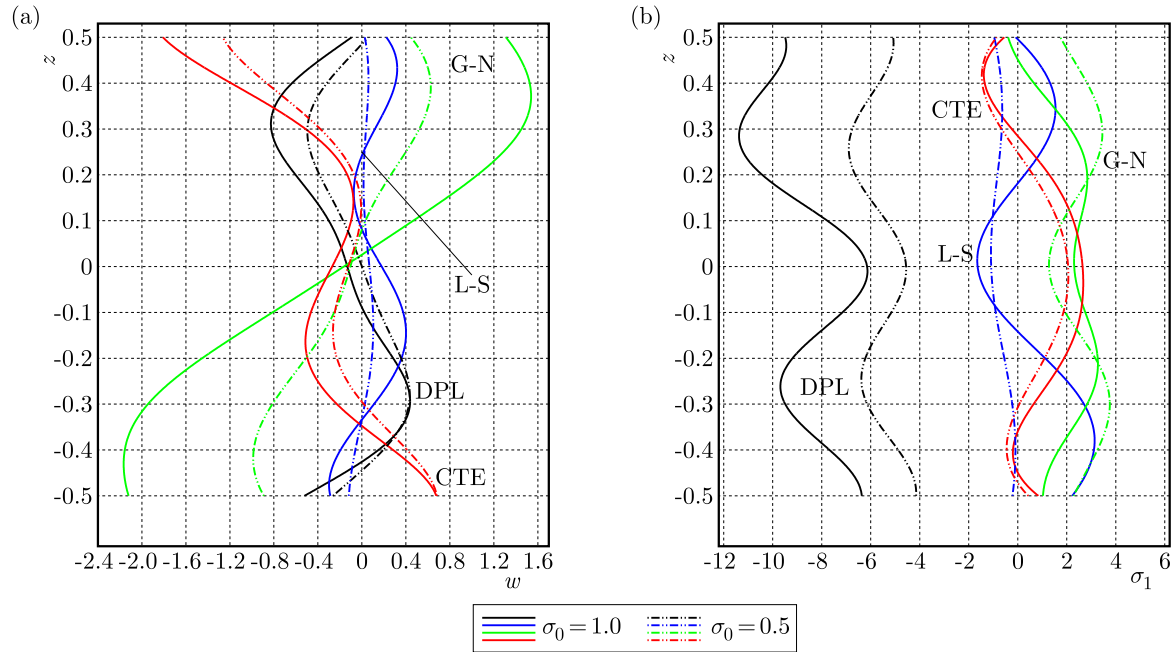


Fig. 6. Distribution of transverse deflection w (a) and of axial stress σ_1 (b) in the thickness direction for two load parameters

Figure 6a shows the through-the-thickness variation of the dimensionless transverse displacement w at the center $x = 0.5$ of the beam. The deflections due to the DPL and L-S models may be closed to each other. All models may exhibit different behavior through-the-thickness of the beam.

Figure 6b shows the through-the-thickness variation of the dimensionless axial stress σ_1 at the center of the beam $x = 0.5$. The DPL model gives axial stresses more different than those of other models. The axial stresses due to the L-S, G-N and CTE are close to each other. The axial stresses for the DPL when $\sigma_0 = 0.5$ are greater than those of the DPL model when $\sigma_0 = 1$. This is not the same for other models.

Figure 7a shows the through-the-thickness variation of the dimensionless normal stress σ_3 at the center of the beam $x = 0.5$. All models are very sensitive to the variation of the used load.

Figure 7b shows the through-the-thickness variation of the dimensionless transverse shear stress σ_5 at the first edge $x = 0$ of the beam. All models are very sensitive to the variation of the used load, especially in the DPL model. The DPL model gives the smallest compressive stress near the mid-plane of the beam at $z = -0.16$ and tensile axial stress at $z = -0.16$.

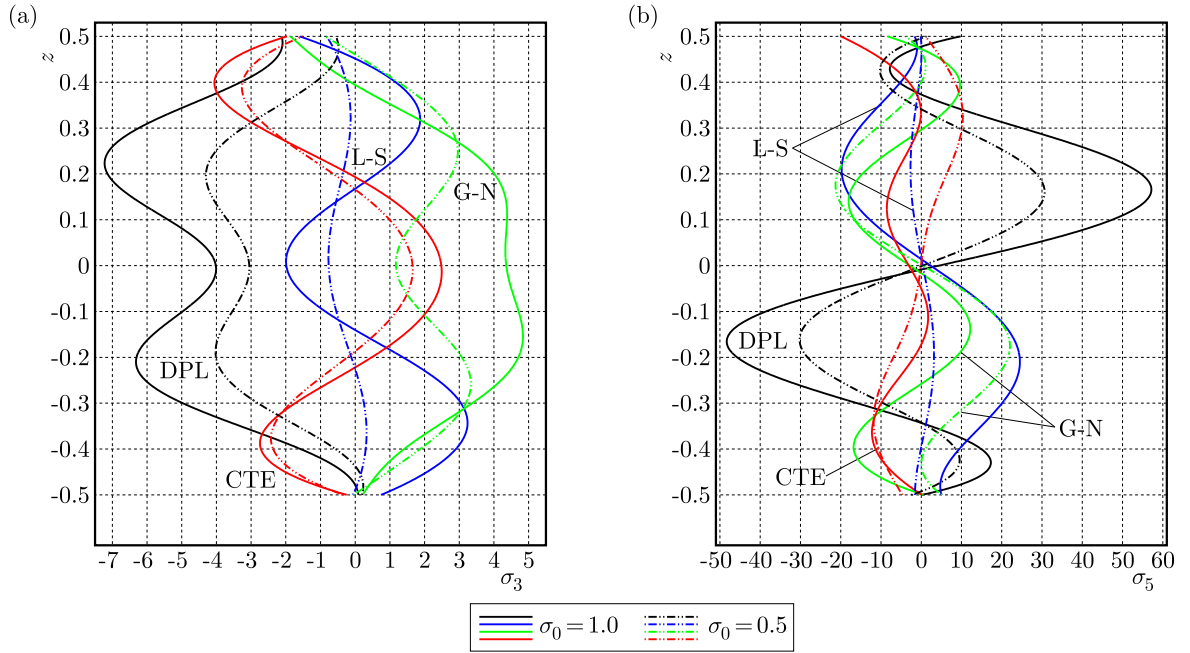


Fig. 7. Distribution of transverse normal stress σ_3 (a) and of transverse shear stress σ_5 in the thickness direction for two load parameters

Figure 8a shows the variation of the dimensionless temperature θ versus the time parameter at the center ($x = 0.5$ and $z = 0$) of the beam. The behavior of all models may be different. The sign of temperature for all models (except the G-N model) may be changed from positive to negative. At $t = 1.5$, the CTE model gives the smallest temperature and the G-N model gives the largest temperature for $\sigma_0 = 1$. Also, temperatures for the G-N (L-S) model are directly increasing (decreasing) as t increases. Otherwise, the temperatures are no longer increasing and have their maximum at different values of the time parameter.

Figure 8b shows the variation of the dimensionless axial displacement u versus the time parameter at the first edge $x = 0$ of the mid-plane $z = 0$ of the beam under two different loads. The axial displacement for the DPL (G-N) model are directly increasing (decreasing) as t increases for the two cases $\sigma_0 = 0.5$ and $\sigma_0 = 1$. The axial displacement for the CTE model are directly increasing as t increases for $\sigma_0 = 0.5$ and decreasing as t increases for $\sigma_0 = 1$.

Figure 9a shows the variation of the transverse displacement w versus the time parameter at the center ($x = 0.5$ and $z = 0$) of the beam. The deflections for the L-S model are directly increasing as t increases for the two cases $\sigma_0 = 0.5$ and $\sigma_0 = 1$. However, the deflections for the other models are directly decreasing as t increases for the two cases $\sigma_0 = 0.5$ and $\sigma_0 = 1$.

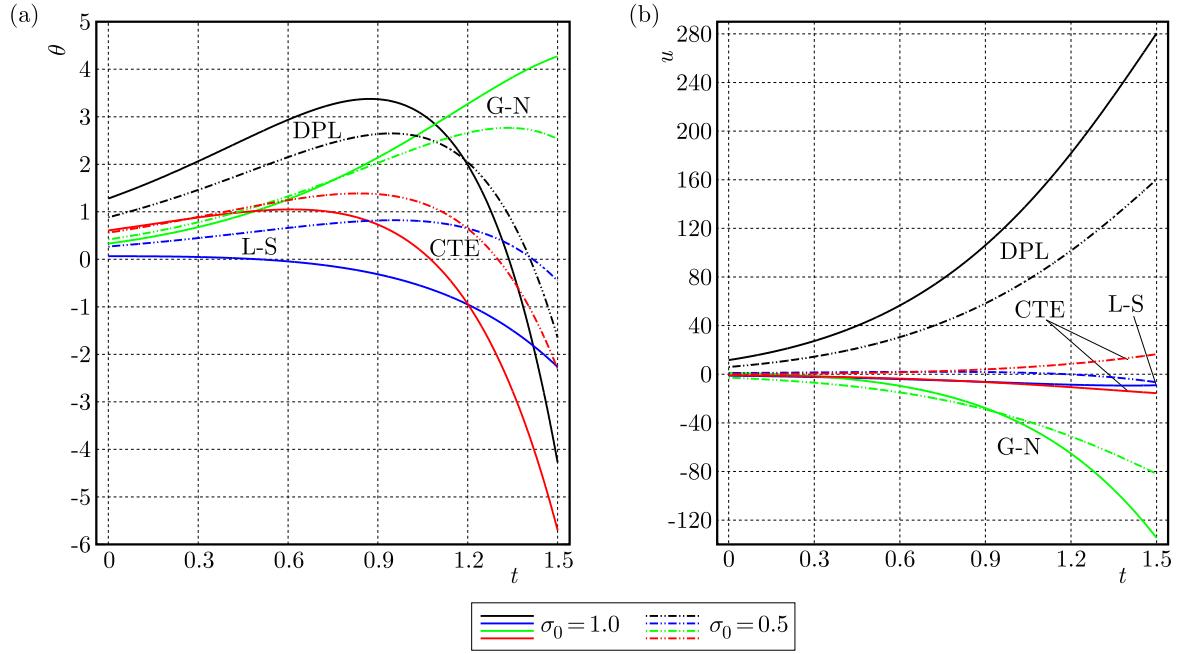


Fig. 8. Variation of temperature θ (a) and of axial displacement u (b) versus the time parameter for two load parameters

Figure 9b shows the variation of the dimensionless axial stress σ_1 versus the time parameter at the center $x = 0.5$ of the upper surface $z = 0.5$ of the beam. The axial stress for the G-N (DPL) model are directly increasing (decreasing) as t increases for the two cases $\sigma_0 = 0.5$ and $\sigma_0 = 1$. The axial stress for the CTE model are directly decreasing as t increases for $\sigma_0 = 0.5$.

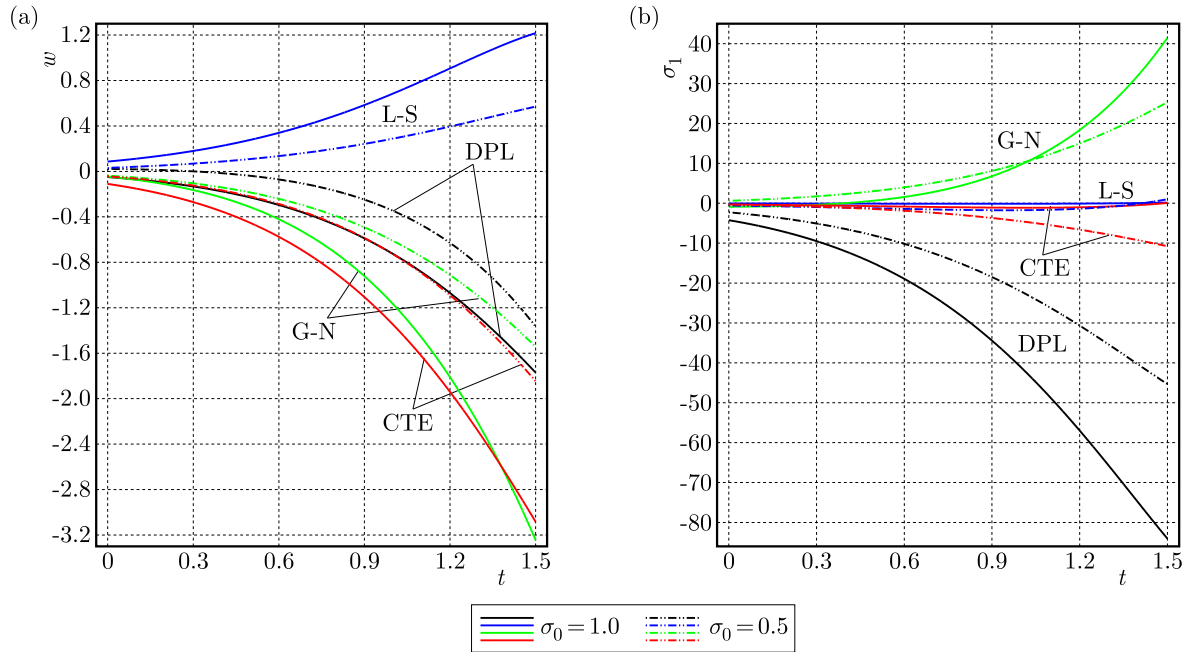


Fig. 9. Variation of transverse deflection w (a) and of axial stress σ_1 (b) versus the time parameter for two load parameters

Figure 10a shows the variation of the dimensionless normal stress σ_3 versus the time parameter at the center $x = 0.5$ of the upper surface $z = 0.5$ of the beam. Most transverse normal stresses are no longer decreasing, and finally increase as t increases. For $\sigma_0 = 0.5$, σ_3 in the DPL

model is directly increasing with an increase in the time parameter while σ_3 for the CTE model is directly decreasing.

Figure 10b shows the variation of the dimensionless transverse shear stress σ_5 versus the time parameter at the first edge of the mid-plane ($x = 0, z = 0$) of the beam. The shear stresses for the L-S (G-N) model are increasing (decreasing) as t increases for $\sigma_0 = 1$ and $\sigma_0 = 0.5$. For $\sigma_0 = 0.5$, σ_5 for the DPL (CTE) model is decreasing (increasing) as t increases. For $\sigma_0 = 1$, σ_5 for the DPL model is no longer increasing and its maximum is at $t = 1.1$, and then it is decreasing again while σ_5 for the CTE model is decreasing as t increases.

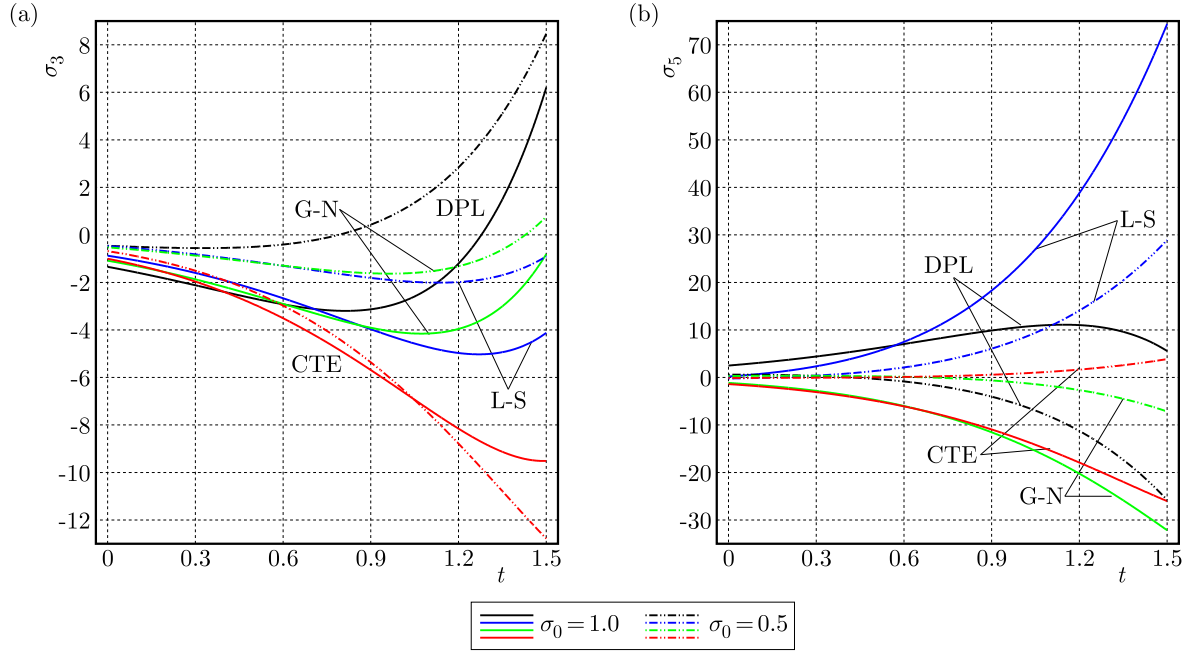


Fig. 10. Variation of transverse normal stress σ_3 (a) and of transverse shear stress σ_5 (b) versus the time parameter for two load parameters

For the sake of completeness and comparison, some plots for the field quantities are displayed through-the-thickness of the beam using the DPL model only. Here, the upper surface of the beam is considered to be thermally insulated and subjected to a mechanical load while the bottom surface is subjected to both mechanical load and heating source. So, the beam is subjected to the following boundary conditions

$$\begin{aligned} \theta\left(x, -\frac{h}{2}, t\right) &= \theta_0 \sin(\mu x) e^{\omega t} & \frac{\partial \theta}{\partial z} \Big|_{z=+\frac{h}{2}} &= 0 \\ \sigma_5\left(x, \pm \frac{h}{2}, t\right) &= 0 & \sigma_3\left(x, -\frac{h}{2}, t\right) &= \left\{ \sigma_3\left(x, \frac{h}{2}, t\right) \right\} = \{-\bar{\sigma}_0, \bar{\sigma}_0\} \sin(\mu x) e^{\omega t} \end{aligned} \quad (5.2)$$

In this case, the initial temperature and stresses are fixed as $\theta_0 = 1$, $\bar{\sigma}_0 = 0.25$ and $\bar{\sigma}_0 = 0.75$. Figure 11a shows the through-the-thickness variation of the dimensionless temperature θ at the center $x = 0.5$ of the beam according to different time parameters. The temperature increases with an increase in z and t . Figure 11b shows the through-the-thickness variation of the axial displacement u at the first edge $x = 0$ of the beam according to different time parameters. The axial displacement is very sensitive to variation of the time parameter. The magnitude of the axial displacement wave is increasing as t increases.

Figure 12a shows the through-the-thickness variation of the dimensionless transverse displacement w at the center $x = 0.5$ of the beam according to different time parameters. Also, the

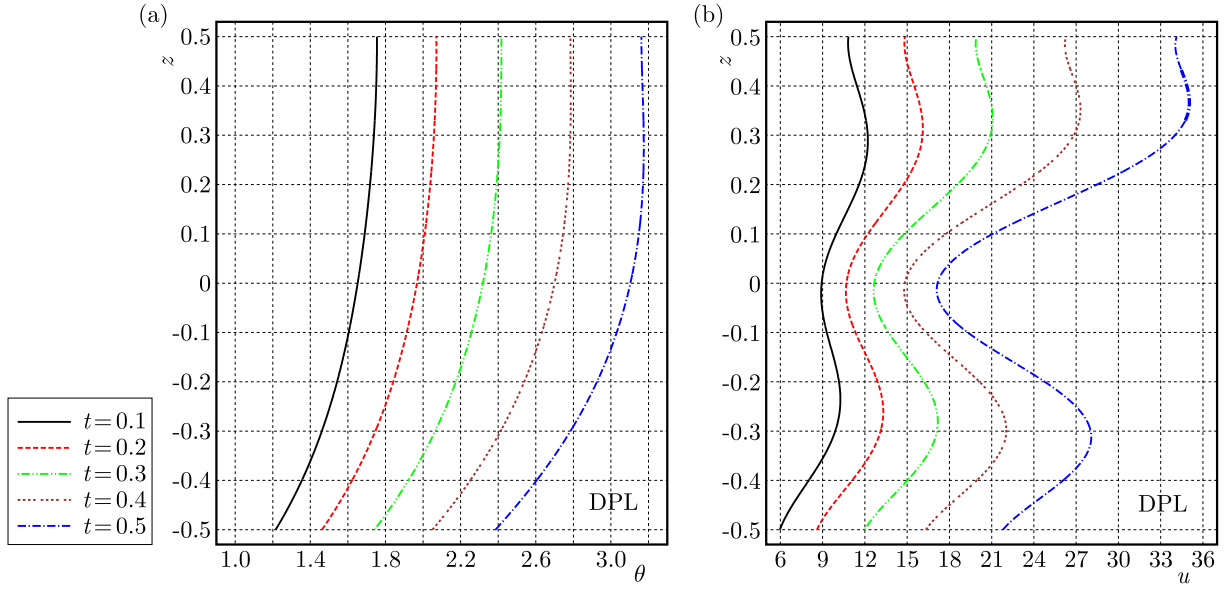


Fig. 11. Distribution of temperature θ (a) and of axial displacement u (b) through-the-thickness of the beam at different time parameters

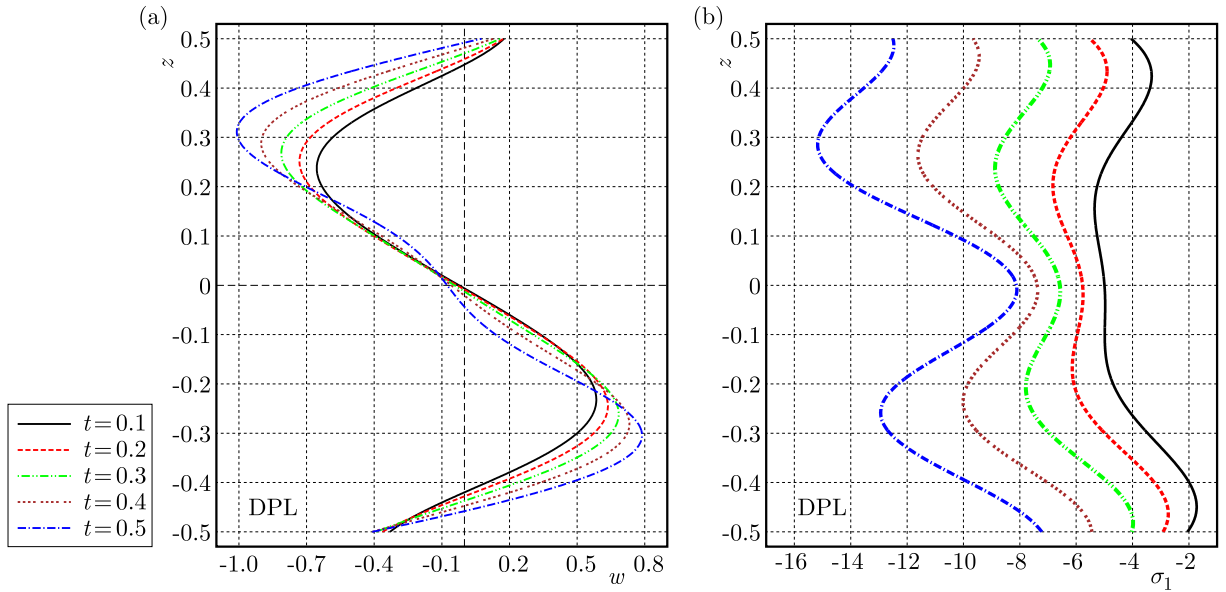


Fig. 12. Distribution of transverse deflection w (a) and of axial stress σ_1 (b) through-the-thickness of the beam at different time parameters

deflection is very sensitive to variation of the time parameter. The magnitude of the deflection wave is increasing as t increases. Figures 12b and 13a show the through-the-thickness variation of the dimensionless axial stress σ_1 and the transverse normal stress σ_3 at the center $x = 0.5$ of the beam according to different time parameters. The stresses themselves are decreasing as t increases while the magnitudes of their waves are increasing. Finally, Figure 13b shows the through-the-thickness variation of the dimensionless transverse shear stress σ_5 at the first edge $x = 0$ of the beam according to different time parameters. The shear stress is very sensitive to variation of the time parameter. The magnitude of the transverse shear stress wave is increasing as t increases.

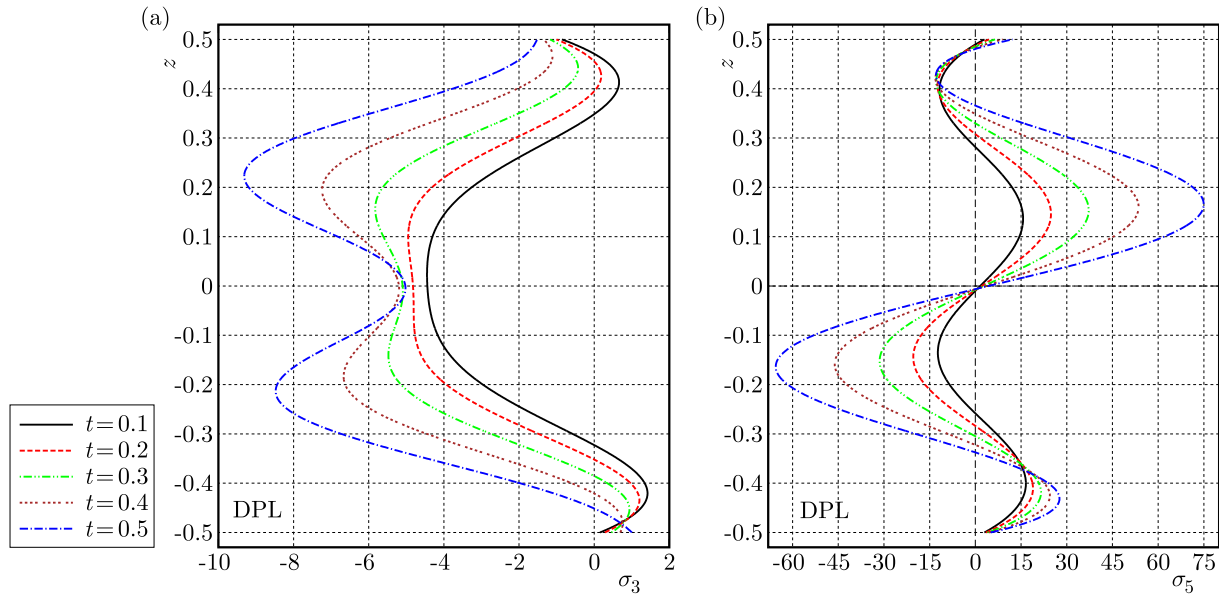


Fig. 13. Distribution of σ_3 (a) and σ_5 (b) through-the-thickness of the beam at different time parameters

6. Conclusions

The exact presentations of temperature, displacements and stresses in the axial and thickness directions of a generalized thermoelastic beam are considered in this article. The model of generalized thermoelasticity with dual-phase-lagging is constructed and other known thermoelastic models may be considered as special cases. The exact 2D general solution is applied to the present beam subjected to various heating sources or thermomechanical loads. The comparisons are shown along the axial and thickness directions of the beam. The field quantities are very sensitive to the applied thermal and mechanical loads and variation of the time parameter. The method used here may be applicable to a wide range of problems in thermodynamics and thermoelasticity. The numerical results presented here may be considered as more general in the sense that they include exact analysis of different field quantities. It is concluded from the graphical results presented here that the effect of dual-phase-lag parameters plays a significant role on all the physical quantities. Some models may fail to treat the thermoelastic response of many structures.

References

1. ABBAS I.A., ZENKOUR A.M., 2014, Dual-phase-lag model on thermoelastic interactions in a semi-infinite medium subjected to a ramp-type heating, *Journal of Computational and Theoretical Nanoscience*, **11**, 642-645
2. ABOUELREGAL A.E., ZENKOUR A.M., 2014, Effect of phase lags on thermoelastic functionally graded microbeams subjected to ramp-type heating, *Iranian Journal of Science and Technology, Transactions of Mechanical Engineering* **38**, 321-335
3. ALLAM M.N., ELSIBAI K.A. ABOUELREGAL A.E., 2009, Electromagneto-thermoelastic problem in a thick plate using Green and Naghdi theory, *International Journal of Engineering Science*, **47**, 680-690
4. BIOT M.A., 1956, Thermoelasticity and irreversible thermodynamics, *Journal of Applied Physics*, **27**, 240-253
5. CHANDRASEKHARAIH D.S., 1998, Hyperbolic thermoelasticity: a review of recent literature, *Applied Mechanics Reviews*, **51**, 705-729

6. GREEN A.E., LINDSAY K.A., 1972, Thermoelasticity, *Journal of Elasticity*, **2**, 1-7
7. GREEN A.E., NAGHDI P.M., 1991, A re-examination of the basic postulates of thermomechanics, *Proceedings of the Royal Society*, **432**, 171-194
8. GREEN A.E., NAGHDI P.M., 1992, On undamped heat waves in an elastic solid, *Journal of Thermal Stresses*, **15**, 253-264
9. GREEN A.E., NAGHDI P.M., 1993, Thermoelasticity without energy dissipation, *Journal of Elasticity*, **31**, 189-209
10. GUO F.L., WANG G.Q., ROGERSON G.A., 2012, Analysis of thermoelastic damping in micro- and nano-mechanical resonators based on dual-phase-lagging generalized thermoelasticity theory, *International Journal of Engineering Science*, **60**, 59-65
11. KOBZAR' V.N., FIL'SHTINSKII L.A., 2008, The plane dynamic problem of coupled thermoelasticity, *Journal of Applied Mathematics and Mechanics*, **72**, 611-618
12. LORD H.W., SHULMAN Y., 1967, A generalized dynamical theory of thermoelasticity, *Journal of the Mechanics and Physics of Solids*, **15**, 299-309
13. MUKHOPADHYAY S., 2004, Thermoelastic interactions without energy dissipation in an unbounded body with a spherical cavity subjected to harmonically varying temperature, *Mechanics Research Communications*, **31**, 81-89
14. MUKHOPADHYAY S., KUMAR R., 2008, A study of generalized thermoelastic interactions in an unbounded medium with a spherical cavity, *Applied Mathematics and Computation*, **56**, 2329-2339
15. PRASAD R., KUMAR R., MUKHOPADHYAY S., 2010, Propagation of harmonic plane waves under thermoelasticity with dual-phase-lags, *International Journal of Engineering Science*, **48**, 2028-2043
16. RAM P., SHARMA N., KUMAR R., 2008, Thermomechanical response of generalized thermoelastic diffusion with one relaxation time due to time harmonic sources, *International Journal of Thermal Sciences*, **47**, 315-323
17. TZOU D.Y., 1995a, A unified approach for heat conduction from macro- to micro-scales, *Journal of Heat Transfer*, **117**, 8-16
18. TZOU D.Y., 1995b, Experimental support for the Lagging behavior in heat propagation, *Journal of Thermophysics and Heat Transfer*, **9**, 686-693
19. TZOU D.Y., 1996, *Macro-to-Microscale Heat Transfer: The Lagging Behavior*, Washington, DC, Taylor & Francis
20. ZENKOUR A.M., 2015, Three-dimensional thermal shock plate problem within the framework of different thermoelasticity theories, *Composite Structures*, **132**, 1029-1042
21. ZENKOUR A.M., ABOUELREGAL A.E., 2014, Nonlocal thermoelastic vibrations for variable thermal conductivity nanobeams due to harmonically varying heat, *Journal of Vibroengineering*, **16**, 3665-3678
22. ZENKOUR A.M., ABOUELREGAL A.E., 2015, The nonlocal dual phase lag model of thermoelastic nanobeam subjected to a sinusoidal pulse heating, *Journal for Computational Methods in Engineering Science and Mechanics*, **16**, 53-73
23. ZENKOUR A.M., ABOUELREGAL A.E., 2016, Non-simple magnetothermoelastic solid cylinder with variable thermal conductivity due to harmonically varying heat, *Earthquakes and Structures*, **10**, 681-697
24. ZENKOUR A.M., MASHAT D.S., ABOUELREGAL A.E., 2013, The effect of dual-phase-lag model on reflection of thermoelastic waves in a solid half space with variable material properties, *Acta Mechanica Sinica*, **26**, 659-670

DYNAMIC AND RESONANCE RESPONSE ANALYSIS FOR A TURBINE BLADE WITH VARYING ROTATING SPEED

DAN WANG, ZHIFENG HAO

School of Mathematical Sciences, University of Jinan, Jinan 250022, China

e-mail: danwang2014518@hotmail.com

YUSHU CHEN

School of Astronautics, Harbin Institute of Technology, Harbin 150001, China

YONGXIANG ZHANG

School of Mathematical Sciences, University of Jinan, Jinan 250022, China

A coupling model between turbine blades with a varying rotating speed and oncoming vortices is constructed, where the coupling of the structure and the fluid is simulated by the van der Pol oscillation. Partial differential governing equations of motions for the coupled system are obtained and discretized by using the Galerkin method. The 1:2 subharmonic resonance and the 1:1 internal resonance are investigated with the multiple scale method and first-order averaged equations are then derived. Nonlinear responses and bifurcation characteristics are studied by a numerical integration method. Stability of bifurcation curves is determined by utilizing the Routh-Hurwitz criterion. The effect of system parameters including the detuning parameter, steady-state rotating speed, amplitude of periodic perturbation for the rotating speed and freestream velocity on vibration responses are investigated.

Keywords: varying rotating speed, van der Pol oscillation, multiple scale method, nonlinear response, bifurcation curve

1. Introduction

The blade is an important component in the turbomachinery, such as gas axial compressors, wind turbines, aero-engine turbines, etc. Rotating blades are subjected to high centrifugal and aerodynamic loads which can lead to aeroelastic problems of the blades, like flutter and vortex-induced vibrations (Gostelow *et al.*, 2006). To keep safe running of the turbomachinery, analysis of the dynamic response characteristics is of importance for the blade design.

Owing to a variety of engineering applications, dynamic analysis of rotating blades has received broad interest. Transverse and rotational motion as well as control of vibrations for a rotating uniform Euler-Bernoulli beam were studied by Yang *et al.* (2004). In addition, the early research that focused on the problem of rotating nonconstant speed was done in the work by Kammer and Schlack (1987). Nonlinear vibration of a variable speed rotating beam was studied by Younesian and Esmailzadeh (2010), where the influence of various parameters was investigated. The nonlinear dynamic response of a rotating blade with varying rotating speed was investigated by Yao *et al.* (2012), and the results showed that the dynamic responses of the rotating blade changed from periodic motions to chaotic motions with different rotating speeds. Nonlinear oscillations and steady-state responses of a rotating compressor blade with varying rotating speed were investigated by Yao *et al.* (2014). Staino and Basu (2013) formulated a multi-modal flexible wind turbine model with variable rotor speed by using a Lagrangian approach, and analysed the effect of the rotational speed on the edgewise vibration of the blades. The equations of motion of a rotating composite Timoshenko beam were derived in the study of

Georgiades *et al.* (2014), and the results showed that the variable rotating speed as well as a nonzero pitch angle have important effects on the system dynamics. A more accurate nonlinear model of a rotating cantilever beam was proposed by Kim and Chung (2016). Geometrically nonlinear vibrations of beams with properties periodically varying along the axis were investigated by Domagalski and Jędrysiak (2016). A new model for a spinning beam under deployment was proposed and the dynamic responses and characteristics were analyzed by Zhu and Chung (2016). The study of forced nonlinear vibrations of a simply supported Euler-Bernoulli beam resting on a nonlinear elastic foundation with quadratic and cubic nonlinearities was carried out by Shahlaei-Far *et al.* (2016) with the homotopy analysis method. Vibration of a rotating beam with variable speed/acceleration has been controlled by using the sandwich beam filled with an ER fluid (Wei *et al.*, 2006). Moreover, Warmiński and Latański (2016) applied a nonlinear saturation control strategy to suppress vibration of the rotating hub-beam structure.

The vortex-induced vibration of a rotating blade with the steady-state rotating speed was investigated by Wang *et al.* (2016c), where the time-varying characteristic of the vortex shedding was represented by a van der Pol oscillator. Moreover, the van der Pol oscillator has been introduced as a reduced model in a number of articles to model the time-varying characteristics of the fluid (Hartlen and Currie, 1970; Barron and Sen, 2009; Hemon, 1999; Gabbai and Benaroya, 2005; Wang *et al.*, 2016a) or the fluid-structure interaction (Barron, 2010; Lee *et al.*, 2006; Facchinetti *et al.*, 2004; Keber and Wiercigroch, 2008; Wang *et al.*, 2016b) according to experimental and numerical studies. In addition, the effect of structural vibration on the motion of the fluid was also investigated in the above articles. Under different air flow conditions, the dynamic behaviour of the blades becomes very complex when the rotating speed is time-varying, which could convert to a nonlinear system with the coupling of parametric-excitation and self-excitation.

The motivation of this paper is to investigate the dynamic response and bifurcation characteristics of blades with varying rotating speed. The coupling model of the blade with the varying rotating speed and the time-varying flows is derived based on the results by Wang *et al.* (2016c). The analysis of the 1:2 subharmonic resonance and 1:1 internal resonance is carried out with the multiple scale method. Four-dimensional nonlinear averaged equations are then derived. Bifurcation curves are obtained and the effect of the system parameters on dynamic responses are discussed in detail.

2. Modeling

2.1. Modeling of the coupling for the structure and vortices

The blade with length r and varying rotating speed Ω is assumed as a continuous uniform straight cantilever beam based on the Euler-Bernoulli formulation in the centrifugal force field as shown in Fig. 1.

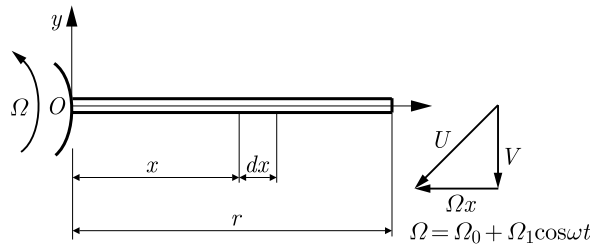


Fig. 1. A beam with varying rotating speed

Similar to the derivation process of formulas in the study by Wang *et al.* (2016c), the governing equation of transverse motion of a uniform cantilever beam with varying rotating speed can be obtained as follows

$$\begin{aligned}
EI \frac{\partial^4 w(x,t)}{\partial x^4} + \tilde{m} \frac{\partial^2 w(x,t)}{\partial t^2} + \tilde{c} \frac{\partial w(x,t)}{\partial t} \\
= F_f - \rho A \Omega^2 x \frac{\partial w(x,t)}{\partial x} + \frac{1}{2} \rho A \Omega^2 (r^2 - x^2) \frac{\partial^2 w(x,t)}{\partial x^2}
\end{aligned} \quad (2.1)$$

where $w(x,t)$ denotes the transverse displacement of the blade, EI is the flexural rigidity of the structure, \tilde{c} is the viscous damping coefficient, $\tilde{m} = (\rho + \rho_f)A$ is the total mass of the structure and fluid, ρ and ρ_f are densities of the structure and air flow, respectively, A is the area of the cross-section of the cantilever beam, $F_f = 0.5\rho_f U^2 \overline{D} C_L(x,t)$ is the lift force effecting the blade and induced by the vortex, $U = \sqrt{V^2 + (\Omega x)^2}$ is the total velocity, V is the freestream velocity, \overline{D} denotes characteristic length of the cross-section of the beam. Here, the varying rotating speed is expressed as $\Omega = \Omega_0 + \Omega_1 \cos \omega t$, representing the periodic perturbation $\Omega_1 \cos \omega t$ on the steady-state rotating speed Ω_0 .

Letting $v(x,t) = w(x,t)/\overline{D}$, $z = x/r$, Eq. (2.1) can be rewritten as

$$\begin{aligned}
\omega_0^2 \frac{\partial^4 v(z,t)}{\partial z^4} + \frac{\partial^2 v(z,t)}{\partial t^2} + \zeta \frac{\partial v(z,t)}{\partial t} \\
= \frac{1}{4\tilde{m}} C_{L0} \rho_f [V^2 + (r\Omega z)^2] q(z,t) - \frac{\rho A \Omega^2}{\tilde{m}} z \frac{\partial v(z,t)}{\partial z} + \frac{\rho A \Omega^2}{2\tilde{m}} (1 - z^2) \frac{\partial^2 v(z,t)}{\partial z^2}
\end{aligned} \quad (2.2)$$

with the boundary conditions $v(0,t) = 0$, $v'(0,t) = 0$, $v''(1,t) = 0$, $v'''(1,t) = 0$, where $\omega_0 = \sqrt{EI/(\tilde{m}r^4)}$, $\zeta = \tilde{c}/\tilde{m}$ is the damping ratio, $q(z,t) = 2C_L/C_{L0}$ represents a time-varying variable of the vortical flows, C_{L0} is the reference lift coefficient.

Similarly, the van der Pol oscillator is applied to simulate time-varying characteristics of the vortices as follows

$$\frac{\partial^2 q(z,t)}{\partial t^2} + s\omega_f [q^2(z,t) - 1] \frac{\partial q(z,t)}{\partial t} + \omega_f^2 q(z,t) = M \frac{\partial^2 v(z,t)}{\partial t^2} \quad (2.3)$$

where ω_f is the shedding frequency of the vortex, s is the van der Pol damping coefficient, M is the linear coupling parameter representing the impact of structural vibration on the fluid motion.

2.2. The Galerkin discretization of the coupled system

Discretization of partial differential equations (2.2) and (2.3) into a finite-dimensional system is done according to the study by Clough and Penzien (2003), Wang *et al.* (2016c), letting

$$v(z,t) = \sum_{i=1}^{\infty} v_i(t) \tilde{v}_i(z) \quad (2.4)$$

represent an arbitrary oscillation of the structure and

$$q(z,t) = \sum_{i=1}^{\infty} q_i(t) \tilde{q}_i(z) \quad (2.5)$$

denote an arbitrary oscillation of the vortical flows.

The modal functions of the structure and the fluid are expressed as those used in the study of Wang *et al.* (2016c), that is

$$\tilde{v}_i(z) = \cosh(\beta_i z) - \cos(\beta_i z) - \frac{\cosh \beta_i + \cos \beta_i}{\sinh \beta_i + \sin \beta_i} [\sinh(\beta_i z) - \sin(\beta_i z)] \quad (2.6)$$

and

$$\tilde{q}_i(z) = \sin(i\pi z) \quad i = 1, 2, \dots \quad (2.7)$$

where β_i ($i = 1, 2, \dots$) satisfy the equation $\cos \beta \cosh \beta + 1 = 0$ that is obtained from the boundary conditions for the cantilever beam.

Repeating the discretization process again, the first mode motion of the structure and fluid can be derived as follows

$$\begin{aligned} \frac{d^2 v_1(t)}{dt^2} + \zeta \frac{dv_1(t)}{dt} + \omega_0^2 \beta_1^4 v_1(t) + a(\Omega_0 + \Omega_1 \cos \omega t)^2 v_1(t) \\ = [b + \tilde{d}(\Omega_0 + \Omega_1 \cos \omega t)^2] q_1(t) \\ \frac{d^2 q_1(t)}{dt^2} + s\omega_f \left[\frac{3}{4} q_1^2(t) - 1 \right] \frac{dq_1(t)}{dt} + \omega_f^2 q_1(t) = M \frac{d^2 v_1(t)}{dt^2} \end{aligned} \quad (2.8)$$

where

$$\begin{aligned} a &= \frac{\rho A}{2\tilde{m}} \frac{\int_0^1 \frac{d\tilde{v}_1(z)}{dz} \tilde{v}_1(z) z \, dz - \int_0^1 \frac{d^2 \tilde{v}_1(z)}{dz^2} (1 - z^2) \tilde{v}_1(z) \, dz}{\int_0^1 \tilde{v}_1^2(z) \, dz} \\ b &= \frac{C_{L0} \rho_f V^2}{4\tilde{m}} \frac{\int_0^1 \tilde{q}_1(z) \tilde{v}_1(z) \, dz}{\int_0^1 \tilde{v}_1^2(z) \, dz} \quad \tilde{d} = \frac{C_{L0} \rho_f r^2}{4\tilde{m}} \frac{\int_0^1 \tilde{q}_1(z) \tilde{v}_1(z) z^2 \, dz}{\int_0^1 \tilde{v}_1^2(z) \, dz} \end{aligned}$$

Equations (2.8) model the interactions between the vortical flows and the structure, which is also a Mathieu-van der Pol type oscillation.

3. Analysis with the multiple scale method

The research by Hao and Cao (2015), Hao *et al.* (2016) showed that nonlinear systems can present rich dynamic characteristics when the resonance occurs, like the primary resonance, superharmonic/subharmonic resonance as well as the internal resonance, etc. The multiple scale method is often utilized to understand qualitative characteristics of the system which present resonant conditions (Nayfeh and Mook, 1979).

Introducing the scaling parameters $\zeta \rightarrow \varepsilon \zeta$, $C_{L0} \rightarrow \varepsilon C_{L0}$, $s \rightarrow \varepsilon s$, $\Omega_1 \rightarrow \varepsilon \Omega_1$, $M \rightarrow \varepsilon M$ into Eqs. (2.8), one can obtain

$$\begin{aligned} \frac{d^2 v_1(t)}{dt^2} + \varepsilon \zeta \frac{dv_1(t)}{dt} + \omega_s^2 v_1(t) + a(\varepsilon^2 \Omega_1^2 \cos^2 \omega t + 2\varepsilon \Omega_0 \Omega_1 \cos \omega t) v_1(t) \\ = [\varepsilon b + \varepsilon \tilde{d}(\Omega_0 + \varepsilon \Omega_1 \cos \omega t)^2] q_1(t) \\ \frac{d^2 q_1(t)}{dt^2} + \varepsilon s \omega_f \left[\frac{3}{4} q_1^2(t) - 1 \right] \frac{dq_1(t)}{dt} + \omega_f^2 q_1(t) = \varepsilon M \frac{d^2 v_1(t)}{dt^2} \end{aligned} \quad (3.1)$$

where $\omega_s = \sqrt{\omega_0^2 \beta_1^4 + a \Omega_0^2}$ denotes the uncoupled natural frequency of the first-order mode of the beam.

Considering the possible 1:1 internal resonance between the structure and the fluid as well as the 1:2 subharmonic resonance conditions, the relations of frequencies can be expressed as $\omega = 2\omega_s + \varepsilon \sigma$, $\omega_f = \omega_s + \varepsilon \sigma_1$, where σ , σ_1 are the detuning parameters, respectively.

Assume the approximate form of the solutions as shown in the following

$$\begin{aligned} v_1(t) &= v_{10}(T_0, T_1) + \varepsilon v_{11}(T_0, T_1) + \dots \\ q_1(t) &= q_{10}(T_0, T_1) + \varepsilon q_{11}(T_0, T_1) + \dots \end{aligned} \quad (3.2)$$

Substituting solutions (3.2) into Eqs. (3.1) and equating the coefficients of like powers of ε , one can obtain:

— order ε^0

$$\begin{aligned} D_0^2 v_{10}(T_0, T_1) + \omega_s^2 v_{10}(T_0, T_1) &= 0 \\ D_0^2 q_{10}(T_0, T_1) + \omega_f^2 q_{10}(T_0, T_1) &= 0 \end{aligned} \quad (3.3)$$

— order ε^1

$$\begin{aligned} D_0^2 v_{11}(T_0, T_1) + 2D_0 D_1 v_{10}(T_0, T_1) + \omega_s^2 v_{11}(T_0, T_1) &= b q_{10}(T_0, T_1) + \tilde{d} \Omega_0^2 q_{10}(T_0, T_1) \\ &\quad - \zeta D_0 v_{10}(T_0, T_1) - 2a v_{10}(T_0, T_1) \Omega_0 \Omega_1 \cos \omega t \\ D_0^2 q_{11}(T_0, T_1) + 2D_0 D_1 q_{10}(T_0, T_1) + \omega_f^2 q_{11}(T_0, T_1) &= M D_0^2 v_{10}(T_0, T_1) \\ &\quad - s \omega_f \left[\frac{3}{4} q_{10}^2(T_0, T_1) - 1 \right] D_0 q_{10}(T_0, T_1) \end{aligned} \quad (3.4)$$

where

$$\frac{d}{dt} = D_0 + \varepsilon D_1 + \varepsilon^2 D_2 + \dots \quad \frac{d^2}{dt^2} = D_0^2 + 2\varepsilon D_0 D_1 + \dots \quad D_n = \frac{\partial}{\partial T_n}$$

General solutions to Eqs. (3.3) can be obtained in the complex form

$$\begin{aligned} v_{10} &= A(T_1) e^{i\omega_s T_0} + \overline{A}(T_1) e^{-i\omega_s T_0} \\ q_{10} &= B(T_1) e^{i\omega_f T_0} + \overline{B}(T_1) e^{-i\omega_f T_0} \end{aligned} \quad (3.5)$$

Substituting (3.5) into Eqs. (3.4) and considering the resonance conditions yields

$$\begin{aligned} D_0^2 v_{11} + \omega_s^2 v_{11} &= b B e^{i(\omega_s T_0 + \sigma_1 T_1)} + \tilde{d} \Omega_0^2 B e^{i(\omega_s T_0 + \sigma_1 T_1)} - i \zeta \omega_s A e^{i\omega_s T_0} \\ &\quad - a \Omega_0 \Omega_1 \left[A e^{i(\omega_s T_0 + \sigma_1 T_1)} + \overline{A} e^{i(\omega_s T_0 + \sigma_1 T_1)} \right] - 2i \omega_s D_1 A e^{i\omega_s T_0} + c.c. \\ D_0^2 q_{11} + \omega_f^2 q_{11} &= -M \omega_s^2 A e^{i(\omega_f - \varepsilon \sigma_1) T_0} - 2i \omega_f D_1 B e^{i\omega_f T_0} \\ &\quad - i s \omega_f^2 \left[\frac{3}{4} B^3 e^{3i\omega_f T_0} + \left(\frac{3}{4} B \overline{B} - 1 \right) B e^{i\omega_f T_0} \right] + c.c. \end{aligned} \quad (3.6)$$

where *c.c.* stands for the complex conjugate of the proceeding terms.

The solvability conditions of Eqs. (3.6) can be obtained by equating the coefficients of secular terms to zero, which reads

$$\begin{aligned} b B e^{i\sigma_1 T_1} + \tilde{d} \Omega_0^2 B e^{i\sigma_1 T_1} - i \zeta \omega_s A - a \Omega_0 \Omega_1 \overline{A} e^{i\sigma T_1} - 2i \omega_s D_1 A &= 0 \\ -M \omega_s^2 A e^{-i\sigma_1 T_1} - i s \omega_f^2 \left(\frac{3}{4} B \overline{B} - 1 \right) B - 2i \omega_f D_1 B &= 0 \end{aligned} \quad (3.7)$$

The derivatives of amplitudes A and B with respect to T_1 can be obtained by Eqs. (3.7), that is

$$\begin{aligned} D_1 A &= \frac{1}{2\omega_s} \left[-i b B e^{i\sigma_1 T_1} - i \tilde{d} \Omega_0^2 B e^{i\sigma_1 T_1} - \zeta \omega_s A + i a \Omega_0 \Omega_1 \overline{A} e^{i\sigma T_1} \right] \\ D_1 B &= \frac{1}{2\omega_f} \left[i M \omega_s^2 A e^{-i\sigma_1 T_1} - s \omega_f^2 \left(\frac{3}{4} B \overline{B} - 1 \right) B \right] \end{aligned} \quad (3.8)$$

Assume that the functions A and B are expressed in polar co-ordinates, which reads

$$A(T_1) = \frac{a_1(T_1)}{2} e^{i\theta_1(T_1)} \quad B(T_1) = \frac{a_2(T_1)}{2} e^{i\theta_2(T_1)} \quad (3.9)$$

where a_k, θ_k ($k = 1, 2$) represent the amplitudes and phase angles of the responses, respectively. The first-order averaged equations can be obtained after separating the real and imaginary parts by substituting (3.9) into Eqs. (3.8), that is

$$\begin{aligned} a_1' &= \frac{1}{2\omega_s}[(b + \tilde{d}\Omega_0^2)t)a_2 \sin \varphi - \zeta\omega_s a_1 - a\Omega_0\Omega_1 a_1 \sin \phi] \\ \theta_1' &= \frac{1}{2a_1\omega_s}[-(b + \tilde{d}\Omega_0^2)a_2 \cos \varphi + a\Omega_0\Omega_1 a_1 \cos \phi] \\ a_2' &= \frac{1}{2\omega_f}\left[M\omega_s^2 a_1 \sin \varphi - s\omega_f^2\left(\frac{3}{16}a_2^2 - 1\right)a_2\right] \\ \theta_2' &= \frac{1}{2a_2\omega_f}M\omega_s^2 a_1 \cos \varphi \end{aligned} \quad (3.10)$$

where $(')$ denotes the derivatives with respect to T_1 and $\varphi = \theta_2 + \sigma_1 T_1 - \theta_1$, $\phi = \sigma T_1 - 2\theta_1$.

The derivatives of φ and ϕ with respect to T_1 can be derived by eliminating θ_1 and θ_2 from Eqs. (3.10)_{2,4}

$$\begin{aligned} \varphi' &= \frac{M\omega_s^2 a_1 \cos \varphi}{2a_2\omega_f} + \sigma_1 + \frac{(b + \tilde{d}\Omega_0^2)a_2 \cos \varphi - a\Omega_0\Omega_1 a_1 \cos \phi}{2a_1\omega_s} \\ \phi' &= \sigma + \frac{(b + \tilde{d}\Omega_0^2)a_2 \cos \varphi - a\Omega_0\Omega_1 a_1 \cos \phi}{a_1\omega_s} \end{aligned} \quad (3.11)$$

The equilibrium solutions of Eqs. (3.10)_{1,3} and (3.11) correspond to periodic motions of the coupled system. The steady-state solutions for system (2.8) can be obtained when assuming $a_1' = 0$, $a_2' = 0$, $\varphi' = 0$, $\phi' = 0$.

4. The nonlinear response and bifurcation analysis with different system parameters

The research of Facchinetti *et al.* (2004), Keber and Wiercigroch (2008), Wang *et al.* (2016c) showed that during the interaction process of the fluid and structure, the structural motion can affect formation of the fluid as well. Therefore, the effects of the system parameters including the detuning parameter σ , steady-state rotating speed Ω_0 and the amplitude of periodic perturbation Ω_1 as well as freestream velocity V on the amplitudes and phase angles of the responses under different coupling parameters M are investigated. The bifurcation curves are computed and stability is determined by examining the eigenvalues of the corresponding characteristic equation to Eqs. (3.10)_{1,3} and (3.11).

Figures 2 and 3 show the varying trends of the amplitudes a_1 and a_2 and phase angles φ and ϕ (mod T) with respect to the detuning parameter σ for the coupling parameters $M = 0.1, 0.2, 0.3$, respectively. The other parameters are fixed at $A = 4.2 \cdot 10^{-4} \text{ m}^2$, $\rho = 7800 \text{ kg/m}^3$, $\rho_f = 1.225 \text{ kg/m}^3$, $EI = 300 \text{ N m}$, $V = 110 \text{ m/s}$, $\Omega_0 = 350 \text{ rad/s}$, $\Omega_1 = 0.1 \text{ rad/s}$, $\overline{D} = 0.1 \text{ m}$, $r = 0.3 \text{ m}$, $\tilde{c} = 6 \text{ N s/m}$, $C_{L0} = 0.01$, $\omega_f = 552.64 \text{ rad/s}$, $s = 0.03$, respectively.

It can be seen from Figs. 2a,b and 3a,b that as the detuning parameter σ increases, the trivial solutions of the amplitudes a_1 , a_2 and the phase angles φ , ϕ jump to large two-mode solutions via a saddle-node bifurcation at SN_1 , leading to the occurrence of a stable and an unstable solution. Similarly, as the detuning parameter σ decreases, the trivial solutions of the amplitudes a_1 and a_2 and the phase angles φ , ϕ become other two-mode solutions via a saddle-node bifurcation at SN_2 , resulting in a stable and an unstable solution, respectively.

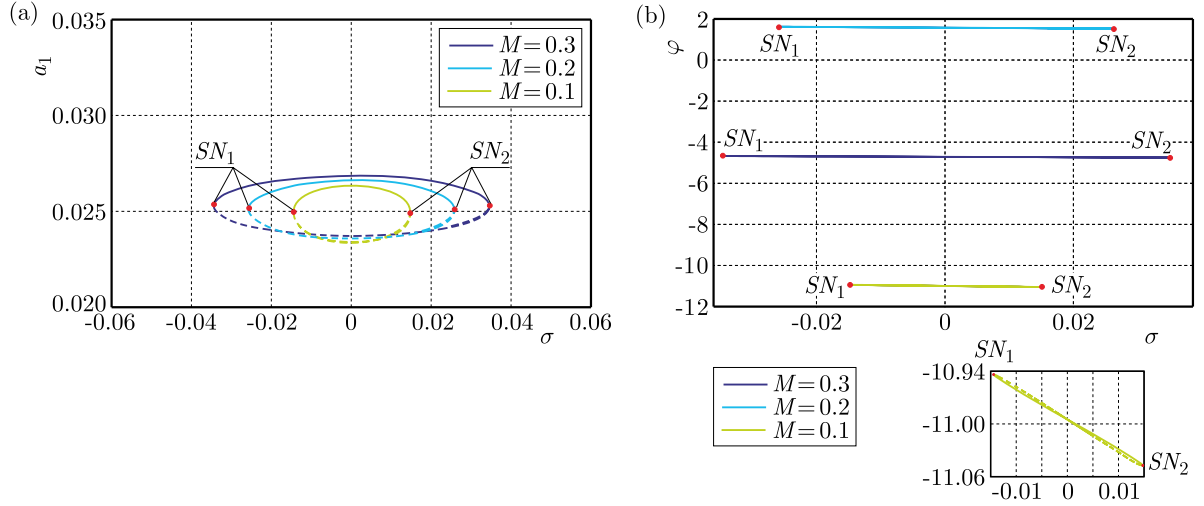


Fig. 2. Frequency-response curves of the amplitude a_1 and the phase angle φ of the structure with respect to the detuning parameter σ

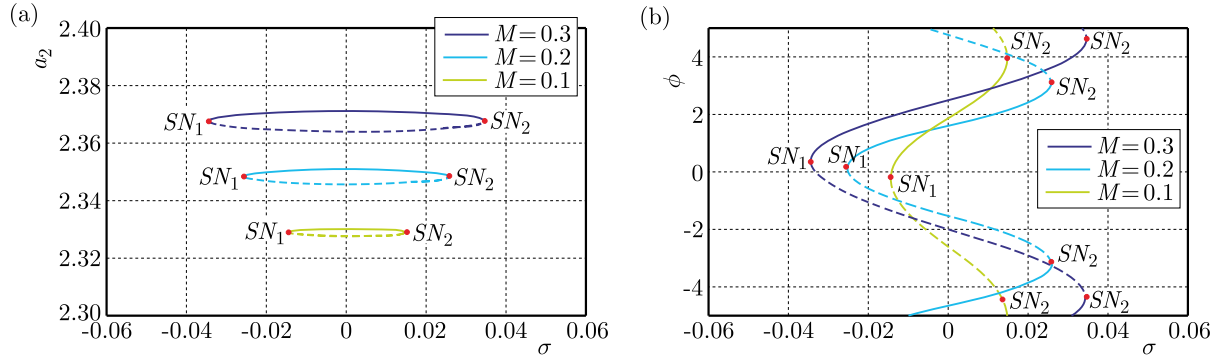


Fig. 3. Bifurcation curves of the amplitude a_2 and the phase angle ϕ of the fluid with respect to the detuning parameter σ

Figures 2a and 3a show that the amplitudes a_1 and a_2 have the same varying trends with respect to the varying detuning parameter. The phase angles φ and ϕ have the opposite varying trends with respect to the varying detuning parameter, which means that there is transformation between the two vibration modes. In addition, Figs. 2 and 3 show that the absolute value of σ for the critical bifurcation increases and the amplitudes as well as the period of the steady-state solutions can be increased as the coupling parameter M increases.

Figures 4 and 5 show the varying trends of the responses with respect to the steady-state rotating speed Ω_0 for the coupling parameters $M = 0.1, 0.2, 0.3$, respectively. The other parameters are fixed at $A = 4.2 \cdot 10^{-4} \text{ m}^2$, $\rho = 7800 \text{ kg/m}^3$, $\rho_f = 1.225 \text{ kg/m}^3$, $EI = 300 \text{ N m}$, $V = 110 \text{ m/s}$, $\Omega_1 = 0.1 \text{ rad/s}$, $\overline{D} = 0.1 \text{ m}$, $r = 0.3 \text{ m}$, $\tilde{c} = 6 \text{ N s/m}$, $C_{L0} = 0.01$, $\omega_f = 552.64 \text{ rad/s}$, $s = 0.03$, $\sigma = 0.01$, respectively.

It can be seen from Figs. 4 and 5 that the trivial solution jumps to large solutions via a saddle-node bifurcation, resulting in the occurrence of a two-mode solution consisting of a stable solution and an unstable one. Figure 4a shows that the steady-state solutions of the amplitude a_1 decrease as the steady-state rotating speed Ω_0 increases, which indicates that the increasing of the steady-state rotating speed can suppress the large-amplitude vibrations of the structure. Figure 5a shows that the steady-state solutions of the amplitude a_2 increase as the steady-state rotating speed Ω_0 increases, which displays an inverse varying trend of the responses comparing with those for the amplitude a_1 . By comparison, the stable and unstable solutions for the phase angle φ as shown in Fig. 4b increase simultaneously as the steady-state rotating

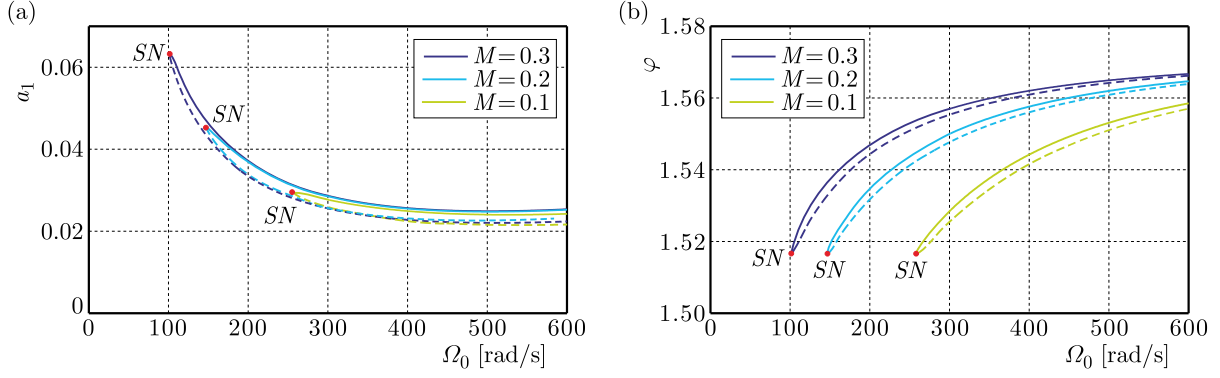


Fig. 4. Bifurcation curves of the amplitude a_1 and the phase angle φ of the structure with respect to the steady-state rotating speed Ω_0

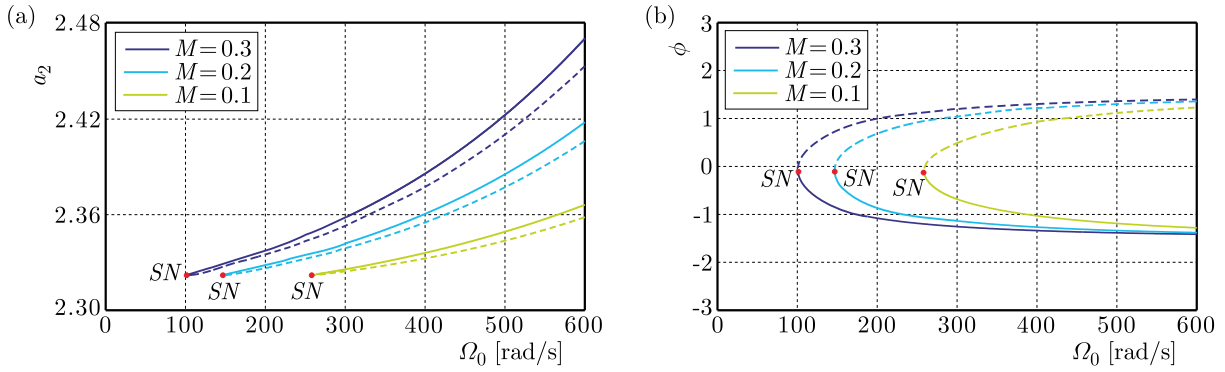


Fig. 5. Bifurcation curves of the amplitude a_2 and the phase angle ϕ of the fluid with respect to the steady-state rotating speed Ω_0

speed Ω_0 increases while the stable solutions of the phase angle ϕ decrease and the unstable one increases when the steady-state rotating speed Ω_0 increases, as shown in Fig. 5b. Moreover, the critical steady-state rotating speed can decrease for the saddle-node bifurcation as the coupling parameter M increases, that is: $\Omega_0 = 257.9793$ rad/s for $M = 0.1$, $\Omega_0 = 146.8258$ rad/s for $M = 0.2$, $\Omega_0 = 101.3993$ rad/s for $M = 0.3$, respectively. In addition, an increase in the coupling parameter M can increase the amplitudes a_1 and a_2 of the responses. It can be illustrated from system (2.8) that the increasing of the coupling parameter M can excite large vibrations of the fluid, which can in turn promote the oscillations of the structure.

Figures 6 and 7 show the bifurcation characteristics of the system responses with respect to the amplitude Ω_1 of the periodic perturbation for different coupling parameters M . The other parameters are fixed at $A = 4.2 \cdot 10^{-4}$ m², $\rho = 7800$ kg/m³, $\rho_f = 1.225$ kg/m³, $EI = 300$ N m, $V = 110$ m/s, $\Omega_0 = 350$ rad/s, $\overline{D} = 0.1$ m, $r = 0.3$ m, $\tilde{c} = 6$ N s/m, $C_{L0} = 0.01$, $\omega_f = 552.64$ rad/s, $s = 0.03$, $\sigma = 0.01$, respectively.

It can be seen from Figs. 6 and 7 that the trivial solution jumps to the large solution via a saddle-node bifurcation (SN), leading to the occurrence of a two-mode solution including a stable solution and an unstable one as the parameter Ω_1 increases. Figures 6a and 7a display that the varying trends of the amplitudes a_1 and a_2 with respect to the parameter Ω_1 are the same to each other, that is, the stable solutions of the amplitudes a_1 and a_2 increase as Ω_1 increases while the unstable solutions decrease as Ω_1 increases. In comparison, the stable and unstable solutions of the phase angles φ and ϕ have the opposite varying trend. In addition, the increasing of the coupling parameter M can make the critical bifurcation value of the parameter Ω_1 smaller, that is, $\Omega_1 = 0.0674$ rad/s for $M = 0.1$, $\Omega_1 = 0.0383$ rad/s for $M = 0.2$ and $\Omega_1 = 0.0286$ rad/s for $M = 0.3$, respectively.

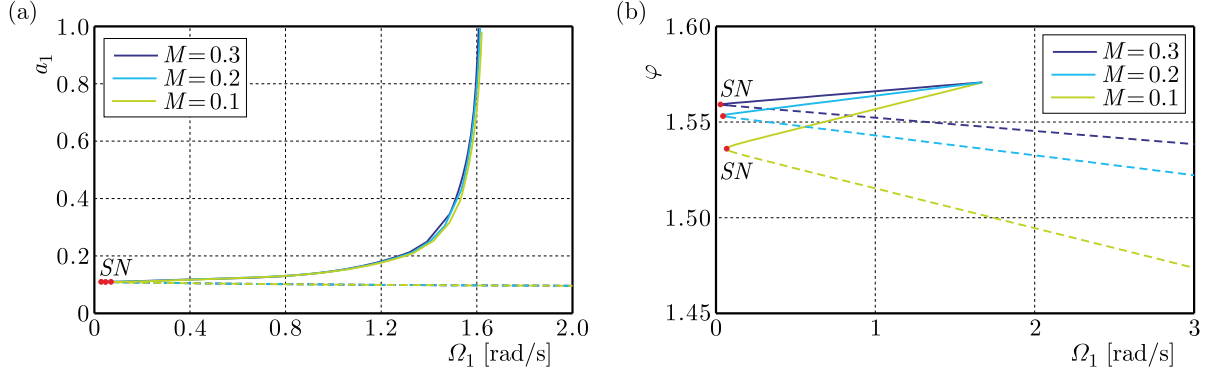


Fig. 6. Bifurcation curves of the amplitude a_1 and the phase angle φ of the structure with respect to the amplitude Ω_1 of the periodic perturbation

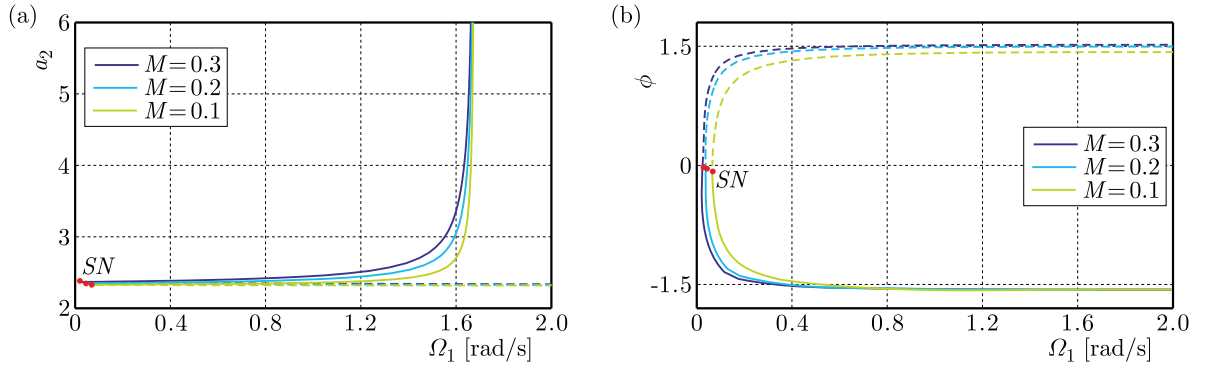


Fig. 7. Bifurcation curves of the amplitude a_2 and the phase angle ϕ of the fluid with respect to the amplitude Ω_1 of the periodic perturbation

Figures 8 and 9 display the varying trends of the responses with respect to the freestream velocity V under different values of the coupling parameter M . The other parameters are fixed at $A = 4.2 \cdot 10^{-4} \text{ m}^2$, $\rho = 7800 \text{ kg/m}^3$, $\rho_f = 1.225 \text{ kg/m}^3$, $EI = 300 \text{ N m}$, $\Omega_0 = 350 \text{ rad/s}$, $\Omega_1 = 0.1 \text{ rad/s}$, $\bar{D} = 0.1 \text{ m}$, $r = 0.3 \text{ m}$, $\tilde{c} = 6 \text{ N s/m}$, $C_{L0} = 0.01$, $s = 0.03$, $\sigma = 0.01$, respectively.

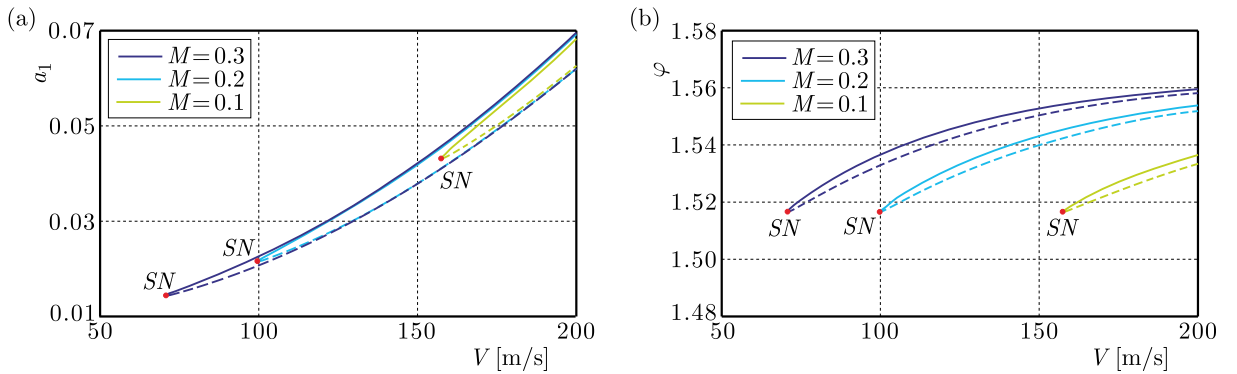


Fig. 8. Bifurcation curves of the amplitude a_1 and the phase angle φ of the structure with respect to the freestream velocity V

It can be seen from Figs. 8 and 9 that the trivial solution jumps to a large solution via a saddle-node bifurcation as the freestream velocity V increases, resulting in the occurrence of a two-mode solution consisting of a stable solution and an unstable one. The stable and unstable solutions of the amplitudes a_1 and a_2 increase when the freestream velocity V increases, as shown in Figs. 8a and 9a which present the similar varying trends for the solutions of the amplitudes

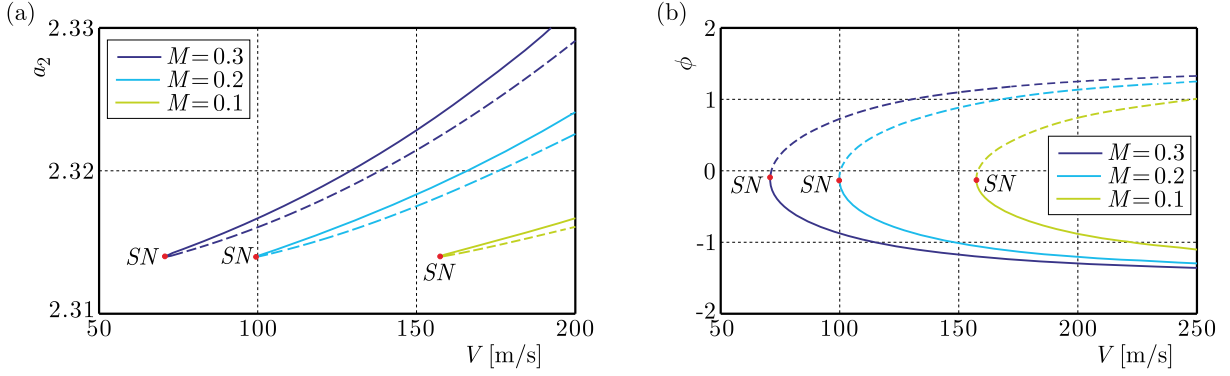


Fig. 9. Bifurcation curves of the amplitude a_2 and the phase angle ϕ of the fluid with respect to the freestream velocity V

a_1 and a_2 . Figures 8b and 9b indicate the opposite varying trends for the stable solutions of the phase angles φ and ϕ , namely, the solution of the phase angle φ increases while the solution of the phase angle ϕ decreases as the freestream velocity V increases. Similarly, the increasing of the coupling parameter M can decrease the critical freestream velocity V for the saddle-node bifurcation of the responses.

5. Conclusions

The dynamic responses and bifurcation characteristics of turbine blades under variable rotating speed have been investigated, where the rotating blade was modeled as a cantilever beam and the effect of the oncoming vortices was represented as the van der Pol oscillation. And the acceleration coupling was considered to simulate the influence of the vibration of the beam on the van der Pol oscillation. The first-order mode vibrations of the coupled system were obtained by the Galerkin discretization. The 1:2 subharmonic resonance and the 1:1 internal resonance for the coupled system were studied by using the multiple scale method. The averaged equations were derived and the bifurcation curves were computed. Effects of the system parameters including the detuning parameter σ , the steady-state rotating speed Ω_0 , the amplitude Ω_1 of the periodic perturbation as well as the freestream velocity V on the responses were investigated.

The phenomenon of saddle-node bifurcation was found to occur under certain parameter conditions. The bifurcation analysis indicates that the increasing of the coupling parameter M can delay the saddle-node bifurcation of the responses with respect to the detuning parameter while the increasing of the coupling parameter M can make the saddle-node bifurcation occur earlier for the responses with respect to the steady-state rotating speed Ω_0 , the amplitude Ω_1 of the periodic perturbation as well as the freestream velocity V . Moreover, the increasing of the steady-state rotating speed can suppress large vibration of the structure. The amplitudes of vibrations of the structure and fluid can be increased as the freestream velocity V increases. The opposite varying trends for the amplitudes and phase angles with respect to the system parameters indicate the energy transfer between the vibrations of the fluid and the structure. The results can help one to understand the interaction of the fluid and the structure.

Acknowledgement

The authors acknowledge the financial support from the National Natural Science Foundation of China (No. 11702111, 11572205, 11732014), the Natural Science Foundation of Shandong Province (No. ZR2017QA005, ZR2017BA031) and the University of Jinan (No. 160100210).

References

1. BARRON M.A., SEN M., 2009, Synchronization of coupled self-excited elastic beams, *Journal of Sound and Vibration*, **324**, 209-220
2. BARRON M.A., 2010, Vibration analysis of a self-excited elastic beam, *Journal of Applied Research and Technology*, **8**, 2, 227-239
3. CLOUGH R.W., PENZIEN J., 2003, *Dynamics of structures*, Computers and Structures, Inc., 3rd edition
4. DOMAGALSKI Ł., JĘDRYSIAK J., 2016, Nonlinear vibrations of periodic beams, *Journal of Theoretical and Applied Mechanics*, **54**, 4, 1095-1108
5. FACCHINETTI M.L., DE LANGREE E., BIOLLEY F., 2004, Coupling of structure and wake oscillators in vortex-induced vibrations, *Journal of Fluids and Structures*, **19**, 123-140
6. GABBAI R., BENAROYA H., 2005, An overview of modeling and experiments of vortex-induced vibration of circular cylinders, *Journal of Sound and Vibration*, **282**, 575-616
7. GEORGIADES F., LATALSKI J., WARMIŃSKI J., 2014, Equations of motion of rotating composite beam with a nonconstant rotation speed and an arbitrary preset angle, *Meccanica*, **49**, 1833-1858
8. GOSTELOW J.P., PLATZER M.F., CARSCALLEN W.E., 2006, On vortex formation in the wake flows of transonic turbine blades and oscillating airfoils, *Journal of Turbomachinery-ASME*, **128**, 528-535
9. HARTLEN R., CURRIE I., 1970, Lift-oscillator model of vortex induced vibration, *Journal of Engineering Mechanics-ASCE*, **96**, 577-591
10. HAO Z.F., CAO Q.J., 2015, The isolation characteristics of an archetypal dynamical model with stable-quasi-zero-stiffness, *Journal of Sound and Vibration*, **340**, 61-79
11. HAO Z.F., CAO Q.J., WIERCIGROCH M., 2016, Two-sided damping constraint control for high-performance vibration isolation and end-stop impact protection, *Nonlinear Dynamics*, **86**, 2129-2144
12. HEMON P., 1999, An improvement of the time delayed quasi-steady model for the oscillations of circular cylinders in cross-flow, *Journal of Fluids and Structures*, **13**, 291-307
13. KAMMER D.C., SCHLACK A.L., 1987, Effects of nonconstant spin rate on the vibration of a rotating beam, *Journal of Applied Mechanics*, **54**, 2, 305-310
14. KEBER M., WIERCIGROCH M., 2008, A reduced order model for vortex-induced vibration of a vertical offshore riser in lock-in, *IUTAM Symposium on Fluid-Structure Interaction in Ocean Engineering*, *Iutam Bookseries*, **8**, 155-166
15. KIM H., CHUNG J., 2016, Nonlinear modeling for dynamic analysis of a rotating cantilever beam, *Nonlinear Dynamics*, **86**, 1981-2002
16. LEE Y., VAKAKIS A., BERGMAN L., MCFARLAND M., 2006, Suppression of limit cycle oscillations in the van der Pol oscillator by means of passive nonlinear energy sinks, *Structural Control and Health Monitoring*, **13**, 41-75
17. NAYFEH A.H., MOOK D.T., 1979, *Nonlinear Oscillations*, New York, 331-338
18. SHAHLAEI-FAR S., NABARRETE A., BALTHAZAR J.M., 2016, Homotopy analysis of a forced nonlinear beam model with quadratic and cubic nonlinearities, *Journal of Theoretical and Applied Mechanics*, **54**, 4, 1219-1230
19. STAINO A., BASU B., 2013, Dynamics and control of vibrations in wind turbines with variable rotor speed, *Engineering Structures*, **56**, 58-67
20. WANG D., CHEN Y.S., WIERCIGROCH M., CAO Q.J., 2016a, A three-degree-of-freedom model for vortex-induced vibrations of turbine blades, *Meccanica*, **51**, 2607-2628

21. WANG D., CHEN Y.S., HAO Z.F., CAO Q.J., 2016b, Bifurcation analysis for vibrations of a turbine blade excited by air flows, *Science China Technological Sciences*, **59**, 8, 1217-1231
22. WANG D., CHEN Y.S., WIERCIGROCH M., CAO Q.J., 2016c, Bifurcation and dynamic response analysis of rotating blade excited by upstream vortices, *Applied Mathematics and Mechanics*, **37**, 9, 1251-1274
23. WARMIŃSKI J., LATALSKI J., 2016, Saturation control for a rotating thin-walled composite beam structure, *Procedia Engineering*, **144**, 713-720
24. WEI K., MENG G., ZHOU S., LIU J., 2006, Vibration control of variable speed/acceleration rotating beams using smart materials, *Journal of Sound and Vibration*, **298**, 4/5, 1150-1158
25. YANG J.B., JIANG L.J., CHEN D.C., 2004, Dynamic modelling and control of a rotating Euler-Bernoulli beam, *Journal of Sound and Vibration*, **274**, 863-875
26. YAO M.H., CHEN Y.P., ZHANG W., 2012, Nonlinear vibrations of blade with varying rotating speed, *Nonlinear Dynamics*, **68**, 487-504
27. YAO M.H., ZHANG W., CHEN Y.P., 2014, Analysis on nonlinear oscillations and resonant responses of a compressor blade, *Acta Mechanica*, **225**, 3483-3510
28. YOUNESIAN D., ESMAILZADEH E., 2010, Non-linear vibration of variable speed rotating viscoelastic beams, *Nonlinear Dynamics*, **60**, 193-205
29. ZHU K., CHUNG J., 2016, Dynamic modeling and analysis of a spinning Rayleigh beam under deployment, *International Journal of Mechanical Sciences*, **115-116**, 392-405

Manuscript received January 10, 2017; accepted for print July 15, 2017

REDUCED NUMBER OF DESIGN PARAMETERS IN OPTIMUM PATH SYNTHESIS WITH TIMING OF FOUR-BAR LINKAGE

JACEK BUŚKIEWICZ

Poznan University of Technology, Institute of Applied Mechanics, Poznań, Poland

e-mail: jacek.buskiewicz@put.poznan.pl

The paper presents the method for the optimal synthesis of four-link mechanism generating open/closed paths with time prescription. Although the method is suitable for both closed and open paths, it enables decreasing the number of design parameters describing dimensions, orientation and position of a path generator. Compared to the methods presented in the references, this is a one-phase synthesis method; although the number of design parameters is reduced, the method does not require affine transformations to be performed on the synthesised mechanism. The effectiveness of the method is discussed based on examples of three paths, with two taken from the literature.

Keywords: path synthesis, evolutionary algorithm, four-bar linkage

1. Introduction

Recent literature reveals a great variety of problems related to the path synthesis in which dimensions of a mechanism are sought, the point of which traces a desired path. This diversification may be classified with respect to:

1. Methods of solutions: analytical, computer (deterministic, heuristic).
2. Formulation of the problem: closed- or open-path synthesis, path synthesis with or without timing, one- or two-phase path synthesis.
3. Type of method: direct or indirect synthesis method (based on an atlas of coupler curves).

Owing to great mathematical complexity (Erdman *et al.*, 2001), computer methods are mainly developed. The prevalent techniques are based on the genetic/evolutionary algorithms and other heuristic methods patterned upon biological systems and social behaviours (Avilés *et al.*, 2010; Bulatović *et al.*, 2013, 2016; Buśkiewicz, 2009, 2015; Buśkiewicz *et al.*, 2010; Cabrera *et al.*, 2007, 2011; Ebrahimi and Payvandy, 2015; Gogate and Matekar, 2012; Kafash and Nahvi, 2015; Kunjur and Krishnamurty, 1997; Lin, 2010; Matekar and Gogate, 2012; Nadal *et al.*, 2015; Penunuri *et al.*, 2011; Shiakolas *et al.* 2002, 2005). Frequently, the methods are devoted to a single specific path-synthesis task: synthesis of open-path generators, synthesis of closed-path generators, path synthesis with and without timing (time prescription). In the path synthesis with timing, each position of the coupler point corresponds to a prescribed angular position of the active link. In many cases, this correspondence is of less significance. In the open-path synthesis, a part of the coupler trajectory is prescribed.

The two-phase synthesis (Buśkiewicz *et al.*, 2009; Buśkiewicz, 2010; Lin, 2014, 2015; McGarva and Mullineux, 1993; Nadal *et al.*, 2015; Sanchez Marin and Gonzalez, 2004; Smaili and Diab, 2007; Sun *et al.*, 2015; Ullah and Kota, 1997) for the direct synthesis method consists of two steps. At first the shape synthesis is carried out followed by scale-rotation-translation transformations. The first step reduces the number of design variables. This number is important when a synthesis method is based on deterministic-probabilistic algorithms for optimal parameter determination.

Every additional parameter increases the dimension of the solution space and may increase the computational cost. In general, the effectiveness of a method depends essentially on the number of design parameters, by which the objective function is expressed.

This paper deals with the direct synthesis method dedicated for an open/closed-path synthesis with timing. The mathematical foundations of the usage of the Fourier descriptors (FDs) as shape signatures (descriptors) of a closed curve were formulated by Zahn and Roskies (1972). Although a prevailing number of these methods may be used for closed paths, the wavelet transform has been used to describe open paths by Sun *et al.* (2015). Smaili and Diab (2007) presented the two-phase synthesis method based on the so-called cyclic angular deviation vector. Buśkiewicz *et al.* (2009) proposed a two-phase synthesis method in which the shape was described by means of the curvature-based Fourier descriptors. The centroid, the direction of the major principal axis and the perimeter of a curve enabled translation, rotation and scaling of the mechanism to the desired configuration. Buśkiewicz (2010) also proposed a two-phase synthesis method using the function of the distance of the curve from its centroid, to describe the curve shape in terms of its normalised Fourier coefficients. Sanchez Marin and Gonzalez (2004) utilised geometric properties to describe the path (without addressing harmonic series theories) and to reduce the number of optimised parameters to five in the open-path synthesis.

The methods using decomposition of the path into normalised parameters, invariant with respect to affine transformation, also belongs to the so-called indirect synthesis method (Chu and Sun, 2010; Galán-Marín *et al.*, 2009; Hoeltzel and Chieng, 1990; McGarva, 1994; Mullineux, 2011; Sun and Chu, 2009; Vasiliu and Yannou, 2001; Yu *et al.*, 2007, 2012). The second phase consists of searching through a computerised atlas database of normalised descriptors which are linked to dimensions of the mechanisms generating closed paths. Nonetheless, most techniques are one-phase syntheses which either introduce new error functions or develop algorithms evaluating an objective function (Acharyya and Mandal, 2009; Avilés *et al.*, 2010; Bulatović and Dordević, 2009; Bulatović *et al.*, 2013, 2016; Cabrera *et al.*, 2002, 2007, 2011; Ebrahimi and Payvandy, 2015; Gogate and Matekar, 2012; Khorshidi *et al.*, 2011; Kinzel *et al.*, 2006; Kunjur and Krishnamurty, 1997; Lio 1997; Lio *et al.*, 2000; Lin, 2010; Lin and Hsiao, 2017; Matekar and Gogate, 2012; Penunuri *et al.*, 2011; Sancibrian *et al.*, 2004; Schmiedeler *et al.*, 2014; Shiakolas *et al.*, 2002, 2005; Smaili *et al.*, 2005). The number of design parameters is as large as necessary to define the problem. In the optimum synthesis with timing the design variables are not only mechanism dimensions and orientation but also angular positions of the input link corresponding with the prescribed coupler points.

The number of techniques for open/closed-path synthesis with timing, defined by the decreased number of design parameters, is rather small (Nadal *et al.*, 2015; Kafash and Nahvi, 2015). The paper presents the method for the optimal synthesis of a four-link planar mechanism generating open paths with time prescription, enabling a decrease in the number of design parameters describing dimensions, orientation and position of the path generator. Compared with the methods presented in the references, this is a one-phase synthesis method; i.e. although the number of design parameters is reduced, the method does not require affine transformations to be performed on the synthesised mechanism. The paper is a continuation of the work (Buśkiewicz, 2015) dealing with the one-phase path synthesis without timing, defined by means of a reduced number of design parameters.

2. Method description

2.1. Mathematical foundations

The method for path synthesis with timing is aimed at minimising the number of design variables being optimised using a heuristic algorithm. The coupler curve is defined by means of the discrete number of points. When the input link rotates by a given angle, the coupler point

passes between two neighbouring curve points. The geometric scheme of the four-bar linkage is shown in Fig. 1a.

The design variables optimised by means of the algorithm are (Fig. 1b):

- coordinates of the input link pivot: x_{O1}, y_{O1} ,
- input link length: l_1 , and coupler AB length: l_2 ,
- angle between arms AD and AB of the coupler: θ_4 ,
- angular position of the input link θ_{10} corresponding with the first coupler point.

Six parameters define the four-bar linkage instead of the 10 required in the classical approach to path synthesis with timing $(l_1, l_2, l_3, l_4, l_5, x_{O1}, y_{O1}, \theta_4, \gamma, \theta_{10})$.

The input data are given as set $\{(x_i, y_i, \theta_{1i}), i = 1, \dots, n\}$, where (x_i, y_i) are the coordinates of the points to be drawn by the coupler point D for the input link angular position $\theta'_{1i} = \theta_{1i} + \theta_{10}$. It means that passing from the point i to the point $i + 1$ is accompanied by rotation of the input link by the angle $\theta_{1i+1} - \theta_{1i}$. The angle γ is determined in the phase of the computations and is not known in the initial phase. This is why the angular position of the input link θ_1 is measured from the horizontal line. Let us assume that we have a set of arbitrary values of the design variables defining a candidate for the optimum mechanism. One has to evaluate how accurately this mechanism approximates the given performance.

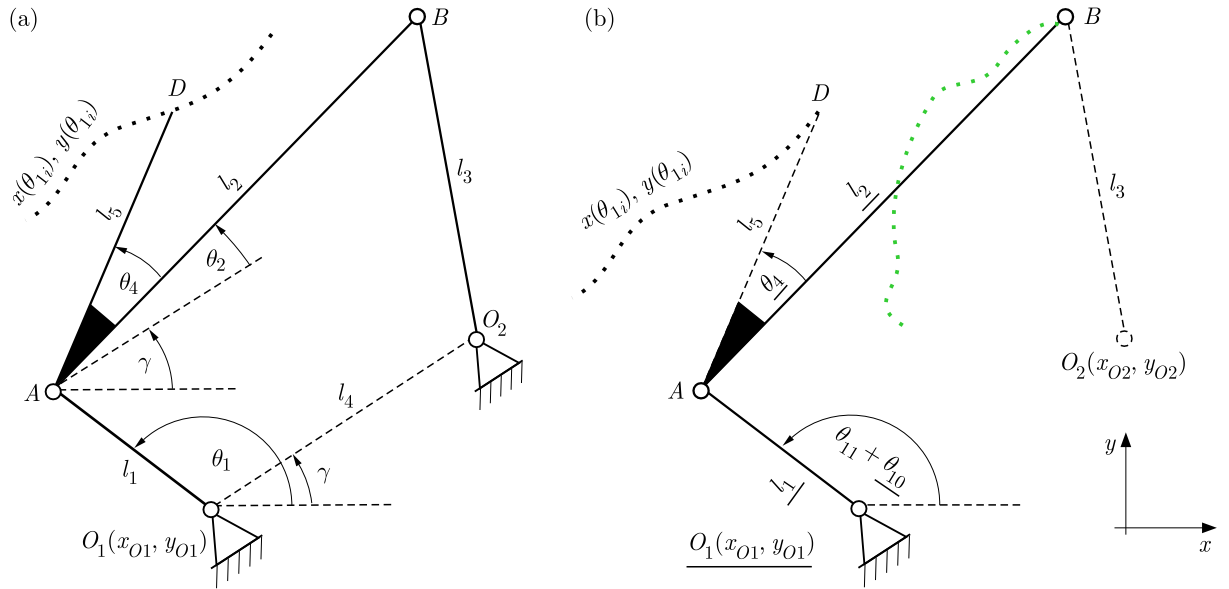


Fig. 1. (a) General geometric scheme of the four-bar linkage, (b) design variables (underlined) and variables determined using design variables

The algorithm for determination of the remaining dimensions of the mechanism is as follows.

Having certain design variables x_{O1}, y_{O1}, l_1 and θ_{10} , the positions of the joint A on the input link for $i = 1, \dots, n$ are computed

$$x_{Ai} = x_{O1} + l_1 \cos(\theta_{1i} + \theta_{10}) \quad y_{Ai} = y_{O1} + l_1 \sin(\theta_{1i} + \theta_{10}) \quad (2.1)$$

Subsequently, the lengths are computed

$$|A_i D_i| = \sqrt{(x_{Ai} - x_i)^2 + (y_{Ai} - y_i)^2} \quad (2.2)$$

as well as the trigonometric functions between the section $A_i D_i$ and the horizontal line

$$\cos \alpha_i = \frac{x_i - x_{Ai}}{|A_i D_i|} \quad \sin \alpha_i = \frac{y_i - y_{Ai}}{|A_i D_i|} \quad (2.3)$$

The optimum length of the arm $|AD|$ minimises, in the sense of the least square method, the sum of the squared deviations of the prescribed point D positions from the points generated by dyad O_1AD , defined by x_{O1} , y_{O1} , l_1 , θ_{10} and l_5 for the prescribed angular positions of the link O_1A

$$E_1 = \sum_{i=1}^n [(x_{Ai} + l_5 \cos \alpha_i - x_i)^2 + (y_{Ai} + l_5 \sin \alpha_i - y_i)^2] \quad (2.4)$$

As l_5 is not known, differentiating E_1

$$\frac{\partial E_1}{\partial l_5} = 2 \sum_{i=1}^n [(x_{Ai} + l_5 \cos \alpha_i - x_i) \cos \alpha_i + (y_{Ai} + l_5 \sin \alpha_i - y_i) \sin \alpha_i] = 0 \quad (2.5)$$

one can obtain

$$l_5 = \frac{1}{n} \sum_{i=1}^n [(x_{Ai} - x_i) \cos \alpha_i + (y_{Ai} - y_i) \sin \alpha_i] \quad (2.6)$$

which equals the average value of $|A_i D_i|$ for all i .

Then the desired design variables minimise the deviations of $|A_i D_i|$ from l_5 . The next set of design variables are the angle between the coupler arms AD and $AB - \theta_4$ and the coupler AB length $-l_2$. Having these values, one can compute the position of the joint B connecting the coupler and the output link. Using the complex number notation, we have the subsequent positions of the link AB corresponding with the positions of the link AD

$$\begin{aligned} \mathbf{A}_i \mathbf{B}_i &= (x_{Bi} - x_{Ai}) + j(y_{Bi} - y_{Ai}) = l_2 \frac{\mathbf{A}_i \mathbf{D}_i}{|A_i D_i|} e^{j(-\theta_4)} \\ &= l_2 (\cos \alpha_i + j \sin \alpha_i) [\cos(-\theta_4) + j \sin(-\theta_4)] \end{aligned} \quad (2.7)$$

Hence, the coordinates

$$x_{Bi} = x_{Ai} + l_2 \cos(\alpha_i - \theta_4) \quad y_{Bi} = y_{Ai} + l_2 \sin(\alpha_i - \theta_4) \quad (2.8)$$

are obtained by clockwise rotating the unit vector $\mathbf{A}_i \mathbf{D}_i$ by the angle θ_4 and multiplying the result by l_2 . It is expected that the position of the joint B can be approximated by a circular arc. The radius of the arc that best fits into these points equals the length of the output link O_2B , and the centre of the arc becomes the pivot of this link. The parameters of this circular arc may be computed using the method described in (Buřkiewicz, 2015). Let l_{3i} denote the radius of the circle with the centre at (x_{O2i}, y_{O2i}) passing through three points: B_i , $B_{i'}$ and $B_{i''}$, where: $i = 1, \dots, n$, $i' = i + 2$, $i'' = i' + 2$, and the number point greater than n is diminished by n . The centre coordinates of the i -th circle are

$$x_{O2i} = \frac{b_1 a_{22} - b_2 a_{12}}{a_{11} a_{22} - a_{12} a_{21}} \quad y_{O2i} = \frac{b_2 a_{11} - b_1 a_{21}}{a_{11} a_{22} - a_{12} a_{21}} \quad (2.9)$$

where

$$\begin{aligned} a_1 &= 2(x_{Bi} - x_{Bi'}) & a_{12} &= 2(y_{Bi} - y_{Bi'}) \\ a_{21} &= 2(x_{Bi} - x_{Bi''}) & a_{22} &= 2(y_{Bi} - y_{Bi''}) \\ b_1 &= x_{Bi}^2 + y_{Bi}^2 - x_{Bi'}^2 - y_{Bi'}^2 & b_2 &= x_{Bi}^2 + y_{Bi}^2 - x_{Bi''}^2 - y_{Bi''}^2 \end{aligned}$$

Then, the coordinates of the ground pin are

$$x_{O2} = \frac{1}{n} \sum_{i=1}^n x_{O2i} \quad y_{O2} = \frac{1}{n} \sum_{i=1}^n y_{O2i} \quad (2.10)$$

Similarly, the average radius is taken as the length of the output link

$$l_3 = \frac{1}{n} \sum_{i=1}^n l_{3i} = \frac{1}{n} \sum_{i=1}^n |O_2 B_i| \quad (2.11)$$

The final step is to compute the length of the immovable link, and cosine and sine of the angle γ

$$l_4 = |O_1 O_2| \quad \cos \gamma = \frac{x_{O2} - x_{O1}}{l_4} \quad \sin \gamma = \frac{y_{O2} - y_{O1}}{l_4} \quad (2.12)$$

An alternative method for measuring the similarity of the set of points to the circular curve has recently been presented by Kafash and Nahvi (2015). The Circular Proximity Function is defined as

$$CPF = \sum_{i=1}^n [(x_{Bi} - x_{O2})^2 + (y_{Bi} - y_{O2})^2 - R^2] \quad (2.13)$$

where the average value of the squared distances between the points B and the centre of the hypothetical circle is as follows:

$$R = \frac{1}{n} \sum_{i=1}^n [(x_{Bi} - x_{O2})^2 + (y_{Bi} - y_{O2})^2] \quad (2.14)$$

The optimum circle centre coordinates minimises the CPF .

2.2. Objective function and Euclidian error

The four-bar linkage realises exactly the desired motion when the sum of deviations of the arm length l_5 from real distances $|A_i D_i|$ and deviations of the length of the output link from computed real distances $|O_2 B_i|$ (the measure of the deviation of the path of the joint B from an ideal circular arc)

$$\delta = \frac{\max |A_i D_i| - \min |A_i D_i|}{l_5} + \frac{\max |O_2 B_i| - \min |O_2 B_i|}{l_3} \quad (2.15)$$

equals 0. Then δ is the minimised objective function and, simultaneously, it is the indirect measure of the inaccuracy of the method. This error bears no information about the Euclidian deviation between given points and points traced by the mechanism obtained. For the determined dimensions of the four-bar linkage, the coordinates of the coupler points for the given angular positions of the input link are computed. For this purpose, the angular position of the coupler and the output link $O_2 B$

$$\theta_{21,2} = 2 \arctan \frac{-K_E \pm \sqrt{K_E^2 - 4K_D K_F}}{2K_D} \quad \theta_{31,2} = 2 \arctan \frac{-K_B \pm \sqrt{K_B^2 - 4K_A K_C}}{2K_A} \quad (2.16)$$

are determined, where

$$\begin{aligned} K_A &= K_3 - K_1 + (1 - K_2) \cos(\theta_1 - \gamma) & K_B &= -2 \sin(\theta_1 - \gamma) \\ K_C &= K_1 + K_3 - (1 + K_2) \cos(\theta_1 - \gamma) & K_D &= K_5 - K_1 + (1 + K_4) \cos(\theta_1 - \gamma) \\ K_E &= -2 \sin(\theta_1 - \gamma) & K_F &= K_1 + K_5 + (K_4 - 1) \cos(\theta_1 - \gamma) & K_1 &= \frac{l_4}{l_1} \\ K_2 &= \frac{l_4}{l_3} & K_3 &= \frac{l_1^2 - l_2^2 + l_3^2 + l_4^2}{2l_1 l_3} & K_4 &= \frac{l_4}{l_2} & K_5 &= \frac{-l_1^2 - l_2^2 + l_3^2 - l_4^2}{2l_1 l_2} \end{aligned}$$

Each solution corresponds to the two configurations of the four-bar linkage in which the mechanism can be assembled for the pre-set dimensions and the angular position of link O_1A . At this stage, the mechanism whose configuration has been generated is not known, therefore the errors for both signs at the square roots in Eqs. (2.16) are computed and the more accurate solution is taken into account.

Then the position of the point D at the instant when the angular position of the input link measured from the horizontal line equals to $\theta_{1i} + \theta_{10}$ is determined from the equations

$$\begin{aligned} x_{Di} &= x_{O1} + l_1 \cos(\theta_{1i} + \theta_{10}) + l_5 \cos[\theta_2(\theta_{1i} + \theta_{10} - \gamma) + \theta_4 + \gamma] \\ y_{Di} &= y_{O1} + l_1 \sin(\theta_{1i} + \theta_{10}) + l_5 \sin[\theta_2(\theta_{1i} + \theta_{10} - \gamma) + \theta_4 + \gamma] \end{aligned} \quad (2.17)$$

The angular position of the crank with respect to the axis O_1O_2 equals $\theta_{1i} + \theta_{10} - \gamma$. Therefore, this angle is taken to compute θ_2 from Eq. (2.16). In the references, the absolute Euclidian error between the points given and generated is defined as follows

$$E = \sum_{i=1}^n [(x_{Di} - x_i)^2 + (y_{Di} - y_i)^2] \quad (2.18)$$

2.3. Optimisation technique

The evolutionary algorithm (EA) (Goldberg, 1989) minimises the objective function (Eq. (2.15)). The technique is described in depth in (Buřkiewicz, 2010, 2015). Preliminary numerical simulations were performed to establish the parameters controlling the EA:

- The size of the population $N_{max} = 80$ (case I), $N_{max} = 50$ (cases II and III).
- The number of individuals to be crossed over in each generation $l_{cr} = 30$.
- The number of randomly generated individuals introduced to each population in the place of the worst fitted ones $l_{rnd} = 25$.
- A feature of the new individual (N) is inherited from the parent (I) with the probability $p_b = 0.75$ (from parent (II) with the probability 0.25).
- The initial value of the mutation coefficient $\lambda = 0.05$ (the value is gradually decreased to 0.005), the initial disturbance coefficient $\mu = 0.001$ is gradually decreased to 0.00001).
- The minimum value of the error function (objective function) E_{min} depends on the case being solved.
- The maximum number of iterations executed (generations) in the case of not achieving the prescribed minimum value of the error function $L_g = 10\,000$.

3. Numerical solutions

To prove the effectiveness of the method, three examples are solved and discussed. Two of them are taken from references and comparative analysis is carried out.

For all cases presented the points are gathered in sets in the forms as follows: $tab = \{(x_i, y_i, \theta_{1i}), i = 1, \dots, n\}$. The coordinates are non-dimensional, the angles are in radians.

Case 1

The first case was presented by Acharyya and Mandal (2009). The authors of this paper considered the synthesis with timing defined by data given in tab_1

$$\begin{aligned} tab_1 = \{ & (0, 0, 0.5236), (1.9098, 5.878, 1.0472), (6.9098, 9.511, 1.5708), (13.09, 9.511, 2.0944), \\ & (18.09, 5.878, 2.618), (20, 0, 3.1416) \} \end{aligned}$$

The input geometric constraints were:

- the range of the coordinates of the crank pivot: $-50 \leq x_{O1}, y_{O1} \leq 50$,
- the lengths of the crank: $5 \leq l_1 \leq 50$, and of the coupler: $5 \leq l_2 \leq 50$.

The computational time was 00:01:14 with 1000 iterations (generations in EA – 80 000 evaluations of the objective function) performed. The evaluations of chosen parameters are shown in Fig. 2a. The progress of the absolute Euclidian error is presented in Fig. 2b.

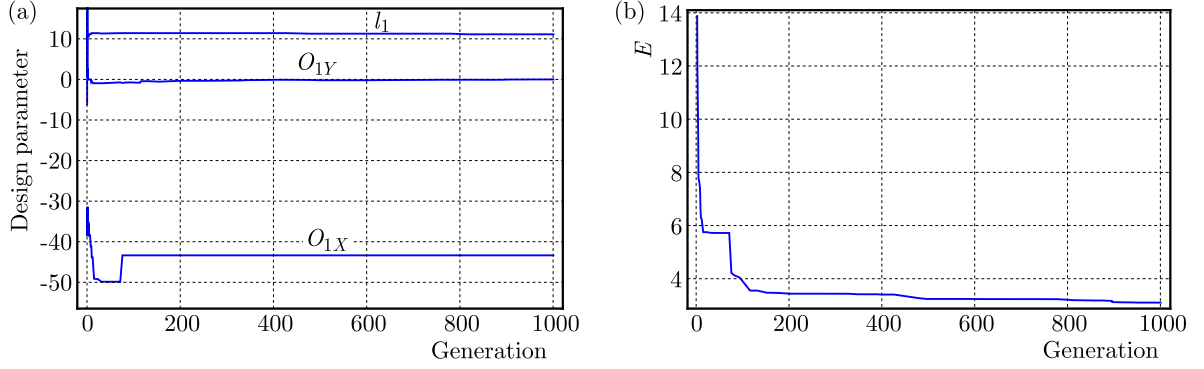


Fig. 2. (a) Evaluation of the crank length and crank pivot coordinates. (b) Evaluation of the Euclidian distance

It is visible from Figs. 2a,b that the areas surrounding the found values of parameters are localised in the first 200 iterations. The best solution of the problem with installing parameters for the first position (Fig. 3) is: $l_1 = 11.1149$, $l_2 = 42.6226$, $\theta_4 = -0.1368$ rad, $\gamma = 6.2819$ rad, $\theta_{10} = 3.29$ rad, $l_3 = 11.9381$, $l_5 = 52.4112$, $l_4 = 43.30492$, $O_1(-43.3598, -0.0067)$, $O_2(-0.0549, -0.0609)$, $D(-0.143478, 0.271792)$, $A(-52.058, -6.92637)$, $B(-11.032, 4.63172)$ and $\theta_1 = \theta_{10} + \theta_{11}(= \text{tab}_{11,3}) = 3.8136$ rad (the angle is measured from the horizontal line).

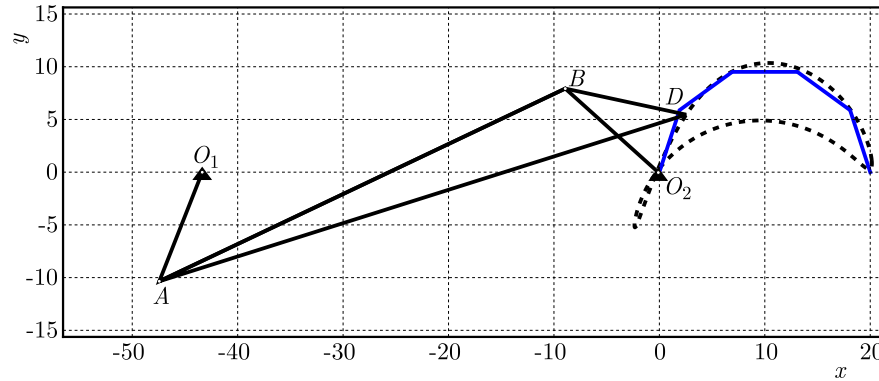


Fig. 3. Case 1: Synthesised four-bar linkage with paths given (continuous line) and generated (dashed line)

The method error $\delta = 2.767$, and the absolute Euclidian error $E = 2.10037$. Three EAs namely Genetic Algorithm (GA), Particle Swarm Optimization (PSO) and Differential Evolution (DE) were applied separately in (Acharyya and Mandal, 2009). The best solution obtained using DE is presented in Table 1. The error reported by the authors is 2.349649, whereas the error computed for the corresponding mechanism dimensions is 5.52074 – this difference was also observed by Ebrahimi and Payvandy (2015). In all addressed methods 100 000 or 200 000 evaluations of the objective function were performed, whereas in the presented paper there were 80 000. The four-bar linkages generating this path were also determined in (Ebrahimi and Payvandy, 2015) using: imperialist competitive algorithm (ICA) and parallel simulated annealing

(SA). The best solution is also presented in Table 1. Ebrahimi and Payvandy also solved the problem of the path synthesis with workspace limits, which is not here considered. The ICA and EA differ from each other in terms of the structure and, therefore, it is difficult to compare their computational costs of the evaluations of the objective functions.

Table 1. Path 1: comparison of results

	Acharyya and Mandal (2009) DE	Ebrahimi and Payvandy (2015) ICA	Proposed
l_1	5	5	11.1149
l_2	5.905345	7.08248	42.6226
l_3	50	48.05733	11.9381
l_4	50	50	43.30492
l_5	18.819312	21.3969	52.4112
θ_4	0	0.6956	-0.1368
x_{O1}	14.373772	11.88034	-43.3598
y_{O1}	-12.444295	-16.08766	-0.0067
γ	0.463633	6.2831853	6.2819
θ_{10}	–	–	3.29
E	5.52074	2.5998	2.10037

Case 2

Kunjur and Krishnamurty (1997) presented the synthesis with timing of the path given by 18 points:

$$\begin{aligned}
 tab_2 = \{ & (0.5, 1.1, 0.3491), (0.4, 1.1, 0.6981), (0.3, 1.1, 1.0472), (0.2, 1.0, 1.3963), \\
 & (0.1, 0.9, 1.7453), (0.05, 0.75, 2.0944), (0.02, 0.6, 2.4435), (0, 0.5, 2.7925), (0, 0.4, 3.1416), \\
 & (0.03, 0.3, 3.4907), (0.1, 0.25, 3.8397), (0.15, 0.2, 4.1888), (0.2, 0.3, 4.5379), \\
 & (0.3, 0.4, 4.8869), (0.4, 0.5, 5.2360), (0.5, 0.7, 5.5851), (0.6, 0.9, 5.9341), (0.6, 1, 6.2832) \}
 \end{aligned}$$

The range for the coordinates of the crank pivot is: $-50 \leq x_{O1}, y_{O1} \leq 50$. The lengths of the crank and coupler l_1, l_2 cannot exceed 50. The computational time is 00:00:36. Within this time, 200 iterations have been performed – the number of evaluations of the objective function is 10 000. The optimum solution is expressed as follows: $l_1 = 0.4102$, $l_2 = 1.2166$, $\theta_4 = 0.8342853$ rad, $\gamma = 0.1110$ rad, $l_3 = 1.1230$, $l_5 = 0.7859$, $l_4 = 1.5395$, $\theta_{10} = 0.8721$ rad.

These parameters are completed with installing parameters for the first position (Fig. 4): $O_1(0.363, -0.0874)$, $O_2(1.8931, 0.0831)$, $D(0.516114, 1.08379)$, $A(0.503501, 0.297987)$, $B(1.41786, 1.10058)$, $\theta_1 = \theta_{10} + \theta_{11}(= tab_{21,3}) = 1.2212$ rad.

The absolute Euclidian error $E = 0.0185453$, and the method error $\delta = 0.1821$. Taking into account the solutions obtained by means of the EAs (Kunjur and Krishnamurty, 1997; Cabrera *et al.* 2011; Nadal *et al.* 2015), the method presented in this paper gives the best solution. The number of evaluations of the objective functions in these methods is 5000. In order to provide higher repeatability, when 34 in 100 algorithm executions give the solution with error $E < 0.02$, twice as many evaluations of the objective function in the presented method are taken. In order to obtain more accurate solutions, Lin and Hsiao (2017) employed the Cuckoo Search (CS) and teaching-learning-based optimization (TLBO) algorithms (200 001 evaluations of the objective function – twice as many evaluations resulted only in the smaller values of the mean error

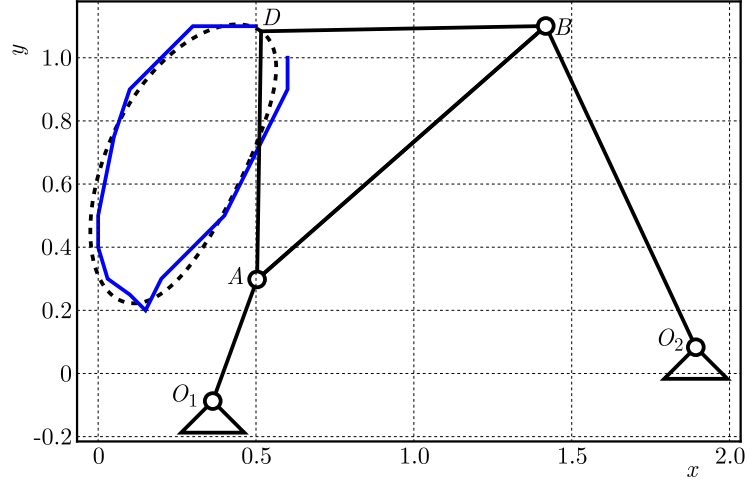


Fig. 4. Case 2: Synthesised four-bar linkage with paths given (continuous line) and generated

and standard deviation). The Modified Krill Herd algorithm applied by Bulatović *et al.* (2016) produced the same degree of accuracy. The number of the objective function evaluations in the MKH algorithm is the product of the number of iterations and the number of repetitions – both parameters are equal to 50. Compared with the EAs, the computational cost of one evaluation of the objective function seems to be higher. This issue, however, was not discussed in (Bulatović *et al.*, 2016) since the MKH, as was the case with the ICA, differed from the EA in performance. All the results are summarised in Table 2.

Table 2. Path 2: comparison of the results

	Kunjur and Krishnamurty (1997)	Cabrera <i>et al.</i> (2011)	Nadal <i>et al.</i> (2015)	Bulatović <i>et al.</i> (2016)	Lin and Hsiao (2017)	Proposed
l_1	0.274853	0.297057	0.239834	0.4218	0.4238752	0.4102
l_2	1.180253	3.913095	0.941660	0.87821	0.9142488	1.2166
l_3	2.138209	0.849372	3.164512	0.58013	0.5989170	1.1230
l_4	1.879660	4.453772	2.462696	1.00429	1.0539434	1.5395
l_5	0.91561	2.65198	0.4834	0.5234	0.54481	0.7859
θ_4	3.5680854	2.464734	1.5638233	0.8147729	0.822721	0.8342853
x_{O1}	1.132062	-1.309243	0.569026	0.26886	0.2676546	0.363
y_{O1}	0.663433	2.806964	0.350557	0.17715	0.1546514	-0.0874
γ	4.354224	2.7387359	4.788536	0.29294	0.2848225	0.1110
θ_{10}	2.558625	4.853543	2.47266	0.88595	0.8915568	0.8721
E	0.043	0.0196	0.113595	0.00911	0.0090289	0.0185453

Case 3

The set tab_3 presents the straight line discretised by 6 points with the crank positions assigned to

$$tab_3 = \left\{ (5.0000, 1.000, 0.3491), (4.0000, 1.000, 0.6981), (3.0000, 1.000, 1.0472), \right. \\ \left. (2.0000, 1.000, 1.3963), (1.0000, 1.000, 1.7453), (0.0000, 1.000, 2.0944) \right\}$$

The input geometric constraints define the range for the crank pivot coordinates: $-25 \leq x_{O1}$, $y_{O1} \leq 25$, and the maximum permissible lengths of the crank and coupler equal to 15. The

computational time is 00:00:47 with 1000 iterations performed for $N_{max} = 50$. The geometric parameters of the optimum mechanism are as follows: $l_1 = 1.7930$, $l_2 = 6.6176$, $\theta_4 = 0.4732$ rad, $\gamma = 2.6679$ rad, $\theta_{10} = 4.5633$ rad, $l_3 = 6.6175$, $l_5 = 11.7914$, $l_4 = 3.475$.

The absolute Euclidian error $E = 0.0000173$, and method error $\delta = 0.0038$. Taking into account the absolute error, one can state that the solution is very accurate. The installing parameters for the first position (Fig. 5) are: $O_1(5.5219, -9.0021)$, $O_2(2.4294, -7.4167)$, $D(4.99683, 0.99906)$, $A(5.87813, -10.7594)$, $B(8.44532, -4.65988)$. $\theta_1 = \theta_{10} + \theta_{11}(= \text{tab}_{31,3}) = 4.9124$ rad.

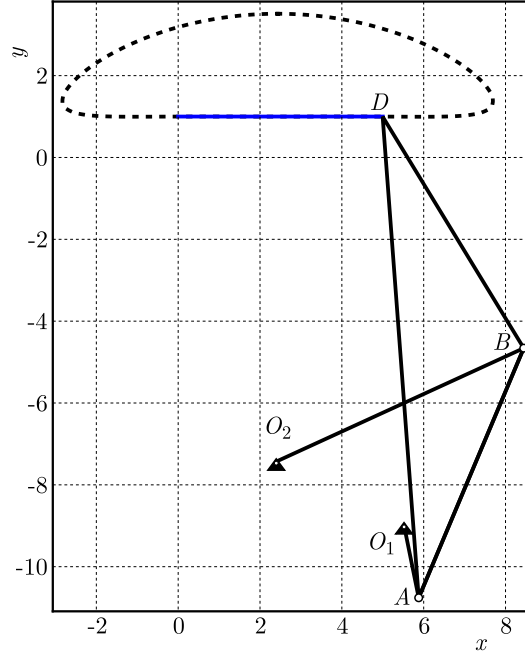


Fig. 5. Case 3: Synthesised four-bar linkage with paths given (continuous line) and generated

4. Conclusion

As mentioned in the introduction, two main branches have been developed recently in the field of mechanism synthesis. The first one deals with the enhancement of probabilistic deterministic algorithms. The other focuses on the minimisation of the number of design variables. It is difficult to find papers on the reduction of the number of design parameters in the case of open/closed-path synthesis with timing in the one-phase path synthesis. The presented method tries to overcome these difficulties and this is the distinctive feature of the method. Free paths are considered to investigate the effectiveness of the method. Although the algorithm employed in this paper utilizes the classical EA, the results of the synthesis are comparable to the best of those presented in the literature. The analysis performed is encouraging for further studies in developing the methods decreasing the number of design parameters, which may be an alternative to more complex, frequently hybrid, new optimisation algorithms. The method, although presented on the example of a four-bar linkage, can be applied in synthesis of other four-link planar mechanisms: crank-slider mechanism and mechanism with slotted links using techniques described in (Buśkiewicz, 2015).

One can formulate some general observations on the way the results obtained by many authors are compared. First of all, it seems reasonable to take into account some measure which reflects the ratio of sizes of the mechanism and the synthesised path. Frequently, the working space occupied by the optimal mechanism when tracing the path is much larger than the space enclosed by the path alone. Such a solution is frequently useless for practical implementation.

Moreover, in the case of an open-path synthesis, the general tendency is that a better solution is characterised by a smaller ratio of the length of the synthesised part to the total path length. This means that the path is generated for a very small angle of rotation of the input link, and the greater part of the mechanism motion is dead motion. Therefore, the comparison of different methods based on the values of the objective functions should only be concluded very carefully.

Such an approach to mechanism synthesis, which consists of reducing the number of design parameters, imposes distinction between the problems with and without timing. In other methods, when the problem without timing is considered, the orientations of the input link corresponding with the coupler point synthesis are treated as additional design parameters.

Acknowledgment

This research was funded by Polish Ministry of Science and Higher Education (the grant DS 02/21/DSPB/3493).

References

1. ACHARYYA S.K., MANDAL M., 2009, Performance of EAs for four-bar linkage synthesis, *Mechanism and Machine Theory*, **44**, 9, 1784-1794
2. AVILÉS R., VALLEJO J., FERNÁNDEZ DE BUSTOS I., AGUIRREBEITIA J., AJURIA G., 2010, Optimum synthesis of planar linkages using a strain-energy error function under geometric constraints, *Mechanism and Machine Theory*, **45**, 65-79
3. BULATOVIĆ R.R., DORDEVIĆ S.R., 2009, On the optimum synthesis of a four-bar linkage using differential evolution and method of variable controlled deviations, *Mechanism and Machine Theory*, **44**, 235-246
4. BULATOVIĆ R.R., DORDEVIĆ S.R., DORDEVIĆ V.S., 2013, Cuckoo Search algorithm: A meta-heuristic approach to solving the problem of optimum synthesis of a six-bar double dwell linkage, *Mechanism and Machine Theory*, **61**, 1-13
5. BULATOVIĆ R.R., MIODRAGOVIĆ G., BOŠKOVIĆ M.S., 2016, Modified Krill Herd (MKH) algorithm and its application in dimensional synthesis of a four-bar linkage, *Mechanism and Machine Theory*, **95**, 1-21
6. BUŚKIEWICZ J., 2010, Use of shape invariants in optimal synthesis of geared five-bar linkage, *Mechanism and Machine Theory*, **45**, 273-290
7. BUŚKIEWICZ J., 2015, A method for optimal path synthesis of four-link planar mechanisms, *Inverse Problems in Science and Engineering*, **23**, 818-850
8. BUŚKIEWICZ J., STAROSTA R., WALCZAK T., 2009, On the application of the curve curvature in path synthesis, *Mechanism and Machine Theory*, **44**, 1223-1239
9. CABRERA J.A., NADAL F., MUNOZ J.P., SIMON A., 2007, Multiobjective constrained optimal synthesis of planar mechanisms using a new evolutionary algorithm, *Mechanism and Machine Theory*, **42**, 791-806
10. CABRERA J.A., ORTIZ A., NADAL F., CASTILLO J.J., 2011, An evolutionary algorithm for path synthesis of mechanisms, *Mechanism and Machine Theory*, **46**, 127-141
11. CABRERA J.A., SIMON A., PRADO M., 2002, Optimal synthesis of mechanisms with genetic algorithms, *Mechanism and Machine Theory*, **37**, 10, 1165-1175
12. CHU J., SUN J., 2010, Numerical atlas method for path generation of spherical four-bar mechanism, *Mechanism and Machine Theory*, **45**, 6, 867-879
13. EBRAHIMI S., PAYVANDY P., 2015, Efficient constrained synthesis of path generating four-bar mechanisms based on the heuristic optimization algorithms, *Mechanism and Machine Theory*, **85**, 189-204

14. ERDMAN A.G., SANDOR G.N., KOTA S.S., 2001, *Mechanism Design: Analysis and Synthesis*, 4th Ed. (Web Enhanced), Volume I, Prentice-Hall
15. GALÁN-MARÍN G.F., ALONSO J., DEL CASTILLO J.M., 2009, Shape optimization for path synthesis of crank-rocker mechanisms using a wavelet-based neural network, *Mechanism and Machine Theory*, **44**, 6, 1132-1143
16. GOGATE G.R., MATEKAR S.B., 2012, Optimum synthesis of motion generating four-bar mechanisms using alternate error functions, *Mechanism and Machine Theory*, **54**, 41-61
17. GOLDBERG D.E., 1989, *Genetic Algorithms in Search, Optimization and Machine Learning*, Addison Wesley, Massachusetts
18. HOELTZEL D.A., CHIENG W.H., 1990, Pattern matching synthesis as an automated approach to mechanical design, *Journal of Mechanical Design*, **112**, 2, 190-199
19. KAFASH S.H., NAHVI A., 2015, Optimal synthesis of four-bar motion generator linkages using circular proximity function, *Proceedings of the Institution of Mechanical Engineers Part C Journal of Mechanical Engineering Science*, **203-210**, 1989-1996
20. KHORSHIDI M., SOHEILYPOUR M., PEYRO M., ATAI A., PANAH M.S., 2011, Optimal design of four-bar mechanisms using a hybrid multi-objective GA with adaptive local search, *Mechanism and Machine Theory*, **46**, 10, 1453-1465
21. KINZEL E.C., SCHMIEDELER J.P., PENNOCK G.R., 2006, Kinematic synthesis for finitely separated positions using geometric constraint programming, *Journal of Mechanical Design*, **128**, 5, 1070-1079
22. KUNJUR A., KRISHNAMURTY S., 1997, Genetic algorithms in mechanical synthesis, *Journal of Applied Mechanisms and Robotics*, **4**, 2, 18-24
23. LIN W.Y., 2010, A GA-DE hybrid evolutionary algorithm for path synthesis of four-bar linkage, *Mechanism and Machine Theory*, **45**, 8, 1096-1107
24. LIN W.Y., 2014, Optimization of scale-rotation-translation synthesis after shape synthesis for path generation of planar mechanisms, *Journal of the Chinese Institute of Engineers*, **37**, 4, 497-505
25. LIN W.Y., 2015, Optimum synthesis of planar mechanisms for path generation based on a combined discrete Fourier descriptor, *Journal of Mechanisms and Robotics*, **7**, 4, 041023-041023
26. LIN W.Y., HSIAO K.M., 2017, Cuckoo search and teaching-learning-based optimization algorithms for optimum synthesis of path-generating four-bar mechanisms, *Journal of the Chinese Institute of Engineers*, **40**, 1, 66-74
27. LIO M.D., 1997, Robust synthesis of linkages—synthesis by solving non-linear optimization problem, *Mechanism and Machine Theory*, **32**, 8, 921-932
28. LIO M.D., COSSALTER V., LOT R., 2000, On the use of natural coordinates in optimal synthesis of mechanisms, *Mechanism and Machine Theory*, **35**, 10, 1367-1389
29. MATEKAR S.B., GOGATE G.R., 2012, Optimum synthesis of path generating four-bar mechanisms using differential evolution and a modified error function, *Mechanism and Machine Theory*, **52**, 158-179
30. MCGARVA J., MULLINEUX G., 1993, Harmonic representation of closed curves, *Applied Mathematical Modelling*, **17**, 4, 213-218
31. MCGARVA J.R., 1994, Rapid search and selection of path generating mechanisms from a library, *Mechanism and Machine Theory*, **29**, 2, 223-235
32. MULLINEUX G., 2011, Atlas of spherical four-bar mechanisms, *Mechanism and Machine Theory*, **46**, 11, 1811-1823
33. NADAL F., CABRERA J.A., BATALLER A., CASTILLO J.J., ORTIZ A., 2015, Turning functions in optimal synthesis of mechanisms, *Journal of Mechanical Design*, **137**, 6, 062302 (10 pages)

34. PENUNURI F., PEÓN-ESCALANTE R., VILLANUEVA C., PECH-OY D., 2011, Synthesis of mechanisms for single and hybrid tasks using differential evolution, *Mechanism and Machine Theory*, **46**, 10, 1335-1349
35. SANCHEZ MARIN F.T., GONZALEZ. A.P., 2004, Open-path synthesis of linkages through geometrical adaptation, *Mechanism and Machine Theory*, **39**, 943-955
36. SANCIBRIAN R., VIADERO F., GARCÍA P., FERNÁNDEZ A., 2004, Gradient-based optimization of path synthesis problems in planar mechanisms, *Mechanism and Machine Theory*, **39**, 8, 839-856
37. SCHMIEDELER J.P., CLARK B.C., KINZEL E.C., PENNOCK G.R., 2014, Kinematic synthesis for infinitesimally and multiply separated positions using geometric constraint programming, *Journal of Mechanical Design*, **136**, 3, 034503 (7 pages)
38. SHIAKOLAS P.S., KOLADIYA D., KEBRLE J., 2002, On the optimum synthesis of four-bar linkages using differential evolution and the geometric centroid of precision positions, *Inverse Problems in Science and Engineering*, **10**, 6, 485-502
39. SHIAKOLAS P.S., KOLADIYA D., KEBRLE J., 2005, On the optimum synthesis of six-bar linkages using differential evolution and the geometric centroid of precision positions technique, *Mechanism and Machine Theory*, **40**, 319-335
40. SMAILI A., DIAB N., 2007, A new approach to shape optimization for closed-path synthesis of planar mechanisms, *Journal of Mechanical Design*, **129**, 9, 941-948
41. SMAILI A.A., DIAB N.A., ATALLAH N.A., 2005, Optimum synthesis of mechanisms using Tabu-Gradient search Algorithm, *Journal of Mechanical Design*, **127**, 917-923
42. SUN J., LIU W., CHU J., 2015, Dimensional synthesis of open-path generator of four-bar mechanisms using the haar wavelet, *Journal of Mechanical Design*, **137**, 8, 082303 (8 pages)
43. SUN J.W., CHU J.K., 2009, Fourier method to function synthesis of an RCCC mechanism, *Proceedings of the Institution of Mechanical Engineers, Part C: Journal of Mechanical Engineering Science*, **223**, 2, 503-513
44. ULLAH I., KOTA S., 1997, Optimal synthesis of mechanisms for path generation using Fourier descriptors and global search methods, *Journal of Mechanical Design*, **119**, 504-510
45. VASILIU A., YANNOU B., 2001, Dimensional synthesis of planar mechanisms using neural networks: application to path generator linkage, *Mechanism and Machine Theory*, **36**, 2, 299-310
46. YU H., TANG D., WANG Z., 2007, Study on a new computer path synthesis method of a four-bar linkage, *Mechanism and Machine Theory*, **42**, 4, 383-392
47. YUE C., SU H.J., GE Q.J., 2012, A hybrid computer-aided linkage design system for tracing open and closed planar curves, *Computer-Aided Design*, **44**, 11, 1141-1150
48. ZAHN T., ROSKIES R.Z., 1972, Fourier descriptors for plane closed curves, *IEEE Transactions on Computers*, **21**, 3, 269-281

ANNULAR ROTATING DISKS OPTIMAL WITH RESPECT TO MIXED CREEP RUPTURE

ANETA USTRZYCKA

Institute of Fundamental Technological Research, Polish Academy of Sciences, Warsaw, Poland
e-mail: austrzycka@ippt.pan.pl

KRZYSZTOF SZUWALSKI

Cracow University of Technology, Faculty of Mechanical Engineering, Institute of Applied Mechanics, Cracow, Poland

Optimal shapes in the class of polynomial functions for rotating annular disks with respect to the mixed creep rupture time are found. Two effects leading to damage: diminishing of transversal dimensions and growth of micro-cracks are simultaneously taken into account. The first of them requires the finite strain analysis, the latter is described by Kachanov's evolution equation. Behaviour of the material is described by nonlinear Norton's law, generalized for true stresses and logarithmic strains, and the shape change law in form of similarity of true stresses and logarithmic strains deviators. For optimal shapes of the disk, changes of geometry and a continuity function are presented. The theoretical considerations based on the perception of the structural components as some highlighted objects with defined properties is presented.

Keywords: annular disk, mixed creep rupture, optimal design

1. Introduction

The problems of optimal design in creep conditions are rather new ones, they started at the end of the last century. The difficulty, first of all, is connected with a new additional variable – time. On the other hand, such problems offer new possibilities of formulation of optimization problems (Betten, 2001). Życzkowski (1971, 1988) pointed out some new optimization criteria such as: stress relaxation, limitation of displacements or their velocities at a given time, and time to creep rupture, which seems to be the most important one. Many solutions were found for structures with maximal time to brittle creep rupture (Białkiewicz, 1986; Ganczarski and Skrzypek, 1976; Piechnik and Chrzanowski, 1970; Rysz, 1987). Such problems are comparatively simpler, because they may be solved within the framework of the small strain theory. Optimal shapes often coincide with shapes of uniform initial strength. Much more complicated are problems of optimization using other theories of creep rupture: ductile and mixed. Both of them are connected with large deformations and require the finite strain theory. Therefore, solutions of optimal design with respect to ductile (Hoff, 1953) or mixed rupture time (Kachanov, 1960, 1999) are rather scarce. Till now, only optimal rotating bars and rotating disks with respect to ductile rupture were found by Szuwalski (1989, 1995). Some problems of prismatic rods under tension were discussed by Golub *et al.* (2008). The ductile creep rupture analysis for elastoplastic disks was carried by Dems and Mróz (1992), Ahmet and Erslan (2003), Çalloğlu *et al.* (2006), Farshi and Bidabadi (2008), Jahed *et al.* (2005) and Gun (2008). Modifications of the Hoff model was proposed by Golub and Teteruk (1994). The influence of boundary conditions on the optimal shape was investigated by Pedersen (2001) and Szuwalski and Ustrzycka (2013). Even more difficult are problems of optimal design with respect to mixed creep rupture time as, besides large strains, they take into account damage development. The first solutions for optimal structures were found by Szuwalski and Ustrzycka (2012, 2013).

2. Formulation of the problem

In the present paper, the initial shape of a rotating annular disk of given internal and external radii A and B and given volume V (Fig. 1) ensuring the longest time to mixed creep rupture time is sought. For the annular disk of the given volume V , initial thickness H and initial radii A, B rotating with constant angular velocity ω , made of a material with known properties with mass M uniformly distributed at the outer edge, the optimization problem is stated as follows:

- for given $V, A, B, \omega, \gamma, M$
- we look for the initial profile of the disk $H(R; b_0, b_1, b_2) = b_0 + b_1 R + b_2 R^2$
- that $t_*^{(m)} \rightarrow \max$

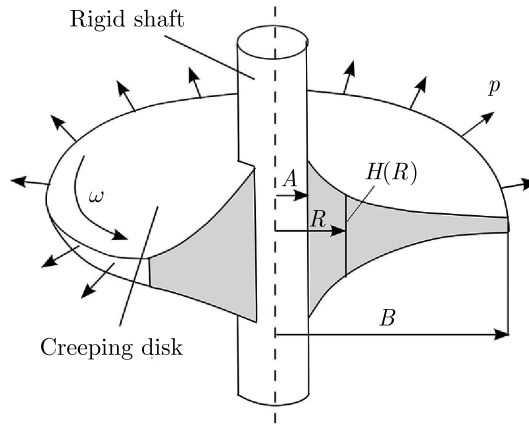


Fig. 1. Model of the annular rotating disk

The problem seems to be of great importance because in such a way rotors of jet engines, power plant turbines working in high temperatures may be calculated. In such structures, the creep effects must be taken into account, additionally of great importance are body forces. The axially symmetric problem (all variables depend only on one material coordinate, radius) is described using the material, Lagrangean coordinate denoted by capital R . The corresponding special coordinate r is the radius of the considered point of the disk after deformation and R is the radius of the considered point of the disk prior to deformation. The external loading of the disk results from the centrifugal force acting on the blades of total mass M put at the outer edge of the disk on the assumption that they are uniformly distributed. Moreover, the body forces connected with own mass of the disk are taken into consideration. What makes the problem more difficult is that both loadings depend on the spatial coordinate and change within the creep process. The condition of internal equilibrium derived for an already deformed element of the disk takes form

$$\frac{1}{hr'} \frac{\partial}{\partial R} (h\sigma_r) + \frac{\sigma_r - \sigma_\vartheta}{r} + \frac{\gamma}{g} \omega^2 r = 0 \quad (2.1)$$

where r' denotes the derivative of spatial coordinate with respect to the material one, h – current thickness of the disk. By “primes” in all formulas are denoted derivatives with respect to the material coordinate, while by overdots – with respect to time. The disk rotates with constant angular velocity ω and is made of a material with the specific weight γ . Radial and circumferential stresses are true stresses related to already deformed cross-sections. The stress orthogonal to the plane of the disk is disregarded (plane stress state assumption). Consequently, for large deformations, the logarithmic strains are introduced. They are connected with true stresses by Norton’s law

$$\dot{\epsilon}_e = k\sigma_e^n \quad (2.2)$$

here expressed by true stresses and logarithmic strains and generalized for complex stress state with the help of the Huber-Mises-Hencky hypothesis

$$\sigma_e = \sqrt{\sigma_r^2 + \sigma_\vartheta^2 - \sigma_r \sigma_\vartheta} \quad (2.3)$$

The shape change law is adopted in form of similarity of true stresses and logarithmic strains deviators, in which the creep modulus φ_c is equal to

$$\varphi_c = k\sigma_e^{n-1} \quad (2.4)$$

This leads to the relationship

$$\frac{\dot{r}}{r} = \frac{1}{2}k\sigma_e^{n-1}(2\sigma_\vartheta - \sigma_r) \quad (2.5)$$

Additionally, the compatibility equation for axially symmetric logarithmic strains

$$\varepsilon_r = \varepsilon_\vartheta + \ln\left(1 + R\frac{\partial\varepsilon_\vartheta}{\partial R}\right) \quad (2.6)$$

expressed, with the help of the shape change law, by stresses, takes form

$$\sigma'_\vartheta = \frac{6\sigma_e^2(\sigma_r - \sigma_\vartheta)\frac{r'}{r} - \sigma'_r[(n-1)(2\sigma_r - \sigma_\vartheta)(2\sigma_\vartheta - \sigma_r) - 2\sigma_e^2]}{(n-1)(2\sigma_\vartheta - \sigma_r)^2 + 4\sigma_e^2} \quad (2.7)$$

The general assumption of incompressibility of the material may be written

$$HR dR = hr dr \quad (2.8)$$

Large deformations of the disk are accompanied by development of micro-cracks whose effect is described by Kachanov's evolution law

$$\frac{\partial\Psi}{\partial t} = -D\left(\frac{\sigma_e}{\Psi}\right)^m \quad (2.9)$$

where Ψ stands for the continuity function describing the degree of damage of material, D and m stand for material constants. With the help of the above presented equations, the five unknowns: true radial σ_r and circumferential σ_ϑ stresses, spatial coordinate r , current thickness h and continuity function Ψ may be calculated. This can be done only by numerical integration of the derived earlier equations. All unknowns are functions of two independent variables: material coordinate R and time t . For numerical calculations, the dimensionless quantities must be introduced. The full, flat, motionless disk of volume V and radius B subjected to the uniform radial traction s resulting from centrifugal force caused by mass M uniformly distributed at radius B , serves as a comparative disk

$$s = \frac{M\omega^2}{2\pi h_m} = \frac{M\omega^2 B^2}{2V} \quad (2.10)$$

where h_m stands for constant thickness of the comparative disk. The dimensionless stress is related to s (2.10), whereas the dimensionless time is defined as

$$\hat{t} = \frac{t}{t_0^{(d)}} \quad (2.11)$$

where $t_0^{(d)}$ stands for the time of ductile rupture for the full plane disk. To evaluate the time of ductile rupture $t_0^{(d)}$ for the full plane disk, the following equation may be used

$$\dot{\varepsilon}_z = \frac{\dot{h}}{h} = \frac{3}{2}k\sigma_e^{n-1}(\sigma_z - \sigma_m) \quad (2.12)$$

In the problem under consideration, the effective stress is

$$\sigma_e = \sigma_r = \sigma_\vartheta = p \quad (2.13)$$

while the mean stress

$$\sigma_m = \frac{2}{3}p \quad (2.14)$$

The implementation of these substitutions to (2.12) leads to the equation

$$\frac{1}{h} \frac{dh}{dt} = -k \left(\frac{M\omega^2}{2\pi h} \right)^n \quad (2.15)$$

describing the change of thickness in time. The initial condition takes form

$$\text{for } t = 0 \quad h = h_m \quad (2.16)$$

The condition of ductile rupture: $h \rightarrow 0$, enables calculation of the time of ductile rupture $t_0^{(d)}$

$$t_0^{(d)} = \frac{1}{nk \left(\frac{M\omega^2}{2\pi h_m} \right)^n} = \frac{1}{nks^n} \quad (2.17)$$

Finally, dimensionless time (2.11) is defined as

$$\hat{t} = nks^n t \quad (2.18)$$

The dimensionless radii are related to external radius B of the comparative disk and dimensionless thickness to its constant thickness h_m .

Finally, the set of five differential dimensionless equations takes form

$$\begin{aligned} \hat{\sigma}'_r &= \frac{\hat{r}'}{\hat{r}} (\hat{\sigma}_\vartheta - \hat{\sigma}_r) - 2\hat{r}\hat{r}'\mu - \frac{\hat{h}'}{\hat{h}} \hat{\sigma}_r \\ \hat{\sigma}'_\vartheta &= \frac{6\hat{\sigma}_e^2 (\hat{\sigma}_r - \hat{\sigma}_\vartheta) \frac{\hat{r}'}{\hat{r}} - \hat{\sigma}'_r [(n-1)(5\hat{\sigma}_r\hat{\sigma}_\vartheta - 2\hat{\sigma}_r^2 - 2\hat{\sigma}_\vartheta^2) - 2\hat{\sigma}_e^2]}{(n-1)(2\hat{\sigma}_\vartheta - \hat{\sigma}_r)^2 + 4\hat{\sigma}_e^2} \end{aligned} \quad (2.19)$$

and

$$\frac{d\hat{r}}{d\hat{t}} = \frac{\hat{r}}{2n} (\hat{\sigma}_r^2 + \hat{\sigma}_\vartheta^2 - \hat{\sigma}_r\hat{\sigma}_\vartheta)^{\frac{n-1}{2}} (2\hat{\sigma}_\vartheta - \hat{\sigma}_r) \quad \hat{h} = \frac{\hat{H}\hat{R}}{\hat{r}'\hat{r}} \quad (2.20)$$

and

$$\frac{\partial \Psi}{\partial \hat{t}} = \frac{-1}{(m+1)\Theta} \left(\frac{\hat{\sigma}_e}{\Psi} \right)^m \quad (2.21)$$

where all dimensionless quantities are denoted by $(\hat{\bullet})$ over the symbol, and additional parameters μ and Θ are introduced

$$\mu = \frac{\gamma V}{gM} \quad (2.22)$$

where μ is the ratio of own mass of the disk to the mass M uniformly distributed at the outer edge, and Θ contains and replaces four material constants from Norton's law and the evolution equation

$$\Theta = \frac{t_{pr}^{(b)}}{t_{pr}^{(d)}} = \frac{nk}{(m+1)D} s^{n-m} \quad (2.23)$$

and is defined as the ratio of brittle and ductile creep rupture time of prismatic bars subject to tension with stress s (2.10). This parameter may be also treated as a measure of sensitivity on the kind of creep rupture.

We define the rupture criterion in the following form

$$\exists R : \quad R \in \langle 0, l \rangle \wedge \Psi \in \langle 1, 0 \rangle \wedge \Psi(\sigma) \Big|_{t_*^{(m)}} \rightarrow 0 \quad (2.24)$$

The time after which the continuity function diminishes to zero is the time of mixed rupture $t_*^{(m)}$. The criterion of rupture is adopted in form of diminishing to zero the value of the continuity function at least at one nodal point.

3. Numerical calculations

To obtain unique solutions for the above presented set of differential equations, initial and boundary conditions must be formulated. At the beginning of the creep process, the shape of the disk is described by the assumed equation $H(R)$. As the initial condition serves the coincidence of the spatial and material coordinate

$$\hat{r}(\hat{R}, 0) = \hat{R} \quad \hat{h}(\hat{R}, 0) = \hat{H}(\hat{R}) \quad (3.1)$$

The boundary condition at the inner radius A may be formulated in several ways. In the case when the disk is connected with a rigid shaft

$$\hat{\sigma}_r(\beta, \hat{t}) = 2\hat{\sigma}_\vartheta(\beta, \hat{t}) \quad (3.2)$$

the radial stress is two times larger than the circumferential one, but their values are unknown. The parameter β stands for the ratio of radii of the disk: $\beta = A/B$. On the other hand, at the outer radius, the radial stress must be equal to tension caused by the centrifugal force acting on the mass M placed there

$$\hat{\sigma}_r(1, \hat{t}) = \frac{1}{\hat{h}(1, \hat{t})} \quad (3.3)$$

For this reason, a recurrential procedure must be used. Assuming various values of stresses at the radius A , we must finally find such values which will make it possible to satisfy condition (3.3). The numerical algorithm consists of three steps:

- first step – for given geometry of the disk, the true stresses distribution is established (from Eqs. (2.19)). We do not know the values of stresses at the inner edge of the disk, so we assume them arbitrarily. The boundary condition at the outer edge of the disk must be fulfilled (see Fig. 2).
- second step – from the first step, the distribution of true stresses is known. It is possible to establish the new, changed geometry of the disk (from Eqs. (2.20)). The mixed creep rupture can occur earlier than the ductile creep rupture. Therefore, it is necessary to check whether the thickness is not small enough (h_{adm}), which finishes the procedure.
- third step – the distribution of the continuity function Ψ is calculated from Eq. (2.21). If its minimum value satisfies the rupture criterion, the creep process is finished – the time to mixed rupture has been found.

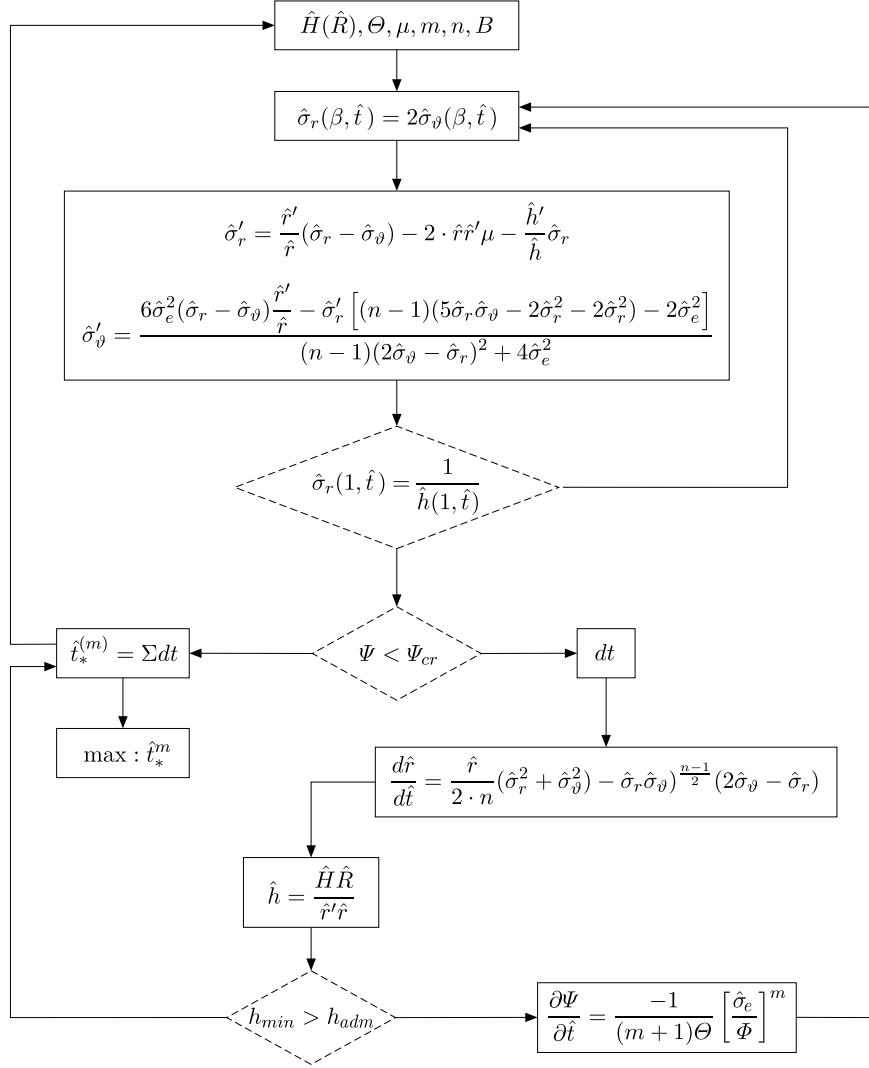


Fig. 2. Algorithm of numerical calculations – flow chart

4. Uniparametric optimization

Due to the inability of explicitly writing the objective function (mixed rupture time) as a function of the optimization parameters (initial profile of the disk), the parametric optimization is applied (search method). Initially, the optimal solution is sought among conical disks whose initial shape is described by the formula

$$\hat{H}(\hat{R}; u_0, u_1) = u_0 + u_1 \hat{R} \quad (4.1)$$

From the condition of constant volume this leads to

$$u_1 = \frac{3}{2}(1 - u_0) \quad (4.2)$$

so only one free parameter u_0 remains.

4.1. Conical disk clamped on a rigid shaft

The optimal solutions of the disks clamped on a rigid shaft for various parameters Θ are presented in Fig. 3.

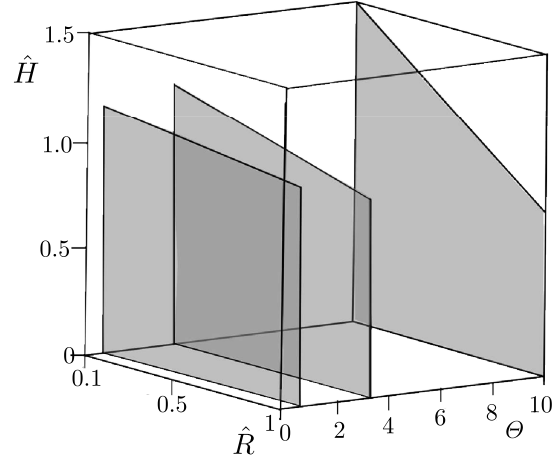


Fig. 3. Optimal profiles of a conical disk clamped on a rigid shaft, $\beta = 0.1$, $\mu = 0.1$

For $\Theta = 0.4$ the optimal profile of the conical disk becomes almost flat. For higher values of the parameter Θ , the mass moves toward the inner edge.

4.2. Conical disk with the free inner edge

The boundary condition at the inner radius is described in the following way

$$\hat{\sigma}_r(\beta, \hat{t}) = 0 \quad (4.3)$$

and at the outer radius by the following equations

$$\hat{\sigma}_r(1, \hat{t}) = \frac{1}{\hat{h}(1, \hat{t})} \quad (4.4)$$

The optimal profiles for the conical disk found according to the algorithm presented in Fig. 2 as a function of the parameter Θ are plotted in Fig. 4.

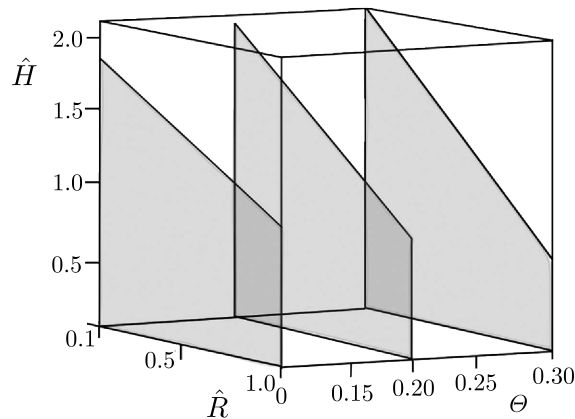


Fig. 4. Optimal profiles of the conical disk with the free inner edge, $\beta = 0.1$, $\mu = 0.1$

The optimal profiles of conical disks with the free inner edge are characterized by a significant reduction of thickness at the outer radius, even larger than that for the disk clamped on a rigid shaft.

5. Biparametric optimization

It is expected that the earlier presented results could be improved by expanding the class of functions, in which the optimal solution is sought. In the next step, biparametric optimization is used. The initial shape is defined by a quadratic function

$$\widehat{H}(\widehat{R}; b_0, b_1, b_2) = b_0 + b_1 \widehat{R} + b_2 \widehat{R}^2 \quad b_2 \neq 0 \quad (5.1)$$

From the three parameters in this function, only two may be treated as free ones, the third results from the given volume of the disk

$$b_2 = 2 - 2b_0 - \frac{4}{3}b_1 \quad (5.2)$$

The search process for biparametric optimization is much more time-absorbing. For the given parameter b_0 , the time to the mixed rupture for various parameters b_1 is calculated. In such a way one may find the parameter b_1 leading to the longest lifetime. This procedure is repeated for subsequent values b_0 . At last the optimal solution is established as “maximum maximorum” of all investigated disks (sometimes almost hundred).

5.1. Parabolic disk clamped on a rigid shaft

The creep process of the annular rotating disk is considered for three different boundary conditions. As the first, the disk clamped on a rigid shaft will be analyzed (e.g. welded connections). Then, despite condition (3.2), an additional condition must be satisfied

$$\widehat{h}(\beta, \widehat{t}) = \widehat{H}(\beta, 0) \quad (5.3)$$

Optimal shapes of the disks for biparametric optimization are shown in Fig. 5.

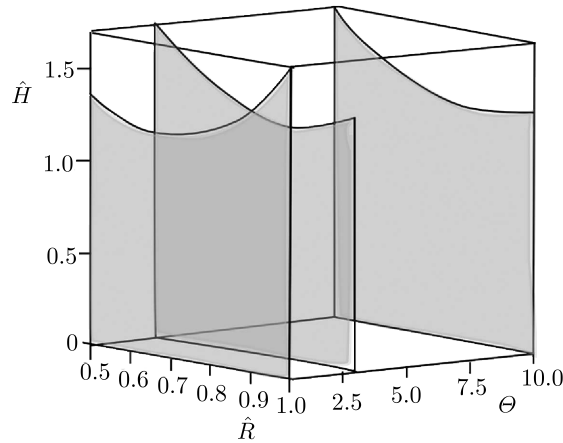


Fig. 5. Optimal shapes of disks clamped on the rigid shaft, $\beta = 0.5$, $\mu = 0.1$

For $\Theta = 0.4$ the optimal shape of the disk is characterized by a large increase of thickness at the external edge. In spite of larger centrifugal forces, the outer edge works as a kind of reinforcement slowing down the creep process. For larger values of the parameter Θ , this effect does not occur.

The course of the creep process for finding the optimal disk with the initial profile described by the function

$$\widehat{H}(\widehat{R}) = 3.51 - 5\widehat{R} + 2.76\widehat{R}^2 \quad (5.4)$$

is presented in Fig. 6 showing changes of the shape (a) and of the distribution of the continuity function (b) in terms of time. The distribution of the continuity function at the moment of rupture is not uniform, the criterion of rupture is fulfilled inside the disk at one point. For other radii, values of the function Ψ are non-zero, and at the inner and outer edge they are quite large. This effect is related only to disks with the initial profile described by quadratic function (5.4).

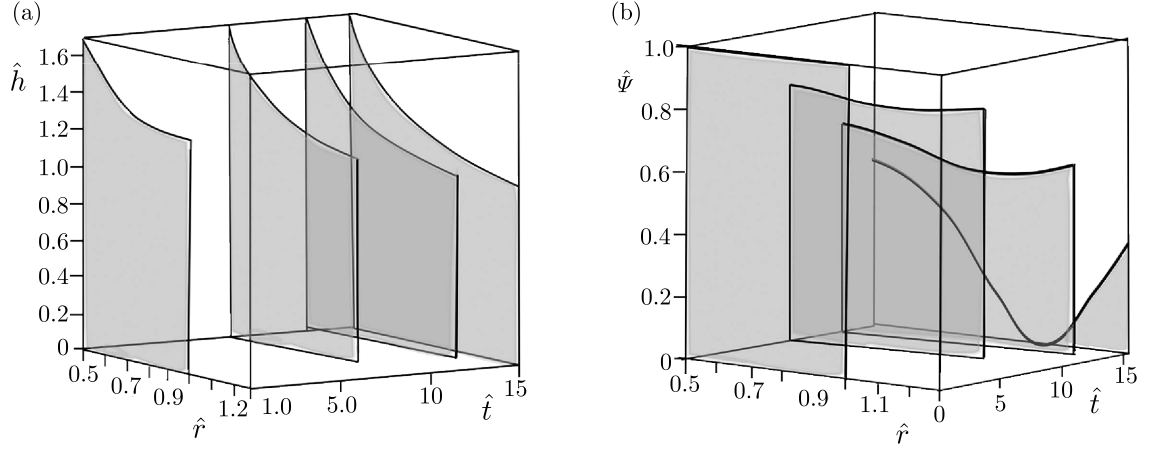


Fig. 6. Time cross-section of the creep process for $\beta = 0.5$, $\mu = 0.1$ and $\Theta = 3$

5.2. Parabolic disk fastened on the rigid shaft with thickness allowed to change

Optimal shapes of disks fastened on a rigid shaft (radial displacement is possible) but with possibility of thickness changing (e.g. spline joint) are shown in Fig. 7.

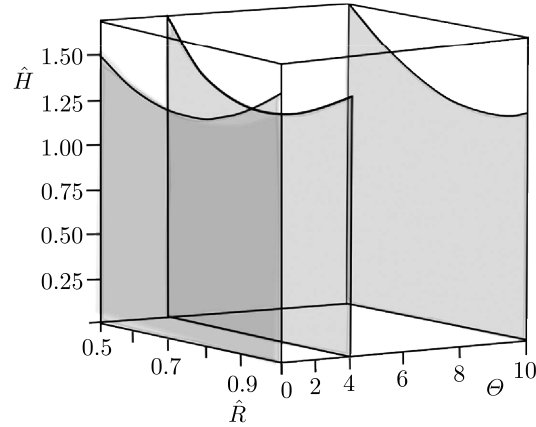


Fig. 7. Optimal shapes of disks fastened on the rigid shaft $\beta = 0.5$, $\mu = 0.1$

For $\Theta = 0.4$ and $\Theta = 3$ the optimal shapes of the disk have a reinforcement of the outer edge (increase of the thickness). For $\Theta = 10$ this effect is smaller.

The above figure drawn for the optimal disk

$$\hat{H}(\hat{R}) = 4.39 - 8\hat{R} + 5.05\hat{R}^2 \quad (5.5)$$

shows the time cross-section of the optimal profile of the annular disk fastened on the rigid shaft (Fig. 8a) and the continuity function (Fig. 8b). The geometrical changes of the profile of the disk in the creep process are not significant. Due to small width of the disk, the change of thickness at the inner edge, although permissible, is not too large.

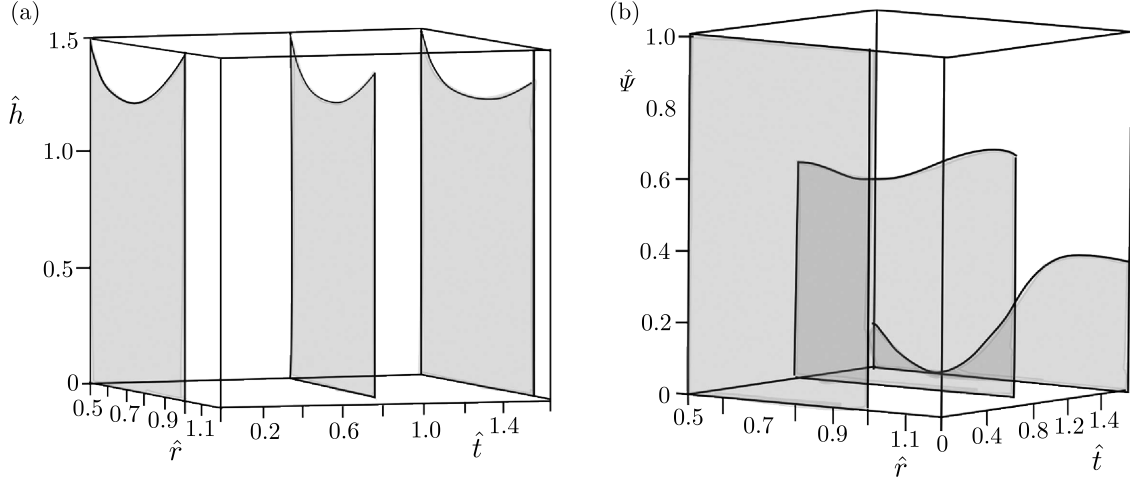


Fig. 8. Time cross-section of the creep process for $\beta = 0.5$, $\mu = 0.1$, $\Theta = 3$

5.3. Parabolic disk with the free inner edge

Optimal shapes of the free disks (4.3) for biparametric optimization are shown in Fig. 9.

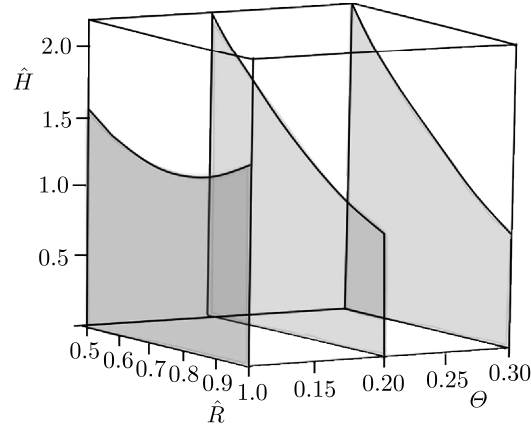


Fig. 9. Optimal shape of the disk with the free inner edge, $\beta = 0.5$, $\mu = 0.1$

The reinforcement of the outer edge of the disk is observed for $\Theta = 0.1$. For $\Theta = 0.2$ and $\Theta = 0.3$ the optimal shapes are characterized by reduction of the thickness of the disk toward the outer edge.

As an example of the found optimal profiles is

$$\hat{H}(\hat{R}) = 4.09 - 5.01\hat{R} + 1.79\hat{R}^2 \quad (5.6)$$

The time cross-section for this optimal profile of the free disk and the continuity function is shown respectively in Figs. 10a and 10b.

The time cross sections of the continuity function indicate that the criterion of rupture of the disk is fulfilled at the inner edge, despite the significant reinforcement of thickness at this point.

6. Corrected disks of uniform initial strength

We expect that disks of uniform initial strength, in which the radial and circumferential stresses are equal and independent of radius, would be close to the optimal profiles with respect to the

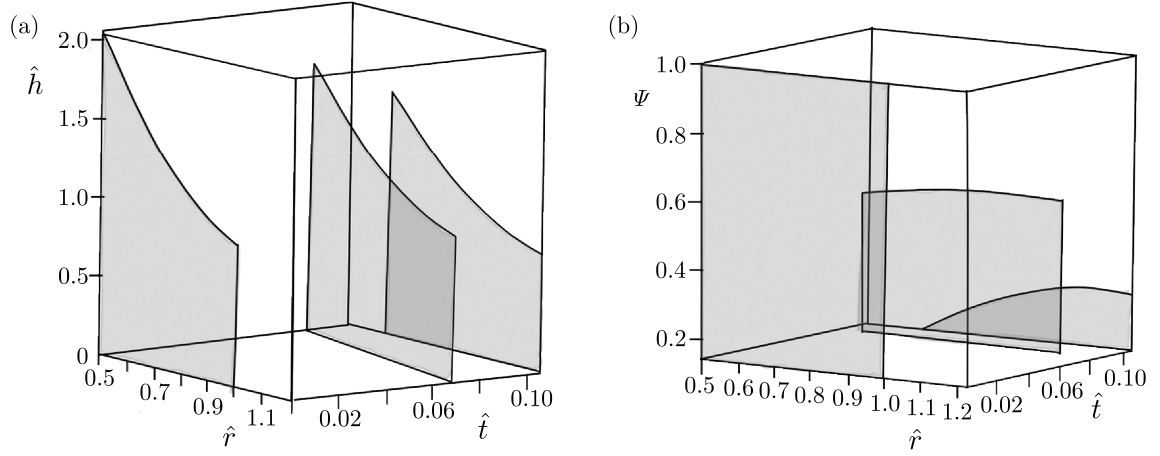


Fig. 10. Time cross-sections of the creep process for the free edge, $\Theta = 0.2$, $\beta = 0.5$, $\mu = 0.1$

mixed rupture time. For a homogeneous material of the uniform initial strength disk, for $t = 0$, the radial Σ_r and circumferential Σ_ϑ stresses are the same

$$\Sigma_r = \Sigma_\vartheta = \Sigma = \text{const}(R) \quad (6.1)$$

and the stress perpendicular to the middle surface of the disk is assumed to be equal to zero ($\sigma_z \equiv 0$).

The shape of uniform initial strength disks results from the internal equilibrium equation

$$\hat{H}_{us}(\hat{R}) = \frac{1}{\hat{\Sigma}} \exp\left[\frac{\mu}{\hat{\Sigma}}(1 - \hat{R}^2)\right] \quad (6.2)$$

where $\hat{\Sigma}$ denotes the dimensionless equalized initial stress calculated from the condition of constant volume

$$\hat{\Sigma} = \frac{\mu}{\ln(1 + \mu)} \quad (6.3)$$

The correction of shape (6.2) is imposed, which is adopted here in form of a third degree polynomial function without linear term

$$\hat{H}_{cor} = p_0 + p_2 \hat{R}^2 + p_3 \hat{R}^3 \quad (6.4)$$

Finally, the initial profile of the disk is described by the equation

$$\hat{H}(\hat{R}) = \hat{H}_{us}(\hat{R}) + \hat{H}_{cor}(\hat{R}) \quad (6.5)$$

Numerical calculations have been carried out for the set of parameters: $\mu = 0.1$, $\Theta = 3$, and exponents: in Norton's law $n = 6$, in Kachanov's law $m = 2$. It turns out that the optimal correction takes form

$$\hat{H}_{cor} = -0.3 - 0.04 \hat{R}^2 + 9.47 \hat{R}^3 \quad (6.6)$$

The optimal shape of the corrected disk of uniform initial strength compared with the profiles obtained with uni- and biparametric optimizations is presented in Fig. 11. Additionally, the time to rupture for all those solutions is given.

The corrected profile of uniform initial strength disks provides the longest time to mixed rupture. It is characterized by significant strengthening of the middle and outer part of the disk, which seems to be very reasonable taking into account the results shown in Fig. 11.

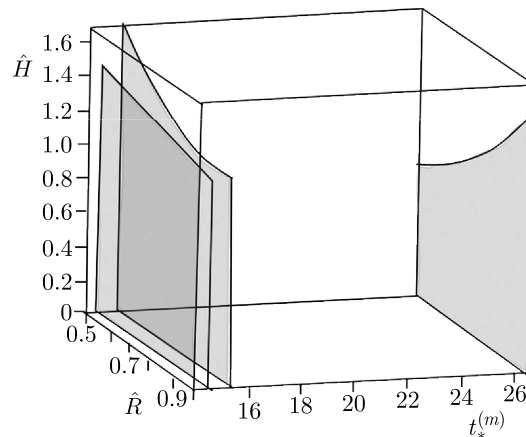


Fig. 11. Optimal shape of the uniform initial strength disks compared with uni- and biparametric optimization

7. Conclusions

The problems of optimal design in creep conditions are very difficult due to a new additional factor-time. When the time to ductile or mixed creep rupture is involved, the difficulties even grow. Such problems require the finite strain approach, i.e. resignation of the rigidification theorem and analysis of the already deformed body using true stresses and logarithmic strains. For this reason, the parametric optimization is applied – the initial shape of the disk is described by a polynomial function. The obtained solutions strongly depend on boundary conditions at the inner edge of the annular disk. For disks fastened on a rigid shaft, the time to rupture is much longer than for disks with free inner edges. Better results – longer times to mixed creep rupture are obtained for biparametric optimization – the initial shape described by a quadratic function. The best results are obtained for the disk of uniform initial strength corrected by a polynomial function of the third degree. A significant influence on the optimal solution of the parameter Θ describing the sensitivity of the material to brittle or ductile rupture is observed. Also the ratio of own mass of the disk and mass placed at the outer edge μ is of great importance.

Acknowledgement

This work has been supported by the National Science Centre through the Grant No. 2014/15/B/ST8/04368.

References

1. AHMET N., ERASLAN., 2003, Elastic-plastic deformations of rotating variable thickness annular disks with free, pressurized and radially constrained boundary conditions, *International Journal of Mechanical Sciences*, **45**, 4, 643-667
2. BETTEN J., 2001, Mathematical modeling of materials behavior under creep conditions, *Applied Mechanics Reviews*, **54**, 2, 107-132
3. BIAŁKIEWICZ J., 1986, Dynamic creep rupture of a rotating disk of variable thickness, *International Journal of Mechanical Sciences*, **28**, 10, 671-681
4. ÇALLIOĞLU H., TOPCU M., TARAKCILAR A.R., 2006, Elastic-plastic stress analysis on orthotropic rotating disc, *International Journal of Mechanical Sciences*, **48**, 985-990
5. DEMS K., MRÓZ Z., 1992, Shape sensitivity analysis and optimal design of disks and plates with strong discontinuities of kinematic fields, *International Journal of Solids and Structures*, **29**, 4, 437-463

6. FARSHI B., BIDABADI J., 2008, Optimum design of inhomogeneous rotating discs under secondary creep, *International Journal of Pressure Vessels and Piping*, **85**, 507-515
7. GANCZARSKI A., SKRZYPEK J., 1976, Optimal shape of prestressed disks in creep, *Journal of Structural Mechanics*, **2**, 141-160
8. GOLUB V.P., ROMANOV A.V., ROMANOVA N.V., 2008, Nonlinear creep and ductile creep rupture of perfectly elastoplastic rods under tension, *International Applied Mechanics*, **44**, 4, 459-470
9. GOLUB V.P., TETERUK R.G., 1994, Evaluating the time to ductile fracture under creep conditions, *International Applied Mechanics*, **30**, 11, 898-905
10. GUN H., 2008, Two-dimensional boundary element analysis of creep continuum damage problems with plastic effects, *Computational Materials Science*, **41**, 3, 322-329
11. HOFF N.J., 1953, The necking and rupture of rods subjected to constant tensile loads, *Journal of Applied Mechanics – Transactions of ASME*, **20**, 105-112
12. JAHED H., FARSHI B., BIDABADI J., 2005, Minimum weight design of inhomogeneous rotating discs, *International Journal of Pressure Vessels and Piping*, **82**, 35-41
13. KACHANOV L.M., 1960, *Creep Theory*, Fizmatgiz, Moscow
14. KACHANOV L.M., 1999, Rupture time under creep conditions, *International Journal of Fracture*, **97**, xi-xviii
15. PEDERSEN P., 2001, On the influence of boundary conditions, Poisson's ratio and material non-linearity on the optimal shape, *International Journal of Solids and Structures*, **38**, 3, 465-477
16. PIECHNIK S., CHRZANOWSKI M., 1970, Time of total creep rupture of a beam under combined tension and bending, *International Journal of Solids and Structures*, **6**, 4, 453-477
17. RYSZ M., 1987, Optimal design of a thick-walled pipeline cross-section against creep rupture, *Acta Mechanica*, **1**, 4, 83-102
18. SZUWALSKI K., 1989, Optimal design of bars under nonuniform tension with respect to ductile creep rupture, *Mechanics of Structures and Machines*, **3**, 303-319
19. SZUWALSKI K., 1995, Optimal design of disks with respect to ductile creep rupture time, *Structural Optimization*, **10**, 54-60
20. SZUWALSKI K., USTRZYCKA A., 2012, Optimal design of bars under nonuniform tension with respect to mixed creep rupture time, *International Journal of Non-Linear Mechanics*, **47**, 55-60
21. SZUWALSKI K., USTRZYCKA A., 2013, The influence of boundary conditions on optimal shape of annular disk with respect to ductile creep rupture time, *European Journal of Mechanics*, **37**, 79-85
22. ŻYCZKOWSKI M., 1971, Optimal structural design in rheology, *Journal of Applied Mechanics*, **38**, 1, 39-46
23. ŻYCZKOWSKI M., 1988, Optimal structural design under creep conditions, *Applied Mechanics Reviews*, **12**, 453-461

AN ANALYTICAL STUDY ON BUCKLING BEHAVIOR OF CNT/POLYMER COMPOSITE PLATES USING THE FIRST ORDER SHEAR DEFORMATION THEORY

PRAMOD KUMAR PEYYALA, V.V. SUBBA RAO

Jawaharlal Nehru Technological University Kakinada, India

e-mail: pramod.330@gmail.com; rao703@yahoo.com

Most plates used in engineering structures such as aircraft wings, ship ducts and buildings, although quite capable of resisting tensile loads, are poor in withstanding compression. In order to avoid premature failure under compression, it is important to know buckling behavior of the plate. This article primarily deals with the analytical study of buckling behavior of a carbon nanotube reinforcing polymer composite plates based on the first order shear deformation theory by employing Mori-Tanaka micromechanics approach to obtain elastic properties. In this investigation, an attempt is made for evaluating the effect of plate thickness, CNT volume fraction, stacking sequence and CNT radii on the buckling of plates.

Keywords: buckling, carbon nanotube, composite plates, micromechanics, FSDT

1. Introduction

Since the recognized discovery of Carbon Nanotubes (CNTs), Iijima (1991), they have attracted an intense interest among researchers in various disciplines due to their stupendous mechanical, electrical and thermal properties (Saito *et al.*, 1999; Ounaies *et al.*, 2003; Weisenberger *et al.*, 2003). The remarkable electrical properties have made CNTs excellent candidates to act as reinforcement in a wide range of applications such as nanosensors and atomic transportation (Arash and Wang, 2013; Wang, 2008). In addition, the outstanding physical and mechanical properties of CNTs, for example an ultra-high Young's modulus of the order of 1 TPa and tensile strength of 200 GPa (Lau and Hui, 2002; Demczyk *et al.*, 2002), stimulated the interest in using CNTs as filler materials in polymer composites to make ultra light structural materials with enhanced mechanical properties.

In the past decade, the wide-ranging experimental and theoretical studies conducted on carbon nanotubes have focused on mechanical characterization and modeling aspects of reinforced polymer composites to assist the development of nanocomposites (Xiao *et al.*, 2005; Zhang Z. *et al.*, 2010; Zhang Y. *et al.*, 2013; Arash *et al.*, 2014; Silani *et al.*, 2014; Gates *et al.*, 2005; Tserpes and Papnikos, 2005). Even though these studies are fairly useful in estimating properties of the nanomaterials, their use in actual structural applications is the ultimate idea behind the development of this highly sophisticated class of materials. However, the literature shows that much of work in this direction is not accomplished. As such, there is a need to examine the macro behavior of the material in actual structural elements such as beams and plates. The behavior of beams under a static loading was studied by Wuite and Adali (2005) for different CNT volume of fractions and nanotube diameters. Based on different assumptions for displacement fields, different theories for plate analysis have been devised. These theories can be divided into three major categories, individual layer theories, equivalent single-layer (ESL) theories, and

three-dimensional elasticity solution procedures. These categories are further divided into sub-theories by the introduction of different assumptions. For example, the second category includes the classical laminate plate theory (CLPT), the first-order and higher-order shear deformation theories (FSDT and HSDT). Analytical observations on static and dynamic behavior of plates by using CLPT were made by Madhu *et al.* (2012).

For the implementation of Carbon nanotube reinforced polymer (CNRP) composites in structural applications, accurate property-microstructure relations are required in the form of micro-mechanics models. In the present investigation, micromechanics properties of CNRP are computed using Mori-Tanaka method as given in (Popov *et al.*, 2000; Shi *et al.*, 2004; Wuite and Adali, 2005; Madhu *et al.*, 2012). The effects of the characteristics developed in these models are investigated on the buckling behavior of CNRP composite plates using FSDT with a view towards assessing the effectiveness of these materials in the design of structural nanocomposites.

2. Micro-mechanics model

The micro-mechanical model involves an elastic and isotropic polymer reinforced with straight, aligned and infinitely long single walled carbon nanotubes (SWCNT). The plate under the study is composed of polystyrene as the matrix with the Young modulus and Poisson's ratio of $E_m = 1.9$ GPa and $\nu_m = 0.3$, respectively. Each SWCNT is considered to be solid and transversely isotropic, and their Hill's elastic constants are taken from Popov *et al.* (2000). The SWCNT radius is assumed to be 10 \AA for all the cases, otherwise mentioned, for which the representative values of the elastic constants are: $n_r = 450$ GPa, $k_r = 30$ GPa, $m_r = p_r = 1$ GPa and $l_r = 10$ GPa. The bonding at the nanotube-polymer interface is taken to be perfect. The resulting composite is also considered as transversely isotropic and its constitutive stress strain relations $\sigma = C\varepsilon$ can be expressed as follows

$$\begin{Bmatrix} \sigma_{11} \\ \sigma_{22} \\ \sigma_{33} \\ \sigma_{23} \\ \sigma_{13} \\ \sigma_{12} \end{Bmatrix} = \begin{bmatrix} n & l & l & 0 & 0 & 0 \\ l & k+m & k-m & 0 & 0 & 0 \\ l & k-m & k+m & 0 & 0 & 0 \\ 0 & 0 & 0 & 2m & 0 & 0 \\ 0 & 0 & 0 & 0 & 2p & 0 \\ 0 & 0 & 0 & 0 & 0 & 2p \end{bmatrix} \begin{Bmatrix} \varepsilon_{11} \\ \varepsilon_{22} \\ \varepsilon_{33} \\ \varepsilon_{23} \\ \varepsilon_{13} \\ \varepsilon_{12} \end{Bmatrix} \quad (2.1)$$

where k is the plane-strain bulk modulus normal to the fiber direction, n is the uni-axial tension modulus in the fiber direction (1), l is the associated cross modulus, m and p are the shear moduli in planes normal and parallel to the fiber direction, respectively, and they are Hill's elastic constants. A composite with a reinforcing phase volume fraction c_r , matrix Young's modulus E_m and matrix Poisson's ratio ν_m is considered. Using the Mori-Tanaka method, Hill's elastic moduli are found to be (Popov *et al.*, 2000; Shi *et al.*, 2004; Wuite and Adali, 2005; Madhu *et al.*, 2012)

$$\begin{aligned} k &= \frac{E_m \{E_m c_m + 2k_r(1 + \nu_m)[1 + c_r(1 - 2\nu_m)]\}}{2(1 + \nu_m)[E_m(1 + c_r - 2\nu_m) + 2c_m k_r(1 - \nu_m - 2\nu_m^2)]} \\ l &= \frac{E_m \{c_m \nu_m [E_m + 2k_r(1 + \nu_m)] + 2c_r l_r(1 - \nu_m^2)\}}{(1 + \nu_m)[2c_m k_r(1 - \nu_m - 2\nu_m^2) + E_m(1 + c_r - 2\nu_m)]} \\ n &= \frac{E_m^2 c_m(1 + c_r - c_m \nu_m) + 2c_m c_r(k_r n_r - l_r^2)(1 + \nu_m)^2(1 - 2\nu_m)}{(1 + \nu_m)[2c_m k_r(1 - \nu_m - 2\nu_m^2) + E_m(1 + c_r - 2\nu_m)]} \\ &\quad + \frac{E_m[2c_m^2 k_r(1 - \nu_m) + c_r n_r(1 - 2\nu_m + c_r) + 4c_m c_r l_r \nu_m]}{2c_m k_r(1 - \nu_m - 2\nu_m^2) + E_m(1 + c_r - 2\nu_m)} \end{aligned} \quad (2.2)$$

$$p = \frac{E_m[E_m c_m + 2(1 + c_r)p_r(1 + \nu_m)]}{2(1 + \nu_m)[E_m(1 + c_r) + 2c_m p_r(1 + \nu_m)]}$$

$$m = \frac{E_m[E_m c_m + 2m_r(1 + \nu_m)(3 + c_r - 4\nu_m)]}{2(1 + \nu_m)\{E_m[c_m + 4c_r(1 - \nu_m)] + 2c_r m_r(3 - \nu_m - 4\nu_m^2)\}}$$

where k_r , l_r , m_r , n_r and p_r are Hill's elastic moduli for the reinforcing phase. The expressions for the moduli of the CNTRC as functions of the stiffness constants are determined for a unidirectional composite as follows

$$E_1 = n - \frac{l^2}{k} \quad E_2 = \frac{4m(kn - l^2)}{kn - l^2 + mn} \quad G_{12} = 2p \quad \nu_{12} = \frac{l}{2k} \quad (2.3)$$

3. Basic equations

The buckling behavior of a symmetric laminated carbon nanotube reinforced polymer square plate is to be studied under the first order shear deformation theory (FSDT), and the basic equations are summarized in this section.

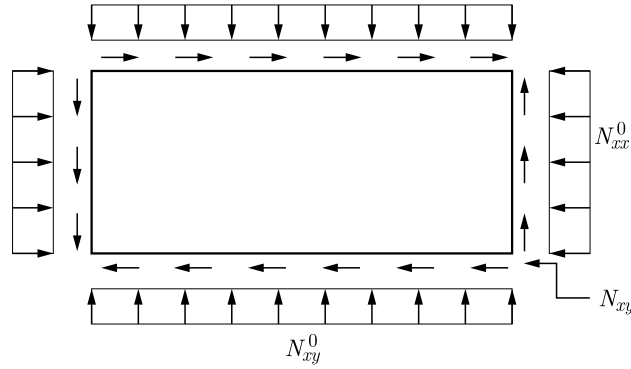


Fig. 1. Buckling of a plate under in-plane compressive edge forces

For laminated composite plates subjected to only in-plane loads, the constitutive relations for the buckling under FSDT are taken from Reddy (2004). A parametric study is carried out to find the minimum buckling load for laminated composite plates which occurs at $m = n = 1$. In the buckling analysis, it is assumed that the loads are in-plane forces only.

For simplicity

$$\hat{N}_{xx} = -N_0 \quad \hat{N}_{yy} = -kN_0 \quad k = \frac{\hat{N}_{yy}}{\hat{N}_{xx}} \quad (3.1)$$

Therefore:

— for uniaxial compression $k = 0$

$$\hat{N}_{xx} = -N_0 \quad \hat{N}_{yy} = 0 \quad (3.2)$$

— for biaxial compression $k = 1$

$$\hat{N}_{xx} = -N_0 \quad \hat{N}_{yy} = -N_0 \quad (3.3)$$

The critical buckling load is nondimensionalised by using

$$\bar{N} = N_{cr} \frac{a^2}{E_2 h^2} \quad (3.4)$$

here \bar{N} is the nondimensionalised critical buckling load, N_{cr} is the critical buckling load, a is length of the plate, E_2 is Young's modulus in the transverse direction and h is thickness of the laminated composite plate.

4. Buckling analysis

A proficient MATLAB code is developed for the buckling analysis using FSDT of carbon nanotube reinforced polymer (CNRP) composite plates. A twofold validation is done to the code, one for validating the elastic properties of CNRP and the other for validating the critical buckling load of composite plates under FSDT. First, the elastic properties of CNRP obtained from Mori-Tanaka micromechanics model are validated with the published results (Wuite and Adali, 2005) and presented in Fig. 2.

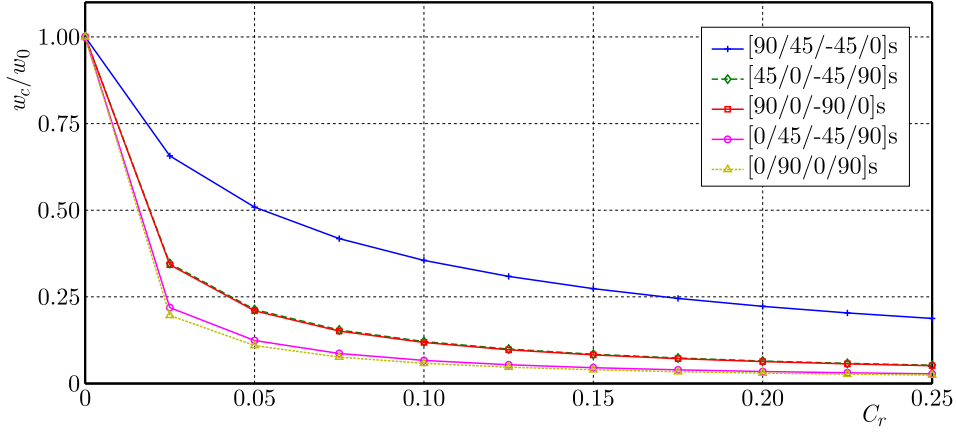


Fig. 2. Curves of the maximum deflection plotted against the fiber volume fraction for various stacking sequences for a simply supported beam subjected to CPL

Further to validate the buckling with the published results, the effect of shear deformation on the nondimensionalised critical buckling loads \bar{N} of symmetric laminated plates with elastic properties $E_1 = 25E_2$, $G_{12} = G_{13} = 0.5E_2$, $G_{23} = 0.2E_2$, $\nu_{12} = 0.25$, $K = 5/6$ is calculated for uniaxial as well as biaxial compression and presented in Table 1 along with the corresponding published results (Reddy, 2004).

Table 1. Comparison of the nondimensionalised critical buckling load with the published results

a/h	[0/90/0]		[0/90/0/90/0]	
	\bar{N}	Reddy (2004)	\bar{N}	Reddy (2004)
Uniaxial compression				
10	15.248	15.289	16.254	16.309
20	20.602	20.628	21.094	21.125
25	21.552	21.568	21.893	21.917
50	22.971	22.978	23.071	23.078
100	23.361	23.363	23.384	23.389
Biaxial compression				
10	7.569	7.644	8.070	8.154
20	10.293	10.314	10.522	10.562
25	10.771	10.784	10.930	10.958
50	11.486	11.489	11.531	11.539
100	11.681	11.682	11.692	11.695

The results obtained are found to be in excellent agreement with the published results. Having validated the composite plate results, the MATLAB code is extended to the CNRP

composite plate to make an attempt to analyze the buckling behavior of these plates under FSDT.

An eight-layer simply supported symmetric square CNRP composite plate is subjected to both uniaxial and biaxial compression to study the buckling behavior. For the CNRP composite plate, the critical buckling load occurs at $m = n = 1$, and the variation in critical buckling load with respect to side-to-thickness ratio a/h of the plate and CNT volume fraction (fiber volume fraction) for various stacking sequences is shown in Figs. 3 and 4.

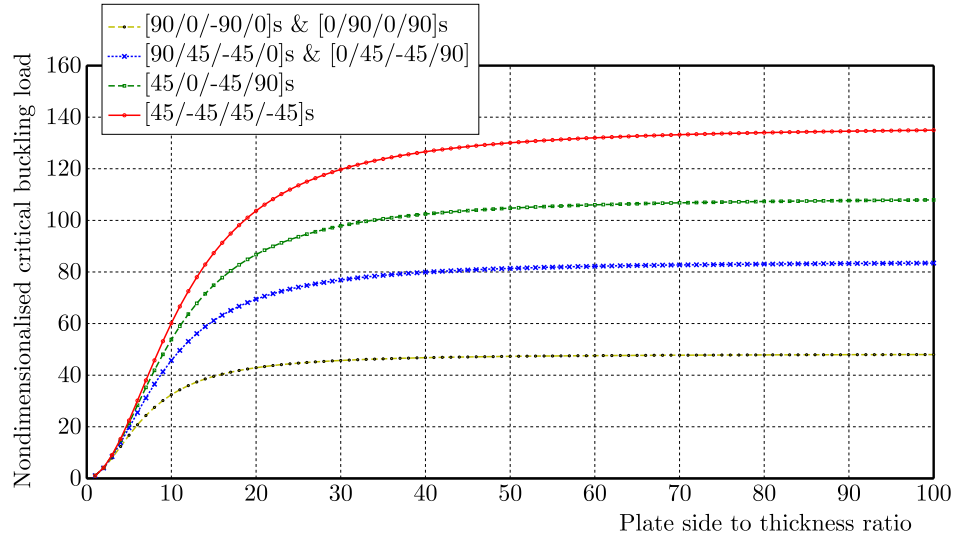


Fig. 3. Curves of the nondimensionalised critical buckling load plotted against the plate side-to-thickness ratio for various stacking sequences for a simply supported plate subjected to uniaxial compression

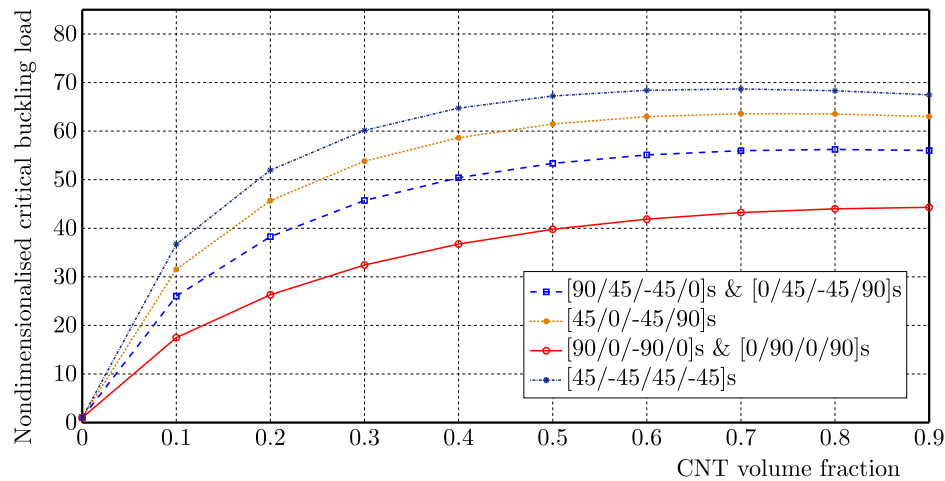


Fig. 4. Curves of the nondimensionalised critical buckling load plotted against the CNT volume fraction for various stacking sequences for a simply supported plate subjected to uniaxial compression

From the above results, it is observed that the angle-ply stacking sequence $[45/-45/45/-45]_s$ exhibits more resistance to buckling than the cross-ply laminating schemes $[0/90/0/90]_s$ and $[90/0/-90/0]_s$ for the same percentage of CNT reinforcement. For all the stacking sequences, the effect of shear deformation on the critical buckling load is clearly observed in thick plates ($0 < a/h \leq 20$), and it is insignificant in the case of thin plates ($a/h > 20$) (Reddy, 2004). However, the effect of shear deformation across the thickness on the critical buckling load is the same even the plate is subjected to biaxial compression ($k = 1$) with actual values lesser than those of uniaxial compression ($k = 0$). The comparison between the nondimensionalised critical

buckling loads of uniaxial and biaxial compression for the stacking sequence $[90/45/-45/0]_s$ at CNT volume fraction 0.3 is shown in Fig. 5.

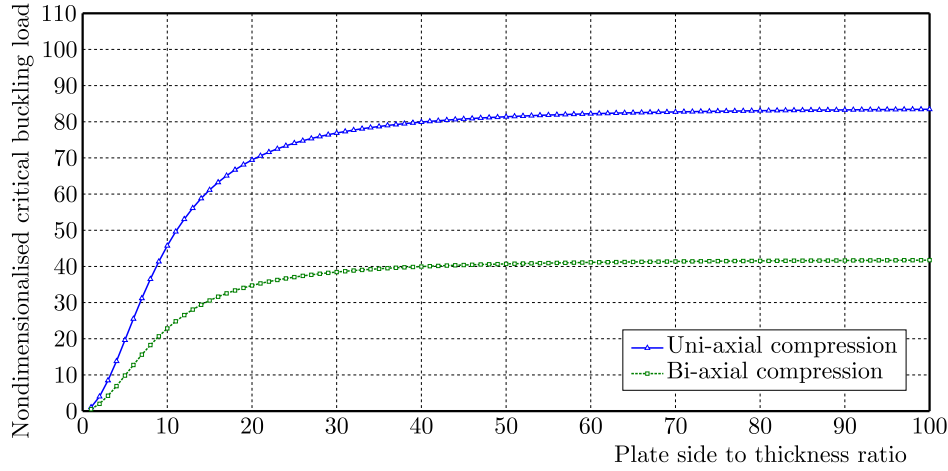


Fig. 5. Curves of the nondimensionalised critical buckling load plotted against the plate side-to-thickness ratio for various loads and stacking sequences $[90/45/-45/0]_s$ for a simply supported plate

It is knowledgeable that the nondimensionalised critical buckling load in biaxial compression is about 0.5 times lesser than that of uniaxial compression for various stacking sequences, CNT radii and for various fiber volume fractions. So the results are presented only for uniaxial compression hereafter.

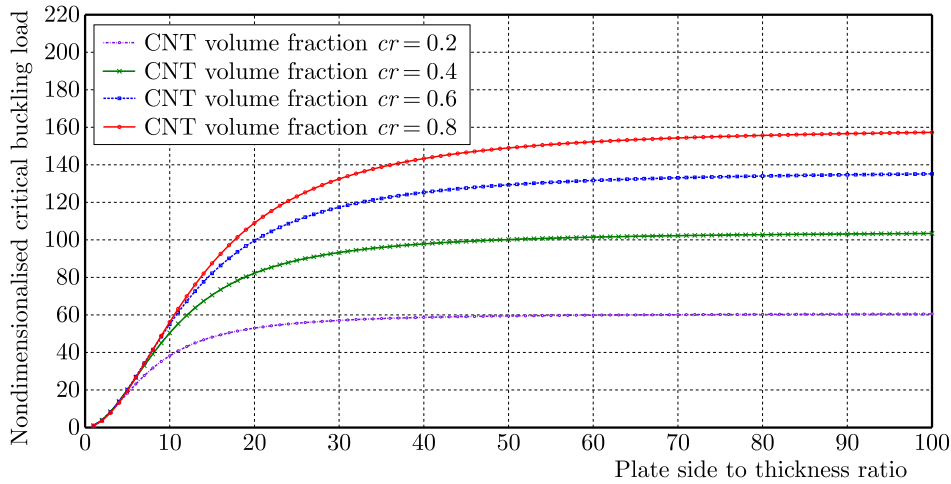


Fig. 6. Curves of the nondimensionalised critical buckling load plotted against the plate side-to-thickness ratio for fiber volume fractions and stacking sequences $[90/45/-45/0]_s$ for a simply supported plate subjected uniaxial compression

The effect of fiber volume fraction on the critical buckling load is presented in Fig. 6. It is obvious that the critical buckling load increases as the fiber volume fraction in the composite increases, as CNTs are stiffer and stringer. It is further investigated to discover the effect of CNT radius on the critical buckling load, and it is observed from the following graph (Fig. 7) that for the same stacking sequence, the effect of nanotube radius on the critical buckling load is insignificant. The same is observed for various stacking sequences, and the results are shown in Fig. 8.

From the above results, it is noticeable that a higher stiffness can be obtained by reinforcing CNTs with smaller diameters and, thereby, a decrease in the critical buckling load can also be achieved.

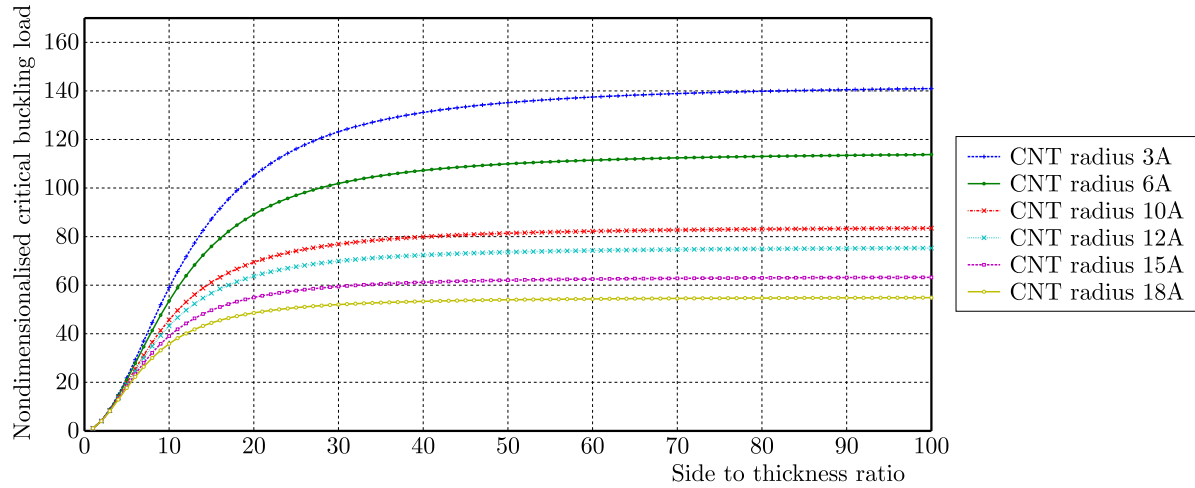


Fig. 7. Curves of the nondimensionalised critical buckling load plotted against the plate side-to-thickness ratio for various CNT radii and stacking sequences $[90/45/-45/0]_s$ for a simply supported plate subjected uniaxial compression

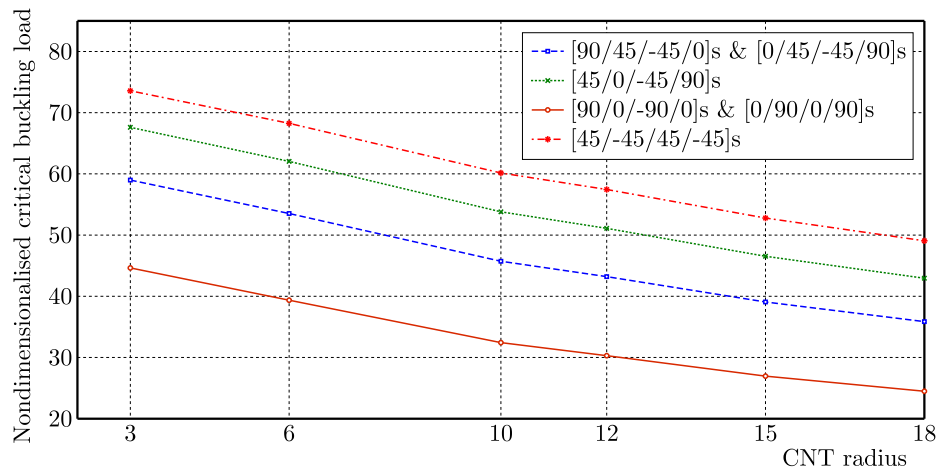


Fig. 8. Curves of the nondimensionalised critical buckling load plotted against CNT radii for various stacking sequences for a simply supported plate subjected uniaxial compression ($k = 0$)

5. Conclusions

The buckling behavior of a CNT reinforced polymer composite plate is studied by using a MATLAB code. The Mori-Tanaka micromechanics model is adopted for determining the elastic constants of the CNT reinforced polymer composite material in terms of nanotube volume fractions. It is shown that they are in good agreement with the published results. The first order shear deformation theory (FSDT) is considered for determination of the critical buckling loads of plates.

A twofold validation is done to the code; one is to validate the elastic constants of the CNRP composite and the second to validate the FSDT. In the case of CNRP composite plates under FSDT, it is found that the effect of side to thickness ratio on the critical buckling load of thick plates is phenomenal. The results markedly show the diminishing effect of transverse shear deformation on the critical buckling load of thick plates, the effect being negligible for side to thickness ratios greater than 20 i.e., for thin plates. It is also investigated that the stacking sequence of the laminated plate is yet another important parameter for determination of the buckling behavior of the plates. It is observed that the buckling resistance of the angle-ply

laminating scheme is less than that of other stacking sequences considered in the study. The influence of CNT radii is also examined on the buckling of the plates, and it is proposed to use a smaller radius to obtain a higher buckling resistance. The effect of the volume fraction of the CNT reinforcements on the buckling of the plate is studied, and it is found that the increase in the fiber volume fraction decreases the critical buckling load.

References

1. ARASH B., WANG Q., 2013, Detection of gas atoms with carbon nanotubes, *Scientific Reports*, **3**
2. ARASH B., WANG Q., VARADAN V., 2014, Mechanical properties of carbon nanotube/polymer composites, *Scientific Reports*, **4**
3. DEMCZYK B.G., WANG Y.M., CUMINGS J., HETMAN M., HAN W., ZETTL A., RITCHIE R.O., 2002, Direct mechanical measurement of the tensile strength and elastic modulus of multiwalled carbon nanotubes, *Material Science Engineering*, **A334**, 173-178
4. GATES T., ODEGARD G., FRANKLAND S., CLANCY T. 2005, Computational materials: multi-scale modeling and simulation of nanostructured materials, *Composite Science Technology*, **65**, 15, 2416-2434
5. IJIMA S., 1991, Helical microtubules of graphitic carbon, *Nature*, **354**, 56-58
6. LAU K.-T., HUI D., 2002, The revolutionary creation of new advanced materials – carbon nanotube composites, *Composites: Part B*, **33**, 263-277
7. MADHU S., SUBBA RAO V.V., PRAMOD KUMAR P., CHANDRAMOULI K., 2012, Static and dynamic analysis of carbon nanotube reinforced polymer composite plates, *Material science Research Journal*, **6**, 3-4
8. OUNAIES Z., PARK C., WISE K.E., SIOCHI E.J., HARRISON J.S., 2003, Electrical properties of single wall carbon nanotube reinforced polyimide composites, *Composite Science Technology*, **63** 1637-1646
9. POPOV V.N., DOREN V.E., BALKANSKI M., 2000, Elastic properties of crystals of single-walled carbon nanotubes, *Solid State Communications*, **114**, 359-399
10. REDDY J.N., 2004, *Mechanics of Laminated Composite Plates and Shells: Theory and Analysis*, 2nd edition, CRC Press
11. SAITO R., DRESSELHAUS G., DRESSELHAUS M.S., 1999, *Physical Properties of Carbon Nanotubes*, Imperial College Press, London
12. SHI D.L., FENG X.Q., HUANG Y.Y., HWANG K.C., GAO H., 2004, The effect of nanotube waviness and agglomeration on the elastic property of carbon nanotube-reinforced composites, *Journal of Engineering Materials and Technology*, **126**, 250-257
13. SILANI M., TALEBI H., ZIAEI-RAD S., KERFRIDEN P., BORDAS S.P., RABCZUK T., 2014, Stochastic modelling of clay/epoxy nanocomposites, *Composite Structures*, **118**, 241-249
14. TSERPEIS K.I., PAPNIKOS P., 2005, Finite element modelling of single-walled carbon nanotubes, *Composites: Part B*, **36**, 468-477
15. WANG Q., 2008, Atomic transportation via carbon nanotubes, *Nano Letters*, **9**, 1, 245-249
16. WEISENBERGER M.C., GRULKE E.A., JACQUES D., RANTELL T., ANDREWS R., 2003, Enhanced mechanical properties of polyacrylonitrile/multiwall carbon nanotube composite fibers, *Journal of Nanoscience Nanotechnology*, **3**, 6
17. WUITE J., ADALI S., 2005, Deflection and stress behaviour of nanocomposite reinforced beams using a multiscale analysis, *Composite Structures*, **71**, 3-4, 388-396

18. XIAO J.R., GAMA B.A., GILLESPIE JR J.W., 2005, An analytical molecular structural mechanics model for the mechanical properties of carbon nanotubes, *International Journal of Solids Structures*, **42**, 3075-3092
19. ZHANG Y., ZHAO J., WEI N., JIANG J., GONG Y., RABCUK T., 2013, Effects of the dispersion of polymer wrapped two neighbouring single walled carbon nanotubes (swnts) on nanoengineering load transfer, *Composites: Part B Engineering*, **45**, 1, 1714-1721
20. ZHANG Z., LIU B., HUANG Y., HWANG K., GAO H., 2010, Mechanical properties of unidirectional nanocomposites with non-uniformly or randomly staggered platelet distribution, *Journal of Mechanics and Physics of Solids*, **58**, 10, 1646-1660

Manuscript received July 25, 2016; accepted for print July 18, 2017

A LOCALLY MODIFIED SINGLE-PHASE MODEL FOR ANALYZING MAGNETOHYDRODYNAMIC BOUNDARY LAYER FLOW AND HEAT TRANSFER OF NANOFLUIDS OVER A NONLINEARLY STRETCHING SHEET WITH CHEMICAL REACTION

POORIA AKBARZADEH

School of Mechanical Engineering, Shahrood University of Technology, Shahrood, Iran
e-mail: akbarzad@ut.ac.ir; p.akbarzadeh@shahroodut.ac.ir

The problem of boundary layer flow and heat transfer of nanofluids over nonlinear stretching of a flat sheet in the presence of a magnetic field and chemical reaction is investigated numerically. In this paper, a new locally modified single-phase model for the analysis is introduced. In this model, the effective viscosity, density and thermal conductivity of the solid-liquid mixtures (nanofluids) which are commonly utilized in the homogenous single-phase model, are locally combined with the prevalent single-phase model. Similarity transformation is used to convert the governing equations into three coupled nonlinear ordinary differential equations. These equations depend on five local functions of the nanoparticle volume fraction viz., local viscosity ratio, magnetic, Prandtl, Brownian motion and thermophoresis functions. The equations are solved using Newton's method and a block tridiagonal matrix solver. The results are compared to the prevalent single-phase model. In addition, the effect of important governing parameters on the velocity, temperature, volume fraction distribution and the heat and mass transfer rates are examined.

Keywords: nanofluid, magnetohydrodynamic, nonlinear stretching sheet, similarity transformation, locally modified single-phase model

1. Introduction

The enhancement of heat transfer in an industrial process such as cooling of electronic devices, guide or thrust bearings, high-speed sliding surfaces, strips or filaments, and etc., may create energy savings, reduce the process time, increase efficiency and lengthen the working life of equipment. Convective heat transfer can be improved by changing flow geometry, boundary conditions, or by enhancing thermal conductivity of the fluid (Wang and Mujumdar, 2007). One way to increase the thermal conductivity of base fluids is the use of nanoparticles (such as Cu, Ag, Al, and etc. as metallic solid, CuO, Al₂O₃, TiO₂ and etc., as metallic oxide particles, multi walled nanotubes (MWNTs) and single wall nanotubes (SWNTs) (as metallic nanotubes) suspended in the fluids. Indeed, the Brownian motion of the nanoparticles in these suspensions is one of the potential contributors to this enhancement (Choi, 1995; Choi *et al.*, 2001; Xie *et al.*, 2003; Li and Peterson, 2007; Aminossadati and Ghasemi, 2009; Hamad and Ferddows, 2012). Apparently, Choi (1995) was the first researcher who introduced the term nanofluids to refer to the fluid with suspended nanoparticles, and up from this time, many researchers focused on numerical or experimental studies in the field of thermophysical and also heat and fluid flow properties of nanofluids such by Choi (1995), Choi *et al.* (2001), Xie *et al.* (2003), Li and Peterson (2007), Aminossadati and Ghasemi (2009), Hamad and Ferddows (2012), Wen and Ding Y. (2004), Heris *et al.* (2006), Abu-Nada and Chamkhac (2010), Sheikhzadeh *et al.* (2011) and to name but a few.

As aforesaid, cooling of continuous strips or filaments by drawing them through a motionless fluid is one of the heat transfer processes in the industry. In these respects, the feature of the final product (e.g. plastic and polymer sheets manufactured by extrusion, glass-fiber and paper production, metal spinning, etc.) depends on the cooling rate and the process of stretching (Rana and Bhargava, 2012). Therefore, simulation of boundary layer behavior of fluid flow over the stretching surface (strips or filaments) can be useful for predicting heat transfer characteristics of such a process. The basic and elementary works on Boundary Layer Flow (BLF) over a continuous moving surface (with constant velocity) were reported by Sakiadis (1961a,b,c). After that, Crane (1970) published a report about the exact temperature distribution of the steady BLF of a viscous fluid caused by stretching a flat isothermal sheet (with a linearly variable velocity). The temperature and concentration distributions of BLF over an isothermal moving plate with blowing or suction were found by Gupta and Gupta (1977). The same problem was studied by Chen and Char (1988) in which the sheet was subjected to a prescribed temperature and heat flux.

The boundary layer and thermal characteristics of fluid flow over a nonlinear stretching sheet were examined for the first time by Vajravelu (2001). Then, Vajravelu and Cannon (2006) investigated the existence of a solution for the nonlinear problem by using the Schauder theory. Afterwards, Cortell (2007) analyzed flow and heat transfer over a nonlinear stretching sheet for the prescribed and constant surface temperature as boundary conditions. Prasad *et al.* (2010) presented a numerical solution for Magneto-Hydrodynamics (MHD) flow of an electrically conducting viscous fluid over a stretching sheet with variable fluid properties. They assumed that the stretching velocity and the transverse magnetic field varied as a power function of the distance from the origin. Postelnicu and Pop (2011) explored steady 2D laminar BLF of a non-Newtonian power-law fluid past a permeable non-linear stretching wedge. And recently, Vajravelu *et al.* (2014) published a paper on the subject of MHD flow and heat transfer of a non-Newtonian power-law fluid over an unsteady stretching isothermal sheet.

Since using nanofluids may improve heat transfer behavior of an engineering process, many researchers examined the effect of those fluids on the boundary layer and thermal characteristics of flow caused by stretching a surface. In this respect, Bachok *et al.* (2010) studied the steady BLF of nanofluids over a continuous moving surface (with constant velocity). Khan and Pop (2010) obtained the temperature distribution of steady BLF of nanofluids over a linear isothermal stretching flat sheet. Gorder *et al.* (2010) presented the similarity solution for the nano-BLFs over a linearly stretching sheet, in which on the surface sheet the velocity slip was assumed to be proportional to the local shear stress. Hassani *et al.* (2011) obtained an analytical solution for BLF of a nanofluid past a linearly stretching sheet using the homotopy analysis method (HAM). Rana and Bhargava (2012) studied numerically flow and heat transfer of a nanofluid over a nonlinearly stretching sheet. They used the finite difference, finite element, and variational method in their computations. Nadeem *et al.* (2014) analyzed flow of a three-dimensional water-based nanofluid over an exponentially stretching sheet. And recently, Das (2015) investigated the problem of BLF of a nanofluid over a non-linear permeable stretching sheet at a predestined surface temperature in the presence of partial slip.

The study of Magneto-Hydrodynamics (MHD) flow of an electrically conducting fluid due to a stretching sheet is important in modern engineering processes. Metallurgy, metalworking, metal fusion in an electrical furnace, and etc., are some examples of such processes (Ibrahim and Shanker, 2014). The MHD flow analysis over a stretching sheet with various aspects such as types of fluids, magnetic effect, stagnation geometry and the temperature effect can be seen in works of many researchers such as Ishak *et al.* (2008), Fadzilah *et al.* (2011), Mahapatra *et al.* (2009), Prasad *et al.* (2010), and to name but a few. Ibrahim *et al.* (2013) studied the MHD stagnation-point flow and heat transfer due to a nanofluid towards a stretching sheet using the Runge-Kutta fourth order numerical method. They analyzed the effect of the velocity

ratio parameter on both the local Nusselt number and local Sherwood number. In the same year, Ibrahim and Shankar (2013) investigated MHD boundary layer flow and heat transfer of a nanofluid past a permeable stretching sheet with velocity, thermal and solutal slip boundary conditions. Recently, Ibrahim and Shankar (2014) studied MHD boundary layer flow and heat transfer of a nanofluid over a non-isothermal stretching sheet. Their analysis was done for two different cases, namely a prescribed surface temperature and prescribed heat flux.

The above mentioned literature review shows that in order to investigate the heat transfer characteristics of nanoparticles (or generally small solid particles) suspended in a fluid, two main approaches have been adopted by researchers. The first approach is the two-phase model which considers both the fluid phase and the solid particles behavior in the heat transfer process. The second one is the single-phase model in which both phases are in thermal and hydrodynamic equilibrium state (this approach is simpler and more computationally efficient). Generally in nanofluids, there are several factors that affect heat transfer enhancement. Some of the more important factors are Brownian motion (including diffusion, sedimentation, and dispersion), gravity, layering at the solid/liquid interface, particle clustering, friction between the fluid and the solid particles, etc. Therefore, in the absence of any experimental data and suitable theoretical studies, the existing macroscopic two-phase model has not enough precision for analyzing nanofluids. Consequently, the modified single-phase, considering some of the above factors, is more convenient than the two-phase model if the main interest of analysis is the heat transfer process (Khanafer *et al.*, 2003). Therefore, in order to improve the results of the single-phase model for analyzing the nanofluids flow, some modifications are needed. In this paper, a new modified single-phase model for analyzing flow and heat transfer in nanofluids is introduced for the first time. In this model, all effective properties of nanofluids such as density, viscosity and thermal conductivity, which are normally used for the effective single-phase model (as constant values), are incorporated locally with the governing equations (as non-constant values). This approach is used for examining the BLF behavior and thermal characteristics of nanofluids flow over a nonlinear stretching sheet in the presence of a magnetic field and chemical reaction. The results for Cu and Al₂O₃ nanoparticles are compared to the prevalent single-phase model. This comparison depicts that the prevalent single-phase model has a considerable deviation for predicting the behavior of nanofluids flow, especially in dimensionless temperature and nanoparticle volume fraction. In addition, the effects of important governing parameters such as the transverse magnetic field, chemical reaction strength, thermophoresis parameter, nanoparticle volume fraction near the surface, etc., on the velocity, temperature, volume fraction distribution and dimensionless heat and mass transfer rates are examined.

2. Mathematical governing equations

The steady-state two-dimensional BLF of a nanofluid past a stretching sheet is considered with the nonlinear velocity $u_w = a_u x^n$, where a_u is a positive constant, n is the nonlinear stretching parameter and x is the coordinate measured along the stretching surface, as shown in Fig. 1. Because of the impermeability characteristic of the sheet, the vertical velocity of the fluid on the surface is $v_w = 0$. In this problem, the stretching surface is a non-isothermal face with the relation of $T_w(x) = T_\infty + a_T x^r$, where a_T is a positive constant, r is the surface temperature parameter in the prescribed surface temperature boundary condition and T_∞ is the temperature of the fluid far away from the stretching sheet. In addition, the fluid is under a transverse magnetic field with strength $B(x)$ which is applied in the vertical direction, given by the special form of $B(x) = B_0 x^{n-1}$, where B_0 is a positive constant. Also, it is assumed that the first-order homogeneous chemical reaction with the non-linear rate of $K = K_0 x^{n-1}$ occurs in the fluid (K_0 is the constant chemical reaction parameter). According to (Ibrahim and Shanker, 2014;

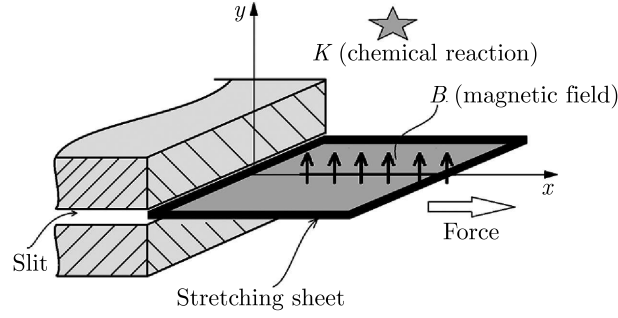


Fig. 1. Physical model of the stretching sheet and the coordinate system

Buongiorno, 2006; Yazdi *et al.*, 2011), the following four governing equations of BLF include the continuity, momentum, energy, and nanoparticles concentration, respectively

$$\begin{aligned}
 \frac{\partial u}{\partial x} + \frac{\partial v}{\partial y} &= 0 & u \frac{\partial u}{\partial x} + v \frac{\partial u}{\partial y} &= \nu_{nf} \frac{\partial^2 u}{\partial y^2} - \frac{\sigma B}{\rho_{nf}} u \\
 u \frac{\partial T}{\partial x} + v \frac{\partial T}{\partial y} &= \alpha_{nf} \frac{\partial^2 T}{\partial y^2} + \frac{(\rho c)_p}{(\rho c)_{nf}} \left[D_B \frac{\partial \varphi}{\partial y} \frac{\partial T}{\partial y} + \frac{D_T}{T_\infty} \left(\frac{\partial T}{\partial y} \right)^2 \right] \\
 u \frac{\partial \varphi}{\partial x} + v \frac{\partial \varphi}{\partial y} &= D_B \frac{\partial^2 \varphi}{\partial y^2} + \frac{D_T}{T_\infty} \frac{\partial^2 T}{\partial y^2} - K \varphi
 \end{aligned} \tag{2.1}$$

here, T is temperature of the fluid, u and v are velocity components along the x and y -axis respectively, φ is the nanoparticle concentration (or volume fraction), D_T is the thermophoretic diffusion coefficient, D_B is the Brownian diffusion coefficient, c is specific heat capacity, ρ is density, $\alpha = k/(\rho c)$ is thermal diffusivity, ν is kinematic viscosity, k is thermal conductivity, and σ is electrical conductivity of the fluid. The subscripts p and nf refer to the nanoparticles and nanofluid, respectively. In this study, a new local Modified Single-Phase Model (here it is named as MSPM) for analyzing nanofluids flow and heat transfer is introduced. In this manner, the parameters ν_{nf} , k_{nf} , ρ_{nf} , and c_{nf} of the above governing equations may be introduced by the following four relations (Oztop and Abu-Nada, 2008)

$$\begin{aligned}
 \frac{(\rho c)_{nf}}{(\rho c)_f} &= 1 - \varphi + \varphi \frac{(\rho c)_p}{(\rho c)_f} & \frac{\rho_{nf}}{\rho_f} &= 1 - \varphi + \varphi \frac{\rho_p}{\rho_f} \\
 \frac{\nu_{nf}}{\nu_f} &= \frac{1}{(1 - \varphi)^{2.5} (1 - \varphi + \varphi \rho_p / \rho_f)} & \frac{k_{nf}}{k_f} &= \frac{k_p + 2k_f - 2\varphi(k_f - k_p)}{k_p + 2k_f + \varphi(k_f - k_p)}
 \end{aligned} \tag{2.2}$$

where, the subscript f refers to the base fluid. The associated boundary conditions for the problem are

$$\begin{aligned}
 u(x, 0) &= u_w(x) = a_u x^n & v(x, 0) &= v_w(x) = 0 \\
 T(x, 0) &= T_w(x) = a_T x^r + T_\infty & \varphi(x, 0) &= \varphi_w \\
 u(x, \infty) &= 0 & v(x, \infty) &= 0 & T(x, \infty) &= T_\infty & \varphi(x, \infty) &= \varphi_\infty
 \end{aligned} \tag{2.3}$$

where φ_w and φ_∞ are the nanoparticle volume fraction neighborhood to the surface and far away from the stretching sheet, respectively. By considering the following similarity transformations (Ibrahim and Shankar, 2013)

$$\begin{aligned}
 \eta &= y \beta x^{\frac{n-1}{2}} & u &= a_u x^n f'(\eta) & v &= -\gamma x^{\frac{n-1}{2}} \left(f + \frac{n-1}{n+1} \eta f' \right) \\
 \theta(\eta) &= \frac{T - T_\infty}{T_w - T_\infty} & \psi(\eta) &= \frac{\varphi - \varphi_\infty}{\varphi_w - \varphi_\infty}
 \end{aligned} \tag{2.4}$$

where, $\beta = \sqrt{a_u(n+1)/(2\nu_f)}$ and $\gamma = \sqrt{a_u\nu_f(n+1)/2}$, BLF governing equations (2.1) are transformed into three non-linear ordinary differential equations as follows

$$\begin{aligned} f''' + F(\varphi)\left(f f'' - \frac{2n}{n+1}f'^2\right) - G(\varphi)\frac{2}{n+1}f' &= 0 \\ \frac{1}{Pr(\varphi)}\theta'' + f\theta' - \frac{2r}{n+1}f'\theta + Nb(\varphi)\psi'\theta' + Nt(\varphi)\theta'^2 &= 0 \\ \psi'' + \overline{Le}f\psi' + \frac{\overline{Nb}}{\overline{Nb}}\theta'' - \frac{2R}{n+1}\overline{Le}\psi &= 0 \end{aligned} \quad (2.5)$$

where $F(\varphi)$ is the local viscosity ratio function, $G(\varphi)$, $Pr(\varphi)$, $Nb(\varphi)$ and $Nt(\varphi)$ are the local magnetic, local Prandtl, local Brownian and local thermophoresis functions are defined as

$$\begin{aligned} F(\varphi) &= (1-\varphi)^{2.5}\left(1-\varphi+\varphi\frac{\rho_p}{\rho_f}\right) & G(\varphi) &= M(1-\varphi)^{2.5} \\ Nb(\varphi) &= \frac{\overline{Nb}}{1-\varphi+vp(\rho c)_p/(\rho c)_f} & Nt(\varphi) &= \frac{\overline{Nt}}{1-\varphi+\varphi(\rho c)_p/(\rho c)_f} \\ Pr(\varphi) &= \frac{\nu_f}{\alpha_{nf}} = Pr_f \frac{k_p/k_f + 2 + 2\varphi(1-k_p/k_f)}{k_p/k_f + 2 - \varphi(1-k_p/k_f)} \left(1-\varphi+\varphi\frac{(\rho c)_p}{(\rho c)_f}\right) \end{aligned} \quad (2.6)$$

In the set of equations (2.6), $M = \sigma B_0/(a_u \rho_f)$ is the magnetic parameter, $Pr_f = \nu_f/\alpha_f$ is the fluid Prandtl number, $\overline{Le} = \nu_f/D_B$ is the Lewis number, $\overline{Nb} = [(\rho c)_p D_B (\varphi_w - \varphi_\infty)]/[\nu_f (\rho c)_f]$ is the Brownian motion number, $\overline{Nt} = [(\rho c)_p D_T (T_w - T_\infty)]/[T_\infty \nu_f (\rho c)_f]$ is the thermophoresis parameter and, finally, $R = K_0/a_u$. It is clear that \overline{Nb} is related to \overline{Le} as follows

$$\overline{Nb} = \frac{(\rho c)_p (\varphi_w - \varphi_\infty)}{\overline{Le} (\rho c)_f} \quad (2.7)$$

It should be noted that the enhancement of nanofluids thermal conductivity is because of four major mechanisms: (1) Brownian motion of nanoparticles, (2) nanolayer, (3) clustering, and (4) nature of heat transport in the nanoparticles. Also, some important parameters which affect the thermal conductivity of nanofluids are particle volume fraction, temperature, particles size and the size and property of the nanolayer. Therefore, a considerable number of studies can be found on the modelling of thermal conductivity of nanofluids, such as the Maxwell model, Hamilton-Crosser model, Bruggeman model, Wasp model, Maxwell-Garnett (MG) model, Gupta model, and to name but a few. However, there is a lack of reliable and comprehensive model which includes all mechanisms and influenced parameters for thermal conductivity of nanofluids (Esfe *et al.*, 2014; Kumar *et al.*, 2015). As a matter of fact, the present study does not focus on a comprehensive thermal conductivity model of nanofluids (so the Maxwell model (Eqs. (2.5) is selected as the model). The novelty of this study can be found in Eqs. (2.5) and (2.6). In Eqs. (2.5), $F(\varphi)$, $Pr(\varphi)$, $Nb(\varphi)$, and $Nt(\varphi)$ are not constant during the calculation and they are updated locally based on the third relation of Eq. (2.5), which is more physical. It means that three relations of Eqs. (2.5) should be solved together. By considering Eqs. (2.3), non-linear ordinary differential equations (2.5) are solved subject to the following boundary conditions

$$\begin{aligned} f'(0) &= 1.0 & \theta(0) &= 1.0 & \psi(0) &= 1.0 & f(0) &= 0 \\ f'(\infty) &= 0 & \theta(\infty) &= 0 & \psi(\infty) &= 0 \end{aligned} \quad (2.8)$$

By introducing the local Reynolds number via $Re_x = u_w(x)x/\nu_f = a_u x^{n+1}/\nu_f$, the surface heat flux through $q_w = k_{nf}(\partial T/\partial y)_{y=0}$, the surface mass flux via $q_m = D_B(\partial \varphi/\partial y)_{y=0}$, the local nanofluid Nusselt number through $Nu_{nf} = xq_w/[k_{nf}(T_w - T_\infty)]$ and the local nanofluid

Sherwood number by means of $Sh_{nf} = xq_m/[D_B(\varphi_w - \varphi_\infty)]$, the following relation can be established

$$\frac{Nu_{nf}}{\sqrt{Re_x}} = \sqrt{\frac{n+1}{2}}|\theta'(0)| \quad \frac{Sh_{nf}}{\sqrt{Re_x}} = \sqrt{\frac{n+1}{2}}|\psi'(0)| \quad (2.9)$$

where $Nu_{nf}/\sqrt{Re_x}$ and $Sh_{nf}/\sqrt{Re_x}$ are known as dimensionless heat and mass transfer rates, respectively. Without loss of generality, one can assume that the nanoparticle volume fraction far away from the stretching sheet is zero or $\varphi_\infty = 0$. In this paper, the fluid is a water based nanofluid containing different types of prevalent nanoparticles: copper (Cu) and alumina (Al_2O_3). Based on (Oztop and Abu-Nada, 2008), the thermophysical properties of the fluid (water) and the mentioned nanoparticles are given in Table 1.

Table 1. Thermophysical properties of the fluid (water) and three nanoparticles

Properties	Fluid phase (water)	Cu	Al_2O_3
c [J/kgK]	4179	385	765
ρ [kg/m ³]	997.1	8933	3970
k [W/mK]	0.613	400	40
Pr_f	6.83	—	—
$(\rho c)_p/(\rho c)_f$	—	0.825	0.729
k_p/k_f	—	652.53	65.25

3. Algorithm of numerical solution

The algorithm of numerical calculation (computer programming procedure) of non-linear differential equations (2.5)-(2.7) with boundary conditions (2.8) is given via items (i) to (viii). It should be noted that for step (ii), by assuming $\varphi_\infty = 0$, the initial guess can be $\psi(\eta) = \varphi(\eta)/\varphi_w = [1 - \exp(\eta - \eta_{max})]/[1 - \exp(-\eta_{max})]$ as an example, where η_{max} is the maximum value of η in the numerical calculation.

- (i) Specify input data of the base fluid and nanoparticles: ρ_p/ρ_f , $(\rho c)_p/(\rho c)_f$, k_p/k_f , Pr_f , \overline{Nb} , \overline{Nt} , \overline{Le} , φ_w
- (ii) Set an initial guess for $\varphi(\eta)$ or its dimensionless parameter, i.e. $\psi(\eta)$
- (iii) Calculate $F(\varphi)$, $G(\varphi)$, $Nb(\varphi)$, $Nt(\varphi)$, and $Pr(\varphi)$ based on step (i) and profile of φ
- (iv) Solve the 1st relation of equation (2.5) to obtain $f(\eta)$ by using Newton's method
- (v) Solve the 2nd relation of equation (2.5) to obtain $\theta(\eta)$ by using Newton's method
- (vi) Solve the 3rd relation of equation (2.5) to update $\psi(\eta)$ or $\varphi(\eta)$ by using Newton's method
- (vii) Check the error between the updated $\psi(\eta)$ and the guessed one
- (viii) If the maximum error $\leq 10^{-5}$ then the procedure is finished; else go to step (iii)

4. Validation of the numerical solution

With reference to many studies such as Khan and Pop (2010), Das (2015), Ibrahim and Shankar (2013), Ibrahim and Shankar (2014) and etc., it is evident that the MSPM is reduced to the old Prevalent Single-Phase Model (PSPM) by considering the relations: $F(\varphi) = 1.0$, $G(\varphi) = M$, $Nb(\varphi) = \overline{Nb}$, $Nt(\varphi) = \overline{Nt}$, and $Pr(\varphi) = Pr$. In order to check the validity of the present computational programming code, governing equations (2.5)-(2.7) subject to boundary conditions (2.8) are solved numerically for some values of the governing parameters of the PSPM. The results

for the reduced Nusselt number $|\theta'(0)|$ and the reduced Sherwood number $|\psi'(0)|$ are compared with those obtained by Khan and Pop (2010) in Table 2. In this simulation, the default values of the parameters are considered as $Pr = 10$, $\overline{Le} = 10$, $n = 1$, $r = 0$, $M = 0$, $R = 0$ and $\eta_{max} = 20$. Also, Table 3 shows the comparison of the magnitude of the velocity gradient at the wall, $|f''(0)|$, between the present code results and that obtained previously by Fang *et al.* (2009) for the case of $n = 1$, $\eta_{max} = 20$, and $M = 0.25$ -4.0. It can be seen from Tables 2 and 3 that the present results are in very good agreement with those reported by other researchers. Therefore, it is clear that the results obtained in this study are accurate.

Table 2. Comparison of $|\theta'(0)|$ and $|\psi'(0)|$ for $Pr = 10$, $\overline{Le} = 10$, $n = 1$, $r = 0$, $R = 0$, $M = 0$, $\eta_{max} = 20$

Parameter	Present result		Khan and Pop (2010)	
	$ \theta'(0) $	$ \psi'(0) $	$ \theta'(0) $	$ \psi'(0) $
$\overline{Nb} = 0.1, \overline{Nt} = 0.1$	0.95238	2.12939	0.9524	2.1294
$\overline{Nb} = 0.1, \overline{Nt} = 0.3$	0.52007	2.52863	0.5201	2.5286
$\overline{Nb} = 0.1, \overline{Nt} = 0.5$	0.32105	3.03514	0.3211	3.0351
$\overline{Nb} = 0.3, \overline{Nt} = 0.1$	0.25215	2.41002	0.2522	2.4100
$\overline{Nb} = 0.3, \overline{Nt} = 0.3$	0.13551	2.60882	0.1355	2.6088
$\overline{Nb} = 0.3, \overline{Nt} = 0.5$	0.08329	2.75187	0.0833	2.7519
$\overline{Nb} = 0.5, \overline{Nt} = 0.1$	0.05425	2.38357	0.0543	2.3836
$\overline{Nb} = 0.5, \overline{Nt} = 0.3$	0.02913	2.49837	0.0291	2.4984
$\overline{Nb} = 0.5, \overline{Nt} = 0.5$	0.01792	2.57310	0.0179	2.5731

Table 3. Comparison of results for $|f''(0)|$ when $n = 1$, and $\eta_{max} = 20$

Parameter	Present result $ f''(0) $	Fang <i>et al.</i> (2009) $ f''(0) $
$M = 0.25$	1.11803	1.1180
$M = 4.0$	2.23606	2.2361

5. Results and discussion

In this Section, the numerical results for profiles of dimensionless velocity $f'(\eta)$, temperature $\theta(\eta)$, nanoparticle concentration $\psi(\eta)$, and etc., are presented for different values of the governing parameters. The obtained results are displayed through graphs in Figs. 2-7. For all simulations and their corresponding figures, the used governing parameters are given in Table 4. It should be noted that the value of the Brownian motion number \overline{Nb} for the MSPM is calculated by equation (2.7), while for PSPM this is considered as the average of \overline{Nb} for Cu and Al_2O_3 nanoparticles. In order to compare the effect of using MSPM and PSPM on the results, the linear and non-linear stretching sheet problems for two different nanoparticles (i.e. Cu and Al_2O_3) are considered. These comparisons for six dimensionless profiles (i.e. $f, f', \theta, \theta', \psi$ and ψ') are presented in Fig. 2 (linear stretching sheet problem) and Fig. 3 (non-linear stretching sheet problem). The illustrated results in both Figs. 2 and 3 confirm that the temperature and nanoparticle volume fraction profiles (i.e. θ and ψ) converge quicker than the horizontal velocity profiles (i.e. f') for both PSPM and MSPM. Nevertheless, it is evident from the figures that the PSPM has a remarkable deviation for predicting the behavior of nanofluids flow, especially in dimensionless temperature θ and nanoparticle concentration ψ . Also, the comparison between the results presented in Figs. 2 and 3 displays that this deviation is intensified when the sheet is

stretched nonlinearly. It should be noted that discussions about the PSPM and its effect on the results of the stretching sheet problem were recently reported in many studies such as Khan and Pop (2010), Hassani *et al.* (2011), Ibrahim and Shankar (2013), Ibrahim and Shanker (2014), and to name but a few. Therefore, for the next simulations, the MSPM is only considered. Also, based on the results shown in Figs. 2 and 3, one can observe that the boundary layer behavior and thermal characteristics of both nanoparticle flows are approximately the same. Hence, the further results and discussions are focused only on the Cu-water nanofluid flow (using the MSPM).

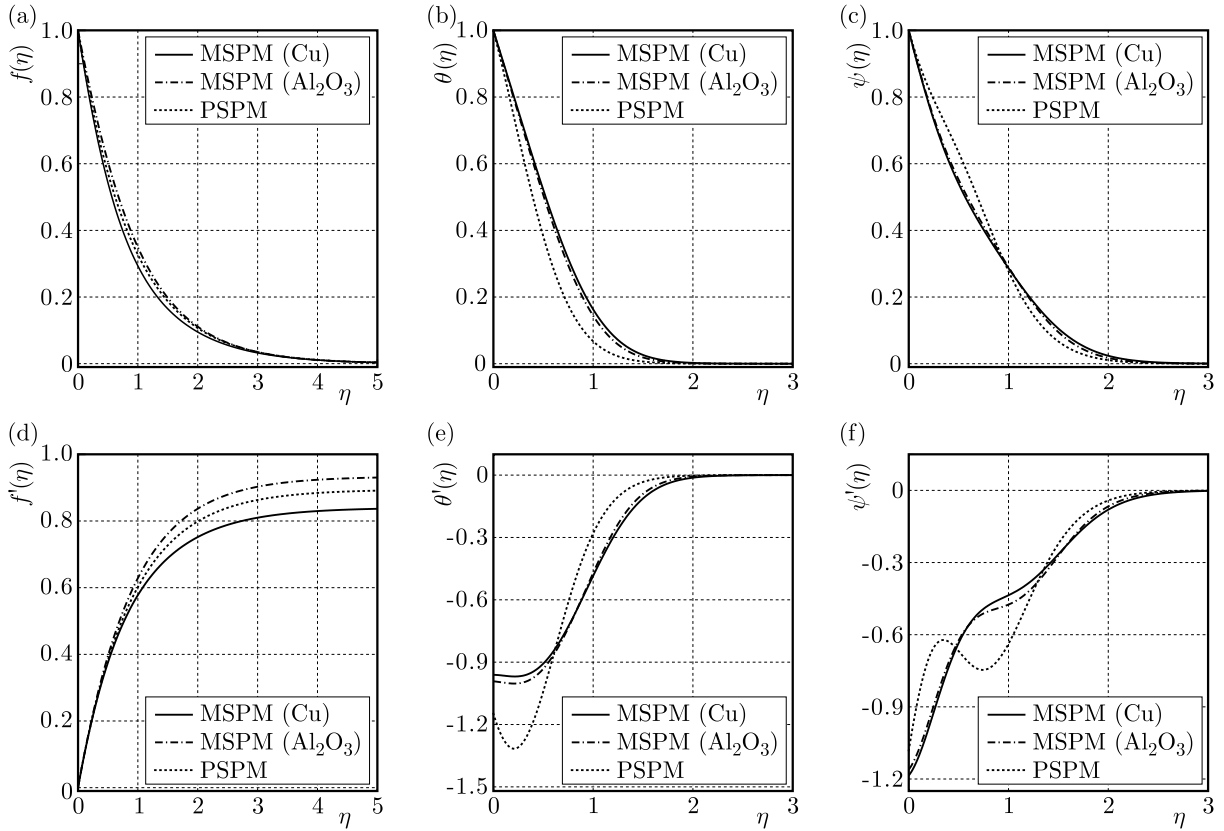


Fig. 2. Effect of the MSPM and PSPM on the dimensionless profiles for $n = 1$ and $r = 0$

Table 4. The governing parameters for nanofluid flow simulations

Fig.	n	r	\overline{Nt}	\overline{Le}	φ_w	M	R	Nb		
								MSPM (Cu)	MSPM (Al ₂ O ₃)	PSPM
2	1	0	0.1	5	0.5	0.25	0.1	0.0825	0.0729	0.0777
3	5	5	0.1	5	0.5	0.25	0.1	0.0825	0.0729	0.0777
4	5	5	0.1	5	0.5	0.0-4.0	0.1	0.0825	—	—
5	5	5	0.1	5	0.5	2.0	0.0-10	0.0825	—	—
6	5	5	0.1	1	0.1-0.5	2.0	5	0.0825-0.4125	—	—
7a	5	5	0.1	5	0.5	0.0-4.0	0.1	0.0825	—	—
7b	5	5	0.1	5	0.5	2.0	0.0-10	0.0825	—	—
7c	5	5	0.1	1	0.1-0.5	2.0	5	0.0825-0.4125	—	—

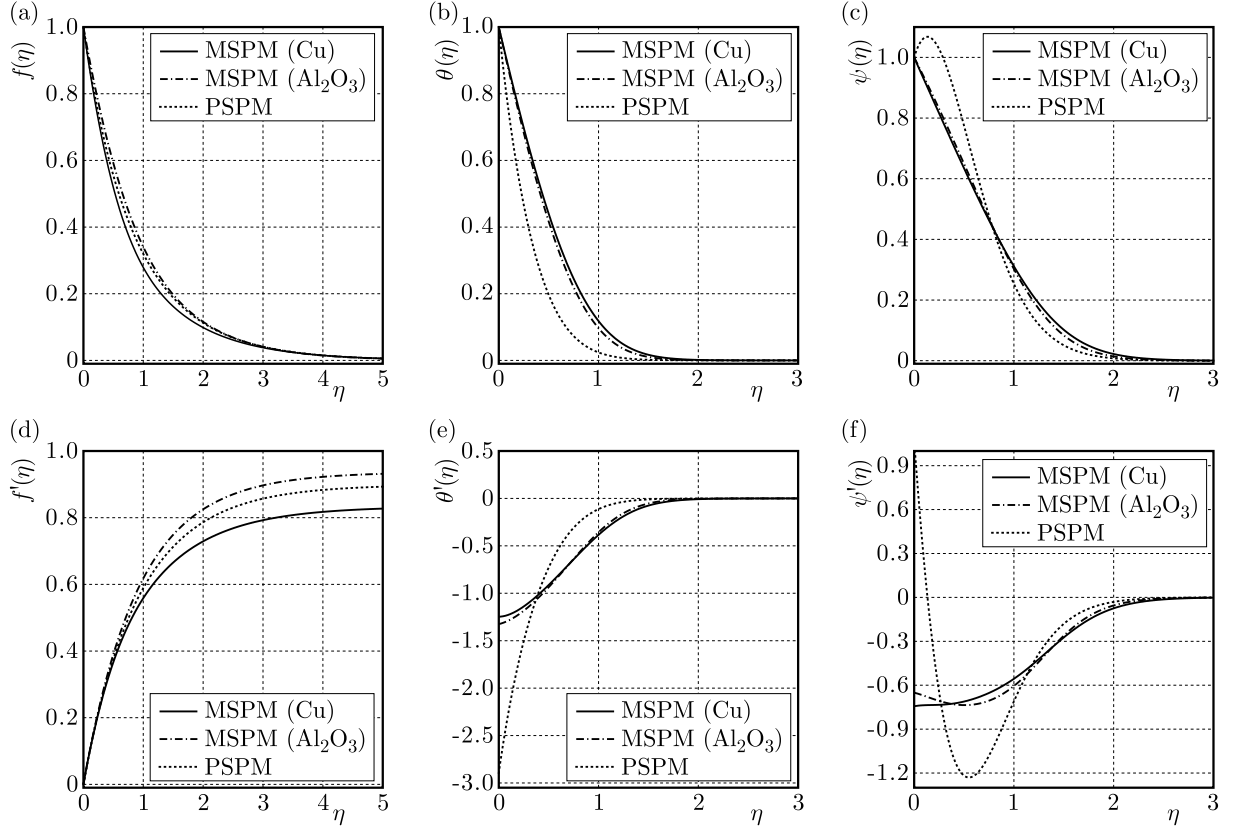


Fig. 3. Effect of the MSPM and PSPM on the dimensionless profiles for $n = 5$ and $r = 5$

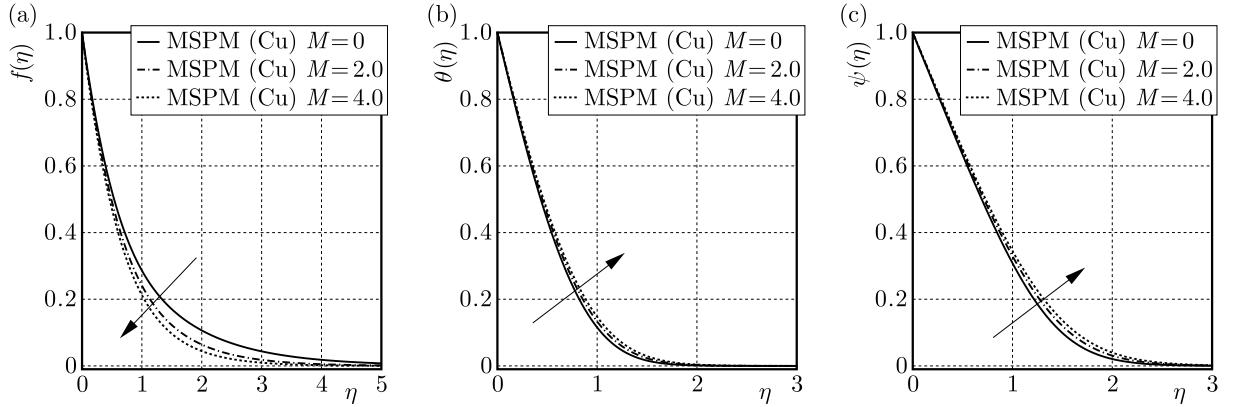


Fig. 4. Effect of M on the dimensionless profiles for $n = 5$ and $r = 5$

The first analysis is related to the effects of the transverse magnetic field M on the flow and thermal characteristics. By applying a transverse magnetic field, a Lorentz force is created, which results in a retarding force on the velocity of the flow (Ibrahim and Shanker, 2014). Therefore, as M increases (and, consequently, increasing the retarding force), the velocity of the fluid decreases. This fact can be observed in Fig. 4a. In addition, Fig. 4b illustrates the impact of the transverse magnetic field on the temperature profile. The results show that as the magnetic parameter M increases, the temperature profile and the thermal boundary layer thickness increase. Also, from Fig. 4c it is seen that the behavior of dimensionless concentration is the same as the temperature profile when the values of the magnetic parameter M increase.

Chemical reaction is an important process that should be considered in micro-mixing of biological systems such as cell-activation and protein-folding, particularly when the mixing of reactants for initiation is necessary. Lorentz forces produced by a magnetic field are able to move nano-liquids in a mixing process. Hence, one of the active methods of micro-mixing of biological samples is using a magnetic field in the presence of chemical reaction (Yazdi *et al.*, 2011). Therefore, the second examination belongs to the effects of the chemical reaction strength R on the nanofluids BLF characteristics. Figure 5 demonstrates the influence of the chemical reaction strength on the velocity, temperature and concentration graph. From Fig. 5a, it is evident that the values of R has not any significant effect on the dimensionless velocity profile. But, by increasing the values of the chemical reaction parameter, the temperature gradient (Fig. 5b) and concentration gradient (Fig. 5c) on the wall intensify. In fact, for the case of the higher nanoparticle concentration gradient near the wall, the nanoparticle concentration decreases rapidly as η increases. Therefore, the conductive heat transfer process is weakened.

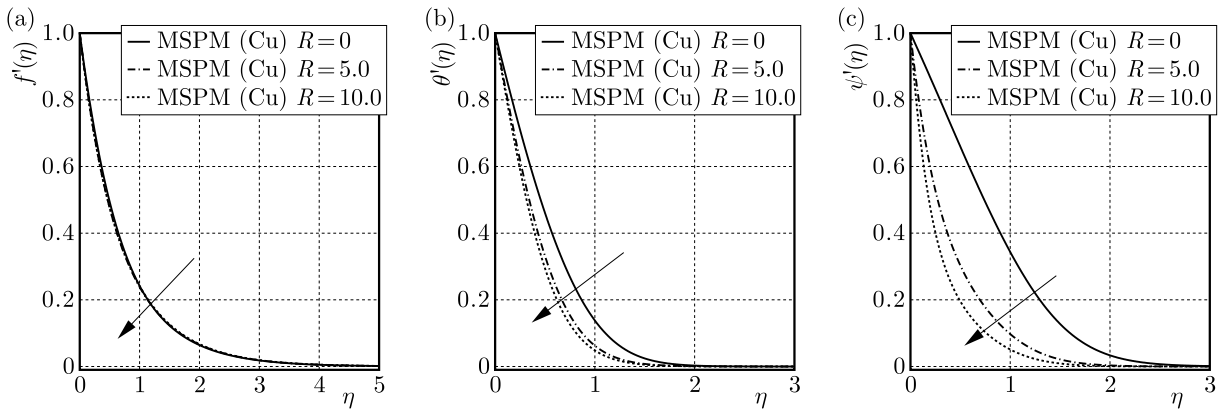


Fig. 5. Effect of R on the dimensionless profiles for $n = 5$ and $r = 5$

As the MSPM depends on the value of the nanoparticle volume fraction near the surface φ_w , it is of great worth to investigate the effects of φ_w on dynamic and thermal characteristics of the nanofluids flow. As it is predicted, when the value of the magnetic parameter M does not change, variation of φ_w has no significant influence on the velocity graph (see Fig. 6a). However, as it is noticed from Fig. 6b, increasing the nanoparticle volume fraction near the surface increases the thermal boundary layer thickness. And finally for Fig. 6c, since $\psi = \varphi/\varphi_w$, comparing the concentration graphs for various φ_w has no any important consequence.

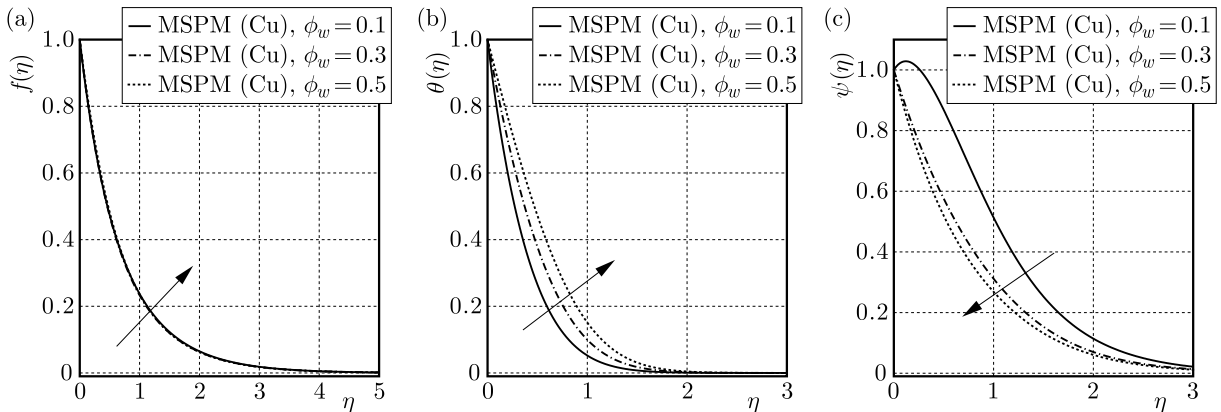


Fig. 6. Effect of φ_w on the dimensionless profiles for $n = 5$ and $r = 5$

The last results are about the effect of M , R , and φ_w on the dimensionless heat $Nu_{nf}/\sqrt{Re_x}$ and mass transfer rates $Sh_{nf}/\sqrt{Re_x}$ on the wall. This information is presented in Fig. 7. Figure 7a illustrates that the heat and mass transfer rates on the stretching wall decrease with an increase in the transverse magnetic field M . In fact, the magnetic field generates more heat in the boundary layer region and, hence, this reduces the wall heat transfer rate. Figure 7b depicts that the wall mass transfer rate and the wall heat transfer rate increase with an increase in the chemical reaction parameter R . In addition, a decrease in the dimensionless heat transfer and an increase in the dimensionless mass transfer on the wall are observed with an increase in φ_w . These are shown in Fig. 7c.

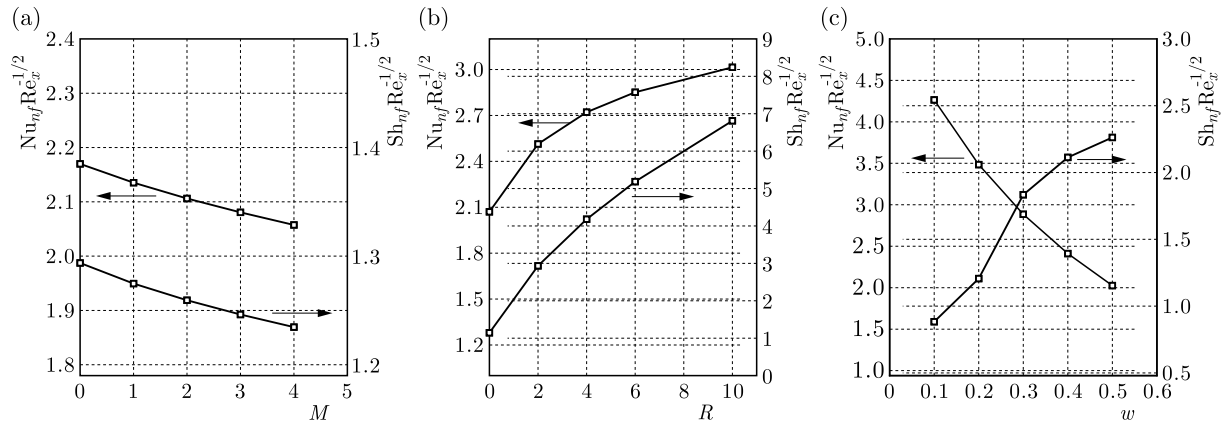


Fig. 7. Effect of M , R , and φ_w on the dimensionless heat and mass transfer rates for $n = 5$ and $r = 5$

6. Conclusion

The problem of boundary layer flow and heat transfer of nanofluids over a nonlinear stretching sheet in the presence of a magnetic field and chemical reaction is examined numerically. In this study, a modified single-phase model for analyzing nanofluids flow and heat transfer is initiated. In this modified model, the effective density and viscosity of nanofluids and the effective thermal conductivity of the solid-liquid mixture which are prevalently used in the effective single-phase model (as constant values) are incorporated locally with the governing equations (as non-constant values). A similarity solution is proposed which depends on the local Prandtl number, local Brownian motion number, local Lewis number and the local thermophoresis number. The results for Cu and Al_2O_3 nanoparticles are compared to the prevalent single-phase model. This comparison shows that the prevalent single-phase model has a noticeable deviation for predicting the behavior of the nanofluids flow, especially in dimensionless temperature and nanoparticle volume fraction. In addition, the results exhibit that the heat and mass transfer rates on the stretching surface decrease with increase in the transverse magnetic field. Also, the wall mass transfer rate and the wall heat transfer rate increase with an increase in the chemical reaction parameter.

Acknowledgments

The author would like to acknowledge the Shahrood University of Technology which supported this project.

References

1. ABU-NADA E., CHAMKHAC A.J., 2010, Mixed convection flow in a lid-driven inclined square enclosure filled with a nanofluid, *European Journal of Mechanics B/Fluids*, **29**, 472-482

2. AMINOSSADATI S.M., GHASEMI B., 2009, Natural convection cooling of a localised heat source at the bottom of a nanofluid-filled enclosure, *European Journal of Mechanics B/Fluids*, **28**, 630-640
3. BACHOK N., ISHAK A., POP, I., 2010, Boundary-layer flow of nanofluids over a moving surface in a flowing fluid, *International Journal of Thermal Sciences*, **49**, 1663-1668
4. BUONGIORNO J., 2006, Convective transport in nanofluids, *ASME Journal of Heat Transfer*, **128**, 240-250
5. CHEN C.K., CHAR M. I., 1988, Heat transfer of a continuous stretching surface with suction or blowing, *Journal Mathematical Analysis and Applications*, **135**, 568-580
6. CHOI S.U.S., 1995, Enhancing thermal conductivity of fluids with nanoparticles, *ASME Fluids Engineering Division*, **231**, 99-105
7. CHOI S.U.S., ZHANG Z.G., YU W., LOCKWOOD F.E., GRULKE E.A., 2001, Anomalous thermal conductivity enhancement in nanotube suspensions, *Applied Physics Letters*, **79**, 14, 2252-2254
8. CORTELL R., 2007, Viscous flow and heat transfer over a nonlinearly stretching sheet, *Applied Mathematics and Computation*, **184**, 864-873
9. CRANE L.J., 1970, Flow past a stretching plate, *Kurze Mitteilungen-Brief Reports-Communications Breves*, **21**, 645-647
10. DAS K., 2015, Nanofluid flow over a non-linear permeable stretching sheet with partial slip, *Journal of the Egyptian Mathematical Society*, **23**, 2, 451-456
11. ESFE M.H., SAEDODIN S., MAHIAN O., WONGWISES S., 2014, Thermal conductivity of Al_2O_3 /water nanofluids – Measurement, correlation, sensitivity analysis, and comparisons with literature reports, *Journal of Thermal Analysis and Calorimetry*, **117**, 2, 675-681
12. FADZILAH M., NAZAR R., NORIHAN M., POP I., 2011, MHD boundary-layer flow and heat transfer over a stretching sheet with induced magnetic field, *Journal of Heat and Mass Transfer*, **47**, 155-162
13. FANG T., ZHANG J., YAO S., 2009, Slip MHD viscous flow over a stretching sheet – An exact solution, *Communications in Nonlinear Science and Numerical Simulation*, **14**, 3731-3737
14. GORDER R.A.V., SWEET E., VAJRARELU K., 2010, Nano boundary layers over stretching surfaces, *Communications in Nonlinear Science and Numerical Simulation*, **15**, 1494-1500
15. GUPTA P.S., GUPTA A.S., 1977, Heat and mass transfer on a stretching sheet with suction or blowing, *The Canadian Journal of Chemical Engineering*, **55**, 744-746
16. HAMAD M.A.A., FERDDOWS M., 2012, Similarity solutions to viscous flow and heat transfer of nanofluid over nonlinearly stretching sheet, *Applied Mathematics and Mechanics (English Edition)*, **33**, 7, 923-930
17. HASSANI M., MOHAMMAD TABAR NEMATI H., DOMAIRRY G., NOORI F., 2011, An analytical solution for boundary layer flow of a nanofluid past a stretching sheet, *International Journal of Thermal Sciences*, **50**, 2256-2263
18. HERIS S.Z., ETEMAD S.G., ESFAHANY M.N., 2006, Experimental investigation of oxide nanofluids laminar flow convective heat transfer, *International Communications in Heat and Mass Transfer*, **33**, 529-535
19. IBRAHIM W., SHANKAR B., 2013, MHD boundary layer flow and heat transfer of a nanofluid past a permeable stretching sheet with velocity, thermal and solutal slip boundary conditions, *Computer and Fluids*, **75**, 1-10
20. IBRAHIM W., SHANKAR B., NANDEPPANAVAR M.M., 2013, MHD stagnation point flow and heat transfer due to nanofluid towards a stretching sheet, *International Journal of Heat and Mass Transfer*, **56**, 1-9
21. IBRAHIM W., SHANKER B., 2014, Magnetohydrodynamic boundary layer flow and heat transfer of a nanofluid over non-isothermal stretching sheet, *ASME Journal of Heat Transfer*, **136**, 051701-9

22. ISHAK A., NAZAR R., POP I., 2008, Hydro magnetic flow and heat transfer adjacent to a stretching vertical sheet, *Journal of Heat and Mass Transfer*, **44**, 921-927
23. KHAN W.A., POP I., 2010, Boundary-layer flow of a nanofluid past a stretching sheet, *International Journal of Heat and Mass Transfer*, **53**, 2477-2483
24. KHANAFER K., VAFAI K., LIGHTSTONE M., 2003, Buoyancy-driven heat transfer enhancement in a two-dimensional enclosure utilizing nanofluids, *International Journal of Heat and Mass Transfer*, **46**, 3639-3653
25. KUMAR P.M., KUMAR J., TAMILARASAN R., SENDHILNATHAN S., SURESH S., 2015, Review on nanofluids theoretical thermal conductivity models, *Engineering Journal*, **19**, 1, 67-83
26. LI C.H., PETERSON G.P., 2007, Mixing effect on the enhancement of the effective thermal conductivity of nanoparticle suspensions (nanofluids), *International Journal of Heat and Mass Transfer*, **50**, 4668-4677
27. MAHAPATRA T.R., NANDY S.K., GUPTA A.S., 2009, Magnetohydrodynamic stagnation point flow of a power-law fluid towards a stretching sheet, *International Journal of Non-Linear Mechanics*, **44**, 124-129
28. NADEEM S., HAQ R.U., KHAN Z.H., 2014, Heat transfer analysis of water-based nanofluid over an exponentially stretching sheet, *Alexandria Engineering Journal*, **53**, **219-224**
29. OZTOP H.F., ABU-NADA E., 2008, Numerical study of natural convection in partially heated rectangular enclosures filled with nanofluids, *International Journal of Heat and Fluid Flow*, **29**, 1326-1336
30. POSTELNICU A., POP I., 2011, Falkner-Skan boundary layer flow of a power-law fluid past a stretching wedge, *Applied Mathematics and Computation*, **217**, 4359-4368
31. PRASAD K.V., VAJRARELU K., DATTI P.S., 2010, Mixed convection heat transfer over a non-linear stretching surface with variable fluid properties, *International Journal of Non-Linear Mechanics*, **45**, 320-330
32. RANA P., BHARGAVA R., 2012, Flow and heat transfer of a nanofluid over a nonlinearly stretching sheet: A numerical study, *Communications in Nonlinear Science and Numerical Simulation*, **17**, 212-226
33. SAKIADIS B.C., 1961a, Boundary layer behavior on continuous moving solid surfaces. I. Boundary layer equations for two-dimensional and axis-symmetric flow, *American Institute of Chemical Engineer Journal*, **7**, 1, 26-28
34. SAKIADIS B.C., 1961b, Boundary layer behavior on continuous moving solid surfaces. II. Boundary layer on a continuous flat surface, *American Institute of Chemical Engineer Journal*, **7**, 2, 221-225
35. SAKIADIS B.C., 1961c, Boundary layer behavior on continuous moving solid surfaces. III. Boundary layer on a continuous cylindrical surface, *American Institute of Chemical Engineer Journal*, **7**, 3, 467-472
36. SHEIKHZADEH G.A., AREFMANESH A., KHEIRKHAH M.H., ABDOLLAHI R., 2011, Natural convection of Cu-water nanofluid in a cavity with partially active side walls, *European Journal of Mechanics B/Fluids*, **30**, 2, 166-176
37. VAJRARELU K., 2001, Viscous flow over a nonlinearly stretching sheet, *Applied Mathematics and Computation*, **124**, 281-288
38. VAJRARELU K., CANNON J.R., 2006, Fluid flow over a nonlinearly stretching sheet, *Applied Mathematics and Computation*, **181**, 609-618
39. VAJRARELU K., PRASAD K.V., DATTI P.S., RAJU B.T., 2014, MHD flow and heat transfer of an Ostwald-de Waele fluid over an unsteady stretching surface, *Ain Shams Engineering Journal*, **5**, 157-167
40. WANG X.Q., MUJUMDAR A.S., 2007, Heat transfer characteristics of nanofluids: a review, *International Journal of Thermal Sciences*, **46**, 1-19

41. WEN D., DING Y., 2004, Experimental investigation into convective heat transfer of nanofluids at the entrance region under laminar flow conditions, *International Journal of Heat and Mass Transfer*, **47**, 5181-5188
42. XIE H.Q., LEE H., YOUN W., CHOI M., 2003, Nanofluids containing multiwalled carbon nanotubes and their enhanced thermal conductivities, *Journal of Applied Physics*, **94**, 8, 4967-4971
43. YAZDI M.H., ABDULLAH S., HASHIM I., SOPIAN K., 2011, Slip MHD liquid flow and heat transfer over non-linear permeable stretching surface with chemical reaction, *International Journal of Heat and Mass Transfer*, **54**, 3214-3225

Manuscript received May 15, 2017; accepted for print July 25, 2017

BENDING ANALYSIS OF PLATES BY SUPERPOSING CYLINDRICAL DEFLECTIONS¹

GRZEGORZ E. JEMIELITA

Warsaw University of Life Sciences, Faculty of Civil and Environmental Engineering, Warsaw, Poland
e-mail: g.jemielita@il.pw.edu.pl

In this paper, the present exact solutions in the plate theory using the cylindrical deflection method and represented by the Fourier series corresponding to the oblique or Cartesian coordinates are given for a hingely supported triangular plate subject to a distributed load in form of a hexagonal pyramid and for a rectangular hingely supported plate subject to loading in form of a truncated octagonal pyramid. In the case of the rectangular hingely supported plate under the truncated octagonal pyramid load, a series of parametric solutions has been obtained. The solutions depend on the parameter ε . For various values of the parameter ε , various load cases are found.

Keywords: plate, reference solution, cylindrical deflection, superposing, Fourier series

1. Introduction

Accuracy assessment of FEM results can be carried out by comparing it with results obtained by using analytical methods. Comparative analysis between benchmark solutions and the FEM results is of practical importance. "The benchmark should have some educational merit" (Becker, 1998). Performing comparative analyses is an excellent and timely topic. This is evidenced by studies in different fields of mechanics. For example: within the framework of linear and non-linear plate and shell theories, particular attention shall be paid to research by Robinson (1985), Kamoulakos *et al.* (1986), NAFEMS (1990), Prinja and Clegg (1993), Becker (2001), Sze *et al.* (2004), within vibration theory see Abbassian *et al.* (1987), theory of composites – Hardy (2001), thermal stresses – Burrows (1985), linear elastic fracture mechanics – Pang and Leggatt (2001), etc. The benchmark reference solutions for thin and thick plates of various shapes can be found in NAFEMS (1990), Davies *et al.* (1992) where linear analysis of bending a skew plate, thick plate, free thin square plate, clamped thin rhombic plate, cantilevered thin square plate, simply-supported 'solid' square plate is carried out. Finding benchmark solutions is of great importance in the process of verification of the FEM results.

Within the framework of the plate theory, such benchmark solutions include closed form solutions obtained by Z. Kączkowski in his doctoral thesis in 1953. The thesis of Zbigniew Kączkowski *On anisotropic plates bending analysis by superposing folded deflections*, published in 1953 (Kączkowski, 1953, 1954) is an exceptional piece of work. Without any doubt, this is both valuable and pioneering research paper created with great imagination and cleverness. The proposed method of superimposing the folded deflections (as called by the Author) makes it possible, by appropriate superposition of cylindrical bending deflections referring to the infinitely long plate, to arrive at closed form solutions of anisotropic plates in form of parallelograms, rectangles and triangles resting on Winkler's foundation, subject to some in-plane normal tractions and subjected to transverse loading of a certain class. The majority of solutions refer to the plates

¹For Dear Professor and my Master Zbigniew Kączkowski in his 96th Jubilee

being hingely supported, yet Zbigniew Kączkowski showed some other boundary conditions that could tackled as in the case of rectangular plates clamped at the opposite parallel edges or fully clamped.

In his famous monograph *Plates. Statical Analysis* (1968), about which prof. Witold Nowacki wrote that this had been the best world wide monograph on plates, prof. Kączkowski put forward a series of examples of triangular plates, not solved in the pioneering work of 1953.

In this beautiful monograph, Professor wrote (p.191): “It is recommended to the reader to find a closed form solution of the deflection of a triangular plate subject to the loading distributed in form of a hexagonal pyramid, Fig. 1.”

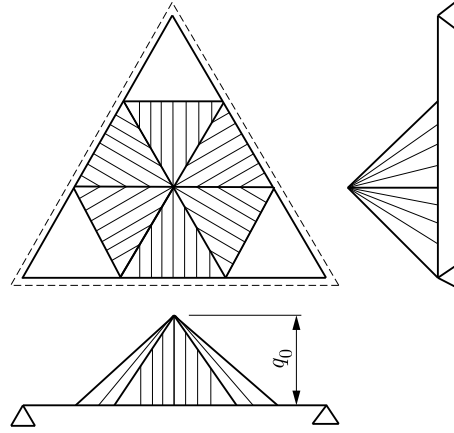


Fig. 1. Scheme of a triangular plate subject to loading distributed in form of a hexagonal pyramid (Kączkowski, 1968, p. 191)

In the available literature, I was not able to find the solution to this still open problem. This and one similar solution will be presented here in closed form solutions and represented by the Fourier series corresponding to the oblique or Cartesian coordinates.

2. A hingely supported triangular plate subject to a distributed load in form of a hexagonal pyramid

Let us consider an infinite isotropic plate subject to normal load p_1 that is a periodic function of a variable x_1 with the period c , antisymmetric with respect to both the original and central points of each period. Due to the load of that kind, we obtain a folded surface that can be represented by a function $w_1(x_1)$ with the folds making the angle of 60° with the axis x . When, apart from the aforementioned load, the plate is also subject to the load $p_2(x_2) = -p_1(x_2)$ due to which the plate deflection surface is $w_2(x_2) = -w_1(x_2)$ as well as to the load $p_3(y) = p_1(y)$ due to which the plate deflection surface is $w_3(y) = w_1(y)$. The “sum” of all three surfaces will satisfy the conditions for the simple support along the edge of the equilateral triangle of side a and height $c = a\sqrt{3}/2$ (Fig. 3).

For the resulting formulae to be more compact, let us introduce a new oblique co-ordinate system $x = \bar{x}$, $y = \bar{y}$, the co-ordinates of which make the angle of 60° (Kączkowski, 1953).

The shape of the loading is shown in Fig. 2.

The plate domain parameterization is assumed as in Fig. 3. Let us introduce non-dimensional coordinates, cf Fig. 3.

$$\begin{aligned} \xi_1 = \frac{x_1}{c} = \frac{\bar{x}}{a} = \bar{\xi} & \quad \bar{\eta} = \frac{x_3}{c} = \frac{\bar{y}}{a} & \quad \frac{x_2}{c} = \bar{\xi} + \bar{\eta} & \quad \xi = \frac{x}{a} \\ \eta = \frac{y}{a} & \quad \bar{\xi} = \xi - \frac{\sqrt{3}}{3}\eta & \quad \bar{\eta} = \frac{2\sqrt{3}}{3}\eta \end{aligned} \quad (2.1)$$

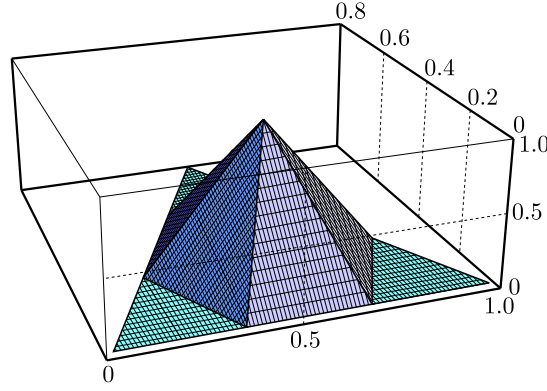


Fig. 2. The shape of the loading

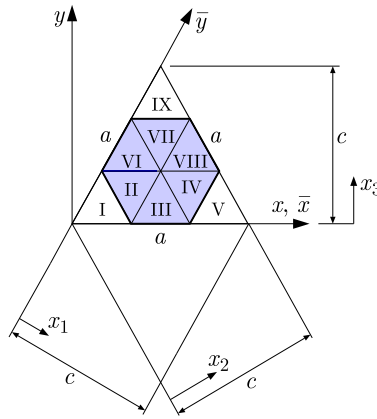


Fig. 3. Parameterization of the plate domain and the coordinates

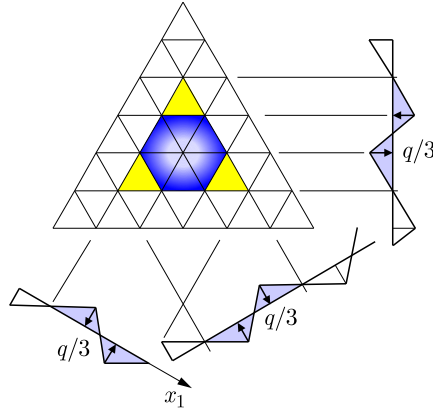


Fig. 4. Decomposition of the hexagonal pyramid load

The loading in Fig. 2 can be viewed as a sum of three loadings acting on an infinite plate, see Fig. 4, hence one can write down this decomposition as

$$q(\bar{\xi}, \bar{\eta}) = q_1(\xi_1) - q_1(\xi_1 + \bar{\eta}) + q_1(\bar{\eta}) \quad (2.2)$$

in which

$$q_1(\xi_1) = \left\{ \begin{array}{ll} q_{11} = q_0 \xi_1 & \text{for } 0 \leq \xi_1 \leq \frac{1}{3} \\ q_{12} = q_0(1 - 2\xi_1) & \text{for } \frac{1}{3} \leq \xi_1 \leq \frac{2}{3} \\ q_{13} = -q_0(1 - \xi_1) & \text{for } \frac{2}{3} \leq \xi_1 \leq 1 \end{array} \right\} = -q_0 \sum_{n=1}^{\infty} \frac{16 \cos \frac{n\pi}{2} \sin^3 \frac{n\pi}{6}}{n^2 \pi^2} \sin(n\pi \xi_1) \quad (2.3)$$

Depending on the subdomain considered, the loading function can be presented as below

$$q(\bar{\xi}, \bar{\eta}) = [q_I, q_{II}, q_{III}, q_{IV}, q_V, q_{VI}, q_{VII}, q_{VIII}, q_{IX}] \quad (2.4)$$

where

$$\begin{aligned} \frac{q_I}{q_0} &= q_{11}(\bar{\xi}) - q_{11}(\bar{\xi} + \bar{\eta}) + q_{11}(\bar{\eta}) = 0 \\ \frac{q_{II}}{q_0} &= q_{11}(\bar{\xi}) - q_{12}(\bar{\xi} + \bar{\eta}) + q_{11}(\bar{\eta}) = -1 + 3\bar{\xi} + 3\bar{\eta} \\ \frac{q_{III}}{q_0} &= q_{12}(\bar{\xi}) - q_{12}(\bar{\xi} + \bar{\eta}) + q_{11}(\bar{\eta}) = 3\bar{\eta} & \frac{q_{IV}}{q_0} &= q_{12}(\bar{\xi}) - q_{13}(\bar{\xi} + \bar{\eta}) + q_{11}(\bar{\eta}) = 2 - 3\bar{\xi} \\ \frac{q_V}{q_0} &= q_{13}(\bar{\xi}) - q_{13}(\bar{\xi} + \bar{\eta}) + q_{11}(\bar{\eta}) = 0 & \frac{q_{VI}}{q_0} &= q_{11}(\bar{\xi}) - q_{12}(\bar{\xi} + \bar{\eta}) + q_{12}(\bar{\eta}) = 3\bar{\xi} \\ \frac{q_{VII}}{q_0} &= q_{11}(\bar{\xi}) - q_{13}(\bar{\xi} + \bar{\eta}) + q_{12}(\bar{\eta}) = 2 - 3\bar{\eta} & \frac{q_{IX}}{q_0} &= q_{11}(\bar{\xi}) - q_{13}(\bar{\xi} + \bar{\eta}) + q_{13}(\bar{\eta}) = 0 \\ \frac{q_{VIII}}{q_0} &= q_{12}(\bar{\xi}) - q_{13}(\bar{\xi} + \bar{\eta}) + q_{12}(\bar{\eta}) = 3(1 - \bar{\xi} - \bar{\eta}) \end{aligned}$$

or in the form of the Fourier series referred to the Cartesian, yet non-orthogonal system (\bar{x}, \bar{y})

$$\begin{aligned} q(\bar{\xi}, \bar{\eta}) &= -q_0 \sum_{n=1}^{\infty} \frac{16 \cos \frac{n\pi}{2} \sin^3 \frac{n\pi}{6}}{n^2 \pi^2} [\sin(n\pi \bar{\xi}) - \sin(n\pi(\bar{\xi} + \bar{\eta})) + \sin(n\pi \bar{\eta})] \\ &= -32q_0 \sum_{n=1}^{\infty} \frac{\cos \frac{n\pi}{2} \sin^3 \frac{n\pi}{6}}{n^2 \pi^2} \left[\sin(n\pi \bar{\xi}) \sin^2 \frac{n\pi \bar{\eta}}{2} + \sin(n\pi \bar{\eta}) \sin^2 \frac{n\pi \bar{\xi}}{2} \right] \end{aligned} \quad (2.5)$$

or to the orthogonal system (x, y)

$$q(\xi, \eta) = -32q_0 \sum_{n=1}^{\infty} \frac{\cos \frac{n\pi}{2} \sin^3 \frac{n\pi}{6}}{n^2 \pi^2} \left[\left(\cos \frac{n\pi \eta}{\sqrt{3}} - \cos(n\pi \xi) \right) \sin \frac{n\pi \eta}{\sqrt{3}} \right] \quad (2.6)$$

The solution to the differential equations

$$\frac{d^4 w_1(\xi_1)}{d\xi_1^4} = \frac{q_0 c^4}{D} \left\{ \begin{array}{ll} \xi_1 & \text{for } 0 \leq \xi_1 \leq \frac{1}{3} \\ 1 - 2\xi_1 & \text{for } \frac{1}{3} \leq \xi_1 \leq \frac{2}{3} \\ -1 + \xi_1 & \text{for } \frac{2}{3} \leq \xi_1 \leq 1 \end{array} \right. \quad (2.7)$$

reads

$$w_1(\xi_1) = \frac{q_0 c^4}{D} \left\{ \begin{array}{ll} w_{11}(\xi_1) & \text{for } 0 \leq \xi_1 \leq \frac{1}{3} \\ w_{12}(\xi_1) & \text{for } \frac{1}{3} \leq \xi_1 \leq \frac{2}{3} \\ w_{13}(\xi_1) & \text{for } \frac{2}{3} \leq \xi_1 \leq 1 \end{array} \right. \quad (2.8)$$

where

$$\begin{aligned} w_{11}(\xi_1) &= \xi_1 \frac{10 - 60\xi_1^2 + 81\xi_1^4}{9720} & w_{12}(\xi_1) &= \frac{1 - 5\xi_1 + 90\xi_1^2 - 330\xi_1^3 + 405\xi_1^4 - 162\xi_1^5}{9720} \\ w_{13}(\xi_1) &= \frac{-31 + 235\xi_1 - 630\xi_1^2 + 750\xi_1^3 - 405\xi_1^4 + 81\xi_1^5}{9720} \end{aligned} \quad (2.9)$$

or it can be represented by the following Fourier series

$$w_1(\xi_1) = -16 \frac{q_0 c^4}{D} \sum_{n=1}^{\infty} \frac{\cos \frac{n\pi}{2} \sin^3 \frac{n\pi}{6}}{n^6 \pi^6} \sin(n\pi\xi_1) = -9 \frac{q_0 a^4}{D} \sum_{n=1}^{\infty} \frac{\cos \frac{n\pi}{2} \sin^3 \frac{n\pi}{6}}{n^6 \pi^6} \sin(n\pi\xi_1) \quad (2.10)$$

The plate deflection referring to the subdomains I to IX (Fig. 3) can be put in the form

$$w(\bar{\xi}, \bar{\eta}) = \frac{q_0 c^4}{D} [w_I, w_{II}, w_{III}, w_{IV}, w_V, w_{VI}, w_{VII}, w_{VIII}, w_{IX}] \quad (2.11)$$

where

$$\begin{aligned} w_I(\bar{\xi}, \bar{\eta}) &= w_{11}(\bar{\xi}) - w_{11}(\bar{\xi} + \bar{\eta}) + w_{11}(\bar{\eta}) = \frac{\bar{\xi}\bar{\eta}}{216} (\bar{\xi} + \bar{\eta}) [4 - 9(\bar{\xi}^2 + \bar{\xi}\bar{\eta} + \bar{\eta}^2)] \\ w_{II}(\bar{\xi}, \bar{\eta}) &= w_{11}(\bar{\xi}) - w_{12}(\bar{\xi} + \bar{\eta}) + w_{11}(\bar{\eta}) = \frac{1}{9720} \left\{ (\bar{\xi} + \bar{\eta}) [15 - 90(\bar{\xi} + \bar{\eta}) \right. \\ &\quad \left. + 330(\bar{\xi} + \bar{\eta})^2 - 405(\bar{\xi} + \bar{\eta})^3 + 162(\bar{\xi} + \bar{\eta})^4] - 1 - 60(\bar{\xi}^3 + \bar{\eta}^3) + 81(\bar{\xi}^5 + \bar{\eta}^5) \right\} \\ w_{III}(\bar{\xi}, \bar{\eta}) &= w_{12}(\bar{\xi}) - w_{12}(\bar{\xi} + \bar{\eta}) + w_{11}(\bar{\eta}) = \frac{\bar{\eta}}{3240} [81\bar{\eta}^4 - 135\bar{\eta}^3(1 - 2\bar{\xi}) \\ &\quad + 90\bar{\eta}^2(1 - 6\bar{\xi} + 6\bar{\xi}^2) - 30\bar{\eta}(1 - 11\bar{\xi} + 27\bar{\xi}^2 - 18\bar{\xi}^3) + 5(1 - 12\bar{\xi} + 66\bar{\xi}^2 - 108\bar{\xi}^3 + 54\bar{\xi}^4)] \\ w_{IV} &= w_{12}(\bar{\xi}) - w_{13}(\bar{\xi} + \bar{\eta}) + w_{11}(\bar{\eta}) = \frac{1}{9720} \left\{ (1 - \bar{\xi}) [405\bar{\eta}^4 - 810(1 - \bar{\xi})\bar{\eta}^3 \right. \\ &\quad \left. - 45(1 - \bar{\xi})\bar{\eta}(5 - 18\bar{\xi} + 9\bar{\xi}^2) + 90\bar{\eta}^2(7 - 18\bar{\xi} + 9\bar{\xi}^2)] + (2 - 3\bar{\xi})^5 \right\} \\ w_V &= w_{13}(\bar{\xi}) - w_{13}(\bar{\xi} + \bar{\eta}) + w_{11}(\bar{\eta}) \\ &= \frac{\bar{\eta}}{216} (1 - \bar{\xi}) [-5 + 9\bar{\eta}^2(2\bar{\xi} + \bar{\eta} - 2) + \xi(23 - 27\bar{\xi} + 9\bar{\xi}^2) + 2\bar{\eta}(7 - 18\bar{\xi} + 9\bar{\xi}^2)] \\ w_{VI} &= w_{11}(\bar{\xi}) - w_{12}(\bar{\xi} + \bar{\eta}) + w_{12}(\bar{\eta}) = \frac{\bar{\xi}}{3240} [5 + 270\bar{\eta}^4 - 540\bar{\eta}^3(1 - \bar{\xi}) \\ &\quad - 3\bar{\xi}(10 - 30\bar{\xi} + 45\bar{\xi}^2 - 27\bar{\xi}^3) - 30\bar{\eta}^2(11 - 27\bar{\xi} + 18\bar{\xi}^2) - 30\bar{\eta}(1 - \bar{\xi})(2 - 9\bar{\xi} + 9\bar{\xi}^2)] \\ w_{VII} &= w_{11}(\bar{\xi}) - w_{13}(\bar{\xi} + \bar{\eta}) + w_{12}(\bar{\eta}) = \frac{1}{9720} [30 + (1 - \bar{\eta})(2 - 3\bar{\eta} + 87\bar{\eta}^2 - 243\bar{\eta}^3 + 162\bar{\eta}^4) \\ &\quad + \bar{\xi}(10 - 60\bar{\xi}^2 + 81\bar{\xi}^4) - 235(\bar{\xi} + \bar{\eta}) + 630(\bar{\xi} + \bar{\eta})^2 - 750(\bar{\xi} + \bar{\eta})^3 \\ &\quad + 405(\bar{\xi} + \bar{\eta})^4 - 81(\bar{\xi} + \bar{\eta})^5] \\ w_{VIII} &= w_{12}(\bar{\xi}) - w_{13}(\bar{\xi} + \bar{\eta}) + w_{12}(\bar{\eta}) = \frac{1}{9720} [31 \\ &\quad + (1 - \bar{\eta})(2 - 3\bar{\eta} + 87\bar{\eta}^2 - 243\bar{\eta}^3 + 162\bar{\eta}^4) - 2\bar{\xi} - \bar{\xi}(1 - \bar{\xi})(3 - 87\bar{\xi} + 243\bar{\xi}^2 - 162\bar{\xi}^3) \\ &\quad - 235(\bar{\xi} + \bar{\eta}) + 630(\bar{\xi} + \bar{\eta})^2 - 750(\bar{\xi} + \bar{\eta})^3 + 405(\bar{\xi} + \bar{\eta})^4 - 81(\bar{\xi} + \bar{\eta})^5] \\ w_{IX} &= w_{11}(\bar{\xi}) - w_{13}(\bar{\xi} + \bar{\eta}) + w_{13}(\bar{\eta}) = \frac{\bar{\xi}}{216} (1 - \bar{\eta}) [(1 - \bar{\xi})(-5 + 9\bar{\xi} - 9\bar{\xi}^2) \\ &\quad + 9\bar{\eta}^2(-3 + 2\bar{\xi} + \bar{\eta}) + \bar{\eta}(23 - 36\bar{\xi} + 18\bar{\xi}^2)] \end{aligned}$$

Alternatively, this function can be represented by the Fourier series corresponding to the oblique coordinates

$$\begin{aligned} w(\bar{\xi}, \bar{\eta}) &= -9 \frac{q_0 a^4}{D} \sum_{n=1}^{\infty} \frac{\cos \frac{n\pi}{2} \sin^3 \frac{n\pi}{6}}{n^6 \pi^6} [\sin(n\pi \bar{\xi}) - \sin(n\pi(\bar{\xi} + \bar{\eta})) + \sin(n\pi \bar{\eta})] \\ &= -9 \frac{q_0 a^4}{D} \sum_{n=1}^{\infty} \frac{\cos \frac{n\pi}{2} \sin^3 \frac{n\pi}{6}}{n^6 \pi^6} \left[\sin(n\pi \bar{\xi}) \sin^2 \frac{n\pi \bar{\eta}}{2} + \sin(n\pi \bar{\eta}) \sin^2 \frac{n\pi \bar{\xi}}{2} \right] \end{aligned} \quad (2.12)$$

or to the orthogonal coordinates

$$w(\xi, \eta) = -18 \frac{q_0 a^4}{D} \sum_{n=1}^{\infty} \frac{\cos \frac{n\pi}{2} \sin^3 \frac{n\pi}{6}}{n^6 \pi^6} \left[\left(\cos \frac{n\pi \eta}{\sqrt{3}} - \cos(n\pi \xi) \right) \sin \frac{n\pi \eta}{\sqrt{3}} \right] \quad (2.13)$$

The maximum deflection for $\bar{\xi} = 1/3$, $\bar{\eta} = 1/3$ equals

$$w_{max} = w_{II} \left(\frac{1}{3}, \frac{1}{3} \right) = \frac{13}{29160} \frac{q_0 c^4}{D} = \frac{13}{51840} \frac{q_0 a^4}{D} \approx 0.000250772 \frac{q_0 a^4}{D} \quad (2.14)$$

or

$$\begin{aligned} w_{max} &= w \left(\bar{\xi} = \frac{1}{3}, \bar{\eta} = \frac{1}{3} \right) = -36 \frac{q_0 a^4}{D} \sum_{n=1}^{\infty} \frac{\cos \frac{n\pi}{2} \sin^5 \frac{n\pi}{6} \sin \frac{n\pi}{3}}{n^6 \pi^6} \\ &= -72 \frac{q_0 a^4}{D} \sum_{n=2,4,6}^{\infty} \frac{\sin^6 \frac{n\pi}{6} \cos \frac{n\pi}{6}}{n^6 \pi^6} \approx 0.000250772 \frac{q_0 a^4}{D} \\ w_{max} &= w \left(\xi = \frac{1}{2}, \eta = \frac{\sqrt{3}}{6} \right) = -18 \frac{q_0 a^4}{D} \sum_{n=1}^{\infty} \frac{\cos \frac{n\pi}{2} \sin^3 \frac{n\pi}{6}}{n^6 \pi^6} \left[\left(\cos \frac{n\pi}{6} - \cos \frac{n\pi}{2} \right) \sin \frac{n\pi}{6} \right] \\ &\approx 0.000250772 \frac{q_0 a^4}{D} \end{aligned} \quad (2.15)$$

3. A rectangular hingely supported plate under loading in form of a truncated octagonal pyramid

Let us find deflection of a hingely supported rectangular plate under the load shown in Fig. 5. For various values of the parameters $\varepsilon = e/c$, $0 \leq \varepsilon \leq 1/2$, we find various load cases, as shown in Fig. 6, by making use of non-dimensional coordinates

$$\left. \begin{aligned} \xi &= \frac{x}{a} & \eta &= \frac{y}{b} \\ 0 \leq \xi \leq 1 & & 0 \leq \eta \leq 1 \end{aligned} \right\} \quad \text{for} \quad \varepsilon = 0, \quad \varepsilon = \frac{1}{4}, \quad \varepsilon = \frac{1}{2} \quad (3.1)$$

The same loading cases, represented by the Fourier series, are shown in Fig. 7

The loading shown in Fig. 6 is a sum of two loads acting on the infinite plate, cf Fig. 8.

The non-dimensional coordinates $\xi_1 = x_1/c$, $\xi_2 = x_2/c$ are linked with ξ and η

$$\xi_1 = \xi - \eta \quad \xi_2 = \xi + \eta \quad (3.2)$$

The loadings $q_1(\xi_1)$, $q_2(\xi_2)$ are expressed by

$$q_1(\xi_1) = \frac{q_0}{2} \begin{cases} 1 & \text{for } 0 \leq \xi_1 \leq \varepsilon \\ \frac{1-2\xi_1}{1-2\varepsilon} & \text{for } \varepsilon \leq \xi_1 \leq 1-\varepsilon \\ -1 & \text{for } 1-\varepsilon \leq \xi_1 \leq 1 \end{cases} \quad q_2(\xi_2) = -q_1(\xi_1) \quad (3.3)$$

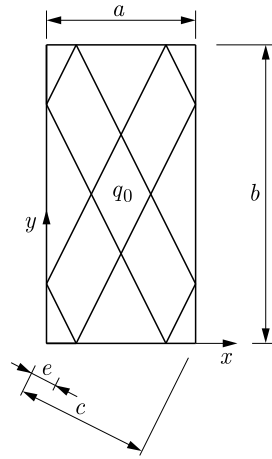


Fig. 5. The load acting on the plate

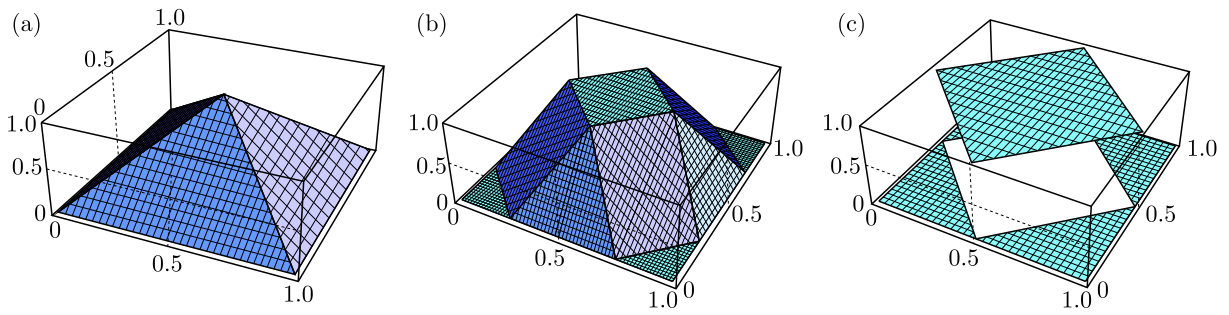
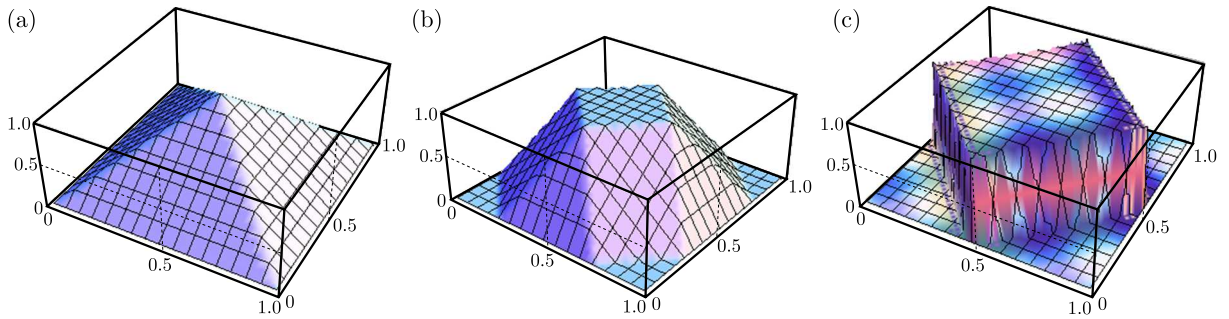
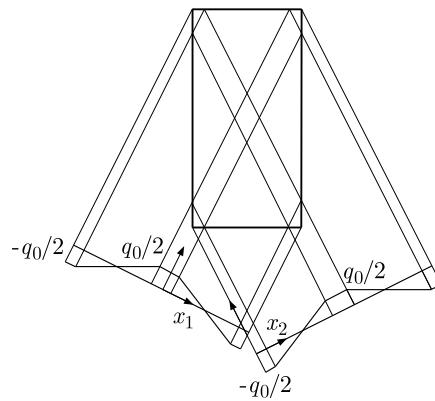

 Fig. 6. Various load cases, (a) $\varepsilon = 0$, (b) $\varepsilon = 1/4$, (c) $\varepsilon = 1/2$

 Fig. 7. Load cases represented by the Fourier series, (a) $\varepsilon = 0$, (b) $\varepsilon = 1/4$, (c) $\varepsilon = 1/2$


Fig. 8. The loading shown in Fig. 6a

while the loading $q(\xi, \eta)$, composed of two loadings as shown in Fig. 8, is represented by

$$q(\xi, \eta) = q_1(\xi - \eta) - q_1(\xi + \eta) \quad (3.4)$$

The function $q_1(x_1)$ can be put in the form of the Fourier series

$$q_1(x_1) = \begin{cases} 2 \sum_{n=1}^{\infty} \frac{\cos[n\pi(-1 + \varepsilon)] - \cos(n\pi\varepsilon)}{n^2\pi^2(-1 + 2\varepsilon)} \cos(n\pi\xi_1) & \text{for } 0 \leq \varepsilon < \frac{1}{2} \\ 8 \sum_{n=1}^{\infty} \frac{\cos \frac{n\pi}{4} \sin^3 \frac{n\pi}{4}}{n\pi} \cos(n\pi\xi_1) & \text{for } \varepsilon = \frac{1}{2} \end{cases} \quad (3.5)$$

while the function $q(\xi, \eta)$ is expressed as follows

$$q(\xi, \eta) = \begin{cases} 4 \sum_{n=1}^{\infty} \frac{\cos[n\pi(-1 + \varepsilon)] - \cos(n\pi\varepsilon)}{n^2\pi^2(-1 + 2\varepsilon)} \sin(n\pi\xi) \sin(n\pi\eta) & \text{for } 0 \leq \varepsilon < \frac{1}{2} \\ 16 \sum_{n=1}^{\infty} \frac{\cos \frac{n\pi}{4} \sin^3 \frac{n\pi}{4}}{n\pi} \sin(n\pi\xi) \sin(n\pi\eta) & \text{for } \varepsilon = \frac{1}{2} \end{cases} \quad (3.6)$$

Similarly, the plate deflection can be written down as

$$w(\xi, \eta) = w_1(\xi - \eta) - w_1(\xi + \eta) \quad (3.7)$$

The function $w_1(\xi_1)$ is of the form

$$w_1(\xi_1) = \frac{q_0 c^4}{D} \begin{cases} w_{11}(\xi_1) & \text{for } 0 \leq \xi \leq \varepsilon \\ w_{12}(\xi_1) & \text{for } \varepsilon \leq \xi \leq 1 - \varepsilon \\ w_{13}(\xi_1) & \text{for } 1 - \varepsilon \leq \xi \leq 1 \end{cases} \quad (3.8)$$

where

$$\begin{aligned} w_{11}(\xi_1) &= \frac{\xi_1^2}{48} [-1 + \xi_1^2 - 2\varepsilon(1 - \varepsilon)] \\ w_{12}(\xi_1) &= \frac{-5\xi_1^2 + 5\xi_1^4 - 2\xi_1^5 + 30\xi_1^2\varepsilon^2 - 20\xi_1^3\varepsilon^2 - 10\xi_1\varepsilon^4 + 2\varepsilon^5}{240(1 - 2\varepsilon)} \\ w_{13}(\xi_1) &= \frac{1}{240} [20\xi_1^3 - 5\xi_1^4 + 10\xi_1(1 - 2\varepsilon + 2\varepsilon^2) - 5\xi_1^2(5 - 2\varepsilon + 2\varepsilon^2) \\ &\quad - 2(1 - 3\varepsilon + 4\varepsilon^2 - 2\varepsilon^3 + \varepsilon^4)] \end{aligned}$$

The deflection of the plate is expressed through functions defined on some subdomains, as shown in Fig. 9.

The relevant functions are

$$\begin{aligned} w(\xi, \eta) &= \frac{q_0 c^4}{D} [w_{11}(\xi, \eta), w_{12}(\xi, \eta), w_{13}(\xi, \eta), w_{14}(\xi, \eta), w_{21}(\xi, \eta), w_{22}(\xi, \eta), \\ &\quad w_{23}(\xi, \eta), w_{24}(\xi, \eta), w_{31}(\xi, \eta), w_{32}(\xi, \eta), w_{33}(\xi, \eta), w_{34}(\xi, \eta), w_4(\xi, \eta)] \\ &= \frac{q_0 c^4}{D} \begin{cases} 4 \sum_{n=1}^{\infty} \frac{\cos[n\pi(-1 + \varepsilon)] - \cos(n\pi\varepsilon)}{n^6\pi^6(-1 + 2\varepsilon)} \sin(n\pi\xi) \sin(n\pi\eta) & \text{for } 0 \leq \varepsilon < \frac{1}{2} \\ 16 \sum_{n=1}^{\infty} \frac{\cos \frac{n\pi}{4} \sin^3 \frac{n\pi}{4}}{n^5\pi^5} \sin(n\pi\xi) \sin(n\pi\eta) & \text{for } \varepsilon = \frac{1}{2} \end{cases} \end{aligned} \quad (3.9)$$

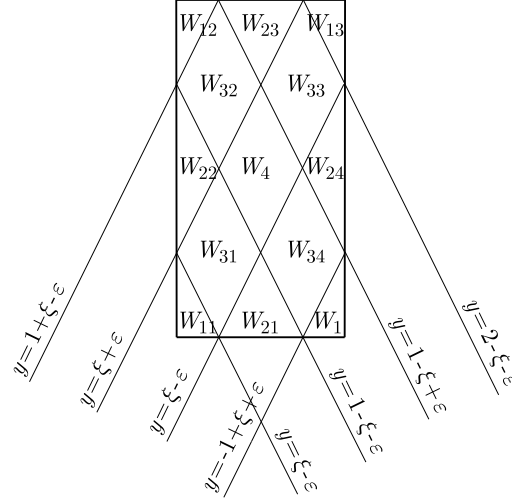


Fig. 9. The deflection of the plate in some subdomains

where

$$\begin{aligned}
 w_{11}(\xi, \eta) &= w_1(\xi - \eta) - w_1(\xi + \eta) = \frac{1}{96}\xi\eta[11 - 16(\xi^2 + \eta^2)] \\
 w_{12}(\xi, \eta) &= \frac{1}{96}\xi(-1 + \eta)[5 + 16(\xi^2 + \eta^2) - 32\eta] \\
 w_{13}(\xi, \eta) &= \frac{1}{96}(1 + \xi)(-1 + \eta)[21 + 16(\xi^2 + \eta^2) - 32(\xi + \eta)] \\
 w_{14}(\xi, \eta) &= \frac{1}{96}(1 - \xi)\eta[11 - 16(1 - \xi)^2 - 16\eta^2] \\
 w_{21}(\xi, \eta) &= w_2(\xi - \eta) - w_2(\xi + \eta) = \frac{1}{7680}\eta[5 - 2560\xi^3 + 1280\xi^4 + 160\eta^2 \\
 &\quad + 256\eta^4 - 160\xi(-5 + 16\eta^2) + 160\xi^2(3 + 16\eta^2)] \\
 w_{22}(\xi, \eta) &= w_2(-\xi + \eta) - w_2(\xi + \eta) = \frac{1}{7680}\xi[256\xi^4 + 160\xi^2(1 - 16\eta + 16\eta^2) \\
 &\quad + 5(1 + 160\eta + 96\eta^2 - 512\eta^3 + 256\eta^4)] \\
 w_{23}(\xi, \eta) &= w_{21}(\xi, 1 - \eta) = \frac{1}{7680}(1 - \eta)\{5 + 160\xi(5 + 3\xi - 16\xi^2 + 8\xi^3) \\
 &\quad + 32(1 - \eta)^2[5 + 8(1 - \eta)^2 - 80\xi + 80\xi^2]\} \\
 w_{24}(\xi, \eta) &= w_{22}(1 - \xi, \eta) = \frac{1}{7680}(1 - \xi)\{5 + 160\eta(1 - \eta)(5 + 8\eta - 8\eta^2) \\
 &\quad + 32(1 - \xi)^2[5 + 8(1 - \xi)^2 - 80\eta + 80\eta^2]\} \\
 w_{31}(\xi, \eta) &= w_1(\xi - \eta) - w_2(\xi + \eta) = \frac{1}{240}\left\{\frac{5}{8}(\xi - \eta)^2[8(\xi - \eta)^2 - 11] - \frac{1}{256} \right. \\
 &\quad \left. + \frac{\xi + \eta}{64}[5 + 8(\xi + \eta)(50 + 20(\xi + \eta) - 80(\xi + \eta)^2 + 32(\xi + \eta)^3)]\right\} \\
 w_{32}(\xi, \eta) &= w_{31}(\xi, 1 - \eta) = \frac{1}{240}\left\{\frac{5}{8}(\xi + \eta - 1)^2[8(\xi + \eta - 1)^2 - 11] - \frac{1}{256} \right. \\
 &\quad \left. + \frac{1 + \xi - \eta}{64}[5 + 8(1 + \xi - \eta)(50 + 20(1 + \xi - \eta) - 80(1 + \xi - \eta)^2 + 32(1 + \xi - \eta)^3)]\right\} \\
 w_{33}(\xi, \eta) &= w_{32}(1 - \xi, \eta) = \frac{1}{240}\left\{\frac{5}{8}(\eta - \xi)^2[8(\eta - \xi)^2 - 11] - \frac{1}{256} \right. \\
 &\quad \left. + \frac{2 - \xi - \eta}{64}[5 + 8(2 - \xi - \eta)(50 + 20(2 - \xi - \eta) - 80(2 - \xi - \eta)^2 + 32(2 - \xi - \eta)^3)]\right\}
 \end{aligned}$$

$$\begin{aligned}
w_{34}(\xi, \eta) &= w_{31}(1 - \xi, \eta) = \frac{1}{240} \left\{ \frac{5}{8} (1 - \xi - \eta)^2 [8(1 - \xi - \eta)^2 - 11] - \frac{1}{256} \right. \\
&\quad \left. + \frac{1 - \xi + \eta}{64} [5 + 8(1 - \xi + \eta)(50 + 20(1 - \xi + \eta) - 80(1 - \xi + \eta)^2 + 32(1 - \xi + \eta)^3)] \right\} \\
w_4(\xi, \eta) &= w_1(\xi - \eta) - w_3(\xi + \eta) = \frac{1}{240} \left\{ \frac{121}{128} + \frac{5}{8} (\xi - \eta)^2 [8(\xi - \eta)^2 - 11] \right. \\
&\quad \left. - \frac{\xi + \eta}{8} [50 - 185(\xi + \eta) + 160(\xi + \eta)^2 - 40(\xi + \eta)^3] \right\}
\end{aligned}$$

The plate deflection for subsequent values of the parameter ε is shown in Fig. 10.

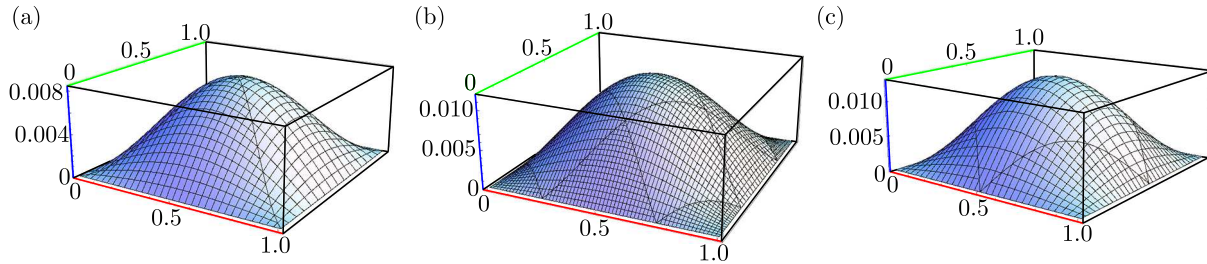


Fig. 10. The plate deflection for subsequent values of the parameter ε , (a) $\varepsilon = 0$, (b) $\varepsilon = 1/4$, (c) $\varepsilon = 1/2$

The maximum deflections $w_{max}(\varepsilon)$ for $\varepsilon = 0$, $\varepsilon = 1/4$, $\varepsilon = 1/2$ are given by

$$\begin{aligned}
w_{max}(0) &= \frac{256}{30720} \frac{q_0 c^4}{D} & w_{max}\left(\frac{1}{4}\right) &= \frac{361}{30720} \frac{q_0 c^4}{D} \\
w_{max}\left(\frac{1}{2}\right) &= \frac{400}{30720} \frac{q_0 c^4}{D}
\end{aligned} \tag{3.10}$$

The exact solutions $w_{max}(0)$ and $w_{max}(1/2)$ are compatible with those reported by Kączkowski (1968).

References

1. ABBASSIAN F., DAWSWELL D.J., KNOWLES N.C., 1987, *Free Vibration Benchmarks*, vol. 2, Department of Trade and Industry, National Engineering Laboratory
2. BECKER A.A., 1998, *Background to Material Non-Linear Benchmarks*, NAFEMS, p. 114
3. BECKER A.A., 2001, *Understanding Non-linear Finite Element Analysis through Illustrative Benchmarks*, NAFEMS, p. 171
4. BURROWS D.J., 1985, *Benchmark Tests in Thermal Stress Analysis Using Finite Element Methods*, NAFEMS, p. 32
5. DAVIES G.A.O., FENNER R.T., LEWIS R.W., 1992, *NAFEMS Background to Benchmarks*, NAFEMS, p. 139
6. HARDY S., 2001, *Composite Benchmarks*, Issue 1, p. 19, University of Cornell, Ithaca, NY, United States, Issue 2, 2010, NAFEMS, Ref: R0031, 38 p.
7. KAMOULAKOS A., HITCHINS D., DAVIES G.A.O., 1986, *Benchmark Tests for Various Finite Element Assemblies – Thin Shells*, NAFEMS, p. 53
8. KĄCZKOWSKI Z., 1953, Anisotropic plates bending analysis by superposing folded deflections (in Polish), *Archiwum Mechaniki Stosowanej*, **5**, 3, 455-496
9. KĄCZKOWSKI Z., 1954, Berechnung anisotroper Platten nach der Methode der Supperposition von Wellenflächen, *Bulletin of the Polish Academy of Sciences. Technical Sciences*, **2**, 2, 79-84

10. KĄCZKOWSKI Z., 1968, *Plates. Static analysis* (in Polish), Arkady, Warszawa (1980 – 2nd edition, 2000 – 3rd edition, 1984 – in Russian, Strojinzdat, Moskva)
11. NAFEMS, 1990, *The Standard NAFEMS Benchmarks*, p. 58
12. PANG H.L.J., LEGGATT R.H., 2001, *2D Test Cases in Linear Elastic Fracture Mechanics (Summary)*, NAFEMS, Glasgow, U.K.
13. PRINJA K., CLEGG R.A., 1993, *Assembly Benchmark Tests for 3D Beams and Shell Exhibiting Geometric Non-Linear Behaviour*, NAFEMS, p. 160
14. ROBINSON J., 1985, *Basic and Shape Sensitivity Tests for Membrane and Plate Bending Finite Elements*, NAFEMS, p. 32
15. SZE K.Y., LIU X.H., LO S.H., 2004, Popular benchmark problems for geometric nonlinear analysis of shells, *Finite Elements in Analysis and Design*, **40**, 11, 1551-1569

Manuscript received June 24, 2016; accepted for print July 25, 2017

AN ANALYTICAL INVESTIGATION OF A 2D-PPMS HOLLOW INFINITE CYLINDER UNDER THERMO-ELECTRO-MECHANICAL (TEM) LOADINGS

MOHSEN MESHKINI

School of Science and Engineering, Sharif University of Technology, International Campus, Kish Island, Iran

e-mail: meshkini@kish.sharif.edu

KEIKHOSROW FIROOZBAKHSH

Department of Mechanical Engineering, Sharif University of Technology, Tehran, Iran

e-mail: firoozbakhsh@sharif.edu

MOHSEN JABBARI

Department of Mechanical Engineering, South Tehran Branch, Islamic Azad University, Iran

e-mail: m_jabbari@azad.ac.ir

ALI SELKGHAFARI

School of Science and Engineering, Sharif University of Technology, International Campus, Kish Island, Iran

e-mail: a_selkgafari@sharif.edu

The analytical solution of steady-state asymmetric thermo-electro-mechanical loads of a hollow thick infinite cylinder made of porous piezoelectric materials (2D-PPMs) based on two-dimensional equations of thermoelasticity is considered. The general form of thermal and mechanical boundary conditions is considered on the inside and outside surfaces. A direct method is used to solve the heat conduction equation and the non-homogenous system of partial differential Navier equations using the complex Fourier series and the power-exponential law functions method. The material properties are assumed to depend on the radial and circumferential variable and are expressed as power-exponential law functions along the radial and circumferential direction.

Keywords: piezoelectric, porothermoelasticity, 2D-PPMs, hollow cylinder, TEM

1. Introduction

Porous piezoelectric materials (PPMs) have lower acoustic impedance and can be incorporated in medical ultrasonic imaging devices. They are widely used for applications such as low frequency hydrophones, accelerometers, vibratory sensors and contact microphones. The classical method of analysis is to combine equilibrium equations with stress-strain and strain-displacement relations to arrive at governing equations in terms of displacement components, namely the Navier equations (Hetnarski and Eslami, 2009). Li *et al.* (2003) presented fabrication and evaluation of porous piezoelectric ceramics and porosity-graded piezoelectric actuators. Zielinski (2010) discussed the fundamentals of multi physics modeling of piezo-poro-elastic structures. The processing and properties of porous piezoelectric materials with high hydrostatic figures of merit was given by Bowen *et al.* (2004). The porous piezoelectric composites with extremely high reception was discussed by Topolov and Turik (2001). Ciarletta and Scarpetta (1996) gave some results on thermoelasticity for porous piezoelectric materials. Batifol *et al.* (2007) presented a finite-element study of a piezoelectric/poroelastic sound package concept. Zeng *et al.* (2007) have discussed the processing and piezoelectric properties of porous PZT ceramics. Ivanov *et al.* (2002) used the porous piezoelectric ceramics materials for ultrasonic flaw detection and medical

diagnostics. Ding *et al.* (2004) presented an analytical solution of a special non-homogeneous piezoelectric hollow cylinder for piezothermoelastic axisymmetric plane strain dynamic problems. Akbari Alashti *et al.* (2013) presented thermo-elastic analysis of a functionally graded spherical shell with piezoelectric layers by differential quadrature method. Jabbari *et al.* (2012, 2016) studied mechanical and thermal stresses in FGPPM hollow cylinders. Meshkini *et al.* (2017) studied an asymmetric mechanical and thermal stresses in 2D-FGPPMs hollow cylinder. The applied separation of variables and the complex Fourier series to solve the heat conduction and Navier equations.

In this study, an analytical method is presented for mechanical and thermal stress analysis for a hollow infinite cylinder made of fluid saturated porous piezoelectric materials (2D-PPMs). In present study, the material properties are assumed to be expressed by power functions in the radial and circumferential direction. The effects of compressibility, pore volume fraction (porosity), and electric potential coefficient on displacements, electric potential and stresses are studied. Temperature distribution is considered in the steady state asymmetric case and mechanical and thermal boundary conditions by satisfying the stress and displacement boundary condition.

2. Governing equations

2.1. Stress analysis

The strain-displacement relations and electric intensity are (Ding *et al.*, 2004)

$$\begin{aligned} \varepsilon_{rr} &= \frac{\partial u}{\partial r} & \varepsilon_{\theta\theta} &= \frac{1}{r} \frac{\partial v}{\partial \theta} + \frac{u}{r} & \varepsilon_{r\theta} &= \frac{1}{2} \left(\frac{1}{r} \frac{\partial u}{\partial \theta} + \frac{\partial v}{\partial r} - \frac{v}{r} \right) \\ E_r &= \frac{\partial \psi}{\partial r} & E_\theta &= \frac{1}{r} \frac{\partial \psi}{\partial \theta} \end{aligned} \quad (2.1)$$

Stress-strain relations of a 2D-PPM cylinder for the asymmetric condition are (Meshkini *et al.*, 2017)

$$\begin{aligned} \sigma_{rr} &= C_{11}\varepsilon_{rr} + C_{12}\varepsilon_{\theta\theta} + e_{21}E_r - \gamma p - C_1^T T(r, \theta) \\ \sigma_{\theta\theta} &= C_{12}\varepsilon_{rr} + C_{22}\varepsilon_{\theta\theta} + e_{22}E_r - \gamma p - C_2^T T(r, \theta) \\ \sigma_{zz} &= C_{12}(\varepsilon_{rr} + \varepsilon_{\theta\theta}) + e_{23}E_r - \gamma p - C_3^T T(r, \theta) \\ \sigma_{r\theta} &= 2C_{44}\varepsilon_{r\theta} + e_{24}E_\theta & D_{rr} &= e_{21}\varepsilon_{rr} + e_{22}\varepsilon_{\theta\theta} - \varepsilon_{22}E_r + g_{21}T(r, \theta) \\ D_{\theta\theta} &= 2e_{24}\varepsilon_{r\theta} - \varepsilon_{21}E_\theta + g_{22}T(r, \theta) \end{aligned} \quad (2.2)$$

where p is related to Biot's modulus, volumetric strain and the variation of the fluid content. Considering the undrained conditions ($\xi = 0$) as (Jabbari *et al.*, 2012)

$$p = M(\xi - \gamma(\varepsilon_{rr} + \varepsilon_{\theta\theta})) = -M\gamma(\varepsilon_{rr} + \varepsilon_{\theta\theta}) \quad (2.3)$$

Using relations (2.2) and (2.3), the stress-strain relations of the 2D-PPM for the asymmetric condition are (Meshkini *et al.*, 2017)

$$\begin{aligned} \sigma_{rr} &= \hat{C}_{11}\varepsilon_{rr} + \hat{C}_{12}\varepsilon_{\theta\theta} + e_{21}E_r - C_1^T T(r, \theta) \\ \sigma_{\theta\theta} &= \hat{C}_{12}\varepsilon_{rr} + \hat{C}_{22}\varepsilon_{\theta\theta} + e_{22}E_r - C_2^T T(r, \theta) \\ \sigma_{zz} &= \hat{C}_{12}(\varepsilon_{rr} + \varepsilon_{\theta\theta}) + e_{23}E_r - C_3^T T(r, \theta) \\ \sigma_{r\theta} &= 2\hat{C}_{44}\varepsilon_{r\theta} + e_{24}E_\theta & D_{rr} &= e_{21}\varepsilon_{rr} + e_{22}\varepsilon_{\theta\theta} - \varepsilon_{22}E_r + g_{21}T(r, \theta) \\ D_{\theta\theta} &= 2e_{24}\varepsilon_{r\theta} - \varepsilon_{21}E_\theta + g_{22}T(r, \theta) \end{aligned} \quad (2.4)$$

and

$$\hat{C}_{11} = C_{11} + C_M \quad \hat{C}_{12} = C_{12} + C_M \quad \hat{C}_{22} = C_{22} + C_M \quad \hat{C}_{44} = C_{44} \quad (2.5)$$

where $C_M = M\gamma^2$ and C_i^T are thermal moduli which can be expressed by elastic constants and linear thermal expansion coefficients α_i (Ding *et al.*, 2004)

$$C_1^T = C_{11}\alpha_r + 2C_{12}\alpha_\theta \quad C_2^T = 2C_{12}\alpha_r + C_{22}\alpha_\theta \quad (2.6)$$

under consideration $\alpha_r = \alpha_\theta = \alpha$ (Hetnarski and Eslami, 2009). Therefore,

$$C_1^T = (C_{11} + 2C_{12})\alpha \quad C_2^T = (2C_{12} + C_{22})\alpha \quad C_3^T = C_1^T \quad (2.7)$$

The equilibrium equations in the radial and circumferential direction, disregarding the body force and the inertia terms, are (Ding *et al.*, 2004)

$$\begin{aligned} \frac{\partial \sigma_{rr}}{\partial r} + \frac{1}{r} \frac{\partial \sigma_{r\theta}}{\partial \theta} + \frac{1}{r} (\sigma_{rr} - \sigma_{\theta\theta}) &= 0 & \frac{\partial \sigma_{r\theta}}{\partial r} + \frac{1}{r} \frac{\partial \sigma_{\theta\theta}}{\partial \theta} + \frac{2}{r} \sigma_{r\theta} &= 0 \\ \frac{\partial D_{rr}}{\partial r} + \frac{1}{r} \frac{\partial D_{\theta\theta}}{\partial \theta} + \frac{1}{r} D_{rr} &= 0 \end{aligned} \quad (2.8)$$

To obtain the equilibrium equations in terms of displacement components for the 2D-PPM cylinder, the functional relationship of the material properties must be known. Because the cylinder material is assumed to be graded along the radial and circumferential direction, the coefficient of thermal expansion and electric constants are assumed to be described with the power-exponential laws as

$$\begin{aligned} \alpha &= \alpha_0 \tilde{r}^{m_1} e^{n_1 \theta} & C_{ij} &= \bar{C}_{ij} \tilde{r}^{m_2} e^{n_2 \theta} & K &= k_0 \tilde{r}^{m_3} e^{n_3 \theta} \\ e_{2i} &= \bar{e}_{2i} \tilde{r}^{m_4} e^{n_4 \theta} & \varepsilon_{2i} &= \bar{\varepsilon}_{2i} \tilde{r}^{m_5} e^{n_5 \theta} & g_{2i} &= \bar{g}_{2i} \tilde{r}^{m_6} e^{n_6 \theta} \end{aligned} \quad (2.9)$$

where $\tilde{r} = r/a$ and a is the inner radius.

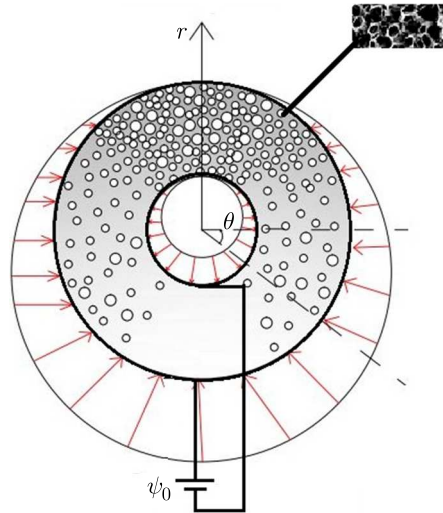


Fig. 1. Geometric model of a 2D-PPM hollow cylinder under two dimensional inner and outer Thermo-Electro-Mechanical (TEM) loads

Using relations (2.4) and (2.9) into (2.8), the Navier equations in terms of the displacement components are

$$\begin{aligned}
& u_{,rr} + \left(m_2 + 1 + (m_2 - 1) \frac{\widehat{\bar{C}}_{12}}{\widehat{\bar{C}}_{11}} \right) \frac{1}{r} u_{,r} + \frac{m_2 \widehat{\bar{C}}_{12} - \widehat{\bar{C}}_{22}}{\widehat{\bar{C}}_{11}} \frac{1}{r^2} u + \frac{n_2 \bar{C}_{44}}{\widehat{\bar{C}}_{11}} \frac{1}{r} v_{,r} - \frac{n_2 \bar{C}_{44}}{\widehat{\bar{C}}_{11}} \frac{1}{r^2} v \\
& + \frac{\bar{C}_{44}}{\widehat{\bar{C}}_{11}} \frac{1}{r^2} u_{,\theta\theta} + \frac{n_2 \bar{C}_{44}}{\widehat{\bar{C}}_{11}} \frac{1}{r^2} u_{,\theta} + \frac{\bar{C}_{12} + \bar{C}_{44}}{\widehat{\bar{C}}_{11}} \frac{1}{r} v_{,r\theta} + \frac{m_2 \bar{C}_{12} - \bar{C}_{22} - \bar{C}_{44}}{\widehat{\bar{C}}_{11}} \frac{1}{r^2} v_{,\theta} \\
& + \left(\frac{\bar{e}_{21}}{\widehat{\bar{C}}_{11}} \psi_{,rr} + \frac{(m_4 + 1) \bar{e}_{21} - \bar{e}_{22}}{\widehat{\bar{C}}_{11}} \frac{1}{r} \psi_{,r} + \frac{\bar{e}_{24}}{\widehat{\bar{C}}_{11}} \frac{1}{r^2} \psi_{,\theta\theta} + \frac{n_4 \bar{e}_{24}}{\widehat{\bar{C}}_{11}} \frac{1}{r^2} \psi_{,\theta} \right) \tilde{r}^{m_4 - m_2} e^{(n_4 - n_2)\theta} \\
& = \left(\frac{(m_1 + m_2 + 1) \bar{C}_{11} + 2(m_1 + m_2) \bar{C}_{12} - \bar{C}_{22}}{\widehat{\bar{C}}_{11}} \frac{1}{r} T + \frac{\bar{C}_{11} + 2 \bar{C}_{12}}{\widehat{\bar{C}}_{11}} T_{,r} \right) \alpha_0 \tilde{r}^{m_1} e^{n_1 \theta} \\
& v_{,rr} + (m_2 + 1) \frac{1}{r} v_{,r} - (m_2 + 1) \frac{1}{r^2} v + n_2 \frac{\widehat{\bar{C}}_{22}}{\bar{C}_{44}} \frac{1}{r^2} v_{,\theta} + \frac{\widehat{\bar{C}}_{22}}{\bar{C}_{44}} \frac{1}{r^2} v_{,\theta\theta} \\
& + \left(m_2 + 1 + \frac{\widehat{\bar{C}}_{22}}{\bar{C}_{44}} \right) \frac{1}{r^2} u_{,\theta} + n_2 \frac{\widehat{\bar{C}}_{12}}{\bar{C}_{44}} \frac{1}{r} u_{,r} + \left(1 + \frac{\widehat{\bar{C}}_{12}}{\bar{C}_{44}} \right) \frac{1}{r} u_{,r\theta} + n_2 \frac{\widehat{\bar{C}}_{22}}{\bar{C}_{44}} \frac{1}{r^2} u \\
& + \left(n_4 \frac{\bar{e}_{22}}{\bar{C}_{44}} \frac{1}{r} \psi_{,r} + \frac{\bar{e}_{22} + \bar{e}_{24}}{\bar{C}_{44}} \frac{1}{r} \psi_{,r\theta} + (m_4 + 2) \frac{\bar{e}_{24}}{\bar{C}_{44}} \frac{1}{r^2} \psi_{,\theta} \right) \tilde{r}^{m_4 - m_2} e^{(n_4 - n_2)\theta} \\
& = \left((n_1 + n_2) \frac{2 \bar{C}_{12} + \bar{C}_{22}}{\bar{C}_{44}} \frac{1}{r} T + \frac{2 \bar{C}_{12} + \bar{C}_{22}}{\bar{C}_{44}} \frac{1}{r} T_{,\theta} \right) \alpha_0 \tilde{r}^{m_1} e^{n_1 \theta} \\
& \psi_{,rr} + (m_5 + 1) \frac{1}{r} \psi_{,r} + n_5 \frac{\bar{e}_{21}}{\bar{e}_{22}} \frac{1}{r^2} \psi_{,\theta} + \frac{\bar{e}_{21}}{\bar{e}_{22}} \frac{1}{r^2} \psi_{,\theta\theta} - \left(\frac{\bar{e}_{21}}{\bar{e}_{22}} u_{,rr} + \frac{(m_4 + 1) \bar{e}_{21} + \bar{e}_{22}}{\bar{e}_{22}} \frac{1}{r} u_{,r} \right. \\
& + \frac{m_4 \bar{e}_{22}}{\bar{e}_{22}} \frac{1}{r^2} u + \frac{n_4 \bar{e}_{24}}{\bar{e}_{22}} \frac{1}{r} v_{,r} - \frac{n_4 \bar{e}_{24}}{\bar{e}_{22}} \frac{1}{r^2} v + \frac{(m_4 + 1) \bar{e}_{22} - \bar{e}_{24}}{\bar{e}_{22}} \frac{1}{r^2} v_{,\theta} \\
& + \left. \frac{\bar{e}_{24}}{\bar{e}_{22}} \frac{1}{r} v_{,r\theta} \right) \tilde{r}^{m_4 - m_5} e^{(n_4 - n_5)\theta} = \left(\frac{(m_6 + 1) \bar{g}_{21} + n_6 \bar{g}_{22}}{\bar{e}_{22}} \frac{1}{r} T + \frac{\bar{g}_{22}}{\bar{e}_{22}} \frac{\partial T}{\partial r} \right. \\
& + \left. \frac{\bar{g}_{22}}{\bar{e}_{22}} \frac{1}{r} \frac{\partial T}{\partial \theta} \right) \tilde{r}^{m_6 - m_5} e^{(n_6 - n_5)\theta}
\end{aligned} \tag{2.10}$$

Navier equations (2.10) are a non-homogeneous system of partial differential equations with non-constant coefficients.

2.2. Heat conduction problem

The first law of thermodynamics for energy equation in the steady-state condition for the 2D-PPM two dimensional cylinder is

$$\frac{1}{r} (kr T_{,r})_{,r} + \frac{1}{r^2} (k T_{,\theta})_{,\theta} = 0 \quad a \leq r \leq b \quad -\pi \leq \theta \leq +\pi \tag{2.11}$$

where $T(r, \theta)$ is temperature distribution, $k(r, \theta)$ is the thermal conduction coefficient and a comma denotes partial differentiation with respect to the space variable.

The thermal boundary conditions are assumed as

$$S_{11} T(a, \theta) + S_{12} T_{,r}(a, \theta) = f_1(\theta) \quad S_{21} T(b, \theta) + S_{22} T_{,r}(b, \theta) = f_2(\theta) \tag{2.12}$$

we assume that the non-homogeneous thermal conduction coefficient $k(r, \theta)$ is a power function of the radial and circumferential coordinates (r, θ) as $k(r, \theta) = k_0 \tilde{r}^{m_3} e^{n_3 \theta}$.

Using the definition for the material properties, the temperature equation becomes

$$T_{,rr} + (m_3 + 1) \frac{1}{r} T_{,r} + \frac{1}{r^2} (n_3 T_{,\theta} + T_{,\theta\theta}) = 0 \tag{2.13}$$

The solution to Eq. (2.13) is written in the form of complex Fourier series, as

$$T(r, \theta) = \sum_{q=-\infty}^{\infty} T_q(r) e^{iq\theta} \quad (2.14)$$

Substituting Eq. (2.14) into Eq. (2.13), the following equation is obtained

$$T_q''(r) + (m_3 + 1) \frac{1}{r} T_q'(r) + \frac{1}{r^2} (iqn_3 - q^2) T_q(r) = 0 \quad (2.15)$$

Equation (2.15) is the Euler equation and has solutions in the form of

$$T_q(r) = A_q r^\beta \quad (2.16)$$

Substituting Eq. (2.16) into Eq. (2.15), the following characteristic equation is obtained

$$\beta^2 + m_3 \beta + (iqn_3 - q^2) = 0 \quad (2.17)$$

the roots of Eq. (2.17) are

$$\beta_{q1,2} = \frac{-m_3}{2} \mp \sqrt{\frac{m_3^2}{4} + q^2 - iqn_3} \quad (2.18)$$

Thus

$$T_q(r) = A_{q1} r^{\beta_{q1}} + A_{q2} r^{\beta_{q2}} \quad (2.19)$$

Substituting Eq. (2.19) into Eq. (2.14) gives

$$T(r, \theta) = \sum_{q=-\infty}^{\infty} (A_{q1} r^{\beta_{q1}} + A_{q2} r^{\beta_{q2}}) e^{iq\theta} \quad (2.20)$$

The constants A_{q1} and A_{q2} are presented in Appendix.

3. Solution of the Navier equation

$$\begin{aligned} u(r, \theta) &= \sum_{q=-\infty}^{\infty} u_q(r) e^{(iq+n_1)\theta} & v(r, \theta) &= \sum_{q=-\infty}^{\infty} v_q(r) e^{(iq+n_1)\theta} \\ \psi(r, \theta) &= \sum_{q=-\infty}^{\infty} \psi_q(r) e^{(iq+n_1)\theta} \end{aligned} \quad (3.1)$$

Substituting Eqs. (2.20) and (3.1) into Eqs. (2.10) yields

$$\begin{aligned} u_q'' + \zeta_1 \frac{1}{r} u_q' + (\tau_2 + i\tau_3) \frac{1}{r^2} u_q + (\tau_4 + i\tau_5) \frac{1}{r} v_q' + (\tau_6 + i\tau_7) \frac{1}{r^2} v_q + \tau_8 \psi_q'' + \tau_9 \frac{1}{r} \psi_q' \\ + (\tau_{10} + i\tau_{11}) \frac{1}{r^2} \psi_q = \frac{1}{a^{m_1}} \left[(\tau_{12} + \beta_{q1} \tau_{13}) A_{q1} r^{m_1 + \beta_{q1} - 1} + (\tau_{12} + \beta_{q2} \tau_{13}) A_{q2} r^{m_1 + \beta_{q2} - 1} \right] \\ v_q'' + \tau_{14} \frac{1}{r} v_q' - (\tau_{15} - i\tau_{16}) \frac{1}{r^2} v_q + (\tau_{17} + i\tau_{18}) \frac{1}{r} u_q' + (\tau_{19} + i\tau_{20}) \frac{1}{r^2} u_q + (\tau_{21} + i\tau_{22}) \frac{1}{r} \psi_q' \\ + (\tau_{23} + i\tau_{24}) \frac{1}{r^2} \psi_q = \frac{1}{a^{m_1}} (\tau_{25} + i\tau_{26}) \left(A_{q1} r^{\beta_{q1} + m_1 - 1} + A_{q2} r^{\beta_{q2} + m_1 - 1} \right) \\ \psi_q'' + \tau_{27} \frac{1}{r} \psi_q' + (\tau_{28} + i\tau_{29}) \frac{1}{r^2} \psi_q - \tau_{30} u_q'' - \tau_{31} \frac{1}{r} u_q' - \tau_{32} \frac{1}{r^2} u_q + (\tau_{33} + i\tau_{34}) \frac{1}{r} v_q' \\ + (\tau_{35} + i\tau_{36}) \frac{1}{r^2} v_q = \frac{1}{a^{m_1}} \left[(\tau_{37} + i\tau_{38} + \beta_{q1} \tau_{39}) A_{q1} r^{\beta_{q1} + m_1 - 1} \right. \\ \left. + (\tau_{37} + i\tau_{38} + \beta_{q2} \tau_{39}) A_{q2} r^{\beta_{q2} + m_1 - 1} \right] \end{aligned} \quad (3.2)$$

Equations (3.2) are a system of ordinary differential equations having general and particular solutions.

The general solutions are assumed as

$$u_q^g(r) = Dr^\eta \quad v_q^g(r) = Er^\eta \quad \psi_q^g(r) = Fr^\eta \quad (3.3)$$

Substituting Eqs. (3.3) into Eqs. (3.2) yields

$$\begin{aligned} & [\eta(\eta - 1) + \tau_1\eta + \tau_2 + i\tau_3]D + [\tau_4\eta + \tau_5 + i(\tau_6\eta + \tau_7)]E \\ & + [\eta(\eta - 1)\tau_8 + \tau_9\eta + \tau_{10} + i\tau_{11}]F = 0 \\ & [\tau_{19} + \tau_{17}\eta + i(\tau_{18}\eta + \tau_{20})]D + [\eta(\eta - 1) + \tau_{14}\eta - \tau_{15} + i\tau_{16}]E \\ & + [\tau_{21}\eta + \tau_{23} + i(\tau_{22}\eta + \tau_{24})]F = 0 \\ & \eta(\eta - 1)\tau_{30} - \tau_{31}\eta - \tau_{32}]D + [\tau_{33}\eta + \tau_{35} + i(\tau_{34}\eta + \tau_{36})]E \\ & + [\eta(\eta - 1) + \tau_{27}\eta + \tau_{28} + i\tau_{29}]F = 0 \end{aligned} \quad (3.4)$$

The constants τ_i are presented in Appendix.

A nontrivial solution is obtained by setting the determinant of the coefficients of Eqs. (3.4) equal to zero, where a six-order polynomial characteristic equation is obtained. It gives six eigenvalues η_{q1} to η_{q6} . Thus, the general solutions are

$$\begin{aligned} u_q^g(r) &= \sum_{j=1}^6 D_{qj} r^{\eta_{qj}} \Rightarrow u_q^g(r) = \sum_{j=1}^6 D_{qj} r^{\eta_{qj}} \\ v_q^g(r) &= \sum_{j=1}^6 E_{qj} r^{\eta_{qj}} \Rightarrow v_q^g(r) = \sum_{j=1}^6 X_{qj} D_{qj} r^{\eta_{qj}} \\ \psi_q^g(r) &= \sum_{j=1}^6 F_{qj} r^{\eta_{qj}} \Rightarrow \psi_q^g(r) = \sum_{j=1}^6 Y_{qj} D_{qj} r^{\eta_{qj}} \end{aligned} \quad (3.5)$$

where X_{qj} is the relation between constants D_{qj} and E_{qj} and Y_{qj} is the relation between constants D_{qj} and F_{qj} . It is obtained from Eqs. (3.4). The constants are presented in Appendix.

The particular solutions $u_q^p(r)$ and $v_q^p(r)$ are assumed as

$$\begin{aligned} u_q^p(r) &= I_{q1} r^{\beta_{q1}+m_1+1} + I_{q2} r^{\beta_{q2}+m_1+1} & v_q^p(r) &= I_{q3} r^{\beta_{q1}+m_1+1} + I_{q4} r^{\beta_{q2}+m_1+1} \\ \psi_q^p(r) &= I_{q5} r^{\beta_{q1}+m_1+1} + I_{q6} r^{\beta_{q2}+m_1+1} \end{aligned} \quad (3.6)$$

Substituting Eqs. (3.6) into the non-homogeneous form of Eqs. (3.2) gives I_{q1} to I_{q6} , as they are presented in Appendix. The complete solutions for $u_q(r)$, $v_q(r)$ and $\psi_q(r)$ are the sum of the general and particular solutions

$$\begin{aligned} u_q(r) &= \sum_{j=1}^6 D_{qj} r^{\eta_{qj}} + I_{q1} r^{\beta_{q1}+m_1+1} + I_{q2} r^{\beta_{q2}+m_1+1} \\ v_q(r) &= \sum_{j=1}^6 X_{qj} D_{qj} r^{\eta_{qj}} + I_{q3} r^{\beta_{q1}+m_1+1} + I_{q4} r^{\beta_{q2}+m_1+1} \\ \psi_q(r) &= \sum_{j=1}^6 Y_{qj} D_{qj} r^{\eta_{qj}} + I_{q5} r^{\beta_{q1}+m_1+1} + I_{q6} r^{\beta_{q2}+m_1+1} \end{aligned} \quad (3.7)$$

Substituting Eqs. (3.7) into Eqs. (3.1) gives

$$\begin{aligned}
 u(r, \theta) &= \sum_{\substack{q=-\infty \\ q \neq 0}}^{\infty} \left(\sum_{j=1}^6 D_{qj} r^{\eta_{qj}} + I_{q1} r^{\beta_{q1}+m_1+1} + I_{q2} r^{\beta_{q2}+m_1+1} \right) e^{(iq+n_1)\theta} \\
 v(r, \theta) &= \sum_{\substack{q=-\infty \\ q \neq 0}}^{\infty} \left(\sum_{j=1}^6 X_{qj} D_{qj} r^{\eta_{qj}} + I_{q3} r^{\beta_{q1}+m_1+1} + I_{q4} r^{\beta_{q2}+m_1+1} \right) e^{(iq+n_1)\theta} \\
 \psi(r, \theta) &= \sum_{\substack{q=-\infty \\ q \neq 0}}^{\infty} \left(\sum_{j=1}^6 Y_{qj} D_{qj} r^{\eta_{qj}} + I_{q5} r^{\beta_{q1}+m_1+1} + I_{q6} r^{\beta_{q2}+m_1+1} \right) e^{(iq+n_1)\theta}
 \end{aligned} \tag{3.8}$$

Substituting Eqs. (3.8) into Eqs. (2.1), the strains and electric intensity are obtained as

$$\begin{aligned}
 \varepsilon_{rr} &= \sum_{\substack{q=-\infty \\ q \neq 0}}^{\infty} \left(\sum_{j=1}^6 \eta_{qj} D_{qj} r^{\eta_{qj}-1} + (\beta_{q1} + m_1 + 1) I_{q1} r^{\beta_{q1}+m_1} \right. \\
 &\quad \left. + (\beta_{q2} + m_1 + 1) I_{q2} r^{\beta_{q2}+m_1} \right) e^{(iq+n_1)\theta} \\
 \varepsilon_{\theta\theta} &= \sum_{\substack{q=-\infty \\ q \neq 0}}^{\infty} \left(\sum_{j=1}^6 (iq + n_1)(X_{qj} + 1) D_{qj} r^{\eta_{qj}-1} + [(iq + n_1) I_{q3} + I_{q1}] r^{\beta_{q1}+m_1} \right. \\
 &\quad \left. + [(iq + n_1) I_{q4} + I_{q2}] r^{\beta_{q2}+m_1} \right) e^{(iq+n_1)\theta} \\
 \varepsilon_{r\theta} &= \frac{1}{2} \sum_{\substack{q=-\infty \\ q \neq 0}}^{\infty} \left(\sum_{j=1}^6 [iq + n_1 + (\eta_{qj} - 1) X_{qj}] D_{qj} r^{\eta_{qj}-1} + [(iq + n_1) I_{q1} \right. \\
 &\quad \left. + (\beta_{q1} + m_1) I_{q3}] r^{\beta_{q1}+m_1} + [(iq + n_1) I_{q2} + (\beta_{q2} + m_1) I_{q4}] r^{\beta_{q2}+m_1} \right) e^{(iq+n_1)\theta} \\
 E_r &= \sum_{\substack{q=-\infty \\ q \neq 0}}^{\infty} \left(\sum_{j=1}^6 \eta_{qj} Y_{qj} D_{qj} r^{\eta_{qj}-1} + (\beta_{q1} + m_1 + 1) I_{q5} r^{\beta_{q1}+m_1} \right. \\
 &\quad \left. + (\beta_{q2} + m_1 + 1) I_{q6} r^{\beta_{q2}+m_1} \right) e^{(iq+n_1)\theta} \\
 E_{\theta} &= \sum_{\substack{q=-\infty \\ q \neq 0}}^{\infty} \left(\sum_{j=1}^6 (iq + n_1) Y_{qj} D_{qj} r^{\eta_{qj}-1} + (iq + n_1) I_{q5} r^{\beta_{q1}+m_1} + (iq + n_1) I_{q6} r^{\beta_{q2}+m_1} \right) e^{(iq+n_1)\theta}
 \end{aligned} \tag{3.9}$$

Substituting Eqs. (3.9) into Eqs. (2.4), the stresses and electric displacement are obtained as

$$\begin{aligned}
 \sigma_{rr} &= \frac{1}{a^{m_2}} \sum_{\substack{q=-\infty \\ q \neq 0}}^{\infty} \left\{ \sum_{j=1}^6 \left(\widehat{C}_{11} [\eta_{qj} D_{qj} r^{\eta_{qj}+m_2-1} + (\beta_{q1} + m_1 + 1) I_{q1} r^{\beta_{q1}+m_1+m_2} \right. \right. \\
 &\quad \left. + (\beta_{q2} + m_1 + 1) I_{q2} r^{\beta_{q2}+m_1+m_2}] - \frac{\alpha_0}{a^{m_1}} \overline{C}_{11} (A_{q1} r^{\beta_{q1}+m_1+m_2} + A_{q2} r^{\beta_{q2}+m_1+m_2}) \right. \\
 &\quad \left. + \widehat{C}_{12} [(iq + n_1)(X_{qj} + 1) D_{qj} r^{\eta_{qj}+m_2-1} + ((iq + n_1) I_{q3} + I_{q1}) r^{\beta_{q1}+m_1+m_2} \right. \\
 &\quad \left. + ((iq + n_1) I_{q4} + I_{q2}) r^{\beta_{q2}+m_1+m_2}] - \frac{2\alpha_0}{a^{m_1}} \overline{C}_{12} (A_{q1} r^{\beta_{q1}+m_1+m_2} + A_{q2} r^{\beta_{q2}+m_1+m_2}) \right\} e^{n_2\theta}
 \end{aligned}$$

$$\begin{aligned}
& + \bar{e}_{21}[\eta_{qj}Y_{qj}D_{qj}r^{\eta_{qj}+m_2-1} + (\beta_{q_1} + m_1 + 1)I_{q_5}r^{\beta_{q_1}+m_1+m_2} \\
& + (\beta_{q_2} + m_1 + 1)I_{q_6}r^{\beta_{q_2}+m_1+m_2}]e^{n_2\theta} \Big\} e^{(iq+n_1)\theta} \\
\sigma_{\theta\theta} = & \frac{1}{a^{m_2}} \sum_{\substack{q=-\infty \\ q \neq 0}}^{\infty} \left\{ \sum_{j=1}^6 \left(\widehat{C}_{12}[\eta_{qj}D_{qj}r^{\eta_{qj}+m_2-1} + (\beta_{q_1} + m_1 + 1)I_{q_1}r^{\beta_{q_1}+m_1+m_2} \right. \right. \\
& + (\beta_{q_2} + m_1 + 1)I_{q_2}r^{\beta_{q_2}+m_1+m_2}] - \frac{\alpha_0}{a^{m_1}}\overline{C}_{12}(A_{q_1}r^{\beta_{q_1}+m_1+m_2} + A_{q_2}r^{\beta_{q_2}+m_1+m_2}) \\
& + \widehat{C}_{22}[(iq + n_1)(X_{qj} + 1)D_{qj}r^{\eta_{qj}+m_2-1} + ((iq + n_1)I_{q_3} + I_{q_1})r^{\beta_{q_1}+m_1+m_2} \\
& + ((iq + n_1)I_{q_4} + I_{q_2})r^{\beta_{q_2}+m_1+m_2}] - \frac{2\alpha_0}{a^{m_1}}\overline{C}_{22}(A_{q_1}r^{\beta_{q_1}+m_1+m_2} + A_{q_2}r^{\beta_{q_2}+m_1+m_2}) \Big) e^{n_2\theta} \\
& + \bar{e}_{22}[\eta_{qj}Y_{qj}D_{qj}r^{\eta_{qj}+m_2-1} + (\beta_{q_1} + m_1 + 1)I_{q_5}r^{\beta_{q_1}+m_1+m_2} \\
& + (\beta_{q_2} + m_1 + 1)I_{q_6}r^{\beta_{q_2}+m_1+m_2}]e^{n_2\theta} \Big\} e^{(iq+n_1)\theta} \\
\sigma_{r\theta} = & \frac{1}{a^{m_2}} \sum_{\substack{q=-\infty \\ q \neq 0}}^{\infty} \left\{ \sum_{j=1}^6 \overline{C}_{44} \left([(iq + n_1) + (\eta_{qj} - 1)X_{qj}]D_{qj}r^{\eta_{qj}+m_2-1} + [(iq + n_1)I_{q_1} \right. \right. \\
& + (\beta_{q_1} + m_1)I_{q_3}]r^{\beta_{q_1}+m_1+m_2} + [(iq + n_1)I_{q_2} + (\beta_{q_2} + m_1)I_{q_4}]r^{\beta_{q_2}+m_1+m_2} \Big) e^{n_2\theta} \\
& - \bar{e}_{24}[(iq + n_1)Y_{qj}D_{qj}r^{\eta_{qj}+m_2-1} + (iq + n_1)I_{q_5}r^{\beta_{q_1}+m_1+m_2} \\
& + (iq + n_1)I_{q_6}r^{\beta_{q_2}+m_1+m_2}]e^{n_2\theta} \Big\} e^{(iq+n_1)\theta} \\
\sigma_{zz} = & \frac{1}{a^{m_2}} \sum_{\substack{q=-\infty \\ q \neq 0}}^{\infty} \left\{ \sum_{j=1}^6 \left(\widehat{C}_{12}[\eta_{qj}D_{qj}r^{\eta_{qj}+m_2-1} + (\beta_{q_1} + m_1 + 1)I_{q_1}r^{\beta_{q_1}+m_1+m_2} \right. \right. \\
& + (\beta_{q_2} + m_1 + 1)I_{q_2}r^{\beta_{q_2}+m_1+m_2} + ((iq + n_1)I_{q_3} + I_{q_1})r^{\beta_{q_1}+m_1+m_2} \\
& + ((iq + n_1)I_{q_4} + I_{q_2})r^{\beta_{q_2}+m_1+m_2} - \frac{3\alpha_0}{a^{m_1}}\overline{C}_{12}(A_{q_1}r^{\beta_{q_1}+m_1+m_2} + A_{q_2}r^{\beta_{q_2}+m_1+m_2}) \Big) e^{n_2\theta} \\
& + \bar{e}_{23}[\eta_{qj}Y_{qj}D_{qj}r^{\eta_{qj}+m_2-1} + (\beta_{q_1} + m_1 + 1)I_{q_5}r^{\beta_{q_1}+m_1+m_2} \\
& + (\beta_{q_2} + m_1 + 1)I_{q_6}r^{\beta_{q_2}+m_1+m_2}]e^{n_2\theta} \Big\} e^{(iq+n_1)\theta} \\
D_{rr} = & \frac{1}{a^{m_2}} \sum_{\substack{q=-\infty \\ q \neq 0}}^{\infty} \left\{ \sum_{j=1}^6 \left(\bar{e}_{21}[\eta_{qj}D_{qj}r^{\eta_{qj}+m_2-1} + (\beta_{q_1} + m_1 + 1)I_{q_1}r^{\beta_{q_1}+m_1+m_2} \right. \right. \\
& + (\beta_{q_2} + m_1 + 1)I_{q_2}r^{\beta_{q_2}+m_1+m_2}] + \bar{e}_{22}[(iq + n_1)(X_{qj} + 1)D_{qj}r^{\eta_{qj}+m_2-1} \\
& + ((iq + n_1)I_{q_3} + I_{q_1})r^{\beta_{q_1}+m_1+m_2} + ((iq + n_1)I_{q_4} + I_{q_2})r^{\beta_{q_2}+m_1+m_2}] \Big) e^{n_2\theta} \\
& - \bar{e}_{22}[\eta_{qj}Y_{qj}D_{qj}r^{\eta_{qj}+m_2-1} + (\beta_{q_1} + m_1 + 1)I_{q_5}r^{\beta_{q_1}+m_1+m_2} \\
& + (\beta_{q_2} + m_1 + 1)I_{q_6}r^{\beta_{q_2}+m_1+m_2}]e^{n_2\theta} \\
& + \frac{\bar{g}_{21}}{a^{m_1}}(A_{q_1}r^{\beta_{q_1}+m_1+m_2} + A_{q_2}r^{\beta_{q_2}+m_1+m_2})e^{(n_1+n_2)\theta} \Big\} e^{(iq+n_1)\theta}
\end{aligned} \tag{3.10}$$

$$\begin{aligned}
D_{\theta\theta} = & \frac{1}{a^{m_2}} \sum_{\substack{q=-\infty \\ q \neq 0}}^{\infty} \left\{ \sum_{j=1}^6 \bar{\varepsilon}_{24} \left([iq + n_1 + (\eta_{qj} - 1)X_{qj}] D_{qj} r^{\eta_{qj} + m_4 - 1} + [(iq + n_1)I_{q_1} \right. \right. \\
& + (\beta_{q_1} + m_1)I_{q_3}] r^{\beta_{q_1} + m_1 + m_4} + [(iq + n_1)I_{q_2} + (\beta_{q_2} + m_1)I_{q_4}] r^{\beta_{q_2} + m_1 + m_4} \left. \right) e^{n_4\theta} \\
& - \bar{\varepsilon}_{21} \left((iq + n_1)Y_{qj} D_{qj} r^{\eta_{qj} + m_5 - 1} + (iq + n_1)I_{q_5} r^{\beta_{q_1} + m_1 + m_5} \right. \\
& \left. + (iq + n_1)I_{q_6} r^{\beta_{q_2} + m_1 + m_5} \right) e^{n_5\theta} + \frac{\bar{g}_{22}}{a^{m_1}} (A_{q_1} r^{\beta_{q_1} + m_1 + m_6} + A_{q_2} r^{\beta_{q_2} + m_1 + m_6}) e^{n_6\theta} \left. \right\} e^{(iq + n_1)\theta}
\end{aligned}$$

To determine the constants D_{qj} , any general form of boundary conditions for displacements, stresses and potential electric is considered as

$$\begin{aligned}
u(a, \theta) = w_1(\theta) & \quad u(b, \theta) = w_2(\theta) & \quad v(a, \theta) = w_3(\theta) \\
v(b, \theta) = w_4(\theta) & \quad \sigma_{rr}(a, \theta) = w_7(\theta) & \quad \sigma_{rr}(b, \theta) = w_8(\theta) \\
\sigma_{r\theta}(a, \theta) = w_9(\theta) & \quad \sigma_{r\theta}(b, \theta) = w_{10}(\theta) & \quad \psi(a, \theta) = w_5(\theta) \\
\psi(b, \theta) = w_6(\theta) & \quad D_{rr}(a, \theta) = w_{11}(\theta) & \quad D_{rr}(b, \theta) = w_{12}(\theta)
\end{aligned} \tag{3.11}$$

It is recalled that Eqs. (3.9) and (3.10) contain six unknowns, $D_{q_1}, D_{q_2}, \dots, D_{q_6}$. Assume that the six boundary conditions are specified from list of Eqs. (3.11). The boundary conditions may be either the given displacements and electric potential or stresses, or combinations. Expanding the given boundary conditions in complex Fourier series gives

$$w_j(\theta) = \sum_{n=-\infty}^{\infty} W_j(q) e^{(iq + n_1)\theta} \quad j = 1, \dots, 6 \tag{3.12}$$

where

$$W_j(q) = \frac{1}{2\pi} \int_{-\pi}^{\pi} w_j(q) e^{-(iq + n_1)\theta} d\theta \quad j = 1, \dots, 6 \tag{3.13}$$

Using the selected six boundary conditions of Eqs. (3.11) with the help of Eqs. (3.12) and (3.13), the six unknown coefficients D_{q_1} to D_{q_6} are calculated.

4. Results and discussion

Consider a thick hollow cylinder of inner radius $a = 1$ m and outer radius $b = 1.2$ m of $\text{Ba}_2\text{NaNb}_5\text{O}_{15}$ material with properties given in Table 1.

The thermal boundary conditions are substituted into Eq. (2.12) to obtain the temperature distribution, where the constants of integration are obtained from the equations given in Appendix. The stress and displacement and electric potential boundary conditions are assumed to be selected such that the mathematical strength of the proposed method can be examined. These type of boundary conditions may not be handled with the potential function method. The constant coefficients of the series expansions are obtained from Eq. (3.13). Here, B is the compressibility coefficient, sometimes named the skempton pore pressure coefficient, and ϕ is the pore volume fraction and is pore per total volume, respectively, which are given in Appendix. Using Eqs. (3.11) and (3.12), the boundary conditions given in terms of the radial and shear stresses as well as electric potential appear in Table 2. These boundary conditions are expanded by the integral series and the unknown coefficients D_{qj} are determined.

Table 1. Material constants of $\text{Ba}_2\text{NaNb}_5\text{O}_{15}$ for 2D-PPM (Akbari Alashti *et al.*, 2013; Jabbari *et al.*, 2012)

Parameter	Value	Parameter	Value	Parameter	Value
α_0 [$1/^\circ\text{C}$]	$1.2 \cdot 10^{-6}$	\bar{C}_{11} [GPa]	239	\bar{e}_{22} [C/m^2]	-0.3
γ	0.75	\bar{C}_{12} [GPa]	104	\bar{e}_{24} [C/m^2]	3.4
ν	0.25	\bar{C}_{22} [GPa]	247	\bar{e}_{21} [$\text{C}^2/\text{N m}^2$]	$1.96 \cdot 10^{-9}$
ν_u	0.3	\bar{C}_{44} [GPa]	76	\bar{e}_{22} [$\text{C}^2/\text{N m}^2$]	$2.01 \cdot 10^{-9}$
k_0 [$\text{W}/\text{m K}$]	13.9	\bar{e}_{21} [C/m^2]	-0.4	\bar{g}_{21} [$\text{C}/\text{m}^2\text{K}$]	$5.4 \cdot 10^{-5}$
m_1, m_2, \dots, m_6	m	n_1, n_2, \dots, n_6	n	\bar{g}_{22} [$\text{C}/\text{m}^2\text{K}$]	$5.4 \cdot 10^{-5}$

Table 2. Boundary condition for 2D-PPM (Jabbari *et al.*, 2012)

$T(a, \theta)$ [$^\circ\text{C}$]	$T(b, \theta)$	$\sigma_{rr}(a, \theta)$ [MPa]	$\sigma_{r\theta}(a, \theta)$ [MPa]	$u(b, \theta)$	$v(b, \theta)$	$\psi(a, \theta)$ [W/A]
$60 \sin(2 \theta)$	0	$400 \sin\left(\frac{\theta^2}{4} - \theta \right)$	$50\theta^2 \cos \theta$	0	0	$\psi_0 \theta^2 \cos(2\theta)$

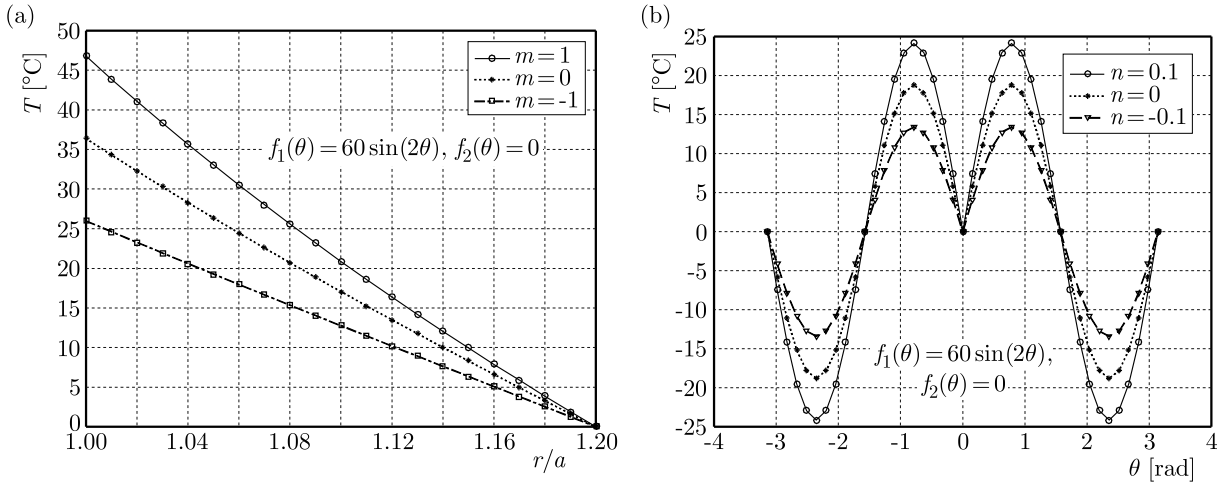
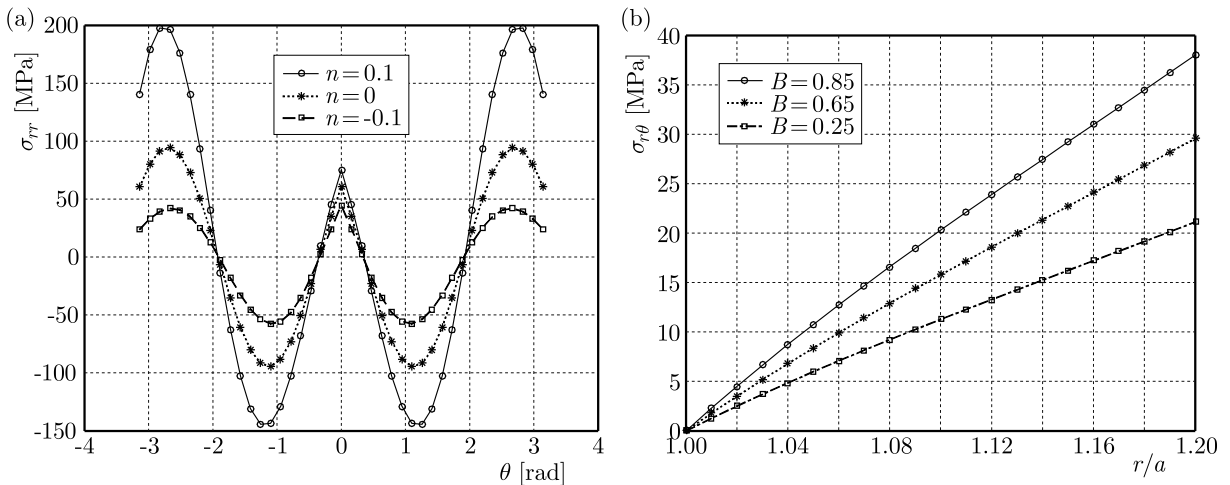
Fig. 2. Temperature distribution in the (a) radial at $\theta = \pi/3$ and (b) circumferential direction at $r = \bar{r}$ Fig. 3. (a) Circumferential distribution of radial thermo-electro-mechanical stresses σ_{rr} at $r = \bar{r}$. (b) Radial distribution of shear thermo-electro-mechanical stresses $\sigma_{r\theta}$ at $\theta = \pi/3$

Figure 2a and 2b shows the effect of the power-exponential law index on the temperature distribution in the wall thickness along the radial and circumferential directions. The effect of the power-exponential law index on the distribution of the radial thermo-electro-mechanical stresses is shown in Fig. 3a. It is shown that as m, n increases, the radial, hoop, shear and axial thermal stresses are increased. This figure is a plot of stresses versus θ at $r = \bar{r} = 1.1$, where \bar{r} is the average inner radius a and the outer radius b . Figure 3b shows the shear thermo-electro-mechanical stresses in the cross section of the cylinder, where the pore compressibility coefficient B is changed and the other parameters are fixed. Figure 4a shows the radial displacement in the cross section of the cylinder, where the based on the pore volume fraction ϕ is changing. Also the electric potential constant in Figs. 1 to 4a is $\psi_0 = 60$ V. Figure 4b shows the circumferential displacements in the cross section of the cylinder, where the based on the versus electric potential coefficient ψ_0 is changing.

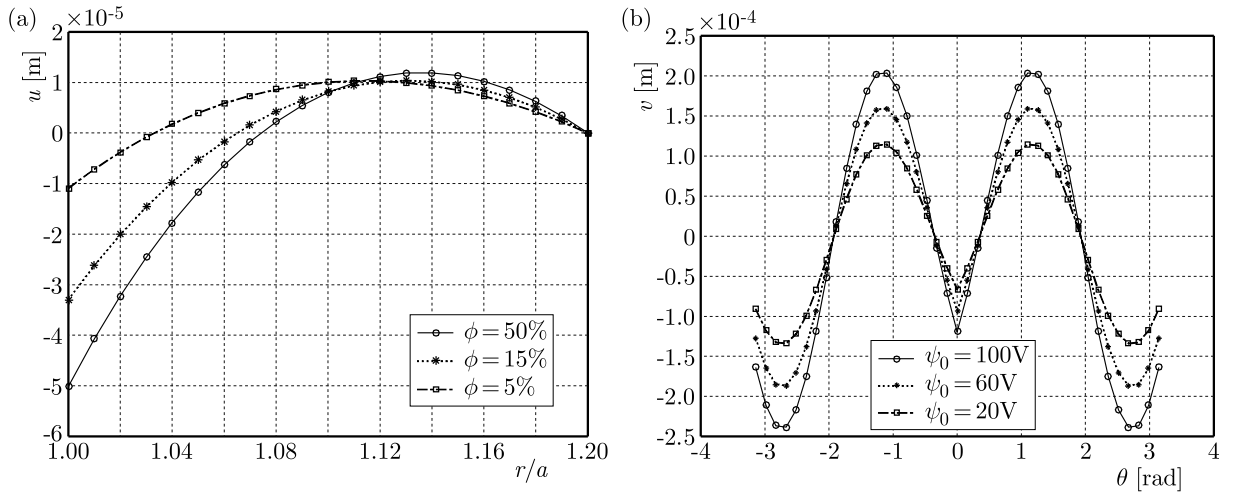


Fig. 4. (a) Radial distribution of u with different porosity coefficient at $\theta = \pi/3$. (b) Circumferential distribution of v with electric potential coefficient at $r = \bar{r}$

5. Conclusions

In the present work, an attempt is made to study the problem of analytical solution for the Thermo-Electro-Mechanical (TEM) in a thick 2D-PPM hollow infinite cylinder where the two-dimensional asymmetric steady-state loads are implied. The method of solution is based on the direct method and uses the power series, rather than the potential function method. The advantage of this method is its mathematical power to handle both simple and complicated mathematical functions for the thermal and mechanical stresses boundary conditions. The potential function method is capable of handling complicated mathematical functions as the boundary conditions. The proposed method does not have mathematical limitations to deal with general types of boundary conditions, which usually occur in the potential function method.

Appendix

$$d_1 = (\beta_{q_1} + m_1 + 1)(\beta_{q_1} + m_1) + \left((m_2 + 1) + (m_2 - 1) \frac{\widehat{\bar{C}}_{12}}{\widehat{\bar{C}}_{11}} \right) (\beta_{q_1} + m_1 + 1) \\ + \frac{m_2 \widehat{\bar{C}}_{12} - \widehat{\bar{C}}_{22}}{\widehat{\bar{C}}_{11}} + [(n_1 + n_2)n_1 + iq(2n_1 + n_2) - q^2] \frac{\bar{C}_{44}}{\bar{C}_{11}}$$

$$\begin{aligned}
d_2 &= (\beta_{q_2} + m_1 + 1)(\beta_{q_2} + m_1) + \left((m_2 + 1) + (m_2 - 1) \frac{\widehat{\overline{C}}_{12}}{\widehat{\overline{C}}_{11}} \right) (\beta_{q_2} + m_1 + 1) \\
&\quad + \frac{m_2 \widehat{\overline{C}}_{12} - \widehat{\overline{C}}_{22}}{\widehat{\overline{C}}_{11}} + [(n_1 + n_2)n_1 + iq(2n_1 + n_2) - q^2] \frac{\overline{C}_{44}}{\widehat{\overline{C}}_{11}} \\
d_3 &= \left((iq + n_1) \frac{\widehat{\overline{C}}_{12}}{\widehat{\overline{C}}_{11}} + (iq + n_1 + n_2) \frac{\overline{C}_{44}}{\widehat{\overline{C}}_{11}} \right) (\beta_{q_1} + m_1 + 1) \\
&\quad + (iq + n_1) \frac{m_2 \widehat{\overline{C}}_{12} - \widehat{\overline{C}}_{22}}{\widehat{\overline{C}}_{11}} - (iq + n_1 + n_2) \frac{\overline{C}_{44}}{\widehat{\overline{C}}_{11}} \\
d_4 &= \left((iq + n_1) \frac{\widehat{\overline{C}}_{12}}{\widehat{\overline{C}}_{11}} + (iq + n_1 + n_2) \frac{\overline{C}_{44}}{\widehat{\overline{C}}_{11}} \right) (\beta_{q_2} + m_1 + 1) \\
&\quad + (iq + n_1) \frac{m_2 \widehat{\overline{C}}_{12} - \widehat{\overline{C}}_{22}}{\widehat{\overline{C}}_{11}} - (iq + n_1 + n_2) \frac{\overline{C}_{44}}{\widehat{\overline{C}}_{11}} \\
d_5 &= \frac{\overline{e}_{21}}{\widehat{\overline{C}}_{11}} (\beta_{q_1} + m_1 + 1)(\beta_{q_1} + m_1) + \frac{(m_4 + 1)\overline{e}_{21} - \overline{e}_{22}}{\widehat{\overline{C}}_{11}} (\beta_{q_1} + m_1 + 1) \\
&\quad + [(n_1 + n_4)n_1 + iq(2n_1 + n_4) - q^2] \frac{\overline{e}_{24}}{\widehat{\overline{C}}_{11}} \\
d_6 &= \frac{\overline{e}_{21}}{\widehat{\overline{C}}_{11}} (\beta_{q_2} + m_1 + 1)(\beta_{q_2} + m_1) + \frac{(m_4 + 1)\overline{e}_{21} - \overline{e}_{22}}{\widehat{\overline{C}}_{11}} (\beta_{q_2} + m_1 + 1) \\
&\quad + [(n_1 + n_4)n_1 + iq(2n_1 + n_4) - q^2] \frac{\overline{e}_{24}}{\widehat{\overline{C}}_{11}} \\
d_7 &= \left(\frac{(m_1 + m_2 + 1)\overline{C}_{11} + 2(m_1 + m_2)\overline{C}_{12} - \overline{C}_{22}}{\widehat{\overline{C}}_{11}} + \frac{\overline{C}_{11} + 2\overline{C}_{12}}{\widehat{\overline{C}}_{11}} \beta_{q_1} \right) \frac{\alpha_0}{a^{m_1}} A_{q_1} \\
d_8 &= \left(\frac{(m_1 + m_2 + 1)\overline{C}_{11} + 2(m_1 + m_2)\overline{C}_{12} - \overline{C}_{22}}{\widehat{\overline{C}}_{11}} + \frac{\overline{C}_{11} + 2\overline{C}_{12}}{\widehat{\overline{C}}_{11}} \beta_{q_2} \right) \frac{\alpha_0}{a^{m_1}} A_{q_2} \\
d_9 &= (\beta_{q_1} + m_1 + 1)(\beta_{q_1} + m_1) + (m_2 + 1)(\beta_{q_1} + m_1 + 1) \\
&\quad - (m_2 + 1) + [(n_1 + n_2) + iq(n_2 + 2) - q^2] \frac{\widehat{\overline{C}}_{22}}{\overline{C}_{44}} \\
d_{10} &= (\beta_{q_2} + m_1 + 1)(\beta_{q_2} + m_1) + (m_2 + 1)(\beta_{q_2} + m_1 + 1) \\
&\quad - (m_2 + 1) + [(n_1 + n_2) + iq(n_2 + 2) - q^2] \frac{\widehat{\overline{C}}_{22}}{\overline{C}_{44}} \\
d_{11} &= \left((iq + n_1) + (iq + n_1 + n_2) \frac{\widehat{\overline{C}}_{12}}{\overline{C}_{44}} \right) (\beta_{q_1} + m_1 + 1) \\
&\quad + (iq + n_1)(m_2 + 1) + (iq + n_1 + n_2) \frac{\widehat{\overline{C}}_{22}}{\overline{C}_{44}} \\
d_{12} &= \left((iq + n_1) + (iq + n_1 + n_2) \frac{\widehat{\overline{C}}_{12}}{\overline{C}_{44}} \right) (\beta_{q_2} + m_1 + 1) \\
&\quad + (iq + n_1)(m_2 + 1) + (iq + n_1 + n_2) \frac{\widehat{\overline{C}}_{22}}{\overline{C}_{44}} \\
d_{13} &= \left((iq + n_1) \frac{\overline{e}_{24}}{\overline{C}_{44}} + (iq + n_1 + n_4) \frac{\overline{e}_{22}}{\overline{C}_{44}} \right) (\beta_{q_1} + m_1 + 1) + (iq + n_1)(m_4 + 2) \frac{\overline{e}_{24}}{\overline{C}_{44}}
\end{aligned}$$

$$d_{14} = \left((iq + n_1) \frac{\bar{e}_{24}}{\bar{C}_{44}} + (iq + n_1 + n_4) \frac{\bar{e}_{22}}{\bar{C}_{44}} \right) (\beta_{q_2} + m_1 + 1) + (iq + n_1)(m_4 + 2) \frac{\bar{e}_{24}}{\bar{C}_{44}}$$

$$d_{15} = (n_1 + n_2 + iq) \frac{2\bar{C}_{12} + \bar{C}_{22}}{\bar{C}_{44}} \frac{\alpha_0}{a^{m_1}} A_{q_1}$$

$$d_{16} = (n_1 + n_2 + iq) \frac{2\bar{C}_{12} + \bar{C}_{22}}{\bar{C}_{44}} \frac{\alpha_0}{a^{m_1}} A_{q_2}$$

$$d_{17} = (\beta_{q_1} + m_1 + 1)(\beta_{q_1} + m_1) + (\beta_{q_1} + m_1 + 1)(m_5 + 1) \\ + [(n_1 + n_5)n_1 + iq(n_5 + 2n_1) - q^2] \frac{\bar{e}_{21}}{\bar{e}_{22}}$$

$$d_{18} = (\beta_{q_2} + m_1 + 1)(\beta_{q_2} + m_1) + (\beta_{q_2} + m_1 + 1)(m_5 + 1) \\ + [(n_1 + n_5)n_1 + iq(n_5 + 2n_1) - q^2] \frac{\bar{e}_{21}}{\bar{e}_{22}}$$

$$d_{19} = -\frac{\bar{e}_{21}}{\bar{e}_{22}} (\beta_{q_1} + m_1 + 1)(\beta_{q_1} + m_1) - \frac{(m_4 + 1)\bar{e}_{21} + \bar{e}_{22}}{\bar{e}_{22}} (\beta_{q_1} + m_1 + 1) - \frac{m_4\bar{e}_{22}}{\bar{e}_{22}}$$

$$d_{20} = -\frac{\bar{e}_{21}}{\bar{e}_{22}} (\beta_{q_2} + m_1 + 1)(\beta_{q_2} + m_1) - \left(\frac{(m_4 + 1)\bar{e}_{21} + \bar{e}_{22}}{\bar{e}_{22}} \right) (\beta_{q_2} + m_1 + 1) - \frac{m_4\bar{e}_{22}}{\bar{e}_{22}}$$

$$d_{21} = (iq + n_1 + n_4) \frac{\bar{e}_{24}}{\bar{e}_{22}} (\beta_{q_1} + m_1 + 1) + (iq + n_1)(m_4 + 1) \frac{\bar{e}_{22}}{\bar{e}_{22}} - (iq + n_1 + n_4) \frac{\bar{e}_{24}}{\bar{e}_{22}}$$

$$d_{22} = (iq + n_1 + n_4) \frac{\bar{e}_{24}}{\bar{e}_{22}} (\beta_{q_2} + m_1 + 1) + (iq + n_1)(m_4 + 1) \frac{\bar{e}_{22}}{\bar{e}_{22}} - (iq + n_1 + n_4) \frac{\bar{e}_{24}}{\bar{e}_{22}}$$

$$d_{23} = \left((m_6 + 1) \frac{\bar{g}_{21}}{\bar{e}_{22}} + (iq + n_6 + \beta_{q_1}) \frac{\bar{g}_{22}}{\bar{e}_{22}} \right) \frac{1}{a^{m_1}} A_{q_1}$$

$$d_{24} = \left((m_6 + 1) \frac{\bar{g}_{21}}{\bar{e}_{22}} + (iq + n_6 + \beta_{q_2}) \frac{\bar{g}_{22}}{\bar{e}_{22}} \right) \frac{1}{a^{m_1}} A_{q_2}$$

$$\hat{N}_{1q_j} = \eta_{q_j}(\eta_{q_j} - 1) + \tau_1\eta + \tau_2 + \tau_3 + i\tau_4$$

$$\hat{N}_{2q_j} = \tau_5\eta_{q_j} + \tau_7 + i(\tau_6 + \tau_8\eta_{q_j})$$

$$\hat{N}_{3q_j} = \eta_{q_j}(\eta_{q_j} - 1)\tau_9 + \tau_{10}\eta_{q_j} + \tau_{11} + i\tau_{12}$$

$$\hat{N}_{4q_j} = \tau_{16} + \tau_{18}\eta_{q_j} + i(\tau_{19}\eta_{q_j} + \tau_{21})$$

$$\hat{N}_{5q_j} = \eta_{q_j}(\eta_{q_j} - 1) + \tau_{15}\eta_{q_j} - \tau_{16} + i\tau_{17}$$

$$\hat{N}_{6q_j} = \tau_{26}\eta_{q_j} + \tau_{28} + i(\tau_{27}\eta_{q_j} + \tau_{29})$$

$$\hat{N}_{7q_j} = \eta_{q_j}(\eta_{q_j} - 1)\tau_{35} - \tau_{36}\eta_{q_j} - \tau_{37}$$

$$\hat{N}_{8q_j} = \tau_{38}\eta_{q_j} + \tau_{40} + i(\tau_{39}\eta_{q_j} + \tau_{41})$$

$$\hat{N}_{9q_j} = \eta_{q_j}(\eta_{q_j} - 1) - \tau_{32}\eta_{q_j} + \tau_{33} + i\tau_{34}$$

$$\begin{bmatrix} \hat{N}_{1q_j} & \hat{N}_{2q_j} & \hat{N}_{3q_j} \\ \hat{N}_{4q_j} & \hat{N}_{5q_j} & \hat{N}_{6q_j} \\ \hat{N}_{7q_j} & \hat{N}_{8q_j} & \hat{N}_{9q_j} \end{bmatrix} \begin{bmatrix} D_{q_j} \\ E_{q_j} \\ F_{q_j} \end{bmatrix} = \begin{bmatrix} 0 \\ 0 \\ 0 \end{bmatrix} \Rightarrow \begin{vmatrix} \hat{N}_{1q_j} & \hat{N}_{2q_j} & \hat{N}_{3q_j} \\ \hat{N}_{4q_j} & \hat{N}_{5q_j} & \hat{N}_{6q_j} \\ \hat{N}_{7q_j} & \hat{N}_{8q_j} & \hat{N}_{9q_j} \end{vmatrix} = 0$$

$$X_{q_j} = \frac{E_{q_j}}{D_{q_j}} = \frac{\hat{N}_{1q_j}\hat{N}_{6q_j} - \hat{N}_{3q_j}\hat{N}_{4q_j}}{\hat{N}_{3q_j}\hat{N}_{5q_j} - \hat{N}_{2q_j}\hat{N}_{6q_j}} \quad Y_{q_j} = \frac{F_{q_j}}{D_{q_j}} = \frac{\hat{N}_{4q_j}\hat{N}_{8q_j} - \hat{N}_{5q_j}\hat{N}_{7q_j}}{\hat{N}_{5q_j}\hat{N}_{9q_j} - \hat{N}_{6q_j}\hat{N}_{8q_j}} \quad j = 1, \dots, 6$$

$$I_{q_1} = \frac{d_7d_9d_{17} - d_3d_{15}d_{17} - d_5d_9d_{23} - d_7d_{13}d_{19} + d_3d_{13}d_{23} + d_5d_{15}d_{19}}{d_1d_9d_{17} - d_3d_{11}d_{17} - d_1d_{13}d_{19} - d_5d_9d_{21} + d_5d_{11}d_{19} + d_3d_{13}d_{21}}$$

$$I_{q_2} = \frac{d_8d_{10}d_{18} - d_4d_{16}d_{18} - d_6d_{10}d_{24} - d_8d_{14}d_{20} + d_4d_{14}d_{24} + d_6d_{16}d_{20}}{d_2d_{10}d_{18} - d_4d_{12}d_{18} - d_2d_{14}d_{20} - d_6d_{10}d_{22} + d_6d_{12}d_{20} + d_4d_{14}d_{22}}$$

$$I_{q_3} = \frac{d_1d_{15}d_{17} - d_7d_{11}d_{17} - d_1d_{13}d_{23} - d_5d_{15}d_{21} + d_5d_{11}d_{23} + d_7d_{13}d_{21}}{d_1d_9d_{17} - d_3d_{11}d_{17} - d_1d_{13}d_{19} - d_5d_9d_{21} + d_5d_{11}d_{19} + d_3d_{13}d_{21}}$$

$$I_{q_4} = \frac{d_2d_{16}d_{18} - d_8d_{12}d_{18} - d_2d_{14}d_{24} - d_6d_{16}d_{22} + d_6d_{12}d_{24} + d_8d_{14}d_{22}}{d_2d_{10}d_{18} - d_4d_{12}d_{18} - d_2d_{14}d_{20} - d_6d_{10}d_{22} + d_6d_{12}d_{20} + d_4d_{14}d_{22}}$$

$$I_{q_5} = \frac{d_1d_9d_{23} - d_1d_{15}d_{19} - d_3d_{11}d_{23} - d_7d_9d_{21} + d_7d_{11}d_{19} + d_3d_{15}d_{21}}{d_1d_9d_{17} - d_3d_{11}d_{17} - d_1d_{13}d_{19} - d_5d_9d_{21} + d_5d_{11}d_{19} + d_3d_{13}d_{21}}$$

$$I_{q_6} = \frac{d_2d_{10}d_{24} - d_2d_{16}d_{20} - d_4d_{12}d_{24} - d_8d_{10}d_{22} + d_8d_{12}d_{20} + d_4d_{16}d_{22}}{d_2d_{10}d_{18} - d_4d_{12}d_{18} - d_2d_{14}d_{20} - d_6d_{10}d_{22} + d_6d_{12}d_{20} + d_4d_{14}d_{22}}$$

$$\begin{aligned}
\tau_1 &= (m_2 + 1) + (m_2 - 1) \frac{\widehat{\overline{C}}_{12}}{\widehat{\overline{C}}_{11}} & \tau_2 &= \frac{m_2 \widehat{\overline{C}}_{12} - \widehat{\overline{C}}_{22} + [(n_1^2 + n_1 n_2) - q^2] \overline{C}_{44}}{\widehat{\overline{C}}_{11}} \\
\tau_3 &= \frac{(2n_1 + n_2) \overline{C}_{44}}{\widehat{\overline{C}}_{11}} q & \tau_4 &= \frac{n_1 \widehat{\overline{C}}_{12} + (n_1 + n_2) \overline{C}_{44}}{\widehat{\overline{C}}_{11}} & \tau_5 &= \frac{\widehat{\overline{C}}_{12} + \overline{C}_{44}}{\widehat{\overline{C}}_{11}} q \\
\tau_6 &= \frac{(m_2 \widehat{\overline{C}}_{12} - \widehat{\overline{C}}_{22}) n_1 - (n_1 + n_2) \overline{C}_{44}}{\widehat{\overline{C}}_{11}} & \tau_7 &= \frac{m_2 \widehat{\overline{C}}_{12} - \widehat{\overline{C}}_{22} - \overline{C}_{44}}{\widehat{\overline{C}}_{11}} q \\
\tau_8 &= \frac{\overline{e}_{21}}{\widehat{\overline{C}}_{11}} & \tau_9 &= \frac{(m_4 + 1) \overline{e}_{21} - \overline{e}_{22}}{\widehat{\overline{C}}_{11}} & \tau_{10} &= [(n_1^2 + n_1 n_4) - q^2] \frac{\overline{e}_{24}}{\widehat{\overline{C}}_{11}} \\
\tau_{11} &= (2n_1 + n_4) \frac{\overline{e}_{24}}{\widehat{\overline{C}}_{11}} q & \tau_{12} &= \frac{\alpha_0 [(m_1 + m_2 + 1) \overline{C}_{11} + 2(m_1 + m_2) \overline{C}_{12} - \overline{C}_{22}]}{\widehat{\overline{C}}_{11}} \\
\tau_{13} &= \alpha_0 \frac{\overline{C}_{11} + 2\overline{C}_{12}}{\widehat{\overline{C}}_{11}} & \tau_{14} &= m_2 + 1 & \tau_{15} &= (m_2 + 1) - [(n_1 + n_2) - q^2] \frac{\widehat{\overline{C}}_{22}}{\overline{C}_{44}} \\
\tau_{16} &= (n_2 + 2) \frac{\widehat{\overline{C}}_{22}}{\overline{C}_{44}} q & \tau_{17} &= n_1 + (n_1 + n_2) \frac{\widehat{\overline{C}}_{12}}{\overline{C}_{44}} & \tau_{18} &= \left(1 + \frac{\widehat{\overline{C}}_{12}}{\overline{C}_{44}}\right) q \\
\tau_{19} &= (m_2 + 1) n_1 + (n_1 + n_2) \frac{\widehat{\overline{C}}_{22}}{\overline{C}_{44}} & \tau_{20} &= \left((m_2 + 1) + \frac{\widehat{\overline{C}}_{22}}{\overline{C}_{44}}\right) q \\
\tau_{21} &= \frac{(n_1 + n_4) \overline{e}_{22} + n_1 \overline{e}_{24}}{\overline{C}_{44}} & \tau_{22} &= \frac{\overline{e}_{22} + \overline{e}_{24}}{\overline{C}_{44}} q & \tau_{23} &= (m_4 + 2) n_1 \frac{\overline{e}_{24}}{\overline{C}_{44}} \\
\tau_{24} &= (m_4 + 2) q \frac{\overline{e}_{24}}{\overline{C}_{44}} & \tau_{25} &= \alpha_0 (n_1 + n_2) \frac{2\overline{C}_{12} + \overline{C}_{22}}{\overline{C}_{44}} \\
\tau_{26} &= \alpha_0 \frac{2\overline{C}_{12} + \overline{C}_{22}}{\overline{C}_{44}} q & \tau_{27} &= m_5 + 1 & \tau_{28} &= [(n_1^2 + n_1 n_5) - q^2] \frac{\overline{e}_{21}}{\overline{e}_{22}} \\
\tau_{29} &= (2n_1 + n_5) q \frac{\overline{e}_{21}}{\overline{e}_{22}} & \zeta_{30} &= -\frac{\overline{e}_{21}}{\overline{e}_{22}} & \tau_{31} &= \frac{(m_4 + 1) \overline{e}_{21} + \overline{e}_{22}}{\overline{e}_{22}} \\
\tau_{32} &= \frac{m_4 \overline{e}_{22}}{\overline{e}_{22}} & \tau_{33} &= (n_1 + n_4) \frac{\overline{e}_{24}}{\overline{e}_{22}} & \tau_{34} &= \frac{\overline{e}_{24}}{\overline{e}_{22}} q \\
\tau_{35} &= \frac{(m_4 + 1) n_1 \overline{e}_{22} - (n_1 + n_4) \overline{e}_{24}}{\overline{e}_{22}} & \tau_{36} &= \frac{(m_4 + 1) \overline{e}_{22} - \overline{e}_{24}}{\overline{e}_{22}} q \\
\tau_{37} &= \frac{(m_6 + 1) \overline{g}_{21} + n_6 \overline{g}_{22}}{\overline{e}_{22}} & \tau_{38} &= \frac{\overline{g}_{22}}{\overline{e}_{22}} q & \tau_{39} &= \frac{\overline{g}_{22}}{\overline{e}_{22}}
\end{aligned}$$

Also

$$B = \frac{3(\nu_u - \nu)}{(1 - 2\nu)(1 + \nu_u)} \quad 0 \leq B \leq 1 \quad \phi = \frac{\gamma(B - k_f)}{B[(1 - \alpha) + k]}$$

where k_f and k are the bulk modulus of the fluid phase and the bulk modulus of the porouselastic medium under the drained condition, respectively

$$M = \frac{2G(\nu_u - \nu)}{\gamma^2(1 - 2\nu)(1 - 2\nu_u)}$$

where M and γ are Biot's modulus, Biot's coefficient of the porouselastic medium, respectively.

Using the boundary conditions (2.12) to determine the constants A_{q_1} , A_{q_2}

$$\begin{aligned} \sum_{q=-\infty}^{\infty} \left[(S_{11}a^{\beta_{q_1}} + S_{12}\beta_{q_1}a^{\beta_{q_1}} - 1)A_{q_1} + (S_{11}a^{\beta_{q_2}} + S_{12}\beta_{q_2}a^{\beta_{q_2}} - 1)A_{q_2} \right] e^{iq\theta} &= f_1(\theta) \\ \sum_{q=-\infty}^{\infty} \left[(S_{21}b^{\beta_{q_1}} + S_{22}\beta_{q_1}b^{\beta_{q_1}} - 1)A_{q_1} + (S_{21}b^{\beta_{q_2}} + S_{22}\beta_{q_2}b^{\beta_{q_2}} - 1)A_{q_2} \right] e^{iq\theta} &= f_2(\theta) \\ (S_{11}a^{\beta_{q_1}} + S_{12}\beta_{q_1}a^{\beta_{q_1}} - 1)A_{q_1} + (S_{11}a^{\beta_{q_2}} + S_{12}\beta_{q_2}a^{\beta_{q_2}} - 1)A_{q_2} &= \frac{1}{2\pi} \int_{-\pi}^{\pi} f_1(\theta) e^{-iq\theta} d\theta \\ (S_{21}b^{\beta_{q_1}} + S_{22}\beta_{q_1}b^{\beta_{q_1}} - 1)A_{q_1} + (S_{21}b^{\beta_{q_2}} + S_{22}\beta_{q_2}b^{\beta_{q_2}} - 1)A_{q_2} &= \frac{1}{2\pi} \int_{-\pi}^{\pi} f_2(\theta) e^{-iq\theta} d\theta \\ A_{q_1} &= \frac{1}{2\pi} \int_{-\pi}^{\pi} \frac{1}{\widehat{S}_1 - \widehat{S}_2} \left[(S_{21}b^{\beta_{q_2}} + S_{22}\beta_{q_1}b^{\beta_{q_2}-1})f_1(\theta) \right. \\ &\quad \left. - (S_{11}a^{\beta_{q_2}} + S_{12}\beta_{q_2}a^{\beta_{q_2}-1})f_2(\theta) \right] e^{-iq\theta} d\theta \\ A_{q_2} &= \frac{1}{2\pi} \int_{-\pi}^{\pi} \frac{1}{\widehat{S}_1 - \widehat{S}_2} \left[(S_{11}a^{\beta_{q_1}} + S_{12}\beta_{q_1}a^{\beta_{q_1}-1})f_2(\theta) \right. \\ &\quad \left. - (S_{21}b^{\beta_{q_1}} + S_{22}\beta_{q_1}b^{\beta_{q_1}-1})f_1(\theta) \right] e^{-iq\theta} d\theta \\ \widehat{S}_1 &= (S_{11}a^{\beta_{q_1}} + S_{12}\beta_{q_1}a^{\beta_{q_1}} - 1)(S_{21}b^{\beta_{q_2}} + S_{22}\beta_{q_2}b^{\beta_{q_2}} - 1) \\ \widehat{S}_2 &= (S_{11}a^{\beta_{q_2}} + S_{12}\beta_{q_2}a^{\beta_{q_2}} - 1)(S_{21}b^{\beta_{q_1}} + S_{22}\beta_{q_1}b^{\beta_{q_1}} - 1) \end{aligned}$$

References

1. AKBARI ALASHTI R., KHORSAND M., TARAHHOMI M.H., 2013, Thermo-elastic analysis of a functionally graded spherical shell with piezoelectric layers by differential quadrature method, *Scientia Iranica B*, **20**, 1, 109-119
2. BATIFOL C., ZIELINSKI T.G., ICHCHOU M.N., GALLAND M.-A., 2007, A finite-element study of a piezoelectric/poroelastic sound package concept, *Smart Materials and Structures*, **16**, 168-177
3. BOWEN C.R., PERRY A., LEWIS A.C.F., KARA H., 2004, Processing and properties of porous piezoelectric materials with high hydrostatic figures of merit, *Journal of the European Ceramic Society*, **24**, 541-545
4. CIARLETTA M., SCARPETTA E., 1996, Some result on thermoelasticity for porous piezoelectric materials, *Mechanics Research Communications*, **23**, 1, 1-10
5. DING H.J., WANG H.M., CHEN W.Q., 2004, Analytical solution of a special non-homogeneous pyroelectric hollow cylinder for piezothermoelastic axisymmetric plane strain dynamic problems, *Applied Mathematics and Computation* **151**, 423-441
6. HETNARSKI R.B., ESLAMI M.R., 2009, *Thermal Stresses – Advanced Theory and Applications*, Library of Congress Control No. 936149
7. IVANOV P.V., EREMkin V.V., SMOTRAKOV V.G., TSIKHOTSKII E.S., 2002, Porous piezoelectric ceramics: materials for ultrasonic flaw detection and medical diagnostics, *Inorganic Materials*, **38**, 4, 408-410
8. JABBARI M., MESHKINI M., ESLAMI M.R., 2012, Nonaxisymmetric mechanical and thermal stresses in FGPPM hollow cylinder, *Journal of Pressure Vessel Technology*, **134**, 061212-1

9. JABBARI M., MESHKINI M., ESLAMI M.R., 2016, Mechanical and thermal stresses in FGPPM hollow cylinder due to radially symmetric loads, *Journal of Pressure Vessel Technology*, **138**, 011207-1
10. LI J.-F., TAKAGI K., ONO M., PAN W., WATANABE R., 2003, Fabrication and evaluation of porous piezoelectric ceramics and porosity-graded piezoelectric actuators, *Journal of the European Ceramic Society*, **86**, 1094-1098
11. MESHKINI M., FIROOZBAKHS K., JABBARI M., SELKGHAFARI A., 2017, Asymmetric mechanical and thermal stresses in 2D-FGPPMs hollow cylinder, *Journal of Thermal Stresses*, **40**, 4, 448-469
12. TOPOLOV V.Y., TURIK A.V., 2001, Porous piezoelectric composites with extremely high reception, *Technical Physics*, **46**, 9, 1093-1100
13. ZENG T., DONG X.L., CHEN S.T., YANG H., 2007, Processing and piezoelectric properties of porous PZT ceramics, *Ceramics International*, **33**, 395-399
14. ZIELINSKI T.G., 2010, Fundamentals of multi physics modeling of piezoporous-elastic structures, *Archives of Mechanics*, **62**, 5, 343-378

Manuscript received January 4, 2017; accepted for print July 25, 2017

A NEW METHOD FOR AUTOMATIC DEFECTS DETECTION AND DIAGNOSIS IN ROLLING ELEMENT BEARINGS USING WALD TEST

AMMAR CHITER, RABAH ZEGADI, RAIS EL'HADI BEKKA, AHMED FELKAOUI

*Applied Precision Mechanics Laboratory, Institute of Optics and Precision Mechanics, Ferhat Abbas University of Setif 1,
Setif, Algeria; e-mail: chiter.ammam@gmail.com*

To detect and to diagnose, the localized defect in rolling bearings, a statistical model based on the sequential Wald test is established to generate a “hypothetical” signal which takes the state zero in absence of the defect, and the state one if a peak of resonance caused by the defect in the bearing is present. The autocorrelation of this signal allows one to reveal the periodicity of the defect and, consequently, one can establish the diagnosis by comparing the frequency of the defect with the characteristic frequencies of the bearing. The originality of this work is the use of the Wald test in the signal processing domain. Secondly, this method permits the detection without considering the level of noise and the number of observations, it can be used as a support for the Fast Fourier Transform. Finally, the simulated and experimental signals are used to show the efficiency of this method based on the Wald test.

Keywords: diagnosis, detection, rolling element bearing, defect, Wald sequential test

1. Introduction

In the industry, a great attention has been given to monitoring conditions and maintenance for the purpose to improve the quality of production. Edwards *et al.* (1998) and Tandon and Choudhury (1999) showed the importance of maintenance as the best way to avoid maintenance problems that are often very expensive. And also how the predictive maintenance techniques have evolved to keep a check of mechanical health by generating information on the machine condition. In rotating machines, the transmission elements: belts, gears and bearings are of major interest in industrial maintenance as the operation of a mechanical system heavily depends on health of these elements. Particularly, the rolling bearing is one of the most critical components that determine machinery health and its remaining life time in modern production machinery (Jayaswal *et al.*, 2008). Robust Predictive Health Monitoring tools are needed to guarantee the healthy state of rolling bearings during the operation. A predictive health monitoring tool indicates upcoming failures which provide sufficient lead time for maintenance planning, as showed by El-Thalji and Jantunen (2015), Mann *et al.* (1995) and Renwick and Babson (1985).

Over the past two decades, several methods have been the subject of studies and developments. Visibly noticed are revolution methods based on mechanical signal processing, which are divided into two main categories, detection and diagnosis, and are based on time-frequency methods and temporal methods or a combination of both. Thus, many methods are born, the scalar indicators such as kurtosis, skew, crest factor (Dron *et al.*, 2004; Pachaud *et al.*, 1997), demodulation and detection of the envelope (Sheen, 2004, 2008), amplitude modulation (Stack *et al.*, 2004), detection of vibration modes (Rizos *et al.*, 1990), de-noising vibratory signals (Bo-laers *et al.*, 2004), the spectral density analysis (Krejcar and Frischer, 2011), the Fast Fourier Transform (Lenort, 1995), the statistical model based on hypothesis test as KS-test Kolmogorov and Smirnov (Kar and Mohanty, 2004; Dong *et al.*, 2011; Yang *et al.*, 2005), scalar and vector statistical time series methods (Kopsaftopoulos and Fassois, 2011), neural networks (Samanta

and Al-Balushi, 2003), wavelets (Bendjama and Boucherit, 2016), blind source separation (Wang *et al.*, 2014), fuzzy logic (Liu *et al.*, 1996). El-Thalji and Jantunen (2015) and Rai and Upadhyay (2016) reviewed almost all the techniques used in the domain predicting defects.

Typical defects in bearings are localized defects that occur generally in form of tiredness cracking under cyclic pressure of contact (El-Thalji and Jantunen, 2015; Fajdiga and Sraml, 2009; Glaeser and Shaffer, 1996; Ismail *et al.*, 1990; Tauqir *et al.*, 2000). Thus, the detection of cracking is frequently based on detection of the attack. During an abnormal operation, a series of wide band impulses will be generated when the rolling element of the bearing (ball or roller) (Brie, 2000; Ou *et al.*, 2016) goes above the defect at a frequency determined by the shaft speed, geometry of the bearing and the site of the defect (Barkov, 1999; Dyer and Stewart, 1978; Feng *et al.*, 2016; Ma and Li, 1995; Tandon and Choudhury, 1999). The site of the defect depending on the characteristic frequencies gives the possibility of detecting the presence of the defect and performing the diagnosis of the defective part.

The difficulty of detection of localized defects (Niu *et al.*, 2015) is related to the bearing energy which will diffuse through a wide band of frequency and hence it can be easily immersed in the noise (Ma and Li, 1995; Van *et al.*, 2016). Thus, under various operating regimes (varying loads and speeds), many methods remain inefficient for the prediction (El-Thalji and Jantunen, 2015), because it may happen that an excited resonance mode at the beginning of the attack may not be excited later when the defect has developed (Ma and Li, 1995; Mikhlin and Mytrokhin, 2008). In this paper, and to refer on the sequential analysis developed by Wald in the 1940s (Schneeweiss, 2005; Wald, 1943, 1945, 1947, 1949; Wald and Wolfowitz, 1943, 1948), a composite hypothesis test is used for the detection and diagnosis of localized defects in rolling bearings. To this end, it is necessary to be provided with a significant and exact variance without any need to estimate when the resonances modes occur.

2. Problem position

2.1. Probability Density Function (PDF) of vibrations of rolling bearings

To characterize vibration of rolling bearings, which is supposed to be a stationary stochastic process, and the PDF can describe the percentage in time when the signal reaches a given amplitude x . For the given amplitude, the PDF is estimated by

$$P(x) = \lim_{\Delta x \rightarrow 0} \frac{P_r \{x \leq x(t) \leq x + \Delta x\}}{\Delta x} = \lim_{\Delta x \rightarrow 0} \frac{1}{\Delta x} \sum_{i=1}^j \frac{\Delta t_i}{T} \quad (2.1)$$

where T is the total time of observation and Δt_i is the i -th duration while $x(t)$ is inside the interval $[x, x + \Delta x]$. For vibration without a defect, which represents healthy functioning, the distribution of the amplitude can be considered as a Gaussian process. This vibratory signature will have a well-defined variance σ_0^2 which is different from the variance σ_1^2 of a signal with a localized fault (Fig. 1) and, consequently, the overall vibration of the bearing will be constituted by two alternately periodic parts with different variances (Ma and Li, 1995).

2.2. Sequential Probability Test (SPRT)

Introduce now the sequential probability test (SPRT) of a simple null hypothesis H_0 which indicates the good operating condition and a simple alternative hypothesis H_1 which indicates the presence of a defect, based on N independent observations x_1, x_2, \dots, x_N having a common probability density function developed by Wald (1945, 1949) and Weiss (1956).

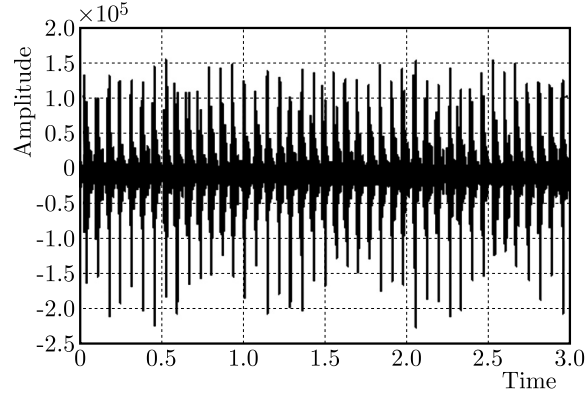


Fig. 1. Real signal of the rolling bearing with a defect

The hypotheses are

$$\begin{aligned} H_0 : \quad P(\mathbf{x}/H_0) &= \frac{1}{\sqrt{(2\pi)^N \sigma_0^N}} \exp \left(- \sum_{i=1}^N \frac{x_i^2}{2\sigma_0^2} \right) \\ H_1 : \quad P(\mathbf{x}/H_1) &= \frac{1}{\sqrt{(2\pi)^N \sigma_1^N}} \exp \left(- \sum_{i=1}^N \frac{x_i^2}{2\sigma_1^2} \right) \end{aligned} \quad (2.2)$$

where $\mathbf{x} = [x_1, x_2, \dots, x_N]$ and σ_i^2 are the variances with $\sigma_0^2 < \sigma_1^2$.

For the analysis of any vibratory signal, certainly one of the two variances will be retained outside the test hypothesis H_1 and one will have information whether or not it occurs with one of the characteristic frequencies of the rolling bearings (inner race, outer race, ball and cage). In the case of healthy rolling bearings, during a time Δt for the signal $x(t)$, all measurements of M observations will have a Gaussian distribution given by relation (2.2)₁. In the case of a defective bearing given by (2.2)₂ and by varying the number M of observations in the time Δt , and as soon as M is sufficiently large, and it is always possible to calculate the estimated variance σ_1^2 of the acquired vibratory signal with the defect in the rolling bearing. The variances σ_0^2 for healthy rolling bearings could be calculated by

$$\sigma_0^2 = \frac{1}{M} \sum_{i=1}^M x_i^2 \quad (2.3)$$

and $\sigma_1^2 = M^{-1} \sum_{i=1}^M x_i^2$ is considered as an estimated variance of the defect signal. Such an estimate will lead to a test for probability of both detection or false alarm (Ma and Li, 1995).

3. Sequential test

3.1. The likelihood ratio test with simple choice

The likelihood ratio test (PRT) of the σ_1^2 measurement could then be expressed as follows (Ma and Li, 1995; Paulson, 1947)

$$\begin{cases} \text{if} & \xi(\mathbf{x}) > \mu & \text{choose } H_1 \\ \text{if} & \xi(\mathbf{x}) < \mu & \text{choose } H_0 \end{cases} \quad (3.1)$$

where $\xi(\mathbf{x})$ is the likelihood ratio, which is defined by

$$\xi(\mathbf{x}) = \frac{P(\mathbf{x}/H_1)}{P(\mathbf{x}/H_0)} = \frac{\sigma_1^N}{\sigma_0^N} \exp \left(\frac{\sigma_1^2 - \sigma_0^2}{2\sigma_0^2\sigma_1^2} \sum_{i=1}^N x_i^2 \right) \quad (3.2)$$

By taking the natural logarithm of the two parts, the test can be simplified into

$$\begin{cases} \text{if} & f(\mathbf{x}) > \gamma & \text{choose } H_1 \\ \text{if} & f(\mathbf{x}) < \gamma & \text{choose } H_0 \end{cases} \quad (3.3)$$

where

$$f(\mathbf{x}) = \sum_{i=1}^N x_i^2 \quad \gamma = \frac{2\sigma_0^2\sigma_1^2}{\sigma_1^2 - \sigma_0^2} \ln\left(\frac{\sigma_1^N}{\sigma_0^N} \mu\right) \quad (3.4)$$

Then probability P_f of the false alarm and the detection probability P_d of the PRT are

$$\begin{aligned} P_f &= P(f(\mathbf{x}) > \gamma/H_0) = P\left(\sum x_i^2 > \gamma/H_0\right) = \int_{\sum x_i^2 > \gamma} P(\mathbf{x}/H_0) d\mathbf{x} \\ P_d &= P(f(\mathbf{x}) > \gamma/H_1) = P\left(\sum x_i^2 > \gamma/H_1\right) = \int_{\sum x_i^2 > \gamma} P(\mathbf{x}/H_1) d\mathbf{x} \end{aligned} \quad (3.5)$$

From equations (2.2) and (3.5)₁, the P_f is a decreasing monotone function of the parameter γ .

Integration of equations (3.5) leads to

$$P_f = \exp\left(\frac{-\gamma}{2\sigma_0^2}\right) \quad P_d = \exp\left(\frac{-\gamma}{2\sigma_1^2}\right) \quad (3.6)$$

where σ_0^2 is the variance measured during healthy operation, σ_1^2 –variance measured during unspecified operation and γ – the threshold of the test determined by

$$\gamma = -2\sigma_0^2 \ln P_f \quad (3.7)$$

while combining P_d with P_f we will have

$$P_d = P_f^{\frac{\sigma_0^2}{\sigma_1^2}} \quad (3.8)$$

Using equation (3.5)₁ to determine the probability of the false alarm P_f which corresponds to threshold equation (3.7) on the one hand and, on the other, using this same threshold will give the maximum probability of detection P_d defined by equation (3.5)₂ related to the variance σ_1^2 which is an unknown parameter estimated in one duration of the previously signal fixed. It can be deduced that the uniformly most powerful test (UMP) exists in the sense of Neyman-Pearson criterion which maximizes P_d (3.8) for a given P_f because the optimal probability rate test (PRT) (3.3) for each $\sigma_1^2 > \sigma_0^2$ could be completely defined apart from the knowledge of the true variance σ_1^2 of the signal defect. Finally, the UMP test is defined by system (3.3) and is constructed by equations (3.1), (3.2) with a determined γ by the pre-established false alarm probability α , where α is the threshold of significance

$$P_f(\gamma) = \alpha \quad (3.9)$$

3.2. Wald sequential test

Contrarily to the classical test (test with a simple choice), one is not obliged to make a choice between the two hypotheses H_0 and H_1 , consequently, one deals with another type of test. If the size of observations is fixed, the construction of the test leads to the sharing of possible values

of the statistical domain in three regions (Wald, 1945; Berger and Wald, 1949; Wolfowitz, 1949; Sobel and Wald, 1949)

$$\Psi^{(n)} = \Psi(x_1, x_2, \dots, x_n) \quad (3.10)$$

that is the region of probable values and the region of improbable values (knowing that the basic hypothesis H_0 is true). If a given value of $\Psi(x_1, x_2, \dots, x_n)$ falls into the region of improbable values, the basic hypothesis is rejected. The sequential test, that is, the test based on a sequential procedure of observation, is built up as follows. For each value of

$$\nu = 1, 2, \dots, n, n+1 \quad (3.11)$$

the domain Γ_ν of possible values of the critical statistics $\Psi(x_1, x_2, \dots, x_n)$ is divided into three disjointed regions: $\Gamma_\nu^{H_0}$ – region of probable values, $\Gamma_\nu^{H_1}$ – region of improbable values and Γ_ν^* – region of doubtful values (knowing that H_0 is true)

$$\Gamma_\nu = \Gamma_\nu^{H_0} \cup \Gamma_\nu^{H_1} \cup \Gamma_\nu^* \quad (3.12)$$

where $\nu = 1, 2, \dots$ with each step ν of the sequential procedure of observation. After having recorded the observations x_1, \dots, x_ν , $\nu = 1, 2, \dots$ one makes a decision relying on the following rule which defines the Wald test: if $\Psi(x_1, x_2, \dots, x_n) \in \Gamma_\nu^{H_0}$ one accepts H_0 ; if $\Psi(x_1, x_2, \dots, x_n) \in \Gamma_\nu^{H_1}$ one accepts H_1 and if $\Psi(x_1, x_2, \dots, x_n) \in \Gamma_\nu^*$ the problem remains open until the ν -th observation. For this reason, the region Γ_ν^* is called the region of indetermination or the region of the observation pursuit.

For the establishment of the Wald test of probability, one considers two simple hypotheses of the following form, see Wald (1945, 1947) and Wald and Wolfowitz (1948)

$$\begin{aligned} H_0 & \quad \text{The observation is extracted from a density population } f(x, \theta_0) \\ H_1 & \quad \text{The observation is extracted from a density population } f(x, \theta_1) \end{aligned} \quad (3.13)$$

The critical statistics of this test is defined by the relation (Wald, 1945, 1947; Paulson, 1947)

$$\Psi^{(\nu)} = \ln \frac{f(x_1, \theta_1) \cdots f(x_i, \theta_1)}{f(x_1, \theta_0) \cdots f(x_i, \theta_0)} = \sum_{i=1}^{\nu} \ln \frac{f(x_i, \theta_1)}{f(x_i, \theta_0)} \quad (3.14)$$

where: $f(x_i, \theta_0) = P(\mathbf{x}/H_0)$ with $\theta_0 = \sigma_0^2$ and $f(x_i, \theta_1) = P(\mathbf{x}/H_1)$ with $\theta_1 = \sigma_1^2$.

$P(\mathbf{x}/H_0)$ and $P(\mathbf{x}/H_1)$ could be drawn from equation (2.2). So, one establishing the likelihood ratio, the critical statistics would be expressed as follows

$$\Psi^{(\nu)} = \ln \left\{ \left[\frac{\exp\left(-\frac{1}{2\sigma_1^2} \sum_{i=1}^{\nu} x_i^2\right)}{\sqrt{(2\pi)^\nu \sigma_1^\nu}} \right] \middle/ \left[\frac{\exp\left(-\frac{1}{2\sigma_0^2} \sum_{i=1}^{\nu} x_i^2\right)}{\sqrt{(2\pi)^\nu \sigma_0^\nu}} \right] \right\} \quad (3.15)$$

After simplification of equation (3.15) and arrangement of the logarithmic term, one gets

$$\Psi^{(\nu)} = \frac{\sigma_1^2 - \sigma_0^2}{2\sigma_0^2\sigma_1^2} \sum_{i=1}^{\nu} x_i^2 + \frac{\nu}{2} \ln \frac{\sigma_1^2}{\sigma_0^2} \quad (3.16)$$

The three regions are defined roughly by relations (3.11), (3.12), (3.13) and (3.16) that define the completely Wald test (WT) (Aivazian, 1986; Wald, 1947; Weiss, 1956)

$$\begin{aligned} \Gamma_\nu^{H_0} &= \left\{ \Psi : \Psi^{(\nu)} \leq \ln \frac{\beta}{1-\alpha} \right\} & \Gamma_\nu^{H_1} &= \left\{ \Psi : \Psi^{(\nu)} \leq \ln \frac{1-\beta}{\alpha} \right\} \\ \Gamma_\nu^* &= \left\{ \Psi : \ln \frac{\beta}{1-\alpha} \leq \Psi^{(\nu)} \leq \ln \frac{1-\beta}{\alpha} \right\} \end{aligned} \quad (3.17)$$

Wald test (3.17) is more optimal than all tests between hypotheses (3.13) with risks of the first and second species lower than the respective given values α and β .

Values of α and β (Aivazian, 1986) are: 0.1, 0.05, 0.025, 0.01, 0.005, 0.001, 0.002.

4. Rolling element bearings defects detection

4.1. Detection procedure

The detection procedure is divided into many steps which can be stated as follows:

- 1 – Take the discrete vibration for M samples, which is larger than the amount of the characteristic period of the defect.
- 2 – Select a window of size N for the test.
- 3 – Estimate the variance σ_0^2 by using equation (2.3).
- 4 – Suggest a choice of α and β .
- 5 – Position the window at the beginning of recording of the vibration.
- 6 – Compute $\Psi^{(N)}$ by using equation (3.16).
- 7 – Define the intervals of the three regions by the terminals $a = \ln[\beta/(1 - \alpha)]$ and $b = \ln[(1 - \beta)/\alpha]$.
- 8 – Make the test by using equation (3.17).
- 9 – Generate a hypothetical signal defined by

$$h(i) = \begin{cases} 0 & \text{if } H_0 \text{ is true } (\Psi \leq a) \\ 1 & \text{if } H_1 \text{ is true } (\Psi \geq b) \end{cases}$$

If $a \leq \Psi \leq b$, carry on with pursue for data opening another window (here, one does not make a decision but only increases the size of the window).

- 10 – After generation of the hypothetical signal, if a defect is present, there will be a data vector composed of two values 0 and 1. If 1, then appears periodically with a period of the characteristic frequency of the bearing and is considered defective.
- 11 – To compare the detected frequency with the main characteristic frequencies of the rolling bearings, it would be very easy to locate the defect so the diagnosis could be established by comparing the multiple of this frequency detected with that of the most well-known defects.

4.2. Test plan

Based on the detection procedure described in Section 4.1, a test plan can be established which is shown by the procedure diagram shown in Fig. 2. So that the experiment is valid, one chooses N as a small fraction of the characteristic period of the defect, that is to say one fifth (Ma and Li, 1995). By examining step 10 in the detection procedure in Section 4.1 (to show if there is periodicity), one uses autocorrelation of the signal, a peak in the autocorrelation function reveals the periodicity of the signal, and the value of the time of this peak will give the period of the defect T_d . Consequently, one can determine the frequency of the defect f_d , and comparing it with the characteristic frequency f_c , one can establish the diagnosis.

5. Validation of the model by simulated and experimental signals

5.1. Validation of the model by simulated signals

5.1.1. Generation of the simulated signals

To simulate the defect, a bearing of the type NJ2204ECP has been used. The shaft speed is $n = 1500$ rpm, the characteristic frequencies are determined by the relations from Appendix A1,

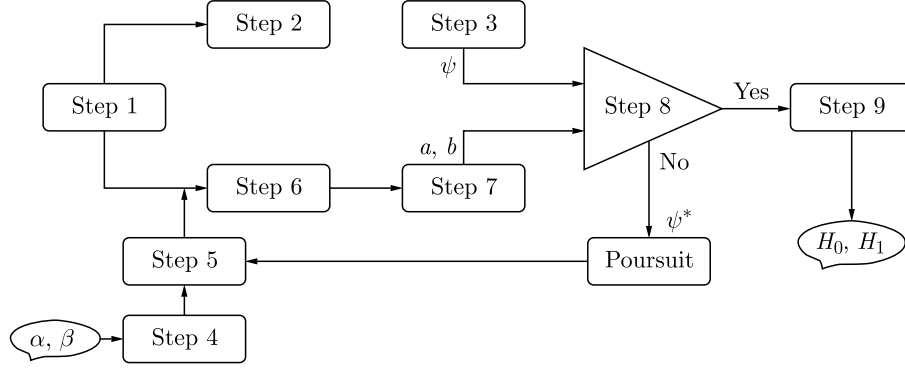


Fig. 2. Test plan

where the frequency of the cage is: $f_{cage} = 0.39fr$ (9.74 Hz), the frequency of the outer race: $f_{or} = 0.39Zfr$ (87.68 Hz), the frequency of the inner race $f_{ir} = 0.61Zfr$ (137.32 Hz), and the frequency of the ball: $f_{re} = 4.754fr$ (118.85 Hz); where: $fr = 25$ Hz, Z is the number of balls. For NJ2204ECP: $Z = 9$, $d = 7.5$ mm, $D = 34$ mm, $\alpha = 0$. The reference signal (Fig. 3a) is taken as a sinusoid of frequency 25 Hz, amplitude equal to unit and a null phase. The simulated defect signal (Fig. 3b) is considered as the sum of a sinusoid of frequency 25 Hz, amplitude equal to unit and the null phase, a sinusoid of frequency 87 Hz of amplitude 10 times the unit (representing a defect of frequency 87 Hz, which corresponds to the frequency of the outer race, as one can use the function `pulstran` available in Matlab which generates a series of impulses), and a Gaussian white noise centered with variance equal to 1 generated by the function “`randn`” available in Matlab with a signal noise ratio $SNR = 20$ dB. The thresholds of significances are fixed at $\alpha = 0.05$ and $\beta = 0.002$.

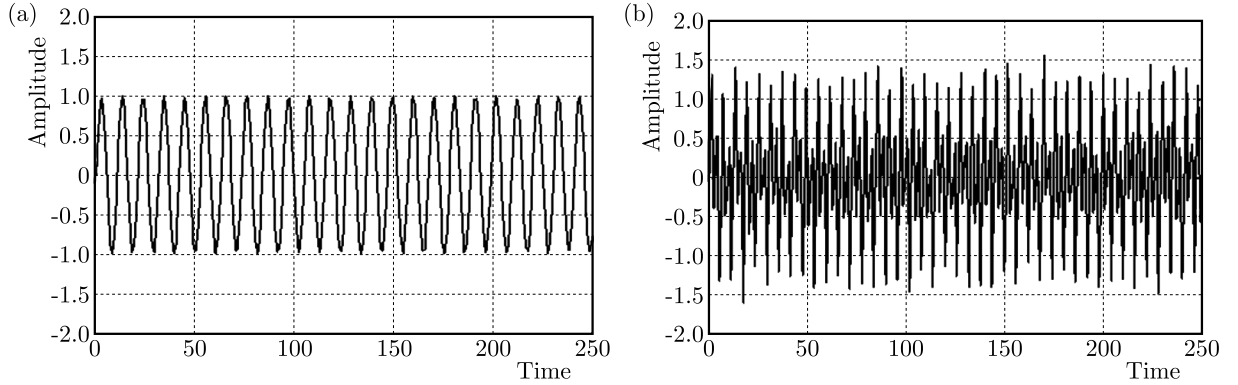


Fig. 3. (a) Reference signal, (b) defect signal

5.1.2. Interpretation

One can say that periodicity of a hypothetical signal (h -signal, Fig. 4a) appeared in the function of autocorrelation (Fig. 4b) reveals the existence of a defect. To determine its frequency, one carries out Fourier fast transform (FFT) of the hypothetical signal, which reveals visually the frequency of the defect (87 Hz) which corresponds indeed to the characteristic frequency of the outer race (Fig. 4c). Consequently, one can affirm that the plan suggested for detection and diagnosis of the defect in the bearing has succeeded and to made diagnosis of the defective part. During healthy running, the hypothetical signal will be zero, the autocorrelation of the h -signal will not reveal any periodicity, and the FFT will confirm the absence of the defect.

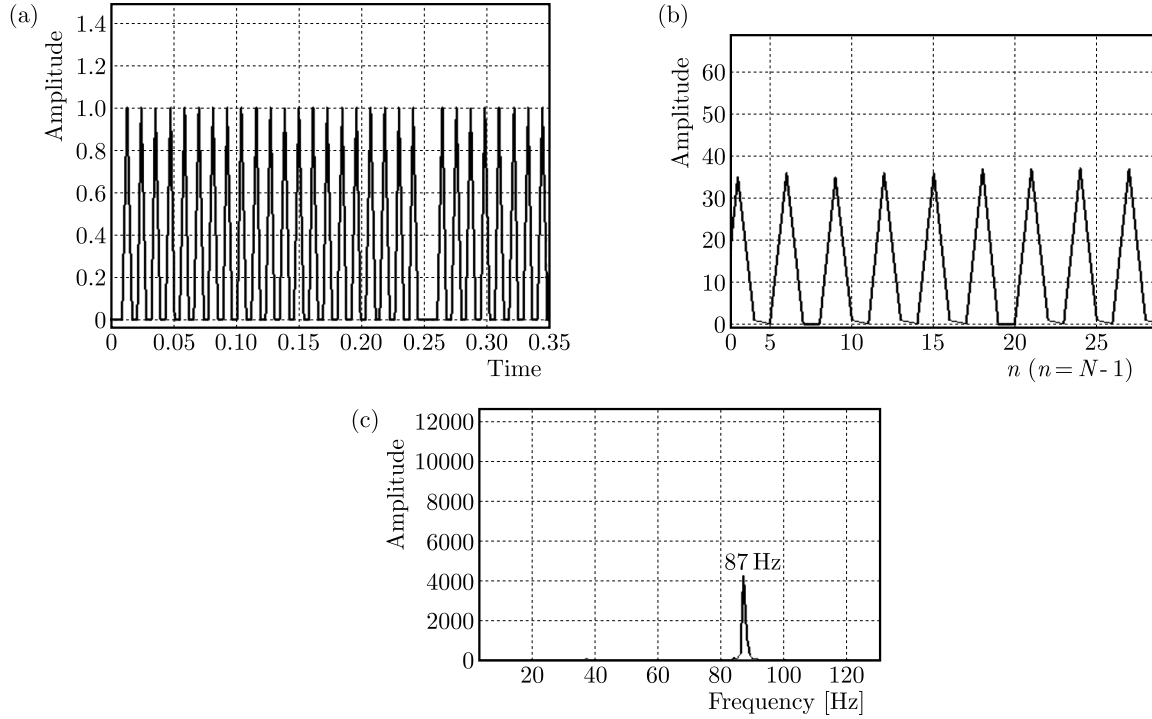


Fig. 4. (a) Hypothetical signal, (b) autocorrelation of hypothetical signal, (c) FFT of hypothetical signal

5.2. Validation of the model by experimental signals

5.2.1. Generation of the experimental signals

The test stand consists of a reinforced concrete frame, isolated from the ground by shock-absorbing studs. Two rows of shafts each having diameter of 60 mm and length of 680 mm are mounted in an open loop and fixed to the chassis by four rolling bearings with an average stiffness of $3 \cdot 10^7$ daN/m as shown in Fig. 5.

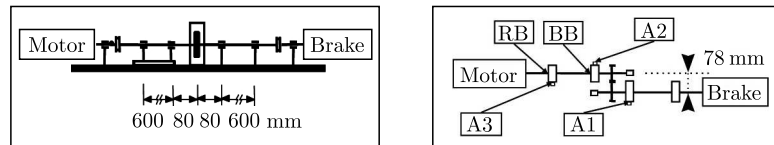


Fig. 5. Architecture of the teststand (RB – roller bearing, BB – ball bearing)

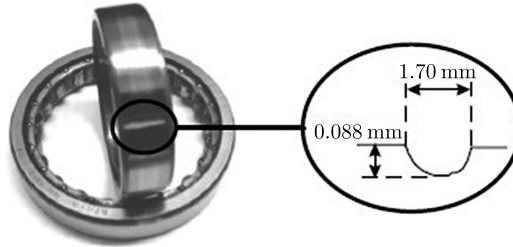
The bearings in the vicinity of the test gear pair have ball bearings of the type 6012, while the outer bearings are roller bearings of the type NU1013. The shaft lines are connected in rotation by test gears. The applied speed and torque are measured by an electronic device composed of a motor and a brake.

The dynamic behavior of the system can be studied using measurements of the acceleration, transmission error and noise. The accelerations are measured using piezoelectric accelerometers ENDEVCO 224C whose resonance frequency is 32 kHz. The accelerometers are mounted by gluing small duralumin pellets onto the accelerometers which are screwed. The tests are carried out on a spur gear with helical teeth. The gear ratio is 36/38 with modulus $m = 2$. The geometric characteristics of the ball and roller bearing are given in Table 1.

Type of defect: To simulate the scaling on the bearings, a notch of 1.7 mm and depth of 0.088 mm is made using a fine grinder as shown in Fig. 6. The roller bearing is removable without “NU type” destruction or specialized tooling.

Table 1. Geometric characteristics of the ball and roller bearing

Geometric characteristics	Ball bearing	Roller bearing
Middle diameter to center of balls D [mm]	77.7	80.55
Diameter of ball d [mm]	9	7
Number of balls Z	14	21
Angle of contact α	0	0

**Fig. 6.** Defective inner race geometry of the roller bearing

Monitoring conditions: The applied load is equal to 12 daN m and 4300 rpm speed test. The characteristic frequencies of the ball bearing and the roller bearing are calculated by the geometrical formulas given in Appendix A1.

Table 2. Characteristic frequencies of the ball and roller bearings

Bearing type	F_r [Hz]	F_{cage} [Hz]	F_{or} [Hz]	F_{ir} [Hz]	F_{er} [Hz]
6012	71.67	31.68	443.56	559.77	627.02
NU1013	71.67	32.72	687.11	817.89	830.91

F_r – rotating frequency, F_{cage} – frequency of the cage,

F_{or} – frequency of the outer race, F_{ir} – frequency of the inner race,

F_{er} – frequency of the ball or roller

Experimental signals: The acquired reference signal and the acquired signal defect are shown in Fig. 7a and 7b.

5.2.2. Interpretation

The detection and diagnostic plan applied to the experimental signals shown in Fig. 7a and Fig. 7b is able to detect the fault frequency applied to the bearing inner ring shown in Fig. 8a. It shows the presence of state “1” of the hypothetical signal and Fig. 8b shows a frequency of 814 Hz very close to the fault frequency which is equal to 817.89 Hz. It indicates that the plan has reacted well in establishing a correct diagnosis.

6. Diagnosis plan

To establish a good diagnosis of defects, it is necessary to know a significant number of defects. Thus, by comparing the frequency detected by the Wald test presented before with the characteristic frequencies we can locate the defect. By comparing the defect frequency with the main defects of the rolling bearings (Barkov, 1999), we can establish the diagnosis by using the frequency of modulation presented in the work of Barkov (1999). For the plan suggested by Fig. 2 it is possible to establish the diagnosis of the bearing defective part and its nature.

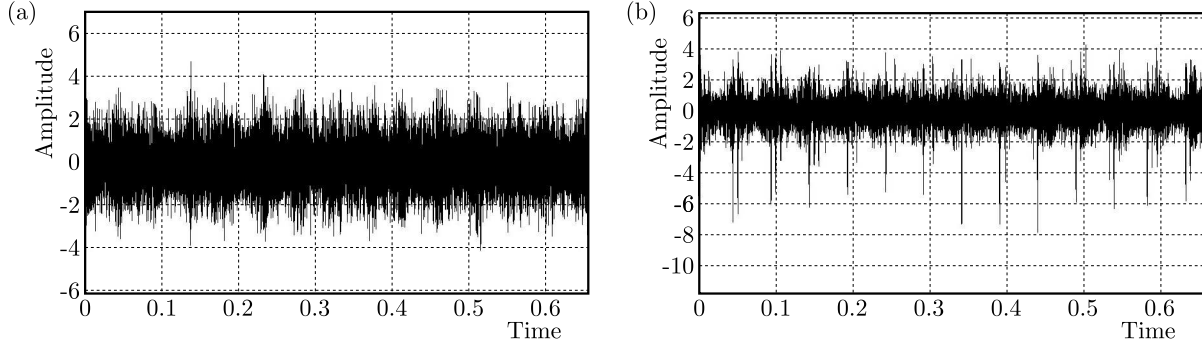


Fig. 7. (a) Experimental reference signal, (b) experimental defect signal

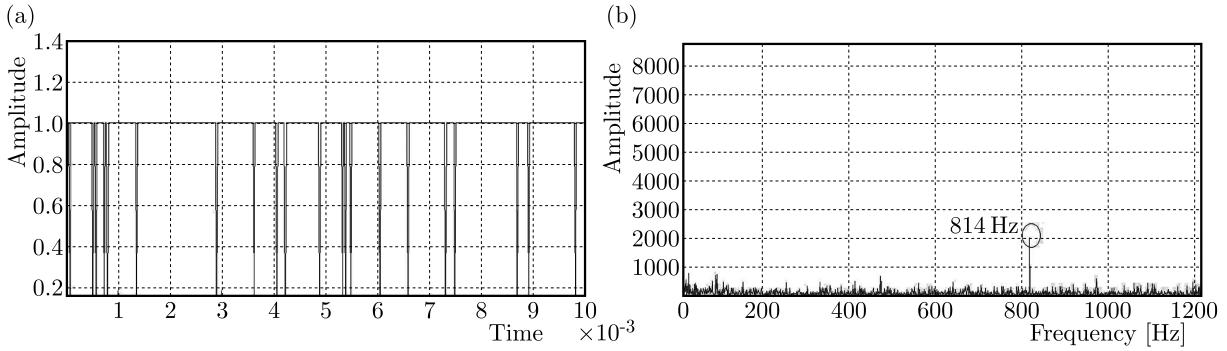


Fig. 8. (a) Experimental hypothetical signal, (b) FFT of the experimental hypothetical signal

7. Conclusion

The detection and diagnosis plan based on the Wald test is described. This plan can be applied to measurements of the bearings vibration signals with and without defects under various loads and speeds. The effectiveness of the suggested detection plan is illustrated in Fig. 4 for the simulated signal and in Fig. 8 for the experimental signal. The plan works very well with vibratory signals of wide bands. Finally, the plan is very promising for automatic detection and diagnostic applications.

Acknowledgment

I address all my gratitude to the Dynamics and Control of Structure team of the Contacts and Structures Mechanics Laboratory (LaMCoS), research unit (UMR5259) of INSA Lyon France and CNRS (INSIS, Institute of Engineering Sciences and Systems) for providing me with the experimental signals realized on their own test stands and, particularly, Associate Professor Mahfoud Jarir, also the director of LaMCoS laboratory.

Appendix 1

Characteristic frequencies of the bearing (Barkov, 1999):

— frequency of the cage

$$f_{cage} = \frac{f_r}{2} \left(1 - \frac{d}{D} \cos \alpha \right)$$

— frequency of the outer race

$$f_{or} = Z \frac{f_r}{2} \left(1 - \frac{d}{D} \cos \alpha \right)$$

— frequency of the inner race

$$f_{ir} = Z \frac{f_r}{2} \left(1 + \frac{d}{D} \cos \alpha \right)$$

— frequency of the ball

$$f_{re} = f_r \frac{d}{D} \left[1 + \left(\frac{D}{d} \right)^2 \cos \alpha \right]$$

where α is the angle of contact, d [mm] – diameter of the ball, D [mm] – middle distance to the center of balls, Z – number of balls, f_r [Hz] – rotating frequency ($f_r = n/60$), n [rpm] – shaft speed.

References

1. AÏVAZIAN S., ÉNUKOV I., MÉCHALKINE, 1986, *Modeling Element and Primary Data Processing* (in French), Mir Moscou
2. BARKOV A.V., BARKOVA N.A., YUDIN I.A., ROGOV S.N., 1999, *The Peculiarities of Rolling Element Bearing Vibroacoustic Diagnostics for Transportation Applications*, Vibrotek
3. BENDJAMA H., BOUCHERIT M.S., 2016, Wavelets and principal component analysis method for vibration monitoring of rotating machinery, *Journal of Theoretical and Applied Mechanics*, **54**, 2, 659-670
4. BERGER A., WALD A., 1949, On distinct hypotheses, *The Annals of Mathematical Statistics*, **20**, 1, 104-109
5. BOLAERS F., COUSINARD O., MARCONNET P., RASOLOFONDRAIBE L., 2004, Advanced detection of rolling bearing spalling from de-noising vibratory signals, *Control Engineering Practice*, **12**, 181-190
6. BRIE D., 2000, Modelling of the spalled rolling element bearing vibration signal : An overview and some results, *Mechanical Systems and Signal Processing*, **14**, 3, 353-369
7. DONG Y., LIAO M., ZHANG X., WANG F., 2011, Faults diagnosis of rolling element bearings based on modified morphological method, *Mechanical Systems and Signal Processing*, **25**, 1276-1286
8. DRON J.P., BOLAERS F., RASOLOFONDRAIBE L., 2004, Improvement of the sensitivity of the scalar indicators (crest factor, kurtosis) using a de-noising method by spectral subtraction: application to the detection of defects in ball bearings, *Journal of Sound and Vibration*, **270**, 270, 61-73
9. DYER D., STEWART R.M., 1978, Detection of rolling element bearing damage by statistical vibration analysis, *Journal of Mechanical Design*, **100**, 229
10. EDWARDS D.J., HOLT G.D., HARRIS F.C., 1998, Predictive maintenance techniques and their relevance to construction plant, *Journal of Quality in Maintenance Engineering*, **4**, 1, 25-37
11. EL-THALJI I., JANTUNEN E., 2015, A summary of fault modelling and predictive health monitoring of rolling element bearings, *Mechanical Systems and Signal Processing*, **60-61**, 252-272
12. FAJDIGA G., SRAML M., 2009, Fatigue crack initiation and propagation under cyclic contact loading, *Engineering Fracture Mechanics*, **76**, 1320-1335
13. FENG Z., MA H., ZUO M.J., 2016, Vibration signal models for fault diagnosis of planet bearings, *Journal of Sound and Vibration*, **370**, 372-393
14. GLAESER W.A., SHAFFER S.J., 1996, Contact fatigue, *ASM Handbook, Fatigue and Fracture*, **19**, 331-336
15. ISMAIL F., IBRAHIM A., MARTIN H.R., 1990, Identification of fatigue cracks from vibration testing, *Journal of Sound and Vibration*, **140**, 2, 305-317

16. JAYASWAL P., WADHWANI A.K., MULCHANDANI K.B., 2008, Machine fault signature analysis, *International Journal of Rotating Machinery*, DOI: 10.1155/2008/583982
17. KAR C., MOHANTY A.R., 2004, Application of KS test in ball bearing fault diagnosis, *Journal of Sound and Vibration*, **269**, 439-454
18. KOPSAFTOPOULOS F.P., FASSOIS S.D., 2011, Scalar and vector time series methods for vibration based damage diagnosis in a scale aircraft skeleton structure, *Journal of Theoretical and Applied Mechanics*, **49**, 3, 727-756
19. KREJCAR O., FRISCHER R., 2011, Non destructive defect detection by spectral density analysis, *Sensors*, **11**, 2334-2346
20. LENORT F., 1995, A Fast Discrete Fourier Transform with unequally-spaced frequencies, *Journal of Theoretical and Applied Mechanics*, **33**, 1, 73-81
21. LIU T.I., SINGONAHALLI J.H., IYER N.R., 1996, Detection of roller bearing defects using expert system and fuzzy logic, *Mechanical Systems and Signal Processing*, **10**, 5, 595-614
22. MA J., LI J.C., 1995, Detection of localised defects in rolling element bearing via composite hypothesis test, *Mechanical Systems and Signal Processing*, **9**, 1, 63-75
23. MANN JR L., SAXENA A., KNAPP G.M., 1995, Statistical-based or condition-based preventive maintenance, *Journal of Quality in Maintenance Engineering*, **1**, 46-59
24. MIKHLIN Y., MYTROKHIN S., 2008, Non linear vibration modes of the tracked road vehicle, *Journal of Theoretical and Applied Mechanics*, **46**, 3, 581-596
25. NIU L., CAO H., HE Z., LI Y., 2015, A systematic study of ball passing frequencies based on dynamic modeling of rolling ball bearings with localized surface defects, *Journal of Sound and Vibration*, **357**, 207-232
26. OU L., YU D., YANG H., 2016, A new rolling bearing fault diagnosis method based on GFT impulse component extraction, *Mechanical Systems and Signal Processing*, **81**, 162-182
27. PACHAUD C., SALVETAT R., FRAY C., 1997, Crest factor and kurtosis contributions to identify defects inducing periodical impulsive forces, *Mechanical Systems and Signal Processing*, **11**, 6, 903-916
28. PAULSON E., 1947, A note on the efficiency of the Wald sequential test, *The Annals of Mathematical Statistics*, **18**, 3, 447-450
29. RAI A., UPADHYAY S.H., 2016, A review on signal processing techniques utilized in the fault diagnosis of rolling element bearings, *Tribology International*, **96**, 289-306
30. RENWICK J.T., BABSON P.E., 1985, 1985, Vibration analysis-a proven technique as a predictive maintenance tool, *IEEE Transactions on Industry Applications*, **IA-21**, 2
31. RIZOS P.F., ASPRAGATHOS N., DIMAROGONAS A.D., 1990, Identification of crack location and magnitude in a cantilever beam from the vibration modes, *Journal of Sound and Vibration*, **138**, 3, 381-388
32. SAMANTA B., AL-BALUSHI K.R., 2003, Artificial neural network based fault diagnosis for rolling element bearings using time-domain features, *Mechanical Systems and Signal Processing*, **17**, 2, 317-328
33. SCHNEEWEISS H., 2005, *Abraham Wald*, Department of Statistics, University of Munich, Collaborative Research Center, 386, 439
34. SHEEN Y.-T., 2004, A complex filter for vibration signal demodulation in bearing defect diagnosis, *Journal of Sound and Vibration*, **276**, 105-119
35. SHEEN Y.-T., 2008, An envelope detection method based on the first-vibration-mode of bearing vibration, *Measurement*, **41**, 797-809
36. SOBEL M., WALD A., 1949, A sequential decision procedure for choosing one of three hypotheses concerning the unknown mean of a normal distribution, *The Annals of Mathematical Statistics*, **20**, 4, 502-522

37. STACK J.R., HARLEY R.G., HABETLER T.G., 2004, An amplitude modulation detector for fault diagnosis in rolling element bearings, *IEEE Transactions on Industrial Electronics*, **51**, 5, 1097-1102
38. TANDON N., CHOUDHURY A., 1999, A review of vibration and acoustic measurement methods for the detection of defects in rolling element bearings, *Tribology International*, **32**, 8, 469-480
39. TAUQIR A., SALAM I., UL HAQ A., KHAN A.Q., 2000, Causes of fatigue failure in the main bearing of an aero-engine, *Engineering Failure Analysis*, **7**, 127-144
40. VAN M., FRANCIOSA P., CEGLAREK D., 2016, Rolling element bearing fault diagnosis using integrated nonlocal means de-noising with modified morphology filter operators, *Mathematical Problems in Engineering*, DOI: 10.1155/2016/9657285
41. WALD A., 1943, On the efficient design of statistical investigations, *The Annals of Mathematical Statistics*, **14**, 2, 134-140
42. WALD A., 1945, Sequential tests of statistical hypotheses, *The Annals of Mathematical Statistics*, **16**, 2, 117-186
43. WALD A., 1947, *Sequential Analysis*, John Wiley and Sons, New York
44. WALD A., 1949, Statistical decision functions, *The Annals of Mathematical Statistics*, **20**, 2, 165-205
45. WALD A., WOLFOWITZ J., 1943, An exact test for randomness in the non-parametric case based on serial correlation, *The Annals of Mathematical Statistics*, **14**, 4, 378-388
46. WALD A., WOLFOWITZ J., 1948, Optimum character of the sequential probability ratio test, *The Annals of Mathematical Statistics*, **19**, 3, 326-339
47. WANG H., LI R., TANG G., YUAN H., ZHAO Q., CAO X., 2014, A compound fault diagnosis for rolling bearings method based on blind source separation and ensemble empirical mode decomposition, *Journals Plos*, **9**, 10
48. WEISS L., 1956, On the uniqueness of Wald sequential tests, *The Annals of Mathematical Statistics*, **27**, 4, 1178-1181
49. WOLFOWITZ J., 1949, On Wald's proof of the consistency of the maximum likelihood estimate, *The Annals of Mathematical Statistics*, **20**, 4, 601-602
50. YANG H., MATHEW J., MA L., 2005, Fault diagnosis of rolling element bearings using basis pursuit, *Mechanical Systems and Signal Processing*, **19**, 341-356

MODIFIED MODEL FOR SHEAR STRESS DISTRIBUTION USING TRI-1 LUNAR SOIL SIMULANT

S. JAYALEKSHMI, PALA GIREESH KUMAR

Civil Engineering Department, National Institute of Technology, Tiruchirappalli, Tamil Nadu, India

e-mail: jaya@nitt.edu; jaynagu@gmail.com; gireeshnitt04@gmail.com

In the present study, research is carried out on deriving modified analytical equations for finding shear stress distribution and known as Modified Shear Stress models (SSM) beneath plain wheels (small and large) on TRI-1 lunar soil simulant. In all four models, the Reece model, Bekker model, Wong-Reece model and Iagnemma model, normal stress and shear stress are determined, and the shear stress determination is based on the Janosi and Hana-moto (1961) model. There exists ample scope for modifying this model. A modified model for shear stress distribution is developed and the same is discussed in this paper.

Keywords: TRI-1, lunar soil simulant, modified model, shear stress distribution

1. Introduction

Investigating mobility performance of planetary rovers is a very difficult task due to presence of more obstacles, sloping conditions (steep, adverse) and environmental conditions that exist on the Moon/Mars. In such a case, knowing the performance and overcoming the problem (by means of optimizing wheel parameters, introducing sensors, etc.) result in giving a better performance. This can be done by calculating the performance parameters (drawbar pull DP, sinkage, torque, rolling resistance) for planetary rovers. This involves terrain parameters and wheel parameters which have to be determined in advance. In the present study, two plain wheels of different sizes are considered. The experiments were carried out in a fabricated single wheel test bed (Sreenivasulu, 2014) on TRI-1 lunar soil simulant.

Wheel-soil interaction has a vital role in vehicle-terrain mobility (Bekker, 1969). A rover moving (travelling) on various terrains will have different mobility characteristics. Normally, the mobility level can be determined in terms of relative performance indices (entry angle, drawbar pull coefficient, resistance coefficient, drawbar pull efficiency, tractive coefficient and tractive efficiency) and absolute performance indices (drawbar pull, driving torque and sinkage) (Liu *et al.*, 2008; Ishigami *et al.*, 2011). For example, the drawbar pull is very important and a positive drawbar pull indicates that the rover can generate forward motion on the terrain it is travelling (traversing), whereas a negative drawbar pull implies that forward motion is difficult or impossible, which is one of the reasons for mission failure (Wong and Reece, 1967; Iagnemma *et al.*, 2004). Determination of absolute performance indices depends on normal stress and shear stress.

Many research works are carried out on study of grouzers on motion performance (Liu *et al.*, 2008), study of motion dynamics and control of planetary rovers (Yoshida *et al.*, 2001), study on stability control of a wheel-lugged rover (Grand *et al.*, 2002), terrain parameter estimation for planetary rovers (Iagnemma *et al.*, 2004) and study on motion performance of a rover which is evaluated by its drawbar pull, driving torque which is related to normal stress and shear stress distribution produced by the wheel at the wheel-soil interface (Wong, 2001; Sutoh *et al.*, 2010). Hence, determination of normal stresses and shear stresses plays a major role in the wheel-soil

interaction. There are several models available, out of which four models are considered for the study (Reece, Bekker, Wong-Reece and Iagnemma model) for normal stress and shear stress distribution analysis that develops beneath the wheel when it interacts with the soil and moving on the terrain. The objective of this paper is to develop a model called the modified Shear Stress Model (SSM). A preliminary comparative study on these models resulted in refinements and culminated in the Modified Shear Stress Model (Modified SSM)

2. Stress distribution models

When a wheel travels over a loose soil, normal stress and shear stress develops beneath the surface. These stresses are used in the calculation of forces. The motion performance of a rover is usually evaluated by its Drawbar Pull (DP) and Driving Torque (DT), which are related to the normal and shear force distributions produced by the wheel at the wheel-soil interface. In the present study, four models are considered for analysis of wheel (small and large) that travels on TRI-1 soil simulant, and modified SSM for shear stress distribution is derived. The models considered are explained in Sections 2.1, 2.2, 2.3 and 2.4.

2.1. Reece normal stress model

When a wheel travels over a loose soil, normal stress and shear stress develop beneath the surface as shown in Fig. 1.

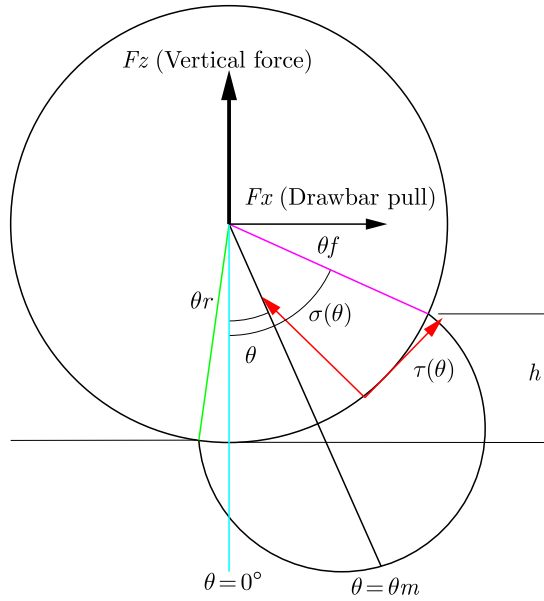


Fig. 1. Wheel-soil interaction

The maximum normal stress is found to occur at the transition point between two zones, the forward and rearward zones.

Normal stress is given as

$$\sigma(\theta) = \begin{cases} \sigma_{max}(\cos \theta - \cos \theta_f)^n & \text{for } \theta_m \leq \theta \leq \theta_f \\ \sigma_{max} \left[\cos \left(\theta_f - \frac{\theta - \theta_r}{\theta_m - \theta_r} (\theta_f - \theta_m) \right) - \cos \theta_f \right]^n & \text{for } \theta_r \leq \theta \leq \theta_m \end{cases} \quad (2.1)$$

where

$$\sigma_{max} = (ck_c + \rho k_\phi b) \left(\frac{r}{b} \right)^n \quad (2.2)$$

where h , b , r is the wheel sinkage, width and radius, respectively, n – sinkage exponent, c – cohesion stress of the soil, ρ – soil bulk density, k_c , k_ϕ – pressure-sinkage moduli. θ_f is the entry angle (the angle from the vertical to the point at which the wheel initially makes contact with the soil)

$$\theta_f = \cos^{-1}\left(1 - \frac{h}{r}\right) \quad (2.3)$$

θ_r – departure angle (the angle from the vertical to where the wheel departs from the soil, and this value is generally assumed to be zero), i.e., $\theta_r \cong 0$, θ_m – maximum angle (the specific wheel angle where the normal stress is maximum)

$$\theta_m = (a_0 + a_1 s)\theta_f \quad (2.4)$$

a_0 and a_1 are parameters depending on the wheel-soil interaction ($a_0 \cong 0.4$, $0 \leq a_1 \leq 0.3$, are assumed values as given by Wong (1965)).

Estimation of the maximum specific angle at which normal stress and shear stress are maximum can be found using Eq. (2.4) for the other models (Bekker and Wong-Reece).

The shear stress distribution model was given by Janosi and Hanamoto (1961) and the same was considered by Reece (1965) to find the shear stress developed beneath the wheel, as shown in Fig. 1.

Shear stress is given as

$$\tau_x = [c + \sigma(\theta) \tan \phi] \left[1 - \exp\left(-\frac{j(\theta)}{k}\right)\right] \quad (2.5)$$

where

$$j(\theta) = r[\theta_f - \theta - (1 - s)(\sin \theta_f - \sin \theta)] \quad (2.6)$$

and ϕ is the internal friction angle of the soil, k – shear deformation modulus (depending on the shape of the wheel surface), j – soil deformation, s – wheel slip (given as the ratio of the wheel width to the wheel radius).

Similarly, the same Janosi shear stress distribution model was used to determine shear stresses for the normal stress distribution models considered by Reece, Bekker, Wong-Reece and Iagnemma.

2.2. Bekker normal stress model

When a wheel rolls on a loose soil, normal and shear stresses are generated under the wheel. These stresses are used in the calculation of the forces. The stresses are modeled as shown in Fig. 1.

Normal stress is given as

$$\sigma(\theta) = \begin{cases} \sigma_{max} \left(\frac{\cos \theta - \cos \theta_f}{\cos \theta_m - \cos \theta_f} \right)^n & \text{for } \theta_m < \theta < \theta_f \\ \sigma_{max} \left[\frac{\cos \left(\theta_f - \frac{\theta - \theta_r}{\theta_m - \theta_r} (\theta_f - \theta_m) \right) - \cos \theta_f}{\cos \theta_m - \cos \theta_f} \right]^n & \text{for } \theta_r < \theta < \theta_m \end{cases} \quad (2.7)$$

where

$$\sigma_{max} = (ck + c + \rho k_\phi b) \left(\frac{r}{b} \right)^n (\cos \theta_m - \cos \theta_f)^n \quad (2.8)$$

and h , b , r are the wheel sinkage, width and radius, respectively, n – soil sinkage exponent, c – cohesion stress of the soil, ρ – soil bulk density, k_c , k_ϕ – cohesion and friction modulus

coefficients. θ_f and θ_r are the entry and exit angles along the wheel surface, and are functions of the soil compaction and recovery. The values for θ_f and θ_r are obtained as

$$\theta_f = \cos^{-1}\left(1 - \frac{h}{r}\right) \quad \theta_r = \cos^{-1}\left(1 - \frac{kh}{r}\right) \quad (2.9)$$

where h defines how much the wheel initially compacts the soil when it contacts with the soil surface, kh defines how much the soil recovers in height following the wheel when it departs the soil surface, k is the wheel sinkage ratio (which denotes the ratio between the front and rear sinkages of the wheel).

The value of k depends on the wheel surface pattern, slip ratio and soil characteristics. The value of k lies below 1.0 when soil compaction occurs, but can be more than 1.0 when the soil is dug by the wheel and transported to the region behind the wheel (Bekker, 1969; Yoshida and Hamano, 2001).

2.3. Wong-Reece normal stress model

When a wheel rolls on a loose soil, normal and shear stresses are generated under the wheel. These stresses are used in the calculation of the forces. The stresses are modeled as shown in Fig. 2.

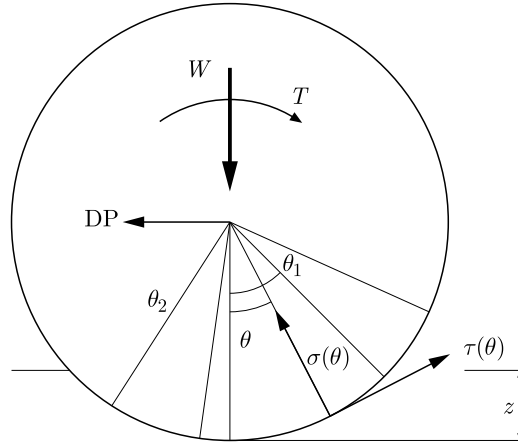


Fig. 2. Stress distribution model of plain wheel

Normal stress is given as

$$\sigma(\theta) = \begin{cases} \left(\frac{k_c}{b} + k_\phi\right)r^N(\cos \theta - \cos \theta_1)^N & \text{for } \theta_m \leq \theta \leq \theta_1 \\ \left(\frac{k_c}{b} + \rho k_\phi\right)r^N \left[\cos\left(\theta_1 - \frac{\theta - \theta_2}{\theta_m - \theta_2}(\theta_1 - \theta_m)\right) - \cos \theta_1 \right]^N & \text{for } \theta_2 \leq \theta \leq \theta_m \end{cases} \quad (2.10)$$

where

$$N = n_0 + n_1 s$$

and n_0 and n_1 are parameters related to the wheel-soil interaction, b denotes wheel width, r – wheel radius, c – cohesion stress of the soil, z – sinkage, k_c , k_ϕ – cohesion and friction modulus coefficients.

For wheels without lugs, the entry and exit angles can be calculated using the following equations. θ_1 is the entry angle (the angle from the vertical to the point at which the wheel initially makes contact with the soil)

$$\theta_1 = \cos^{-1}\left(1 - \frac{z}{r}\right) \quad (2.11)$$

θ_2 is the departure angle (the angle from the vertical to where the wheel departs from the soil, and this value is generally assumed to be zero). In this model, it is not assumed as zero, hence it can be calculated as

$$\theta_2 = \cos^{-1}\left(1 - \frac{kz}{r}\right) \quad (2.12)$$

2.4. Iagnemma normal stress model

When a wheel rolls on a loose soil, radial and tangential stresses are generated under the wheel. These stresses are used in the calculation of the forces. The stresses are modeled as in Fig. 2.

Radial stress is given as

$$\sigma(\theta) = \begin{cases} \sigma_1(\theta) & \text{for } \theta_m < \theta < \theta_1 \\ \sigma_2(\theta) & \text{for } \theta_2 < \theta < \theta_m \end{cases} \quad (2.13)$$

where

$$\begin{aligned} \sigma_1(\theta) &= \left(\frac{k_c}{b} + k_\phi\right) [r(\cos \theta - \cos \theta_1)]^n \\ \sigma_2(\theta) &= \left(\frac{k_c}{b} + k_\phi\right) \left[r \left(\cos \left(\theta_1 - \frac{\theta - \theta_2}{\theta_m - \theta_2} (\theta_1 - \theta_m) \right) - \cos \theta_1 \right)\right]^n \end{aligned} \quad (2.14)$$

and z , b , r are the wheel sinkage, width and radius, respectively, n is the sinkage exponent, c – cohesion stress of the soil, ρ – soil bulk density, k_c , k_ϕ – coefficient of cohesion and friction modulus, σ_1 – radial stress profile between θ_1 and θ_m , σ_2 – radial stress profile between θ_m and θ_2 , θ – angular location of the wheel rim, θ_1 – entry angle (the angle from the vertical to the point at which the wheel initially makes contact with the soil)

$$\theta_1 = \cos^{-1}\left(1 - \frac{z}{r}\right) \quad (2.15)$$

θ_2 is the departure angle (the angle from the vertical to where the wheel departs from the soil, and this value is generally assumed to be zero), i.e., since θ_2 is generally small in practice for low cohesion soils, $\theta_2 \cong 0$. θ_m is the maximum angle (angular location of the maximum normal stress). The location of the point of the maximum radial stress is at

$$\theta_m = \frac{\theta_1 + \theta_2}{2} \quad (2.16)$$

3. Modified stress distribution models

Using the above normal stress models and the shear stress model for plain wheels, small wheels (160 mm×32 mm) and large wheels (210 mm×50 mm), the normal stress and shear stresses are determined and the modified shear stress distribution model is developed from the obtained results of previous models. The shear stress distribution model was given by Janosi and Hanamoto (1961) and the same model was used by Reece, Bekker, Wong and Iagnemma normal stress distribution (where the shear stress was a function of the normal stress).

Hence, there exists space in deriving modified shear stress distribution models. The developed mathematical model for the shear stress distribution is based on the Janosi and Hana-moto (1961) model which has been used for both wheels (small: 160 mm×32 mm and large: 210 mm×50 mm) moving on TRI-1 (Tiruchirappalli-1) soil simulant. An analytical method for predicting the shear stress distribution beneath the wheel when it interacts with the soil has been found based on the results obtained from all four models which are considered in the study. The derived shear stress model for TRI-1 soil simulant predicts the shear stress very well and close to the Janosi model. The modified shear stress model (SSM) is not a function of the normal stress, whereas the earlier one is a function of the normal stress. In this modified SSM, the constants like A , B and F are introduced and the model expressed is in terms of b/R and the maximum specific angle θ_m . The modified SSM for all models considered are given as below.

Model 1 (Reece model)

Table 1. Equation for the modified SSM, $A = 3.409k - 0.112$, $B = -90.90k + 2.2361$

No.	Condition		F	Equation for shear stress
1	max ss k_1	S	$\frac{bd}{W} \left(64.84 \frac{b}{R} - 9.635 \right)$	$\tau = F \frac{w}{bd} \left(A \frac{\theta_m}{\theta_{ref}} + B \right)$ $\theta_{ref} = 1^\circ$ (assumption)
2		L		
3	min ss k_1	S	$\frac{bd}{W} \left(39.25 \frac{b}{R} - 5.51 \right)$	
4		L		
5	max ss k_2	S	$\frac{bd}{W} \left(164.60 \frac{b}{R} - 49.58 \right)$	
6		L		
7	min ss k_2	S	$\frac{bd}{W} \left(101.40 \frac{b}{R} - 30.38 \right)$	
8		L		
9	max ss k_3	S	$\frac{bd}{W} \left(188.30 \frac{b}{R} - 59.03 \right)$	
10		L		
11	min ss k_3	S	$\frac{bd}{W} \left(113.40 \frac{b}{R} - 35.18 \right)$	
12		L		

In Table 1, A and B are shear deformation constants (depending on k , shear deformation modulus obtained from a direct shear test, k for TRI-1 soil simulant is 1.02 ± 0.76 cm) and are given in the above table. S denotes small wheel, L – large wheel, ss – shear stress, W – wheel weight, b – wheel width and d – wheel diameter. Similarly, for other modified SSM also, it is same (k remains the same for TRI-1 soil simulant and varies for different types of simulants, A and B varies, W , b and d also vary).

For both small (160 mm×32 mm) and large wheels (210 mm×50 mm), the modified SSM is the same, where A and B for each model are given separately. The modified SSM is given for both minimum and maximum density. The model is the same for each case but it changes with respect to the shear deformation modulus k and a factor F (Table 1). Similarly, for other models, the modified SSM are as follows.

Model 2 (Bekker model)

Findings of the shear stress coefficient F and shear deformation constants A and B are explained in Figs. 3 to 8. The shear deformation constants are derived in terms of the shear deformation modulus for different models and are presented in these figures.

Table 2. Equation for the modified SSM, $A = 3.623k - 0.116$, $B = -90.90k + 2.236$

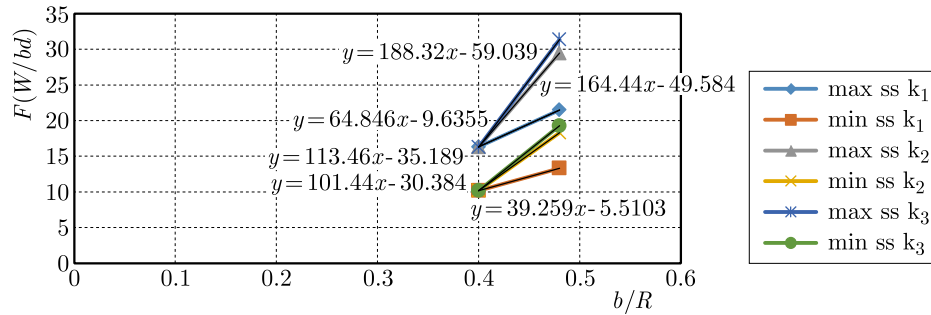
No.	Condition		F	Equation for shear stress
1	max ss k_1	S	$\frac{bd}{W} \left(85.94 \frac{b}{R} - 18.08 \right)$	$\tau = F \frac{w}{bd} \left(A \frac{\theta_m}{\theta_{ref}} + B \right)$ $\theta_{ref} = 1^\circ$ (assumption)
2		L	$\frac{bd}{W} \left(85.94 \frac{b}{R} - 18.08 \right)$	
3	min ss k_1	S	$\frac{bd}{W} \left(52.25 \frac{b}{R} - 10.70 \right)$	
4		L	$\frac{bd}{W} \left(52.25 \frac{b}{R} - 10.70 \right)$	
5	max ss k_2	S	$\frac{bd}{W} \left(171.50 \frac{b}{R} - 52.36 \right)$	
6		L	$\frac{bd}{W} \left(171.50 \frac{b}{R} - 52.36 \right)$	
7	min ss k_2	S	$\frac{bd}{W} \left(105.50 \frac{b}{R} - 32.01 \right)$	
8		L	$\frac{bd}{W} \left(105.50 \frac{b}{R} - 32.01 \right)$	
9	max ss k_3	S	$\frac{bd}{W} \left(191.00 \frac{b}{R} - 60.15 \right)$	
10		L	$\frac{bd}{W} \left(191.00 \frac{b}{R} - 60.15 \right)$	
11	min ss k_3	S	$\frac{bd}{W} \left(117.40 \frac{b}{R} - 36.79 \right)$	
12		L	$\frac{bd}{W} \left(117.40 \frac{b}{R} - 36.79 \right)$	

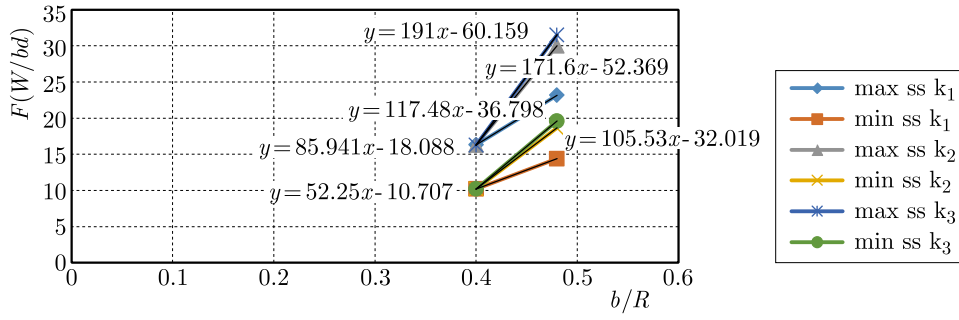
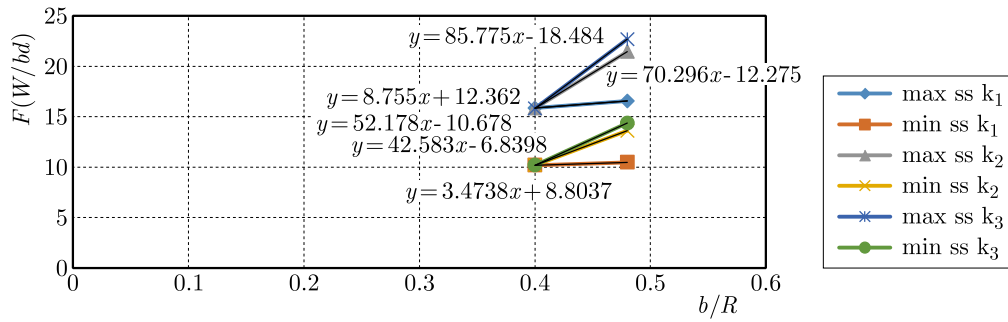
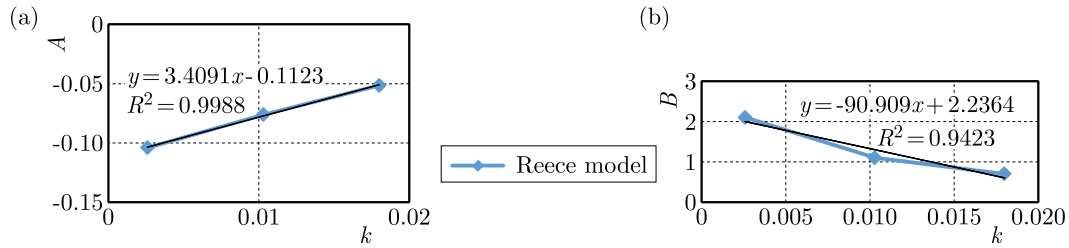
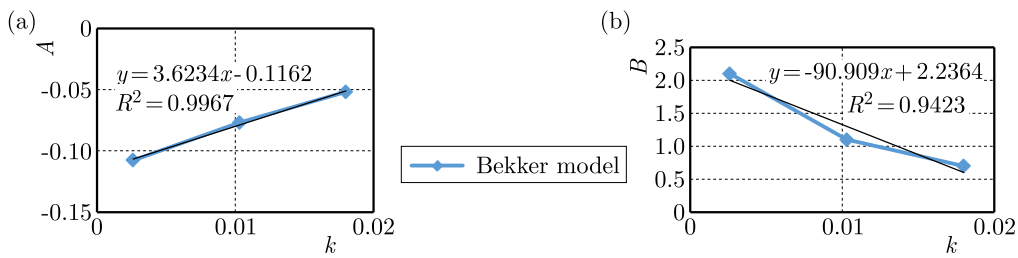
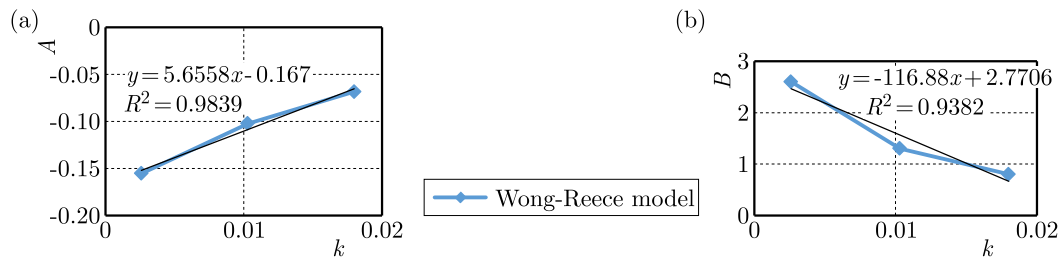
Model 3 (Wong-Reece model)**Table 3.** Equation for the modified SSM, $A = 5.655k - 0.167$, $B = -116.80k + 2.770$

No.	Condition		F	Equation for shear stress
1	max ss k_1	S	$\frac{bd}{W} \left(8.755 \frac{b}{R} - 12.36 \right)$	$\tau = F \frac{w}{bd} \left(A \frac{\theta_m}{\theta_{ref}} + B \right)$ $\theta_{ref} = 1^\circ$ (assumption)
2		L	$\frac{bd}{W} \left(8.755 \frac{b}{R} - 12.36 \right)$	
3	min ss k_1	S	$\frac{bd}{W} \left(3.473 \frac{b}{R} - 8.803 \right)$	
4		L	$\frac{bd}{W} \left(3.473 \frac{b}{R} - 8.803 \right)$	
5	max ss k_2	S	$\frac{bd}{W} \left(70.29 \frac{b}{R} - 12.27 \right)$	
6		L	$\frac{bd}{W} \left(70.29 \frac{b}{R} - 12.27 \right)$	
7	min ss k_2	S	$\frac{bd}{W} \left(42.58 \frac{b}{R} - 6.839 \right)$	
8		L	$\frac{bd}{W} \left(42.58 \frac{b}{R} - 6.839 \right)$	
9	max ss k_3	S	$\frac{bd}{W} \left(85.77 \frac{b}{R} - 18.48 \right)$	
10		L	$\frac{bd}{W} \left(85.77 \frac{b}{R} - 18.48 \right)$	
11	min ss k_3	S	$\frac{bd}{W} \left(52.17 \frac{b}{R} - 10.67 \right)$	
12		L	$\frac{bd}{W} \left(52.17 \frac{b}{R} - 10.67 \right)$	

The modified shear stress models have been determined and are shown in Tables 1 to 3.

The modified shear stress model (SSM) is a function of F , A , B and F . The shear deformation constants A and B shown in Figs. 3 to 8.

**Fig. 3.** Reece model – determination of F

Fig. 4. Bekker model – determination of F Fig. 5. Wong-Reece model – determination of F Fig. 6. Reece model – (a) determination of A , (b) determination of B Fig. 7. Bekker model – (a) determination of A , (b) determination of B Fig. 8. Wong-Reece model – (a) determination of A , (b) determination of B

4. Results and discussions

- The shear deformation constants A and B , F are introduced as a function of the shear stress. The derived modified shear stress models (SSM) are presented from Tables 1 to 3, for the Reece, Bekker and Wong-Reece models, respectively.
- The modified shear stress model (SSM) is derived based on the results obtained for both small (160 mm×32 mm) and large wheels (210 mm×50 mm) from the Reece, Bekker and Wong-Reece models.
- Initially, the SSM was found for each case, later the equations were minimized by doing an extensive work and are presented in Section 3 in Tables 1 to 3.
- From Tables 1 to 3, it is found that the modified shear stress model is the same for all models (Reece, Bekker and Wong-Reece) but it varies with F and shear deformation constants A , B . Hence, for various simulants, F , A , B will be different.
- From Figs. 3 to 5, it is found that the shear stress coefficient F depends on the b/R and bd/W ratio, and it changes for each case in all models (Reece, Bekker and Wong-Reece) with respect to a change in the b/R and bd/W ratios.
- From Tables 1 to 3, it is inferred that for the maximum and minimum density, the derived equation for the modified shear stress model remains the same, but F varies with respect to density irrespective of the type of wheel (both wheels – small 160 mm×32 mm and large 210 mm×50 mm).
- From Figs. 6a and 6b, it is found that the shear deformation modulus k is a function of the shear deformation constants A and B . A is plotted versus k and B versus k to determine expressions for the shear deformation constants A and B in terms of k . This expression is the same and applicable to various types of simulants where A and B vary with respect to k . The obtained expression for the shear deformation constants is for the Reece model.
- Similarly, from Figs. 7 and 8, the shear deformation constants A and B are derived in terms of k (TRI-1 soil simulant) for the remaining models (Bekker and Wong-Reece).
- From Tables 1 to 3, it is found that the shear deformation constants A and B remains the same for a particular k value in all models but change with respect to a change in k .
- The modified shear stress model (SSM) is given by the authors of this paper in the following form

$$\tau = F \frac{w}{bd} \left(A \frac{\theta_m}{\theta_{ref}} + B \right)$$

where A and B are constants for both wheels (small – 160 mm×32 mm and large – 210 mm×50 mm) with respect to density (minimum (1.15 g/cc) and maximum (1.88 g/cc) – TRI-1 soil simulant) and varying with respect to k , whereas F is the same for both wheels (small – 160 mm×32 mm and large – 210 mm×50 mm) with respect to k but varies with respect to density (minimum and maximum – TRI-1 soil simulant), see Tables 1 to 3.

5. Conclusions

An analytical model has been developed for shear stress distribution based on the Janosi and Hanamoto (1961) shear stress distribution model. An extensive work has been carried out to derive a modified shear stress model (SSM) for small (160 mm×32 mm) and large wheels (210 mm×50 mm) moving on TRI-1 soil simulant to find the maximum shear stress generated beneath the wheel when it interacts with the soil. Shear deformation constants A , B are introduced along with a shear stress coefficient F , and expressions are derived for both shear

deformation constants and F for the SSM in all models. The modified shear stress model (SSM) has been derived for three models (Reece, Bekker, Wong-Reece) to determine shear stress on TRI-1 soil simulant. The results of SSM satisfy the Janosi model considered in the study. The SSM presents an alternative approach to analysis based on geometrical parameters of the wheel. The study can be extended to other simulants and wheel-soil interactions conducted on them.

Acknowledgment

The technical support received from National Institute of Technology Tiruchirappalli for the research work is gratefully acknowledged. We also acknowledge with grateful thanks to the Ministry of Human Resource Development (MHRD), India, for the Ph.D. Scholarship received to carry out the research work.

References

1. BEKKER M.G., 1969, *Introduction to Terrain-Vehicle Systems*, Ann Arbor: University of Michigan Press
2. DING L., GAO H., DENG Z., NAGATANI K., YOSHIDA K., 2011, Experimental study and analysis on driving wheels' performance for planetary exploration rovers moving indeformable soil, *Journal of Terramechanics*, **48**, 27-45
3. GRAND C., BEN AMAR, PLUMET F., BIDAUD, 2002, *Stability Control of a Wheel-Lugged Mini-Rover*, University de Paris VI
4. IAGNEMMA K., KANG S., SHIBLY H., DUBOWSKY S., 2004), Online terrain parameter estimation for wheeled mobile robots with application to planetary rovers, *IEEE Transactions on Robotics*, **20**, 5, October
5. ISHIGAMI G., OTSUKI M., KUBOTA T., IAGNEMMA K., 2011, Modelling of flexible and rigid wheels for exploration rover on rough terrain, *28th International Symposium on Space Technology and Science*, Okinawa, Japan, 5-12 June
6. JANOSI Z., HANAMOTO B., 1961, Analytical determination of drawbar pull as a function of slip for tracked vehicles in deformable soils, *Proceedings of the 1st International conference on Terrain-Vehicle Systems*, Turin, Italy, 707-736
7. LIU J., GAO H., DENG Z., 2008, Effect of straight grousers parameters on motion performance of small rigid wheel on loose sand, *Information Technology Journal*, **7**, 8, 1125-1132
8. SREENIVASULU S., 2014, *Development and Characterisation of TRI-1: an Engineered Lunar Soil Simulant and Studies on Wheel Soil Interaction*, Ph.D. Thesis, Department of Civil Engineering, National Institute of Technology, Tiruchirappalli
9. SUTOH M., YUSA J., NAGATANI K., YOSHIDA K., 2010, Travelling performance evaluation of planetary rovers on weak soil, *Journal of Field Robotics*, Sapporo, Japan
10. WONG J.Y., 2001, *Theory of Ground Vehicles*, 3rd ed., New York: Wiley-Interscience
11. WONG J.Y., REECE A., 1967, Prediction on rigid wheel performance based on the analysis of soil-wheel stresses: Part 1. Performance of driven rigid wheels, *Journal of Terramechanics*, **4**, 1, 81-98
12. YOSHIDA K., HAMANO H., 2001, *Motion Dynamics and Control of a Planetary Rover With Slip-Based Traction Model Robotics*, Laboratory in Tsukuba Space Center, NASDA, Japan

ON AXISYMMETRIC HEAT CONDUCTION PROBLEM FOR MULTILAYER GRADED COATED HALF-SPACE

DARIUSZ M. PERKOWSKI, ROMAN KULCHYTSKY-ZHYHAILO, WALDEMAR KOŁODZIEJCZYK

Białystok University of Technology, Faculty of Mechanical Engineering, Białystok, Poland

e-mail: perkowski.d.m@gmail.com; r.kulczycki@pb.edu.pl; w.kolodziejczyk@pb.edu.pl

The technique of integral Hankel transform to find the solution of heat conduction in half-space coated by a multilayered package of homogenous laminae is applied. The half-space is heated by the given heat flux on the boundary surface. The temperature and heat flux distribution in the radial direction is analyzed for two types of coatings: 1) when the heat conductivity coefficient is described by a power or exponential function of the distance to the boundary surface; 2) multilayered coating has a periodic structure.

Keywords: temperature, heat flux, FGM, composite, homogenized model

1. Introduction

Modern engineering construction require the use of materials with appropriate thermal and mechanical properties which make them more and more complicated structures. To such materials belong media with functionally changing gradation properties (i.e. gradient materials). Furthermore, the surface coverage of gradient materials significantly affect the behaviour of the bodies under the influence of mechanical and thermal loads.

The formulations of the problems lead to boundary value problems of partial differential equations with varying coefficients. For the power (or exponential) law of variation of the heat conduction coefficient (or Young's modulus), the analytical methods of solutions are known (Guler and Erdogan, 2004, 2006; Liu and Wang, 2008; Matysiak *et al.*, 2011; Kulchytsky-Zhyhailo and Bajkowski, 2015). If the thermal and mechanical properties are described by other functions, obtaining analytical solutions encounters considerable mathematical difficulties. Parallel with the application of analytical methods for the solution of partial differential equations, inhomogeneous layers are also modeled by using an approach according to which the coating is replaced by a package of homogeneous or inhomogeneous layers (Ke and Wang, 2006, 2007; Kulchytsky-Zhyhailo and Bajkowski, 2012, 2015; Liu T.-J. *et al.*, 2008; Liu and Wang, 2009; Liu J. *et al.*, 2011, 2012). Most studies are based on two-dimensional problems of elasticity or thermoelasticity (Barik *et al.*, 2008; Choi and Paulino, 2008; Diao, 1999; Diao *et al.*, 1994; Liu J. *et al.*, 2011, 2012). However, the axisymmetric and three-dimensional problems are dealt with in a much lesser degree.

A special type of graded coating is the multilayered coating with periodic structure (Farhat *et al.*, 1997; Vevodin *et al.*, 2001). In the modeling of laminated half-spaces or coatings with periodic structures, it is customary to use two different approaches. In the first of these approaches the layers are considered as separate continuous media. The second approach is based on the analysis of a homogenized uniform coating whose properties are determined on the basis of the material properties and geometric characteristics of the strip of periodicity (Matysiak and Woźniak, 1987; Woźniak, 1987). The solution obtained for the laminated half-space is compared with Kulchytsky-Zhyhailo and Matysiak (2005).

In the present work, we consider an axisymmetric problem of heat conductivity for half-space with a multilayered coating. The boundary surface is heated by the given heat flux. In parallel, we obtain: 1) analytical solutions of the problems for the coating whose heat conductivity coefficient is described by a continuous function of the distance to the boundary surface; 2) the solution for the multilayered coating with a periodic structure which is described by a homogenized uniform layer (Matysiak and Woźniak, 1987; Woźniak, 1987). We analyze the difference between the temperature and heat flux in the non-homogeneous half-space caused by the use of two different models of nonuniform coatings. The obtaining of the smallest deviations in consideration of the heat conduction problem will be a strong argument in favor for application of the proposed methods for solving axisymmetric and three-dimensional problems of thermoelasticity for the functionally graded coated half-space.

2. Formulation of the problem

Assume that the surface $z = h$ of the non-homogeneous half-space is heated by a heat flux $q(r)$ on the circle of radius a , where r, z are dimensionless cylindrical coordinates referred to the linear size $a, h = H/a, H$ is thickness of the coating (Fig. 1).

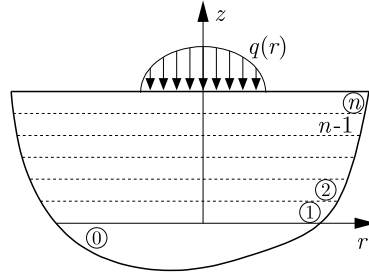


Fig. 1. The scheme of the body

The non-homogeneous half space is formed by the homogeneous half-space with the heat conductivity coefficient K_0 and a system of non-homogeneous layers with thicknesses H_i and the heat conductivity coefficients $K_i, i = 1, 2, \dots, n$, respectively, where the value of the parameter n corresponds to the number of the layer in the package. Assume that the conditions of perfect thermal contact are realized between the layers of the coating and between the coating and the base.

The analyzed problem of theory of heat conduction is reduced to the solution of the following partial differential equations

$$\frac{\partial^2 T_i}{\partial r^2} + \frac{1}{r} \frac{\partial T_i}{\partial r} + \frac{1}{K_i} \frac{\partial}{\partial z} \left(K_i \frac{\partial T_i}{\partial z} \right) = 0 \quad i = 0, 1, \dots, n \quad (2.1)$$

with boundary conditions imposed on the surface of the non-homogeneous half-space

$$\frac{\partial T_n}{\partial z} = \frac{q(r)a}{K_n} H(1 - r) \quad z = h \quad (2.2)$$

conditions of perfect thermal contact between the components of the considered half-space

$$\begin{aligned} T_i &= T_{i+1} & K_i(h_i^*) \frac{\partial T_i}{\partial z} &= K_{i+1}(h_i^*) \frac{\partial T_{i+1}}{\partial z} \\ z &= h_i^* & i &= 0, \dots, n-1 \end{aligned} \quad (2.3)$$

and conditions imposed at infinity

$$T_i \rightarrow 0 \quad r^2 + z^2 \rightarrow \infty \quad i = 0, 1, \dots, n \quad (2.4)$$

where T_i is the temperature in the i -th component of the non-homogenous medium, the index $i = 0$ describes the parameters and functions of state in the homogeneous half-space, h_i^* is the coordinate z of the upper surface of the i -th component of the non-homogenous half-space, $h_0^* = 0$, $h_i^* = h_{i-1}^* + h_i$, $h_i = H_i/a$, $i = 1, \dots, n$, $h_n^* = h$, $H(r)$ – Heaviside step function.

3. Method of solution

The solution of the boundary value problem is sought by applying the Hankel integral transformation (see Sneddon, 1966)

$$\tilde{T}_i(s, z) = \int_0^\infty T_i(r, z) r J_0(sr) dr \quad (3.1)$$

where $J_0(sr)$ is the Bessel function. The solution to equation (2.1) was determined by Hankel integral transformation technique (3.1). The temperature for the homogeneous half-space in the Hankel transform space which satisfies the regularity conditions at infinity (2.4) can be written in the form

$$\tilde{T}_0(s, z) = t_0(s) \exp(sz) \quad (3.2)$$

where $t_0(s)$ is the unknown function.

We considered the following cases.

Case A

Let $n = 1$. The dependence of the heat conductivity coefficient on the coordinate z is described by the formula

$$K_1(z) = K_0 \exp(\alpha z) \quad \alpha = \frac{1}{h} \ln\left(\frac{K_S}{K_0}\right) \quad 0 \leq z \leq h \quad (3.3)$$

where K_S is the heat conductivity coefficient on the surface of the inhomogeneous half-space. The general solution to differential equation (2.1) in the Hankel transform space specified in the coating can be written in the form

$$\tilde{T}_1(s, z) = t_1(s) \exp(\alpha^{(-)} z) + t_2(s) \exp(\alpha^{(+)} z) \quad (3.4)$$

where $2\alpha^{(\pm)} = -\alpha \pm \sqrt{\alpha^2 + 4s^2}$, $t_1(s)$ and $t_2(s)$ are the unknown functions.

Case A'

Let $n = 1$. The dependence of the heat conductivity coefficient on the coordinate z is described by the power function

$$K_1(z) = K^* (c \pm z)^\alpha \quad c = \pm h \left(\left(\frac{K_S}{K_0} \right)^{1/\alpha} - 1 \right)^{-1} \quad (3.5)$$

$$K^* = \frac{K_0}{c^\alpha} \quad 0 \leq z \leq h$$

In equation (3.5) for the case $K_0 < K_S$, we take sign “+”, when $K_0 > K_S$ – sign “–”.

The Hankel transform of temperature in the coating can be written in the form

$$\tilde{T}_1(s, z) = t_1(s) \zeta^p I_p(s\zeta) + t_2(s) \zeta^p K_p(s\zeta) \quad (3.6)$$

where $2p + \alpha = 1$, $\zeta = c \pm z$, $I_p(s\zeta)$, $K_p(s\zeta)$ are modified Bessel functions.

Moreover, if the analytical solution of partial differential equation with variable coefficient (2.1) is not known, the non-homogeneous coating can be replaced by a multilayered system of homogeneous layers. Their thermal properties are described by their heat conductivity coefficients

$$K_i = \frac{1}{h_i} \int_{h_{i-1}^*}^{h_i^*} K_1(z) dz \quad (3.7)$$

Case B

The coating composed of n homogeneous layers. The general solution to equations (2.1) expressed in the Hankel transform domain takes the form

$$\tilde{T}_i = t_{2i-1}(s) \sinh[s(h_i^* - z)] + t_{2i}(s) \cosh[s(h_i^* - z)] \quad i = 1, 2, \dots, n \quad (3.8)$$

where $t_i(s)$, $i = 1, \dots, 2n$ are the unknown functions.

Case C

The multilayered coating with a microperiodical structure. Assume that the repeated fundamental layer comprises two homogeneous elastic sublayers with different thicknesses (h_I and h_{II}) and thermal conductivities (K_I and K_{II}). A large number of equations and boundary conditions on the interfaces complicates the solution of the problem. Another approach is using a homogenized model (Choi and Paulino, 2008; Diao, 1999) in which properties of the homogenized coating are determined on the base of properties of the components.

Applying the homogenized model to the coating, we solve the boundary value problem described by the equation (Matysiak and Woźniak, 1987; Woźniak, 1987)

$$\frac{\partial^2 T_1}{\partial r^2} + \frac{1}{r} \frac{\partial T_1}{\partial r} + \frac{1}{p_1^2} \frac{\partial^2 T_1}{\partial z^2} = 0 \quad (3.9)$$

where T_1 is the temperature in the homogenized coating

$$\begin{aligned} p_1^2 &= \widetilde{K} K_c^{-1} & K_c &= \frac{K_I K_{II}}{(1 - \eta) K_I + \eta K_{II}} \\ \widetilde{K} &= \eta K_I + (1 - \eta) K_{II} & \eta &= \frac{h_I}{h_I + h_{II}} \end{aligned} \quad (3.10)$$

the boundary condition imposed on the surface of the non-homogeneous half-space

$$\frac{\partial T_1}{\partial z} = \frac{q(r)a}{K_c} H(1 - r) \quad z = h \quad (3.11)$$

and boundary conditions of perfect thermal contact between the homogenized coating and the substrate

$$T_0 = T_1 \quad K_0 \frac{\partial T_0}{\partial z} = K_c \frac{\partial T_1}{\partial z} \quad z = 0 \quad (3.12)$$

Boundary conditions (2.4) stay without change. The general solution to equation (3.9) in the Hankel transform takes the form

$$\tilde{T}_1 = t_1(s) \sinh[(h - z)sp_1] + t_2(s) \cosh[(h - z)sp_1] \quad (3.13)$$

Equations (3.2), (3.4), (3.6), (3.8) and (3.13) contain the unknown functions $t_i(s)$. These functions are obtained satisfying boundary conditions (2.2) and (2.3) (or (3.11)) and (3.12) in Case C. Satisfying the boundary conditions, the functions $t_i(s)$ may be written as

$$t_i(s) = \frac{\tilde{q}(s)a}{\widehat{K}_s} \widehat{t}_i(s) \quad (3.14)$$

where the functions $\widehat{t}_i(s)$ are obtained from the solution to linear equations (see Appendix A), $\tilde{q}(s)$ is the Hankel transform of heat flux, $\widehat{K} = K_n$ in Case A, A', B and $\widehat{K} = K_cp_1$ in Case C.

Applying the inverse Hankel transform to equations (3.2), (3.4), (3.6), (3.8) and (3.13), temperature can be found at the desired location (see Sneddon, 1966)

$$T_i(r, z) = \int_0^\infty s \widehat{T}_i(s, z) J_0(sr) ds \quad (3.15)$$

At internal points of the non-homogeneous half space ($z < h$) the integrals are evaluated numerically using the Gaussian quadrature (Abramowitz and Stegun, 1964). On the surface $z = h$, we take into account the asymptotic behaviour of the functions $t_{2n-1}(s)$ and $t_{2n}(s)$ as $s \rightarrow \infty$. The continuity of the results when $z \rightarrow h$ has been also verified.

4. Numerical results and discussion

Assume that the heat flux is elliptically distributed as follows

$$q(r) = \begin{cases} Q_0 \sqrt{1-r^2} & \text{for } r < 1 \\ 0 & \text{for } r \geq 1 \end{cases} \quad (4.1)$$

where $r = r^*/a = 1$ is radius of the circle heat zone and the heat flux (4.1) in the Hankel transform space takes the form (Gradshteyn and Ryzhik, 2015)

$$\tilde{q}(s) = \sqrt{\frac{\pi}{2}} Q_0 \frac{J_{3/2}(s)}{s^{3/2}} \quad (4.2)$$

where $J_{3/2}(s)$ is the Bessel function.

The analysis of the original relations in Case A (or A') shows that the solution of the problem of modeling of the inhomogeneous coating by the package of homogeneous layers depends on three (Case A) or four (Case A') dimensionless parameters: thickness of the coating h , ratio of heat conductivity coefficients on the surfaces of the non-homogeneous half space and the substrate K_S/K_0 , parameter α (only for Case A') and the number of layers in the package n . A similar solution obtained for an inhomogeneous coating with regard to the continuous dependence of thermal properties on the coordinate is independent of the parameter n . In what follows, we assume that $h = 0.4$, $K_0/K_S = 2, 4$, or 8 , $\alpha = 1$ (only for Case A'), and $n = 10, 20, 40$, or 80 .

The temperature and the heat flux in the radial direction r on the considered nonhomogeneous surface are shown in Figs. 2 and 3 ((a) – Case A, (b) – Case A'). In this figures, the continuous lines correspond to the solution of the problem with continuous variation of the thermal properties. The rhombi correspond to the results obtained for the package formed by 40 homogeneous layers. The results of calculations presented in Fig. 2 show good agreement between the solutions obtained using the analyzed two models of the coating. As follows from Fig. 3, the maximum absolute error of calculation of the radial heat flux component can be observed on the end of the heated zone for $r = 1$.

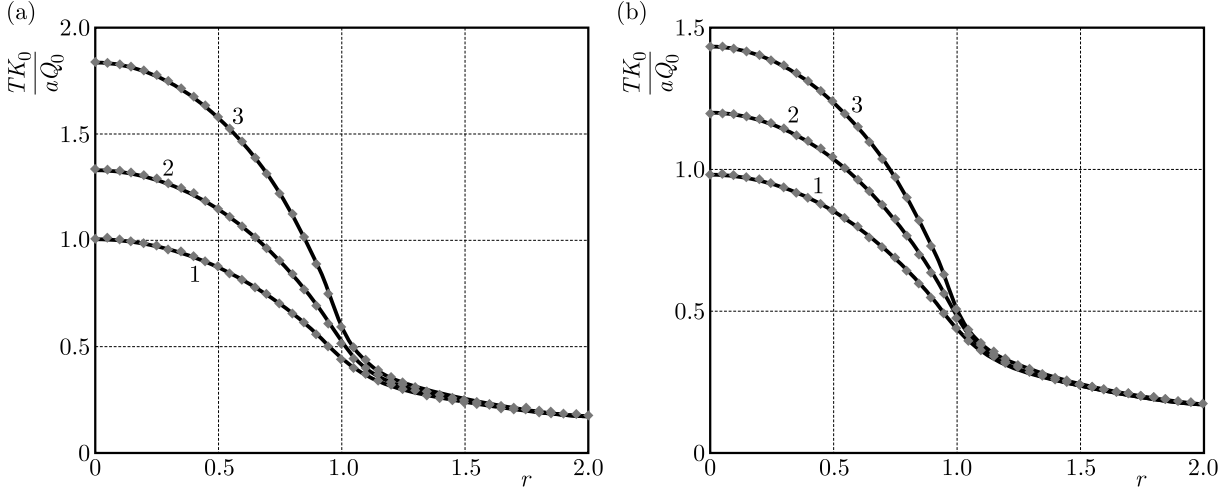


Fig. 2. The dimensionless temperature distribution on the surface $z = h$: (a) – Case A, (b) – Case A';
 1 – $K_0/K_S = 2$, 2 – $K_0/K_S = 4$, 3 – $K_0/K_S = 8$; $h = 0.4$

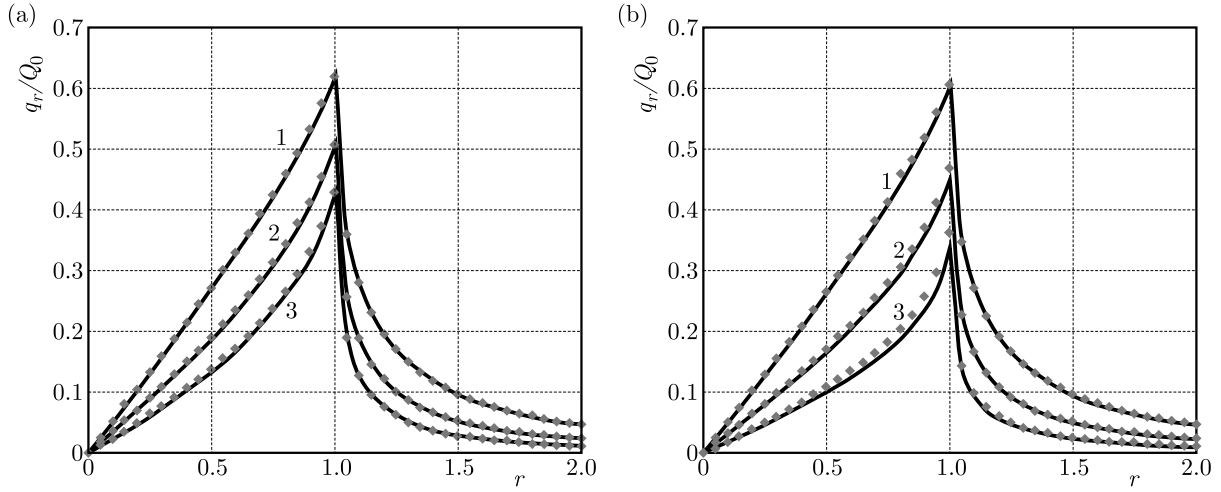


Fig. 3. The dimensionless radial heat flux on the surface $z = h$: (a) – Case A, (b) – Case A';
 1 – $K_0/K_S = 2$, 2 – $K_0/K_S = 4$, 3 – $K_0/K_S = 8$; $h = 0.4$

The values of the radial heat flux in this point are presented in Table 1. The analytical solution is presented in the rows of Table 1 with $n \rightarrow \infty$. The relative error of their evaluation with the help of modeling of the inhomogeneous coating by the package of n homogeneous layers is given in columns with $n = 10, 20, 40$, and 80 . It is easy to see that as the number of layers becomes twice larger, the corresponding error becomes almost twice lower. In the case where there are 80 layers in the package and $K_0/K_S \leq 8$, the error of finding the heat flux at the point $r = 1, z = h$ does not exceed 2.2%.

Estimating the original relations, we conclude that the distributions of temperature and heat flux in the problem of homogenized coating (Case C) depend on four dimensionless parameters: thickness of the coating h , ratios of heat conductivity coefficients K_I/K_0 and K_{II}/K_0 and the ratio of the thicknesses of layers in the strip of periodicity h_I/h_{II} . Similar distributions for the non-uniform coating additionally depend on the number of layers in the coating n . To decrease the number of input parameters, we assume that the thermal properties of one layer in the strip of periodicity coincide with the thermal properties of the base ($K_I/K_0 = 1$ or $K_{II}/K_0 = 1$) and the thicknesses of all layers in the stack are identical ($h_I/h_{II} = 1$). We also assume that K_0/K_I (or K_0/K_{II}) = 4, $h = 0.2, 0.4$, or 0.8 , and $n = 10, 20, 40$, or 80 .

Table 1. The dimensionless radial heat flux at the point $r = 1$, $z = h$ ($n \rightarrow \infty$) and the errors of their evaluation as a result of modeling of the inhomogeneous coating by the package of n homogeneous layers $n = 10, 20, 40$, and 80

K_0/K_S	$n = 10$	$n = 20$	$n = 40$	$n = 80$	$n \rightarrow \infty$
Case A					
2	2.79%	1.43%	0.68%	0.29%	0.6169
4	5.40%	2.73%	1.29%	0.54%	0.5021
8	7.79%	3.90%	1.82%	0.71%	0.4236
Case A'					
2	3.95%	2.03%	0.98%	0.43%	0.6022
4	11.00%	5.68%	2.72%	1.14%	0.4562
8	23.00%	11.97%	5.65%	2.18%	0.3435

The dimensionless temperature at the centre of the heating area for different thicknesses of the coating and different numbers of layers is presented in Table 2. The temperature calculated for the homogenized model is in the last column. The relative differences between the temperature in the non-homogeneous coating and the temperature in the homogenized coating are presented in columns with $n = 10, 20, 40$, and 80 . The upper numbers in cells have been calculated for the case $K_0/K_I = 4$, $K_0/K_{II} = 1$, the lower numbers were obtained for the case $K_0/K_I = 1$, $K_0/K_{II} = 4$. It can be seen that as the number of layers becomes twice larger, the errors become twice lower then. For the same value of the parameter $\delta = h/n$ (for example: $h = 0.2$, $n = 10$; $h = 0.4$, $n = 20$; and $h = 0.8$, $n = 40$), these errors are in the same order of magnitude.

Table 2. The dimensionless temperature at the centre of the heating zone at the point $r = 0$, $z = h$ ($n \rightarrow \infty$) and the errors of their evaluation as a result of modeling of the inhomogeneous coating by the package of n homogeneous layers $n = 10, 20, 40$, and 80

h	$n = 10$	$n = 20$	$n = 40$	$n = 80$	$n \rightarrow \infty$
0.2	1.12%	0.56%	0.28%	0.14%	1.0841
	-1.13%	-0.56%	-0.28%	-0.14%	
0.4	3.35%	1.67%	0.83%	0.41%	1.2481
	-3.26%	-1.64%	-0.83%	-0.42%	
0.8	7.99%	3.92%	1.94%	0.96%	1.3887
	-7.31%	-3.76%	-1.90%	-0.96%	

Figures 4a and 4b show the dimensionless radial heat flux as functions of z for $r = 1$ and two numbers of layers ($n = 20$ and $n = 40$). In Fig. 4, the rhombi mark the numerical results obtained for the non-homogeneous laminated coating, whereas the solid lines correspond to the homogenized coating. It should be emphasized that in the case of homogenized coating, we do not know which layer of the slip of periodicity is located at the analyzed point of the coating. Hence, the radial heat flux at every point of the coating is described by the two curves. Curves 1 and 2 correspond to the heat flux acting in the layers with smaller and larger heat conductivity coefficients, respectively. In the homogeneous substrate, curves 1 and 2 coincide.

Comparing the heat flux obtained in both analyzed problems, we conclude that only in the case of the heat flux acting in the homogeneous substrate we get deviations comparable with the deviations of temperature. In the layers of the coating, the deviations of heat flux vary from 1%-5% ($K_0/K_I \leq 4$, $n = 20$) up to 10%-20% for the heat flux acting on the boundary of the region of heating. The indicated deviations strongly depend on the gradient of the analyzed parameter in the investigated layer of the slip of periodicity, which explains the following obse-

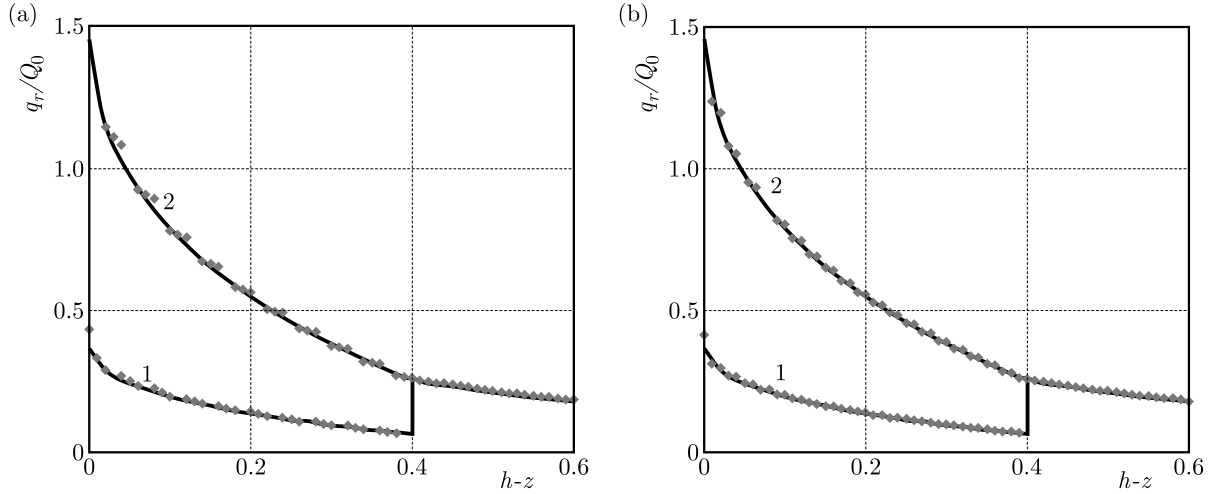


Fig. 4. The dimensionless radial heat flux on the line $r = 1$: (a) – $n = 20$, (b) – $n = 40$; $K_0/K_I = 4$, $h = 0.4$, $h_I/h_{II} = 1$

rvations: in the layers with lower heat conductivity coefficients, the deviations are much smaller (Fig. 4) and the maximum deviations are observed at the point $(1, h)$. As could be expected, the agreement between the solutions improves as the number of layers in the coating increases.

5. Conclusions

This paper provides the solution to the problem of the inhomogeneous half-space heated by the heat flux. It is shown that the solution to the problem for a package of 20-80 homogeneous layers is in good agreement with the analytical solution to the problem for the coating whose dependence of the heat conductivity coefficient on the coordinate z is described by an exponential (or power) function. This is a strong argument for the possibility of modeling of the gradient coating with continuous variation of thermal and mechanical properties by a package of homogeneous layers.

It is shown that the solution of the axisymmetric problem of heat conductivity for the half-space with a laminated coating of the periodic structure heated by heat flux is in good agreement with the solution of the problem in which the coating is modeled by a homogenized coating. The smallest deviations are obtained while finding the temperature and heat flux in the homogeneous substrate.

A. Appendix

A system of linear equations for determination of the functions $\hat{t}_i(s)$, $i = 0, 1, 2$:

— Case A

$$\begin{aligned} -\hat{t}_0(s) + \hat{t}_1(s) + \hat{t}_2(s) &= 0 \\ -\hat{t}_0(s) + \alpha^{(-)} s^{-1} \hat{t}_1(s) + \alpha^{(+)} s^{-1} \hat{t}_2(s) &= 0 \\ \alpha^{(-)} s^{-1} \hat{t}_1(s) \exp(\alpha^{(-)} h) + \alpha^{(+)} s^{-1} \hat{t}_2(s) \exp(\alpha^{(+)} h) &= 1 \end{aligned} \quad (\text{A.1})$$

— Case A'

$$\begin{aligned} -\hat{t}_0(s) + \hat{t}_1(s) c^p I_p(sc) + \hat{t}_2(s) c^p K_p(sc) &= 0 \\ \hat{t}_0(s) \mp \hat{t}_1(s) c^p I_{p-1}(sc) \pm \hat{t}_2(s) c^p K_{p-1}(sc) &= 0 \\ \hat{t}_1(s) (c \pm h)^p I_{p-1}(s(c \pm h)) - \hat{t}_2(s) (c \pm h)^p K_{p-1}(s(c \pm h)) &= \pm 1 \end{aligned} \quad (\text{A.2})$$

— Case C

$$\begin{aligned} -\hat{t}_0(s) + \hat{t}_1(s) \sinh(sp_1 h) + \hat{t}_2(s) \cosh(sp_1 h) &= 0 \\ K_0(K_c p_1)^{-1} \hat{t}_0(s) + \hat{t}_1(s) \cosh(sp_1 h) + \hat{t}_2(s) \sinh(sp_1 h) &= 0 \\ \hat{t}_1(s) &= -1 \end{aligned} \quad (\text{A.3})$$

A system of linear equations for determination of the functions $\hat{t}_i(s)$, $i = 0, 1, \dots, 2n$ in Case B

$$\begin{aligned} -\hat{t}_0(s) + \hat{t}_1(s) \sinh(sh_1) + \hat{t}_2(s) \cosh(sh_1) &= 0 \\ K_0 K_1^{-1} \hat{t}_0(s) + \hat{t}_1(s) \cosh(sh_1) + \hat{t}_2(s) \sinh(sh_1) &= 0 \\ -\hat{t}_{2i}(s) + \hat{t}_{2i+1}(s) \sinh(sh_{i+1}) + \hat{t}_{2i+2}(s) \cosh(sh_{i+1}) &= 0 \quad i = 1, \dots, n-1 \\ -K_i K_{i+1}^{-1} \hat{t}_{2i-1}(s) + \hat{t}_{2i+1}(s) \cosh(sh_{i+1}) + \hat{t}_{2i+2}(s) \sinh(sh_{i+1}) &= 0 \quad i = 1, \dots, n-1 \\ \hat{t}_{2n-1}(s) &= -1 \end{aligned} \quad (\text{A.4})$$

Acknowledgments

This work was carried out within the project “selected problems of thermomechanics for materials with temperature dependent properties”. The project was financed by the National Science Centre awarded based on the decision number DEC-2013/11/D/ST8/03428.

References

1. ABRAMOWITZ M., STEGUN I.A., 1964, *Handbook of Mathematical Functions: with Formulas, Graphs, and Mathematical Tables*, United States Department of Commerce, National Bureau of Standards
2. BARIK S.P., KANORIA M., CHAUDHURI P.K., 2008, Steady state thermoelastic contact problem in a functionally graded material, *International Journal of Engineering Science*, **46**, 775-789
3. CHOI H.J., PAULINO G.H., 2008, Thermoelastic contact mechanics for a flat punch sliding over a graded coating/substrate system with frictional heat generation, *Journal of the Mechanics and Physics of Solids*, **56**, 4, 1673-1692
4. DIAO D.F., 1999, Finite element analysis on local yield map and critical maximum contact pressure for yielding in hard coating with an interlayer under sliding contact, *Tribology International*, **32**, 25-32
5. DIAO D.F., KATO K., HAYASHI K., 1994, The maximum tensile stress on a hard coating under sliding friction, *Tribology International*, **27**, 4, 267-272
6. FARHAT Z.N., DING Y., NORTHWOOD D.O., APLAS A.T., 1997, Nanoindentation and friction studies on Ti-based nanolaminated films, *Surface and Coatings Technology*, **89**, 24-30
7. GRADSHTEYN I.S., RYZHIK I.M., 2015, *Table of Integrals, Series and Products*, Academic Press
8. GULER M.A., ERDOGAN F., 2004, Contact mechanics of graded coatings, *International Journal of Solids and Structures*, **41**, 3865-3889
9. GULER M.A., ERDOGAN F., 2006, Contact mechanics of two deformable elastic solids with graded coatings, *Mechanics of Materials*, **38**, 633-647
10. KE L.-L., WANG Y.-S., 2006, Two-dimensional contact mechanics of functionally graded materials with arbitrary spatial variations of material properties, *International Journal of Solids and Structures*, **43**, 18/19, 5779-5798
11. KE L.-L., WANG Y.-S., 2007, Two-dimensional sliding frictional contact of functionally graded materials, *European Journal of Mechanics – A/Solids*, **26**, 171-188

12. KULCHYTSKY-ZHYHAILO R., BAJKOWSKI A., 2012, Analytical and numerical methods of solution of three-dimensional problem of elasticity for functionally graded coated half-space, *International Journal of Mechanical Sciences*, **54**, 105-112
13. KULCHYTSKY-ZHYHAILO R., BAJKOWSKI A., 2015, Three-dimensional analytical elasticity solution for loaded functionally graded coated half-space, *Mechanics Research Communications*, **65**, 43-50
14. KULCHYTSKY-ZHYHAILO R., MATYSIAK S.J., 2005, On some heat conduction problem in a periodically two-layered body. Comparative results, *International Communications in Heat and Mass Transfer*, **32**, 3-4, 332-340
15. LIU J., KE L.-L., WANG Y.-S., 2011, Two-dimensional thermoelastic contact problem of functionally graded materials involving frictional heating, *International Journal of Solids and Structures*, **48**, 18, 2536-2548
16. LIU J., KE L.-L., WANG Y.-S., YANG J., ALAM F., 2012, Thermoelastic frictional contact of functionally graded materials with arbitrarily varying properties, *International Journal of Mechanical Sciences*, **63**, 1, 86-98
17. LIU T.-J., WANG Y.-S., 2008, Axisymmetric frictionless contact problem of a functionally graded coating with exponentially varying modulus, *Acta Mechanica*, **199**, 151-165
18. LIU T.-J., WANG Y.-S., 2009, Reissner-Sagoci problem for functionally graded materials with arbitrary spatial variation of material properties, *Mechanics Research Communications*, **36**, 322-329
19. LIU T.-J., WANG Y.-S., ZHANG C., 2008, Axisymmetric frictionless contact of functionally graded materials, *Archive of Applied Mechanics*, **78**, 267-282
20. MATYSIAK S., KULCHYTSKY-ZHYHAILO R., PERKOWSKI D., 2011, Reissner-Sagoci problem for a homogeneous coating on a functionally graded half-space, *Mechanics Research Communications*, **38**, 4, 320-325
21. MATYSIAK S.J., WOŹNIAK C., 1987, On the modelling of heat conduction problem in laminated bodies, *Acta Mechanica*, **65**, 223-238
22. SNEDDON I.N., 1966 The Reissner-Sagoci problem, *Proceedings of the Glasgow Mathematical Association*, **7**, 136-144
23. VOEVODIN A.A., IARVE E.V., RAGLAND W., ZABINSKI J.S., DONALDSON S., 2001, Stress analyses and in-situ fracture observation of wear protective multilayer coatings in contact loading, *Surface and Coatings Technology*, **148**, 38-45
24. WOŹNIAK C., 1987, A nonstandard method of modelling of thermoelastic periodic composites, *International Journal of Engineering Science*, **25**, 483-499

Manuscript received January 31, 2017; accepted for print July 31, 2017

A PREDICTION METHOD FOR LOAD DISTRIBUTION IN THREADED CONNECTIONS

DONGMEI ZHANG

School of Mechanical and Electrical Engineering, North University of China, Taiyuan, China

e-mail: dongmei_zhang@163.com

SHIQIAO GAO, SHAOHUA NIU, HAIPENG LIU

State Key Laboratory of Explosion Science and Technology, Beijing Institute of Technology, Beijing, China

A new method has been developed for predicting the load distribution along the thread portion of a bolt and nut connection. The calculated results were validated by comparison with three-dimensional finite element analysis and Yamamoto's method. It was shown that the load distribution predicted by the model in this paper was in good agreement with the results from finite element model, and the load ratio on the first thread by the prediction model and finite element model was slightly larger than the results from Yamamoto's method. In addition, the results of calculation and finite element analysis indicated that the decreasing of the lead angle could improve the load distribution, the increasing of the length of thread engaged could significantly improve the load bearing capacity of the first thread, and the adopting of a material with low stiffness for the nut with respect to the bolt could improve the load distribution slightly.

Keywords: load distribution, threaded connections, finite element analysis

1. Introduction

The bolted joint is a typical connection that is widely used for construction of structures from components. In order to ensure functionality of the joint, the load distribution in threaded connections is of concern.

The load distribution in threaded connections has been studied since the beginning of the century, but only a few of the most essential papers are referenced here (Goodier, 1940; Hetenyi, 1943; Motosh, 1975; Kenny and Patterson, 1985; Brutti and D'Eramo, 1987; Patterson and Kenny, 1986). The Sopwith (1948) theory for predicting the load distribution of thread fasteners is the most well known analytical model. The action of a number of strains is formulated by the axial extension of the bolt and compression of the nut. These strains include bending deflection of the thread, axial recession due to radial compression of the threads, and axial recession due to axial contraction of the bolt and expansion of the nut caused by radial pressure of the joints. Alternatively, Yamamoto (1980) proposed a procedure for calculating the deflection due to bending moment, shear loading and radial contraction and expansion on the bolt and the nut.

Due to the progress of the modern finite element method, the solution of contact problem becomes possible by using finite element software. Grosse and Mitchell (1990), Wileman *et al.* (1991), Lehnhoff and Wistehuff (1996), Chaaban and Muzzo (1991) and Chaaban and Jutras (1992) studied stresses in threaded connections by axisymmetrical finite element models by ASME Code. In order to investigate the helical effect on the thread connection, Chen and Shih (1999) built a three-dimensional bolt-nut assembly by ABAQUS. But there was a small hole on

the center of the bolt, which slightly reduced the area of the applied load. Moreover, Eraslan and Inan (2010) built 3D finite element models of screws by Solidworks.

In order to achieve a more convenient prediction for the load distribution in screw threads, we developed a new analytical model to calculate the load distribution in the thread connection. Comparing the previous methods, especially Yamamoto's method which includes five deflections, there are only two main thread deflections in our method. In addition, we fully consider the ununiformity of load distribution on thread and use unit deflection per unit width under unit force. Meanwhile, a three-dimensional finite element model of the bolt-nut assembly is built to validate the prediction method.

2. The new analytical model

According to Sopwith's theory, the ISO triangle thread can be simplified into a cantilever beam with a variable cross section. The strain in the thickness direction is considered to be zero, namely, it is a plane strain problem. A coordinate system for the thread under axial concentrated load is established. The length direction of the thread is the y -axis, the depth direction is the x -axis, and the origin is located at the root of the thread, as shown in Fig. 1a. The original cross section of the thread is a triangle. The semi-angle of the thread is α , the thread length is $2a$, and the pitch diameter is D , as shown in Fig. 1b.

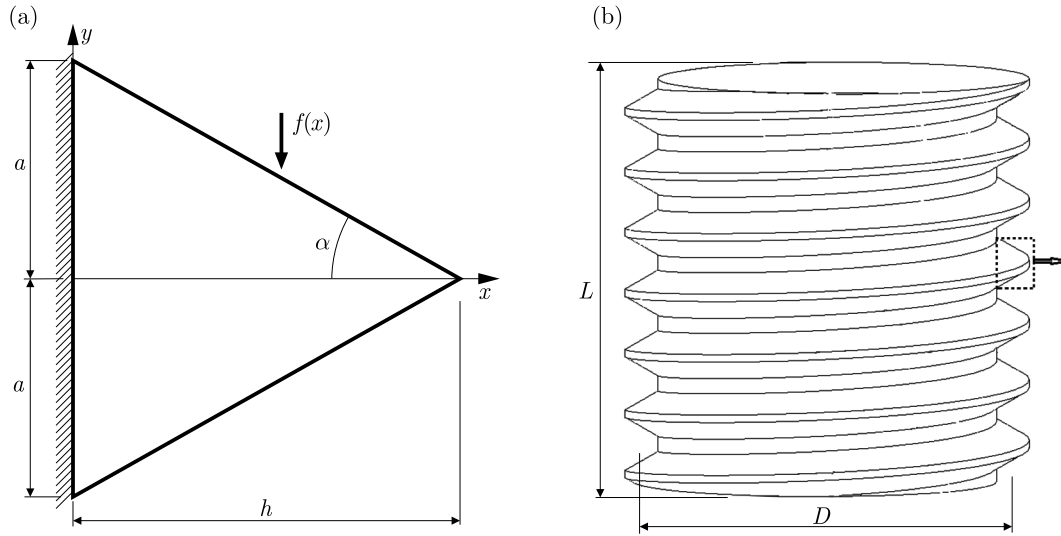


Fig. 1. (a) Thread structure and coordinate system, (b) bolt structure

The geometric equation of the upper half of the thread is

$$y = a - kx \quad (2.1)$$

where $k = \tan \alpha$ and $\alpha = 30^\circ$.

The geometric equation of the lower half of the thread is

$$y = kx - a \quad (2.2)$$

The moment of inertia of one thread is

$$I(x) = \iint_{S(x)} y^2(x) dS = \frac{2\pi D}{3} (a - kx)^3 \quad (2.3)$$

where $a = kh$, h is depth of the thread (as shown in Fig. 1a), therefore

$$I(x) = \iint_{S(x)} y^2(x) dS = \frac{2\pi D}{3} k^3 (h - x)^3 \quad (2.4)$$

2.1. The elastic deflection of thread

According to Sopwith's theory, the thread under axial loading will deform due to several reasons. Owing to the above assumption, these deflections mainly include bending and shearing deflection of the thread. An ISO triangle thread can be seen as a cantilever beam under a concentrated load P at $x = l_1$, which is shown in Fig. 2. The bending deflection δ_1 and shearing deflection δ_2 along the axial direction at $x = l_1$ can be obtained by the following functions.

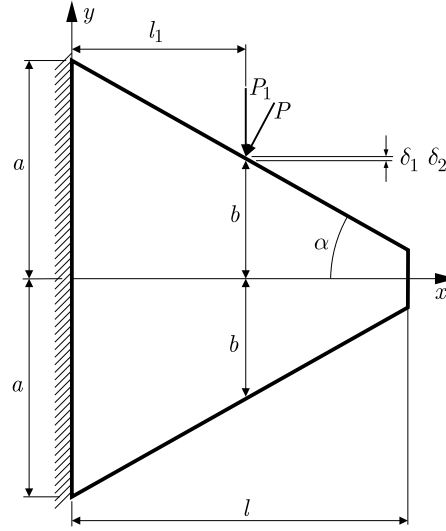


Fig. 2. Bending deflection and shearing deflection

2.1.1. The deflection due to bending moment

For a thread shown in Fig. 2, according to the theory of mechanics of materials, the static bending equation is

$$EI(x) \frac{\partial^2 w}{\partial x^2} = P_1(l_1 - x) \quad x < l_1 \quad (2.5)$$

where P_1 is the axial force on one thread, $I(x)$ is the moment of inertia, l_1 is the distance from the action point of the force to the root of the thread, E is Young's modulus and w is the bending deflection. Substituting Eq. (2.4) into (2.5) leads to

$$\frac{\partial^2 w}{\partial x^2} = \frac{3P_1}{2\pi DEk^3} \frac{l_1 - x}{(x - l)^3} \quad x < l_1 \quad (2.6)$$

where l is height of the thread as shown in Fig. 2.

Primary integration of Eq. (2.6) is conducted in accordance with the assumption that the deflection angle at the root of the thread is zero, i.e., the boundary condition $\partial w / \partial x = 0$ at $x = 0$ and the deflection angle can be expressed as

$$\frac{\partial w}{\partial x} = \frac{-3P_1}{2\pi DEk^3} \left(\frac{1}{x - l} + \frac{l - l_1}{2(x - l)^2} + \frac{1}{l} - \frac{l - l_1}{2l^2} \right) \quad x < l_1 \quad (2.7)$$

Primary integration of Eq. (2.7) is conducted on the assumption that the displacement at the root of the thread is zero, i.e., the boundary condition $w = 0$ at $x = 0$ is

$$w = \frac{-3P_1}{2\pi DEk^3} \left[\ln \frac{l-x}{l} - \frac{l-l_1}{2(x-l)} + \left(\frac{1}{l} - \frac{l-l_1}{2l^2} \right) x - \frac{l-l_1}{2l} \right] \quad x < l_1 \quad (2.8)$$

Under the unit force, the bending deflection of one thread at $x = l_1$ is

$$\delta_1 = \frac{-3}{2\pi DEk^3} \left[\ln \frac{l-l_1}{l} + \frac{1}{2} + \left(\frac{1}{l} - \frac{l-l_1}{2l^2} \right) l_1 - \frac{l-l_1}{2l} \right] \quad (2.9)$$

Because the deformation of thread is treated as a plane deformation, under the unit force, the unit deflection due to bending moment can be expressed as

$$\delta_1 = \frac{-3(1-\nu^2)}{2\pi DEk^3} \left[\ln \frac{l-l_1}{l} + \frac{1}{2} + \left(\frac{1}{l} - \frac{l-l_1}{2l^2} \right) l_1 - \frac{l-l_1}{2l} \right] \quad (2.10)$$

2.1.2. The deflection due to shear loading

At $x = l_1$, the shear stress for the thread can be expressed as

$$\tau(x) = \frac{P_1}{\pi D} \frac{1}{2(a-kx)} \quad (2.11)$$

Therefore, the shearing deflection of one thread should be

$$\Delta(x) = \frac{\tau(x)}{G} L \quad (2.12)$$

where the L is total length of the thread as shown in Fig. 1b.

The shearing deflection of the unit length ($L \equiv 1$) is

$$\delta_U(x) = \frac{\tau(x)}{G} \quad (2.13)$$

where G is shear modulus, and $G = E[2(1+\nu)]$. Therefore, the unit shearing deflection of one thread under the unit force ($P_1 \equiv 1$) can be expressed as

$$\delta(x) = \frac{1+\nu}{E\pi D} \frac{1}{a-kx} \quad (2.14)$$

According to the boundary condition $\delta(x) = 0$ for $x = 0$ and $\delta(x) = \delta_2$ for $x = l_1$, integration of Eq. (2.14) leads to

$$\delta_2 = \frac{1+\nu}{E\pi D} \int_0^{l_1} \frac{dx}{a-kx} = \frac{1+\nu}{kE\pi D} \ln \frac{a}{b} \quad (2.15)$$

According to Yamamoto (1980), the load P is located at the center of the original triangle of the thread, namely

$$l_1 = \frac{1}{2}l \quad b = \frac{1}{2}a \quad (2.16)$$

Therefore, for the bolt and nut under the unit force, substituting of Eqs. (2.16) into Eqs. (2.10) and (2.15), respectively, the elastic deformation of unit length thread in the direction of the helix is

$$\begin{aligned} \delta_b &= \delta_{1b} + \delta_{2b} = \frac{0.5(1-\nu_b^2) + 1.2(1+\nu_b)}{\pi DE_b} \\ \delta_n &= \delta_{1n} + \delta_{2n} = \frac{0.5(1-\nu_n^2) + 1.2(1+\nu_n)}{\pi DE_n} \end{aligned} \quad (2.17)$$

where δ_{1b} and δ_{2b} represent the bending and shearing deflection of bolt, respectively, δ_{1n} and δ_{2n} represent the bending and shearing deflection of the nut. For the ISO triangle thread, there is $k = \tan 30^\circ$. For the threaded connection structure composed of the bolt and nut, the total elastic deformation of the unit length thread in the direction of the helix is

$$\delta_y = \delta_b + \delta_n \quad (2.18)$$

where δ_b and δ_n represent the total deflection of the bolt and nut, respectively.

2.2. Thread stiffness

For the thread on the bolt, the stiffness of the unit length thread under the unit force in the direction of the helix is

$$k_{bu} = \frac{1}{\delta_b} \quad (2.19)$$

Because the total length of the thread is πD , the total axial stiffness of the thread on the bolt under the unit force is

$$K_b = \pi D k_{bu} = \frac{\pi D}{\delta_b} \quad (2.20)$$

Similarly, for the thread on the nut, the stiffness of the unit length under the unit force in the direction of the helix is

$$k_{nu} = \frac{1}{\delta_n} \quad (2.21)$$

The thread stiffness of the thread on the nut under the unit force is

$$K_n = \pi D k_{nu} = \frac{\pi D}{\delta_n} \quad (2.22)$$

If one thread is considered to be a spring, the threaded connection that consists of several threads is a parallel spring. Thus, for the bolt, the total stiffness of n thread is nK_b . If the pitch is p , then the stiffness of the unit axial length under the unit force is regarded as

$$k_{by} = \frac{K_b}{p} = \frac{\pi D k_{bu}}{p} \quad (2.23)$$

If the lead angle of the helix is β , then $\tan \beta = p/(\pi D)$. For the bolt and nut, the stiffness of the unit axial length under the unit force is respectively

$$k_{by} = \frac{k_{bu}}{\sin \beta} = \frac{1}{\delta_b} \sin \beta \quad k_{ny} = \frac{k_{nu}}{\sin \beta} = \frac{1}{\delta_n} \sin \beta \quad (2.24)$$

For the threaded connection structure composed of the bolt and nut, the total stiffness of the unit axial length is

$$k_y = \frac{1}{\frac{1}{k_{by}} + \frac{1}{k_{ny}}} = \frac{1}{(\delta_b + \delta_n) \sin \beta} = \frac{1}{\delta_y \sin \beta} \quad (2.25)$$

Because the stiffness is the ratio of the force to deflection, the axial deflection of the thread body is

$$\Delta_y = \frac{1}{k_y} \frac{\partial P}{\partial y} \quad (2.26)$$

where $\partial P/\partial y$ is the axial force on the unit length thread. The preceding equation indicates that the axial deflection of the thread body varies directly with load distribution.

2.3. Axial load distribution in threaded connection

Figure 3 shows that the threaded connection structure includes a fixed nut body and a bolt body. In the bolt body under a compressing force f_B , the force will be transferred to the nut body through the threads. The structure is elastic. Thus, the bolt body, the nut body or the thread body will exhibit deflection under the force. However, the forms of forces on the bolt body and the nut body differ from those on the thread body. Furthermore, their load distributions also vary. Thus, the deformation modes of the bolt body and the nut body differ from those of the thread body. However, the bolt body and the nut body are joined by the thread body. Thus, their deformations are compatible.

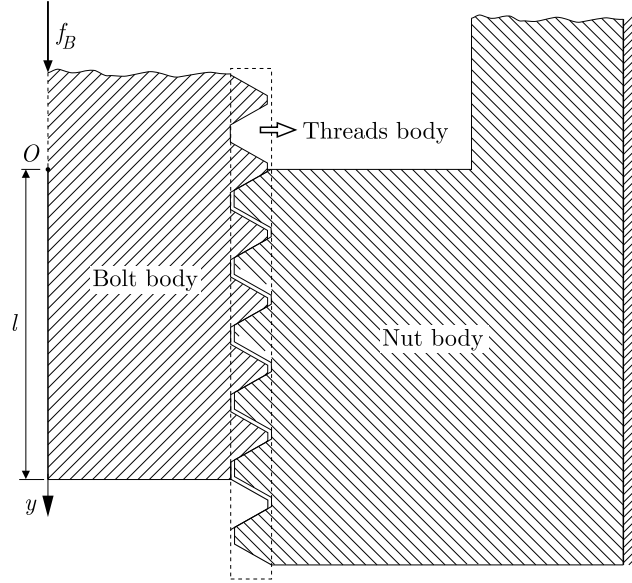


Fig. 3. Threaded connection structure

The region of the compressing force on the thread body ranges from 0 to l , where l is the engaged length of the bolted joint. Thus, the strain ε_b generated by the bolt body under the compressing force $f(y)$ at the location y is

$$\varepsilon_b = \frac{f(y)}{S_b E_b} \quad (2.27)$$

where S_b is the cross-sectional area of the bolt body.

Similarly, strain ε_n generated by the bolt body under the compressing force $f(y)$ is

$$\varepsilon_n = \frac{f(y)}{S_n E_n} \quad (2.28)$$

where S_n is the cross-sectional area of the nut body.

For the thread body, the load f is distributed along the direction of the helix and along the axial direction y . The thread deformation analysis indicates that the deflection and displacement of threads on the bolt body is related to the gradient of force distribution, i.e.,

$$\delta_b = \frac{1}{k_{by}} \frac{\partial f}{\partial y} \quad (2.29)$$

Similarly, the deflection of the thread body on the nut body is

$$\delta_n = \frac{1}{k_{ny}} \frac{\partial f}{\partial y} \quad (2.30)$$

Their displacement gradients are respectively

$$\frac{\partial \delta_b}{\partial y} = \frac{1}{k_{by}} \frac{\partial^2 f}{\partial y^2} \quad \frac{\partial \delta_n}{\partial y} = \frac{1}{k_{ny}} \frac{\partial^2 f}{\partial y^2} \quad (2.31)$$

In order to make the deformation compatible, ε_b , ε_n , δ_b and δ_n must meet the following relationship

$$\varepsilon_b + \varepsilon_n = \frac{\partial \delta_b}{\partial y} + \frac{\partial \delta_n}{\partial y} \quad (2.32)$$

Substitution of Eqs. (2.27), (2.28) and (2.31) into Eq. (2.32) leads to

$$\lambda^2 f = \frac{\partial^2 f}{\partial y^2} \quad (2.33)$$

where

$$\lambda = \sqrt{\frac{\frac{1}{S_b E_b} + \frac{1}{S_n E_n}}{\frac{1}{k_{ny}} + \frac{1}{k_{by}}}}$$

The solution to Eq. (2.32) is

$$f = C_1 \sinh \lambda y + C_2 \cosh \lambda y \quad (2.34)$$

By the boundary conditions $f(y) = f_B$ for $y = 0$ and $f(y) = 0$ for $y = l$, we can obtain

$$C_2 = f_B \quad C_1 = -\frac{\cosh \lambda l}{\sinh \lambda l} f_B$$

Substituting C_1 and C_2 into Eq. (2.34) leads to

$$f(y) = f_B \left(-\frac{\cosh \lambda l}{\sinh \lambda l} \sinh \lambda y + \cosh \lambda y \right) \quad (2.35)$$

where f_B is the load on the first thread of the bolt. The load along the axial direction y can be calculated by Eq. (2.35). This distribution is more precise than Yamamoto's method because we considered the load distribution along the helix of the screw.

3. Finite element model

A group of ISO metric screw threads M36 are used to study the load distribution and the effect of pitch, material and length of the thread engagement. The parameters of all screws are listed in Table 1. Commercial finite element software ANSYS is used for modeling and analysis. The model geometry is meshed by 8 node hexahedron elements (SOLID185). The contact and target elements are TARGE169 and CONTA172, respectively. The friction coefficient changes between 0.15 0.2 according to the material of the thread. Figure 4 shows 3-D finite element models of the standard bolt assembly and the stress distribution on the screw under the external load. There is no sliding between the bolt and nut threads because friction coefficients are large enough to prevent sliding. In the models, the axial loading is applied to the top surface of the bolt, and the outer bottom surface of nut is assumed fixed. Convergence study is carried out on the initial finite element model by decreasing the element size near the threads. The smallest element size is 0.25 mm by 0.25 mm and the total number of element is about 80000. There is no significant improvement in the accuracy by using smallest elements.

Table 1. Parameters of the thread

Speci- men No.	Nominal diameter of thread d [mm]	Pitch p [mm]	Engaged length of bolted joints l [mm]	Materials	
				bolt	nut
1	36	4	28	steel	steel
2	36	3	28		
3	36	2	28		
4	36	1.5	28		
5	36	4	24		
6	36	4	20		
7	36	4	16		
8	36	4	12		
9	36	4	28	steel	copper
10	36	4	28	steel	brass
11	36	4	28	steel	aluminum
12	36	4	28	aluminum	steel

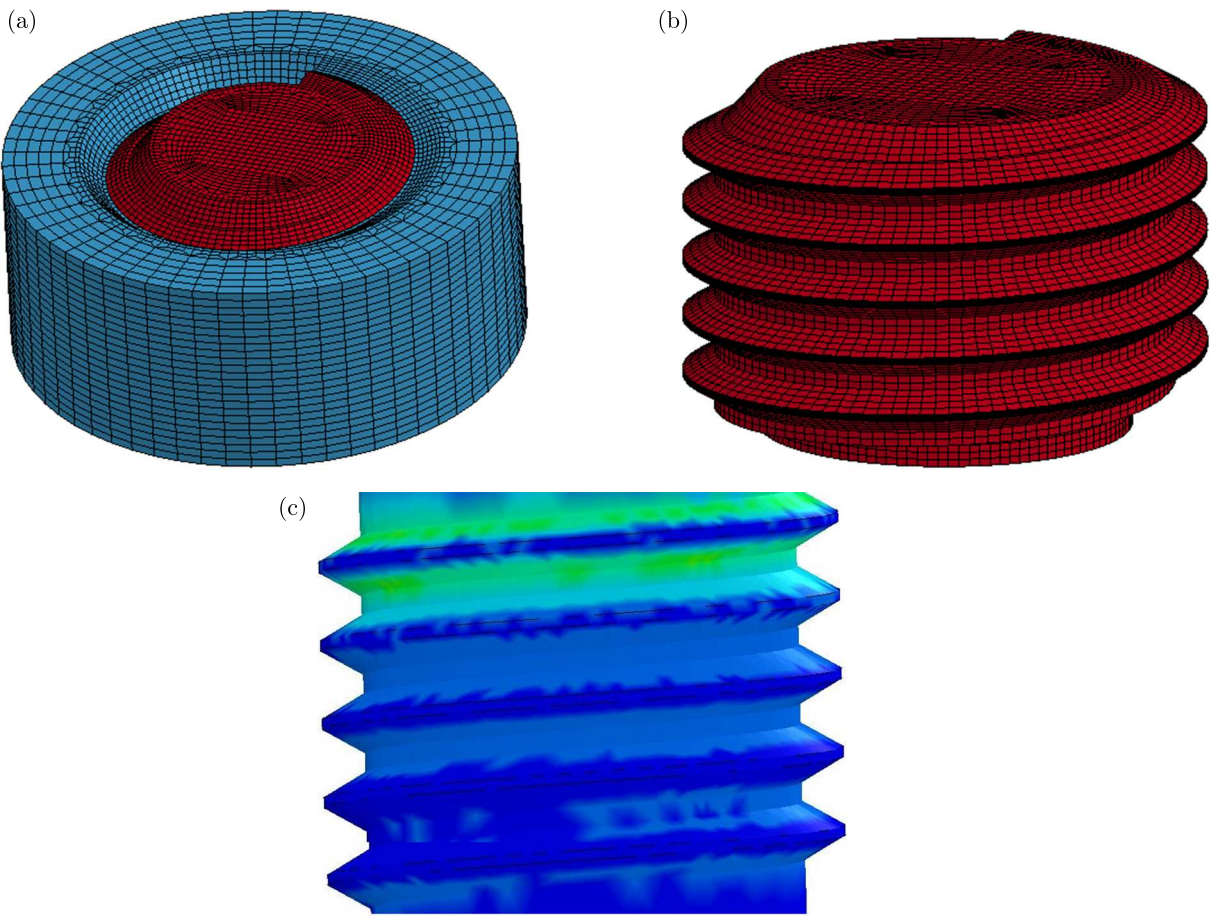


Fig. 4. 3-D model mesh of standard threaded connection: (a) bolted joint assembly, (b) bolt, (c) contour plot of the screw stress

Table 2. Parameters of material

Material	Young's modulus E [GPa]	Poisson's ratio ν [-]	Density ρ [kg/m ³]
Steel	211	0.269	7890
Copper	137	0.310	8980
Brass	105	0.320	8500
Aluminum	69	0.330	2700

An elastic material is used throughout this work. A uniform pressure loading p is applied to the top root surface of the bolt. So, the total force due to the applied pressure can be expressed as

$$f_B = p \frac{\pi d^2}{4} \quad (3.1)$$

where d is the nominal diameter of the bolt.

4. Result and discussion

For thread No. 1, the result of the load distribution on each thread by Yamamoto's method, finite element model and the prediction model developed in this paper can be shown in Fig. 5.

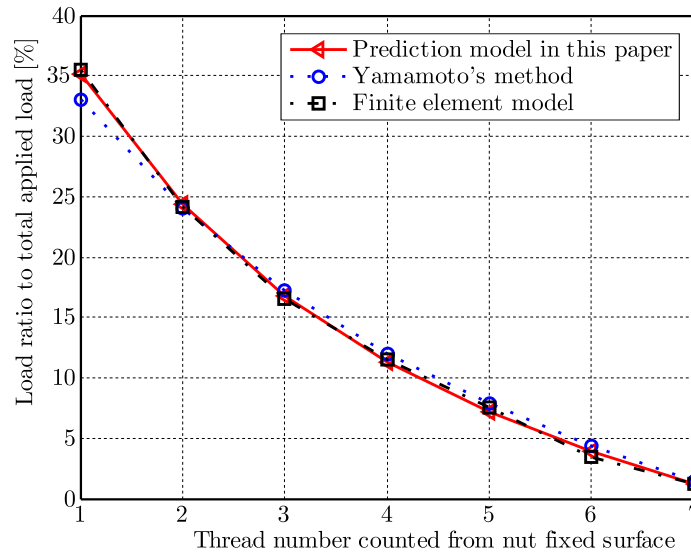


Fig. 5. The load ratio on each thread for bolted joints No. 1

Figure 5 shows that the load distribution obtained from the model in this paper are in a close agreement with the finite element analysis. It is a load corresponding to the pitch section of the thread. The load distribution with prediction from the analytical model and finite element model is shown to be slightly larger than the results of Yamamoto's method. For the FEM calculation, the axial component of stress is utilized for the load on thread and the load ratio is the ratio of the load on thread to the load on the surface of the bolt. The load on thread can be calculated by equation (2.32) for the prediction model, and it is the average value of some element (all the elements along the thread edge) for the FEM calculation. From the figure, we can see that the loading ratio is quite similar on each thread in the case of the analytical model and finite element model for all specimens.

There are four pitches which have been used in this Section, namely 4 mm, 3 mm, 2 mm, 1.5 mm, and the corresponding lead angles are 2.1804° , 1.6068° , 1.0511° , 0.7810° , respectively. The load ratio of the prediction model in this paper with different pitch in Fig. 6 shows that the decreasing of the pitch can improve the load distribution and reduces the load bearing on the first thread.

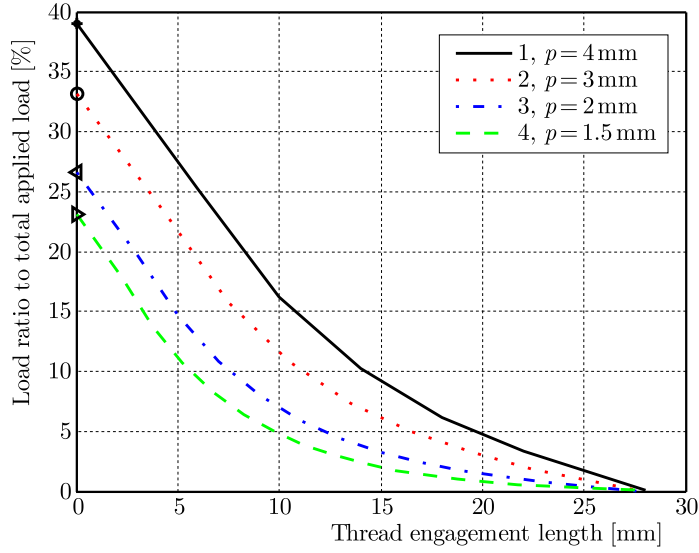


Fig. 6. The load ratio on each thread for bolted joints No. 1, 2, 3, and 4

Figure 7 is the load ratio of the prediction model and finite element model with length of thread engagement 28 mm, 24 mm, 20 mm, 16 mm, 12 mm, respectively. The figures show that the load ratio is modified greatly with the increasing of thread engagement length. And the longer the length of thread engagement, the smaller the load bearing on the first thread. But when the length is more than 20 mm, the effect is very slight.

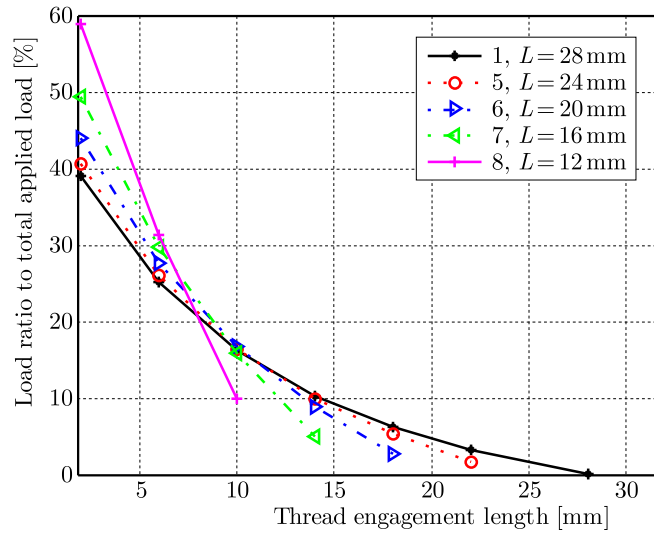


Fig. 7. The load ratio on each thread for bolted joints No. 1, 5, 6, 7 and 8

In addition, when Young's modulus of bolt E_b is larger than that of the nut E_n , the load distribution is improved slightly. The calculation result by the prediction model for specimens No. 1, 9, 10, 11, 12 whose bolts and nuts are made of different materials, are shown in Fig. 8.

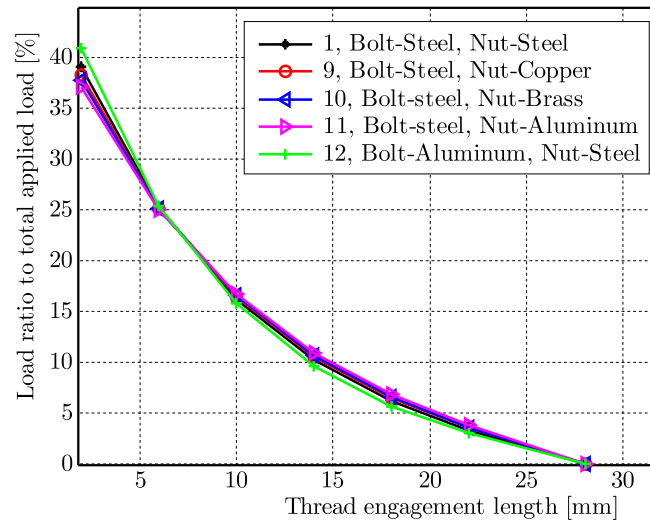


Fig. 8. The load ratio on each thread for bolted joints No. 1, 9, 10, 11 and 13

5. Conclusions

The load distributions on the thread connection by the analytical model and finite element model have been studied. The results can be concluded as follows.

1. The load distributions obtained from the model in this paper are in good agreement with finite element analysis and Yamamoto's method.
2. The results of the analytical model in this paper are nearer to the finite element analysis than Yamamoto's method, because we considered the load distribution along the helix of the screw.
3. The effect of pitch on the load distribution of the threaded assembly is very obvious. A decrease in the pitch not only can improve the load distribution, but also can reduce the load ratio in the first thread.
4. The load distribution of the first thread is significantly decreased by a properly increased length of the thread engagement.
5. Adopting a material with low stiffness for the nut with respect to the bolt can improve the load distribution slightly.

References

1. BRUTTI C., D'ERAMO M., 1987, Methods to evaluate load distribution in screw threads, *Proceedings of 2th Canadian Conference of Applied Mechanics*, Edmonton, 74-75
2. CHAABAN A., JUTRAS M., 1992, Static analysis of buttress threads using the finite element method, *Journal of Pressure Vessel Technology*, **114**, 209-212
3. CHAABAN A., MUZZO U., 1991, Finite element analysis of residual stresses in threaded end closure, *Journal of Pressure Vessel Technology*, **113**, 398-401
4. CHEN J.J., SHIH Y.S., 1999, A study of the helical effect on the thread connection by three dimensional finite element analysis, *Nuclear Engineering and Design*, **191**, 2, 109-116
5. ERASLAN O., INAN O., 2010, The effect of design on stress distribution in a solid screw implant: a 3D finite element analysis, *Clinical Oral Investigations*, **14**, 411-416
6. GOODIER J.N., 1940, The distribution of load on the threads of screws, *Transactions ASME*, **62**, 10-16

7. GROSSE I.R., MITCHELL L.D., 1990, Non-linear axial stiffness characteristic of axisymmetric bolted joint, *Journal of Mechanical Design*, **112**, 442-449
8. HETENYI M., 1943, A photoelastic study of bolt and nut fastenings, *Transactions ASME*, **65**, 93-100
9. KENNY B., PATTERSON E.A., 1985, Load and stress distribution in screw threads, *Experimental Mechanics*, **25**, 208-213
10. LEHNHOFF T.F., WISTEHUFF W.E., 1996, Non-linear effects on the stress and deformations of bolted joints, *Journal of Mechanical Design*, **118**, 54-58
11. MOTOSH N., 1975, Load distribution on threads of titanium tension nut and steel bolts, *Transactions ASME*, **97**, 162-166
12. PATTERSON E.A., KENNY B., 1986, A modification to the theory for the load distribution in conventional nuts and bolts, *Proceedings of the Institution of Mechanical Engineers*, **21**, 1, 17-23
13. SOPWITH D.G., 1948, The distribution of load in screw threads, *Proceedings of the Institution of Mechanical Engineers*, **159**, 373-383
14. WILEMAN J., CHOUDHURY M., GREEN I., 1991, Computation of member stiffness in bolted connections, *Journal of Mechanical Design*, **113**, 432-437
15. YAMAMOTO A., 1980, *The Theory and Computation of Threads Connection* (in Japanese), Yoken-do, Tokyo

Manuscript received June 12, 2016; accepted for print August 7, 2017

DETERMINATION OF THE INTERNAL RESISTANCE OF A HAMMER DRILL CHISEL

NIKOLAY NIKOLOV

Technical University – Sofia, Strength of Materials Department, Sofia, Bulgaria
e-mail: nyky@tu-sofia.bg

PETKO SINAPOV

Technical University – Sofia, Department of Mechanics, Sofia, Bulgaria
e-mail: p.sinapov@tu-sofia.bg

The present work examines damped oscillations of a chisel, represented as a distributed parameters system. The system is discretized with the finite element method. Rayleigh's law is used for the modelling of the resistance. The internal resistance of the mechanical system has been determined by an experiment, then enshrined in the numerical model. Comparison and analysis of the results have been made.

Keywords: free damped oscillations, FEM, Rayleigh damping matrix, damping coefficients

1. Introduction

Precise determination of the internal resistance is a crucial point in the research on the distributed parameter dynamics of mechanical systems. Without knowing its value, it would be impossible to study numerically different processes, such as free damped or forced oscillations, nonlinear oscillations, shock occurrences and others. The Rayleigh law is most commonly used to describe the internal resistance

$$\mathbf{C} = \alpha \mathbf{M} + \beta \mathbf{K} \quad (1.1)$$

where \mathbf{C} is the Rayleigh damping matrix, α is a coefficient taking into account the influence of the mass distribution on the resistance, β is a coefficient accounting for the influence of the system elasticity on the resistance, while \mathbf{M} and \mathbf{K} are, respectively, mass and stiffness matrices. According to many researchers (Stelzmann *et al.*, 2008), the coefficients α and β are to be determined for each specific structure. It turns out that by varying these two coefficients, certain oscillation frequencies could be suppressed, while others prevail. A number of studies have shown (Man and Corman, 1995) that the α -damping affects low frequencies, and the β -damping affects high frequencies, as shown in Fig. 1. A great advantage when using the Rayleigh law is that after orthogonal transformation the system of n differential equations, describing motion of the system, can be represented by n independent equations (Chowdhury and Dasgupta, 2003), i.e. it can break the connection between the equations.

Different methods could be used for determining the α and β (Craig and Kurdila, 2006; Alipour and Zareian, 2008; Adhikari, 2001). If ω_1^* and ω_2^* are the first two frequencies of the system damped oscillations, then for the most common method it is assumed that at both ends of the frequency range $[\omega_1^*; \omega_2^*]$ the damping ratio ξ has equal values (Fig. 1). When a mechanical system is dominated by free oscillations with frequencies within the mentioned range, the values of α and β are determined by the equations

$$\alpha = \xi \frac{2\omega_1^* \omega_2^*}{\omega_1^* + \omega_2^*} \quad \beta = \xi \frac{2}{\omega_1^* + \omega_2^*} \quad (1.2)$$

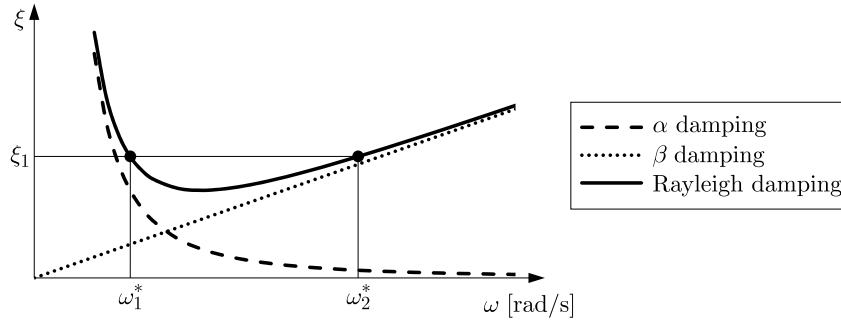


Fig. 1. Rayleigh damping

The damping ratio ξ depends on the material and the studied structure. Information about the value of ξ for steel can be found in the bibliography. For example, the following intervals from 0.02 to 0.08; from 0.02 to 0.03 and from 0.0008 to 0.0025 are given respectively in (Chowdhury and Dasgupta, 2003; Chopra, 1995; Dresig and Holzweissig, 2006). In (Mevada and Patel, 2016) ξ was experimentally determined and the obtained value was 0.0069. It was found by Stevenson (1980) that ξ depended on the dynamic values of the stresses and strains, and the value for steel was set to 0.01. In (Zare *et al.*, 2011) ξ has the value of 0.03 and in (Sangeetha *et al.*, 2014) ξ has the value of 0.2. It appears that for each structure the resistance is strictly individual and it often depends even on the operation mode.

The purpose of the present work is to model damping oscillations of the mechanical system once the internal resistance has been experimentally determined.

2. Research object

A schematic drawing of a hammer drill is shown on Fig. 2. It is well known that this type of machine use a set of working tools with different shape, size and weight. As parts of the mechanical system, these working tools also affect the force of the impact. Therefore, the working tools, just like the operating modes, are subject to optimization in order to maximize the machine efficiency. The present study is focused only on the chisel.

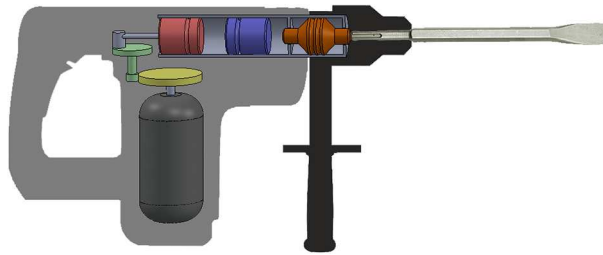


Fig. 2. Schematic drawing of a hammer drill

A suitable dynamic model has to be developed in order to give a numerical representation of the law for amending the force of impact. All parameters involved should be set down with their real values, preferably determined by an experiment.

After being created, the model should be validated with experimental data from the actual working process of the machine. The present study is the first step to the creation of such a model. It is aimed at determining the coefficients α and β of the working tool of the hammer drill.

3. Dynamic model

Drilling machines whose tool performs complex motion including rotation are examined in (Khulief *et al.*, 2005; Yigit *et al.*, 1998; Zare *et al.*, 2011). In our case, the chisel moves only in the axial direction and it is assumed that the oscillations along this axis will be the most significant. Bending and twisting vibrations due to additional factors at this stage are neglected. Figure 3 shows the studied mechanical system which consists of a chisel and support. The latter is a pair of metal jaws clenching the chisel.

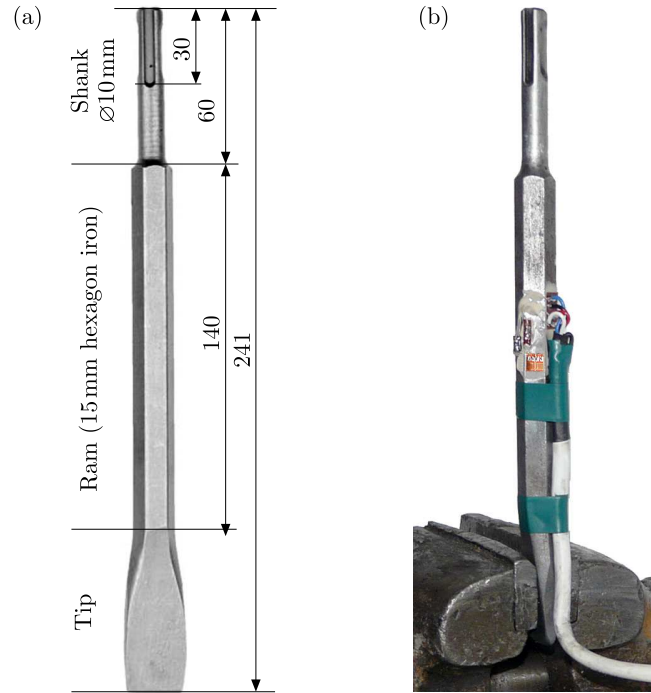


Fig. 3. Mechanical system: (a) sections and dimensions of the chisel, (b) fixing of the chisel

Figure 4 shows the dynamic model of the mechanical system. For the purpose of the modeling, the system is presented as a rod, fixed at its lower end, oscillating in the axial direction.

The movement of each section of the rod with constant cross-section is described with the following partial differential equation

$$\frac{E}{\rho} \frac{\partial^2 u_i(x, t)}{\partial x^2} - \frac{\partial^2 u_i(x, t)}{\partial t^2} = 0 \quad (3.1)$$

where E is the elasticity modulus, ρ – density of the material, $u_i(x, t)$ – coordinate, describing oscillations of the i -cross section of the rod. Since the cross section of the chisel is variable, it is divided into four sections, as shown in Fig. 3a (the dimensions are given in mm):

- upper part of the shank, with diameter 10 mm and cut out channels,
- lower part of the shank, cylindrical, with diameter 10 mm,
- ram – hexagonal, with diameter of the inscribed circle 15 mm,
- tip with a relatively complex shape and cross section, decreasing from the ram to the end.

The finite element method has been used for solving equation (3.1). The rod is represented by 15 finite elements, shown in Fig. 4. The tip is discretized with 3 finite elements and all the other areas – with 4 elements. The cross section of the upper part of the shank is reduced by 20% compared to its lower part, due to fixing channels. The lengths of the ram elements are chosen

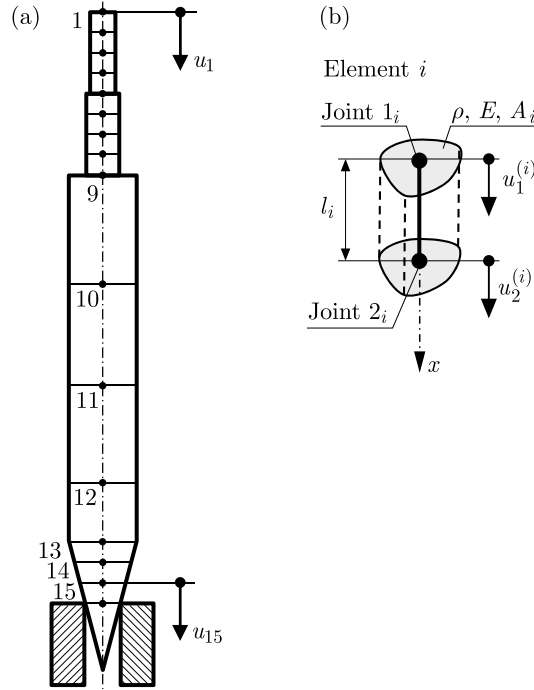


Fig. 4. Dynamic model with finite elements: (a) arrangement of the finite elements, (b) single finite element

in such a way as to obtain a node at the place of bonding of the strain gauges, as shown in Fig. 3b. The elements of the tip are 10 mm long and thus its lower part (No. 15 in Fig. 4a) reaches the support. The cross section area of each element at the top is set according to the actual geometry.

All finite elements are of type shown in Fig. 4b (Reddy, 1984; Rao, 2004; Stelzmann *et al.*, 2008). Each node has one degree of freedom, i.e. the finite element has two local degrees of freedom ($u_1^{(i)}$ and $u_2^{(i)}$). The mass and stiffness matrices for the finite element used are as follows

$$\mathbf{M}^{(e)} = \frac{\rho A_i l_i}{6} \begin{bmatrix} 2 & 1 \\ 1 & 2 \end{bmatrix} \quad \mathbf{K}^{(e)} = \frac{EA_i}{l_i} \begin{bmatrix} 1 & -1 \\ -1 & 1 \end{bmatrix} \quad (3.2)$$

It is more convenient to work with global coordinates for the formation of global matrices. The following connections between local and global coordinates should be taken into account during the transition to such global matrices

$$u_1^{(1)} = u_1 \quad u_2^{(1)} = u_1^{(2)} = u_2 \quad etc.$$

where $u^{(i)}$ ($i = 1, 2, \dots, 15$) are the global coordinates (Reddy, 1984). Thus, equations (3.1) turn into a system of 15 ordinary differential equations of the second order, which take into account the boundary conditions.

The differential equation describing motion of the mechanical system is

$$\mathbf{M}\ddot{\mathbf{q}} + \mathbf{C}\dot{\mathbf{q}} + \mathbf{K}\mathbf{q} = \mathbf{0} \quad (3.3)$$

where \mathbf{M} is the mass matrix (15×15), \mathbf{K} is the stiffness matrix (15×15), $\mathbf{C} = \alpha\mathbf{M} + \beta\mathbf{K}$ is the Rayleigh damping matrix, $\mathbf{q} = [u_1, u_2, \dots, u_{15}]^T$ is the coordinate vector, $\mathbf{0}$ is zero matrix (15×1).

The natural frequencies of the system are calculated in Matlab by solving equation (3.3) and without taking into account the internal resistance, i.e.

$$\mathbf{M}\ddot{\mathbf{q}} + \mathbf{K}\mathbf{q} = \mathbf{0} \quad (3.4)$$

Equation (3.4) is brought into a normal appearance (Genov *et al.*, 2007)

$$\dot{\mathbf{X}} = \tilde{\mathbf{A}}\mathbf{X} \quad (3.5)$$

by introducing the following vector

$$\mathbf{X} = [q, \dot{q}]^T \quad (3.6)$$

and the matrix $\tilde{\mathbf{A}}$ is

$$\tilde{\mathbf{A}} = \begin{bmatrix} \mathbf{O}_{15 \times 15} & \mathbf{E}_{15 \times 15} \\ -\mathbf{MK} & -\mathbf{MO}_{15 \times 15} \end{bmatrix} \quad (3.7)$$

In equation (3.7), $\mathbf{O}_{15 \times 15}$ is the zero matrix, $\mathbf{E}_{15 \times 15}$ is the identity matrix.

The natural frequencies of the system are obtained by determining the eigenvalues of the matrix $\tilde{\mathbf{A}}$ by *Q-R* algorithm – orthogonal projections (Watkins, 2004).

The first four values of the natural frequencies of the system thus obtained are given in Table 1.

Table 1. Natural frequencies

Natural frequencies	f_i [Hz]	ω_i [rad/s]
1	5640	35419
2	16920	106257
3	26810	168366
4	39530	248248

4. Influence of the internal resistance

It has been assumed that the occurrence of the first two natural frequencies at free oscillations in the longitudinal direction is physically possible in the research model. The interval in Fig. 1 has been chosen to be from 35419 to 106257 rad/s (according to Table 1). According to equations (1.1), different values of the coefficients α and β have been obtained for different values of the damping ratio ξ , as given in Table 2.

Table 2. Values of α and β depending on ξ

ξ	α	β
0.001	53.1288	$1.41 \cdot 10^{-8}$
0.010	531.288	$1.41 \cdot 10^{-7}$
0.100	5312.88	$1.41 \cdot 10^{-6}$

Differential equations (3.3) describing motion have been solved numerically by Matlab-Simulink, using the scheme in Fig. 5. For that purpose, the dimensions from Fig. 2 as well as the following values of the physical constants: $E = 2.1 \cdot 10^{11}$ Pa and $\rho = 7850$ kg/m³ have been taken.

The numerical solution of the problem using the values from Table 2, returned the results shown in Fig. 6. The figure shows the relative deformation variation in time $\varepsilon = (u_{11} - u_{10})/l_{10}$. Figure 6 shows that for the three values of ξ , the movement differs considerably (the time of damping is different), i.e. for successful modelling, it is of particular importance to set the exact value of ξ .

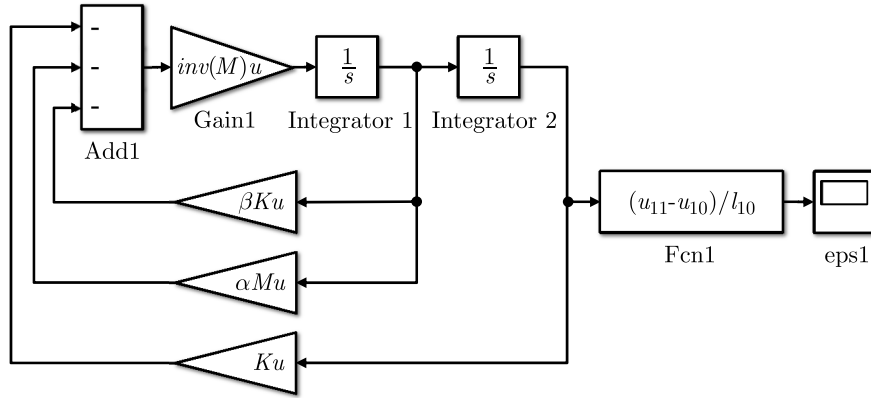


Fig. 5. Scheme for solving the differential equations in Matlab-Simulink

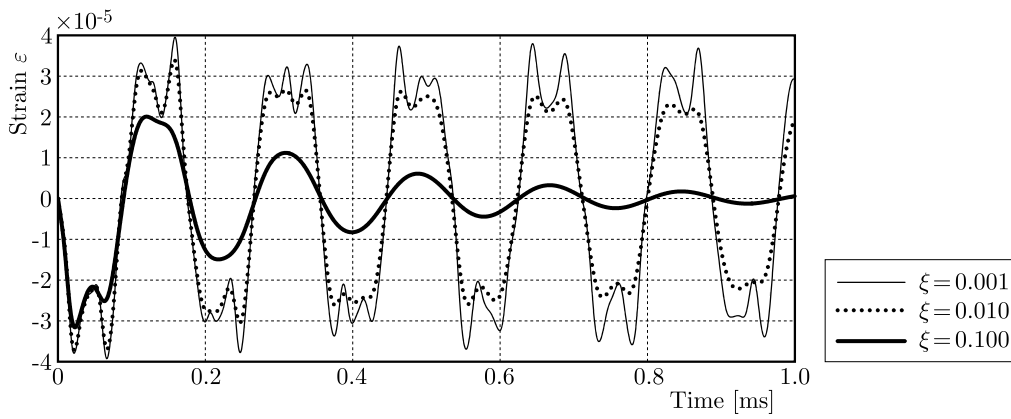


Fig. 6. Damped oscillations for different values of ξ

5. Experimental determination of the chisel internal resistance by the method of damping oscillations

One of the future goals of this project will be to measure the impact force of the machine under real operating conditions. Therefore, a decision has been taken to make tensometrical (strain) measurements. Free damped oscillations of the chisel arising from shock impact, have been thus registered in the course of the present study.

Figure 7 shows a scheme of the experimental installation. Strain gauges have been glued at two opposite points in the middle of the ram (Fig. 3b). Two equal half bridge T-rosettes have been used, each with two serially connected strain gauges, one of them in the longitudinal and the other – in the transverse direction to the chisel axis. The rosettes are connected in a full bridge circuit. The oscillation frequencies of the studied object are high, which makes the standard tensometric equipment inapplicable for strain registration. It has been, therefore, decided to use a high-frequency universal system for data acquisition (DAQ system) – National Instruments NI USB-6211 (250 kS/s, 16 bit). Excitation voltage is applied to the bridge circuit with a suitable 12V Li-ion rechargeable battery. The incoming information from the DAQ system is processed and recorded using software package LabVIEW®. Calibration with reference weights has been made before the experiment. The chisel has been consecutively loaded with increasing weights of pure pressure in order to check the linearity and establish the conversion factors stress/strain.

In Fig. 7, the T-rosettes are not in their actual positions.

Figure 8 shows the recordings of damped oscillations after the impact on the studied system. Three recordings have been made with random forces of the impact, designated as FDO1, FDO2

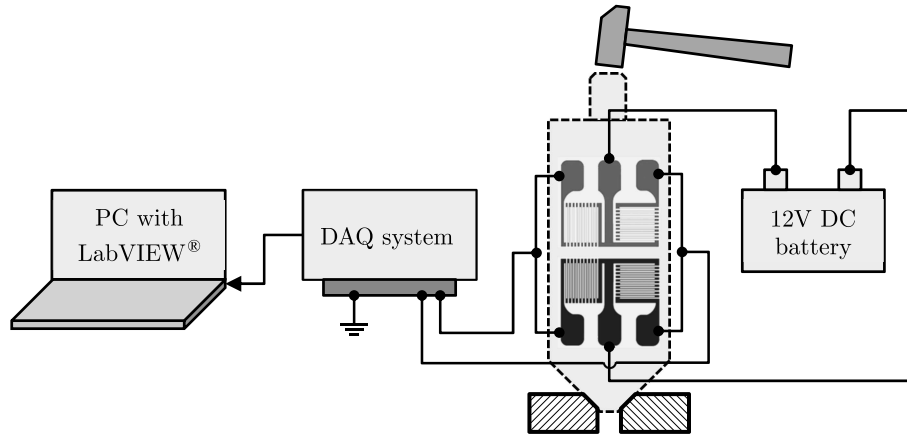


Fig. 7. Experimental installation scheme for registering strain upon impact

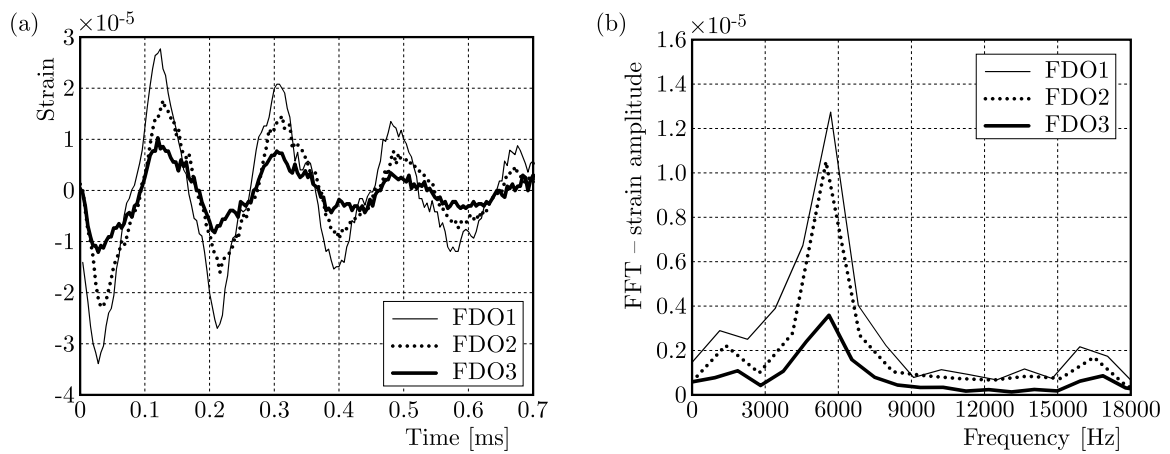


Fig. 8. Measurement results and frequency analysis

and FDO3 (FDO – free damping oscillations). On the left, the relative strain ε is shown as a function of time and on the right – frequency analysis determining the damped oscillations frequency. Fast Fourier Transform (FFT) algorithm in Matlab is used for frequency analysis. The values obtained for the first and second frequency of the damped oscillations are given in Table 3. The results from the processing of all three recordings are similar.

Table 3. Frequencies of the damped oscillations

Recording	f_{e1}^* [Hz]	f_{e2}^* [Hz]
FDO1	5682	15882
FDO2	5495	16483
FDO3	5618	16854

Let us consider the first recording from Fig. 8 – FDO1. Damped oscillations have been observed with frequencies ($f_{e1}^* = 5682$ Hz and $f_{e2}^* = 15882$ Hz) close to the first two natural frequencies of the mechanical system (Table 1). It is assumed that the specific resistance coefficient ξ of the damped oscillations is the same for the first and second frequency of the damped oscillations found from the experiment ($\omega_{e1}^* = 2\pi f_{e1}^* = 35683$ rad/s and $\omega_{e2}^* = 2\pi f_{e2}^* = 99739$ rad/s). Then its value can be determined on the basis of the lower frequency ω_{e1}^* .

The differential equation, describing the damped oscillations with frequency ω_{e1}^* , is

$$\ddot{u} + 2\xi\omega_{e1}\dot{u} + \omega_{e1}^2 u = 0 \quad (5.1)$$

The relationship between ξ and ω_{e1} is given by the equation

$$\omega_{e1} = \frac{\omega_{e1}^*}{\sqrt{1 - \xi^2}} \quad (5.2)$$

where ω_{e1}^* is the first frequency of the damped oscillations, determined by Fig. 8. Figure 9 shows four consecutive oscillations from the record, given in Fig. 8.

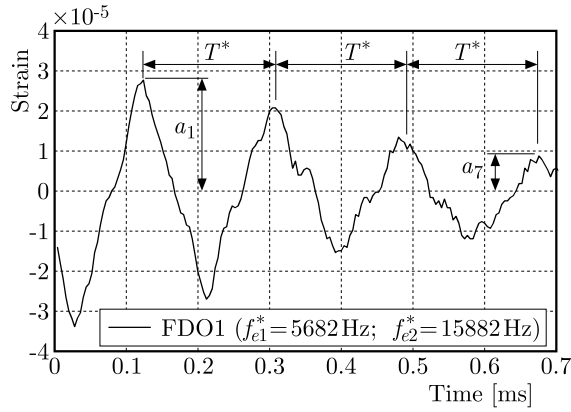


Fig. 9. Determining the resistance of damped oscillations

From Fig. 9 it can be determined that the ratio of the amplitudes a_1 and a_7 is 3.2. The following relation is valid for the amplitudes i and $i + 2k$ (i and k being positive integers)

$$\frac{a_i}{a_{i+2k}} = \exp(k\xi\omega_{e1}\tau^*) \quad (5.3)$$

Equation (5.3) can be resolved in relation to ξ , assuming that: $a_1/a_7 = 3.2$, $i = 1$, $k = 3$, ω_{e1}^* is expressed by (5.2), and the period $\tau^* = 2\pi/\omega_{e1}^*$. The result is $\xi = 0.06$. Replacing ξ with 0.06, ω_{e1}^* with 35683 rad/s and ω_{e2}^* with 99739 rad/s in (1.1), we obtain the Rayleigh law coefficients

$$\alpha = 3153.7 \quad \beta = 8.86 \cdot 10^{-7} \quad (5.4)$$

Setting the values from equations (5.4) in numerical model (3.3) and applying the Q - R algorithm – orthogonal projections (Watkins, 2004), we obtain the damped oscillation frequencies shown in Table 4.

Table 4. Frequencies of the damped oscillations

Natural frequencies	f_i^* [Hz]	ω_i^* [rad/s]
1	5616	35270
2	16837	105737
3	26630	167238
4	39135	245769

The solution to differential equation (2.3) with these coefficients is shown in Fig. 10.

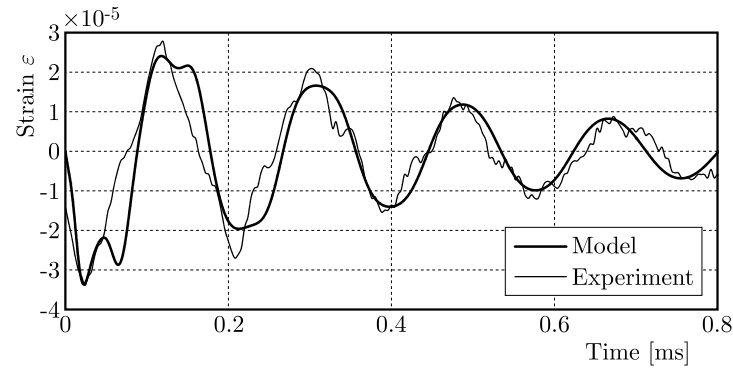


Fig. 10. Simulated and experimentally determined damped oscillations

6. Summary

Free damped oscillations of the chisel represented as a distributed parameters system have been studied in the present work. The dynamic model of the chisel was discretized with FEM and the problem was solved numerically with Matlab. The values of the coefficients α and β (5.4), forming the Rayleigh damping matrix, have been experimentally determined in the given frequency range, after which they have been set in the numerical model. A comparison of the modelled oscillations with a real record has been made – see Fig. 10. The resulting close match shows that the proposed numerical model is acceptable and that the constants set in it have been correctly determined.

References

1. ADHIKARI S., 2001, Damping models for structural vibration, Doctoral dissertation, University of Cambridge, 26-35
2. ALIPOUR A., ZAREIAN F., 2008, Study Rayleigh damping in structures; uncertainties and treatments, *Proceedings of 14th World Conference on Earthquake Engineering*, Beijing, China
3. CHOPRA A.K., 1995, *Dynamics of Structures: Theory and Applications to Earthquake Engineering*, New Jersey: Prentice Hall, 415
4. CHOWDHURY I., DASGUPTA S.P., 2003, Computation of Rayleigh damping coefficients for large systems, *Electronic Journal of Geotechnical Engineering*, **8**, Bundle C
5. CRAIG R.R., KURDILA A.J., 2006, *Fundamentals of Structural Dynamics*, John Wiley & Sons, 501-504
6. DRESIG H., HOLZWEISSIG F., 2006, *Machine Dynamics* (in German), Springer-Verlag, **52**, 417-427
7. GENOV J., POLIHRONOV G., KRALOV I., 2007, *Vibration of Vehicles*, TU-Sofia, **25**
8. KHULIEF Y.A., AL-NASER H., 2005, Finite element dynamic analysis of drillstrings, *Finite Elements in Analysis and Design*, **41**, 13, 1270-1288
9. MAN L., CORMAN D.G., 1995, Formulation of Rayleigh damping and its extensions, *Computers and Structures*, **57**, 2, 277-285
10. MEVADA H., PATEL D., 2016, Experimental determination of structural damping of different materials, *Procedia Engineering*, **144**, 110-115
11. RAO S.S., 2004, *The Finite Element Method in Engineering*, Butterworth-Heinemann, 430-431
12. REDDY J.N., 1984, *An Introduction to the Finite Element Method*, New York: McGraw-Hill, 123-131

13. SANGEETHA N., SATHISH KUMAR P., 2014, A study of vibration analysis for drill string using finite element analysis, *IOSR Journal of Mechanical and Civil Engineering*, **8**, 60-74
14. STELZMANN U., GROTH C., MÜLLER G., 2008, *FEM for Practitioners Volume 2: Structural Dynamics* (in German), Auflage 5, Expert-Verlag, 89-91
15. STEVENSON J.D., 1980, Structural damping values as a function of dynamic response stress and deformation levels, *Nuclear Engineering and Design*, **60**, 2, 211-237
16. WATKINS D.S., 2004, *Fundamentals of Matrix Computations*, John Wiley & Sons, 356-371
17. YIGIT A.S., CHRISTOFOROU A.P., 1998, Coupled torsional and bending vibrations of drillstrings subject to impact with friction, *Journal of Sound and Vibration*, **215**, 1, 167-181
18. ZARE J., HASHEMI S.J., RASHED G., 2011, Finite element analysis of drillstring lateral vibration, *Scientific Research and Essays*, **6**, 13, 2682-2694

Manuscript received May 29, 2017; accepted for print August 30, 2017

FATIGUE CRACK GROWTH AND PROBABILITY ASSESSMENT FOR TRANSVERSE TIG WELDED ALUMINUM ALLOY 6013-T4

GUNAWAN D. HARYADI

Diponegoro University, Department of Mechanical Engineering, Semarang, Indonesia

RANDO TUNGGGA DEWA

Pukyong National University, Department of Mechanical Design Engineering, Busan, Korea

e-mail: rando.td@gmail.com

I.M.W. EKAPUTRA

Sanata Dharma University, Department of Mechanical Engineering, Yogyakarta, Indonesia

The aim of this study is to investigate the fatigue crack growth behavior with post weld heat treatments (T4) on transverse tungsten inert gas-welded Aluminum alloy 6013. All fatigue tests have been carried out using center cracked tension specimens at ambient temperature under a stress ratio of $R = 0.3$. The results revealed that various time of aging in T4 affects its mechanical properties, also the fatigue crack growth behavior as well. It has been observed that in the heat treated samples the crack growth rate is lower than that in the as-welded sample, but higher than the rate in the base metal. To be more specific, samples with 18 hours aging exhibit the highest tensile strength and fatigue resistance compared to the other heat treated samples. The probability assessment has also been used to determine the fatigue crack growth rate and a good linearity has been found.

Keywords: fatigue crack growth, Aluminum alloy 6013-T4, post welding heat treatment, TIG welding

1. Introduction

The aircraft and automotive industries have been long using Aluminum alloys for the prime material construction. This material is normally used in the aerospace industry (for fuselage skins and other applications) and automotive industry (for body panels and bumpers) due to its excellent properties such as preferential strength, corrosion resistance, weld ability and low cost. Various structural components in machines, pressure vessels, transport vehicles, earthmoving equipment and spacecraft are made of welded joints. The butt welds are the most common ones in the fabrication and construction of many structures. The wide applications of butt welds in various structures including offshore and nuclear ones give a large scope for researches to analyze the behavior under different types of loading conditions. This concept was introduced after the works of Yakubovski and Valteris (1989). However, as it is well known, welded joints can exhibit poor fatigue properties. Thus, detail design guidelines are necessary to prevent fatigue failures in welded Aluminum alloy structures. Apart from the basic design of new structures, there is also an increase of interest in methods for assessing the remaining life of existing structures. The previous author's work also revealed the fatigue crack growth behavior of the studied material using longitudinal direction of tungsten inert gas (TIG) welding (Haryadi and Kim, 2011). Prompted by difficulties experienced in reaching a consensus on fatigue performance of welded Aluminum alloys, an animated discussion has been undertaken over the past 10 years (Maddox, 2003).

To produce a high quality weldment component, TIG welding is preferred rather than the other arc welding processes due to the temperature distribution on the welded plate, which may induce distortion. Also the TIG welding process is one of the most well established processes which has capabilities to weld all metals of industrial use. Therefore, many efforts have been done to investigate the fatigue behavior on TIG welded Aluminum alloy joints. The weldment components have lower impact energy and fracture tenacity compared to its parent material. It is well known that the welded structures are also less superior to the parent material as the welding process (thermal interaction) results in microstructure heterogeneity, which brings differences to mechanical properties (Manti *et al.*, 2008). Failure analysis of the weldment indicates that fatigue damage have to be considered to account for most of the disruptive failures. The main problem is that there is an abrupt change in section due to the excess weld reinforcement, undercut, slag inclusion and lack of penetration, and nearly 70% of fatigue cracking occurs in the welded joint (Pakusiewicz *et al.*, 2006). It is also well known that the heat treatment process after welding, i.e. solution treatment and aging, can possibly overcome the degradation of mechanical properties.

To determine the fatigue tendency of the weld structure, the test matrix of tests is more complex as welded joints present microstructure variations over small distances, not to mention complex distributions of residual stresses. The fatigue and fracture tests are performed in accordance with standards and codes devised by the American Society for Testing and Materials (ASTM) E647 based on the concepts of $a - N$ and $(da/dN) - \Delta K$ for fatigue design curves.

This work deals with the dependence of constant-amplitude fatigue crack growth rates on the center cracked tension (CCT) specimens of a material for a variety of heat-treatable thin-sheet Aluminum alloys. The TIG welded 6013 Aluminum alloy transverse joint is of particular interest. A better understanding of the relatively high variability of these rates and the role of material parameters based on the analysis of experimental data are explored and discussed for assessing the remaining lives of existing structures.

2. Experimental section

The material studied is Aluminum alloy 6013 with sheet thickness of 2.5 mm. The chemical composition of Aluminum alloy 6013-T4 and its filler wire Al 5356 can be found in Table 1 (Rooy, 2000). The welding process by using the TIG method on specimens has been performed by Al 5356 filler with 3.2 mm diameter, and the welding was done in the transverse direction. The welding conditions and process parameters can be found in (Haryadi and Kim, 2011). Tensile test specimens were made with dimensions according to the standard test ASTM B-557, and crack propagation tests specimens according to the standard test ASTM E-647 proposed by American Society of Mechanical Engineers (ASME) (ASTM E 647-08, 2008). The specimens were grouped into three kinds of fracture conditions, i.e. cracks without heat treatment, cracks in the welding simulation, and cracks in the welding simulation continued with various T82 artificial aging. The surfaces of the specimens were polished to prevent the formed notches. The geometry and dimensions of specimens are specified in Fig. 1.

Table 1. Chemical composition of Al 6013-T4 and filler wire Al 5356 [wt%]

References	Si	Fe	Cu	Mn	Mg	Cr	Zn	Ti	Al
Al 6013	0.66	0.09	0.80	0.39	1.04	0.07	0.06	0.02	Bal
Al 5356	0.25	0.40	0.10	0.10	5.55	0.20	0.10	0.20	Bal

The heat treatment (T4) on the specimen is hereafter referred to as the specimen experiencing the process of solution treatment (the specimen is heated until it reaches the temperature

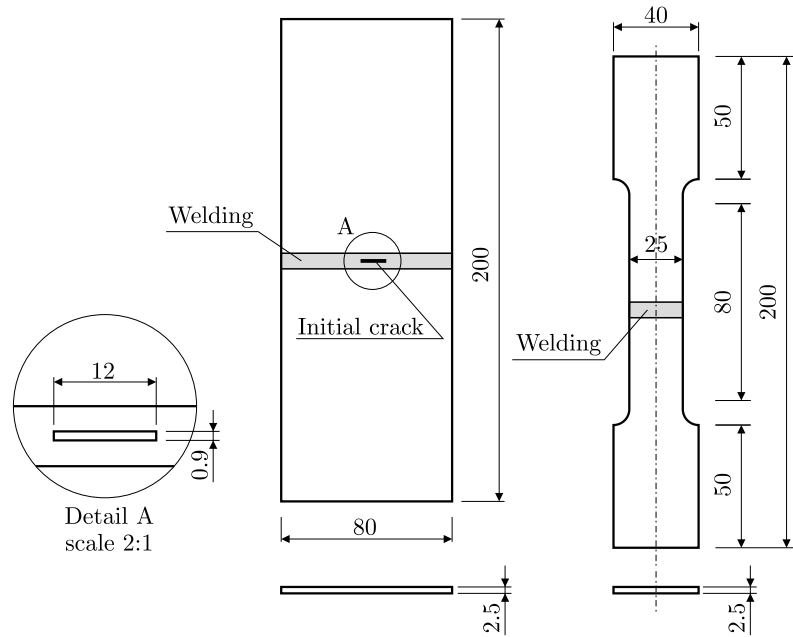


Fig. 1. Specimen configuration for tensile and fatigue crack propagation tests (all units in millimeters)

of 420°C), followed by a process of strain hardening of 2%, and the final process is the artificial aging in temperature of 175°C and the aging time of 6 hours, 18 hours, and 24 hours, respectively. Microhardness measurements have been conducted through fusion boundaries using a Vickers microhardness tester. Vickers hardness measurement was carried out by using a diamond indenter on a metallographically polished section of the welded joint along the central line at a loading of 0.2 kg and loaded time of 5 s. The indentations were set at an interval of 1 mm along the weld center, transverse to the direction of the base metal. The schematic illustration of hardness testing distribution is shown in Fig. 2. The microstructures of all material types are shown in Fig. 3. The as-welded material has a larger grain size compared to the other heat treated samples. Coarser grained by 24 hours aging time samples relatively contained a lower amount of grain boundary areas than the finer grained microstructure.

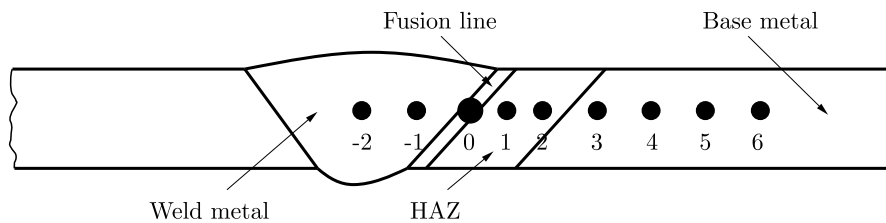


Fig. 2. Welding profiles and a schematic illustration of the hardness testing distribution

Initial cracks for the fatigue crack propagation CCT samples were made using EDM (Electric Discharge Machine) with 12 mm length and 0.9 mm width. The fatigue crack growth tests were carried out using side grooves to ensure the crack propagation occur along a single plane. Five different stress levels (345 MPa, 225 MPa, 138 MPa, 202 MPa, and 170 MPa) were applied under a stress ratio of $R = 0.3$ with a constant frequency of 5-11 Hz. A travelling microscope was used to monitor the crack growth with an accuracy of 0.01 mm. In this work, the applied stress cycle was in the pull mode as the compressive mode usually near the fatigue crack. The data points measured with an accuracy of 0.01 mm were fitted with a smooth curve as in the form of crack length against the number of cycles.

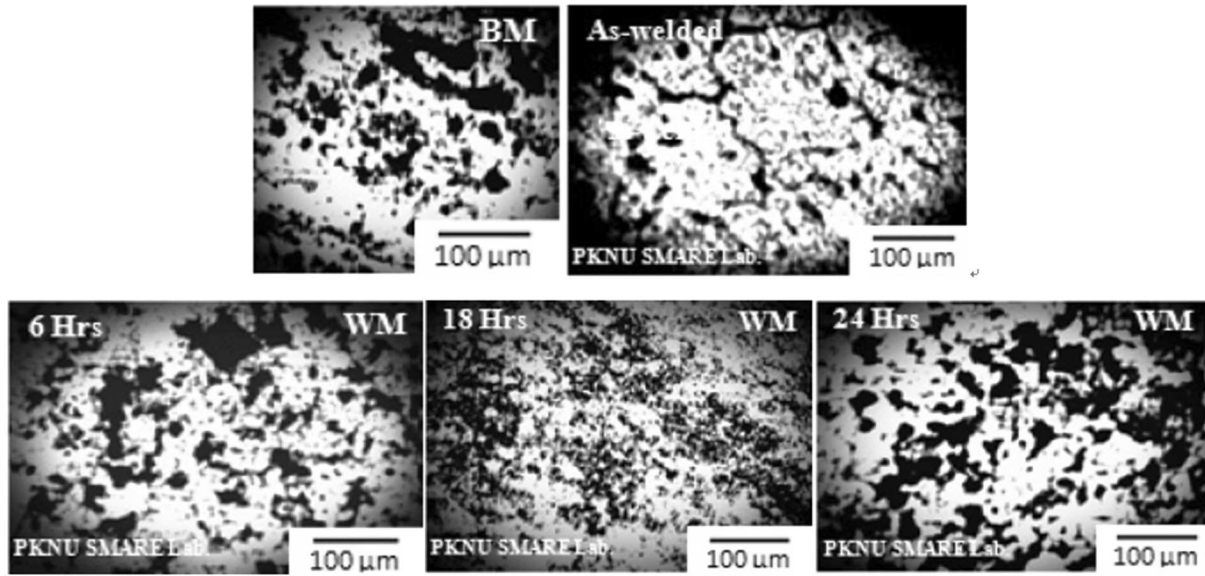


Fig. 3. Microstructures of as-welded and 6013-T4 samples (BM: base metal and WM: Weld metal)

3. Results and discussions

3.1. Tensile properties of 6013-T4

The tensile test results were performed on the base metal, welding without T4, and welding with T4 aging time variations. The results of the tensile tests are mean values of minimum three tests. All tensile test failures occurred in the heat affected zone (HAZ) due to coarser grains as the cast structure of the base material. As such, the reduced section and notched specimens were made to characterize the failure from the welded metal. The yield strength results based on 0.2% offset in the load-elongation diagram and the peak maximum (ultimate tensile) strength are reported in Fig. 4. The unwelded base metal indicates yield strength and tensile strength values of 243 MPa and 346 MPa, respectively. These results are comparable to other literature data (Heinz and Skrotzki, 2002) for 6013-T4 base metal having the yield and ultimate strength approximately 220 and 320 MPa, respectively. Thus, the transverse as-welded sample shows the yield strength and tensile strength values of 141 MPa and 227 MPa, respectively. From this result, we can point out that there is a 52% reduction in strength values due to the TIG welding process in the transverse direction. The as-welded material possesses higher strength or embrittlement, therefore, very slight lateral displacement will result in shearing off the structure. In the case of the as-welded samples, the transverse TIG welded samples with 6 hours aging exhibit the lowest yield strength and tensile strength of 82 MPa and 160 MPa, respectively. This suggests that there is a 42% reduction in strength due to T4 with a 6 hours aging process compared to the transverse as-welded samples. The heat treated specimens with 18 hours aging indicate the highest yield strength and tensile strength of 107 MPa and 202 MPa, respectively. Though these values are lower than those for the base metal and as-welded samples, the strength values are comparatively higher than those of the other samples with T4 process. The 24-hour aged samples show the yield strength and tensile strength of 102 MPa and 194 MPa, respectively, which is 20% higher than the heat treated samples by 6 hours aging. To conclude all those cases, no significant influence of the welding direction compared to the previous study (Haryadi and Kim, 2011) has been reported.

The percentage of elongation in the cross sectional area of the base material and transverse as-welded samples can be seen in Fig. 5. The elongation in the cross sectional area of the base metal and the transverse as-welded samples are 19.42% and 5.83%, respectively. According to

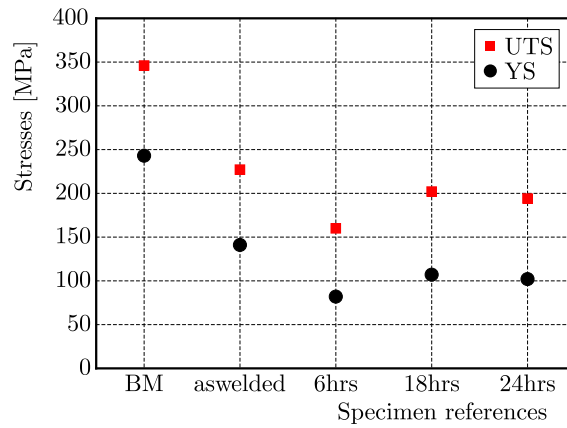


Fig. 4. Results of tensile tests on the strength of various transverse TIG welded 6013-T4 samples

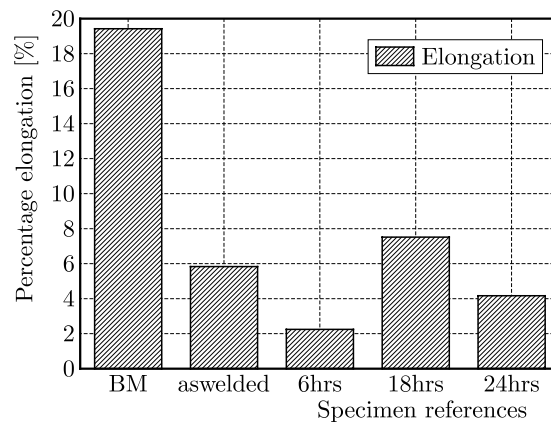


Fig. 5. Reduction in area in terms of elongation [%] of transverse TIG welded 6013-T4

the literature (Heinz and Skrotzki, 2002), the elongation for 6013-T4 base metal is comparable, approximating 20%. The increase of strength of the as-welded samples has been expected as the microstructure hardens due to the solidification process during welding. The transverse TIG welded samples with T4 of 6, 18, and 24 hours exhibit 2.24%, 7.51% and 4.16% of elongation in the cross sectional area, respectively. This suggests that there is a 60% reduction in ductility due to T4 with 6 hours aging with respect to the transverse as-welded samples. Again, the heat aged specimens for 18 hours indicate the highest elongation of 7.51%. The heat treatment process, especially the 18-hour aging, can improve ductility properties significantly.

3.2. Microhardness analysis

The exact extension of the HAZ and welded region are not easily measurable, thus, each indentation of microhardness profiles was drawn based on three average points for the best condition obtained. Hence the mechanical characteristics of heat-treatable Aluminum alloy are largely determined by characteristics of precipitates (i.e. size, volume fraction, composition, distribution, etc.). Precipitates and second phase particles act as obstacles to dislocation movement, which in turn increases hardness and strength but also limits ductility of the material. Precipitation hardening of Al-Mg-Si alloys has also been reported to occur due to increased energy requirement to break Mg-Si bond rather than coherency strains (Haryadi and Kim, 2011). The TIG welding process has proven to affect the original state and distribution of those precipitates. The base metal in its initial number 4-6 condition has the average hardness of about 91 HV approximately, which starts to slightly increase in the HAZ to a minimum of 100 HV. The

hardness is greatly reduced in the welded region irrespective of the welding processes (Fig. 6). This is one of the reasons for location of the failure invariably at the welded region. The closer to the center of the weld, the higher the temperature is reached, which may lead to coarsening of the grain structure. The coarsening becomes an important aspect in the welded region due to the thermally activated phase in this particular zone. Thus, the softening phase caused by precipitation coarsening will also soften the material. The time aging by T4 possesses limits the strength due to high temperatures resulting in finer grains (Effertz *et al.*, 2016), and re-precipitation accompanied by aging. The ductility of this Aluminum alloy can be enhanced by a proper heat treatment process. The T4 sample aged by 6 hours indicates the lowest hardness profiles about 50 HV at the weld center. The T4 sample with 18 hours aging shows the highest hardness of about 71 HV at the welded region. It is important to emphasize that the transverse as-welded sample has the highest hardness of about 77 HV at the welded region.

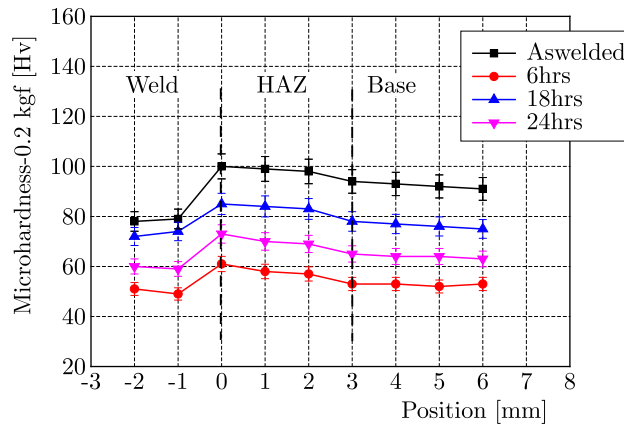


Fig. 6. Vickers microhardness profile distribution across the welded zone

With the combination of tensile properties and microhardness profiles, it is also possible to determine mechanical properties of the transverse welded butt joint with 18 hours aging, which are the most superior compared to other aging processes. The aging by 18 hours is more appropriate for more brittle materials (high strength). After this time of aging, the detriment of the mechanical properties can be observed due to the over aging process.

3.3. Fatigue crack growth properties

It is well known that the growth of the fatigue crack of many materials can be divided into three regimes as shown in Fig. 7. Region I is the fatigue threshold region where ΔK is too low to propagate the crack. Region II involves the rate of crack growth changes roughly linearly with a change in the stress intensity factor (SIF). Lastly, region III with a small increase in the SIF, produces a relatively large increase in the crack growth rate.

Considering the power law region, the experimental results for the crack length a are plotted in da/dN versus ΔK , with N and ΔK being the number of cycles and SIF, respectively, according to the following Paris equation (Paris and Erdogan, 1963)

$$\frac{da}{dN} = C(\Delta K)^m \quad (3.1)$$

where the correlation between the exponent m and the coefficient C in the Paris equation determines the material constants. The crack growth exponent m , which is derived from the relationship existing between the crack growth rate da/dN and the SIF range, is an important parameter to evaluate the fatigue crack growth behavior of materials since it decides about the fatigue crack propagation life of the materials (Dieter, 1988).

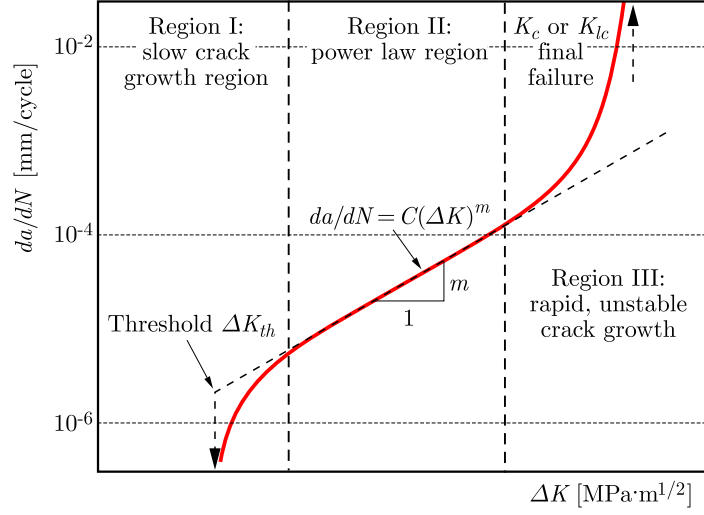


Fig. 7. Fatigue crack propagation curve

The loading variables R , ΔK , and K_{max} are related in accordance with the range of the SIF with the following relationship (Malarvizhi *et al.*, 2008), where σ is a uniform tensile stress perpendicular to the crack plane and Y depends on the geometry of samples

$$\Delta K = Y\sqrt{\pi a} \quad N = \int_{a_i}^{a_f} \frac{1}{C(\Delta K)^m} da \quad (3.2)$$

where a_i and a_f are initial crack length and crack length at the fracture point, respectively. The crack growth rate, da/dN for the propagation stage is calculated for the steady state growth regime at different intervals of crack length increment, against the associated number of cycles to propagation. The SIF values are calculated for different values of the growing fatigue crack length $2a$ using the following expression for the middle tension specimen referring to the ASTM Standard. The measured variation in the crack length $2a$ and the corresponding number of cycles N endured under the action of particular applied stress range are plotted in Fig. 8.

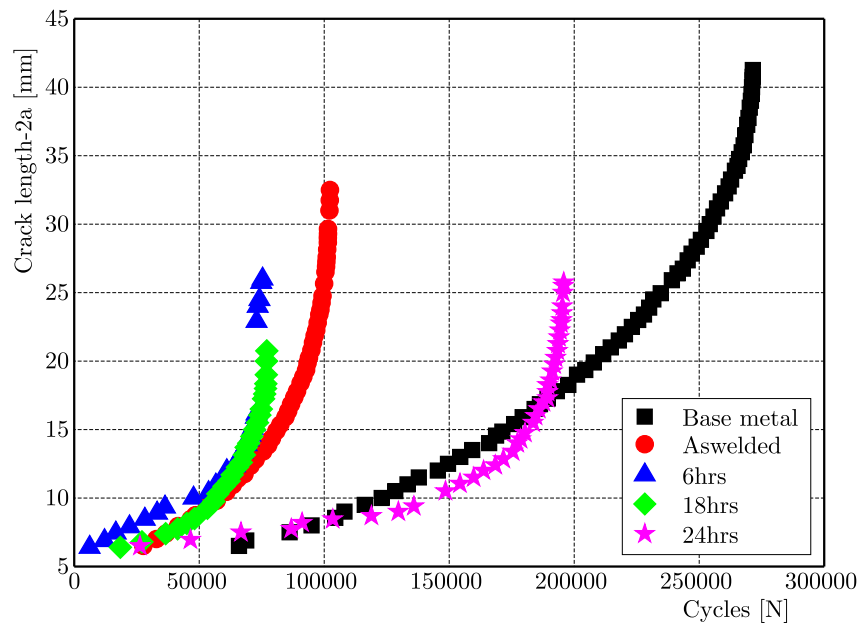


Fig. 8. Fatigue crack propagation curve of transverse TIG welded 6013-T4

The relationship between the SIF and ΔK range and the corresponding crack growth rate da/dN in terms of the best fit lines is shown in Figs. 9a and 9b for all samples. The data points plotted in the graph mostly correspond to the second stage of the Paris sigmoidal relationship ($10E-6$ to $10E-3$ mm/cycle). The exponent m , which is the slope of the line on log-log plot and the intercept C of the line, are determined and presented in Table 2.

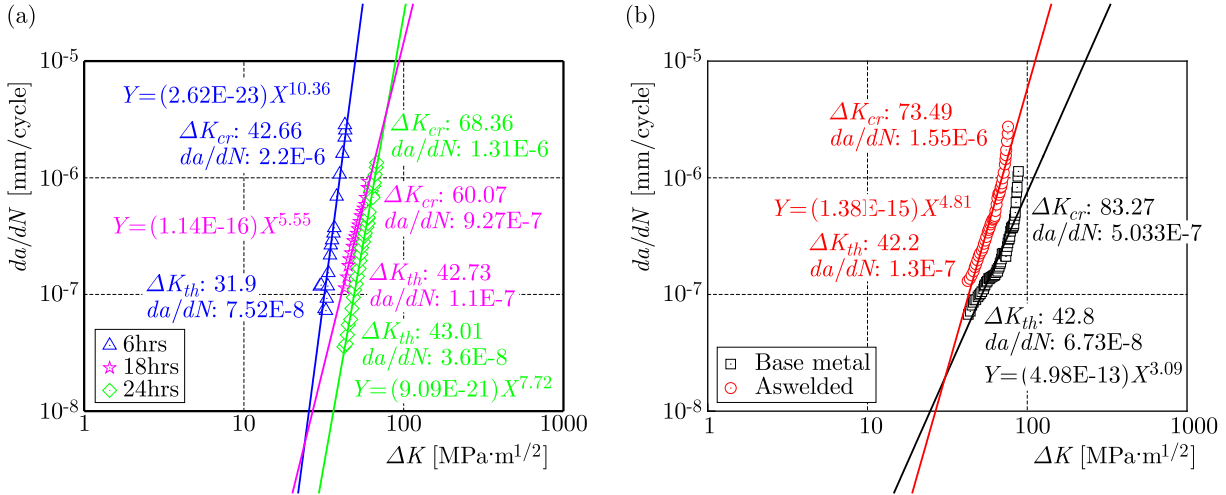


Fig. 9. (a) Fatigue crack growth for Al 6013-T4 (base metal) and the transverse as-welded sample. (b) Measured fatigue crack growth for the transverse TIG welded 6013-T4

Table 2. Fatigue crack growth parameters of transverse TIG welded samples

References	Crack growth exponent m	Coefficient C
Al 6013 base metal	3.09	4.98E10-13
Transverse TIG welded	4.81	1.38E10-15
After 6 hours aging	10.36	2.62E10-23
After 18 hours aging	5.55	1.14E10-16
After 24 hours aging	6.74	9.09E10-21

It can be seen from those figures that at higher crack growth rates, the measured fatigue crack growth rate for the base metal is $5.03E-7$ mm/cycle ($\Delta K_{cr} = 84.2 \text{ MPa}\sqrt{\text{m}}$), and the measured fatigue crack growth rate for transverse as-welded samples is $1.55E-6$ mm/cycle ($\Delta K_{cr} = 73.49 \text{ MPa}\sqrt{\text{m}}$). On the other hand, in Fig. 9b for all T4 samples, at higher crack growth rates for 6 hours aging, 18 hours aging and 24 hours aging samples exhibit $2.2E-6$ mm/cycle ($\Delta K_{cr} = 42.66 \text{ MPa}\sqrt{\text{m}}$), $9.27E-7$ mm/cycle ($\Delta K_{cr} = 60.07 \text{ MPa}\sqrt{\text{m}}$), and $1.31E-6$ mm/cycle ($\Delta K_{cr} = 68.36 \text{ MPa}\sqrt{\text{m}}$), respectively. The unstable crack growth phase occurred and, hence, the corresponding ΔK value is taken as the critical SIF range ΔK_{cr} . Furthermore, the crack growth at a lower rate is found to be dormant, and the corresponding ΔK value is taken as the threshold SIF (ΔK_{th}). At a lower crack growth rate, the measured fatigue crack growth rate for the base metal is $6.73E-8$ mm/cycle ($\Delta K_{th} = 42.8 \text{ MPa}\sqrt{\text{m}}$) and the measured fatigue crack growth rate for transverse as-welded samples is $1.3E-7$ mm/cycle ($\Delta K_{th} = 42.2 \text{ MPa}\sqrt{\text{m}}$). Thus, at a lower crack growth rate for all T4 samples with 6 hours aging, 18 hours aging and 24 hours aging results in $7.52E-8$ mm/cycle ($\Delta K_{th} = 31.9 \text{ MPa}\sqrt{\text{m}}$), $1.1E10-7$ mm/cycle ($\Delta K_{th} = 42.73 \text{ MPa}\sqrt{\text{m}}$), and $3.6E-8$ mm/cycle ($\Delta K_{th} = 43.01 \text{ MPa}\sqrt{\text{m}}$), respectively.

The fatigue crack growth exponent of the Al 6013-T4 Aluminum alloy base metal is lower than that of the transverse TIG samples. On the three heat treated samples with various aging,

the 18 hours aging samples exhibit a very low fatigue crack growth exponent compared to the other heat treated samples. Although, the fatigue crack growth exponent of 18 hours aging samples is approximately 44% higher than in the base metal. It is understood that the 18 hours aging samples exhibit superior fatigue crack growth resistance compared to the other heat treated samples. If this exponent has a larger value, then the slope of the curve is higher what explains lower resistance of the material to the growing fatigue crack and reduction the lifespan (Ambriz *et al.*, 2010; Sivaraj *et al.*, 2014). The reasons for better fatigue crack growth resistance of the 18 hours aging samples is due to superior of mechanical properties. The crack tip plasticity is also the reason of the higher crack growth rate, since the deformation is controlled by the yield strength of the material and mainly concentrated in the welded metal zone. The extension of the plastic zone size (PZS) is limited within the welded metal. This relationship indicates that the local fatigue crack growth rate decreases when the SIF is increased, and can be estimated by the following equation (Sohn *et al.*, 2014)

$$PZS_{(cycle)} = 0.033 \left(\frac{\Delta K}{\sigma_{ys}} \right)^2 \quad (3.3)$$

Eripret and Horner (1994) reported that as soon as the plastic zone reaches the fusion line, plasticity keeps on developing along the interface between the parent material and the weld metal. The triaxial state of stress is high in the weld metal and the relaxation of this stress is poor. The crack driving force needed for this crack extension is small. Hence, the fracture toughness of the lower strength weld metal is not high. On the other hand, if the strength of the weld metal is more or less equal to the base metal, the plastic zone can easily extend into the parent material.

An extensive research by Zhang *et al.* (2016) did not deal with probabilistic viewpoints that define the probability of fracture. In this circumstance, a quantifiable method based on a statistical and probabilistic approach is proposed for assessing fatigue crack growth rate data. As mentioned above, the fatigue crack growth data followed the lognormal distribution well if using the standard deviation σ and mean value μ obtained from the lognormal distribution. The probability density functions (PDF) for this distribution is

$$P(N, loc, scale) = \frac{1}{\sigma\sqrt{2\pi}} \exp \left[-\frac{1}{2} \left(\frac{\ln N - \mu}{\sigma} \right)^2 \right] \quad (3.4)$$

As an example of application, Fig. 10 shows the probability distribution on the fatigue crack growth data for 18 hours aging samples. The fatigue crack growth life was estimated from the initial crack length of 8.5 mm to 17.6 mm. To the author's best knowledge, the lognormal distribution provides a good agreement for the statistical distribution of fatigue crack growth life. The confidence intervals of 90% and 10 % will be the upper and lower limits of conventional prediction for the fastest and lower fatigue crack growth rate according to the concept in the literature (Kim *et al.*, 2011).

To probabilistically predict the fatigue crack growth rate, the probabilistic distributions of da/dN have been determined for various materials. Figure 11 shows a typical result for the probability distribution of the da/dN for various materials. The relationships between the probability and fatigue crack growth life data revealed a linear relationship in the lognormal plot. Although, there are some variability linear equations between material types. The most scattered and widely distributed values are revealed for the 6 hours aging samples. This also proves that the TIG welded microstructure and the heat treatment time process could greatly affect the fatigue crack growth life. Using these fatigue crack growth rate data, it is possible to probabilistically predict the fatigue crack growth rate lines for this class of materials at the operational temperature when the fatigue crack growth data is absent.

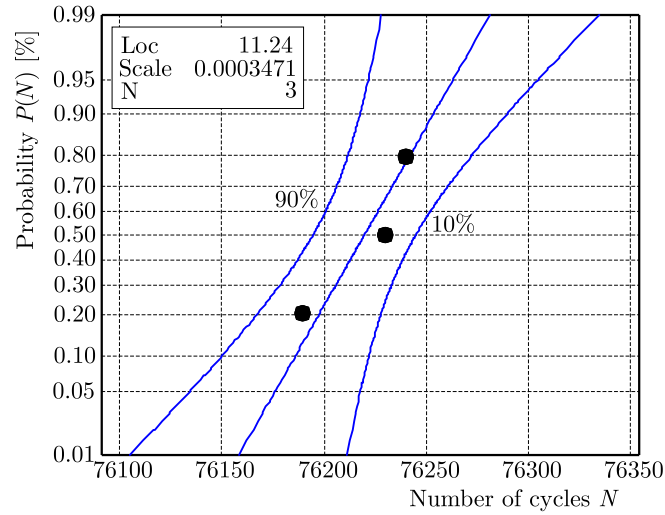


Fig. 10. Probability distribution of the fatigue crack growth life N for 18 hours aging samples

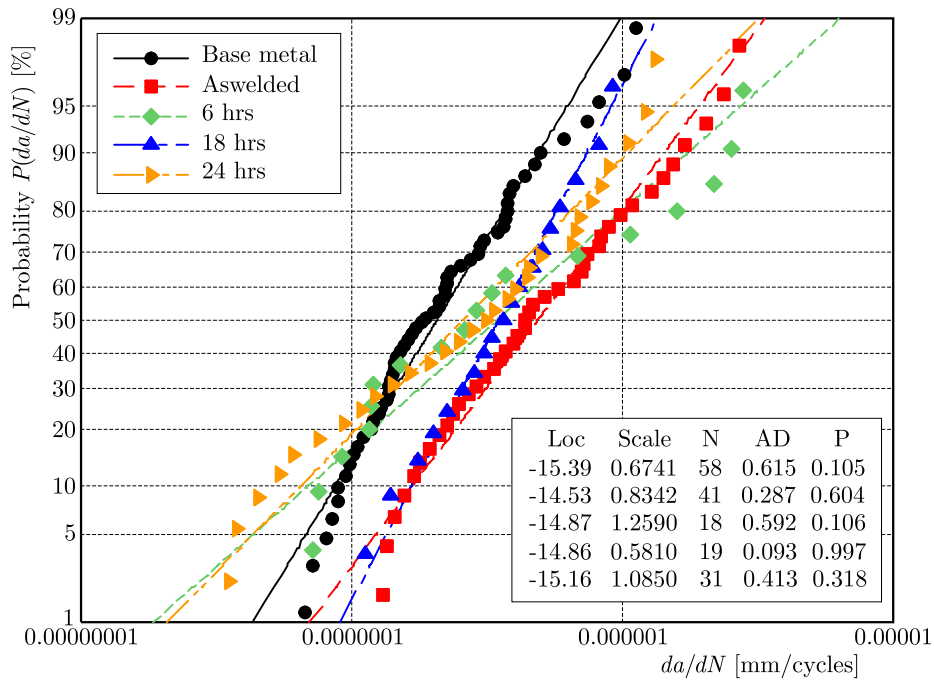


Fig. 11. Log-normal distribution of the fatigue crack growth rate for all tested samples at average N values

4. Concluding remarks

This paper presents results of tensile, hardness profile, fatigue crack growth behavior and probabilistic analysis of transverse TIG welded Al 6013-T4. However, some aspects deserve attention and are discussed in this Section. The following conclusions can be drawn:

- A 52% reduction in strength values due to the TIG welding process in the transverse direction with respect to the base material has been observed. Thus, the heat treatment process also can reduce the strength by about 20% in average despite the percentage of elongation of the respected T4 materials has been increased with respect to the as-welded material.

- The fatigue crack growth resistance and fatigue life of Al 6013-T4 are generally reduced by the TIG welding process. Of the three types of T4 samples, the 18 hours aging samples exhibit a higher fatigue crack growth resistance compared to other heat treated samples.
- The effect of 18 hours aging showed a crack growth exponent m of 5.55 which is the lowest value compared to the other heat treated samples. With a high ΔK (SIF), it causes a dramatic increase in the crack growth resistance compared to the other heat treated samples.
- The relationships between probability and fatigue crack growth life data exhibit linearity of the lognormal plot. The variability of the fatigue crack growth life is influenced by the TIG welded microstructures and T4 aging time.

Acknowledgements

This research was supported through research grant of Diponegoro University and Pukyong National University (2017). Special gratitude is granted to prof. Seon Jin-Kim, PhD (Pukyong National University) for technical discussions and supports.

References

1. AMBRIZ R.R., MESMACQUE G., RUIZ A., AMROUCHE A., LÓPEZ V.H., BENSEDIDQ N., 2010, Fatigue crack growth under a constant amplitude loading of Al-6061-T6 welds obtained by modified indirect electric arc technique, *Science and Technology of Welding and Joining*, **15**, 6, 514-521
2. ASTM E 647-08, 2008, Standard Test Method for Measurement of Fatigue Crack Growth Rates, American Society for Testing Materials (ASTM), New York, U.S.A.
3. DIETER G.E., 1988, *Mechanical Metallurgy*, 4th ed., Tata McGraw Hill, New York, U.S.A.
4. EFFERTZ P.S., INFANTE V., QUINTINO L., SUHUDDIN U., HANKE S., DOS SANTOS J.F., 2016, Fatigue life assessment of friction spot welded 7050-T76 aluminium alloy using Weibull distribution, *International Journal of Fatigue*, **87**, 381-390
5. ERIPRET C., HORNET P., 1994, Prediction of overmatching effects on the fracture of stainless steel cracked welds, [In:] *Miss-Matching of Welds, ESIS 17*, K.H. Schwalbe, M. Koçak (Edit.), London, 685-708
6. HARYADI G.D., KIM S.J., 2011, Influences of post weld heat treatment on fatigue crack growth behavior of TIG welding of 6013-T4 aluminum alloy joint. Part 1. Fatigue crack growth across the weld metal, *Journal of Mechanical Science and Technology*, **25**, 9, 2161-2170
7. HEINZ B., SKROTZKI B., 2002, Characterization of a friction-stir-welded aluminum alloy 6013, *Metallurgical and Materials Transactions B*, **33B**, 489-498
8. KIM W.G., PARK J.Y., HONG S.D., KIM S.J., 2011, Probabilistic assessment of creep crack growth rate for Gr. 91 steel, *Nuclear Engineering and Design*, **241**, 3580-3586
9. MADDOX S.J., 2003, Review of fatigue assessment procedures for welded aluminium structures, *International Journal of Fatigue*, 1359-1378
10. MALARVIZHI S., RAGHUKANDAN K., VISWANATHAN N., 2008, Investigations on the influence of post weld heat treatment on fatigue crack growth behaviour of electron beam welded AA2219 alloy, *International Journal of Fatigue*, **30**, 1543-1555
11. MANTI R., DWIVEDI D.K., ARGAWAL A., 2008, Pulse TIG welding of two Al-Mg-Si alloys, *ASM International*, **17**, 6, 667-673
12. PARIS P.C., ERDOGAN F.A., 1963, Critical analysis of crack propagation laws, *Journal of Basic Engineering, Transactions ASME (Series D)*, **85**, 528-534

13. PUKASIEWICZ A.G.M., HENKE S.L., CASAS W.J.P., 2006, Effect of post-weld heat treatment on fatigue crack propagation in welded joints in CA6NM martensite stainless steel, *Welding International*, **20**, 12, 947-952
14. ROOY E.L., 2000, Introduction to aluminum and aluminum alloys, *ASM Handbook*, **2**
15. SIVARAJ P., KANAGARAJAN D., BALASUBRAMANIAN V., 2014, Fatigue crack growth behaviour of friction stir welded AA7075-T651 aluminium alloy joints, *Transactions of Nonferrous Metals Society of China*, **24**, 2459-2467
16. SOHN H.J., HARYADI G.D., KIM S.J., 2014, Statistical aspects of fatigue crack growth life of base metal, weld metal and heat affected zone in FSWed 7075-T651 aluminum alloy, *Journal of Mechanical Science and Technology*, **28**, 10, 3957-3962
17. YAKUBOVSKI V.V., VALTERIS I.I., 1989, Geometrical parameters of butt and fillet welds and their influence on the welded joint fatigue life, *International Institute of Welding*, Document XIII, 132689
18. ZHANG X., WANG S., YAN X., YUE D., SUN R., ZHOU X., 2016, Probabilistic analysis for the functional and structural fatigue of NiTi wires, *Materials and Design*, **102**, 213-224

Manuscript received March 2, 2017; accepted for print August 31, 2017

MODIFICATION OF THE ALGORITHM FOR CALCULATING FATIGUE LIFE FOR THE CRITERIA BASED ON THE CONCEPT OF THE CRITICAL PLANE

KRZYSZTOF KLUGER, TADEUSZ ŁAGODA

Opole University of Technology, Department of Mechanics and Machine Design, Opole, Poland

e-mail: k.kluger@po.opole.pl; t.lagoda@po.opole.pl

The aim of this paper is to propose an algorithm for fatigue life determination with the use of widely-known criteria for the fatigue life considering proper determination of material characteristics, which are a function of the number of cycles to failure. The application of the modified algorithm has been presented within the criteria of Findley, Matake, Papadopoulos and Dang Van, and the results of calculations have been compared with test results for steels S355J2G3 and Ck45. For both materials analysed, the application of the modified algorithm in the fatigue criteria makes it possible to obtain much more precise results of the calculations for all types of the loading analysed.

Keywords: mean value, bending with torsion, multiaxial fatigue

1. Introduction

One of the research areas are the criteria for the multiaxial fatigue life, which aim at the assessment of fatigue damage of the material to any loadings. The fundamental part of the multiaxial fatigue life is the suggested function that reduces the multiaxial state of stress to the uniaxial state. Among many functions suggested, one group features the assumption that the components of the stress state are responsible for fatigue crack initiation associated with the plane at a specified orientation. This suggestion, called the concept of the critical plane, has attracted a lot of attention (Karolczuk and Macha, 2005a,b; Skibicki, 2007; Skibicki and Pejkowski, 2012; Kluger and Łagoda, 2014; Kluger, 2015). The reduction functions, suggested in the criteria, are used to calculate the fatigue life by comparison of the reduced value of stress σ_{eq} to stress $\sigma(N_f)$ from a fatigue curve (e.g. of Wöhler or Basquin). The reduction functions based on the critical plane are most often linear or nonlinear functions of material characteristics and the shear stress τ_{ns} , normal stress σ_n (on the critical plane), or hydrostatic stress σ_h (stress state invariant). The reduction function properly suggested and applied to any case, but of the same fatigue life, of the uniaxial loading, e.g. torsion, compression, or bending, brings these stress states to the equivalent state. The fatigue criteria in the original form are usually suggested in order to assess the limit state, hence for the so-called fatigue limit. Therefore, the material characteristics are relationships of the fatigue limits from the uniaxial stress states. Unfortunately, the fatigue criteria, or rather reduction functions, applied in order to calculate the so-called limited fatigue life (for steel $N_f < 2 \cdot 10^6$), are usually applied with coefficients which are functions of the fatigue limits (Findley *et al.*, 1956; Dang Van *et al.*, 1989; Papadopoulos, 1994; Papuga, 2011; Carpinteri *et al.*, 2013). Such an approach is correct only for materials that have parallel fatigue curves ($m_\sigma \cong m_\tau$). This fact has been noticed in, among others, papers (Kurek and Łagoda, 2012; Karolczuk and Kluger, 2014; Karolczuk *et al.*, 2016).

The aim of this paper is to suggest an algorithm for fatigue life determination with the use of widely-known criteria for the fatigue life considering proper determination of material characteristics which are the functions of the number of cycles to failure.

2. Short description of the analysed criteria for multiaxial fatigue life

2.1. Findley's criterion

Findley's criterion (Findley *et al.*, 1956) in the form considering the impact of the mean value of stress has been presented in the following form

$$\tau_{ns,a} + k\sigma_{n,max} \leq \tau_{af} \quad (2.1)$$

where k is a material constant that takes into account the impact of the normal stress and, according to Findley, depends on the number of cycles to failure, and $\sigma_{max} = \sigma_m + \sigma_a$. Findley assumed that the main directions under the proportional loadings do not change. He also drew attention to the fact that the constant k depends on the number of cycles to failure N_f , and this formula is in the following form for reduction of the stress state according to (2.1)

$$\frac{\sigma_f(N_f)}{\tau_f(N_f)} = \frac{2}{1 + \frac{k}{\sqrt{1+k^2}}} \quad (2.2)$$

where $\sigma_f(N_f)$ and $\tau_f(N_f)$ are fatigue curves for symmetrical bending and symmetrical torsion, respectively.

2.2. Papadopoulos' criterion

Papadopoulos (Papadopoulos, 1998) offered a form of the criterion being a linear combination of the maximum amplitude of the generic shear stress T_a on the critical plane and the maximum value of the hydrostatic stress σ_H in the mesoscopic scale, which may be written as

$$\max T_a + k\sigma_{H,max} \leq \tau_{af} \quad (2.3)$$

where k is a coefficient determined by uniaxial fatigue tests in the form of

$$k = 3\left(\frac{\tau_{af}}{\sigma_{af}} - \frac{1}{2}\right) \quad (2.4)$$

The maximum value of the generic shear stress amplitude of T_a is defined as the following

$$T_a(\varphi, \theta) = \sqrt{\frac{1}{\pi} \int_{x=0}^{2\pi} \tau_a^2(\varphi, \theta, \chi) d\chi} \quad (2.5)$$

where τ_a is the shear stress amplitude in the direction of \vec{s} determined by the angle x on the normal plane \vec{n} defined by angles φ and θ according to the formula

$$\tau_a(\varphi, \theta, \chi) = \frac{1}{2} [\max_t \tau(\varphi, \theta, \chi, t) - \min_t \tau(\varphi, \theta, \chi, t)] \quad (2.6)$$

2.3. Matake's criterion

Matake (Matake, 1977) simplified criterion (2.1) by changing the definition of the critical plane. According to Matake, the critical plane is the maximum shear stress plane

$$\tau_{ns,a} + k\sigma_{n,max} \leq \tau_{af} \quad (2.7)$$

Under this approach, there is only one coefficient in the criterion, which is determined using the following formula

$$k = 2\frac{\tau_{af}}{\sigma_{af}} - 1 \quad (2.8)$$

2.4. Dang Van's criterion

The Dang Van's criterion (Dang Van, 1983; Dang Van *et al.*, 1989) is based on the analysis of stress in the mesoscopic scale, which differs from the stress in the macroscopic scale with “the deviatoric part of the stabilized residual stress tensor”. The Dang Van's criterion in the macroscopic scale has been applied in this paper

$$\tau_{ns} + k\sigma_{H,max} \leq \tau_{af} \quad k = 3 \frac{\tau_{af}}{\sigma_{af}} - \frac{3}{2} \quad (2.9)$$

3. Enhanced algorithm for calculating the fatigue life

The algorithm for calculating the number of cycles to failure N_{cal} for both proportional and non-proportional loadings considering the variability of the coefficient k according to the number of cycles N is presented in Fig. 1 (Karolczuk *et al.*, 2016).

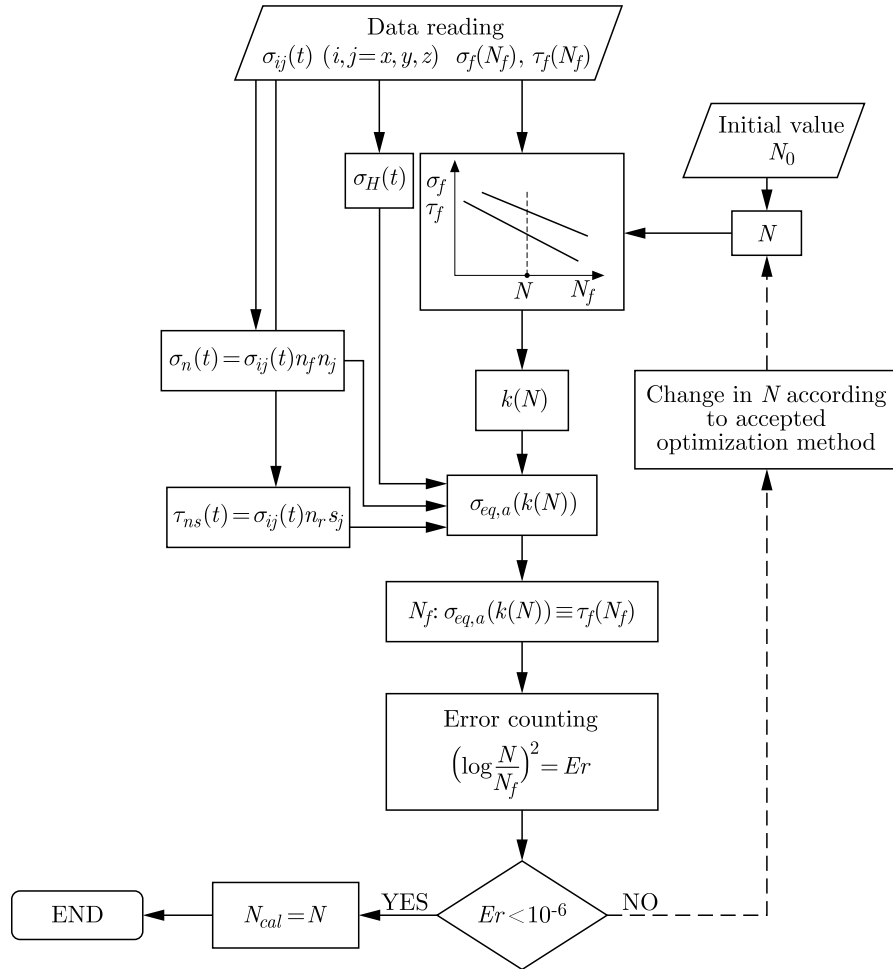


Fig. 1. Algorithm for calculating the fatigue life for proportional loadings considering the variability of the coefficient k according to the number of cycles N

In the first phase, the loading of stress state amplitudes $\sigma_{ij,a}$ takes place for the global coordination system $Oxyz$ and for material constants that define two fatigue curves: $\sigma_f(N_f)$ and $\tau_f(N_f)$. Additionally, a set of unit vectors \mathbf{n} normal to the analysed plane is generated, among which the critical plane orientation is sought. On the basis of $\sigma_{ij,a}$ and for each vector \mathbf{n} , the vector of stress $\mathbf{T} = \boldsymbol{\sigma} \cdot \mathbf{n}$ is calculated by the inner product of the tensor $\boldsymbol{\sigma}$ and vector \mathbf{n} . The

normal stress amplitude $\sigma_{n,a}$ is calculated by the inner product of the vector \mathbf{T} and vector \mathbf{n} . The shear stress amplitude $\tau_{ns,a}$ results from adding the normal and shear stress vectors, that is $\tau_{ns,a}(\mathbf{n}) = \sqrt{\mathbf{T} \cdot \mathbf{T} - \sigma_{n,a}^2}$. In the second path of the algorithm, looped and optimised for the assumed number of cycles N , the value of the coefficient k is calculated on the basis of the assumed fatigue curves $\sigma_f(N_f)$ and $\tau_f(N_f)$. In the next phase, a set of equivalent stress amplitudes $\sigma_{eq,a}$ (in set \mathbf{n}) for the assumed N is calculated. Then the set $\sigma_{eq,a}(\mathbf{n})$ is browsed in order to determine the orientation \mathbf{n}_c of the critical plane according to the criterion adopted. The determined value $\sigma_{eq,a}(\mathbf{n}_c)$ is substituted to fatigue curves $\sigma_f(N_f)$ or $\tau_f(N_f)$ to determine a possible number of cycles to failure N_f . With the use of the objective function

$$\left(\log \frac{N}{N_f}\right)^2 = Er \quad (3.1)$$

the concurrence of the number of cycles N and N_f is determined. If the error Er is less than 10^{-6} , the algorithm is terminated by adopting $N_{cal} = N$. In another case, the value N is altered and the second path of the algorithm is repeated.

4. Experimental data

The suggested algorithm has been verified on the basis of the experimental data concerning steels S355J2G3 (Pawliczek and Prażmowski, 2015; Kluger and Łagoda, 2014) and Ck45, which were taken from the literature (Simbürger, 1975).

Based on the data, the coefficients of fatigue curves have been calculated under uniaxial loadings according to the ASTM standards (ASTM E1049-85(2011)e1, 2003):

— for bending

$$\sigma_f(N_f) : \quad \log N_f = A_\sigma - m_\sigma \log \sigma_f \quad (4.1)$$

— for torsion

$$\tau_f(N_f) : \quad \log N_f = A_\tau - m_\tau \log \tau_f \quad (4.2)$$

where N_f is the estimated number of cycles to failure, A_σ , m_σ , A_τ , m_τ are parameters of the linear regression equation. The basic strength and fatigue parameters of the materials analysed are presented in Table 1. Types of analysed loadings for steel S355J2G3 and Ck45 are presented in Table 2.

Table 1. The basic strength parameters and material constants for fatigue curves (4.1) and (4.2) with the confidence intervals for a probability of 0.95

Material (EN)	E [GPa]	R_e [MPa]	R_m [MPa]	ν	A_σ	m_σ	A_τ	m_τ
S355J2G3	213	394	611	0.31	23.8 ± 4.0	7.2 ± 1.6	32.8 ± 8.7	11.7 ± 3.8
Ck45	210	704	850	0.30	28.5 ± 3.9	9.0 ± 1.5	77.0 ± 13.5	29.3 ± 5.5

The evaluation of the effectiveness of criteria for the multiaxial fatigue of materials for a limited number of cycles to failure typically involves comparison of the calculated strength N_{cal} with the experimental one N_{exp} on a log-log diagram with additionally calculated parameters of the scatter of results (Karolczuk and Kluger, 2014; Kluger, 2015). In order to assess the effectiveness of the algorithm suggested, an original function $\text{Pr}(T)$ has been proposed

$$\text{Pr}(T) = \text{Prob}\left(\frac{N_{exp}}{T} \leq N_{cal} \leq T N_{exp}\right) \quad \text{for} \quad T \geq 1 \quad (4.3)$$

Table 2. Types of the analysed loading for steel S355J2G3 and Ck45

S355J2G3	Ck45
Zero mean stress	
$\sigma_a \neq 0$	$\sigma_a \neq 0$
$\tau_a \neq 0$	$\tau_a \neq 0$
$\sigma_a = \tau_a \neq 0, \varphi = 0^\circ$	$\sigma_a = \tau_a \neq 0, \varphi = 0^\circ$
$\sigma_a = 2\tau_a \neq 0, \varphi = 90^\circ$	$\sigma_a = 1.7\tau_a, \varphi = 60^\circ$
$\sigma_a = 3\tau_a \neq 0, \varphi = 90^\circ$	$\sigma_a = 1.7\tau_a, \varphi = 90^\circ$
Non-zero mean stress	
$\sigma_a \neq 0, \sigma_m \neq 0$	$\sigma_a \neq 0, \sigma_m \neq 0$
$\tau_a \neq 0, \tau_m \neq 0$	$\sigma_a = 1.7\tau_a, \tau_m \neq 0, \varphi = 0^\circ$
$\sigma_a = \tau_a \neq 0, \sigma_m = \tau_m \neq 0, \varphi = 0^\circ$	$\sigma_a = 1.7\tau_a, \sigma_m \neq 0, \varphi = 0^\circ$
	$\sigma_a = 1.7\tau_a, \sigma_m \neq 0, \varphi = 90^\circ$

and

$$T(\text{Pr}) = 0.95 \quad (4.4)$$

Function (4.3) describes the probability that the calculated fatigue life N_{cal} is within the scatter band with the coefficient of T , wherein $T \geq 1$, which means that $T = N_{cal}/N_{exp}$ for $N_{cal} \geq N_{exp}$ or $T = N_{exp}/N_{cal}$ for $N_{cal} < N_{exp}$. This is an increasing function, based on which one can estimate (through interpolation) the scatter band T , which includes, for example, 95% of the specimens, see equation (4.4).

5. Results of calculations and their analysis

The number of cycles to failure N_{cal} has been calculated with the use of two algorithms, which, for the sake of their presentation clarity, have been marked as: *NA* – the new algorithm suggested in this paper that takes into account the variability of the coefficient k according to the number of cycles N ; *CA* – the classical algorithm in which the coefficient k is constant and corresponds to the theoretical limit fatigue, i.e. for $N_f = 2 \cdot 10^6$ cycles. Figures 2 to 9 show a comparison of the experimental number of cycles N_{exp} with the calculated number of cycles to failure. Additionally, each of these figures features dispersion parameters $T(0.95)$ calculated for each type of the loading. The dotted line represents the scatter band for the coefficient equal to 3, and the solid line represents the ideal correspondence. In the case of the parameter T exceeding the value of 50, the precise value of T has not been given since such a high value of dispersion renders the given approach unusable. The scatter band $T(0.95)$ is calculated separately for each type of the loading (σ_a – bending, τ_a – torsion, σ_a - τ_a -proportional bending-torsion and σ_a - τ_a -non-proportional bending-torsion, etc.) and also for the results from all types of the loading treated as a set (a total scatter band). In such a case, not all points N_{exp} - N_{cal} are within the boundaries of graphs in the figure. Such a scattering is due to the imperfections of the analyzed fatigue criteria for some types of the load.

In order to estimate the level of improvement, a proportion between the scatter bands $T(NA)/T(CA)$ is calculated for computations with the use of both the new and classical algorithms. The correlation improvement is achieved for $T(NA)/T(CA) < 1$. The results of the comparison of the scatter bands are presented in Fig. 10.

The graphical comparison of the results obtained with the use of selected comparative fatigue criteria with the experimental results, which are presented in Figs. 2 to 9, has enabled a more

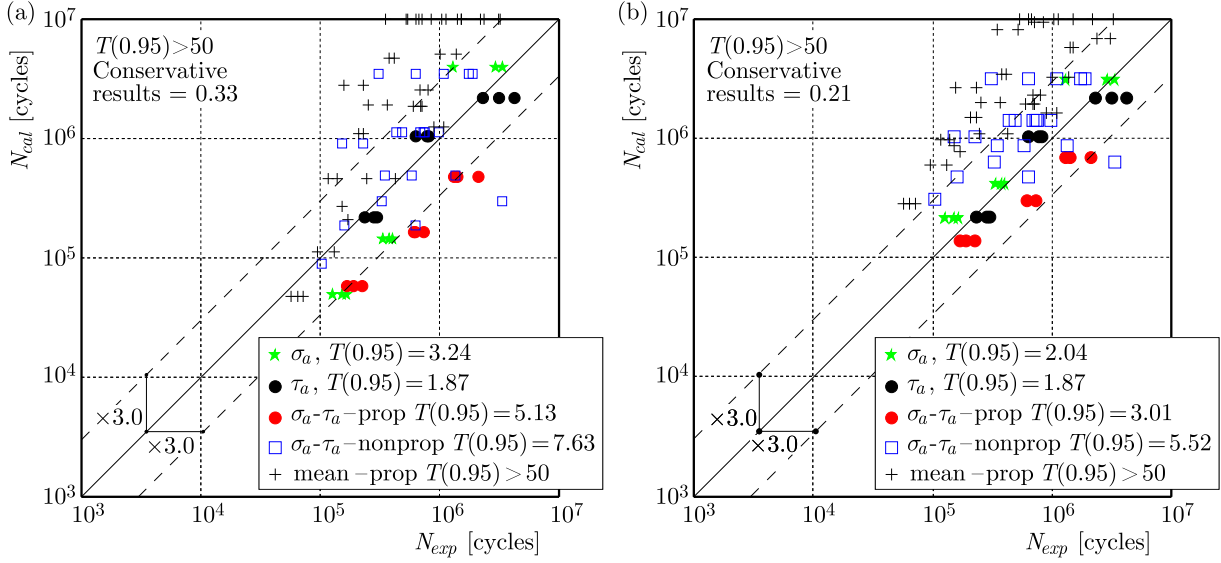


Fig. 2. Comparison of the experimental fatigue life N_{exp} with the calculated fatigue life N_{cal} for the Findley criterion and for S355J2G3 steel, according to: (a) classical algorithm CA , (b) new algorithm NA

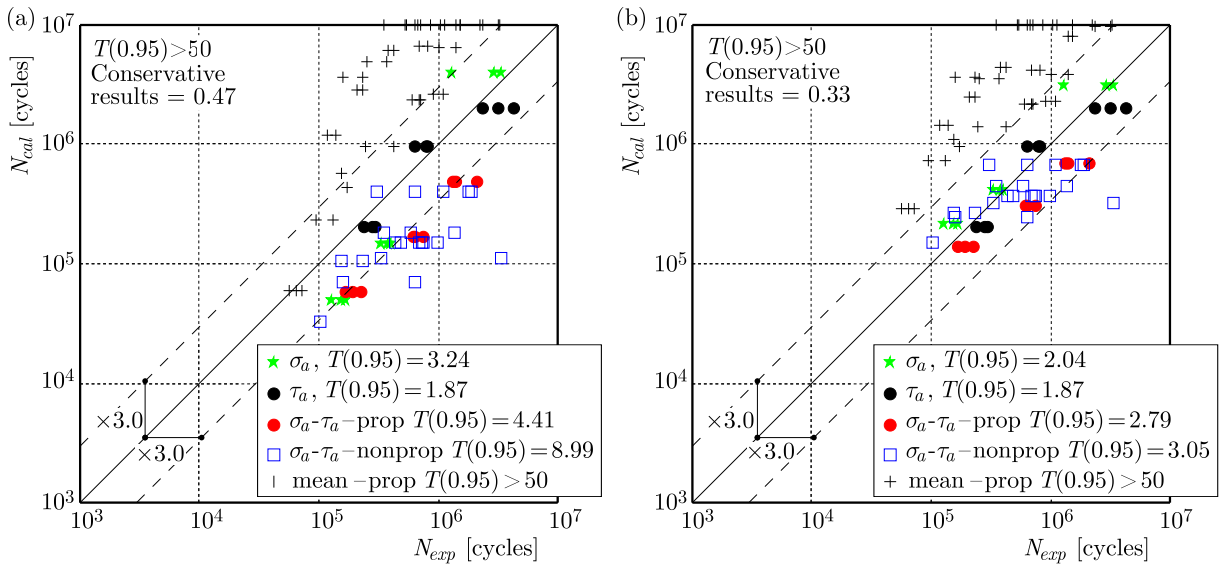


Fig. 3. Comparison of the experimental fatigue life N_{exp} with the calculated fatigue life N_{cal} for the Papadopoulos criterion and for S355J2G3 steel, according to: (a) classical algorithm CA , (b) new algorithm NA

profound assessment of the capacity of applying the algorithms being described in the fatigue criteria, and also given insight into their usefulness for the estimation of the fatigue life of selected construction materials. A considerable increase in the calculation results has been achieved for all materials analysed and for most types of the loading.

The higher scatter bands achieved for loadings in the presence of nominal stress is caused by an insufficient consideration of the nominal stress in the fatigue criteria.

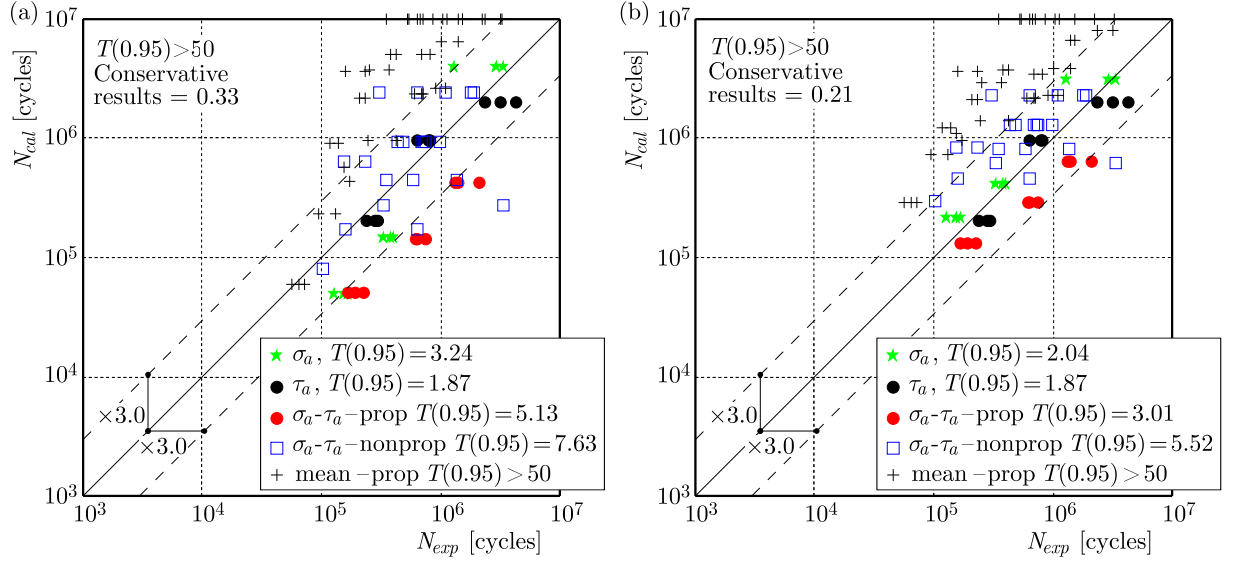


Fig. 4. Comparison of the experimental fatigue life N_{exp} with the calculated fatigue life N_{cal} for the Matake criterion and for S355J2G3 steel, according to: (a) classical algorithm CA , (b) new algorithm NA

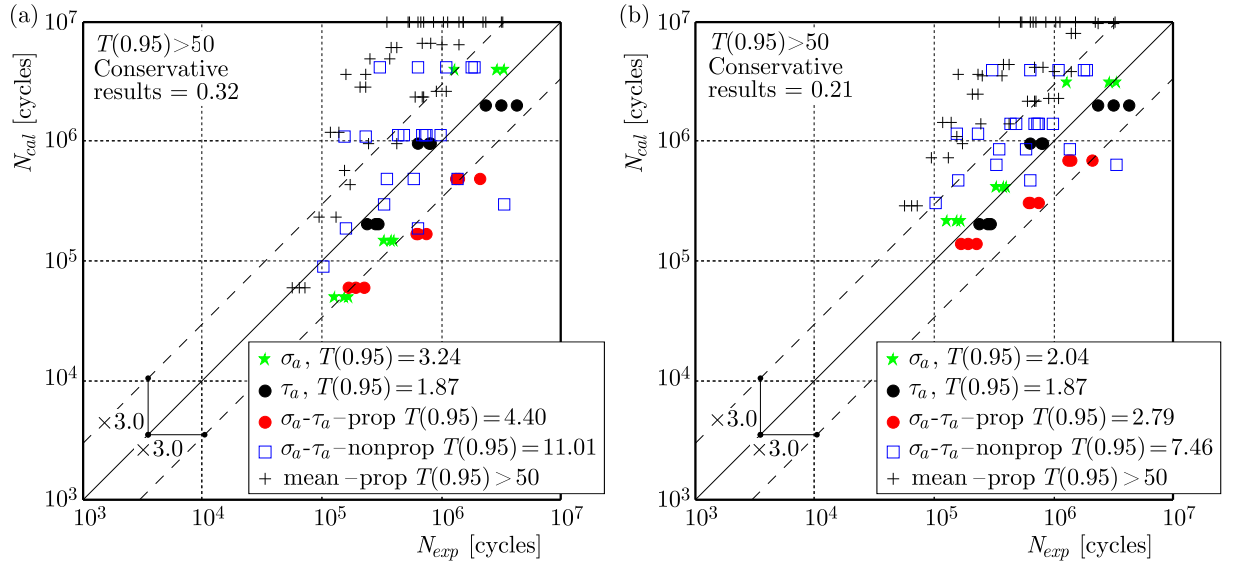


Fig. 5. Comparison of the experimental fatigue life N_{exp} with the calculated fatigue life N_{cal} for the Dang Van criterion and for S355J2G3 steel, according to: (a) classical algorithm CA , (b) new algorithm NA

6. Conclusions

On the basis of the analyses performed, the following conclusions may be drawn:

- The suggested algorithm for calculating the fatigue life that takes into account the variability of the coefficients occurring in the fatigue criteria according to a number of cycles is concurrent in the analysed proportional ranges of proportional and non-proportional cyclic loadings, with non-zero mean stress, both in the presence and absence of the nominal stress.

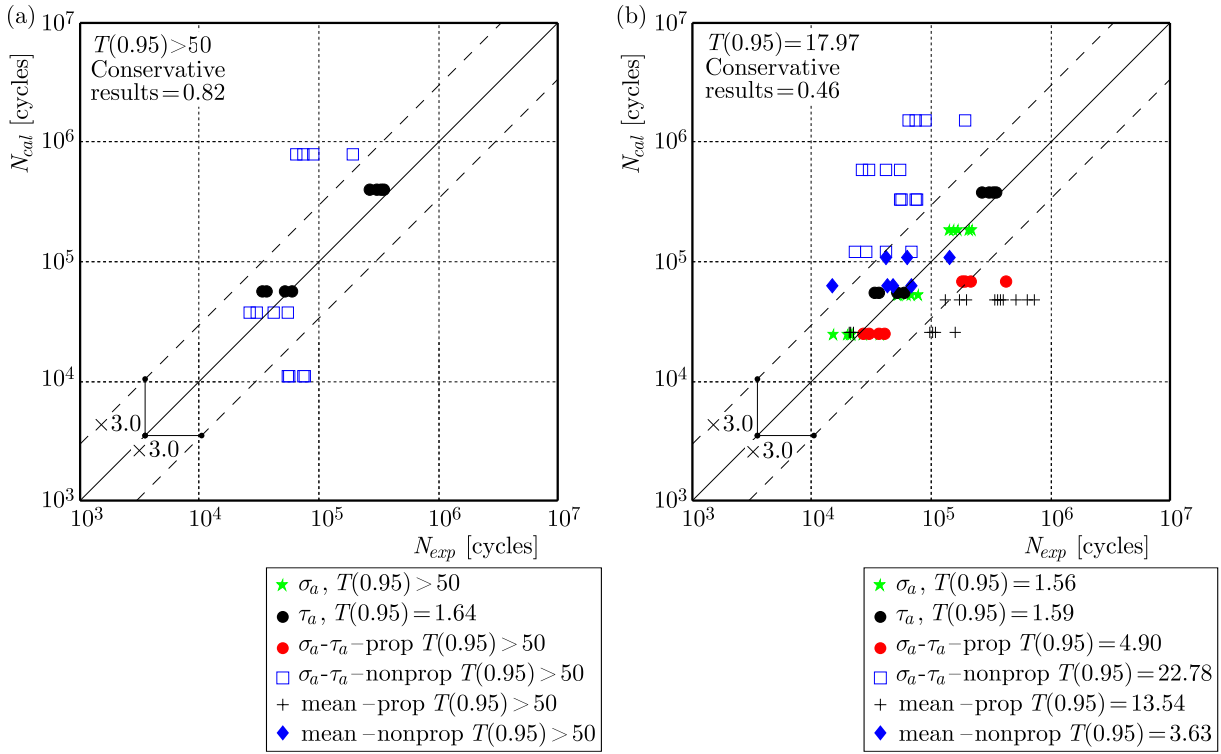


Fig. 6. Comparison of the experimental fatigue life N_{exp} with the calculated fatigue life N_{cal} for the Findley criterion and for Ck45 steel, according to: (a) classical algorithm CA , (b) new algorithm NA

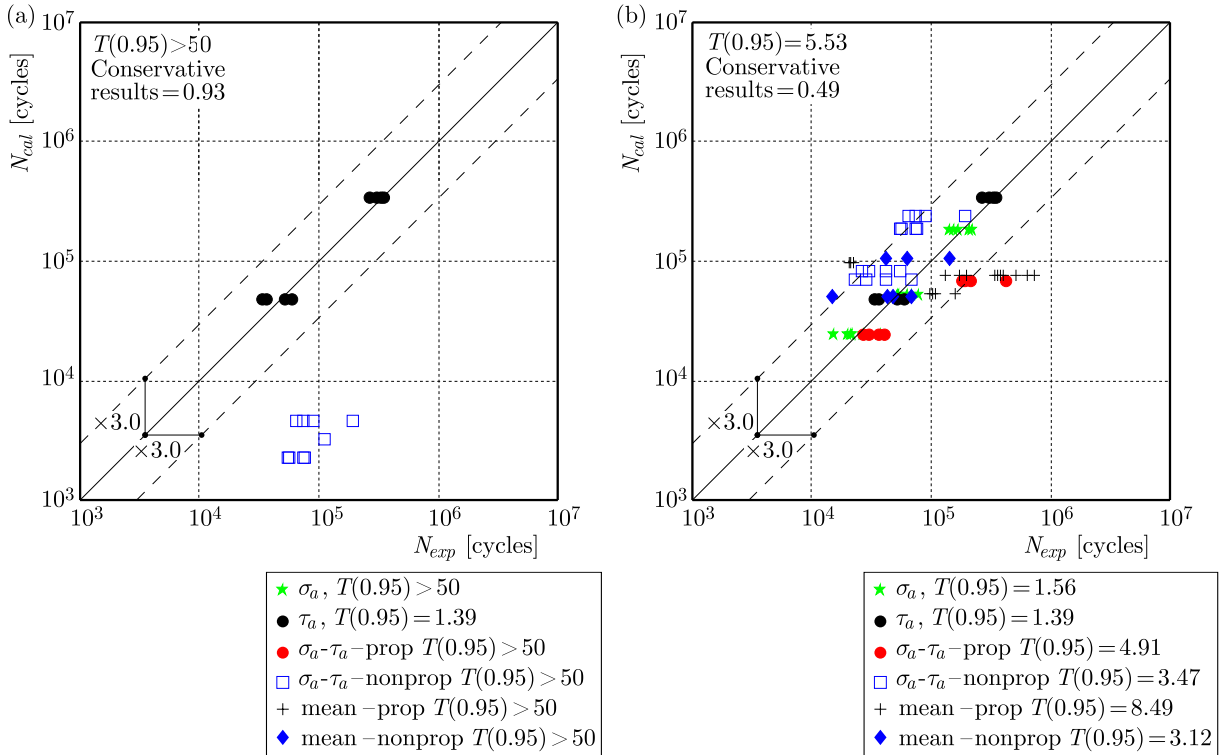


Fig. 7. Comparison of the experimental fatigue life N_{exp} with the calculated fatigue life N_{cal} for the Papadopoulos criterion and for Ck45 steel, according to: (a) classical algorithm CA , (b) new algorithm NA

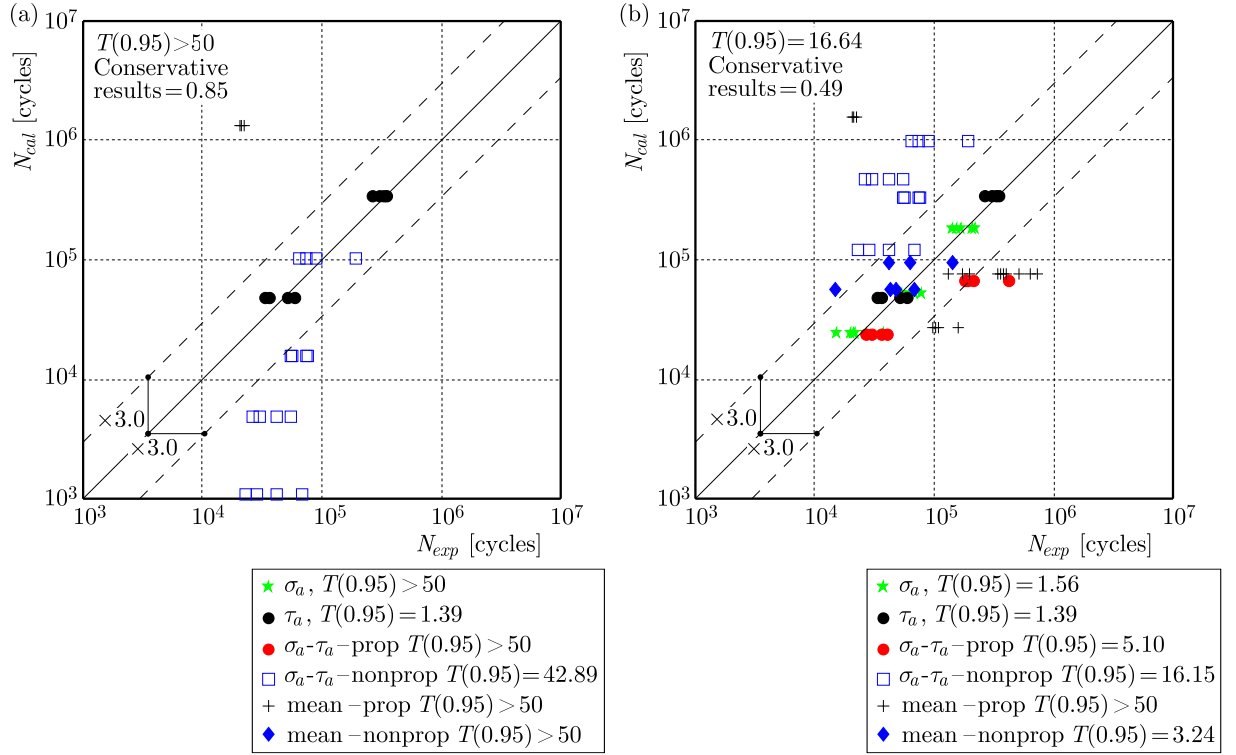


Fig. 8. Comparison of the experimental fatigue life N_{exp} with the calculated fatigue life N_{cal} for the Matake criterion and for Ck45 steel, according to: (a) classical algorithm CA, (b) new algorithm NA

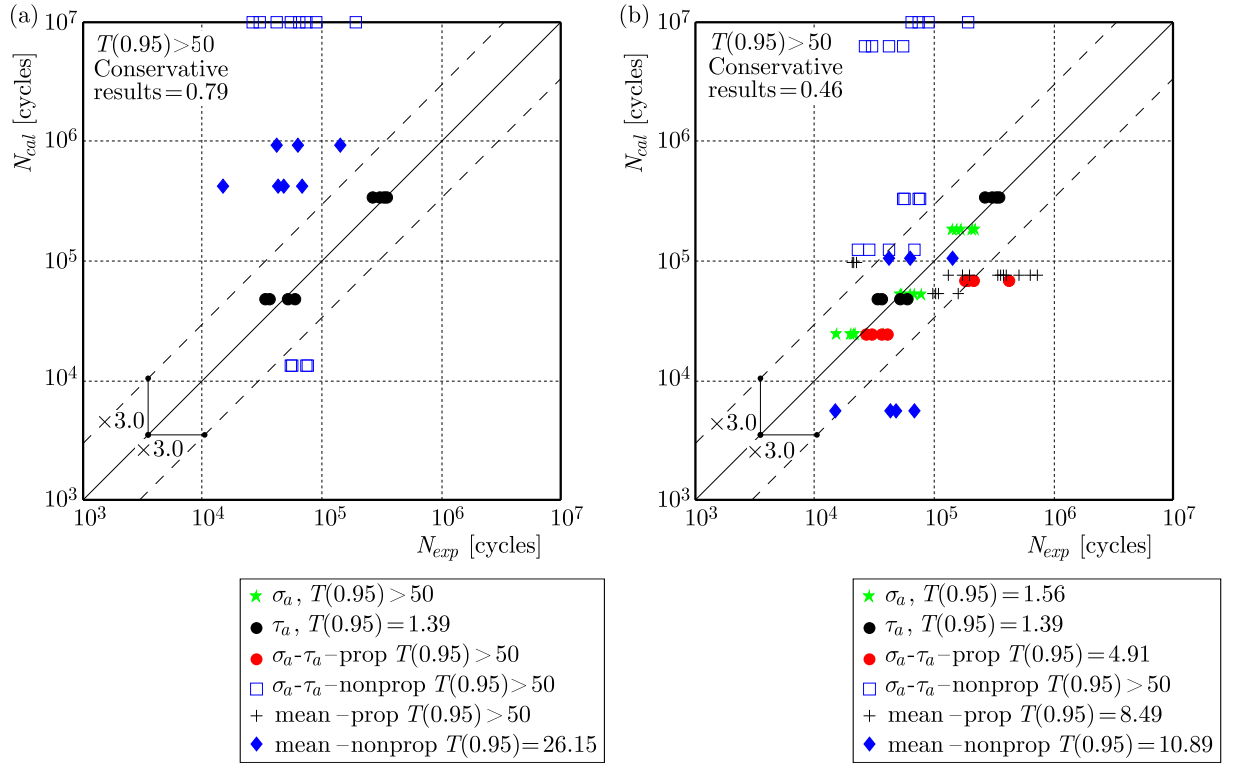


Fig. 9. Comparison of the experimental fatigue life N_{exp} with the calculated fatigue life N_{cal} for the Dang Van criterion and for Ck45 steel, according to: (a) classical algorithm CA, (b) new algorithm NA

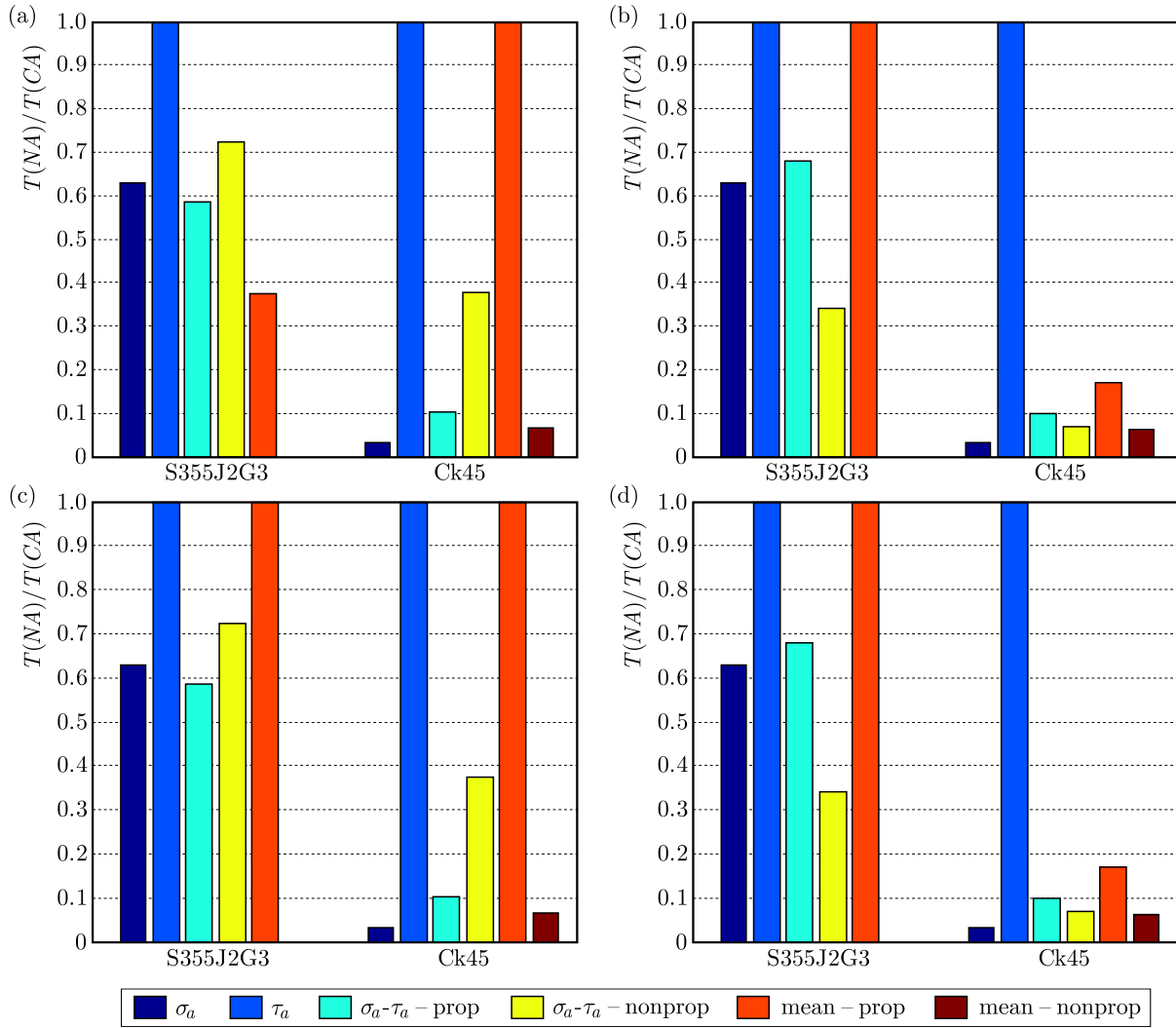


Fig. 10. Comparison of the scatter bands of the new and classical algorithms for the materials and types of the loading analysed: (a) Findley criterion, (b) Papadopoulos criterion, (c) Mataké criterion, (d) Dang Van criterion

- By the variability of the coefficients used in the fatigue criteria according to the number of cycles, a considerable increase in the correspondence between the calculation and experimental results for steel S355J2G3 and Ck45 has been achieved.
- The discrepancies in the results of the experiment and calculations in the presence of the nominal stress are caused by neglecting the shear stress in the criteria analysed.
- The modified algorithm described here may be applied to most criteria in the literature that are based on the concept of the critical plane.

References

1. ASTM E1049-85(2011)e1, 2003, *Standard Practices for Cycle Counting in Fatigue Analysis*, ASTM International, West Conshohocken, PA
2. CARPINTERI A., SPAGNOLI A., VANTADORI S., BAGNI C., 2013, Structural integrity assessment of metallic components under multiaxial fatigue: the C-S criterion and its evolution, *Fatigue and Fracture of Engineering Materials and Structures*, **36**, 9, 870-883

3. DANG VAN K., 1983, Macro-micro approach in high-cycle multiaxial fatigue, *American Society for Testing and Materials STP 1191*, 120-130
4. DANG VAN K., CAILLETAUD G., FLAVENOT J.F., LE DOUARON A., LIEURADE H.P., 1989, Criterion for high cycle fatigue failure under multiaxial loading, *Mechanical Engineering Publications*, London, 459-478
5. FINDLEY W.N., COLEMAN J.J., HANLEY B.C., 1956. Theory for combined bending and torsion fatigue with data for SAE 4340 steel, *International Conference on Fatigue of Metals*, London
6. KAROLCZUK A., KLUGER K., 2014, Analysis of the coefficient of normal stress effect in chosen multiaxial fatigue criteria, *Theoretical and Applied Fracture Mechanics*, **73**, 39-47
7. KAROLCZUK A., KLUGER K., ŁAGODA T., 2016, A correction in the algorithm of fatigue life calculation based on the critical plane approach, *International Journal of Fatigue*, **83**, 174-183
8. KAROLCZUK A., MACHA E., 2005a, Critical planes in multiaxial fatigue, [In:] *Materials Structure and Micromechanics of Fracture*, J. Pokluda (Edit.), Zurich-Uetikon: Trans Tech Publications Ltd, 109-114
9. KAROLCZUK A., MACHA E., 2005b. Fatigue fracture planes and expected principal stress directions under biaxial variable amplitude loading, *Fatigue Fracture of Engineering Materials and Structures*, **28**, 1/2, 99-106
10. KLUGER K., 2015, Fatigue life estimation for 2017A-T4 and 6082-T6 aluminium alloys subjected to bending-torsion with mean stress, *International Journal of Fatigue*, **80**, 22-29
11. KLUGER K., ŁAGODA T., 2014, New energy model for fatigue life determination under multiaxial loading with different mean values, *International Journal of Fatigue*, **66**, 229-245
12. KUREK M., ŁAGODA T., 2012, Estimation of fatigue life of materials with out-of-parallel fatigue characteristics under block loading, *Materials Science Forum*, **726**, 181-188
13. MATAKE T., 1977, An explanation on fatigue limit under combined stress, *Bulletin of the JSME*, **20**, 141, 257-263
14. PAPADOPOULOS I.V., 1994, A new criterion of fatigue-strength for out-of-phase bending and torsion, *International Journal of Fatigue*, **16**, 6, 377-384
15. PAPADOPOULOS I.V., 1998, Critical plane approaches in high-cycle fatigue: on the definition of the amplitude and mean value of the shear stress acting on the critical plane, *Fatigue and Fracture of Engineering Materials and Structures*, **21**, 3, 269-285
16. PAPUGA J., 2011, A survey on evaluating the fatigue limit under multiaxial loading, *International Journal of Fatigue*, **33**, 2, 153-165
17. PAWLICZEK R., PRAŻMOWSKI M., 2015, Study on material property changes of mild steel S355 caused by block loads with varying mean stress, *International Journal of Fatigue*, **80**, 171-177
18. SIMBÜRGER A., 1975, Festigkeitsverhalten zäher Werkstoffe bei einer mehrachsigen phasenverschobenen Schwingbeanspruchung mit körperfesten und veränderlichen Hauptspannungsrichtungen. LBF Darmstadt – Bericht Nr FB-1975.
19. SKIBICKI D., 2007, Experimental verification of fatigue loading nonproportionality model, *Journal of Theoretical and Applied Mechanics*, **45**, 2, 337-348
20. SKIBICKI D., PEJKOWSKI L., 2012, Integral fatigue criteria evaluation for life estimation under uniaxial combined proportional and non-proportional loadings, *Journal of Theoretical and Applied Mechanics*, **50**, 4, 1073-1086

STEADY AND UNSTEADY ANALYSIS OF NACA 0018 AIRFOIL IN VERTICAL-AXIS WIND TURBINE

KRZYSZTOF ROGOWSKI

Warsaw University of Technology, Institute of Aeronautics and Applied Mechanics, Warsaw, Poland

e-mail: krogowski@meil.pw.edu.pl

MARTIN O.L. HANSEN

Technical University of Denmark, DTU Wind Energy, Department of Wind Energy, Lyngby, Denmark

e-mail: molh@dtu.dk

RYSZARD MAROŃSKI

Warsaw University of Technology, Institute of Aeronautics and Applied Mechanics, Warsaw, Poland

e-mail: maron@meil.pw.edu.pl

Numerical results are presented for aerodynamic unsteady and steady airfoil characteristics of the NACA 0018 airfoil of a two-dimensional vertical-axis wind turbine. A geometrical model of the Darrieus-type wind turbine and the rotor operating parameters used for numerical simulation are taken from the literature. Airfoil characteristics are investigated using the same mesh distribution around the airfoil edges and two turbulence models: the RNG $k-\varepsilon$ and the SST Transition. Computed results for the SST Transition model are in good agreement with the experiment, especially for static airfoil characteristics.

Keywords: airfoil characteristics, vertical-axis wind turbine, computational fluid dynamics

1. Introduction

Generally, with respect to the orientation of the rotor shaft, wind turbines can be divided into two main groups: horizontal-axis wind turbines (HAWTs, or axial flow turbines) and vertical-axis wind turbines (VAWTs, or cross-flow turbines) (Maroński, 2016). Wind turbines can also be divided with respect to the principle of operation: lift-driven and drag-driven machines (Rogowski, 2014). Although, HAWTs are now widely used in the industry, large-scale VAWTs are designed as offshore units – floating wind turbines (Madsen *et al.*, 2013; Borg *et al.*, 2014). Aerodynamic efficiency (power coefficient) of drag-driven wind turbines is low, therefore, they are used relatively rarely (Rogowski and Maroński, 2015). In 1931, Georges J.M. Darrieus, a French aeronautical engineer, patented his invention – a new type of windmill designed for power generation (Blackwell, 1974). The Darrieus wind turbine is a lift-driven wind turbine having two or more blades. The rotor of the Darrieus wind turbine can achieve relatively high aerodynamic efficiency (Hau, 2006). Originally, the Darrieus wind turbine had curved blades with a symmetrical airfoil in their cross sections. The curved blade shape, so-called troposkien, was designed to avoid large bending stresses of the blades, especially when applied to large units (Paraschivoiu, 2009). Darrieus-type wind turbines are designed both as large- and small-size wind turbines with both curved and straight blades. The characteristics of the Darrieus-type wind turbines are: slightly lower power coefficient than HAWTs (Amet *et al.*, 2009); the gearbox and the power generator can be installed at the ground level; the yaw system is not needed because the rotor operates regardless of the wind direction. The main shortcomings of these wind turbines are: low starting torque and vibrations of the structure during rotor operation

(Paraschivoiu, 2009). The growing demand for decentralized electricity generation in urban and rural areas is the motivation for studying wind turbines in a small scale.

Darrieus-type vertical-axis wind turbines are relatively simple devices. The movement of a single wind turbine blade is similar to the movement of the pitching blade. During rotation of the rotor, the blade angle of attack, the local Reynolds number and the relative wind velocity vary according to the rotor azimuthal angle. These variations also depend on the relationship between the tangential velocity of the wind turbine blade and wind velocity. For these reasons, many nonlinear phenomena occur in a single cycle of the blade (Laneville and Vittecoq, 1986). The rotor power coefficient defined as the ratio of the power absorbed by the rotor shaft divided by the power available from the air stream flowing through the rotor swept area (Hansen, 2008), depends on the tip speed ratio defined as the ratio of the tangential blade velocity to the wind speed. Typical Darrieus wind turbine achieves the maximum power coefficient of about 0.4 at the tip speed ratio of 5-6 (Hau, 2006). Dynamic effects associated with dynamic stall phenomena occur at low tip speed ratios (below 4). Aerodynamic effects of the rotor elements such as blades, tower, struts, etc., play important role in reduction of the rotor power coefficient at high tip speed ratios (above 6) (Paraschivoiu, 2009).

Although, measurement techniques have been improved in the recent years, only a few experimental tests of unsteady aerodynamic blade loads have been performed. Measurement difficulties are particularly associated with the tangential blade load component (tangential to the rotor swept area) which is responsible for creation of the rotor torque. This is because the tangential blade load is very low compared with the normal blade load component (normal to the rotor swept area). Experiments referring to aerodynamic blade loads of the Darrieus-type vertical-axis wind turbines were performed in a water towing tank at Texas Tech University (Strickland *et al.*, 1979, 1981). Laneville and Vittecoq (1986) conducted investigations of lift and drag airfoil characteristics of a small-size vertical-axis Darrieus-type wind turbine in a wind tunnel. Ferreira *et al.* (2011) showed that it was possible, though crudely, that the blade loading could be extracted from velocity flow fields using a method that they had developed.

Streamtube models and single-wake vortex models are often used in simulations of aerodynamic blade loads of VAWTs (Paraschivoiu, 2009; Ferreira, 2009). Nowadays, computational methods of fluid dynamics (CFD) have become popular in many areas of engineering as they can provide very accurate results when referring to the experiments performed on a full-scaled object (Lichota, 2013; Lichota, 2016). The incorporated turbulence models are in numerical computations a compromise between the available hardware capabilities and accuracy of computations. In order to resolve all scales of turbulence, it is necessary to apply an appropriate mesh with very small grid elements. Using a space-time mesh fine enough to compute all scales of turbulence is still a very difficult task for modern supercomputers. However, the increase in computing power of modern computers has led to the development of computationally expensive turbulence models (Ferreira *et al.*, 2007). Ponta and Jacovkis (2001) investigated the Darrieus-type wind turbine using a combined method consisting of a classic free vortex model and finite element techniques. Amet *et al.* (2009) performed CFD analysis of the two-bladed rotor basing on the experiment of Laneville and Vittecoq (1986) at tip speed ratios of 2 and 7. Many numerical simulations of two-dimensional Darrieus-type wind turbines using different turbulence models were made by Rogowski (2014). 3D simulations of a straight-bladed vertical axis tidal turbines were performed by Marsh *et al.* (2013) using the SST $k-\omega$ turbulence model.

Generally, Darrieus wind turbines operate at low Reynolds numbers. The range of the blade angle of attack is very large. Streamtube models and vortex models require C_L and C_D airfoil characteristics in order to compute aerodynamic blade loads. Aerodynamic characteristics can be computed using CFD methods (Rogowski, 2014; Sarlak *et al.*, 2014) or performed experimentally (Sheldahl and Klimas, 1981; Laneville and Vittecoq, 1986).

The three main objectives of this work are as follows:

- Determination of aerodynamic coefficients for unsteady flow around the wind turbine using a hybrid mesh consisting of a structured quadrilateral mesh close to airfoil edges and an unstructured triangle mesh elsewhere.
- Investigation of steady characteristic of the NACA 0018 airfoil using the same mesh distribution as during the unsteady flow simulation of the VAWT.
- Comparison of the aerodynamic characteristics for two turbulence models: the RNG $k-\varepsilon$ and the SST Transition.

2. Wind turbine parameters

In this paper, the authors present computed airfoil characteristics of a rotating wind turbine blade and of a stationary airfoil. Computed airfoil characteristics are compared with the experiment of Laneville and Vittecoq (1986). The experiment was conducted in an open jet wind tunnel at the Universite de Sherbrooke. The main objective of Laneville and Vittecoq was to measure aerodynamic blade loads for a two-bladed rotor with zero offset pitch angle using strain gauges. Basic geometrical parameters of the investigated wind turbine are given in Table 1. In the central part of the rotor, a torsion-free steel shaft supported by two ball bearings was mounted. The rotor blades made of balsa wood were supported by horizontal arms at the lower part of the rotor and by two guitar wires stretched between the shaft and the blades at the upper part of the rotor. Measuring devices such as force transducers and amplifiers were placed in the lower horizontal arms. During the experiment, a special variable-speed electric motor was used to maintain the correct rotational velocity. The effect of centrifugal forces on aerodynamic blade loads were removed from experimental data. The experimental measured data was not corrected for blockage effects. The method of measurement of aerodynamic blade load components is presented in Fig. 1.

Table 1. Basic parameters of the investigated wind turbine

Parameter	Value
Rotational speed n [rpm]	300
Rotor radius R [m]	0.3
Chord c [m]	0.061
Airfoil	NACA 0018
Number of blades N	2
Tower diameter d [m]	0.0381
Tip speed ratio TSR	5
Wind velocity V_∞ [m/s]	1.88

The static NACA 0018 airfoil characteristics C_L and C_D were measured in the experiment using the same wind turbine and using the same measuring system as described above (Laneville and Vittecoq, 1986).

3. Lift and drag coefficients

In this paper, the angle of attack is an angle between the tangential velocity of the rotor blade V_T ($V_T = \omega R$, where ω is angular velocity of the rotor, R – rotor radius) and relative velocity V_R which is a resultant of the wind speed V_∞ and the tangential velocity V_T taken with the minus sign (Fig. 2)

$$\mathbf{V}_R = \mathbf{V}_\infty - \mathbf{V}_T \quad (3.1)$$

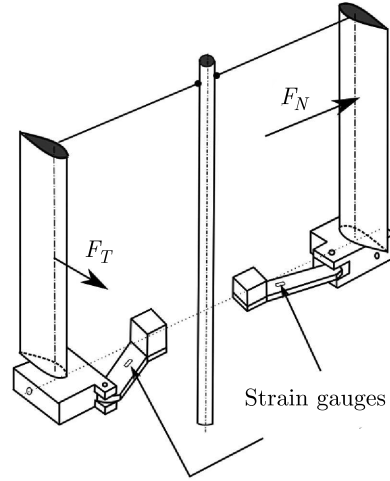


Fig. 1. Silhouette of the turbine rotor and the method of measurement of aerodynamic blade loads (Laneville and Vittecoq, 1986)

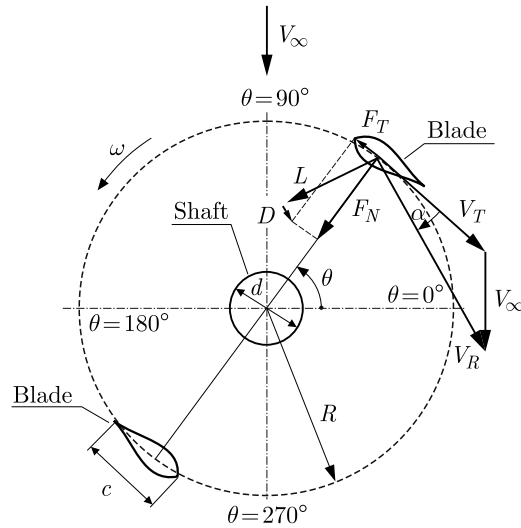


Fig. 2. Geometrical parameters of the rotor. Velocity vectors, angles and aerodynamic loads

From geometrical considerations (Fig. 2), the vector components V_R in the tangential and normal directions to the blade trajectory are respectively

$$V_{Rt} = V_T + V_\infty \cos \theta \quad V_{Rn} = V_\infty \sin \theta \quad (3.2)$$

where θ is the azimuth angle. The tangent angle of attack α is

$$\tan \alpha = \frac{V_{Rn}}{V_{Rt}} = \frac{V_\infty \sin \theta}{V_T + V_\infty \cos \theta} \quad (3.3)$$

Dividing the numerator and denominator of this equation by V_∞ we get

$$\tan \alpha = \frac{\sin \theta}{\frac{V_T}{V_\infty} + \cos \theta} \quad (3.4)$$

TSR is the tip speed ratio defined as

$$TSR = \frac{V_T}{V_\infty} = \frac{\omega R}{V_\infty} \quad (3.5)$$

Taking into account the above formula in equation (3.4), the angle of attack is

$$\alpha = \tan^{-1} \left(\frac{\sin \theta}{\cos \theta + TSR} \right) \quad (3.6)$$

The relative velocity V_R can be defined as

$$V_R = \sqrt{(\omega R + V_\infty \cos \theta)^2 + (V_\infty \sin \theta)^2} \quad (3.7)$$

During wind turbine operation, the blade angle of attack varies with the azimuth θ , whereas the relative wind velocity is associated with a variation in the angle of attack (Fig. 3). The lift and drag coefficients are given by

$$C_L = \frac{L}{\frac{1}{2} \rho c (\omega R)^2} \quad C_D = \frac{D}{\frac{1}{2} \rho c (\omega R)^2} \quad (3.8)$$

where L is the lift force, D – drag, ρ – air density, c – chord.

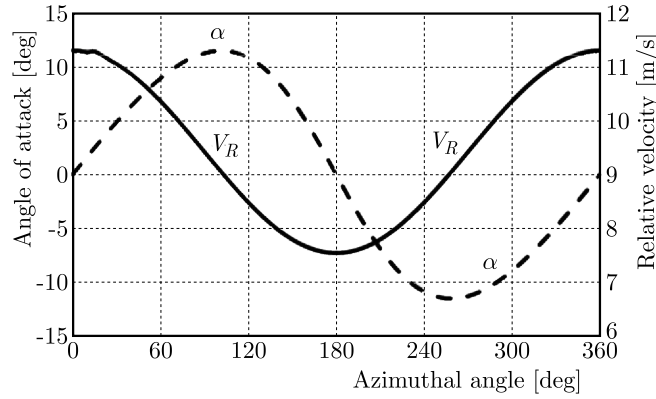


Fig. 3. Evolution of the angle of attack and the relative velocity vs azimuthal angle at the tip speed ratio of 5

The definitions of the lift and drag coefficients contain the tangential velocity of the blade $V_T = \omega R$ instead of the relative velocity V_R . In the case of VAWTs, the relative velocity is constantly changing in both magnitude and incidence. The use of the constant reference velocity in the dynamic pressure is desirable since it is possible to compare force coefficients for different airfoils (Danao *et al.*, 2012; Amet *et al.*, 2009).

4. Numerical model

One of the main objectives of this study is to investigate unsteady aerodynamic characteristics of the wind turbine airfoil and steady aerodynamic characteristics of the same airfoil. The numerical two-dimensional model of the vertical-axis Darrieus-type wind turbine consists of two NACA 0018 airfoils and a tower which has been modeled as a circle (Fig. 2). Simulations of the steady airfoil characteristics have been performed using only a single NACA 0018 airfoil with the same chord.

The model of the wind turbine rotor has been enclosed in a square area of a virtual wind tunnel. According to the previous investigations of the authors (Rogowski, 2014; Rogowski and Maroński, 2015), the length of the virtual wind tunnel should be at least equal to ten rotor diameters. The static characteristics of NACA 0018 have been obtained using one airfoil placed in a square area of the virtual wind turbine with the same length as in the case of the rotating rotor.

The mesh near airfoils has been created using structural quadrilateral elements. The height of the first layer of the structural grid is $7 \cdot 10^{-7}$ m giving $y^+ \leq 1$. The growth rate of each layer of the structured mesh is 1.13. The airfoil edges are divided into small parts with lengths of $2 \cdot 10^{-4}$ m. The growth rate of the unstructured mesh is 1.06. The mesh for unsteady simulations, presented in Fig. 4 contains of 133 366 elements. In the case of the stationary airfoil, the same mesh distribution around the NACA 0018 is used and the number of mesh elements of the virtual wind tunnel is 74 834.

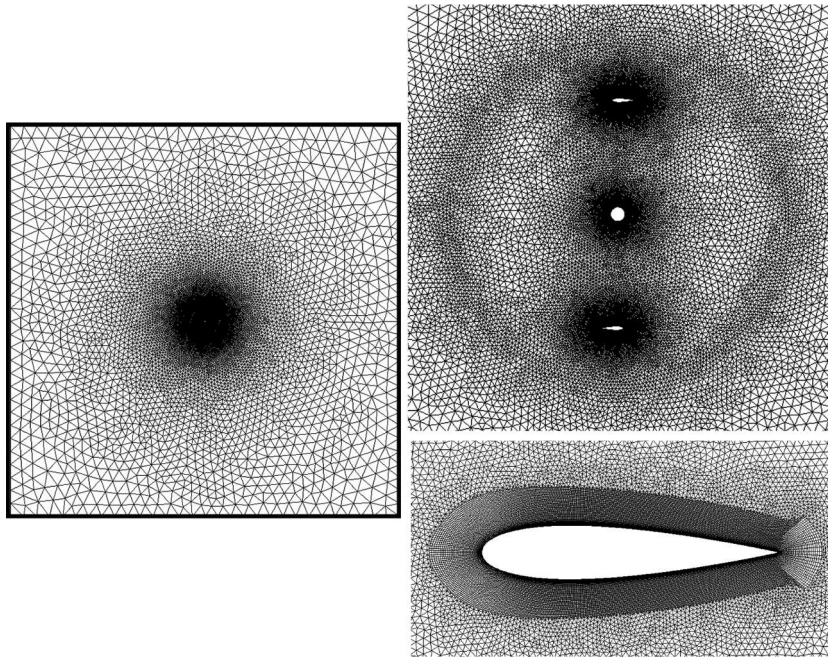


Fig. 4. Mesh distribution

In this paper, two turbulence models are taken into account: the two-equation RNG $k-\varepsilon$ and the four-equation SST Transition. The RNG $k-\varepsilon$ turbulence model closes the average Navier-Stokes equations introducing two transport equations: one for turbulent kinetic energy and one for turbulent dissipation. The SST Transition turbulence model solves the transport equations for the turbulence kinetic energy, the specific dissipation rate, the intermittency and the transition onset criteria. More detailed description of these turbulence models can be found in the ANSYS, Inc.15.0 documentation.

Turbulence parameters of the wind tunnel of the Universite de Sherbrooke are unknown. However, in the case of open jet wind tunnels, the turbulence intensity of the incoming flow is usually high. Therefore, in this simulation, the value of the turbulence intensity is assumed to be 5%.

5. Results

5.1. Unsteady airfoil characteristics of the wind turbine blade

Figures 5a and 5b present drag and lift coefficients as functions of the angle of attack. The airfoil characteristics are computed using two turbulence models: the RNG $k-\varepsilon$ and the SST Transition. The numerical results are compared with the experiment of Laneville and Vittecoq (1986). As it can be seen from Figs. 5a and 5b, the computed results of the drag coefficients are more similar to the experimental results than in the case of the lift coefficient. The differences can be caused by the accuracy of measuring devices. According to Laneville and Vittecoq (1986), with the increasing tip speed ratio, the precision of experimental data decreases, especially for

the lift coefficient. The precision of experimental data has been estimated as follows: $C_D \pm 5\%$ and $C_L \pm 12\%$. Even though the experiment was considered as a two-dimensional (large aspect ratio of the blades), the 3D aerodynamic effects such as tip vortices can reduce the efficiency of the device (Paraschivoiu, 2009; Scheurich *et al.*, 2011). Analyzing the obtained numerical results of airfoil characteristics, hysteresis loops both of the lift and drag coefficients are visible (Figs. 5a and 5b). In the upwind part of the rotor, for the azimuth from 0 deg to 90 deg, a significant increase in the lift and drag coefficients can be observed. Moreover, at the azimuthal angle of zero, which corresponds to the zero angle of attack, the lift coefficients are 0.23 and 0.37 for the SST Transition and the RNG $k-\varepsilon$ turbulence models, respectively. The non-zero value of the lift force may have several reasons. Firstly, the definition of the angle of attack assumed in this paper does not take into account effects associated with the slowdown of the flow close to the rotor. Secondly, during rotation of the rotor the virtual camber of the airfoil occurs at the zero angle of attack caused by curved flow around the rotor blade. This means that the symmetrical airfoil of the vertical-axis wind turbine behaves as a cambered airfoil (Akimoto *et al.*, 2013). Moreover, in the case of the airfoil oscillating around the zero average angle of attack, C_L cannot be equal to zero because of the momentum and the inertia of the fluid (Laneville and Vittecoq, 1986). With the increasing azimuth from 90 deg to 180 deg, the lift and the drag force coefficients decrease. In the downwind part of the rotor, the computed lift coefficients are still positive while experimental results are negative. The values of the lift force coefficients obtained by the SST Transition turbulence model are much better compared with the RNG $k-\varepsilon$ turbulence model.

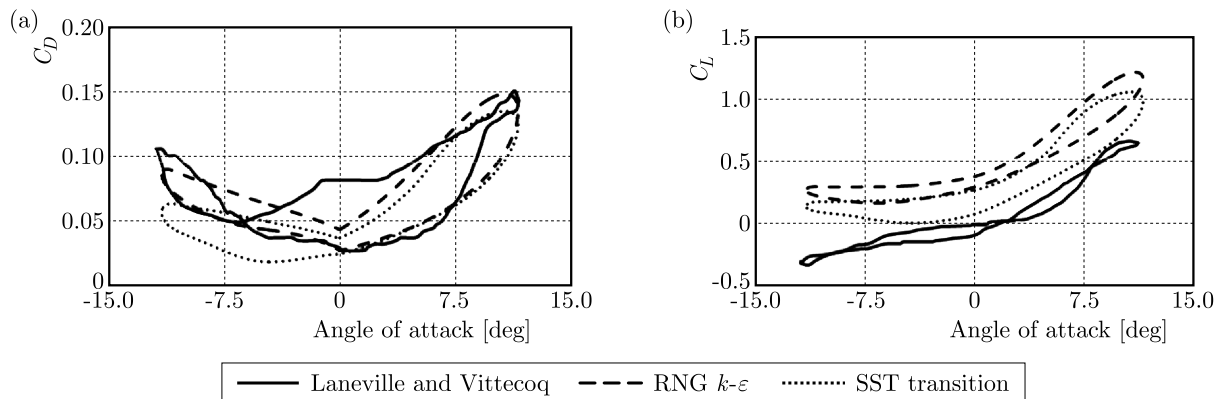


Fig. 5. (a) Drag and (b) lift force coefficient versus the angle of attack at TSR of 5

Figure 6 presents vorticity fields computed using the SST Transition turbulence model at three azimuth positions: 0 deg, 60 deg and 120 deg. Analyzing these figures, it can be noticed that at the azimuthal angle of 0 deg two interactions between the blades and the aerodynamic wake occur. At the azimuth of 120 deg, the rotor blade located at the downwind part of the rotor interacts also with the aerodynamic wake from the rotor shaft.

5.2. Airfoil characteristics of NACA 0018

The second part of this paper concerns the analysis of static airfoil characteristics using the same mesh distribution close to the airfoil and the same turbulence models as during unsteady analysis. The obtained results of aerodynamic loads are compared with the experimental data taken from two independent sources (Laneville and Vittecoq, 1986; Sheldahl and Klimas, 1981). The experimental data from the report of Sheldahl and Klimas (1981) are commonly used in simplified aerodynamic models for Darrieus vertical-axis wind turbines applications. The experiments were performed for the Reynolds numbers of $3.8 \cdot 10^4$ in the Laneville and Vittecoq experiment (1986) and $4 \cdot 10^4$ in the experiment of Sheldahl and Klimas (1981).

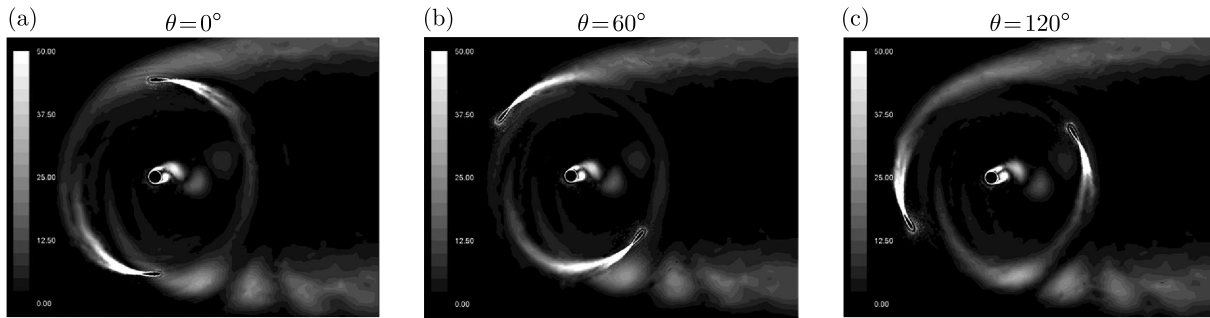


Fig. 6. Evolution of the vorticity field, ω [1/s] – the SST Transition model

The results of aerodynamic force coefficients as a function of the angle of attack are presented in Figs. 7a and 7b. The aerodynamic derivatives $\partial C_L / \partial \alpha$ at the angle of attack range between 0 deg and 5 deg are: 6.0144 for the SST Transition model; 5.78 for the RNG $k-\varepsilon$ turbulence model; 6.19 for the experiment of Laneville and Vittecoq (1986) and 4.72 for the experiment of Sheldahl and Klimas (1981). The maximum values of C_L are: 0.71 at the angle of attack of 8.57 deg for the experiment of Laneville and Vittecoq; 0.473 at the angle of attack of 6 deg for the experiment of Sheldahl and Klimas; 0.91 at the angle of attack of 12.5 deg for the SST Transition model and 1.22 at the angle of attack of 15 deg for the RNG $k-\varepsilon$ model. The minimum values of the drag coefficient at the zero angle of attack are: 0.034 for the experiment of Laneville and Vittecoq; 0.0214 for the experiment of Sheldahl and Klimas; 0.042 for the SST Transition model and 0.032 for the RNG $k-\varepsilon$ model. The largest difference of C_L data between all data series (Fig. 7b) is observed in the static-stall region. Lower drag coefficients by Sheldahl and Klimas (1981) in comparison with those by Laneville and Vittecoq (1986) can be caused by turbulence parameters of the wind tunnel. It is worth noting that the characteristics, both the lift and the drag coefficients, obtained using the SST Transition turbulence model are more comparable with the experimental results of Laneville and Vittecoq (1986) than the experimental results of Sheldahl and Klimas (1981).

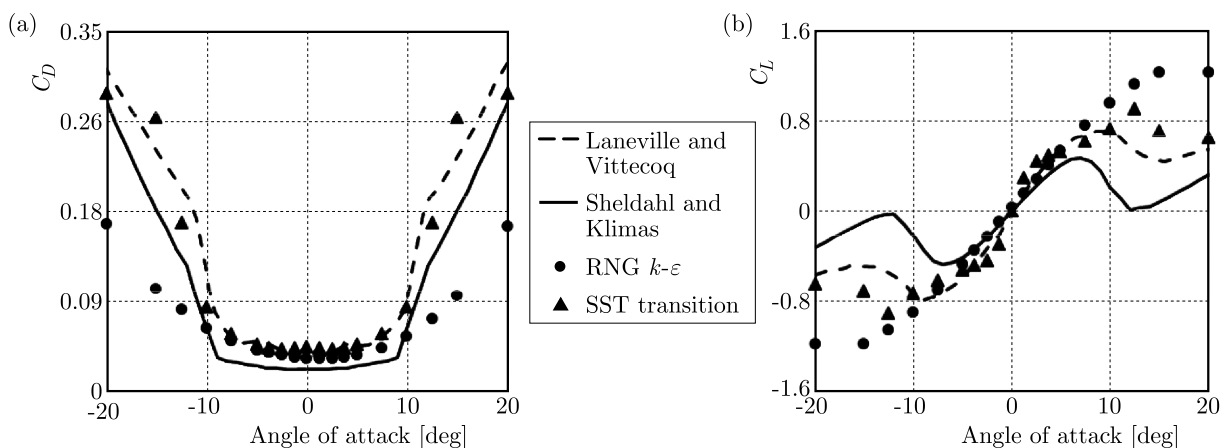


Fig. 7. (a) Drag and (b) lift force coefficients versus the angle of attack

6. Conclusions

The main purposes of this paper are the investigation of steady and unsteady lift and drag coefficients of NACA 0018 airfoil using the same mesh distribution around the airfoil and two turbulence models: the RNG $k-\varepsilon$ and the SST Transition. The analysis shows that:

- For the same mesh around the airfoils, consisting of structural quadrilateral elements near the blades and triangle elements elsewhere, the steady airfoil characteristics are in good agreement with the experimental results. However, 3D effects may cause errors in the experiment.
- The SST Transition turbulence model gives more realistic results of aerodynamic force coefficients than the RNG k - ε model.
- Comparison of the results of the lift force coefficient obtained during two independent experiments shows significant differences in the static stall zones.

This paper gives some preliminary results of steady RANS modeling of the flow past a turbine rotor. The presented simulations are a part of a more extensive numerical study of vertical-axis wind turbines. The results of simulations presented in the paper can be a database for other investigations.

Acknowledgments

This work has been supported by the European Union in the framework of European Social Fund through the “Didactic Development Program of the Faculty of Power and Aeronautical Engineering of the Warsaw University of Technology”.

References

1. AKIMOTO H., HARA Y., KAWAMURA T., NAKAMURA T., LEE Y.-S., 2013, A conformal mapping technique to correlate the rotating flow around a wing section of vertical axis wind turbine and an equivalent linear flow around a static wing, *Environmental Research Letters*, **8**, 044040
2. AMET E., MAÎTRE T., PELLONE C., ACHARD J.-L., 2009, 2D numerical simulations of blade-vortex interaction in a Darrieus turbine, *Journal of Fluids Engineering*, **131**, 111103-1-15
3. BLACKWELL B.F., 1974, The vertical-axis wind turbine “how it works”, Report SLA-74-0160, Sandia Laboratories, USA
4. BORG M., SHIRES A., COLLU M., 2014, Offshore floating vertical axis wind turbines, dynamics modelling state of the art. Part I: Aerodynamics, *Renewable and Sustainable Energy Reviews*, **39**, 1214-1225
5. DANA O. L.A., QIN N., HOWELL R., 2012, A numerical study of blade thickness and camber effects on vertical axis wind turbines, *Proceedings of the Institution of Mechanical Engineers, Part A: Journal of Power and Energy*, **226**, 7, 867-881
6. FERREIRA C., 2009, The near wake of the VAWT: 2D and 3D views of the VAWT aerodynamics, Ph.D. Thesis, Delft University of Technology
7. FERREIRA C., VAN BUSSEL G., VAN KUIK G., 2007, 2D CFD simulation of dynamic stall on a Vertical Axis Wind Turbine: verification and validation with PIV measurements, *45th AIAA Aerospace Sciences Meeting and Exhibit/ASME Wind Energy Symposium*, Reno, 16191-16201
8. FERREIRA C., VAN BUSSEL G.W., VAN KUIK G.M., SCARANO F., 2011, On the use of velocity data for load estimation of a VAWT in dynamic stall, *Journal of Solar Energy Engineering*, **133**, 1, 011006-011006-8
9. HANSEN M.O.L., 2008, *Aerodynamics of Wind Turbines*, Second Edition, Earthscan
10. HAU E., 2006, *Wind Turbines*, Springer
11. LANEVILLE A., VITTECOQ P., 1986, Dynamic stall: the case of the vertical axis wind turbine, *Journal of Solar Energy Engineering*, **108**, 141-145
12. LICHOTA P., 2013, Maximum Likelihood estimation: a method for flight dynamics – angle of attack estimation, *14th International Carpathian Control Conference, IEEE*, Rytro, Poland, 218-221

13. LICHOTA P., 2016, Inclusion of the D-optimality in multisine manoeuvre design for aircraft parameter estimation, *Journal of Theoretical and Applied Mechanics*, **54**, 1, 87-98
14. MADSEN H., LARSEN T., VITA L., PAULSEN U., 2013, Implementation of the actuator cylinder flow model in HAWC2 for aeroelastic simulations on vertical axis wind turbines, *51st AIAA Aerospace Sciences Meeting Including the New Horizons Forum and Aerospace Exposition*, Texas, USA
15. MAROŃSKI R., 2016, *Wind Turbines* (in Polish), Oficyna Wydawnicza Politechniki Warszawskiej, Warszawa
16. MARSH P., RANMUTHUGALA D., PENESIS I., THOMAS G., 2013, Performance predictions of a straight-bladed vertical axis turbine using double-multiple streamtube and computational fluid dynamics models, *Journal of Ocean Technology*, **8**, 1, 87-103
17. PARASCHIVOIU I., 2009, *Wind Turbine Design with Emphasis on Darrieus Concept*, Presses Internationales Polytechnique
18. PONTA F.L., JACOVKIS P.M., 2001, A vortex model for Darrieus turbine using finite element techniques, *Renewable Energy*, **24**, 1, 1-18
19. ROGOWSKI K., 2014, Analysis of performance of the Darrieus wind turbine, Ph.D. Thesis, Warsaw University of Technology, Faculty of Power and Aeronautical Engineering, Warsaw
20. ROGOWSKI K., MAROŃSKI R., 2015, CFD computation of the Savonius rotor, *Journal of Theoretical and Applied Mechanics*, **53**, 1, 37-45
21. SARLAK H., MIKKELSEN R., SARMAST S., SØRENSEN J.N., 2014, Aerodynamic behaviour of NREL S826 airfoil at $Re=100,000$, *Journal of Physics: Conference Series*, **524**, 1
22. SCHEURICH F., FLETCHER T.M., BROWN R.E., 2011. Simulating the aerodynamic performance and wake dynamics of a vertical-axis wind turbine, *Wind Energy*, **14**, 159-177
23. SHELDAHL R.E., KLIMAS P.C., 1981, Aerodynamic characteristics of seven symmetrical airfoil sections through 180-degree angle of attack for use in aerodynamic analysis of vertical axis wind turbines, Energy Report SAND80-2114, Sandia National Laboratories, Albuquerque, New Mexico
24. STRICKLAND J.H., SMITH T., SUN K., 1981, A vortex model of the Darrieus turbine: an analytical and experimental study, Sandia National Laboratories, Technical Report SAND 81-7017
25. STRICKLAND J.H., WEBSTER B.T., NGUYEN T., 1979, A vortex model of the Darrieus turbine: an analytical and experimental study, *Journal of Fluids Engineering*, **101**, 500-505

Manuscript received July 27, 2017; accepted for print August 31, 2017

OLD MATERIALS – NEW CAPABILITIES: LATTICE MATERIALS IN STRUCTURAL MECHANICS

MAREK AUGUSTYNIAK

Gdańsk University of Technology, Department of Technical Physics and Applied Mathematics, Gdańsk, Poland and
DES ART Ltd., Gdynia, Poland; e-mail: maugustyniak@mif.pg.gda.pl

Lattice materials (LM) are a novel concept stemming from the combination of crystallography and structural optimisation algorithms. Their practical applications have become real with the advent of versatile additive layer manufacturing (ALM) techniques and the development of dedicated CAD/CAE tools. This work critically reviews one of the major claims concerning LMs, namely their excellent stiffness-to-weight performance. First, a brief literature review of spatially uniform LMs is presented, focusing on specific strength of standard engineering materials as compared with novel structures. An original modelling and optimisation is carried out on a flat panel subject to combined shear and bending load. The calculated generalised specific stiffness is compared against reference values obtained for a uniform panel and the panel subjected to topological optimisation. The monomaterial, a spatially repetitive solution turns out to be poorly suited for stiff, lightweight designs, because of suboptimal material distribution. Spatially non-uniform and locally size-optimised structures perform better. However, its advantage over manufacturable, topologically-optimised conventional designs can at best be marginal ($< 10\%$). Cubic-cell lattices cannot replace conventional bulk materials in the typical engineering use. The multi-cell-type and multi-material lattice structures, albeit beyond the scope of this article, are more promising from the point of view of mechanical properties. The possibility of approaching the linear scaling reported in the recent literature can make them an attractive option in ultra-low weight designs.

Keywords: lattice materials, additive layer manufacturing, specific stiffness, topological optimisation

1. Introduction

1.1. Definition and classification

The Lattice Material is a structure generated with the aid of Additive Layer Manufacturing consisting of branched beams usually forming repetitive primitive cells having internal structures derived from crystallography (Face-Centered Cubic, Diamond-like, etc.). The edge of a typical cell does not exceed 10 mm, and the beams cross section tends to be of the order of a $1/10$ up to 1 mm square. Smaller diameters are difficult to manufacture, except for very sophisticated low-series techniques (Bauer *et al.*, 2016).

LMs feature an open structure, and their fabrication method (ALM) naturally allows free modulation of the material effective density.

A rigorous classification of LM (also known as: periodic cellular solids, metamaterials, periodic trusses) is difficult, although claimed by Zok *et al.* (2016) to be possible. Several criteria have to be employed, including (but not limited to):

- the material used to form beams: polymer/metal
- the external shape of the primitive cell: hex/wedge/tetra, or compound (more than one cell type)

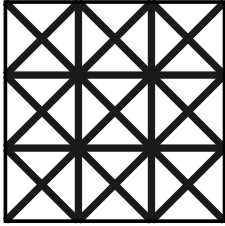
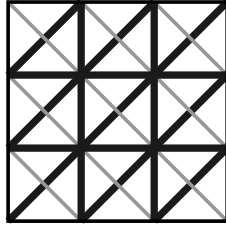
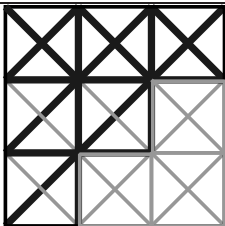
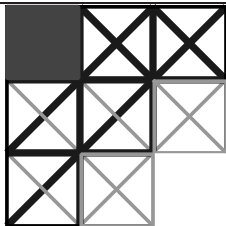
- the internal “crystallographic” layout: BCC, FCC, diamond, Kelvin-cell, etc.
- the fabrication technology: SLS (Selective Laser Sintering) or FDM (Fused Deposition Modelling).

The spatial, long-range configuration of LM introduces further classes:

- fully uniform (cells are reproduced 1:1, and their properties are quasi-isotropic)
- uniform-directional (cells are reproduced 1:1, but their internal structure produces long-range anisotropy)
- beam-optimised (each beam can have a different diameter).

Table 1 represents schematically the mentioned spatial configurations, adding a “blended” structure in which some design regions are solid while some others created from the lattice structure. Both the diameter-optimised and blended designs require a dedicated calculation algorithm (size + topology optimisation). Their generation requires a case-by-case approach tailored for a given component shape and loading conditions.

Table 1. Basic options for the cubic cell Lattice Material spatial layout

(a) Fully uniform		(b) Uniform-directional	
<ul style="list-style-type: none"> • Repetitive cell topology • Repetitive beam cross sections • Quasi-isotropic 		<ul style="list-style-type: none"> • Repetitive cell topology • Repetitive beam cross sections • Designed as anisotropic 	
(c) Diameter-optimised		(d) Blended	
<ul style="list-style-type: none"> • Repetitive cell topology • Beam cross sections differing from one cell to another (optimised) • Inherently anisotropic: tailored for a given set of load conditions 		<ul style="list-style-type: none"> • Repetitive cell topology with added “void” and “solid” cell options • Beam cross sections differing from one cell to another (optimised) • Inherently anisotropic: tailored for a given set of load conditions 	

The multi-cell-type and multi-material lattice structures (with further ramifications, as shown in Table 1) remain largely unexplored. This stems from the difficulties in their optimal design and still very limited access to adequate manufacturing technologies. These solutions, promising as they seem, will not be discussed in this paper.

1.2. Lattice material properties and range of potential applications

LMs are remarkable for their potential multi-functionality, namely the combination of tuneable or even programmable mechanical, thermal, mass-transport and electromagnetic properties. The word “potential” has to be emphasised, because apart from decorative objects, no inherently “lattice-based” technical designs have so far emerged on the market.

Several authors have studied the sensitivity analysis of various thermomechanical properties of LMs including: static stiffness and strength, energy absorption capacity, vibration properties, effective Poisson’s ratio, effective thermal dilatation coefficient and the active surface. In many

cases, the main stake is mass reduction, or more precisely, optimisation of specific stiffness, specific energy absorption (SEA) or other mentioned parameters.

Some authors have been systematically exploring the design space of varying cell configurations and sizes. Mazur *et al.* (2016) focused on strength and stiffness of Ti-6Al-4V lattices. Junyi and Balint (2016) added dispersion properties to monitored variables. Lopatin *et al.* (2017) studied both the intensive (cell structure) and extensive (plate dimensions) parameters in search for the maximum critical buckling load.

Messner (2016) came up with a complete algorithm for generating homogeneous lattice microstructures optimisable from the point of view of the stiffness-to-density ratio. He took the degree of anisotropy into account as well.

The static specific stiffness of LMs has been explored in the context of its:

- maximisation (Messner, 2016; Bauer *et al.*, 2016)
- tuning (for reproduction of human bone stiffness) (Serra-Garcia *et al.*, 2016)
- minimisation (supercompressibility) (Zhu *et al.*, 2015; Jiang and Wang, 2016).

This parameter will be the main focus of this study.

Lattice-type materials have also been discussed in the context of auxetics, i.e. structures with negative Poisson's ratio.

Controlled buckling behaviour, usually studied for fail-safe design or maximisation of energy absorption has been put forward by Lopatin *et al.* (2017), Paulose *et al.* (2015), Yin *et al.* (2017), Hawreliak *et al.* (2016). Vibration characteristics (selective damping) have been studied by Bacigalupo *et al.* (2015), Srivastava (2016) and Pasternak *et al.* (2016).

Thermal and thermo-mechanical properties remain a prominent area of research. Especially, thermal dilatation tuning (e.g. zero CTE for elimination of thermal stresses) has been reported in (Pasternak *et al.*, 2016; Xu and Pasini, 2016; Wang *et al.*, 2016; Toropova and Steeves, 2016). Maximisation of the effective thermal conductivity (heat sinks) appeared in works by Wadley and Queheillalt (2007), Kumar *et al.* (2009), Tian *et al.* (2007). The list is not exhaustive. Notably, there have been attempts to characterise lattice material durability (Hawreliak *et al.*, 2016), mass-transport properties for possible application in electrodes (Bauer *et al.*, 2016; Zhu *et al.*, 2015). A high surface-to-mass ratio allows the development of more efficient energy-storage structures (Zhu *et al.*, 2015; Sullivan *et al.*, 2016). Last but not least, a still active major research area involves interaction of electromagnetic waves with periodic structures (meta-materials) (Srivastava, 2016 and many others).

1.3. Goal of this study

Among several possible functions of LMs, one of the fundamental mechanical properties, namely the stiffness-to-density ratio, is selected for close examination. Several scientific papers hint on the outstanding specific stiffness (and alternatively specific strength) of LMs:

- Mazur *et al.* (2016) – “One can reach properties beyond the capacity of solid material”
- Yin *et al.* (2017) – “Hybrid designs can populate vacant regions in mechanical property charts”
- Messner (2016) – “Previous work demonstrates that lattice materials have excellent stiffness- and strength-to-weight scaling, outperforming natural materials (...) making these structures efficient for lightweight structural applications” (quoted after Zheng *et al.*, 2014).

In the above statements it is implied that the specific stiffness of LMs can be significantly maximised by appropriate selection of their internal layout. These claims are even more pronounced in informal reports:

- Dias (2015) – “LMs also have desirable weight characteristics, and are used as an approach to target weight reduction” (this feature is listed in the third place, after “better performance for stability and larger surface area”)
- Krassenstein and Lyles (2014) – “As we know, lattice structures have been shown to increase strength while reducing weight (...) Without a doubt, there could be hundreds or even thousands of uses for lattices such as this for designing and engineering a whole range of products and architectural designs”.

However, there are some recent papers (e.g. Zok *et al.*, 2016) where the above claims are put at doubt.

The community of structural mechanics indeed awaits novel stiff and light materials. The red contour, sketched by the author on one of the Ashby-plots (Fig. 1, taken from Ashby and Cebon, 1993), encompasses the area of highly desirable specific stiffness levels with 4-sub-areas corresponding to:

- A: structures with a relatively high absolute stiffness, as light as possible, dedicated to a broad engineering use
- B: specialised low and ultra-low density structures exhibiting as little stiffness loss as possible
- C: hybrid area between A and B
- D: most probably infeasible materials.

Another simplified criterion can be set at a straight line corresponding to a constant $E^{1/2}/\rho = 1/100$, with E expressed in GPa and ρ expressed in kg/m^3 .

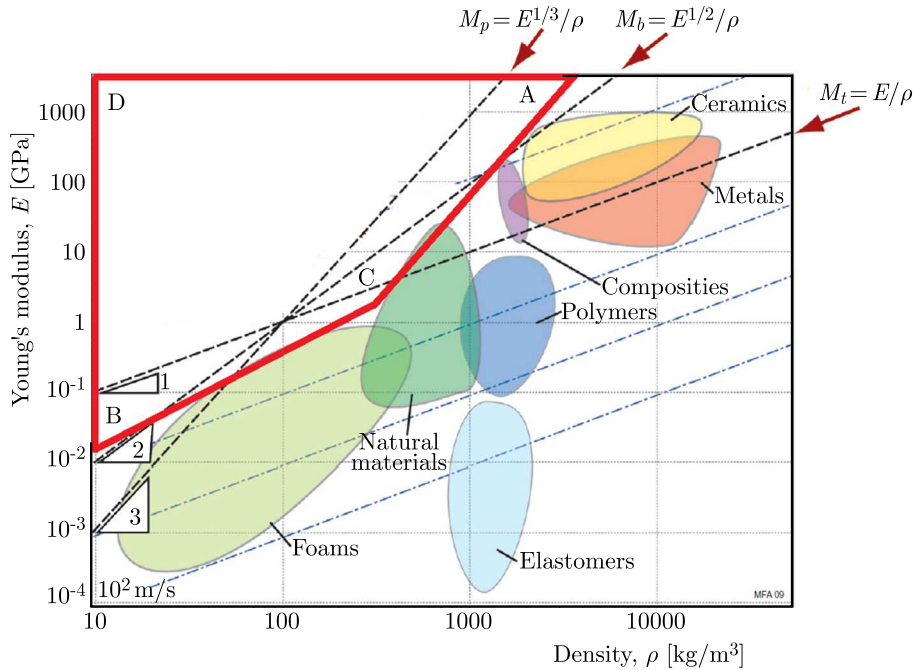


Fig. 1. Material selection chart (Ashby and Cebon, 1993) with sub-areas marked by the author of this article

The key question is: can LMs perform better, at least in terms of increased specific stiffness, than the existing materials, either homogeneous or composite? The areas of the potential widespread engineering use (A and C in Fig. 1) are addressed in this paper.

A brief literature review is carried out first in order to quantify the best solutions hitherto found.

Apart from the literature review, the original contribution of this study consists in the design and numerical optimisation of a series globally and locally optimised lattice structures in search for their actual specific stiffness.

In particular, the sensitivity analysis is carried out on a panel of constant external dimensions and varied internal LM configuration. The finite element computations are performed using OptiStruct 14.0 software by Altair. The modelling is supposed to compare the “latticed” design as compared to the best conventional topologically optimised design.

2. Uniform lattice materials: specific stiffness and strength

Several authors, as shown in the previous Section, have claimed that LMs are very promising in terms of pushing the limits of specific stiffness and strength. It is relevant to quantify and verify the obtained results by comparing them to the representatives of various material families.

At the beginning, it is necessary to note that in the traditional structural design more than one “specific stiffness” can be defined for a given material (for demonstration, see Ashby and Cebon, 1993). Notably, E/ρ is recommended for pure 1D loading (as in struts, stretched cables), $E^{1/2}/\rho$ is adequate for beams carrying bending loads, $E^{1/3}/\rho$ characterizes the shells/plates/panels.

Consequently, if both the stiffness and density decrease proportionally (e.g. both by a factor of 10 typical for LMs as compared with the bulk material), the parameters: $E^{1/2}/\rho$ and $E^{1/3}/\rho$, increase, which is beneficial for lightweight design of beam/plate structures. In the further discussion, special emphasis is put on the “beam-optimised” specific stiffness.

Table 2 puts together selected typical data from metal, polymer and ceramic engineering materials. As expected, the costly carbon-fibre composite turns out to be the best. However, cheap and widely accessible wood comes the second, being particularly well suited for beam-optimised designs. Young’s modulus E is here expressed in GPa and ρ expressed in kg/m^3 . These units shall be kept further on in this study.

Table 2. Juxtaposition of specific strengths for standard engineering materials (source: Cambridge, 2003)

Material	E [GPa]	ρ [kg/m ³]	E/ρ (pure stretch)	$E^{1/2}/\rho$ (beam)	$E^{1/3}/\rho$ (plate)
Flex. polymer foam (VLD)	0.001	35	3E-5	9E-4	3E-3
Polypropylene	1.2	900	1E-3	1E-3	1E-3
WC	650	15600	4E-2	2E-3	6E-4
Plain steel	200	7850	3E-2	2E-3	7E-4
Rigid polymer foam (HD)	0.3	300	1E-3	2E-3	2E-3
Alu	75	2700	3E-2	3E-3	2E-3
Typical wood (longitudinal)	12	700	2E-2	5E-3	3E-3
CFRP	120	1500	8E-2	7E-3	3E-3

What is the performance of LMs in this aspect? Table 3 and corresponding Fig. 2 (data taken from Mazur *et al.*, 2016) shows that one the best type of cubic basic cell behaves on average 2 times better than the bulk base material and slightly outperforms pure aluminium. On the

other hand, the worst case exhibits properties equal to those of polypropylene, which is a very poor outcome for a specialised Ti-Al-V alloy. In terms of beam-optimised specific stiffness, the best LM shows roughly a twofold superiority over plain steel while its absolute stiffness is lower by a factor of 200. As long as such a low stiffness is acceptable in a given design, LM can thus be a valuable alternative to conventional materials.

Table 3. Juxtaposition of specific stiffnesses of the best/worst lattice materials (Mazur *et al.*, 2016)

Material	E [GPa]	ρ [kg/m ³]	E/ρ (pure stretch)	$E^{1/2}/\rho$ (beam)	$E^{1/3}/\rho$ (plate)
Ti-6Al-4V bulk	115	4430	3E-2	2E-3	1E-3
Ti-6Al-4V LM (1% E , 6% ρ), FCCZ-S3 (best)	1.15	266	4E-3	4E-3	4E-3
Ti-6Al-4V LM (1% E , 24% ρ), FBCCZ0-S2 (worst)	1.15	1063	1E-3	1E-3	1E-3

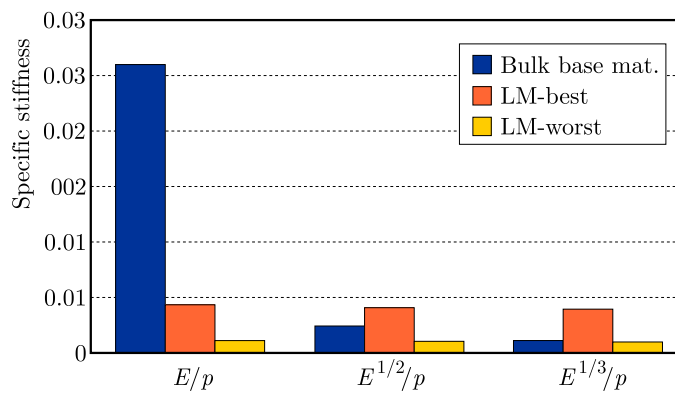


Fig. 2. Juxtaposition of specific stiffnesses of the best/worst lattice materials according to (Mazur *et al.*, 2016)

The recent work by Zheng *et al.* (2014) has revealed a new solution based on lattices made of hollow tubes with average E/ρ of 3E-3 and outstandingly high $E^{1/2}/\rho$ of 3E-2 (with E expressed in GPa and ρ in kg/m³). However, they applied a special octet-truss, a non-cubic structure, and focused on ultra-low density materials which are outside the scope of this research.

It is notable that only few quantitative assessments of specific stiffness (or alternatively specific strength) can be found in literature. Some reports, especially informal ones, are simply misleading. For example, a Purdue researcher working for a commercial 3D printing company (Krassenstein and Lyles, 2014) claims that his “incredible” Kelvin-cell-based aluminium cube supports about 100 000 times its weight. The number can be true, but when closely examined, it turns out to be no better than the natural performance of the bulk aluminium for the same cube dimensions.

Some authors hint on scaling the LM structures down as a method for increasing their stiffness and strength. Jiang and Qiang (2016) declares that under large-strain tension, their moduli follow a linear scaling relationship with their densities regardless of architecture types, which is in sharp contrast to the architecture-dependent modulus power-law of the existing engineering materials. Mazur *et al.* (2016) and Messner (2016) reported a convergence of mechanical properties with the increasing number of unit cells. The quantitative data produced by Bauer *et al.*

(2016) (concerning strength only) did not, however, provide convincing proofs of the superiority over the bulk base material. They aim at exploiting material strengthening size effects and achieving strength-to-density ratios of “nanolattices” 6 times those of other reported microlattices. However, their 1 micrometer-long struts with 200-nanometer diameters made of pyrolysed carbon exhibit compressive specific strength inferior to those of diamond (1.2 GPa at 600 kg/m³ as compared with > 110 GPa at 3500 kg/m³). Thus the carbon-based microlattice is 20× less stress-resistant (and probably just as less stiff) than the diamond while much more expensive to manufacture.

Again, it has to be emphasised, that the best structurally optimised LMs can be beneficial uniquely in very-low-weight designs, where their stiffness can decrease proportionally to the decreasing density, as compared to much more unfavourable scaling relationship of stochastic foams.

Judging from the literature data, the spatially uniform Lattice Materials, regardless of the scale of their structure (meso/micro/nano), are not significantly superior to the existing non-lattice materials in terms of specific stiffness as long as relatively stiff structures (e.g. $E > 100$ MPa) are required. Even if some carefully selected structures show an increased $E^{1/2}/\rho$ over the bulk base material, they do not penetrate deep into the desirable zones on the Ashby plot. It is partly reflected in the conclusion of the paper by Zok *et al.* (2016): “numerous trusses that have been studied in recent years do not appear to be particularly well-suited for use as stiff and strong lightweight structures on their own”.

3. Single-material lattices vs topologically optimised base material: original modelling

The literature review suggests that spatially uniform Lattice Materials are not likely to achieve outstanding specific stiffness. However, spatial variation of the cell type and beam diameters is intuitively beneficial, and has been suggested by some authors (e.g. Messner, 2016). Some simple solutions can be directly borrowed from the classic design rules, e.g. adding of solid skins atop of LM panels in order to increase their bending stiffness. On the other hand, Additive Layer Manufacturing (ALM), costly as it is, offers in exchange almost unlimited freedom in structural shaping, so it is natural to look for arbitrarily “free” non-standard designs often inspired by biological systems. Automatic optimisation procedures including topology and size optimisation have reached maturity, and now are widely used in industry as witnessed by the author in his engineering practice. It is possible that both these approaches are applicable to design of light and stiff LMs. However, such a hybrid methodology has not been widely used yet. The only quantitative data of the beneficial LM effect comes from commercial presentation (Dias, 2015), where a 12% increase in the of stiffness of an actual automotive part is reported as compared with the topologically optimised manufacturable design without a lattice structure. More data is definitely needed.

In this paper, the author generates a relatively simple model which is useful in studying the impact of Topological Optimisation (TO) and LM techniques, separately or in combination.

The model (Fig. 3) involves a 2 mm thick plate made of Nylon12PA, typical for 3D-printing applications, dimensioned 240×32 mm. The plate is supported along its shorter edges and is loaded with a field of uniform concentrated forces at its geometrical centre. The supports are designed so that the mechanism is avoided, but there are no singularities due to overconstraining at the same time.

A series of FEA calculations have been carried out in order to examine the variation of the specific stiffness. No stress constraints have been applied. The studied solutions are presented in Table 4.

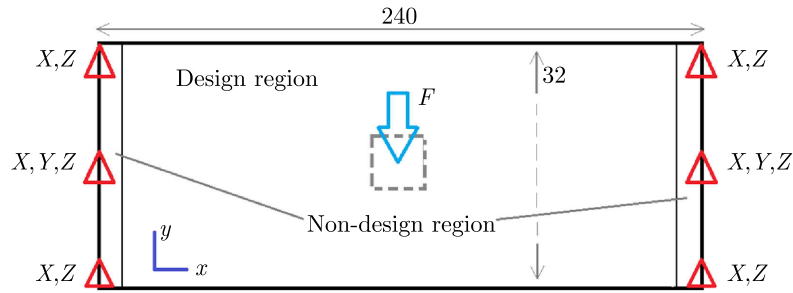


Fig. 3. A schematic view of the design space for specific strength analysis

Table 4. List of structural variants selected for specific strength comparison

100	Starting design: a full plate
200	Topological optimisation with a volume constraint set at 30% of the initial design region volume and objective defined as compliance minimisation
400	A series of LM designs with the total plate volume uniformly transformed into lattice; the beam diameter (equal for every element) is made variable
600	Hybrid, “blended” solution

The analyses refer to the case-specific “generalised” metrics of compliance and stiffness, typical for numerical studies of engineering components. The simplest definition of a generalised compliance is a vector product $\mathbf{F} \cdot \mathbf{u}$ summed over all nodes, where \mathbf{F} is the applied force vector, and \mathbf{u} – vector of resultant displacements. Such a function represents equally strain energy of the component.

Additionally, it is practical to replace the density with the component mass, so that the generalised specific stiffness (GSS) is equal to the generalised stiffness/component mass or alternatively: $1/(\text{generalised compliance} \cdot \text{component mass})$. So defined GSS will be the key parameter in the following discussion.

3.1. Design 100 – starting design, full plate

Standard linear-static analysis has been performed. The displacements plot is presented in Fig. 4.

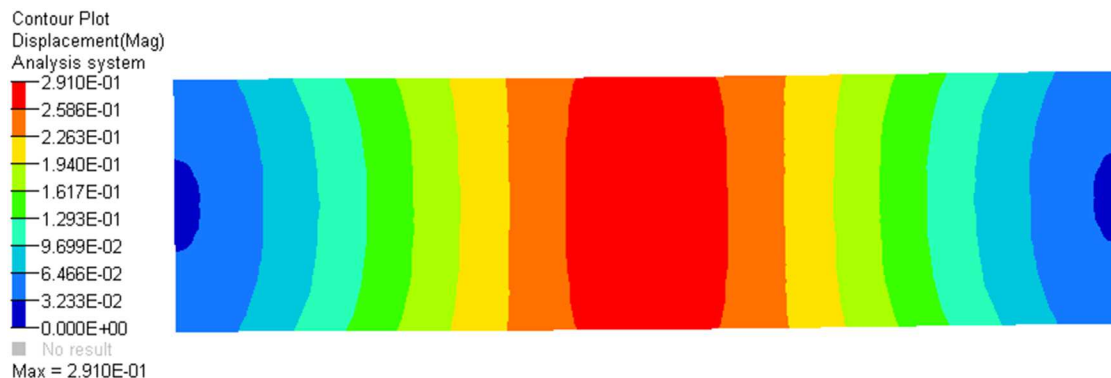


Fig. 4. The magnitude of displacement for the starting, full-plate design (100)

The bulk plate weighs 6.8 g. The behaviour of the plate, both in terms of deflection and stress distribution (not shown here), is consistent with the expectations derived from the classical beam theory. The Generalised Specific Stiffness (GSS) has been calculated, and set as a 100% reference for the subsequent options. The numerical data are presented at the end of the article, in Table 6.

3.2. Design 200 – topological optimisation (TO)

The design space has been subjected to a typical topological optimisation procedure based on the SIMP (Solid Isotropic Material with Penalisation) algorithm. A mass constraint has been set so as to finally reduce the mass of the design region by 30%. The TO algorithm converged after 20 iterations, producing pseudo-density distribution as in Fig. 5. The red areas represent the material which needs to be kept while dark blue zones indicate the redundant material to be removed. The uneven contour boundaries can be manually or automatically smoothened out. An automatic, rough, yet meaningful interpretation of the final design is shown in Fig. 5.

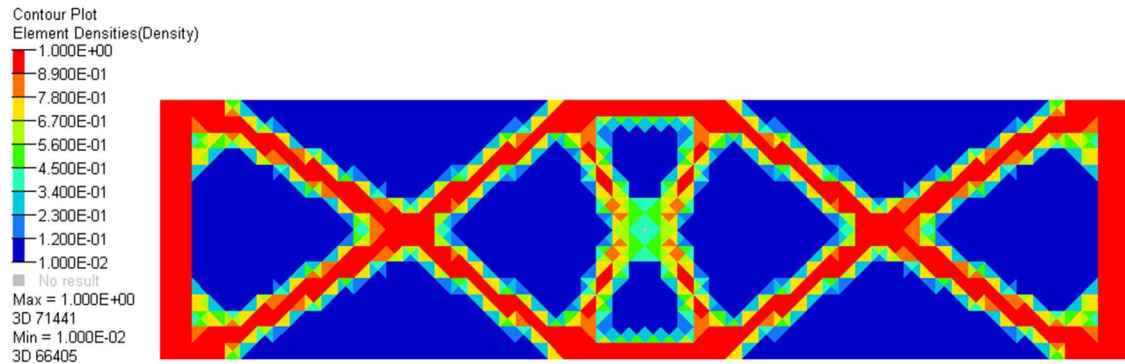


Fig. 5. Element pseudo-density distribution at the final iteration of the topological optimisation process (200)

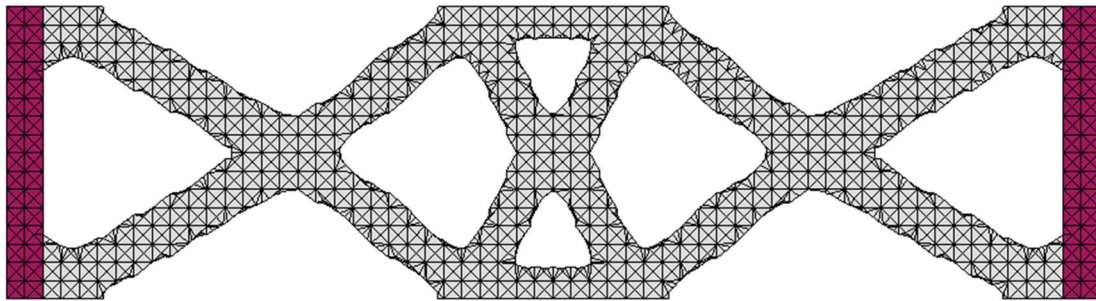


Fig. 6. Rough automatic interpretation of the topologically optimised structure for subsequent reanalysis or manufacturing

The normalised Generalised Specific Stiffness (GSS) for this design is slightly below the reference value and amounts to its 86%. The topological optimisation, in this particular case, does not bring benefits in terms of specific stiffness. However, it allows identifying weakly stressed areas and results in mass reduction which is an obvious advantage in industrial applications as long as constraints on allowable displacements are not violated.

3.3. Design 400 – uniform lattice with variable beam diameter

The entire plate has been transformed into a LM, except for its constrained edge bounds. The elementary cell dimensions are directly inherited from the finite element mesh. The beams are assigned with an arbitrary, constant diameter with the starting value of 0.1 mm.

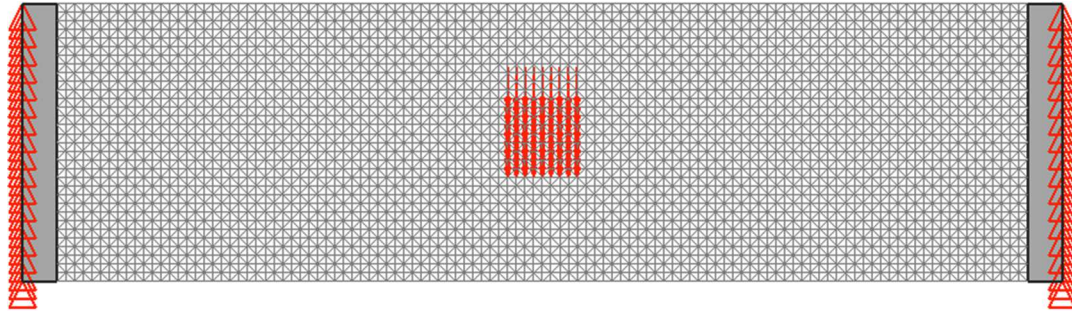


Fig. 7. The plate transformed into an uniform lattice structure (400)

Table 5. Influence of variation of the beam diameter on the generalised specific stiffness

	Relative density [%]	GSS
400 LM-uniform diameter 0.1 mm	12	0.0009
400 LM-uniform diameter 0.2 mm	26	0.0015
400 LM-uniform diameter 0.3 mm	51	0.0018
100 bulk	100	0.0069

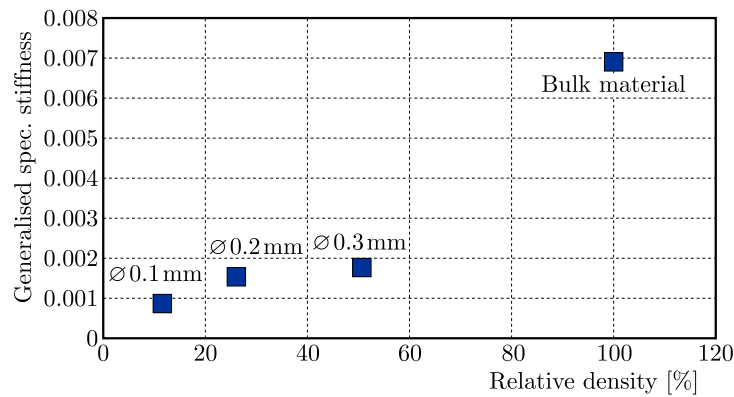


Fig. 8. The influence of variation of the beam diameter on the generalised specific strength: plot related to relative density

The sensitivity analysis is summarised in Table 5 and Fig. 8. Two adverse effects are noticeable:

- 1) Calculation at 50% of the relative density is visibly biased. If beam diameters are significant as compared with their lengths, the problem of overlapping at beam joints arises, and the nominal mass is overestimated. An actual 3D-printed object shall be lighter than the sum of masses of beams included in the FE model.
- 2) The specific stiffness definitely does not improve when replacing the bulk material with a LM. On the contrary, for this design space and set of loads the effect of “latticing” is detrimental. As compared with the starting simple bulk plate, the GSS (for 0.1 mm beams) drops by a factor of 7, which entails about a 60× decrease in the absolute stiffness.

3.4. Design 600 – hybrid (blended) solution

This design combines the results from Topology Optimisation with the partial Lattice transformation according to the lower and upper bounds arbitrarily set by the user. Here the bounds are 0.15 and 0.6, which entails that relative densities below 0.15 are removed (a void remains) while the elements exhibiting densities beyond 0.6 remain as solid.

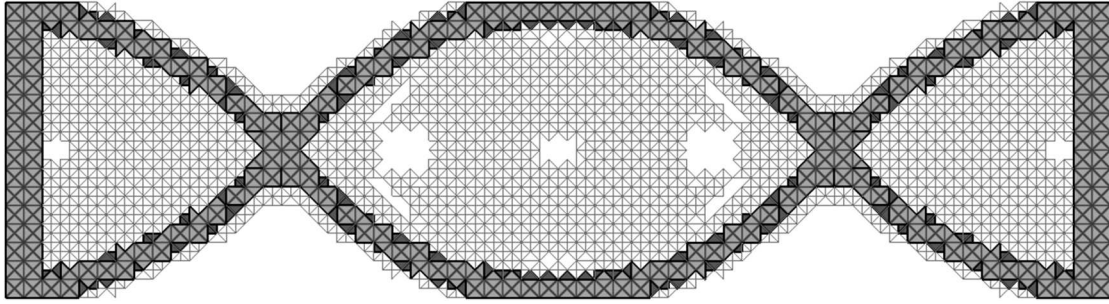


Fig. 9. An example of a “blended” design, combining the TO – resultant core structure and auxiliary lattice

The obtained solution has several remarkable features:

- 1) The GSS for this solution is very close to the one from pure Topological Optimisation, however it can possibly be increased if beam-by-beam size optimisation is employed.
- 2) The entire structure is a “composite” with locally varying stiffnesses and densities, although it is actually made of a single base material.
- 3) The design after smoothening and cleaning up can be manufactured in a single-pass FDM or SLS technology.
- 4) Although in this hybrid solution the lattice does not play a significant role in terms of stiffness or strength, it can serve as a filler or a supportive structure for additional functionalities (e.g. heat exchange, cabling, sensor arrays, etc.).
- 5) The similar, automotive structure redesigned with a “blended” technique has been reported to be $\sim 10\%$ stiffer than the solution by Topological Optimisation only with the imposed manufacturing constraints.

The summary of calculated GSS is presented in Table 6.

Table 6. Complete comparison of generalised specific stiffnesses for the studied design options

	Mass [g]	Generalised compliance [N·mm]	Generalised stiffness	Generalised spec. stiffness (GSS)	Normalised GSS [%]
100 Bulk material	7.3	19.8	0.05	0.0069	100
200a TO, volumic goal of design space set to 30%	2.5	67.5	0.01	0.0059	86
200b TO, volumic goal of design space set to 40%	3.2	48.3	0.02	0.0065	93
400 LM-Uniform diameter 0.1	0.84	1370	0	0.0009	13
400 LM-Uniform diameter 0.2	1.9	343	0	0.0015	22
400 LM-Uniform diameter 0.3	3.7	153	0.01	0.0018	26
600 LM-blended	2.5	67.4	0.01	0.0059	86

4. Conclusions and perspectives

The literature review and original modelling focused on the stiffness performance of lattice materials have led to the following conclusions:

- In the studied case, a simple conversion of the bulk material into a lattice results in a significant decrease of its stiffness; the best uniform LM cases reported in the literature show stiffnesses comparable to that of the bulk base material, however they do never exceed it. The claims of superiority of LMs in terms of light and stiff designs have to be refuted.
- In spite of the literature reports on the beneficial scale effect, one should not expect lattice-related specific strength higher than for the bulk base material, probably even if micrometre-scale elementary cells are produced.
- Some (but not dramatic) improvement of LM-related GSS can be aimed at when performing beam-by-beam size optimisation; such algorithms are already available in scientific and commercial contexts.
- The only convincing report on GSS increase due to application of the LM base on a hybrid (blended) design, in which the topologically optimised “backbone” made of the bulk material plays a dominant role in providing stiffness. In the areas of intermediate resulting densities (30%-70%) it is replaced with lattices. Even if such hybrid optimisation is employed, the reported gain is of the order of 10% as compared with pure topological optimisation with manufacturing constraints. Still the gain requires sophisticated, blended solid/LM designs, based on two-stage optimisation (Topological+Size). The final solution is of the order of magnitude more costly in production than the standard design (bulk material after TO).
- To meet the engineering goals and be economically viable, lattice materials should be:
 - structurally non-uniform to exploit the inherent freedom of design provided by ALM,
 - multifunctional, similarly to foams (cf. Banhart, 2005).

Stiffness and/or strength can only constitute an auxiliary function in lattice-material designs. The primary function can be thermal (e.g. embedded efficient heat exchange), thermo-mechanical (e.g. stress-free intermaterial adapters) or electromagnetic (integrated cables, sensors, screening systems).

- LMs do not deliver a break-through in the area of stiff lightweight design. At present, there are only very limited “hi-tech” fields of their application (aerospace, biomedical, military).

The search for light and stiff micro/macro-optimised solution continues. Interestingly, some authors (Zimińska *et al.*, 2016; Dong and Wadley, 2015) hint on CFRP lattices as being capable of crossing the present limits of available specific stiffnesses. LM multi-material composites can possibly fill the gap of the material selection charts. This, however, is a subject for another study.

References

1. ASHBY M., CEBON D., 1993, Materials selection in mechanical design, *Journal de Physique IV Colloque*, **03**, C7, C7-1-C7-9
2. BACIGALUPO A., LEPIDI M., GNECCO G., GAMBAROTTA L., 2015, Optimal design of auxetic hexachiral metamaterials with local resonators, *Smart Materials and Structures*, **25**, 5
3. BANHART J., 2005, Aluminium foams for lighter vehicles, *International Journal of Vehicle Design*, **37**
4. BAUER J., SCHROER A., SCHWAIGER R., KRAFT O., 2016, Approaching theoretical strength in glassy carbon nanolattices, *Nature Materials*, **15**, 438-443
5. Cambridge Press, 2003, Materials Data Book, 2003 Edition, Cambridge University Engineering Department

6. DIAS W., 2015, <http://insider.altairhyperworks.com/design-and-optimization-of-lattice-structures-for-3d-printing-using-altair-optistruct/>
7. DONG L., WADLEY H., 2015, Mechanical properties of carbon fiber composite octet-truss lattice structures, *Composites Science and Technology*, **119**, 26-33
8. HAWRELIAK J.A., LIND J., MADDOX B., BARHAM M., MESSNER M., BARTON N., JENSEN B.J., KUMAR M., 2016, Dynamic behavior of engineered lattice materials, *Nature Scientific Reports*, **6**, 28094
9. JIANG Y., WANG Q., 2016, Highly-stretchable 3D-architected mechanical metamaterials, *Nature Scientific Report*, **6**, 34147
10. JUNYI L., BALINT D.S., 2016, A parametric study of the mechanical and dispersion properties of cubic lattice structures, *International Journal of Solids and Structures*, **91**, 55-71
11. KRASSENSTEIN E., LYLES D.P., 2014, <https://3dprint.com/29958/3d-printed-aluminum-lattice/>
12. KUMAR V., MANOGHARAN G., CORMIER D.R., 2009, Design of periodic cellular structures for heat exchanger applications, *20th Annual International Solid Freeform Fabrication Symposium*
13. LOPATIN A.V., MOROZOV E.V., SHATOV A.V., 2017, Buckling of the composite anisogrid lattice plate with clamped edges under shear load, *Composite Structures*, **159**, 72-80
14. MESSNER M.C., 2016, Optimal lattice-structured materials, *Journal of the Mechanics and Physics of Solids*, **96**, 162-183
15. MAZUR M., LEARY M., SUN S., VCELKA M., SHIDID D., BRANDTET M., 2016, Deformation and failure behaviour of Ti-6Al-4V lattice structures manufactured by selective laser melting (SLM), *The International Journal of Advanced Manufacturing Technology*, **84**, 5, 1391-1411
16. PASTERNAK E., SHUFRIN I., DYSKIN A., 2016, Thermal stresses in hybrid materials with auxetic inclusions, *Composite Structures*, **138**, 313-321
17. PAULOSE J., MEEUSSEN A.S., VITELLI V., 2015, Selective buckling via states of self-stress in topological metamaterials, *Proceedings of the National Academy of Sciences, USA*, **112**, 7639-7644
18. SERRA-GARCIA M., LYDON J., DARAIO C., 2016, Extreme stiffness tunability through the excitation of nonlinear defect modes, *Physical Review E*, **93**
19. SRIVASTAVA A., 2016, Metamaterial properties of periodic laminates, *Journal of the Mechanics and Physics of Solids*, **96**, 252-263
20. SULLIVAN K.T., ZHU C., DUOSS E.B., GASH A.E., KOLESKY D.B., KUNTZ J.D., LEWIS J.A., SPADACCINI C.M., 2016, Controlling material reactivity using architecture, *Advanced Materials*, **28**, 1934-1939
21. TIAN J., LU T.J., HODSON H.P., QUEHEILLALT D.T., WADLEY H.N.G., 2007, Cross flow heat exchange of textile cellular metal core sandwich panels, *International Journal of Heat and Mass Transfer*, **50**, 2521-2536
22. TOROPOVA M.M., STEEVES C.A., 2016, Bimaterial lattices as thermal adapters and actuators, *Smart Materials and Structures*, **25**, 11
23. WADLEY H.N.G., QUEHEILLALT D.T., 2007, Thermal applications of cellular lattice structures, *Materials Science Forum*, **539-543**, 242-247
24. WANG Q., JACKSON J.A., GE Q., HOPKINS J.B., SPADACCINI C.M., FANG N.X., 2016, Lightweight mechanical metamaterials with tunable negative thermal expansion, *Physical Review Letter*, **117**
25. XU H., PASINI D., 2016, Structurally efficient three-dimensional metamaterials with controllable thermal expansion, *Nature Scientific Reports*, **6**, 34924
26. YIN S., LI J., BINGHE L., KANGPEI M., HUAN Y., NUTT S.R., XU J., 2017, Honeytubes: Hollow lattice truss reinforced honeycombs for crushing protection, *Composite Structures*, **160**, 1147-1154

27. ZHENG X., LEE H., WEISGRABER T.H., SHUSTEFF M., DEOTTE J., DUOSS E.B., KUNTZ J.D., BIENER M.M., GE Q., JACKSON J.A., KUCHEYEV S.O., FANG N.X., SPADACCINI C.M., 2014, Ultralight, ultrastiff mechanical metamaterials, *Science*, **344**, 1373-1377
28. ZHU C., HAN T.Y.-J., DUOSS E.B., GOLOBIC A.M., KUNTZ J.D., SPADACCINI C.M., WORSLEY M.A., 2015, Highly compressible 3D periodic graphene aerogel microlattices, *Nature Communications*, **6**, 6962
29. ZIMINSKA M., DUNNE N., HAMILTON A.R., 2016, Porous materials with tunable structure and mechanical properties via templated layer-by-layer assembly, *ACS Applied Materials and Interfaces*, **8**, 34, 21968-21973
30. ZOK F.W., LATTURE R.M., BEGLEY M.R., 2016, Periodic truss structures, *Journal of the Mechanics and Physics of Solids*, **96**, 184-203

Manuscript received April 28, 2017; accepted for print September 13, 2017

POLYESTER SAIL TECHNICAL WOVEN FABRIC BEHAVIOUR UNDER UNIAXIAL AND BIAXIAL TENSILE TESTS

ANDRZEJ AMBROZIAK, PAWEŁ KŁOSOWSKI

Gdansk University of Technology, Faculty of Civil and Environmental Engineering, Gdańsk, Poland

e-mail: ambrozan@pg.gda.pl; klosow@pg.gda.pl

The paper is focused on the identification of mechanical properties of a sail technical woven fabric (yacht sailcloth polyester) style 480 AP with MTO (Medium Tempered Optimized) finish. The non-linear elastic behaviour of the fabric applied for sails is investigated under uniaxial and biaxial tensile tests. Comparison of non-linear elastic parameters with others polyester coated fabrics is made. This paper is intended to be an introduction to a comprehensive investigation on sail technical woven fabrics.

Keywords: sail fabric, polyester coated fabrics, textiles, mechanical properties, uniaxial tensile test, biaxial tensile tests

1. Introduction

The applications of composites materials are widespread in various branches of industry. Among others, coated woven fabrics (named architectural fabrics or technical woven fabrics) are widely applied. The coated woven fabrics are usually manufactured from polyester fibres, glass fibres or carbon fibres (generally, woven of two families of threads called the warp and weft) covered by a coating material (e.g.: PTFE, PVC) for greater strength and/or environmental resistance. In civil engineering, the technical woven fabrics are applied as membranes, pneumatic and hanging roofs (see e.g. Fig. 1). On the other hand, technical woven fabrics are used also for sailing ships (see Fig. 2). Analysis of sails as flexible membranes with two-dimensional theory started in the sixties of the XX century (see e.g. Nielsen, 1963). In the modern literature one find can papers regarding experimental studies (see e.g. Triki *et al.*, 2011) and the numerical background (see e.g. Gasser *et al.*, 2000; Badel *et al.*, 2008). Only a few papers regarding the experimental analysis of sail cloths can be found, see e.g. Benfratello and Palizzolo (2010), Benfratello *et al.* (2013), where behaviour of the Dacron 360 woven fabric under uniaxial tensile tests with and without finish was investigated. On the other hand, Blicblau *et al.* (2008) investigated the forces applied resultant material deformations and stresses on a novel windsurfer sail. Spalatel-Lazar *et al.* (2008) improved the quality and performances of sails by using an orthotropic membrane model, numerical experimentation and optimization methods. Le Maître *et al.* (1996) proposed an elastic string network model of sails. The equilibrium equation for this model was written in form of a minimization problem.

The parameters given by sailcloth manufactures in order to describe orthotropic and non-linear behaviour of the sail fabric are insufficient for full description of its characteristics. An engineer who is supposed to perform the sail analysis should collect as well all information about the mechanical properties. From the naval engineer's point of view, a material to be used in sail manufacture should, first of all, have a smooth surface, have zero porosity ensuring effective air flow around the sail and be sea water resistant. On the other hand, the fabric of the sail must hold its shape over a wide wind range, and it must achieve long-term durability and ultra violet resistance.



Fig. 1. Factoria amphitheatre in Pruszcz Gdański, Poland



Fig. 2. Sailing vessels in Gdynia harbour, Poland

The aim of the present paper is to analyse, through experimental tests, the behaviour of the yacht sailcloth polyester style 480 AP with MTO finish under uniaxial and biaxial tensile tests and specify the non-linear elastic properties in form of sets of parameters.

2. Material and methods

The yacht sailcloth style 480 AP belongs to the polyester type of base fabric. The sailcloth weight is about 11.2 Sm-oz. (11.2 sailmakers per square yards is equal to about 4.8 N/m^2). Material parameters necessary to design new shapes of sails and analyse their behaviour are not provided in technical specification. In order to perform the relevant assessment of the material, laboratory tests have been carried out.

A special set of constitutive equations must be applied for description of the fabric behaviour. The authors have good experience with the dense net model (see e.g. Ambroziak and Kłosowski, 2011), in which the behaviour of each family of threads is treated individually and is described by the individual longitudinal stiffness F_i . The threads stress increment of the warp $\Delta\sigma_1$ or weft direction $\Delta\sigma_2$ are calculated from the following equations

$$\Delta\sigma_1 = F_1(\varepsilon_1)\Delta\varepsilon_1 \quad \Delta\sigma_2 = F_2(\varepsilon_2)\Delta\varepsilon_2 \quad (2.1)$$

where $F_1(\varepsilon_1)$ and $F_2(\varepsilon_2)$ are material functions of the threads and are called the longitudinal stiffnesses. Several constitutive elastic, viscoplastic or viscoelastic approaches can be used to define these functions. They are usually specified on the basis of the uniaxial, or during more complex investigation, like e.g. biaxial laboratory tests. It should be noted that stress of a technical fabric

is generally given in [N/m] or [kN/m], due to difficulties with thickness measurement, see e.g. Żyliński (1965). In such an approach, the results are thickness independent.

Basing on the geometrical relationship, the threads stress σ_i and threads strain ε_i can be expressed by the stress σ_x and strains ε_x components in the plane stress state as follows

$$\begin{aligned}\varepsilon_\xi &= \begin{Bmatrix} \varepsilon_1 \\ \varepsilon_2 \end{Bmatrix} = \begin{bmatrix} 1 & 0 & 0 \\ \cos^2 \alpha & \sin^2 \alpha & \sin \alpha \cos \alpha \end{bmatrix} \begin{Bmatrix} \varepsilon_{x2} \\ \varepsilon_{x2} \\ \gamma_{x1x2} \end{Bmatrix} = \mathbf{T}_{x\xi} \varepsilon_x \\ \sigma_x &= \begin{Bmatrix} \sigma_{x1} \\ \sigma_{x2} \\ \tau_{x1x2} \end{Bmatrix} = \begin{bmatrix} 1 & \cos^2 \alpha \\ 0 & \sin^2 \alpha \\ 0 & \sin \alpha \cos \alpha \end{bmatrix} \begin{Bmatrix} \sigma_1 \\ \sigma_2 \end{Bmatrix} = (\mathbf{T}_{x\xi})^T \sigma_\xi\end{aligned}\quad (2.2)$$

where α is the inclination angle between the thread families during the deformation process. The angle between the thread families α changes during deformation is calculated in accordance with the current values of stress components σ_{x2} and τ_{x1x2} in the fabric from the relation

$$\alpha = \arctan \frac{\sigma_{x2}}{\tau_{x1x2}} \quad (2.3)$$

Next, the relation between stress and strain in the plane stress state is written in the form

$$\sigma_x = (\mathbf{T}_{x\xi})^T \mathbf{F} \mathbf{T}_{x\xi} \varepsilon_x = \mathbf{D}_x \varepsilon_x \quad (2.4)$$

where

$$\mathbf{D}_x = \begin{bmatrix} F_1(\varepsilon_1) + F_2(\varepsilon_2) \cos^4 \alpha & F_2(\varepsilon_2) \sin^2 \alpha \cos^2 \alpha & F_2(\varepsilon_2) \sin \alpha \cos^3 \alpha \\ F_2(\varepsilon_2) \sin^2 \alpha \cos^2 \alpha & F_2(\varepsilon_2) \sin^4 \alpha & F_2(\varepsilon_2) \sin^3 \alpha \cos \alpha \\ F_2(\varepsilon_2) \sin \alpha \cos^3 \alpha & F_2(\varepsilon_2) \sin^3 \alpha \cos \alpha & F_2(\varepsilon_2) \sin^2 \alpha \cos^2 \alpha \end{bmatrix} \quad (2.5)$$

In uniaxial and biaxial tests, the stiffness values F_i of the families can be determined. These values can be compared with the values obtained from both types of tests.

3. Experimental tests

The uniaxial and biaxial tensile tests with a constant displacement rate are chosen from a large group of experimental tests to model the material behaviour of a technical woven fabric. The uniaxial tensile experiments are the basic group of tests used for determination of mechanical properties of technical fabrics. One of the advantages of such tests is simplicity of preparation and cutting out of specimens which are generally cut along two orthogonal directions of the warp and weft threads. In basic uniaxial tensile tests, it is possible to specify stress and strains along investigated directions. In more sophisticated uniaxial tests, one can additionally specify Poisson's ratio. On the other hand, the biaxial tests are more complicated, and the application of specially designed stands is necessary. The test machines should apply tension in two directions with a different force ratio, constant in time. Good quality of the results depends on the type of an extensometer used to measure deformation in two directions simultaneously. Generally, the feature extraction method or digital image correlation based on artificial marks is used in a video extensometer for strain calculations (see e.g. Bathurst and Shinoda, 2004). In the feature extraction method, on the specimen surface, a non-destructive circles marks are made and then the distance between them is traced during the deformation process. When the specimen is deformed, its image changes accordingly. Following the changes of the marks coordinated on the specimen and the displacements, the strains can be calculated. In the biaxial tests, cross-shaped

specimens are preferred. The biaxial tests reflects well an anisotropic character of technical fabrics.

Uniaxial tensile laboratory tests have been made using the computer-controlled Zwick 020 testing machine (Fig. 3). The experiments have been carried out according to the national standard PN-EN ISO 1421 (2001). Specimens from the same batch of fabric in three directions: along warp, along weft and with an angle of 45° to both threads directions have been prepared. For each direction, five samples have been tested. Their dimensions were: width 50 mm, length 900 mm. The specimens have been subjected to tension with a displacement rate of grip equal to 100 mm/min (constant grip displacement rate). The tests have been controlled by a video extensometer with the base about 50 mm. The gauge length of each specimen (separation of curved grips) has been 100 mm. All tests have been performed at room temperature (about 20°C). All tests have been carried out up to specimen failure.

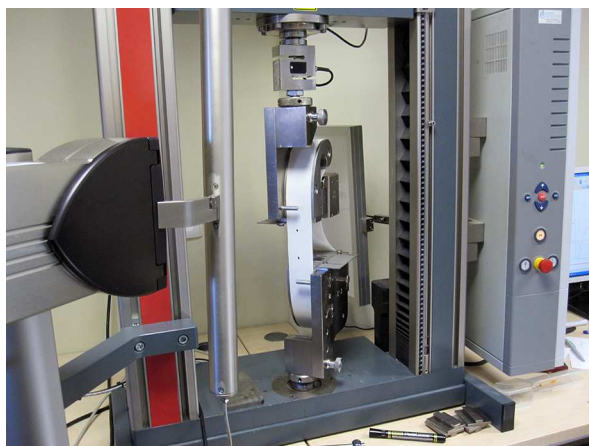


Fig. 3. Uniaxial laboratory test stand

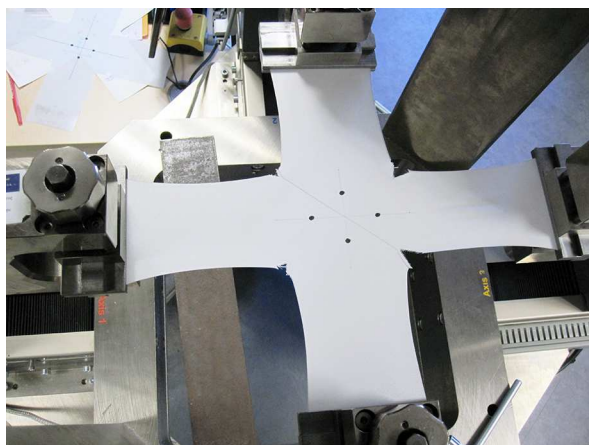


Fig. 4. Biaxial laboratory test stand

The biaxial tensile tests performed on the Zwick system BIAx 020 with a video extensometer attached (see Fig. 4), have been made for the cross-shaped specimens. There is no standard regulation on the method the tests should be performed. The arm width is 100 mm, therefore, on the testing area of $100\text{ mm} \times 100\text{ mm}$ the gage length of about 50 mm in both directions has been chosen. In all tests, the initial grip separation of 300 mm has been used. The specimens have been subjected to tension (base constant force rate of 100 N/s) in the warp, weft and bias directions with load (stress) ratios 1:1, 1:2, 2:1 ($\sigma_{warp} : \sigma_{weft}$). For each stress ratio, two samples up to failure have been tested. In the uniaxial and biaxial tensile tests, the measurements data (time, elongation and force) has been stored by every 0.01 s or force increment of 1 N.

4. Results and discussion

The stress-strain curves under uniaxial tensile tests are shown in Fig. 5. In general, mechanical properties in the weft and warp direction are different. The value of the Ultimate Tensile Strength (UTS) of specimens and the strain at rupture ε_R are collected in Table 1. The UTS is the final stress sustained in a tensile test at the exact moment of rupture of fabric specimens. The results given in Table 1 are presented in the form $\bar{x} \pm \bar{s}_x$, where \bar{x} is the mean value and \bar{s}_x is the standard error of the mean value. The UTS values for the weft and warp are comparable, but the elongation and strain at break for the weft direction is about 50% higher than for the warp direction. The bias direction (45°) has the highest elongation and the smallest UTS value. In this case, the main threads (warp and weft) are angled for the load direction and are not going from one grip to the other.

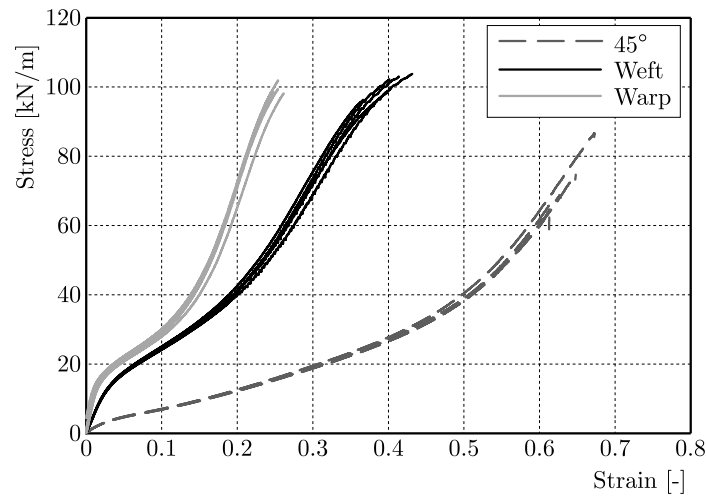


Fig. 5. Uniaxial test results

Table 1. Values of strain at break ε_R and UTS

	ε_R [-]	UTS [kN/m]
Weft	0.40 ± 0.01	101 ± 1
Warp	0.27 ± 0.01	99.2 ± 0.9
45°	0.64 ± 0.01	74 ± 5

Looking at the stress-strain curves (Fig. 5), the characteristic points of the curvature change can be specified. Then, for the strain range, a piecewise linear model (see e.g. Ambroziak, 2015a) can be used. In this concept, it is necessary to specify the longitudinal modules F_i and the intersection points P_j ($j = 1, 2$) for the specified strain values ε_{Pj} which define the range of applicability of a certain longitudinal modulus. The Marquardt-Levensberg algorithm (Marquardt, 1963) has been used to find the parameters that give the best fit between the constitutive equation and the experimental data. The parameters (and their standard deviation) for the piecewise linear model based on the uniaxial tensile test are given in Table 2. The parameters F_1 and F_3 are about 100% higher for the warp than for the weft direction. For the parameter F_2 , the weft and the warp differences of 10% can be observed. These parameters can be easily applied in the dense net model (see e.g. Ambroziak and Kłosowski, 2011) to describe the coated woven fabric behaviour in FEM calculations of structures.

The results of the biaxial tensile tests for 1:1, 1:2, 2:1 load ratios are presented in Figs. 6 and 7. It should be pointed that up to 10 kN/m stress range, the behaviour of the technical

Table 2. Non-linear model parameters – uniaxial tests

	Warp	Weft	45°
F_1 [kN/m]	967 ± 25	491 ± 4	122 ± 2
F_2 [kN/m]	159 ± 2	140 ± 2	60 ± 1
F_3 [kN/m]	633 ± 7	344 ± 4	275 ± 3
ε_{P1} [-]	0.0146 ± 0.0009	0.0297 ± 0.0004	0.004 ± 0.001
ε_{P2} [-]	0.146 ± 0.002	0.203 ± 0.003	0.475 ± 0.003

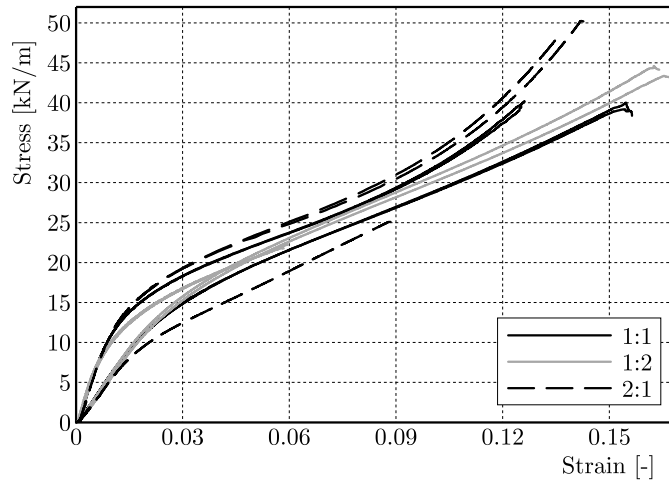


Fig. 6. Biaxial test results: 1:1, 1:2, 2:1

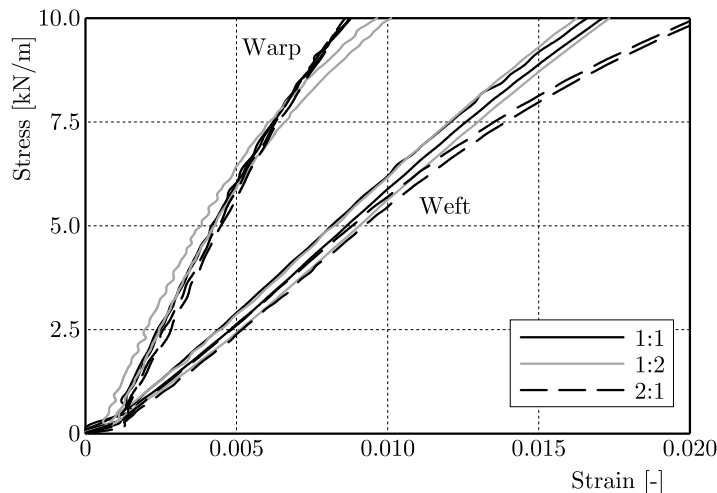


Fig. 7. Biaxial test results: 1:1, 1:2, 2:1 – stress range to 10 kN/m

fabric under biaxial tensile tests is very similar. Biaxial bias direction tests results are given in Fig. 8. The load ratios 1:2_{45°} and 2:1_{45°} exhibit contraction for thread directions which have the smallest stress values. The highly loaded threads straighten while other ones become folded. For the 1:1_{45°} stress ratio, the strains are positive in both directions (expanded in both directions).

The stress and strain values at rupture of the specimens (see Figs. 9 and 10) are given in Table 3. The mean stress value at brake for 1:1 load ratio is about 40 kN/m and is about 40% of the mean uniaxial tensile strength (see Table 1). The bias direction for 1:1_{45°} load ratio reaches a stress value of 18.6 kN/m. It is about 50% of the 1:1 biaxial stress and about 25%

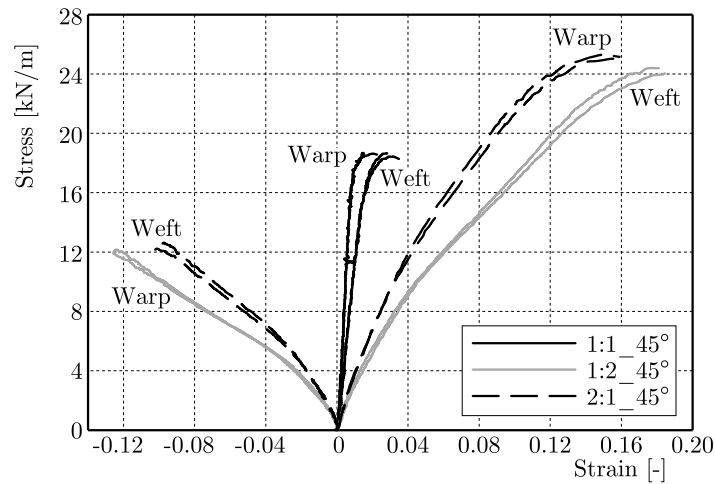


Fig. 8. Biaxial bias directions test results: 1:1.450, 1:2.450, 2:1.450

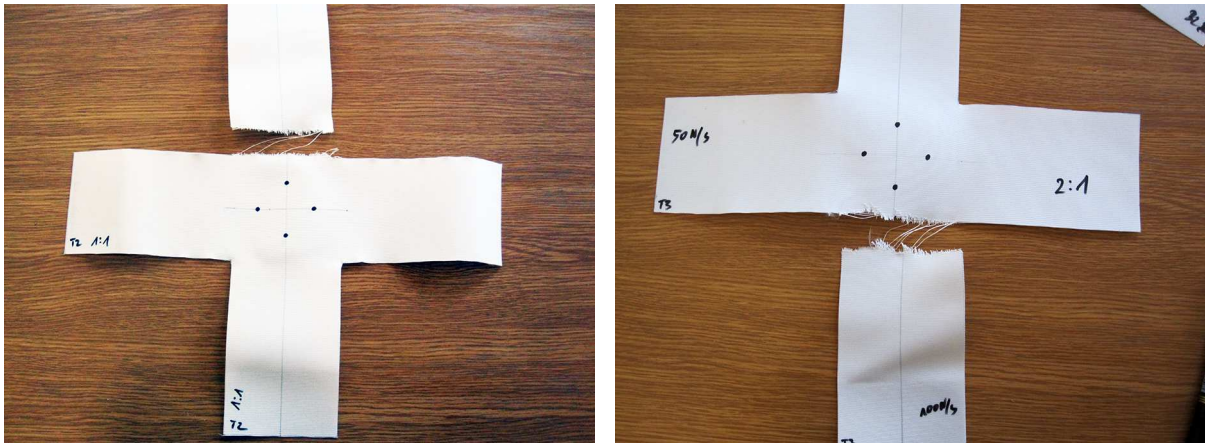


Fig. 9. Damaged specimens – biaxial test results

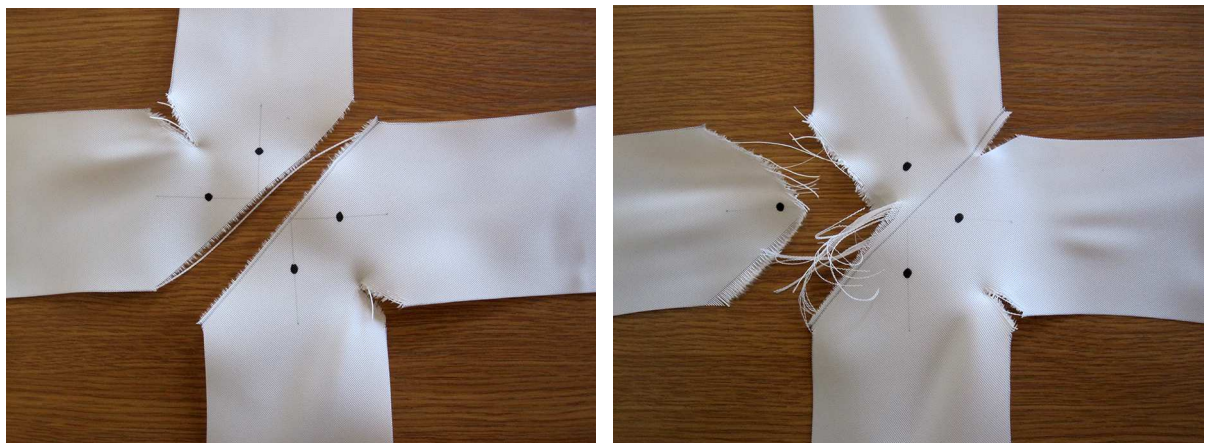


Fig. 10. Damaged 45° specimens – biaxial test results

of the uniaxial bias tensile strength. It should be noted that when the load ratio is 1:2 and 2:1, the strength of the fabric increases by 10%-20% up to 44 kN/m and 49 kN/m, respectively. This result can be explained by the failure mode of the specimen, see Figs. 9 and 10. For the 1:1, 1:2 and 2:1 load ratios, one of the cross arms is damaged. On the other hand, for the bias

directions 1:1_{45°}, 1:2_{45°}, 2:1_{45°} tear of the cross specimen in the central region is observed. The parameters for the piecewise linear model based on the biaxial tensile test are given in Tables 4 and 5. The value of F_1 parameter in the bias direction is about 100% higher than for the 1:1 load ratio in the warp and weft direction.

Table 3. Values of stress and strain at break

Load ratios	σ_{warp} [kN/m]	ε_{warp} [-]	σ_{weft} [kN/m]	ε_{weft} [-]
1:1	39.8 ± 0.3	0.1257 ± 0.0005	39.6 ± 0.4	0.1561 ± 0.0006
1:1 _{45°}	18.6 ± 0.1	0.0198 ± 0.003	18.6 ± 0.1	0.0321 ± 0.003
1:2	22.1 ± 0.3	0.0594 ± 0.0003	44.0 ± 0.6	0.167 ± 0.002
1:2 _{45°}	12.1 ± 0.1	-0.1264 ± 0.0001	24.3 ± 0.2	0.185 ± 0.001
2:1	49.3 ± 1	0.139 ± 0.004	24.6 ± 0.5	0.086 ± 0.003
2:1 _{45°}	25.2 ± 0.2	0.1649 ± 0.0001	12.5 ± 0.2	-0.103 ± 0.005

Table 4. Non-linear model parameters – warp

	1:1	1:1 _{45°}	1:2	2:1
F_1 [kN/m]	1140 ± 2	2240 ± 130	1429 ± 23	1228 ± 6
F_2 [kN/m]	178 ± 1	–	193 ± 1	181 ± 3
F_3 [kN/m]	326 ± 6	–	–	439 ± 6
ε_{P1} [-]	0.0136 ± 0.0001	–	0.0094 ± 0.0003	0.0141 ± 0.0001
ε_{P2} [-]	0.0975 ± 0.0003	–	–	0.102 ± 0.002

Table 5. Non-linear model parameters – weft

	1:1	1:1 _{45°}	1:2	2:1
F_1 [kN/m]	595 ± 2	1110 ± 13	613 ± 14	606 ± 7
F_2 [kN/m]	190 ± 2	–	199 ± 5	219 ± 1
ε_{P1} [-]	0.0248 ± 0.0002	–	0.026 ± 0.001	0.0164 ± 0.0005

Additionally, it can be shown in Fig. 11 that the biaxial tensile tests are comparable with the uniaxial tensile behaviour of the sailing technical fabric in a specific range of load. This characteristic is observed for a polyester type coated fabrics (see e.g. Ambroziak, 2015b). In Figs. 12 and 13 and Tables 6 and 7, uniaxial and biaxial test results for the chosen coated fabrics (AF 9032, FR 8540 and Precontraint 1202S) are compared with the tested 480 AP sail fabric. Detailed investigation on the FR 8540 and Precontraint 1202S coated fabrics are given by Ambroziak (2015a,b), respectively.

The shape and characteristic of the stress-strain curves from the warp and weft under uniaxial tensile tests (see Fig. 12) and 1:1 biaxial tensile tests (see Fig. 13) for the 480 AP fabric are similar to the Precontraint 1202S fabric. It can be concluded that bidirectional tension is applied during the manufacturing (coating) process of both these fabrics, because the shapes of stress-strain curves in the warp and weft directions are similar. For the AF 9032 and FR 8540 fabrics, the shape of stress-strain curves in the warp and weft direction are different. UTS values for the 480 AP, AF 9032 and Precontraint 1202S are comparable. The longitudinal stiffness F_1 in the warp direction for the 480 AP is comparable with the other fabrics. On the other hand, it should be noted that total weights of the AF 9032 and Precontraint 1202S fabrics are two times bigger than the weight of the 480 AP fabric. It can be concluded that a different way of thread weaving of both fabrics has been applied.

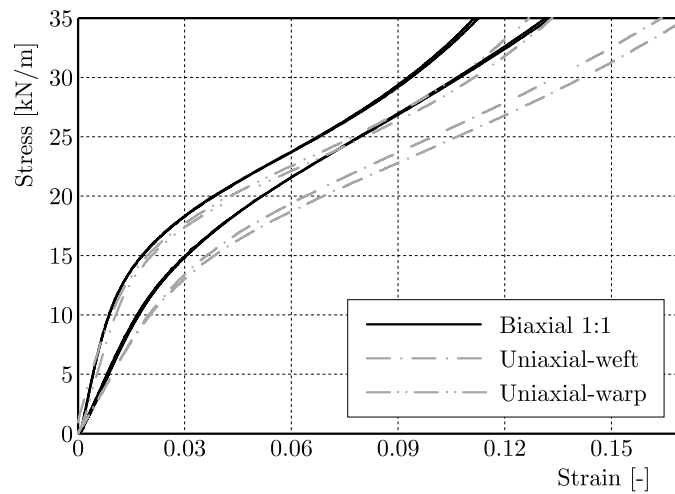


Fig. 11. Comparison of biaxial and uniaxial test results

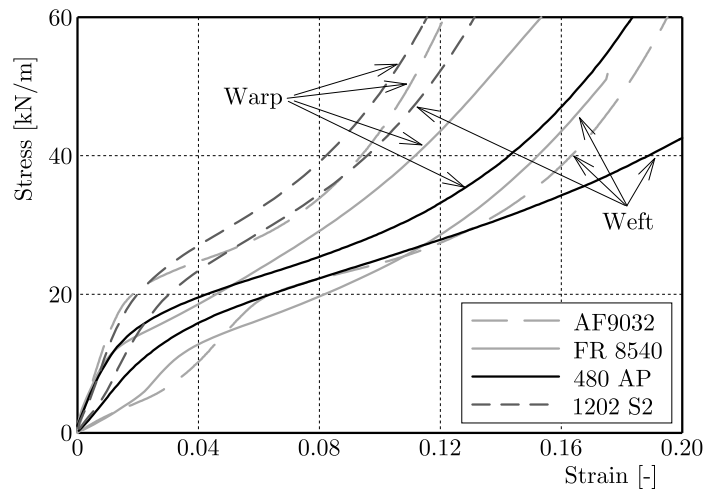


Fig. 12. Comparison of uniaxial test results for polyester fabrics

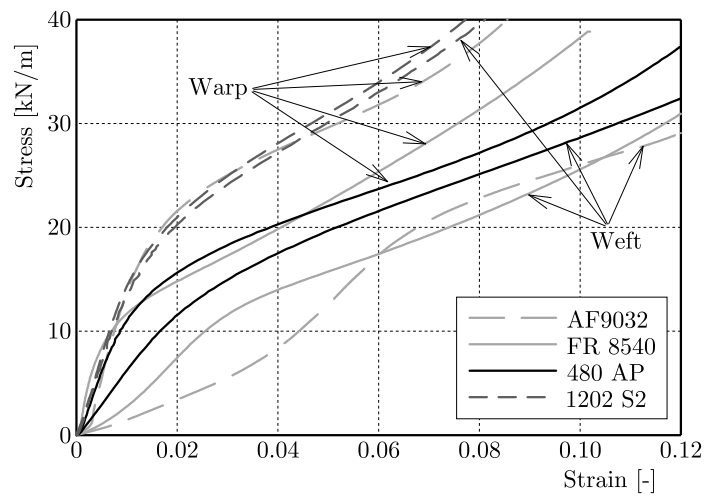


Fig. 13. Comparison of biaxial test results for polyester fabrics

Table 6. Non-linear model parameters – uniaxial tests

Total weight [g/m ²]	480	1085	890	1050
Weft	480 AP	AF 9032	FR 8540	Precontraint 1202S
F_1 [kN/m]	491 ± 4	193 ± 5	241 ± 12	650 ± 26
F_2 [kN/m]	140 ± 2	465 ± 15	437 ± 11	288 ± 3
F_3 [kN/m]	344 ± 4	105 ± 2	183 ± 2	841 ± 8
F_4 [kN/m]	–	880 ± 20	444 ± 5	–
ε_{P1} [–]	0.0297 ± 0.0004	0.034 ± 0.002	0.018 ± 0.002	0.030 ± 0.001
ε_{P2} [–]	0.203 ± 0.003	0.064 ± 0.004	0.035 ± 0.002	0.1144 ± 0.0007
ε_{P3} [–]	–	0.168 ± 0.005	0.124 ± 0.004	–
UTS [kN/m]	101 ± 1	104 ± 2	67.5 ± 0.5	102 ± 1
Warp	480 AP	AF 9032	FR 8540	Precontraint 1202S
F_1 [kN/m]	967 ± 25	1280 ± 15	1070 ± 5	1170 ± 20
F_2 [kN/m]	159 ± 2	197 ± 1	257 ± 2	300 ± 4
F_3 [kN/m]	633 ± 7	1075 ± 5	482 ± 4	897 ± 12
ε_{P1} [–]	0.0146 ± 0.0009	0.0142 ± 0.0004	0.0105 ± 0.0002	0.0164 ± 0.0002
ε_{P2} [–]	0.146 ± 0.002	0.0981 ± 0.0003	0.100 ± 0.001	0.1002 ± 0.0004
UTS [kN/m]	99.2 ± 0.9	116 ± 2	65 ± 1	108 ± 1

Table 7. Non-linear model parameters – biaxial tests (1:1)

Weft	480 AP	AF 9032	FR 8540	Precontraint 1202S
F_1 [kN/m]	595 ± 2	192 ± 4	241 ± 12	1300 ± 10
F_2 [kN/m]	190 ± 2	462 ± 12	437 ± 11	300 ± 5
F_3 [kN/m]	–	167 ± 1	183 ± 2	675 ± 50
F_4 [kN/m]	–	875 ± 12	444 ± 5	–
ε_{P1} [–]	0.0248 ± 0.0002	0.034 ± 0.002	0.018 ± 0.002	0.0145 ± 0.0005
ε_{P2} [–]	–	0.064 ± 0.004	0.035 ± 0.002	0.095 ± 0.001
ε_{P3} [–]	–	0.168 ± 0.005	0.124 ± 0.004	–
Warp	480 AP	AF 9032	FR 8540	Precontraint 1202S
F_1 [kN/m]	1140 ± 2	1732 ± 20	1070 ± 5	1500 ± 10
F_2 [kN/m]	178 ± 1	236 ± 2	257 ± 2	335 ± 5
F_3 [kN/m]	326 ± 6	1045 ± 3	482 ± 4	750 ± 25
ε_{P1} [–]	0.0136 ± 0.0001	0.0142 ± 0.0004	0.0105 ± 0.0002	0.012 ± 0.001
ε_{P2} [–]	0.0975 ± 0.0003	0.0981 ± 0.0003	0.100 ± 0.001	0.095 ± 0.001

5. Conclusions

The study presents test methods to investigate mechanical properties of a sail technical woven fabric. Additionally, several non-linear model parameters for polyester coated fabrics have been collected and compared. The identification of non-linear elastic properties has been successfully performed on the basis of uniaxial and biaxial tension tests for the dense net model. The material parameters, determined above, can be used in a direct way in FE analysis, where the problem of geometric nonlinearity is supplemented by physical nonlinearity of the fabric material. Based on the presented results, it can be concluded that it is possible to indicate the same types

of technical woven fabrics for which the behaviour under biaxial stress state can be described by a uniaxial response (compare Fig. 11 and Fig. 7). One of the deciding factors is the type of textile weave (generally two orthogonal families of warp and weft threads). For engineering calculations in the preliminary design stage, one can apply the dense net model with uniaxial nonlinear parameters to describe biaxial behaviour of a technical woven fabric in the range 1:2 – 1:1 – 2:1 of load ratios. A modern laboratory equipment allows testing in different variants and computer storage of the results, important for a future identification process. Examples of such tests have been presented in the paper in order to understand the behaviour of the sail technical woven fabric better. The investigation confirms that the quality of the yacht sailcloth polyester is sufficiently high. The obtained results encourage the authors to continue the outlined research, also on the basis of extended experiments and to apply other types of constitutive models. This study may provide naval engineers and designers with a theoretical basis for a wide use of sail coated fabrics. Examples of presented laboratory tests and comparison of mechanical parameters make a step towards a better understanding of the behaviour of polyester coated fabrics.

References

1. AMBROZIAK A., 2015a, Mechanical properties of polyester coated fabric subjected to biaxial loading, *Journal of Materials in Civil Engineering*, **27**, 11
2. AMBROZIAK A., 2015b, Mechanical properties of PVDF-coated fabric under tensile tests, *Journal of Polymer Engineering*, **35**, 4, 377-390
3. AMBROZIAK A., KŁOSOWSKI P., 2011, Review of constitutive models for technical woven fabrics in finite element analysis, *AATCC Review*, **11**, 3, 58-67
4. BATHURST R.J., SHINODA M., 2004, Strain measurement of geogrids using a video-extensometer technique, *Geotechnical Testing Journal*, **27**, 5, 456-463
5. BADEL P., VIDAL-SALLE E., BOISSE P., 2008, Large deformation analysis of fibrous materials using rate constitutive equations, *Computers and Structures*, **86**, 11-12, 1164-1175
6. BENFRATELLO S., CIRELLO A., PALIZZOLO L., 2013, Effect of surface finish on the mechanical behaviour of Dacron 360 woven, *Ocean Engineering*, **70**, 88-96
7. BENFRATELLO S., PALIZZOLO L., 2010, Experimental characterization of Dacron 360 woven constitutive behaviour, *Meccanica dei Materiali e delle Strutture*, **1**, 3, 13-23
8. BLICBLAU A.S., SINGH M., MCCONNELL E., PLEANER M., 2008, Stress analysis of a novice windsurfer sail by finite element analysis, *Mathematical and Computer Modelling*, **47**, 11-12, 1108-1116
9. GASSER A., BOISSE P., HANKLAR S., 2000, Mechanical behaviour of dry fabric reinforcements. 3D simulations versus biaxial tests, *Computational Materials Science*, **17**, 1, 7-20
10. LE MAÎTRE O., HUBERSON S., SOUZA DE CURSI J.E., 1996, Application of a non-convex model of fabric deformations to sail cut analysis, *Journal of Wind Engineering and Industrial Aerodynamics*, **63**, 77-93
11. MARQUARDT D.W., 1963, An algorithm for least squares estimation of parameters, *Journal of the Society of Industrial and Applied Mathematics*, **11**, 431-441
12. NIELSEN J.N., 1963, Theory of flexible aerodynamic surfaces, *Journal of Applied Mechanics*, **30**, 435-442
13. PN-EN ISO 1421:2001 Rubber- or plastics-coated fabrics – Determination of tensile strength and elongation at break

14. SPALATELU-LAZAR M., LÉNÉ F., TURBÉ N., 2008, Modelling and optimization of sails, *Computers and Structures*, **86**, 1486-1493
15. TRIKI E., DOLEZ P., VU-KHANH T., 2011, Tear resistance of woven textiles – criterion and mechanisms, *Composites Part B: Engineering*, **42**, 7, 1851-1859
16. ŻYLIŃSKI T., 1965, *Textile Metrology* (in Polish), Wydawnictwo Przemysłu Lekkiego i Spożywczego, Warsaw

Manuscript received December 16, 2016; accepted for print September 14, 2017

DYNAMIC SIMULATION OF A NOVEL “BROOMSTICK” HUMAN FORWARD FALL MODEL AND FINITE ELEMENT ANALYSIS OF THE RADIUS UNDER THE IMPACT FORCE DURING FALL

DARIUSZ GRZELCZYK, PAWEŁ BIESIACKI, JERZY MROZOWSKI, JAN AWREJCIEWICZ

Lodz University of Technology, Department of Automation, Biomechanics and Mechatronics, Łódź, Poland

e-mail: dariusz.grzelczyk@p.lodz.pl; pawel.biesiacki@dokt.p.lodz.pl; jerzy.mrozowski@p.lodz.pl; jan.awrejcewicz@p.lodz.pl

The paper presents dynamic simulation and experimental identification of a human forward fall model describing the process of “falling like a broomstick” on the outstretched arms. The model implemented in Mathematica allows one to estimate time histories of the ground reaction force in different scenarios of the fall process. These time series are applied as time-varying load conditions to the numerical analysis of the human radial bone model created from the computed tomography data. Finally, the obtained numerical results indicate that the strain criterion seems to be more useful for estimating the radius fracture site in comparison to the stress criterion.

Keywords: forward fall, ground reaction force, bone strength, fracture, distal radius

1. Introduction

Falls are common accidents in human daily life. They are severe and inevitable threats during the walking process of the bipedal movement. Despite all population groups are exposed to these risk factors, falls are the most serious social health problem among the elderly (Heijnen and Rietdyk, 2016). As a result, the risk of injuries to hands, torso, head/neck and/or other parts of the human body is possible. These injuries can eventually lead to death, chronic pain, disability and/or loss of independence (Robinovitch *et al.*, 2013).

The vast majority of cases of upper extremity injuries occur as a result of a fall with a direct impact on the extended arms which are exposed to dynamical impact forces (Nevitt and Cummings, 1993; Palvanen *et al.*, 2000). Distal radius fractures are common in elderly women with osteoporosis due to their compromised bone density/quality as well as probably due to the increased risk of falling in this population group. Fractures of the forearm bones represent nearly 20% of all reported fractures worldwide, and the most common type of fracture is the so-called Colles' fracture as an injury of distal radius of the forearm (Johnell and Kannis, 2006).

The aforementioned upper extremity injuries may be a result of forward falls, backward falls or side falls. Colles' fracture, as an injury of the radius, is a direct result of exceeding the maximum value of the force allowable for this bone. For instance, distal radius fractures at a mean force equal to 2260 ± 1010 N were observed by Frykman using 48 cadaveric bones of average age of 65 years (Frykman, 1967). Spadaro and his co-investigators obtained the mean strength of a bone fracture at the level of 1640 ± 980 N (Spadaro *et al.*, 1994). Kim and Ashton-Miller (2009) adopted the value equal to 2400 N as a distal radius fracture threshold. Also in one of the recent papers by Burkhart *et al.* (2013), the estimated values of force causing fracture of the studied bones derived from cadavers were approximately equal to 2150 N.

2. Literature review of the forward fall models

A forward fall is known as the most frequent type of fall, and more than a half of all falls among the elderly occur in the forward direction (Nevitt and Cummings, 1993; O'Neill *et al.*, 1994; Vellas *et al.*, 1998). Recent decades have brought different models related to the impact of the upper extremities to the ground as a result of a forward or backward fall. One of the simplest effective mechanical models of the human falling motion is a single-degree-of-freedom (DoF) linear mass-spring-damper mechanical system subjected to a sudden velocity input or an impulse force input. Such a model can be readily extended to systems with many DoFs. Below we are focused only on the three most well-known, widely available and cited forward fall models.

A fall model proposed by Chiu and Robinovitch (1998) applies to the human forward fall from a low height on the outstretched and fully extended upper extremities as the worst-case scenario of such a fall. It is constructed based on a 2-DoFs lumped-parameter mechanical system containing elastic and damping elements responsible for the operation of human muscles. Davidson *et al.* (2006) completed a study with the aim of developing a “risk factor” value in order to determine whether someone will sustain the radius fracture based on the characteristics of their fall. The mentioned study used a two mass-spring-damper model, referring to the experimental data obtained from 45 clinical cases of children falling off of playground equipment.

DeGoede and Ashton-Miller (2003) employed Adams software to develop a half-body symmetric model of the human forward fall consisting of five segments (legs, torso with head and neck, upper arm, forearm and hand). In that model, the movement of the hand and the pivot point in the ankle toe are fixed, and friction is not taken into account. Moreover, the wrist, elbow and hip joints are adopted as flat joints without friction, whereas the shoulder joint connecting the arm to the body via massless blades is modelled as a linear frictionless sliding joint with the movement axis perpendicular to the longitudinal body axis. The main goal of the authors was to study the possibility of injury in older women. Therefore, to determine the model parameters, baseline height and weight equal to 1.63 m and 62 kg, respectively, were used (Kroemer *et al.*, 1997).

Kim and Ashton-Miller (2009) proposed another flat model of the forward fall as a two DoFs system constructed based on a mechanical model of a double pendulum rotating freely around a pivot corresponding to the ankles of the lower human extremities. To provide a mathematical model, the mechanical system was reduced to a system of linear translational movements with 2-DoFs with spring-damper elements responsible for attenuation action of the human muscles. Numerical simulation for the fall height of 1.5 m showed that the maximum impact force was doubled from 1250 N to a value of 2610 N, depending on the fall scenario. In this way, the authors showed that for the same fall conditions (the same faller falling from the same height), too rapid movement of the arms in comparison to the rest of the body could cause the occurrence of an excessive force acting on the upper extremity more than 2350 N, which caused a fracture of the distal radius.

To conclude, it can be stated that, in general, the considered falling process was usually mathematically modelled based on flat and linear mechanical systems consisting of two rigid bodies with masses moved by transverse motion connected by linear spring-damper elements. These models were usually presented as a set of the second-order ordinary differential equations of motion (Chiu and Robinovitch, 1998), but also the appropriate equations were written in the state space (Kim and Ashton-Miller, 2009). On the other hand, in the case of a more complex mechanical model, numerical simulations were performed only using commercial Adams software (DeGoede and Ashton-Miller, 2003). In the present paper, we propose our own mathematical model of the human forward fall on the outstretched arms. In addition, unlike previous models met in the literature, our model takes into account a direct influence of different human speed

just before the trip over an obstacle and starting the falling process, which affects the final force of impact of the upper extremity on the ground.

3. The proposed “broomstick” forward fall model

3.1. Mathematical modelling

The human “like a broomstick” forward fall on the outstretched arms is schematically shown in Fig. 1a. Equations of motion of the analysed system have been obtained by the Newton-Euler method, and Free Body Diagrams of the system are shown in Fig. 1b.

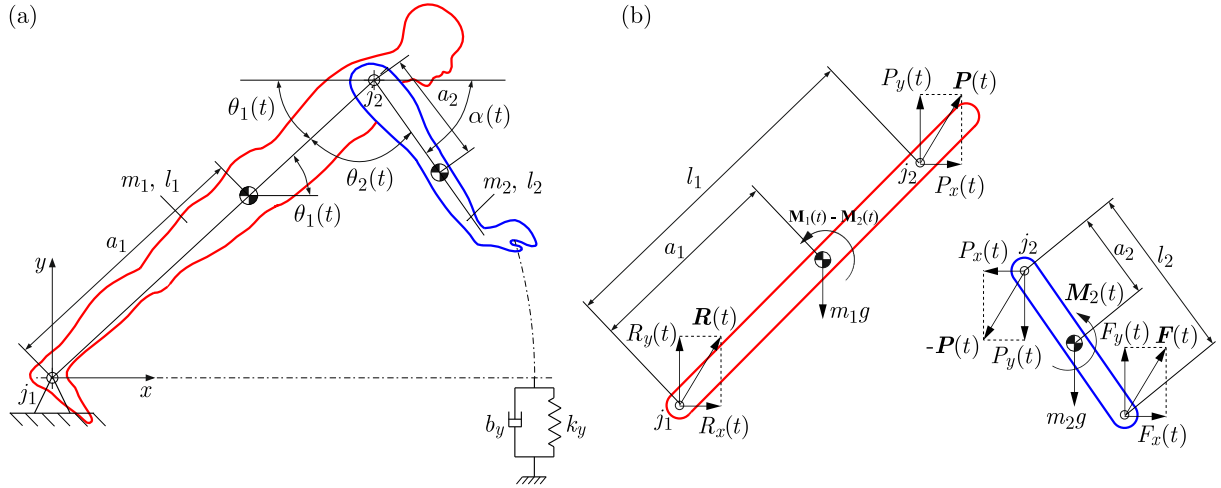


Fig. 1. Mechanical modelling of the forward fall process: (a) the proposed forward fall biomechanical model as a planar mechanical system with 2-DoFs embedded in the Cartesian coordinate system; (b) Free Body Diagrams of the system

The model consists of two rigid bodies, 1 and 2, with masses m_1 , m_2 and moments of inertia I_1 , I_2 around centres of gravity of the bodies, respectively. Body 1 corresponds to the human torso with legs, neck and head, whereas body 2 corresponds to the human upper extremities (including arms, forearms and hands). The parameters a_1 and a_2 represent the distances between the gravity centres of individual bodies and their rotation axes, whereas l_1 and l_2 denote the total lengths of the mentioned bodies, respectively. The angle $\theta_1(t)$ denotes the angle between the horizontal x axis and the longitudinal axis of body 1. The angle $\theta_2(t)$ is the angle measured from the axis of body 1 to the axis of body 2. The ground with non-linear contact law is characterised by stiffness and damping coefficients k_y and b_y , respectively.

In this model, we take the vectors $\boldsymbol{\theta}_1(t) = [0, 0, \theta_1(t)]^T$, $\boldsymbol{\theta}_2(t) = [0, 0, \theta_2(t)]^T$ of the angles in the joints j_1 and j_2 , vectors $\mathbf{r}_{C1}(t)$, $\mathbf{r}_{C2}(t)$ of displacements of gravity centres of the first and the second body, as well as the vectors $\mathbf{l}_1(t)$, $\mathbf{l}_2(t)$ of displacements of the joint j_2 and the end of body 2 which can impact to the ground, respectively, in the following form

$$\begin{aligned} \mathbf{r}_{C1}(t) &= [x_1(t), y_1(t), 0]^T = [a_1 \cos \theta_1(t), a_1 \sin \theta_1(t), 0]^T \\ \mathbf{r}_{C2}(t) &= [x_2(t), y_2(t), 0]^T = [l_1 \cos \theta_1(t) + a_2 \cos \alpha(t), l_1 \sin \theta_1(t) - a_2 \sin \alpha(t), 0]^T \\ \mathbf{l}_1(t) &= [l_1 \cos \theta_1(t), l_1 \sin \theta_1(t), 0]^T \\ \mathbf{l}_2(t) &= [l_1 \cos \theta_1(t) + l_2 \cos \alpha(t), l_1 \sin \theta_1(t) - l_2 \sin \alpha(t), 0]^T \end{aligned} \quad (3.1)$$

where $\alpha(t) = 180^\circ - \theta_1(t) - \theta_2(t)$. The forces $\mathbf{Q}_1 = [0, -m_1g, 0]^T$ and $\mathbf{Q}_2 = [0, -m_2g, 0]^T$ are the gravity forces acting on the gravity centres of bodies 1 and 2, respectively, with the acceleration

of gravity g ($g = 9.81 \text{ m/s}^2$). The force $\mathbf{R}(t) = [R_x(t), R_y(t), 0]^T$ is the reaction force in the joint j1. The unknown force in the joint j2 and presented in the Free Body Diagrams (see Fig. 1b) is denoted as $\mathbf{P}(t) = [P_x(t), P_y(t), 0]^T$. Finally, the force $\mathbf{F}(t) = [F_x(t), F_y(t), 0]^T$ is the ground reaction force acting on body 2 at the moment of its impact to the ground.

Let $\mathbf{M}_1(t) = [0, 0, 0]^T$ and $\mathbf{M}_2(t) = [0, 0, M_2(t)]^T$ denote the torques generated in the joints j1 and j2, respectively. As a result, for the two considered free bodies presented in Fig. 1b, we can write the following equations of motion in the vector form

$$\begin{aligned} m_1 \ddot{\mathbf{r}}_{C1}(t) &= \mathbf{R}(t) + \mathbf{Q}_1 + \mathbf{P}(t) \\ I_1 \ddot{\boldsymbol{\theta}}_1(t) &= \mathbf{M}_1(t) - \mathbf{M}_2(t) - \mathbf{r}_{C1}(t) \times \mathbf{R}(t) + [\mathbf{l}_1(t) - \mathbf{r}_{C1}(t)] \times \mathbf{P}(t) \\ m_2 \ddot{\mathbf{r}}_{C2}(t) &= -\mathbf{P}(t) + \mathbf{Q}_2 + \mathbf{F}(t) \\ I_2 \ddot{\boldsymbol{\theta}}_2(t) &= \mathbf{M}_2(t) - [\mathbf{l}_1(t) - \mathbf{r}_{C2}(t)] \times \mathbf{P}(t) + [\mathbf{l}_2(t) - \mathbf{r}_{C2}(t)] \times \mathbf{F}(t) \end{aligned} \quad (3.2)$$

Equations (3.2) can be reduced to the scalar form

$$\begin{aligned} I_1 \ddot{\theta}_1(t) &= -M_2(t) + a_1 R_x(t) \sin \theta_1(t) - a_1 R_y(t) \cos \theta_1(t) \\ &\quad + (l_1 - a_1) P_y(t) \cos \theta_1(t) - (l_1 - a_1) P_x(t) \sin \theta_1(t) \\ I_2 \ddot{\theta}_2(t) &= M_2(t) + a_2 P_y(t) \cos \alpha(t) + a_2 P_x(t) \sin \alpha(t) \\ &\quad + (l_2 - a_2) F_y(t) \cos \alpha(t) + (l_2 - a_2) F_x(t) \sin \alpha(t) \end{aligned} \quad (3.3)$$

where

$$\begin{aligned} P_x(t) &= F_x(t) - m_2 \ddot{x}_2(t) \\ P_y(t) &= F_y(t) - m_2 \ddot{y}_2(t) - m_2 g \\ R_x(t) &= m_1 \ddot{x}_1(t) - P_x(t) = m_1 \ddot{x}_1(t) + m_2 \ddot{x}_2(t) - F_x(t) \\ R_y(t) &= m_1 \ddot{y}_1(t) + m_1 g - P_y(t) = m_1 \ddot{y}_1(t) + m_2 \ddot{y}_2(t) + m_1 g + m_2 g - F_y(t) \end{aligned} \quad (3.4)$$

At the time of tripping over an obstacle, a human instinctively and quickly pulls his arms to the front in order to arrest and/or to absorb the fall. This process is described by the time histories of the angle $\theta_2(t)$, which can be estimated based on the kinematics of the falling process registered with the use of a digital camera. Based on the second equation of (3.3) and the function $\theta_2(t)$ obtained in this way, we can calculate the torque $M_2(t)$ generated by arms in the joint shoulder during the falling process. Taking the torque $M_2(t)$ in the first Eq. of (3.3), one obtains eventually the following equation of motion around the joint j1

$$\begin{aligned} I_1 \ddot{\theta}_1(t) + I_2 \ddot{\theta}_2(t) &= a_1 R_x(t) \sin \theta_1(t) - a_1 R_y(t) \cos \theta_1(t) + (l_1 - a_1) P_y(t) \cos \theta_1(t) \\ &\quad - (l_1 - a_1) P_x(t) \sin \theta_1(t) + a_2 P_y(t) \cos \alpha(t) + a_2 P_x(t) \sin \alpha(t) \\ &\quad + (l_2 - a_2) F_y(t) \cos \alpha(t) + (l_2 - a_2) F_x(t) \sin \alpha(t) \end{aligned} \quad (3.5)$$

with the function $\theta_1(t)$ as a solution to this equation of motion.

3.2. Ground reaction force

To predict the vertical ground reaction force (GRF) $F_y(t)$, a non-linear model of impact at the wrist-ground interface has been employed in the form

$$F_y(t) = k_y |y(t)|^3 (1 - b_y \dot{y}(t)) J(-y(t)) \quad (3.6)$$

where parameters k_y , b_y denote the ground stiffness and damping coefficients in the vertical direction, respectively, $y(t) = l_1 \sin \theta_1(t) - l_2 \sin \alpha(t)$, and the function $J(-y(t))$ is the step function defined as

$$J(-y(t)) = \begin{cases} 1 & \text{if } y(t) < 0 \\ 0 & \text{if } y(t) \geq 0 \end{cases} \quad (3.7)$$

For instance, this formulation of GRF had been used previously to model the heel strike in running (Gerritsen *et al.*, 1995) and to model GRF at the hand-ground interface (DeGoede and Ashton-Miller, 2003). In our model, we have not included the horizontal force component $F_x(t)$ which is required to prevent the hand from sliding. However, the total GRF is less than 5% greater than the vertical GRF (DeGoede and Ashton-Miller, 2003).

3.3. Initial conditions

The considered model has been reduced to a single DoF model with the function $\theta_1(t)$ as the solution and the following initial conditions: $\theta_1(0)$ -initial angular position, and $\dot{\theta}_1(0)$ -initial angular velocity. At the beginning of the trip ($t = 0$), a human is usually in the standing position, and thus we take $\theta_1(0) = 90^\circ$ (see Fig. 1a). The initial angular velocity $\dot{\theta}_1(0)$ is estimated based on the transverse human speed during walking just before the moment of the trip. For this reason, we assume that the linear speed of the human gait decreases from v_0 to 0, and the rotational velocity $\dot{\theta}_1(t)$ increases from 0 to $\dot{\theta}_1(0)$ at the same time. Taking into account the principle of conservation of momentum, rotary motion of the human body around the pivot axis is governed as

$$I \frac{\Delta \dot{\theta}_1(t)}{\Delta t} = rF \Rightarrow \Delta \dot{\theta}_1(t) = -\frac{(m_1 + m_2)v_0 r}{I} = \dot{\theta}_1(0) \quad (3.8)$$

where $F\Delta t$ is a force impulse causing rotation of the human body around the rotation axis placed in feet (ankles), I is the moment of inertia of the human body around the pivot axis and r is the distance between the human gravity centre and the pivot axis with the upper extremities adjusted along the body (typical position of the human body during walking). On the contrary to the previous investigations met in the literature, the assumption adopted in this paper allows one also to study kinematic and dynamic parameters during the falling process for different walking speeds of the faller just before the moment of the trip over an obstacle.

4. Identification of the fall model parameters

4.1. GrabCAD model of the human body

To determine the human body parameters required in the proposed fall model, the full 3D scanned human body model based on GrabCAD (2016) (see Fig. 2) as well as the appropriate AutoDesk Inventor commands have been used. The mass of the whole body is calculated assuming that the average density equals to $\rho = 1050 \text{ kg/m}^3$, and the model parameters are: $a_1 = 1.01 \text{ m}$, $a_2 = 0.22 \text{ m}$, $l_1 = 1.4 \text{ m}$, $l_2 = 0.53 \text{ m}$, $r = 1.03 \text{ m}$, $m_1 = 61.0 \text{ kg}$, $m_2 = 7.4 \text{ kg}$, $I_1 = 9.9 \text{ kg}\cdot\text{m}^2$, $I_2 = 0.232 \text{ kg}\cdot\text{m}^2$, $I = 82.86 \text{ kg}\cdot\text{m}^2$.

4.2. Kinematics of the fall process

The kinematic analysis of the faller between the moment of tripping over an obstacle and hitting his hands to the ground were observed using an Optitrack optoelectronic motion analysis system installed at the Department of Automation, Biomechanics and Mechatronics, Lodz University of Technology, Lodz, Poland. The front panel of the computer program used to operate this system with the location of the individual markers on the faller's body is presented in Fig. 3, where the process of forward fall from the standing position to the ground is shown. Before the experimental test, the volunteer (one of the authors of this paper) has been instructed to safely fall “like a broomstick”. The fall of the human body was performed using a certificated soft insurance mattress with the full size $2 \text{ m} \times 2 \text{ m} \times 0.3 \text{ m}$, and thus there was no a direct threat of injury to the upper extremities and other body parts.

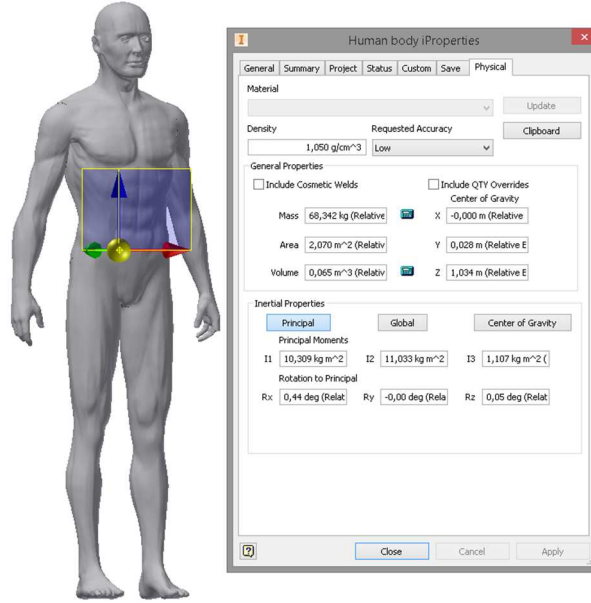


Fig. 2. Three-dimensional scanned human body model used for the estimation of its geometrical and mechanical properties (GrabCAD, 2016)

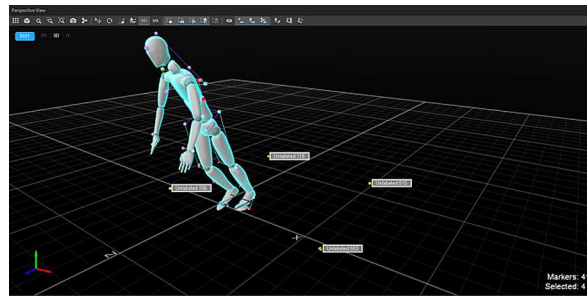


Fig. 3. Forward fall from the standing position to the soft mattress observed by Optitrack system using 37 passive reflective markers distributed on the faller's body

Using Optitrack system we observed that the faller extends his arms from initial position $\theta_{20} \approx 5^\circ$ to the final position $\theta_{2max} \approx 80^\circ$ at the moment of the impact to the ground. That is why, in all further presented investigations we use the time history of angle $\theta_2(t)$ described by the formula

$$\theta_2(t) = \begin{cases} \theta_{20} + (\theta_{2max} - \theta_{20}) \sin^2(\lambda t) & \text{if } t \leq T \\ \theta_{2max} & \text{if } t > T \end{cases} \quad (4.1)$$

where T denotes duration of the fall (the time between tripping and hitting the ground), whereas λ corresponds to the speed of movements of the faller's arms. The parameters λ and T strongly depend on the walking speed of the faller before the trip. The averaged time history of the angle $\theta_2(t)$ obtained from the experiment for $v_0 = 1.5 \text{ m/s}$ and its approximation are presented in Fig. 4.

4.3. Hand-ground contact parameters

Figure 5a shows the schematics (the first frame of our animation created in Mathematica) of the initial configuration of the subject falling in the forward direction from the initial shoulder height of 1 m (DeGoede and Ashton-Miller, 2003). The red line represents the torso with legs, the blue line represents upper extremities, whereas the green circle is the head of the faller.

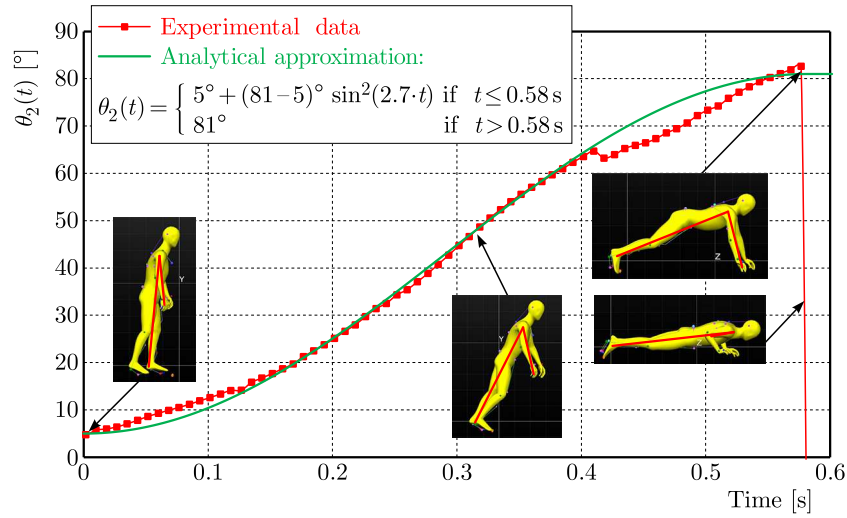


Fig. 4. Time history of the angle $\theta_2(t)$ (red points and red curve) obtained from the experiment and its approximation by an analytical smooth function (green curve). In this experiment, the faller started to fall from not a fully standing position ($\theta_1(0) < 90^\circ$)

The presented initial position was obtained for the following initial conditions: $\theta_1(0) = 45^\circ$, $\dot{\theta}_1(0) = 0$ and $\theta_2(t) = 83.5^\circ = \text{const}$. During numerical experiments we tested different values of the parameters k_y and b_y to obtain GRF which corresponds (both from a qualitative and quantitative point of view) to the GRFs presented by DeGoede and Ashton-Miller (2003). In that paper, the authors tested five healthy young male volunteers aged between 22 and 28 years with the average body mass of 72 ± 7 kg and the overall height of 173 ± 3 cm (DeGoede and Ashton-Miller, 2002). Finally, the best degree of fit was obtained for $k_y = 50\,000$ N/m³ and $b_y = 0.6$ s/m (the obtained results are shown in Fig. 5b).

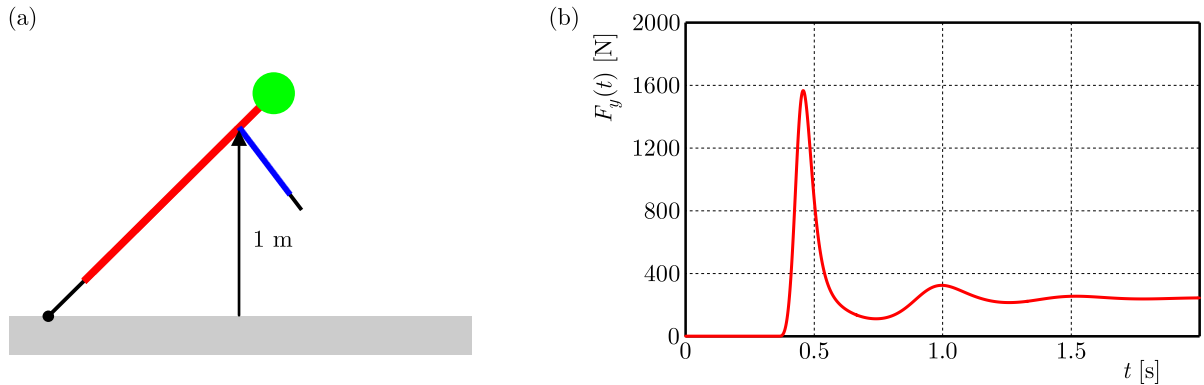


Fig. 5. Initial configuration of the faller's body, i.e. the fall from the shoulder height of 1 m (a), and the time history of GRF obtained numerically for the proposed forward fall model for $k_y = 50\,000$ N/m³ and $b_y = 0.6$ s/m, which corresponds to the GRF obtained experimentally for a representative fall from the shoulder height of 1 m (b) (DeGoede and Ashton-Miller, 2003)

5. Numerical simulation of the forward fall model

5.1. Parameters and relationships used in simulation

Experimental observations confirmed that with an increase in the walking speed v_0 , the human instinctively faster pulls his arms in the forward direction and the value of the mentioned parameter λ also increases. This is why in all our numerical simulations we use the time histories

of the angle $\theta_2(t)$ governed by Eq. (4.1) with different parameters θ_{2max} and λ , depending on the angle ϕ_{Arm} (the angle between the arm and the vertical axis of the Cartesian coordinate system at the moment of the impact to the ground) and the speed v_0 of the human walking just before the trip. Table 1 presents the dependence of the angle θ_{2max} on the angle ϕ_{Arm} , while Table 2 presents the dependence of parameters λ and T on the speed v_0 of the faller before the trip. The parameters of the proposed fall model (identified in Section 4) allow one to conduct broader analysis for different parameters and different fall scenarios.

Table 1. Values of the angle θ_{2max} corresponding to different values of the angle ϕ_{Arm}

ϕ_{Arm} [°]	0	5	10	15	20	25	30
θ_{2max} [°]	67.75	72.85	78.11	83.55	89.16	94.93	100.86

Table 2. Values of parameters T and λ corresponding to different values of walking speed v_0

v_0 [m/s]	0.5	1.0	1.5	2.0	2.5	3.0
T [s]	1.0	0.7	0.58	0.5	0.4	0.35
λ [1/s]	1.58	2.23	2.70	3.15	3.92	4.50

5.2. Time histories of ground reaction forces

Figure 6 shows the time history of GRF obtained for a fall from the full standing position ($\theta_1(0) = 90^\circ$), $v_0 = 1.5$ m/s and $\phi_{Arm} = 15^\circ$, which corresponds to the most common falls met in real situations. In this case, the maximum value of GRF reaches 2400 N, which corresponds to the distal radius fracture threshold (Kim and Ashton-Miller, 2009). Thus, we demonstrated that the taken typical and the most common falling conditions are enough to cause compressive fracture of the distal radius. The investigated falling process has been also observed by using the animation created in Mathematica (see Fig. 7).

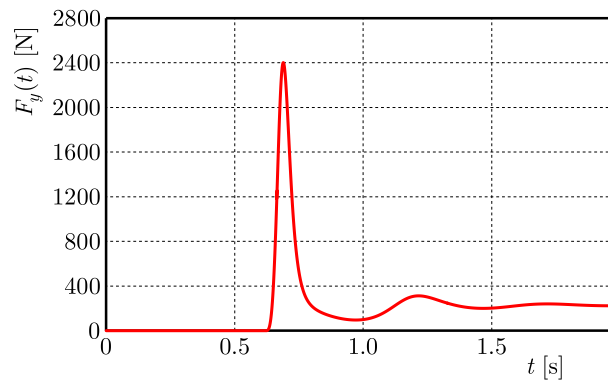


Fig. 6. Time histories of GRF from the standing position and $v_0 = 1.5$ m/s

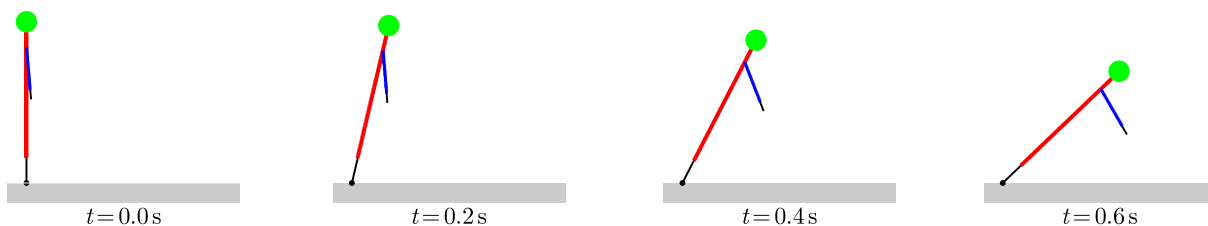


Fig. 7. Animation snapshots of the faller's body plotted in regular time intervals in different phases of the fall from the full standing position and walking speed $v_0 = 1.5$ m/s (obtained in Mathematica software)

Figure 8 illustrates times histories of the force $F_y(t)$ acting on a single hand for $v_0 = 1.5$ m/s and for different values of the angle ϕ_{Arm} . For all three presented cases, the plotted time histories of GRF are similar. However, it can be noticed that the maximum value of GRF increased from 2374 N for $\phi_{Arm} = 0$ to 2486 N for $\phi_{Arm} = 30^\circ$.

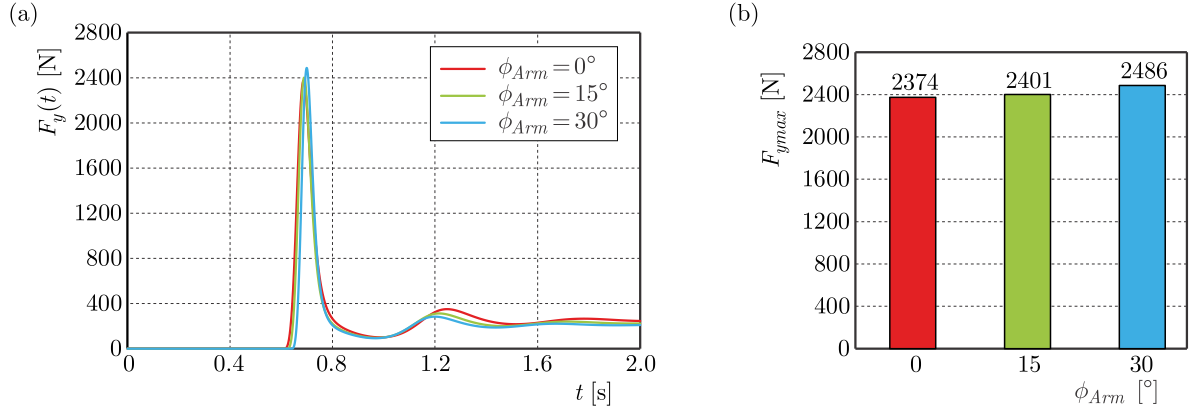


Fig. 8. GRFs for $v_0 = 1.5$ m/s and different values of angle ϕ_{Arm} : (a) time histories $F_y(t)$, (b) maximum values F_{ymax}

The results in Fig. 9 show the influence of different values of the velocity v_0 on time histories of the force $F_y(t)$. For larger values of the parameter v_0 , the duration of the fall is smaller while the maximum value of GRF is greater. The value of GRF increases from 2246 N for $v_0 = 0.5$ m/s to 2534 N for $v_0 = 2.0$ m/s. It means that for a smaller speed v_0 (i.e. $v_0 < 1.5$ m/s), the GRF is less than the distal radius fracture threshold, whereas for larger values of v_0 (i.e. $v_0 > 1.5$ m/s), this threshold is exceeded.

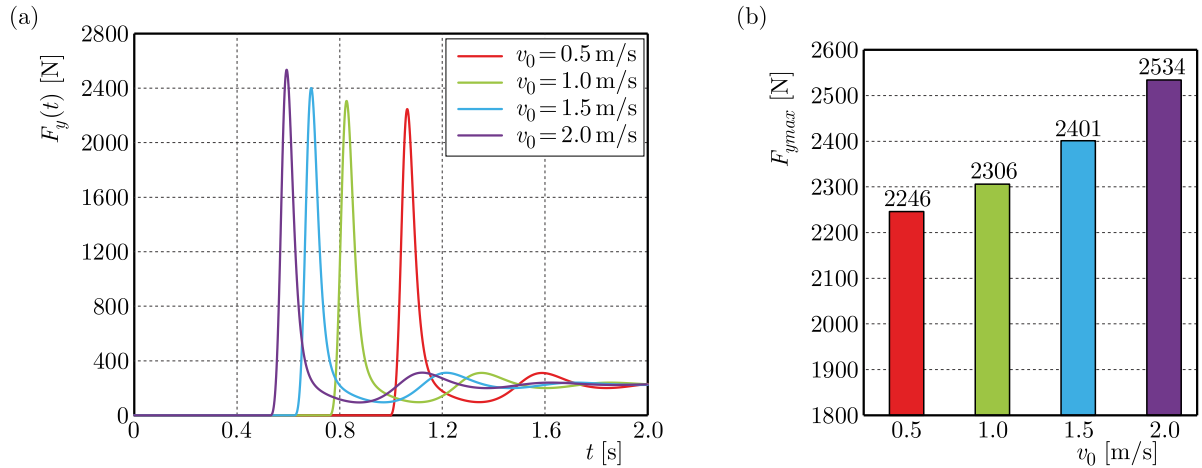


Fig. 9. GRFs for $\phi_{Arm} = 15^\circ$ and different values of the velocity v_0 : (a) time histories $F_y(t)$, (b) maximum values F_{ymax}

Figure 10 presents maximum values of GRF as a function of the velocity v_0 for different values of the angle ϕ_{Arm} . The maximum value of GRF increases with the increasing speed v_0 as well as the angle ϕ_{Arm} . For the lowest presented value of v_0 equal to 0.5 m/s, the maximum value of GRF increases from 2217 N for $\phi_{Arm} = 0$ to 2335 N for $\phi_{Arm} = 30^\circ$. For the largest value of v_0 equal to 3.0 m/s, the maximum value of GRF increases from 2898 N for $\phi_{Arm} = 0$ to 3000 N for $\phi_{Arm} = 30^\circ$. If one considers the case $\phi_{Arm} = 0$, the maximum value of GRF increases from 2217 N for $v_0 = 0.5$ m/s to 2898 N for $v_0 = 3.0$ m/s. In the case of $\phi_{Arm} = 30^\circ$, the maximum value of GRF increases from 2335 N for $v_0 = 0.5$ m/s to 3000 N for $v_0 = 3.0$ m/s.

For small values of v_0 ($v_0 \leq 1$ m/s), the maximum value of GRF is less than the distal radius fracture threshold, regardless of the angle ϕ_{Arm} . In the case of $v_0 = 1.5$ m/s, the maximum value of GRF is less than the mentioned fracture threshold when $0 \leq \phi_{Arm} \leq 10^\circ$, whereas GRF exceeds this threshold for $\phi_{Arm} > 15^\circ$. For $v_0 \geq 2.0$ m/s, the maximum of GRF exceeds the distal radius fracture threshold regardless of the angle ϕ_{Arm} . Concluding, for a small walking speed before the falling process, the value of the angle ϕ_{Arm} does not have a great influence. At a higher speed of human gait, the distal radius fracture threshold is usually exceeded, finally leading to injuries and/or fractures of the upper extremities. In the case of $v_0 = 1.5$ m/s, the correct configuration of the human body (the correct value of the angle ϕ_{Arm}) at the moment of the impact to the ground can reduce the maximum value of GRF and, as a result, can protect the faller from potential injuries or fractures of the upper extremity bones.

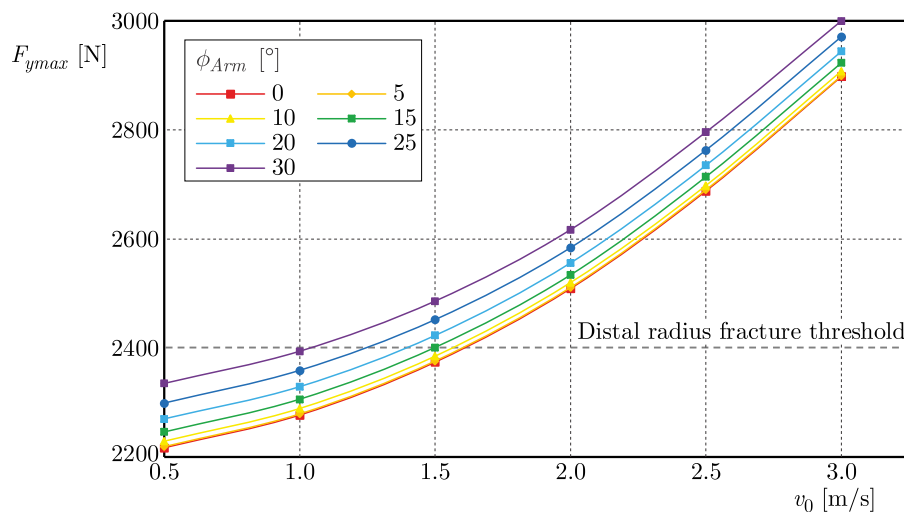


Fig. 10. Maximum values $F_{y\max}$ of GRF as a function of the velocity v_0 for different values of the angle ϕ_{Arm}

6. Finite element analysis of the radial bone

6.1. Geometry and material properties of the radial bone model

The DICOM data used in this paper come from cadavers of 35-years-old man with a height of 1.73 m and weight of 75 kg. These data have been obtained using a Siemens 64 Slice computed tomography (CT) Scanner in the Department of Forensic Medicine, Jagiellonian University Medical College, Cracow, Poland. The DICOM file of all upper extremity bones composed of the total number of 274 slices with the slice thickness equal to 1.5 mm, pixel size equal to 0.977 mm and resolution 512×512 was imported to Mimics. During the next steps, the radius was separated, the computer model of this bone was obtained, and the computational mesh of the radius was corrected to avoid further numerical errors. As a result, the mesh of the radius was reduced to 3444 surface elements, and the correctness of the constructed computational mesh was verified using a Fix Wizard function. Finally, a realistic 3D FE model of the radius consisting of 15751 FEs was obtained and used for the strength analysis in Ansys. We used the SOLID185 FE-shaped tetrahedron element. The assumed in this paper isotropy of the material is not ideal, but the CT data provided only scalar information, and the determination of principal material directions had to be inferred (Neuert *et al.*, 2013).

Material inhomogeneity of the radius was modelled in Mimics based on the CT images. First, we tested three different density-elasticity relationships describing human long bones to obtain the correct range of Young's modulus of the radius based on the CT images and the Hounsfield

Unit scale. Finally, mechanical properties of the considered radial bone were calculated based on the density-elasticity relationships proposed by Rho *et al.* (1995)

$$\rho = 1.067\text{HU} + 131 \quad E = 0.004\rho^{2.01} \quad (6.1)$$

where ρ expressed in $[\text{kg}/\text{m}^3]$ represents density of the bone, HU is the nondimensional Hounsfield Unit, E expressed in $[\text{MPa}]$ denotes Young's modulus, whereas ν is Poisson's ratio. The obtained range of Young's modulus of the radial bone is close to the range of the appropriate values for this bone presented in the literature. Young's moduli of the radius vary in the range 600-12000 MPa (see Fig. 11), whereas Poisson's ratio equals 0.3 for all FEs.

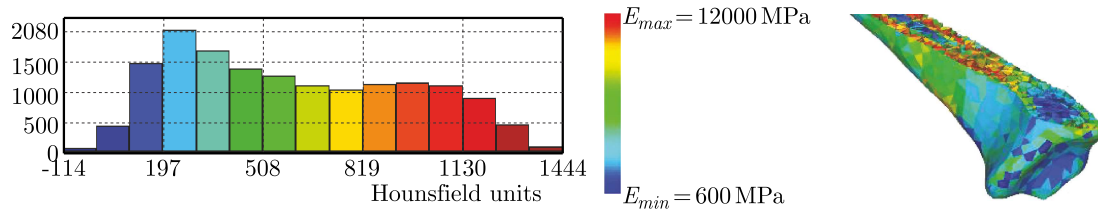


Fig. 11. Histogram and cross-sections of the radius showing quantitative distributions of FEs characterised by different Hounsfield Units and spatial distribution of inhomogeneous material properties

6.2. Load and boundary conditions

Numerical results presented in Fig. 6 were applied as the load conditions of the developed FE upper extremity model analysed in Ansys. These time histories of GRFs correspond to the GRF for the standing position and the walking speed $v_0 = 1.5 \text{ m/s}$. As far as the boundary conditions applied in the analysed numerical FE model of the radius were concerned, all six spatial DoFs in the proximal radius (region of the elbow joint) were fixed. The angle between the longitudinal axis of the radius and axis of the gravity field was equal to ϕ_{Arm} , while the GRF was applied in the region of the radial neck in the vertical direction (direction of the gravity field). In all the investigated cases, we considered the same time-varying load condition (see Fig. 6), but the analysis was conducted for different directions of the GRF acting on the radius (i.e. for different angles ϕ_{Arm}).

6.3. Stress and strain analyses

To predict bone fracture sites, we decided to measure the maximum von Mises stresses as the main criterion first. Moreover, we also measured maximal strains of the bones as another criterion leading to the additional information useful for a better understanding of the upper extremity behaviour under the applied load conditions, i.e. the assessment of the radius fracture site and failure load. The determination of the moment of time when the maximum stresses and strains were the highest enabled finding the fracture site and to investigate the state of the rest of the bones. The mentioned results are presented in Figs. 12 and 13 in the form of von Mises stress and strain distributions.

Values of both the maximal von Mises stress and bone strains significantly depend on the value of the angle ϕ_{Arm} . Namely, with an- increase in the angle ϕ_{Arm} , von Mises stresses and strains also increase. It should be noted that in the case of axial compression of the bone ($\phi_{Arm} = 0$), there are no bending torques and the bone itself is more resistant in such a configuration in comparison to the nonaxial compression. In the case of nonaxial GRF, bending torques are significant and, therefore, there are considerable values of both stresses and strains. For all the considered cases, the maximum values of stress and strain occur for $\phi_{Arm} = 30^\circ$.

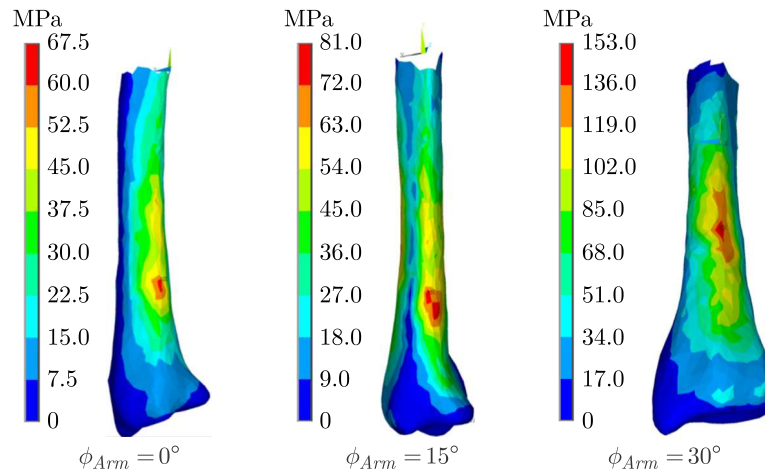


Fig. 12. Stress distributions in the radius for different angles ϕ_{Arm}

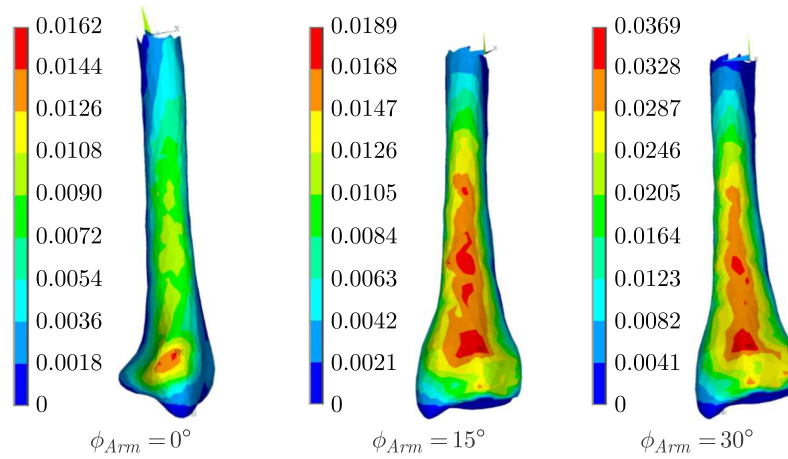


Fig. 13. Strain distributions in the radius for different angles ϕ_{Arm}

The results presented in Figs. 12 and 13 show also other regularity. Namely, the maximum stresses occur on the medial side (diaphysis) of the radius bone while the maximum strains occur in the distal region of this bone. As it is known, Colles' fracture is the most common type of injury related to the forward fall on the outstretched upper extremities. Therefore, the presented results indicate that the strain criterion can be more useful for estimating the radius fracture site (the maximum strains are concentrated in the distal radius, see Fig. 13).

Table 3. Maximum von Mises stress and maximum strains for three different angles ϕ_{Arm}

		Radius	Time [s]
$\phi_{Arm} = 0$	von Mises stress [MPa]	65.54	0.122
	Strain [-]	0.0154	0.126
$\phi_{Arm} = 15^\circ$	von Mises stress [MPa]	78.88	0.132
	Strain [-]	0.0186	0.132
$\phi_{Arm} = 30^\circ$	von Mises stress [MPa]	148.58	0.124
	Strain [-]	0.0363	0.124

In contrast to previous numerous papers dealing usually with resting conditions in our studies we carried out also a transient state analysis in Ansys. Values of maximum stresses and strains of the radius bone for different angles ϕ_{Arm} are presented in Table 3. The maximum values of

the von Mises stress and strains do not occur at the moment of the maximum peak of GRF but later, i.e. at the time about 0.12-0.13 s.

7. Conclusions

The forward fall model proposed in this paper enables one to estimate the vertical ground reaction forces acting on the hands in various scenarios of the human falling process. The obtained numerical simulations fit with other results presented in the literature (Kim and Ashton-Miller, 2009), both from a qualitative and quantitative point of view. Moreover, the simulations show that the parameters describing the human body and parameters modelling biomechanical properties between the palmar cartilages and the ground have an essential influence on the obtained results.

It should be emphasized that the developed model has some limitations. First of all, the movement of the shoulder grid with respect of the torso and stiffness/damping properties of the shoulder joint have not been implemented in our model. Moreover, the horizontal component of the ground reaction force has not been considered. Nevertheless, the mentioned limitations may be of interest for our future study. On the other hand, our further modifications and improvements of the proposed model can be oriented on the increase of the number of DoFs of the mechanical model describing the human body as well as taking into consideration the rotary stiffness and damping properties in each of the human joints.

The choice of a linear material law is justified by small displacements of the radius bone observed during compressive tests presented in the literature (Bosisio *et al.*, 2007). Although all bones have been modelled as a linear elastic isotropic material, in our opinion, the applied simplification should not significantly affect the ability of the proposed model to predict fracture sites and failure load of the radius bone under loads resulting from a forward fall. The variability of Poisson’s ratio has not been evaluated in our investigations.

The performed numerical investigations with the time history of the GRF that occur during the falling process in the forward direction on the outstretched arms are sufficient to determine potential fracture sites and the obtained results agree with numerical/experimental results presented in the literature (Edwards and Troy, 2012). In addition, the obtained results indicate that the angle ϕ_{Arm} and, consequently, the direction of load applied to the radius have a strong impact on the fracture strength of this bone. It means that falls from a standing position on the outstretched arms generate the value of GRF which can exceed the mean human distal radius fracture threshold. Moreover, we have also shown that the maximal strain criterion seems to be more useful for the estimation of the fracture site than the appropriate von Mises stress criterion. Although we obtained various numerical results, unfortunately we were unable to compare these results with own experimental studies from a quantitative point of view. However, the obtained numerical results show that our model provides a realistic estimation of radius bone strain, fracture strength and fracture side estimation under various loading scenarios simulating a forward fall.

Ethical Approval

This article does not contain any studies performed on animals. The presented experimental studies have been performed using one of the author of this paper (Paweł Biesiacki) without any other human participants.

Acknowledgments

The work has been partially supported by the National Science Centre of Poland under the grant OPUS 9 No. 2015/17/B/ST8/01700 for years 2016-2018.

References

1. BOSISIO M.R., TALMANT M., SKALLI W., LAUGIER P., MITTON D., 2007, Apparent Young's modulus of human radius using inverse finite-element method, *Journal of Biomechanics*, **40**, 2022-2028
2. BURKHART T.A., ANDREWS D.M., DUNNING C.E., 2013, Multivariate injury risk criteria and injury probability scores for fractures to the distal radius, *Journal of Biomechanics*, **46**, 973-978
3. CHIU J., ROBINOVITCH S.N., 1998, Prediction of upper extremity impact forces during falls on the outstretched hand, *Journal of Biomechanics*, **31**, 1169-1176
4. DAVIDSON P.L., CHALMERS D.J., STEPHENSON S.C., 2006, Prediction of distal radius fracture in children, using biomechanical impact model and case-control data on playground free falls, *Journal of Biomechanics*, **39**, 503-509
5. DEGOEDE K.M., ASHTON-MILLER J.A., 2002, Fall arrest strategy affects peak hand impact force in a forward fall, *Journal of Biomechanics*, **35**, 843-848
6. DEGOEDE K.M., ASHTON-MILLER J.A., 2003, Biomechanical simulations of forward fall arrests: effects of upper extremity arrest strategy, gender and aging-related declines in muscle strength, *Journal of Biomechanics*, **36**, 413-420
7. EDWARDS W.B., TROY K.L., 2012, Finite element prediction of surface strain and fracture strength at the distal radius, *Medical Engineering and Physics*, **34**, 290-298
8. FRYKMAN G., 1967, Fracture of the distal radius including sequelae shoulder-hand-finger syndrome, disturbance in the distal radio-ulnar joint and impairment of nerve function, *Acta Orthopaedica Scandinavica*, **108**, 1-153
9. GERRITSEN K.G.M., VAN DEN BOGERT A.J., NIGG B.M., 1995, Direct dynamics simulation of the impact phase in heel-toe running, *Journal of Biomechanics*, **28**, 661-668
10. GrabCAD, 2016, Open CAD library (<https://grabcad.com/library>)
11. HEIJNEN M.J.H., RIETDYK S., 2016, Falls in young adults: Perceived causes and environmental factors assessed with a daily online survey, *Human Movement Science*, **46**, 86-95
12. JOHNNELL O., KANNIS J.A., 2006, An estimate of the worldwide prevalence and disability associated with osteoporotic fractures, *Osteoporosis International*, **17**, 1726-1733
13. KIM K.-J., ASHTON-MILLER J.A., 2009, Segmental dynamics of forward fall arrests: A system identification approach, *Clinical Biomechanics*, **24**, 348-354
14. KROEMER K.H.E., KROEMER H.J., KROEMER-ELBERT K.E., 1997, *Engineering Physiology: Bases of Human Factors/Ergonomics*, Van Nostrand Reinhold, New York
15. NEUERT M.A.C., AUSTMAN R.L., DUNNING C.E., 2013, The comparison of density-elastic modulus equations for the distal ulna at multiple forearm positions: a finite element study, *Acta of Bioengineering and Biomechanics*, **15**, 37-43
16. NEVITT M.C., CUMMINGS S.R., 1993, Type of fall and risk of hip and wrist fractures: the study of osteoporotic fractures, *Journal of the American Geriatrics Society*, **41**, 11, 1226-1234
17. O'NEILL T.W., VARLOW J., SILMAN A.J., REEVE J., REID D.M., TODD C., WOOLF A.D., 1994, Age and sex influences on fall characteristics, *Annals of the Rheumatic Diseases*, **53**, 773-775
18. PALVANEN M., KANNUS P., PARKKARI J., PITKAJARVI T., PASANEN M., VUORI I., JARVINEN M., 2000, The injury mechanisms of osteoporotic upper extremity fractures among older adults: a controlled study of 287 consecutive patients and their 108 controls, *Osteoporosis International*, **11**, 822-831
19. RHO J.Y., HOBATHO M.C., ASHMAN R.B., 1995, Relations of mechanical properties to density and CT number in human bone, *Medical Engineering and Physics*, **17**, 347-355

20. ROBINOVITCH S.N., FELDMAN F., YANG Y., SCHONNOP R., LEUNG P.M., SARRAF T., SIMS-GOULD J., LOUGHIN M., 2013, Video capture of the circumstances of falls in elderly people residing in long-term care: an observational study, *The Lancet*, **381**, 47-54
21. SPADARO J.A., WERNER F.W., BRENNER R.A., FORTINO M.D., FAY L.A., EDWARDS W.T., 1994, Cortical and trabecular bone contribute strength to the osteopenic distal radius, *Journal of Orthopaedic Research*, **12**, 211-218
22. VELLAS B.J., WAYNE S.J., GARRY P.J., BAUMGARTNER R.N., 1998, A two-year longitudinal study of falls in 482 community-dwelling elderly adults, *The Journals of Gerontology, Series A, Biological Sciences and Medical Sciences*, **53**, 264-274

Manuscript received June 7, 2017; accepted for print September 21, 2017

EXTENSION OF THE HAMILTONIAN APPROACH WITH GENERAL INITIAL CONDITIONS

HELIO A. NAVARRO

Escola de Engenharia de São Carlos, Universidade de São Paulo, São Paulo, Brazil

e-mail: han@sc.usp.br

LIVIJA CVETICANIN

Faculty of Technical Sciences, University of Novi Sad, Novi Sad, Serbia

e-mail: cveticanin@uns.ac.rs

In this paper, the Hamiltonian approach is extended for solving vibrations of nonlinear conservative oscillators with general initial conditions. Based on the assumption that the derivative of Hamiltonian is zero, the frequency as a function of the amplitude of vibration and initial velocity is determined. A method for error estimation is developed and the accuracy of the approximate solution is treated. The procedure is based on the ratio between the average residual function and the total energy of the system. Two computational algorithms are described for determining the frequency and the average relative error. The extended Hamiltonian approach presented in this paper is applied for two types of examples: Duffing equation and a pure nonlinear conservative oscillator.

Keywords: nonlinear dynamics, Hamiltonian approach, error estimation

1. Introduction

In 2010, the method denominated “Hamiltonian approach” was introduced by He (2010) for solving strong nonlinear oscillatory systems. Since that time, a significant number of papers, where the suggested method is extended and applied, have been published. In the papers of Akbarzade and Kargar (2011a) and Akbarzade and Kargar (2011), the Hamiltonian method is applied for obtaining accurate analytical solutions to nonlinear oscillators. Using this method, He *et al.* (2010) and Bayat *et al.* (2014) obtained the solution for the Duffing-harmonic equation, and Cveticanin *et al.* (2010a, 2012) derived solutions for the generalized nonlinear oscillator with a fractional power. Belendez *et al.* (2011) pointed out that if a first-order trigonometric approximation function was used then there was an equivalence between the Hamiltonian approach and the first-order harmonic balance method. Yildirim *et al.* (2011b) and Belendez *et al.* (2011) specified the method for oscillators with rational and irrational elastic terms. Xu and He (2010) used the Hamiltonian approach to determine the limit cycle motion for strongly nonlinear oscillators. The method was applied for solving some practical problems, such as nonlinear oscillations of a punctual charge in the electric field of a charged ring (Yildirim *et al.*, 2011a), nonlinear vibrations of micro electro mechanical systems (Sadeghzadeh and Kabiri, 2016), nonlinear oscillations in an engineering structure (Akbarzade and Khan, 2012), among others. The Hamiltonian approach has also been applied to improve the accuracy of the solution for nonlinear oscillators, such as higher order approximations (Durmaz *et al.*, 2010; Yildirim *et al.*, 2011c), multiple coupled nonlinear oscillators (Durmaz *et al.*, 2012) and multiple-parameter ones (Khan *et al.*, 2011), among others.

In this study, the accuracy of the Hamiltonian approach is presented by comparing an analytically obtained solution with the numerical solution. Navarro and Cveticanin (2016) used the

method in oscillators with integer or non-integer terms. The authors proposed an error estimation method based on the ratio between the square root of the averaged residual function and the initial constant of energy.

The aim of this paper is to extend the Hamiltonian approach for solving a conservative nonlinear oscillator

$$\ddot{x} + f(x) = 0 \quad (1.1)$$

with the generalized initial conditions

$$x(0) = A \quad \dot{x}(0) = v \quad (1.2)$$

where $f(x)$ is a conservative force. The authors also propose an error procedure to measure the quantitative difference between approximate and numerical solutions. In the present work, the error treatment described by Navarro and Cveticanin (2016) is extended for general initial conditions.

This paper is divided in five Sections. After the Introduction, an extended Hamiltonian approach is considered, in Section 2. In that Section, Algorithm 1, called FREQUENCY, is developed. In Section 3, a method for error estimation is introduced. The error is estimated as the integral of the square of the residual function over the period of vibration. Special attention is given to the computation of relative errors. The error calculation is performed using Algorithm 2, called DELTA. In Section 4, a comparison between approximate and numerical solutions is shown. The suggested method of the Hamiltonian approach and error estimation are applied for a Duffing equation and for a pure nonlinear conservative oscillator with various orders of nonlinearity. Finally, conclusions of the numerical experiments are presented.

2. The approximate solution

Equation (1.1) describes a conservative oscillator with kinetic energy

$$K = \frac{\dot{x}^2}{2} \quad (2.1)$$

and potential energy, $F(x)$, is given by

$$\frac{dF(x)}{dx} = f(x) \quad (2.2)$$

The total mechanical energy of the oscillator corresponds to its Hamiltonian

$$H = \frac{1}{2}\dot{x}^2 + F(x) \quad (2.3)$$

For the conservative oscillator, the total mechanical energy keeps unchanged during motion and, consequently, the Hamiltonian of the system is constant, i.e., $H = H_0 = \text{const}$, and due to initial conditions (1.2)

$$H_0 = \frac{1}{2}v^2 + F(A) \quad (2.4)$$

For nonlinear oscillators, it is generally impossible to obtain a closed form analytical solution to (2.3). Consequently, to obtain an approximate solution, we assumed a trigonometric trial solution in the form

$$x(t) = C \cos(\omega t - \phi) \quad (2.5)$$

where ω is the unknown frequency of vibration, C is the amplitude of the oscillator, and ϕ is the phase of the oscillator. Using Eq. (2.5) and initial conditions (1.2), we find the maximum value of $x(t)$ and the phase given, respectively, by

$$C = \sqrt{A^2 + \left(\frac{v}{\omega}\right)^2} \quad (2.6)$$

and

$$\phi = \tan^{-1}\left(\frac{v}{\omega A}\right) \quad (2.7)$$

Substituting (2.5) into (2.3), we have

$$\tilde{H} = \frac{1}{2}C^2\omega^2 \sin^2(\omega t - \phi) + F(C \cos(\omega t - \phi)) \quad (2.8)$$

Usually, the frequency ω is determined from the derivative of Eq. (2.8)

$$\frac{\partial \tilde{H}}{\partial C} = 0 \quad (2.9)$$

Unfortunately, the obtained result is far from being accurate. To overcome this problem, He (2010) developed the so called Hamiltonian approach. He introduced a new function, \overline{H} that has a similar form of

$$\overline{H} = \int_{t_1}^{t_1+T} \tilde{H} dt \quad (2.10)$$

where T is the period of vibration and t_1 is an arbitrary initial integration time. After integration, it is $\overline{H} = \tilde{H}T$, i.e.

$$\tilde{H} = \frac{\partial \overline{H}}{\partial T} \quad (2.11)$$

According to (2.9) and $T = 2\pi/\omega$, it is

$$\frac{\partial}{\partial C} \left(\frac{\partial \overline{H}}{\partial T} \right) = \frac{\partial}{\partial C} \left(\frac{\partial \overline{H}}{\partial \omega^{-1}} \right) = \frac{\partial}{\partial C} \left(\frac{\partial \overline{H}}{\partial \omega} \right) = 0 \quad (2.12)$$

Solving algebraic equation (2.12), the approximate frequency of the conservative nonlinear oscillator is obtained in function of the amplitude C (see He, 2010). In most cases, by using relations (2.6) and (2.7), we can expressed an explicit relationship for approximate frequency in function of A , v , and other parameters of the system. Thus, for

$$\overline{H}(x, \dot{x}) = \int_{t_1}^{t_1+T} \left(\frac{1}{2} \dot{x}^2 + F(x) \right) dt \quad (2.13)$$

and trial function (2.5), we can express \overline{H} as

$$\overline{H}(C, \omega) = \int_{t_1}^{t_1+T} \left[\frac{1}{2} C^2 \omega^2 \sin^2(\omega t - \phi) + F(C \cos(\omega t - \phi)) \right] dt \quad (2.14)$$

Substituting in Eq. (2.14) the variable $\psi = \omega t$ and the period of vibration $T = 2\pi/\omega$, and defining $\psi^* = t_1/T$, we have

$$\overline{H}(C, \omega) = \int_{2\pi\psi^*}^{2\pi(1+\psi^*)} \left[\frac{1}{2}C^2\omega \sin^2(\psi - \phi) + \omega^{-1}F(C \cos(\psi - \phi)) \right] d\psi \quad (2.15)$$

where ψ^* is an arbitrary value that can be defined as $\psi^* = n/m$, with $n \in \mathbb{N}$ and $m \in \mathbb{N}^*$, to avoid numerical errors. The trivial choice for ψ^* is $\psi^* = 0$ ($t_1 = 0$) so that Eq. (2.15) becomes

$$\overline{H}(C, \omega) = \int_0^{2\pi} \left[\frac{1}{2}C^2\omega \sin^2(\psi - \phi) + \omega^{-1}F(C \cos(\psi - \phi)) \right] d\psi \quad (2.16)$$

Equations (2.12) and (2.16) can be used to determine a relationship for approximate frequency in function of C .

We can see that Eq. (2.5) reaches its maximum value when $\omega t - \phi = 2\pi n$, where $n = 0, \pm 1, \pm 2, \dots$. The maximum value for $n = 0$ occurs when $t = \phi/\omega$. Adopting the initial time $t_1 = \phi/\omega$ and substituting the variable $\tau = t - t_1$ into Eq. (2.14), we obtain

$$\overline{H}(C, \omega) = \int_0^T \left[\frac{1}{2}C^2\omega^2 \sin^2(\omega\tau) + F(C \cos(\omega\tau)) \right] d\tau \quad (2.17)$$

As before, substituting into Eq. (2.17) the variables $\psi = \omega\tau$ and $T = 2\pi/\omega$, we have

$$\overline{H}(C, \omega) = \int_0^{2\pi} \left[\frac{1}{2}C^2\omega \sin^2(\psi) + \omega^{-1}F(C \cos(\psi)) \right] d\psi \quad (2.18)$$

We can note that Eq. (2.18) is the common expression used for determining the frequency-amplitude relationship with particular initial conditions $x(0) = A$, $\dot{x}(0) = 0$ in works developed by several authors (e.g., Akbarzade and Kargar, 2011a,b; He, 2010; Akbarzade and Khan, 2012; Askari, 2013; Belendez *et al.*, 2011; Bayat *et al.*, 2014; Cveticanin *et al.*, 2010a, 2012; Durmaz *et al.*, 2010, 2012; He *et al.*, 2010; Khan *et al.*, 2011; Navarro and Cveticanin, 2016; Sadeghzadeh and Kabiri, 2016; Xu and He, 2010; Yildirim *et al.*, 2011a,b,c, 2012), i.e, when $C = A$ and $\phi = 0$. Comparing Eq. (2.16) with Eq. (2.18), it is observed that both can be used with Eq. (2.12) to determine a relationship for the approximate frequency in function of C and of other parameters of the system. Therefore, it is recommended to use Eq. (2.18) because of the following reasons: (a) it is simpler; (b) it is easy to determine the variation of the signal of the function potential F with the angle ψ , i.e., depending on the signal of F , the limits of integration can vary, for example, from 0 to π or 0 to $\pi/2$.

In some cases, an explicit relationship for the approximate frequency (that is a function of the initial amplitude A , the initial velocity v and parameters of the system) can be derived by Eq. (2.18) (frequency in function of C and parameters of the system) and Eq. (2.6). When it is not possible to derive an explicit relation, the values of the frequency, for specific values of A and v , can be obtained numerically by Algorithm 1, where cs are generic parameters of the system. After computation of the variables ω and C by Algorithm 1, the phase ϕ is determined by Eq. (2.7).

The approximate solution, Eq. (2.5), can also be represented by

$$x(t) = C \sin(\omega t + \phi_1) \quad (2.19)$$

where the phase is given by $\phi_1 = \pi/2 - \phi$, i.e,

$$\phi_1 = \tan^{-1}\left(\frac{\omega A}{v}\right) \quad (2.20)$$

Algorithm 1 Frequency

```

1: procedure FREQUENCY( $A, v, cs$ )
2:    $C_2 \leftarrow \sqrt{A^2 + v^2}$ 
3:   repeat
4:      $\omega_1 \leftarrow \omega(C_2, cs)$  ▷ Using Eqs. (2.12) and (2.18)
5:      $C_1 \leftarrow \sqrt{A^2 + (\frac{v}{\omega_1})^2}$  ▷ Using Eq. (2.6)
6:      $\omega_2 \leftarrow \omega(C_1, cs)$  ▷ Using Eqs. (2.12) and (2.18)
7:      $C_2 \leftarrow \sqrt{A^2 + (\frac{v}{\omega_2})^2}$  ▷ Using Eq. (2.6)
8:   until  $|\frac{\omega_2 - \omega_1}{\omega_2}| < \textit{Tolerance}$ 
9:   return  $\omega_2, C_2$ 

```

3. Error estimation

The Hamiltonian calculated for approximate solution (2.5) differs from the total mechanical energy H_0 . The difference between \tilde{H} and H_0 gives us the instantaneous residual

$$R(t) = \tilde{H} - H_0 = \frac{1}{2}C^2\omega^2 \sin^2(\omega t - \phi) + F(C \cos(\omega t - \phi)) - \left(\frac{1}{2}\dot{v}^2 + F(A)\right) \quad (3.1)$$

As the residual varies in time, to determine the average value, the error is estimated as the integral of the square of the residual function over the period of vibration. The following functional is introduced for error estimation

$$\Delta_2 = \frac{1}{T} \int_{t_1}^{t_1+T} R(t)^2 dt = \frac{1}{T} \int_{t_1}^{t_1+T} (\tilde{H} - H_0)^2 dt \quad (3.2)$$

Substituting (3.1) into (3.2), we have

$$\Delta_2 = \frac{1}{T} \int_{t_1}^{t_1+T} \left[\frac{1}{2}C^2\omega^2 \sin^2(\omega t - \phi) + F(C \cos(\omega t - \phi)) - \left(\frac{1}{2}\dot{v}^2 + F(A)\right) \right]^2 dt \quad (3.3)$$

using $t_1 = \phi/\omega$ and $\tau = t - t_1$

$$\Delta_2 = \frac{1}{T} \int_0^T \left[\frac{1}{2}C^2\omega^2 \sin^2(\omega\tau) + F(C \cos(\omega\tau)) - \left(\frac{1}{2}\dot{v}^2 + F(A)\right) \right]^2 d\tau \quad (3.4)$$

and for $\psi = \omega\tau$, $T = 2\pi/\omega$, and Eq.(2.6)

$$\Delta_2 = \frac{1}{2\pi} \int_0^{2\pi} \left[\frac{1}{2}(A^2\omega^2 + v^2) \sin^2(\psi) + F\left(\frac{1}{\omega} \sqrt{A^2\omega^2 + v^2} \cos(\psi)\right) - \left(\frac{1}{2}\dot{v}^2 + F(A)\right) \right]^2 d\psi \quad (3.5)$$

The obtained solution is a function of the initial amplitude, initial velocity and coefficients of the system: $\Delta_2 = \Delta_2(A, v, c_k)$. The relative error is calculated as the ratio between the square root of the average residual function and the initial constant energy function H_0

$$\Delta = \frac{\sqrt{\Delta_2}}{H_0} \quad (3.6)$$

The relative error is suitable to be presented in the percent form: $\Delta\% = (\sqrt{\Delta_2}/H_0)100\%$. When the explicit relation for the frequency is not available, the average relative error Δ can be determined numerically by Algorithm 2, where cs are generic parameters of the system. Algorithm 2, DELTA, calls Algorithm 1 and uses the integral given by Eq. (3.4).

Next, we apply the procedure proposed in Sections 2 and 3 in two examples: Duffing equation and a pure nonlinear conservative oscillator.

Algorithm 2 Delta

```

1: procedure DELTA( $A, v, cs$ )
2:    $\omega = f(A, v, cs)$  ▷ Analytically or using Algorithm 1
3:   Compute  $C$  ▷ Eq. (2.6)
4:   Create vector:  $\tau_i \leftarrow 0 : \Delta\tau : T$ 
5:    $y_i \leftarrow C \cos(\omega\tau_i)$ 
6:    $\dot{y}_i \leftarrow C\omega \sin(\omega\tau_i)$ 
7:   Compute  $H_0$  ▷ Eq. (2.4)
8:    $\tilde{H}_i \leftarrow \frac{1}{2}\dot{y}_i^2 + F(y_i)$  ▷ F is obtained using Eq. (2.2)
9:    $R_i \leftarrow \tilde{H}_i - H_0$ 
10:   $\Delta_2 \leftarrow \frac{1}{n} \sum_{i=1}^n R_i^2$  ▷ Eq. (3.4)
11:   $\Delta \leftarrow \frac{\sqrt{\Delta_2}}{H_0}$ 
12:  return  $\Delta$ 

```

4. Comparison between approximate and numerical solutions

Consider an oscillator represent by the Duffing equation

$$\ddot{x} + c_1^2 x + c_2^2 x^3 = 0 \quad (4.1)$$

with initial conditions (1.2). The origin of the name of this equation is shown by Cveticanin (2013). Translation of sections from Duffing's original book Duffing (1918) is found in the work of Kovacic and Brennan (2011). Considering Eq. (4.1), the potential energy is written as

$$F(x) = \frac{1}{2}c_1^2 x^2 + \frac{1}{4}c_2^2 x^4 \quad (4.2)$$

and the Hamiltonian of the oscillator is expressed by

$$H = \frac{1}{2}\dot{x}^2 + \frac{1}{2}c_1^2 x^2 + \frac{1}{4}c_2^2 x^4 \quad (4.3)$$

For an approximate solution (2.5), function (2.18) becomes

$$\begin{aligned} \overline{H}(C, \omega) &= 4 \int_0^{\pi/2} \left[\frac{1}{2}C^2\omega \sin^2(\psi) + \omega^{-1} \left(\frac{1}{2}c_1^2 C^2 \cos^2(\psi) + \frac{1}{4}c_2^2 C^4 \cos^4(\psi) \right) \right] d\psi \\ &= \frac{C^2\pi(8c_1^2 + 3C^2c_2^2 + 8\omega^2)}{16\omega} \end{aligned} \quad (4.4)$$

setting Eq. (2.12)

$$\frac{\partial}{\partial C} \left(\frac{\partial \overline{H}}{\partial \omega} \right) = 2\pi C - \frac{3\pi c_2^2 C^3}{8\omega^2} - \frac{\pi C(8c_1^2 + 3c_2^2 C^2 + 8\omega^2)}{8\omega^2} = 0 \quad (4.5)$$

we obtain an approximate frequency relationship with the maximum amplitude

$$\omega = \sqrt{c_1^2 + \frac{3}{4}c_2^2 C^2} \quad (4.6)$$

In this case, we can write an explicit relationship for the approximate frequency in function of the initial amplitude A , initial velocity v , and parameters c_1 and c_2 . Thus, using Eqs. (2.6) and (4.6), the approximate frequency is given by

$$\omega = \sqrt{\frac{c_1^2}{2} + \frac{3}{8}c_2^2 A^2} + \sqrt{\left(\frac{c_1^2}{2} + \frac{3}{8}c_2^2 A^2 \right)^2 + \frac{3}{4}c_2^2 v^2} \quad (4.7)$$

and according Eq. (2.7), the phase is

$$\phi = \tan^{-1} \left(\frac{v}{A \sqrt{\frac{c_1^2}{2} + \frac{3}{8}c_2^2 A^2} + \sqrt{\left(\frac{c_1^2}{2} + \frac{3}{8}c_2^2 A^2\right)^2 + \frac{3}{4}c_2^2 v^2}} \right) \quad (4.8)$$

If $v = 0$, the approximate frequency and phase become, respectively,

$$\omega = \sqrt{c_1^2 + \frac{3}{4}c_2^2 A^2} \quad \phi = 0 \quad (4.9)$$

and for $A = 0$

$$\omega = \frac{\sqrt{2}}{2} \sqrt{c_1^2 + \sqrt{c_1^4 + 3c_2^2 v^2}} \quad \phi = \frac{\pi}{2} \quad (4.10)$$

The approximate period is computed by

$$T = \frac{2\pi}{\omega} = \frac{2\pi}{\sqrt{\frac{c_1^2}{2} + \frac{3}{8}c_2^2 A^2} + \sqrt{\left(\frac{c_1^2}{2} + \frac{3}{8}c_2^2 A^2\right)^2 + \frac{3}{4}c_2^2 v^2}} \quad (4.11)$$

Now, we compare approximate period (4.11) with the numerically obtained one. The ‘exact’ numerical period of vibration T_n is calculated using the numerical solution of Eq. (4.1) with initial conditions (1.2) by the Runge-Kutta method. The vibration period T_n is computed for the time in the interval $0 \leq t \leq T$ with a time-step of Δt , where T is the approximate period, see Eq. (4.11). The relative error in percentage is given by

$$\Delta_T = \left| \frac{T_n - T}{T_n} \right| \cdot 100\% \quad (4.12)$$

Figure 1 illustrates the variation of the relative error in percentage versus the initial amplitude A for three values of the initial velocity, i.e., $v = 0$ (solid line), $v = 10$ (dashed line) and $v = 100$ (dotted line). In Fig. 1, the parameters of the system are $c_1^2 = c_2^2 = 1$ and the amplitude A varies in the interval $0 \leq A \leq 50$ with an increment $\Delta A = 0.5$. The time-step is $\Delta t = 10^{-5}T$. We can note that for $v = 0$ the relative error has a monotonic growth, while for $v = 10$ and $v = 100$ the relative error starts with a higher value and then oscillates converging to $A = 50$.

Table 1 shows the relative errors in percentage, Eq. (4.12), for the parameters $c_1^2 = c_2^2 = 1$ and for several values of initial conditions, amplitude A and velocity v . In Table 1 the time-step used is $\Delta t = 10^{-7}T$. The numbers in Table 1 are rounded to three decimal places. The same behavior obtained in Figure 1 is shown in Table 1. We can also see a monotonic growth for $v = 0$. For values of $v > 0$, the relative error starts in higher values for $A = 0$ and then, increasing A , the relative error decreases up to a minimum value. After that, the relative error starts to increase converging to 2.172% when $A \rightarrow \infty$. We can also observe that for high values of v and $A = 0$, the error is larger and this error converges to 8.264% ($A = 0, v \rightarrow \infty$).

Now, an estimative for the average error between the approximate and exact solutions is computed. For the initial conditions $x(0) = A$ and $\dot{x}(0) = v$, the Hamiltonian of the system is

$$H_0 = \frac{1}{2}v^2 + \frac{1}{2}c_1^2 A^2 + \frac{1}{4}c_2^2 A^4 \quad (4.13)$$

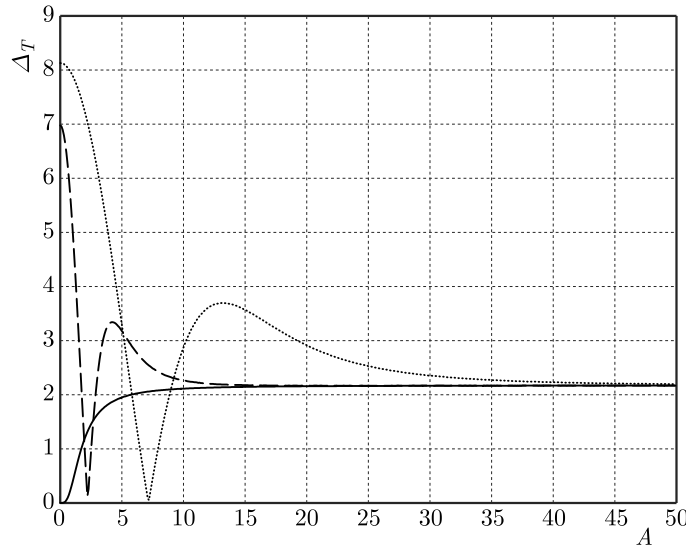


Fig. 1. Relative errors Δ_T , Eq. (4.12), versus the amplitude A for $v = 0$ (solid line), $v = 10$ (dashed line) and $v = 100$ (dotted line)

Table 1. Relative errors Δ_T , Eq. (4.12), for $c_1^2 = c_2^2 = 1$ and various initial conditions A, v

$v \backslash A$	0	1	5	10	50	100	500	1000
0	—	0.385	1.949	2.113	2.170	2.172	2.172	2.172
1	1.354	1.010	1.972	2.115	2.170	2.172	2.172	2.172
5	5.861	2.807	2.431	2.152	2.170	2.172	2.172	2.172
10	6.977	5.070	3.179	2.263	2.170	2.172	2.172	2.172
50	7.993	7.542	0.106	3.615	2.176	2.172	2.172	2.172
100	8.127	7.898	3.294	2.873	2.196	2.173	2.172	2.172
500	8.237	8.190	7.108	4.180	2.707	2.212	2.172	2.172
1000	8.250	8.227	7.675	6.067	3.494	2.327	2.172	2.172

Substituting approximate solution (2.5) into (4.3) and using relations (3.2), (4.13), the error function, according to (3.5), is

$$\Delta_2 = \frac{2}{\pi} \int_0^{\pi/2} \left[\frac{1}{2} C^2 \omega^2 \sin^2(\psi) + \frac{1}{2} c_1^2 C^2 \cos^2(\psi) + \frac{1}{4} c_2^2 C^4 \cos^4(\psi) - \left(\frac{1}{2} v^2 + \frac{1}{2} c_1^2 A^2 + \frac{1}{4} c_2^2 A^4 \right) \right]^2 d\psi \quad (4.14)$$

Using Eqs. (2.6) and (4.7) and after some calculation, Δ_2 is written as

$$\begin{aligned} \Delta_2 = & \frac{A^4 c_1^4}{6} + \frac{23 c_1^8}{1296 c_2^4} + \frac{A^2 c_1^6}{12 c_2^2} + \frac{1}{8} A^6 c_1^2 c_2^2 + \frac{135 A^8 c_2^4}{4096} + \frac{85}{576} A^2 c_1^2 v^2 + \frac{23 c_1^4 v^2}{432 c_2^2} \\ & + \frac{107}{768} A^4 c_2^2 v^2 + \frac{23 v^4}{1152} - \frac{263 A^4 c_1^2 R}{9216} - \frac{23 c_1^6 R}{5184 c_2^4} - \frac{121 A^2 c_1^4 R}{6912 c_2^2} - \frac{121 A^6 c_2^2 R}{12288} \\ & - \frac{49 A^2 v^2 R}{4608} - \frac{23 c_1^2 v^2 R}{3456 c_2^2} \end{aligned} \quad (4.15)$$

where

$$R = \sqrt{16 c_1^4 + 24 A^2 c_1^2 c_2^2 + 9 A^4 c_2^4 + 48 c_2^2 v^2} \quad (4.16)$$

and according to Eqs. (3.6) and (4.13), the error Δ is given by

$$\Delta = \frac{\sqrt{\Delta_2}}{\frac{1}{2}v^2 + \frac{1}{2}c_1^2 A^2 + \frac{1}{4}c_2^2 A^4} \quad (4.17)$$

As before, Fig. 2 illustrates the relative errors Δ , Eq. (4.17) versus the initial amplitude $0 \leq A \leq 50$ ($\Delta A = 0.1$) for three values of the initial velocity, i.e., $v = 0$ (solid line), $v = 10$ (dashed line) and $v = 100$ (dotted line), with $c_1^2 = c_2^2 = 1$. The same pattern shown in Fig. 1 is also obtained for the average relative error Δ .

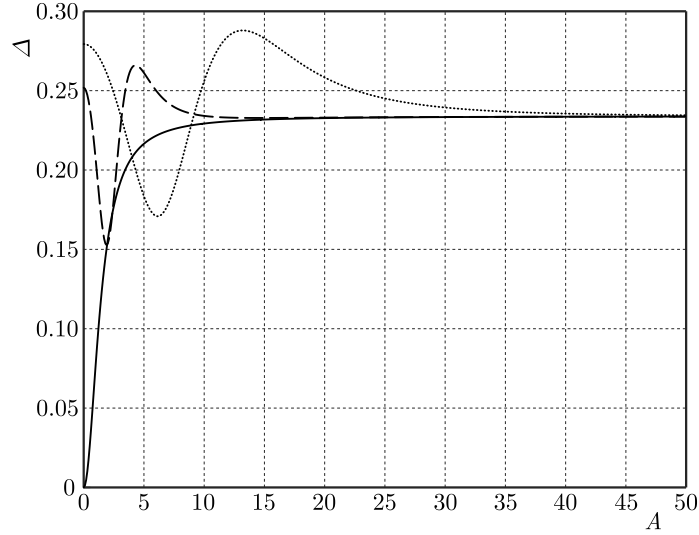


Fig. 2. Relative errors Δ , Eq. (4.17), versus the amplitude A , for $v = 0$ (solid line), $v = 10$ (dashed line) and $v = 100$ (dotted line)

4.1. Pure nonlinear conservative oscillator

Considering the following equation for a pure nonlinear conservative oscillator

$$\ddot{x} + c_1^2 x |x|^{\alpha-1} = 0 \quad (4.18)$$

where α is the order of nonlinearity, integer or non-integer. There are several studies of oscillators where the nonlinearity has an order which is any rational number (integer or non-integer) (see, for example, Cveticanin *et al.*, 2010a,b, 2012; Heriřanu and Marinca, 2010; Kovacic *et al.*, 2010; Cveticanin, 2014; Cveticanin and Pogany, 2012). According to (2.5), the approximate solution is

$$x(t) = C \cos(\omega t - \phi) \quad (4.19)$$

and using Eqs. (2.12) and (2.18), the frequency is

$$\omega^2 = c_1^2 |C|^{\alpha-1} K_\alpha \quad (4.20)$$

with

$$K_\alpha = \frac{2}{\pi} B\left(\frac{1}{2}, \frac{\alpha+2}{2}\right) \quad (4.21)$$

where B is the Euler beta function. If $v = 0$, the approximate frequency and phase become, respectively,

$$\omega = \sqrt{c_1^2 |A|^{\alpha-1} K_\alpha} \quad \phi = 0 \quad (4.22)$$

for $A = 0$

$$\omega = \left(c_1^2 |v|^{\alpha-1} K_\alpha\right)^{\frac{1}{\alpha+1}} \quad \phi = \frac{\pi}{2} \quad (4.23)$$

and for general values of A and v , the frequency is calculated using Eq. (4.20) and Algorithm 1. Then, the amplitude C and phase ϕ are determined by Eqs. (2.6) and (2.7), respectively. The approximate period is given by $T = 2\pi/\omega$, where the frequency is determined by Algorithm 1. The approximate period T is compared with T_n obtained numerically solving Eq. (4.18) with initial conditions (1.2) by the Runge-Kutta method in the time interval $0 \leq t \leq T$ with a time-step $\Delta t = 10^{-7}T$. The relative error Δ_T is computed by Eq.(4.12). The average relative error Δ is calculated by Algorithm 2. In Table 2, the value of relative errors Δ_T and Δ for various values of α and for $c_1^2 = 1$ are shown. When the initial velocity is zero, the errors Δ_T and Δ are independent of the initial amplitude A and of the constant c_1^2 . Table 2 shows that for $\alpha < 1$ the error decreases with an increase in α , and for $\alpha > 1$ occurs the reverse, i.e., the error increases with α . For the linear case, $\alpha = 1$, the approximate solution corresponds to the exact solution, $x(t) = C \cos(|c_1|t - \phi)$ and, apart from this value ($\alpha = 0$ or $\alpha = 3$), the relative errors increase due to nonlinear effects. Navarro and Cveticanin (2016) studied the solutions when $v = 0$ and showed that for high values of α the relative errors diverge. We can also note that $\Delta_T(A, 0) = \Delta_T(A \rightarrow \infty, v)$ and $\Delta(A, 0) = \Delta(A \rightarrow \infty, v)$ for a specific value of α . These equalities can be observed in Table 2 for $v = 10$.

Table 2. Values of relative errors $\Delta_T(A, v)$ and $\Delta(A, v)$ for various values of the power α

α	0	1/2	1	3/2	2	5/2	3
$\Delta_T(A, 0)$	1.5649	0.3103	0	0.2117	0.7203	1.3987	2.1723
$\Delta(A, 0)$	0.11096	0.05957	0	0.06079	0.12047	0.17823	0.23385
$\Delta_T(0, 10)$	23.370	2.7389	0	1.1411	3.3583	5.8275	8.2642
$\Delta(0, 10)$	0.52475	0.17855	0	0.11022	0.18556	0.24056	0.28260
$\Delta_T(1, 10)$	22.164	2.5547	0	0.9867	2.7627	4.5399	6.0783
$\Delta(1, 10)$	0.49605	0.16669	0	0.09817	0.16116	0.20409	0.2379
$\Delta_T(5, 10)$	17.866	1.3809	0	0.1548	1.1174	2.4310	3.4975
$\Delta(5, 10)$	0.39674	0.09721	0	0.05788	0.13734	0.21773	0.28097
$\Delta_T(10, 10)$	13.516	0.3133	0	0.3714	1.0361	1.6631	2.3273
$\Delta(10, 10)$	0.30175	0.05655	0	0.07108	0.13361	0.18736	0.23881
$\Delta_T(20, 10)$	7.4054	0.4490	0	0.2667	0.7731	1.4251	2.1824
$\Delta(20, 10)$	0.18253	0.06318	0	0.06402	0.12251	0.17910	0.23417
$\Delta_T(50, 10)$	0.1732	0.5300	0	0.2181	0.7238	1.3998	2.1725
$\Delta(50, 10)$	0.10583	0.06565	0	0.06115	0.12060	0.17826	0.23386
$\Delta_T(A \rightarrow \infty, 10)$	1.5649	0.3103	0	0.2117	0.7203	1.3987	2.1723
$\Delta(A \rightarrow \infty, 10)$	0.11096	0.05957	0	0.06079	0.12047	0.17823	0.23385

Figures 3 and 4 show, respectively, the period relative errors Δ_T and the average relative errors Δ (Algorithm 2) versus the initial amplitude $0 \leq A \leq 50$ ($\Delta A = 0.1$) for the initial velocity $v = 10$, parameter $c_1^2 = 1$, and three values of the power, i.e., $\alpha = 1/2$ (solid line), $\alpha = 3/2$ (dashed line) and $\alpha = 3$ (dotted line). We can see that in both figures the errors start in a higher value and then oscillate converging when $A = 50$. The minimum values of the relative errors occur for lower values of A with the increase of the power α .

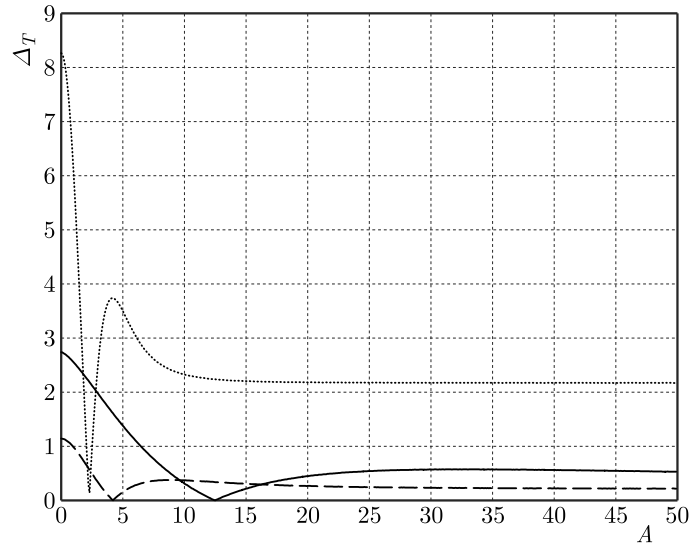


Fig. 3. Relative errors Δ_T , Eq. (4.12) versus the amplitude A for $v = 10$, and $\alpha = 1/2$ (solid line), $\alpha = 3/2$ (dashed line) and $\alpha = 3$ (dotted line)

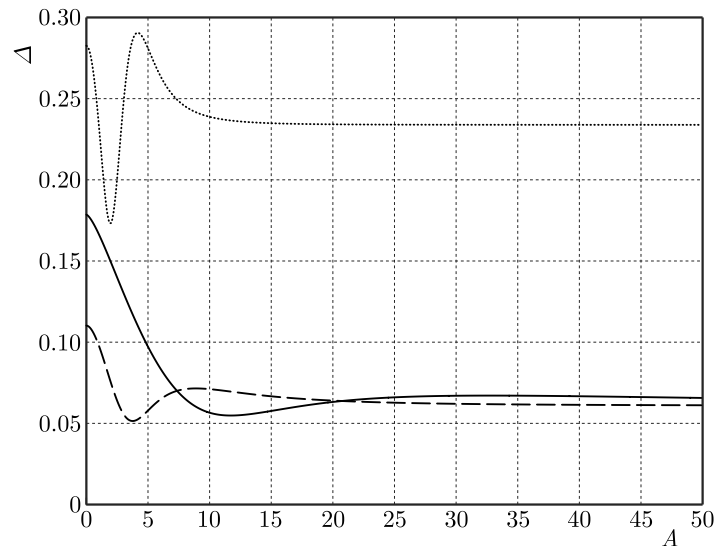


Fig. 4. Relative errors Δ (Algorithm 2) versus the amplitude A for $v = 10$, and $\alpha = 1/2$ (solid line), $\alpha = 3/2$ (dashed line) and $\alpha = 3$ (dotted line)

5. Conclusions

The Hamiltonian approach is extended for nonlinear conservative oscillators with general initial conditions. A method is proposed for obtaining a relationship for the frequency as a function of the initial amplitude, initial velocity and parameters of the system. An error estimation procedure is investigated. Computational algorithms are proposed as an alternative procedure to determine the frequency, amplitude, phase and relative errors in the adopted approximate solution. Considering the obtained results, we have concluded the following:

- In the case of oscillators governed by the Duffing equation, the relative error for the vibration period Δ_T converges to 2.172% for $(A \rightarrow \infty, v)$ and to 8.264% for $(A = 0, v \rightarrow \infty)$. The average relative error Δ converges to 0.233854 for $(A \rightarrow \infty, v)$ and to 0.282597 for $(A = 0, v \rightarrow \infty)$.
- In pure nonlinear conservative oscillators, the relative errors for the vibration period Δ_T , and for the average solution Δ decrease with the increasing α up to $\alpha = 1$, where the

errors are zero. Beyond this point $\alpha > 1$, the relative errors start to increase. According to Table 2, when the velocity $v = 0$, there is a limit or maximum values for the errors, i.e., $\Delta_T(A, 0) = \Delta_T(A \rightarrow \infty, v)$ and $\Delta(A, 0) = \Delta(A \rightarrow \infty, v)$. The minimum values of the relative errors occur for lower values of A with an increase in the power α .

Acknowledgments

Helio A. Navarro thanks “Conselho Nacional de Desenvolvimento Científico e Tecnológico (CNPq – Brazil)” for financial support in the development of this work (project No. 303476/2015-0).

The involvement of Livija Cveticanin was financially supported by the Ministry of Science, Republic of Serbia (Projects No. ON174028 and III41007).

References

1. AKBARZADE M., KARGAR A., 2011a, Accurate analytical solutions to nonlinear oscillators by means of the Hamiltonian approach, *Mathematical Methods in the Applied Sciences*, **34**, 17, 2089-2094
2. AKBARZADE M., KARGAR A., 2011b, Application of the Hamiltonian approach to nonlinear vibrating equations, *Mathematical and Computer Modelling*, **54**, 910, 2504-2514
3. AKBARZADE M., KHAN Y., 2012, Dynamic model of large amplitude non-linear oscillations arising in the structural engineering: analytical solutions, *Mathematical and Computer Modelling*, **55**, 34, 480-489
4. ASKARI H., NIA Z.S., YILDIRIM A., KALAMI YAZDI M., 2013, Application of higher order Hamiltonian approach to nonlinear vibrating systems, *Journal of Theoretical and Applied Mechanics*, **51**, 2, 287-296
5. BAYAT M., PAKAR I., CVETICANIN L., 2014, Nonlinear free vibration of systems with inertia and static type cubic nonlinearities: an analytical approach, *Mechanism and Machine Theory*, **77**, 50-58
6. BELENDEZ A., ARRIBAS E., FRANCES J., PASCUAL I., 2011, Notes on “Application of the Hamiltonian approach to nonlinear oscillators with rational and irrational elastic terms”, *Mathematical and Computer Modelling*, **54**, 11-12, 3204-3209
7. CVETICANIN L., 2013, Ninety year of Duffings equation, *Theoretical and Applied Mechanics*, **40**, 1, 49-63
8. CVETICANIN L., 2014, On the truly nonlinear oscillator with positive and negative damping, *Applied Mathematics and Computation*, **243**, 433-445
9. CVETICANIN L., KALAMI-YAZDI M., ASKARI H., 2012, Analytical approximations to the solutions for a generalized oscillator with strong nonlinear terms, *Journal of Engineering Mathematics*, **77**, 1, 211-223
10. CVETICANIN L., KALAMI-YAZDI M., SAADATNIA Z., ASKARI H., 2010a, Application of Hamiltonian approach to the generalized nonlinear oscillator with fractional power, *International Journal of Nonlinear Sciences and Numerical Simulation*, **11**, 12, 997-1002
11. CVETICANIN L., KOVACIC I., RAKARIC Z., 2010b, Asymptotic methods for vibrations of the pure non-integer order oscillator, *Computers and Mathematics with Applications*, **60**, 9, 2616-2628
12. CVETICANIN L., POGANY T., 2012, Oscillator with a sum of noninteger-order nonlinearities, *Journal of Applied Mathematics*, **2012**, 649050, 1-20
13. DUFFING G., 1918, *Erzwungene Schwingungen bei veranderlicher Eigenfrequenz und ihre technische Bedeutung*, Druck und Verlag von Fridr. Vieweg & Sohn, Braunschweig, Germany
14. DURMAZ S., ALTAY DEMIRBAG S., KAYA M.O., 2010, High order Hamiltonian approach to nonlinear oscillators, *International Journal of Nonlinear Sciences and Numerical Simulation*, **11**, 8, 565-570

15. DURMAZ S., ALTAY DEMIRBAG S., KAYA M.O., 2012, Hamiltonian approach to multiple coupled nonlinear oscillators, *Acta Physica Polonica A*, **121**, 1, 47-49
16. HE J.H., 2010, Hamiltonian approach to nonlinear oscillators, *Physics Letters, Section A: General, Atomic and Solid State Physics*, **374**, 23, 2312-2314
17. HE J.H., ZHONG T., TANG L., 2010, Hamiltonian approach to Duffing-harmonic equation, *International Journal of Nonlinear Sciences and Numerical Simulation*, **11**, 43-46
18. HERIŞANU N., MARINCA V., 2010, Accurate analytical solutions to oscillators with discontinuities and fractional-power restoring force by means of the optimal homotopy asymptotic method, *Computers and Mathematics with Applications*, **60**, 6, 1607-1615
19. KHAN N.A., JAMIL M., ARA A., 2011, Multiple-parameter Hamiltonian approach for higher accurate approximations of a nonlinear oscillator with discontinuity, *International Journal of Differential Equations*, **2011**, 649748
20. KOVACIC I., BRENNAM M.J., eds., 2011, *The Duffing Equation: Nonlinear Oscillators and their Behaviour*, John Wiley & Sons, United Kingdom
21. KOVACIC I., RAKARIC Z., CVETICANIN L., 2010, A non-simultaneous variational approach for the oscillators with fractional-order power nonlinearities, *Applied Mathematics and Computation*, **217**, 8, 3944-3954
22. NAVARRO H.A., CVETICANIN L., 2016, Amplitude-frequency relationship obtained using Hamiltonian approach for oscillators with sum of non-integer order nonlinearities, *Applied Mathematics and Computation*, **291**, 162-171
23. SADEGHZADEH S., KABIRI A., 2016, Application of higher order Hamiltonian approach to the nonlinear vibration of micro electro mechanical systems, *Latin American Journal of Solids and Structures*, **13**, 3, 478-497
24. XU L., HE J.H., 2010, Determination of limit cycle by Hamiltonian approach for strongly nonlinear oscillators, *International Journal of Nonlinear Sciences and Numerical Simulation*, **11**, 12, 1097-1101
25. YILDIRIM A., ASKARI H., KALAMI YAZDI M., KHAN Y., 2012, A relationship between three analytical approaches to nonlinear problems, *Applied Mathematics Letters*, **25**, 11, 1729-1733
26. YILDIRIM A., ASKARI H., SAADATNIA Z., KALAMI YAZDI M., KHAN Y., 2011a, Analysis of nonlinear oscillations of a punctual charge in the electric field of a charged ring via a Hamiltonian approach and the energy balance method, *Computers and Mathematics with Applications*, **62**, 1, 486-490
27. YILDIRIM A., SAADATNIA Z., ASKARI H., 2011, Application of the Hamiltonian approach to nonlinear oscillators with rational and irrational elastic terms, *Mathematical and Computer Modelling*, **54**, 12, 697-703
28. YILDIRIM A., SAADATNIA Z., ASKARI H., KHAN Y., KALAMI YAZDI M., 2011, Higher order approximate periodic solutions for nonlinear oscillators with the Hamiltonian approach, *Applied Mathematics Letters*, **24**, 12, 2042-2051

ON BIFURCATION LOAD OF A THREE-MEMBER SLENDER SYSTEM WITH AN INTERNAL CRACK SUBJECTED TO EULER'S LOAD

SEBASTIAN UZNY, KRZYSZTOF SOKÓŁ

Częstochowa University of Technology, Institute of Mechanics and Machine Design Foundations, Częstochowa, Poland

e-mail: uzny@imipkm.pcz.pl; sokol@imipkm.pcz.pl

The results of numerical simulations presented in this paper are concerned with instability of a three member slender system subjected to Euler load. The investigated column is built up as a flat frame composed of three rods. In the internal one, the defect is present in form of a crack. The boundary problem has been formulated on the basis of a static criterion of instability. The boundary conditions associated with different types of supports are obtained by proper selection of parameters of the generalized load. On the basis of these results, the magnitude of bifurcation load can be determined.

Keywords: column, divergence, conservative load, crack

1. Introduction

Numerical investigations on slender complex systems composed of beam elements with different rigidities have been presented in the papers (Godley and Chilver, 1970; Lueschen *et al.*, 1996; Tomski and Uzny, 2008, Tomski *et al.*; 2014; Uzny, 2011a,b). In those papers, different types of conservative and non conservative loads have been considered. The most common type of a conservative load is the Euler load. The loading force has a constant line of action regardless of the deflection of the system. All known types of conservative loads can be expressed by means of the generalized load (Bochenek and Życzkowski, 2004; Gajewski and Życzkowski, 1970). It is induced by simultaneous actions of longitudinal and transversal forces and bending moments. The generalized load is a theoretical loading, because authors of the papers in which it is used do not present the design of loading heads. When the system is composed of elements with different bending and compression rigidities, the rectilinear and curvilinear forms of static equilibrium are present (Tomski and Uzny, 2008). The compressed system keeps the rectilinear form of static equilibrium up to the bifurcation load magnitude. An increase of the external load causes a change of the equilibrium form from the rectilinear into a curvilinear one. The maximum magnitude of the compressive force is called the critical one. If the constant total bending stiffness of the investigated system is used the change in relation of the bending stiffness between rods, it has no influence on critical load magnitude (Tomski *et al.*, 2007). Only the change of bifurcation load can be observed because of asymmetry of the bending stiffness of the rods. The magnitude of the bifurcation load can be controlled by means of the following parameters: prestressing, additional elements responsible for transversal displacements, loading heads configuration – Tomski load (Tomski and Uzny, 2008; Uzny, 2011a). The change of the bifurcation load magnitude in relation to the rigidity of the system elements has influence on the occurrence of the local instability phenomenon (Tomski and Uzny, 2008; Uzny, 2011a,b). The rod with the lower rigidity is responsible for local instability (it deflects from the rectilinear form of static equilibrium and causes deflection of the whole system). In some cases, the rage of external load which corresponds to the curvilinear form of static equilibrium (from the bifurcation load

magnitude up to the critical one) can be greater than the range of external load in the rectilinear form. The phenomenon of local instability of the discussed systems has a completely different nature than in thin walled structures.

In this paper, the instability of a complex system with consideration of the crack presence in the rod with the lowest rigidity is presented. Cracks in beam elements or columns have been investigated by many scientists (Anifantis and Dimarogonas, 1983; Chati *et al.*, 1997; Kim and Kim, 2000; Krawczuk, 1992; Kukla, 2009; Masoud *et al.*, 1999; Ostachowicz and Krawczuk, 1991; Sokół, 2014). In the literature, different methods of crack modeling can be found. The crack can be modeled as a rotational spring with properly chosen stiffness (Anifantis and Dimarogonas, 1983; Chati *et al.*, 1997; Hjelmstad and Shin, 1996; Kim and Kim, 2000; Krawczuk, 1992; Masoud *et al.*, 1999; Narkis, 1994; Ostachowicz and Krawczuk, 1991; Rizos *et al.*, 1990; Shen and Taylor, 1991). In such a case, the system is composed of two beams or rods connected by a rotational spring in the point of crack location. The stiffness of the spring depends on relation of the crack depth to transverse dimensions and is being calculated with consideration of the fracture mechanics principles (Ostachowicz and Krawczuk, 1999). Identification of characteristic parameters of cracks can be done on the basis of the vibration frequency, shape modes (Tomski *et al.*, 2014) and the amplitude of vibration (Rizos *et al.*, 1990).

A different method of crack modeling is presented in Chandros *et al.* (1998) according to which Crack Disturbance Functions are used. This method is more advanced because stress, strain and displacement are modified in the whole area of the damaged element (not only locally in the point of crack presence). The mentioned crack model is more accurate but at the same time more complex and time consuming. However, when the crack is being modelled by means of a rotational spring, good accuracy of the simulation and experimental results can be found (Chandros *et al.*, 1998). On the basis of the analysis of the natural vibration frequency curves presented in (Chandros *et al.*, 1998), it can be concluded that the difference between the two models (continuous cracked beam model and lumped crack flexibility model) is getting greater with an increase of the crack size. When small cracks are considered (crack smaller than half of the cross section), those differences are insignificant. Taking into account a comparison of experimental data with numerical simulations shown in (Chandros *et al.*, 1998), there is a good foundation to use rotational springs in the modelling process of a small crack.

Zamorska *et al.* (2015) proposed analytical simulations done with the Green function of a cracked beam with a variable cross-sectional area and numerical results in CATIA software. Zhang *et al.* (2009) revealed a crack identification method by means of wavelet analysis with a transform matrix. While Ghadami *et al.* (2013) detected cracks with the use of natural frequencies.

The rotational spring has been used in (Sokół and Uzny, 2015) to simulate a crack in a multi-member slender system composed of three rods (symmetrically placed in relation to the axis of the system) in form of a flat frame. In the internal element, the crack was present. In that study, the investigations of the influence of crack location and size on the natural vibration frequency were done in systems with different boundary conditions subjected to the Euler load. The results presented in (Sokół and Uzny, 2015) can be used in a diagnostic process of supporting systems.

In this paper, a continuation of studies started in (Sokół and Uzny, 2015) is presented. On the basis of those results, it has been stated that detailed studies on the bifurcation load should be done because of presence of discontinuity of curves that describe the change of static equilibrium form. The results shown here are focused on the bifurcation load magnitude at which the change of form of static equilibrium from a rectilinear into curvilinear one takes place. The influence of the crack size and relation of elasticity moduli is also taken into account.

2. Boundary problem formulation

The considered slender system (Fig. 1a) is subjected to a compressive external load with a constant line of action. The column is composed of elements (rods) with different rigidities which are symmetrically placed relative to the axis of the system.

Two external rods have equal rigidities while the third one is characterized by a smaller rigidity relative to the others. Additionally, in the internal element, a defect in form of a crack (slit) is investigated. In this paper, results of numerical simulations for different boundary conditions are presented (Fig. 1b – EUi where i stands for a different type of support 1-5).

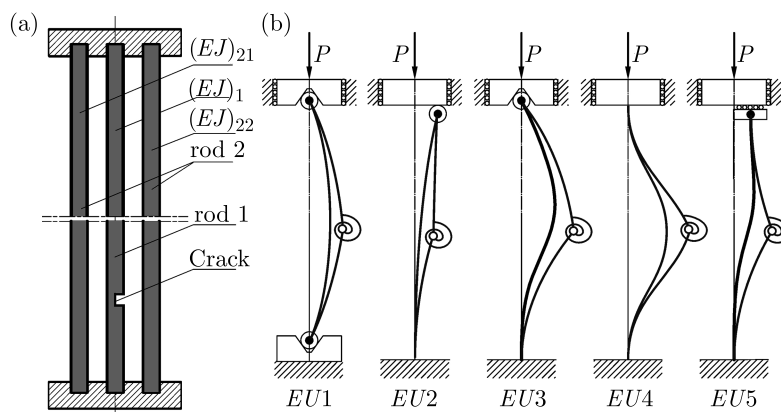


Fig. 1. Investigated multi-member system: (a) physical model of a flat frame with a marked defect – crack, (b) schematic diagrams of the system with different boundary conditions and the installed rotational spring in the point of crack presence

In the problem formulation, a generalized load (see Bochenek and Życzkowski, 2004; Gajewski and Życzkowski, 1970) on both ends of the column is used. The advantage of the theoretical generalized load is that it can be implemented in order to show all known types of conservative loads (therein the Euler load in the system with different boundary conditions). The applied force is a longitudinal external force P . The H_k and M_k components are generalized forces which arise due to the action of P . The index k is introduced and it can take values: 0 for $x_{21} = 0$ and 1 for $x_{21} = l_{21}$.

In the boundary problem formulation process, the four rods are taken into account (Fig. 2) with rigidities E_{11} , E_{12} , E_{21} , E_{22} . Elements 21 and 22 have equal rigidities, while 11 and 22 stand for the cracked element. The crack is simulated by means of a rotational spring of stiffness C and linear characteristics in the point of connection of rods 11 and 12. The function $W_{ij}(x_{ij})$, $i, j = 1, 2$ describes transversal displacements of the rods at a given coordinate x_{ij} . The components H_k and M_k of the generalized load depend on the compressive force P and can be expressed in form (see Gajewski and Życzkowski, 1970)

$$\begin{aligned} H_k &= P \left[-(-1)^k (1 - \varphi_k) \frac{dW_{21}(x_{21})}{dx_{21}} \Big|_{x_{21}=kl_{21}} - \gamma_k W_{21}(kl_{21}) \right] \\ M_k &= P \left[-(-1)^k \rho_k \frac{dW_{21}(x_{21})}{dx_{21}} \Big|_{x_{21}=kl_{21}} + \nu_k W_{21}(kl_{21}) \right] \end{aligned} \quad (2.1)$$

where ϕ_k , γ_k , ρ_k , ν_k are the coefficients which depend on the type of support or loading head. The magnitudes of ϕ_k , γ_k , ρ_k , ν_k for different types of support with consideration of Euler load are presented in Table 1.

The boundary problem formulation is done by means of the static criterion of instability

$$\delta V = 0 \quad (2.2)$$

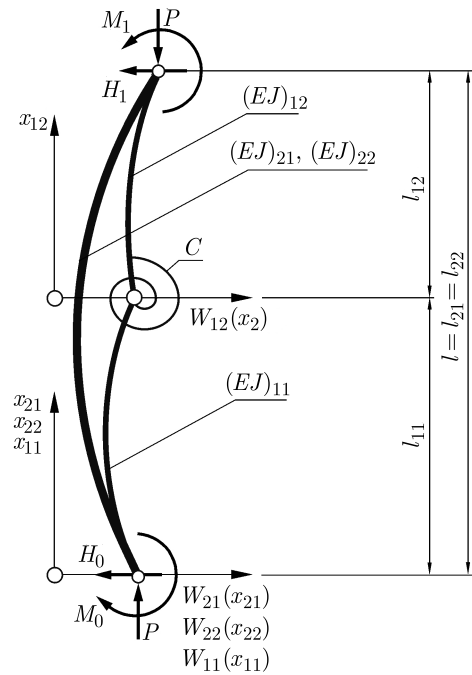


Fig. 2. Calculation model of the considered system subjected to the generalized load on both ends

Table 1. Magnitudes of generalized load parameters

	Type of suport				
	<i>EU1</i>	<i>EU2</i>	<i>EU3</i>	<i>EU4</i>	<i>EU5</i>
ϕ_0	1	1	1	1	1
γ_0	$1/\gamma_0 = 0$	$1/\gamma_0 = 0$	$1/\gamma_0 = 0$	$1/\gamma_0 = 0$	$1/\gamma_0 = 0$
ρ_0	0	$1/\rho_0 = 0$	$1/\rho_0 = 0$	$1/\rho_0 = 0$	$1/\rho_0 = 0$
ν_0	0	1	1	1	1
ϕ_1	1	1	1	1	0
γ_1	$1/\gamma_1 = 0$	0	$1/\gamma_1 = 0$	$1/\gamma_1 = 0$	0
ρ_1	0	0	0	$1/\rho_1 = 0$	$1/\rho_1 = 0$
ν_1	0	0	0	1	1

on the basis of which the estimation of the magnitude of the bifurcation load can be done. The potential energy of the system shown in Fig. 2 is as follows

$$\begin{aligned}
 V = & \frac{1}{2} C \left[\frac{dW_{11}(x_{11})}{dx_{11}} \Big|_{x_{11}=l_{11}} - \frac{dW_{12}(x_{12})}{dx_{12}} \Big|_{x_{12}=0} \right]^2 + \frac{1}{2} \sum_{i=1}^2 \sum_{j=1}^2 (EJ)_{ij} \int_0^{l_{ij}} \left[\frac{d^2 W_{ij}(x_{ij})}{dx_{ij}^2} \right]^2 dx_{ij} \\
 & + \frac{1}{2} \sum_{i=1}^2 \sum_{j=1}^2 (EA)_{ij} \int_0^{l_{ij}} \left[\frac{dU_{ij}(x_{ij})}{dx_{ij}} + \frac{1}{2} \left(\frac{dW_{ij}(x_{ij})}{dx_{ij}} \right)^2 \right]^2 dx_{ij} + PU_{21}(l_{21}) \\
 & + \sum_{i=0}^1 \frac{1}{2} \left\{ -(-1)^i P \left[-(-1)^i \rho_i \frac{dW_{21}(x_{21})}{dx_{21}} \Big|_{x_{21}=il} + \nu_i W_{21}(il) \right] \frac{dW_{21}(x_{21})}{dx_{21}} \Big|_{x_{21}=il_{21}} \right. \\
 & \left. + P \left[-(-1)^i (1 - \varphi_i) \frac{dW_{21}(x_{21})}{dx_{21}} \Big|_{x_{21}=il} - \gamma_i W_{21}(il) \right] W_{21}(il) \right\}
 \end{aligned} \tag{2.3}$$

Geometrical boundary conditions can be written in form

$$\begin{aligned}
 U_{11}(0) = U_{21}(0) = U_{22}(0) = 0 \quad U_{12}(l_{12}) = U_{21}(l_{21}) = U_{22}(l_{22}) \\
 U_{11}(l_{11}) = U_{12}(0) \quad W_{11}(0) = W_{21}(0) = W_{22}(0) \\
 W_{12}(l_{12}) = W_{21}(l_{21}) = W_{22}(l_{22}) \quad W_{11}(l_{11}) = W_{12}(0) \\
 \frac{dW_{11}(x_{11})}{dx_{11}} \Big|_{x_{11}=0} = \frac{dW_{21}(x_{21})}{dx_{21}} \Big|_{x_{21}=0} = \frac{dW_{22}(x_{22})}{dx_{22}} \Big|_{x_{22}=0} \\
 \frac{dW_{12}(x_{12})}{dx_{12}} \Big|_{x_{11}=l_{12}} = \frac{dW_{21}(x_{21})}{dx_{21}} \Big|_{x_{21}=l_{21}} = \frac{dW_{22}(x_{22})}{dx_{22}} \Big|_{x_{22}=l_{22}}
 \end{aligned} \tag{2.4}$$

Introduction of potential energy (2.3) into (2.2) leads to equations of transversal and longitudinal displacements and natural boundary conditions on each end of the system at $x_{11} = x_{21} = x_{22} = 0$; $x_{12} = l_{12}$, $x_{21} = l_{21}$, $x_{22} = l_{22}$ and crack location $x_{11} = l_{11}$, $x_{12} = 0$.

The differential equation of transversal displacements is as follows

$$(EJ)_{ij} \frac{d^4 W_{ij}(x_{ij})}{dx_{ij}^4} + S_{ij} \frac{d^2 W_{ij}(x_{ij})}{dx_{ij}^2} = 0 \tag{2.5}$$

While the longitudinal displacements can be presented in form

$$U_{ij}(x_{ij}) - U_{ij}(0) = -\frac{S_{ij}}{(EA)_{ij}} x_{ij} - \int_0^{x_{ij}} \left(\frac{dW_{ij}(x_{ij})}{dx_{ij}} \right)^2 dx_{ij} \quad \begin{matrix} i = 1, 2 \\ j = 1, 2 \end{matrix} \tag{2.6}$$

Natural boundary conditions are shown below

$$\begin{aligned}
 (EJ)_{11} \frac{d^3 W_{11}(x_{11})}{dx_{11}^3} \Big|_{x_{11}=0} + \sum_{i=1}^2 (EJ)_{2i} \frac{d^3 W_{2i}(x_{2i})}{dx_{2i}^3} \Big|_{x_{2i}=0} + S_{11} \frac{dW_{11}(x_{11})}{dx_{11}} \Big|_{x_{11}=0} \\
 + \sum_{i=1}^2 S_{2i} \frac{dW_{2i}(x_{2i})}{dx_{2i}} \Big|_{x_{2i}=0} - P \left[\gamma_0 W_{21}(0) + (1 - \varphi_0) \frac{dW_{21}(x_{21})}{dx_{21}} \Big|_{x_{21}=0} \right] = 0 \\
 (EJ)_{11} \frac{d^2 W_{11}(x_{11})}{dx_{11}^2} \Big|_{x_{11}=0} + \sum_{i=1}^2 (EJ)_{2i} \frac{d^2 W_{2i}(x_{2i})}{dx_{2i}^2} \Big|_{x_{2i}=0} \\
 + P \left[\nu_0 W_{21}(0) - \rho_0 \frac{dW_{21}(x_{21})}{dx_{21}} \Big|_{x_{21}=0} \right] = 0 \\
 (EJ)_{12} \frac{d^3 W_{12}(x_{12})}{dx_{12}^3} \Big|_{x_{12}=l_{12}} + \sum_{i=1}^2 (EJ)_{2i} \frac{d^3 W_{2i}(x_{2i})}{dx_{2i}^3} \Big|_{x_{2i}=l_{2i}} + S_{12} \frac{dW_{12}(x_{12})}{dx_{12}} \Big|_{x_{12}=l_{12}} \\
 + \sum_{i=1}^2 S_{2i} \frac{dW_{2i}(x_{2i})}{dx_{2i}} \Big|_{x_{2i}=l_{2i}} + P \left[\gamma_1 W_{21}(l_{21}) - (1 - \varphi_1) \frac{dW_{21}(x_{21})}{dx_{21}} \Big|_{x_{21}=l_{21}} \right] = 0 \\
 (EJ)_{11} \frac{d^2 W_{11}(x_{11})}{dx_{11}^2} \Big|_{x_{12}=l_{12}} + \sum_{i=1}^2 (EJ)_{2i} \frac{d^2 W_{2i}(x_{2i})}{dx_{2i}^2} \Big|_{x_{2i}=l_{2i}} \\
 + P \left[\nu_1 W_{21}(l_{21}) + \rho_1 \frac{dW_{21}(x_{21})}{dx_{21}} \Big|_{x_{21}=l_{21}} \right] = 0 \\
 (EJ)_{11} \frac{d^2 W_{11}(x_{11})}{dx_{11}^2} \Big|_{x_{11}=l_{11}} + C_R \left[\frac{dW_{11}(x_{11})}{dx_{11}} \Big|_{x_{11}=l_{11}} - \frac{dW_{12}(x_{12})}{dx_{12}} \Big|_{x_{12}=0} \right] = 0
 \end{aligned} \tag{2.7}$$

$$\begin{aligned}
& (EJ)_{12} \frac{d^2 W_{12}(x_{12})}{dx_{12}^2} \Big|_{x_{12}=0} + C_R \left[\frac{dW_{11}(x_{11})}{dx_{11}} \Big|_{x_{11}=l_{11}} - \frac{dW_{12}(x_{12})}{dx_{12}} \Big|_{x_{12}=0} \right] = 0 \\
& \sum_{i=1}^2 (EJ)_{1i} (-1)^{i+1} \frac{d^3 W_{1i}(x_{1i})}{dx_{1i}^3} \Big|_{x_{1i}=(l_{1i})(2-i)} + S_{11} \frac{dW_{11}(x_{11})}{dx_{11}} \Big|_{x_{11}=l_{11}} \\
& - S_{12} \frac{dW_{12}(x_{12})}{dx_{12}} \Big|_{x_{12}=0} = 0
\end{aligned}$$

and

$$S_{12} + S_{21} + S_{22} - P = 0 \quad (2.8)$$

Complex slender systems are characterized by the presence of rectilinear and curvilinear form of static equilibrium. In this paper, the rectilinear form is only considered. In this case, the internal force S_{ij} in the element is obtained on the basis of the following relations

$$S_{11} = S_{12} \quad S_{21} = S_{22} \quad S_{12} = P \frac{(EA)_{12}}{(EA)_{12}} + 2(EA)_{21} \quad S_{22} = \frac{P - S_{12}}{2} \quad (2.9)$$

The relations between internal forces have been calculated with consideration of boundary conditions (2.4) and (2.8). The presented method of formulation of the boundary problem in which the theoretical generalized load is used shows that numerical simulations can be performed for different types of supports and loads (including Tomski load (see Tomski and Uzny, 2008; Tomski *et al.*, 2007, 2014)). In the boundary conditions, only the parameters ρ_k , ν_k , ϕ_k , γ_k , where $k = 0, 1$, must be introduced.

The solution of the differential equations of transversal displacements has been performed on the basis of the following expression, $i = 1, 2$ and $j = 1, 2$

$$W_{ij}(x_{ij}) = A_{ij} \exp(i\sqrt{P}x_{ij}) + B_{ij} \exp(-i\sqrt{P}x_{ij}) + C_{ij}x_{ij} + D_{ij} \quad (2.10)$$

After introduction of (2.10) into the boundary conditions, one obtains a system of equations for which the matrix determinant equated to zero creates a transcendental equation used for the estimation of the bifurcation load.

3. Results of numerical simulations

The results of numerical simulations performed on the basis of the proposed mathematical model have been presented in the plane bifurcation load – flexural rigidity asymmetry factor μ_a . The coefficient μ_a is defined as a relation of the flexural rigidity of the cracked rod to the sum of rigidities of the external rods

$$\mu_a = \frac{(EJ)_{11}}{(EJ)_{21} + (EJ)_{22}} \quad (3.1)$$

The magnitude of bifurcation load is presented in the non-dimensional form

$$\lambda_b = \frac{Pl_{21}^2}{(EJ)_{11}} + \sum_{i=1}^2 (EJ)_{2i} \quad (3.2)$$

In simulations, a constant total flexural rigidity of the system is used

$$(EJ)_{11} + (EJ)_{21} + (EJ)_{22} = EJ$$

Numerical simulations have been performed for three magnitudes of the parameter ζ_B ($\zeta_B = 0.1, 0.5, 1.0$). The ζ_B shows the relation between the Young modulus of the cracked rod to the uncracked one

$$\zeta_B = \frac{E_{11}}{E_{21}} \quad (3.3)$$

The non-dimensional spring stiffness parameter c which reflects the crack size and the location ζ_A are as follows

$$c = \frac{Cl}{EJ} \quad \zeta_A = \frac{l_{11}}{l} \quad (3.4)$$

The results presented in this paper are done only at $\zeta_A = 0.5$ (central location).

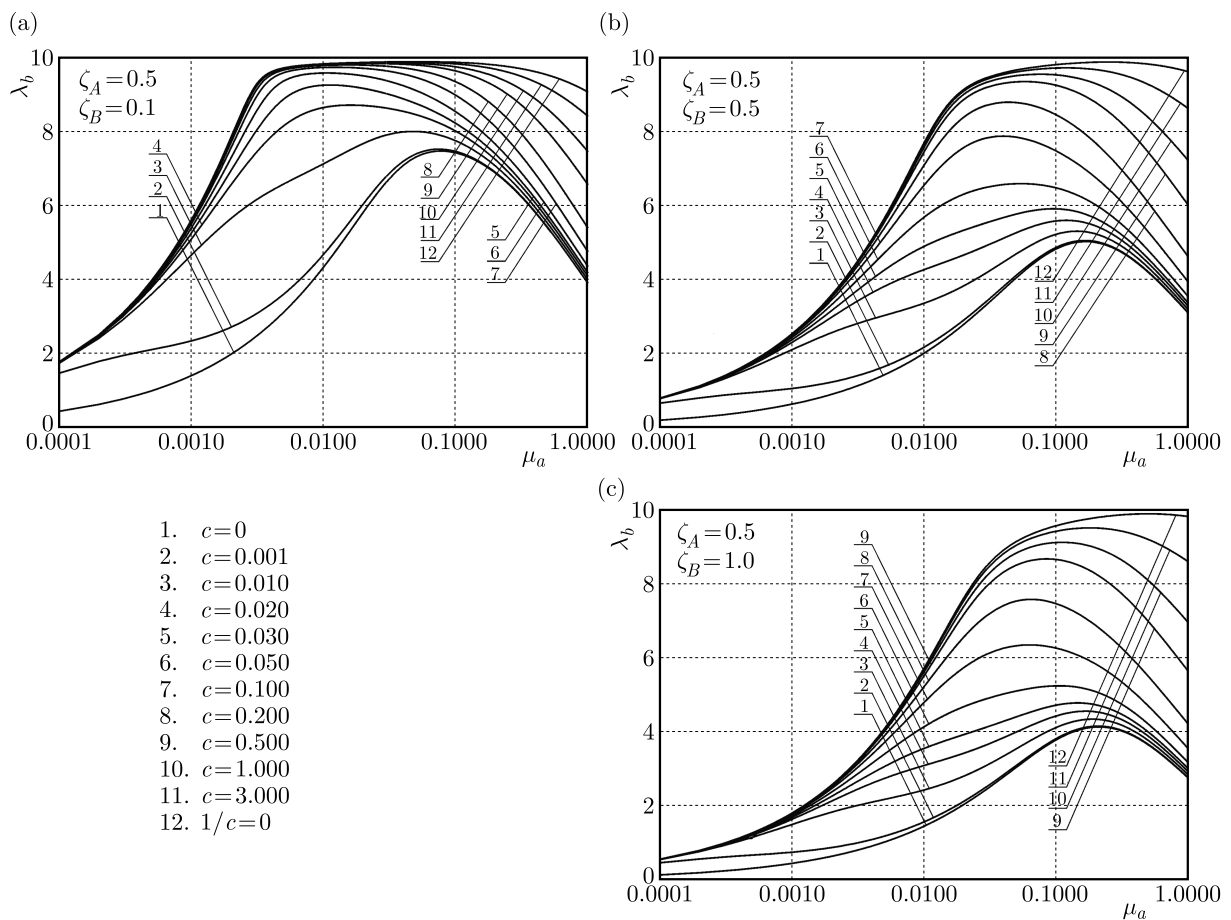


Fig. 3. A change of the bifurcation load parameter λ_b of EU1 column in relation to the flexural rigidity asymmetry factor μ_a at $\zeta_A = 0.5$ and different crack sizes: (a) $\zeta_B = 0.1$, (b) $\zeta_B = 0.5$, (c) $\zeta_B = 1$

On the basis of the results of numerical simulations presented in Figs. 3-7 it have been shown that the crack size has a small influence on the bifurcation load magnitude at a lower level of the bending rigidity asymmetry factor. This influence depends on the boundary conditions and Young modulus of the materials used in the supporting structure. When the materials are comparable (which corresponds to $\zeta_B \approx 1$) the differences in bifurcation loads are the smallest at low μ_a . An increase in the bending rigidity asymmetry factor μ_a causes an increase in bifurcation load to the maximum level above which a further increase of μ_a results in reduction of the loading

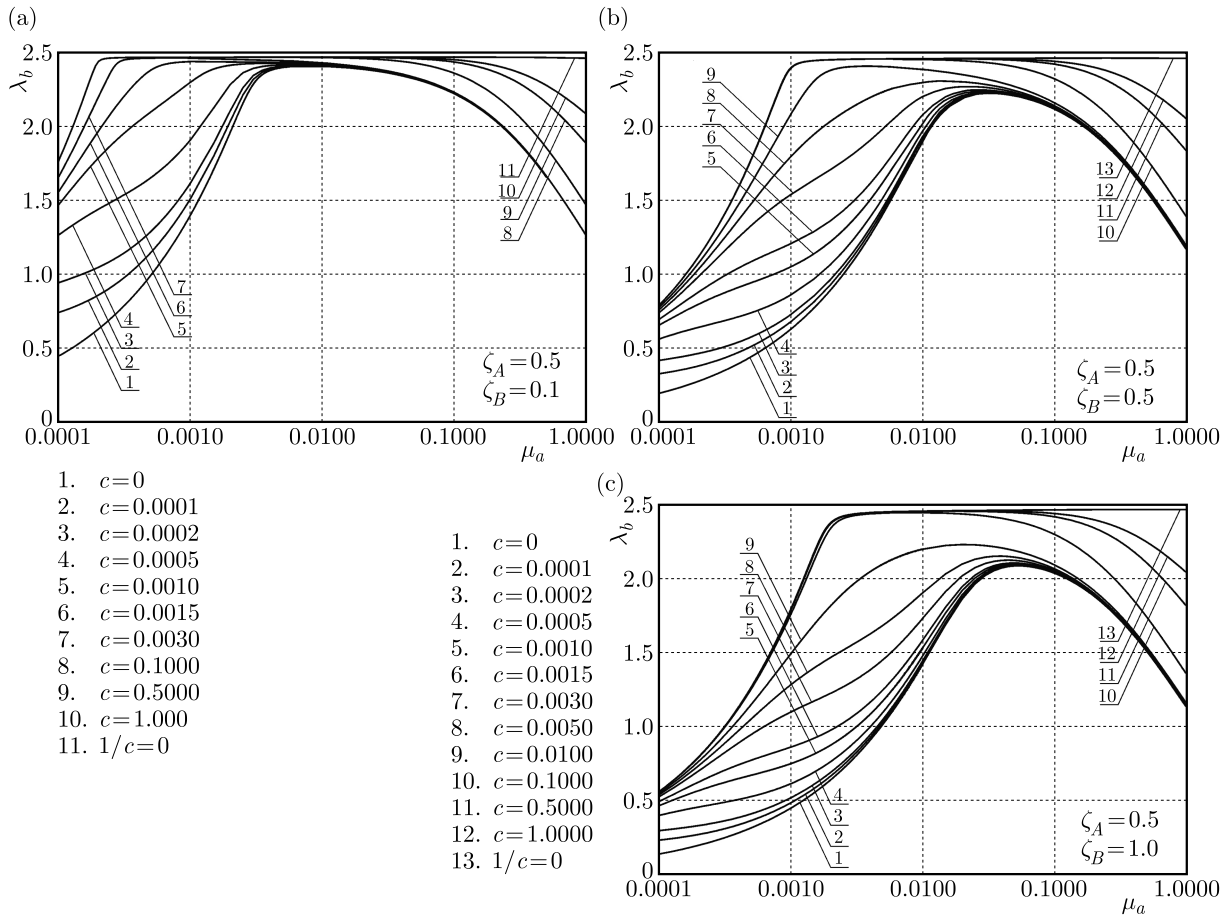


Fig. 4. A change of the bifurcation load parameter λ_b of EU2 column in relation to the flexural rigidity asymmetry factor μ_a at $\zeta_A = 0.5$ and different crack sizes: (a) $\zeta_B = 0.1$, (b) $\zeta_B = 0.5$, (c) $\zeta_B = 1$

capacity. In EU4 and EU5 configurations at higher μ_a , the bifurcation load is constant and independent of the crack size. Furthermore, in EU5 the area of independency of the bifurcation load to μ_a can be found (the smaller crack, the greater the independency area). On the basis of the numerical simulations, it can be concluded that columns EU4 and EU5 at higher μ_a are insensitive to the crack size, which appears in the central element (the one with lower bending rigidity). In all investigated cases such ranges of the crack size can be estimated at which a small change of the bifurcation load regardless of μ_a can be found.

Additionally, it has been shown that in configurations EU4 and EU5, the discontinuity of the curves can be observed in the plane loading parameter – flexural rigidity asymmetry factor $\lambda_b(\mu_a)$. In columns EU4 and EU5, at a sufficiently high flexural rigidity asymmetry factor, a change in buckling mode shapes takes place. The magnitude of this factor at which the change can be observed highly depends on the crack size (rotational spring stiffness c). The smaller crack, the higher μ_a is needed to obtain a change in the buckling mode shape. The buckling mode shapes of the considered systems are presented in Fig. 8. A high difference in the parameter μ_a has been chosen in order to achieve the best presentation of the change of buckling shapes, especially for EU4 and EU5.

In configurations EU1-EU3, an increase of μ_a reveals the presence of the crack. That is why in those three cases an observation of buckling shape modes can easily lead to determination of failure of the structure at high μ_a because the function used to describe the transversal displacements of the cracked element is not a smooth one. The buckling shape modes of EU4 and EU5 systems at a lower magnitude of the μ_a coefficient are characterized by no transversal

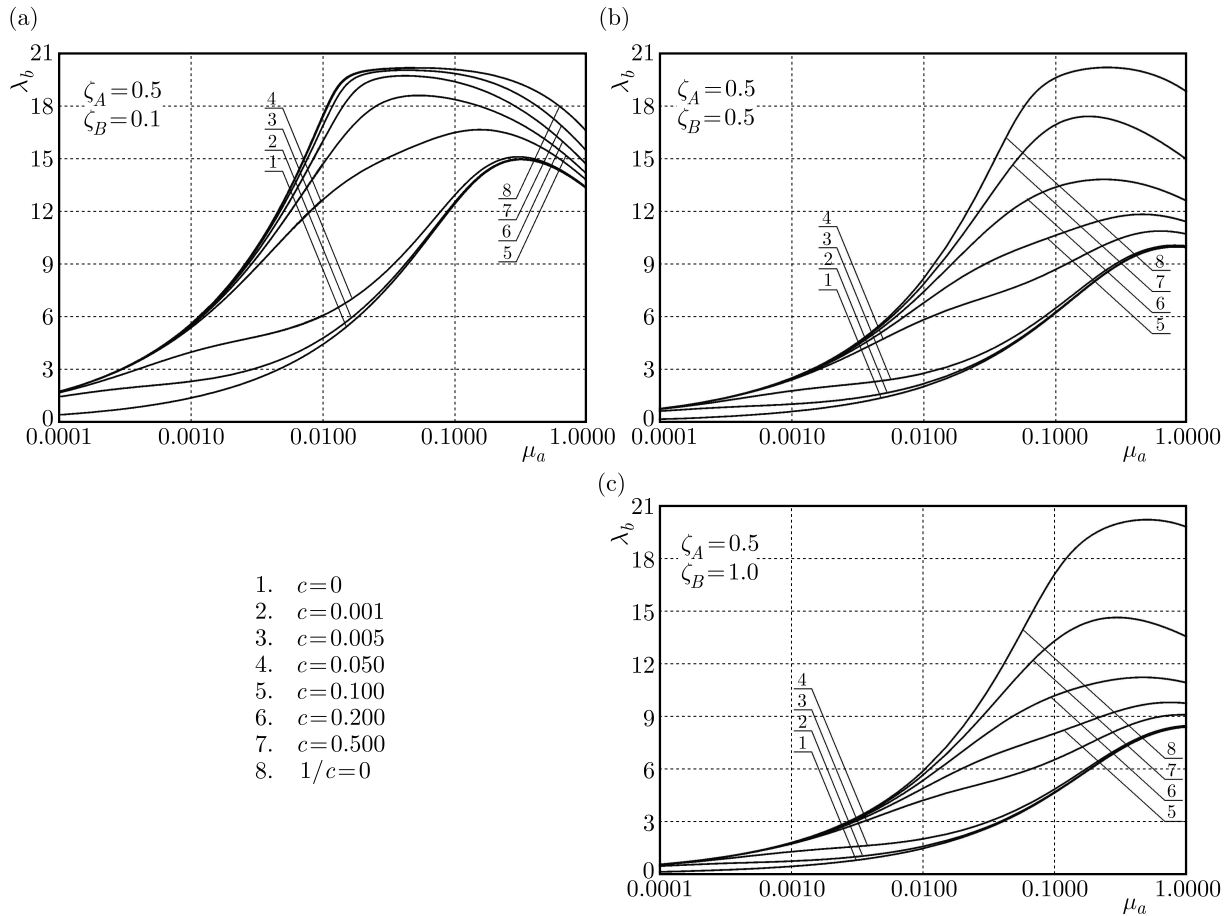


Fig. 5. A change of the bifurcation load parameter λ_b of *EU3* column in relation to the flexural rigidity asymmetry factor μ_a at $\zeta_A = 0.5$ and different crack sizes: (a) $\zeta_B = 0.1$, (b) $\zeta_B = 0.5$, (c) $\zeta_B = 1$

displacement of the uncracked rods (see Fig. 8 – shapes at $\mu_a = 0.01$ – *EU4* and $\mu_a = 0.001$ – *EU5* configurations). At $\mu_a = 0.9$, the buckling shape modes of *EU4* and *EU5* are changing regarding to lower μ_a . The change is related to independency of the bifurcation load of the considered systems from the crack size at higher μ_a magnitudes. Additionally, when columns *EU4* and *EU5* are taken into account, the buckling shape modes are described by a smooth function. In *EU4* and *EU5* configurations, the crack presence is hard to identify on the basis of analysis of buckling shape modes. That is why, the further investigations on the natural vibration frequency must be done (relations: external load-vibration frequency and amplitude-vibration frequency). The solution presented in this paper allows one to choose proper physical and geometrical parameters and reveals the area of drop in the loading capacity in the case of crack presence.

4. Conclusions

In this paper, a slender system with a crack subjected to compressive external load with a constant line of action is considered. The effect of size of the crack, which is present in the internal element, on the bifurcation load magnitude is investigated. Numerical simulations of the bifurcation load have been done at different magnitudes of parameters such as: rotational spring stiffness (size of the crack), flexural rigidity asymmetry factor and longitudinal elasticity modulus. The numerical calculations are also concerned with different types of supports (five configurations have been chosen for presentation).

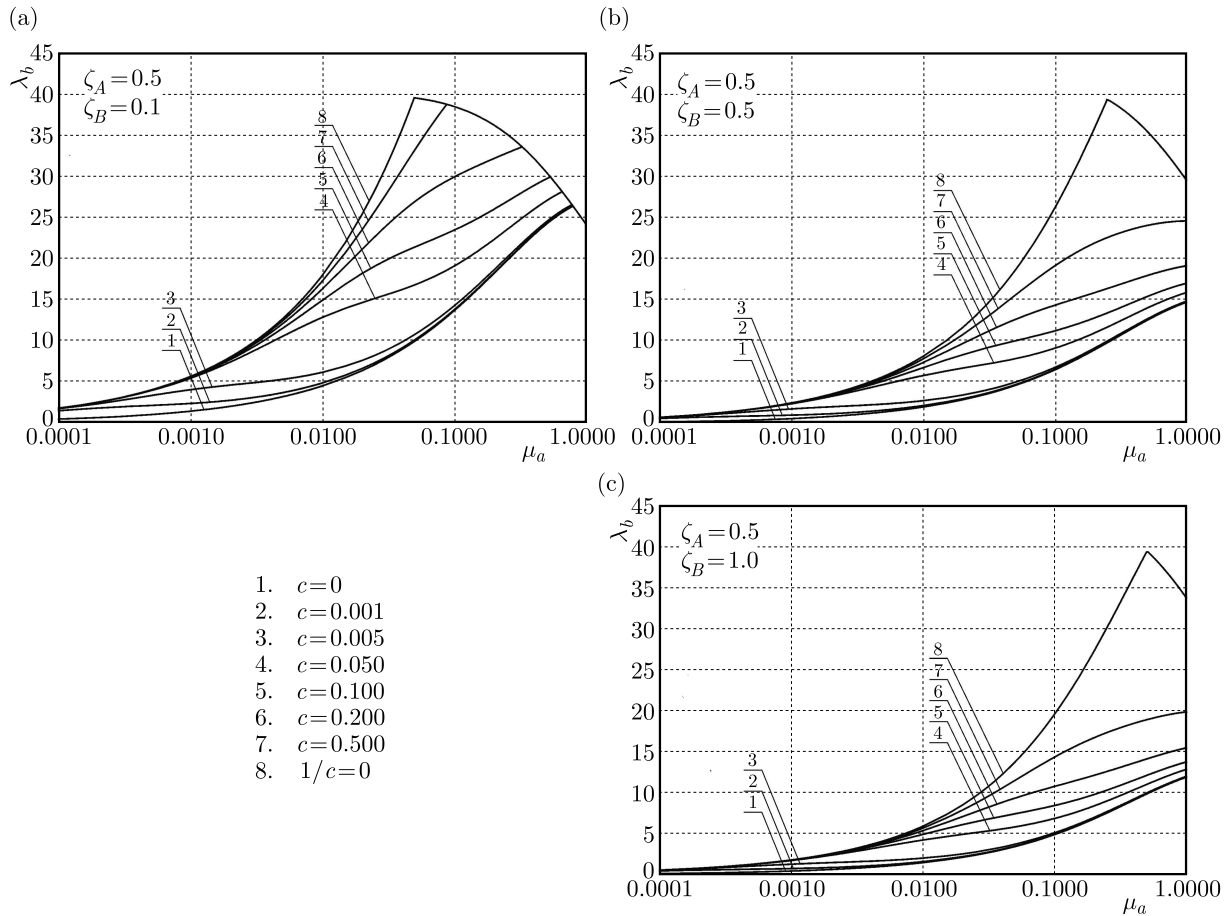


Fig. 6. A change of the bifurcation load parameter λ_b of EU4 column in relation to the flexural rigidity asymmetry factor μ_a at $\zeta_A = 0.5$ and different crack sizes: (a) $\zeta_B = 0.1$, (b) $\zeta_B = 0.5$, (c) $\zeta_B = 1$

On the basis of the results of simulations, the following conclusions can be drawn:

- influence of the crack size on the bifurcation load magnitude highly depends on a combination of the supporting elements (boundary conditions),
- in the systems with the zero deflection angle at both ends, the crack which is present in the element with the lower bending rigidity has no effect on the bifurcation load at high μ_a ,
- for each of the considered systems, the magnitude of the bending rigidity asymmetry factor as a function of the crack size at which the bifurcation load is the highest can be found,
- the magnitude of μ_a which corresponds to the highest bifurcation load strongly depends on the Young modulus parameter ζ_B ,
- when the systems with the zero deflection angle at both ends are considered, such μ_a can be found at which the change of buckling shape modes can be observed; additionally, after this change, the buckling load does not depend on the crack size.

On the basis of the simulations presented in this paper the type of supports have significant influence on the sensitivity of the structure to the crack presence (taking into account the bifurcation load considered in this publication). Additionally, in the future investigations of the influence of the crack on instability of a discussed structure, different types of external load should be introduced. Structures subjected to non-conservative loads may be less vulnerable to the crack presence. A good example of such a type of load is the specific load. An introduction of the specific load modifies investigations on instability and natural vibrations (change of vibration frequencies and shape modes) regarding the classic Euler load. For the specific load (which is a

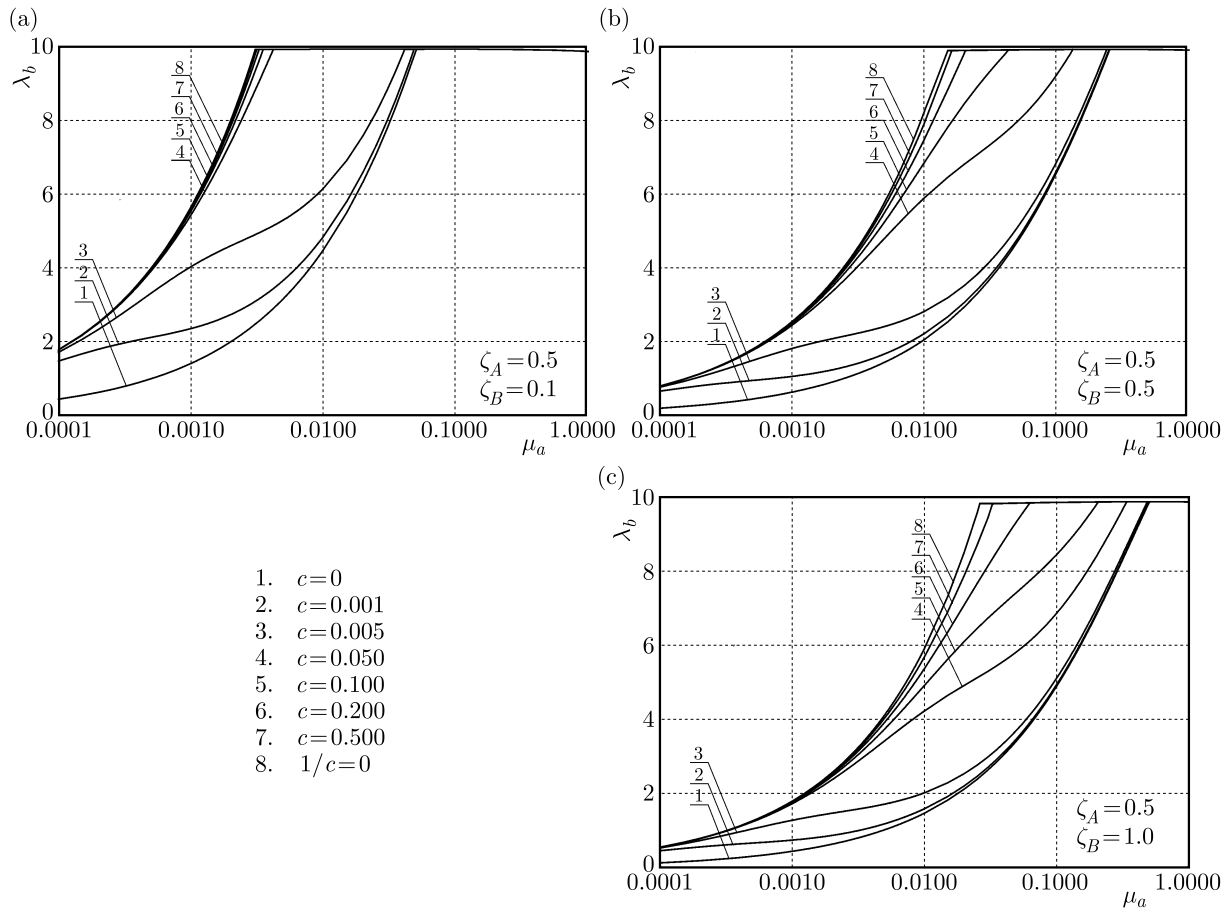


Fig. 7. A change of the bifurcation load parameter λ_b of EU5 column in relation to the flexural rigidity asymmetry factor μ_a at $\zeta_A = 0.5$ and different crack sizes: (a) $\zeta_B = 0.1$, (b) $\zeta_B = 0.5$, (c) $\zeta_B = 1$

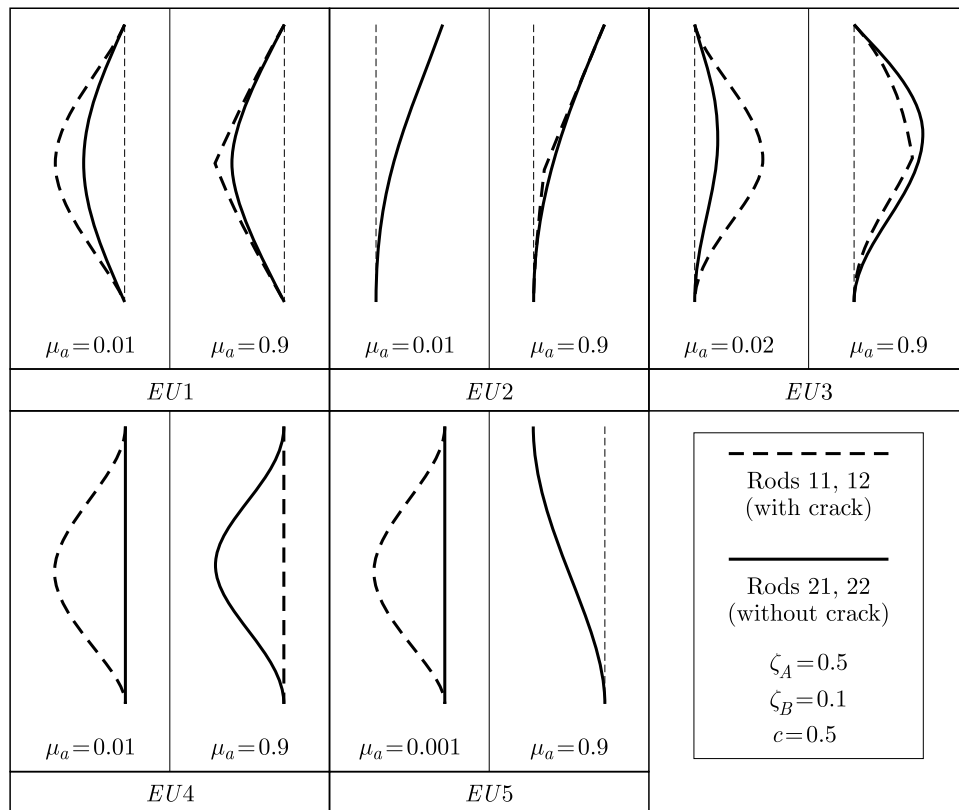


Fig. 8. Buckling mode shapes of the considered systems (EU1-EU5) for $\zeta_B = 0.1$, $c = 0.5$

practical load, see Tomski and Uzny (2008), Tomski *et al.* (2007, 2014)) the parameters allowing the control of the bifurcation load or the critical one as well as the natural vibration frequency can be found. It can be assumed that the parameters of the loading heads of the specific load will also affect the vulnerability of the structure to the crack presence. A continuation of this study in the mentioned way is justified and should be done in the future.

Acknowledgements

The study has been carried out within the statutory funds of the Czestochowa University of Technology (BS/PB-1-101-3020/11/P).

References

1. ANIFANTIS N., DIMAROGONAS A., 1983, Stability of column with a single crack subjected to follower and vertical loads, *International Journal of Solids and Structures*, **19**, 4, 281-291
2. BOCHENEK B., ŻYCZKOWSKI M., 2004, Analytical approach to optimization of columns for post-buckling behavior, *Structural and Multidisciplinary Optimization*, **28**, 252-261
3. CHANDROS T.G., DIMAROGONAS A.D., YAO J., 1998, A continuous cracked beam vibration theory, *Journal of Sound and Vibration*, **215**, 1, 17-34
4. CHATI M., RAND R., MUKHERJEE S., 1997, Modal analysis of a cracked beam, *Journal of Sound and Vibration*, **207**, 2, 249-270
5. GAJEWSKI A., ŻYCZKOWSKI M., 1970, Optimal design of elastic columns subject to the general conservative behaviour of loading, *Journal of Applied Mathematics and Mechanics*, **21**, 806-818
6. GHADAMI A., MAGHSOODI A., MIRADAMADI H.R., 2013, A new adaptable multiple-crack detection algorithm in beam-like structures, *Archives of Mechanics*, **65**, 6, 469-483
7. GODLEY M.H.R., CHILVER A.H., 1970, Elastic buckling of overbraced frame, *International Journal of Mechanical Sciences*, **12**, 4, 238-246
8. HJELMSTAD K.D., SHIN S., 1996, Crack identification in a cantilever beam from modal response, *Journal of Sound and Vibration*, **198**, 5, 527-545
9. KIM K.-H., KIM J.-H., 2000, Effect of a crack on the dynamic stability of a free-free beam subjected to a follower force, *Journal of Sound and Vibration*, **233**, 1, 119-135
10. KRAWCZUK M., 1992, Finite Timoshenko-type beam element with a crack, *Engineering Transactions*, **40**, 2, 229-248
11. KUKLA S., 2009, Free vibrations and stability of stepped columns with cracks, *Journal of Sound and Vibration*, **319**, 1301-1311
12. LUESCHEN G.G.G., BERGMAN L.A., MCFARLAND D.M., 1996, Green's functions for uniform Timoshenko beams, *Journal of Sound and Vibration*, **194**, 1, 93-102
13. MASOUD S., JARRAH M. A., AL-MAAMORY M., 1999, Effect of crack depth on the natural frequency of a prestressed fixed-fixed beam, *Journal of Sound and Vibration*, **214**, 2, 201-212
14. NARKIS Y., 1994, Identification of crack location in vibrating simply supported beams, *Journal of Sound and Vibration*, **172**, 4, 549-558
15. OSTACHOWICZ W. M., KRAWCZUK M., 1991, Analysis of the effect of cracks on the natural frequencies of a cantilever beam, *Journal of Sound and Vibration*, **150**, 2, 191-201
16. RIZOS P.F., ASPRAGATHOS N., DIMAROGONAS A.D., 1990, Identification of crack location and magnitude in a cantilever beam from the vibration modes, *Journal of Sound and Vibration*, **138**, 3, 381-388
17. SHEN M.-H.H., TAYLOR J.E., 1991, An identification problem for vibrating cracked beams, *Journal of Sound and Vibration*, **150**, 3, 457-484

18. SOKÓŁ K., 2014, Linear and nonlinear vibrations of a column with an internal crack, *Journal of Engineering Mechanics*, **140**, 5
19. SOKÓŁ K., UZNY S., 2015, Instability and vibration of multi-member columns subjected to Euler's load, *Archive of Applied Mechanics*, DOI 10.1007/s00419-015-1068-6
20. TOMSKI L., SZMIDLA J., UZNY S., 2007, The local and global instability and vibration of systems subjected to non-conservative loading, *Thin-Walled Structures*, **45**, 10-11, 945-949
21. TOMSKI L., SZMIDLA J., UZNY S., 2014, Active and passive specific loads with respect to the stability and free vibrations of columns, *Journal of Engineering Mechanics*, **140**, 1, 193-205
22. TOMSKI L., UZNY S., 2008, Free vibration and the stability of a geometrically non-linear column loaded by a follower force directed towards the positive pole, *International Journal of Solids and Structures*, **45**, 1, 87-112
23. UZNY S., 2011a, Free vibrations of an elastically supported geometrically nonlinear column subjected to a generalized load with a force directed toward the positive pole, *Journal of Engineering Mechanics*, **137**, 11, 740-748
24. UZNY S., 2011b, Local and global instability and vibrations of a slender system consisting of two coaxial elements, *Thin-Walled Structures*, **49**, 618-626
25. ZAMORSKA I., CEKUS D., MIARA M., 2015, Effect of crack parameters on free vibrations of the Bernoulli-Euler beam, *Journal of Applied Mathematics and Computational Mechanics*, **14**, 4, 167-174.
26. ZHANG W., WANG Z., MA H., 2009, Crack identification in stepped cantilever beam combining wavelet analysis with transform matrix, *Acta Mechanica Sinica*, **22**, 4, 360-368

Manuscript received August 22, 2016; accepted for print September 21, 2017

PRELIMINARY EXPERIMENTAL/NUMERICAL STUDY OF THE VIBRATION ANNOYANCE CONTROL OF A WINDSHIELD WIPER MECHANICAL SYSTEM THROUGH A SYNCHRONIZED SWITCH SHUNT RESONATOR (SSSR) TECHNOLOGY

MASSIMO VISCARDI, ROMEO DI LEO

*University of Naples "Federico II", Department of Industrial Engineering – Aerospace Section, Naples, Italy
e-mail: romeodileo@gmail.com*

MONICA CIMINELLO

C.I.R.A. Italian Aerospace Research Centre, Capua (CE), Italy

MARCO BRANDIZZI

C.R.F. Centro Ricerche Fiat, Orbassano (TO), Italia

The present work focuses on the study and analysis of vibrations generated by the electrical motor of a wiper system on its support bracket referring to an hatchback vehicle passenger car. In the electric motor of the wiper system there can be present an imbalance transmitting vibrations to the main body via the support bracket. In this paper, after a short resume of available synchronized switch shunt damping methods, a preliminary experimental evaluation of their potential performance on noise control of the wiper system is reported. After preliminary experimental measurements of dynamic vibration by the use of vibrometer laser both on the real hatchback car then in laboratory environment, a numerical model has been created to evaluate deformations of the support bracket for comparison with the experimental data. This work realizes the preliminary numerical/experimental characterization activity to set up a new application of a control system based on a semi-active technique, called Synchronized Switch Shunt Resonator (SSSR).

Keywords: vibration control, acoustic, wiper system, semi-active technique, synchronized switch shunt resonator

1. Introduction

In the modern automotive industry, the fundamental topic is noise annoyance inside the car.

The reduction of internal noise is of great importance in order to make the driving experience safer and more comfortable and to prevent that these annoyance sources could be perceived as the low quality indicator. For this reason, great efforts are addressed by the research world to define requirements and specifications for integrated solutions aimed at reduction of noise using different cost effective established technologies such as noise and vibration control, innovative materials and optimized tires, analyzing related risks too. In addition, many new soundproofing solutions are developed and focused, in particular, oriented on internal noises reduction (especially for squeak and rattle noises).

The noise sources in an auto-vehicle can be divided into the primary and secondary sources. In the first group, there are three main sources:

- The power-train: the engine noise is generated by mechanical and chemical processes inside the engine that cause vibrations which are transmitted to the cockpit.
- Interaction road-tires: the road noise is generated by the interaction with the tire interface and the ground and causes broadband vibrations which are transmitted to the structure.

- Aerodynamic flow: the vortex shedding noise which is caused by the fluid (air) and a non-aerodynamic body (car) interaction.

In the other group, there are two main secondary sources:

- Noise generated internally by the passenger compartment (squeaks, etc.).
- Equipment and systems of various kinds (air conditioning, etc.).

Within this frame, the present work focuses on the study and analysis of vibrations generated by the electrical motor of the wiper system transmitted on its support bracket for a hatchback vehicle passenger car application. It has been indeed identified that the electric motor of the wiper system can present an imbalance transmitted to the body through this support bracket. The main goal is to investigate typical vibration modes of the supporting plate in order to design proper control system parameters based on a semi-active technique. This technique uses piezo transducers to convert mechanical into electrical energy and elaborates the related signal within an external electrical circuit.

Piezoelectric materials fall in the category of the so-called smart materials and they can often control and suppress vibration in an efficient and intelligent way without causing much additional weight or cost. In many research activities, piezoelectric materials are satisfactorily applied to control structural materials due to their excellent mechanical-electrical coupling characteristics.

The shunt methods for vibro-acoustic control based on piezoelectric sensors and actuators can be divided into three main classes: passive, active and semi-active. Passive shunt control systems mainly reproduce the dynamic vibration absorber device by means of electrical components, typically resistive-inductive (R-L) circuits (Hollkamp, 1994). This kind of circuits is simple to design but its performance is based on the resonance tuning, so it is sensitive to variations of structural parameters. In addition, R-L shunt systems need large inductance for a low frequency domain, which is improbable in realistic applications.

Active control systems require high-performance digital signal processors and bulky power amplifiers to drive actuators, which is not suitable in many practical applications too. To overcome these disadvantages, several semi-active approaches have been proposed. In the last years, Clark proposed a state-switched method (Clark, 1999) in which piezo-elements were periodically held in an open-circuit state, then switched and held in the short-circuit state synchronously with the structure motion. Another type of semi-active control, which has been receiving much attention in the recent years, is called the pulse switching technique (Richard *et al.*, 1998; Onoda *et al.*, 2003; Makiyara *et al.*, 2005). It consists in fast inversion of voltage on the piezo-element using a few basic electronic elements synchronized with the mechanical vibration.

In the methods proposed by Richard *et al.* (1998), the voltage is switched on the piezoelectric element at each strain extrema or, equally, displacement extrema. These methods are called synchronized switch damping (SSD) techniques (Ciminello *et al.*, 2008).

The present paper reports a preliminary feasibility study of the well established control technology on a new automotive application. The Synchronized Switch Shunt Resonator (SSSR) control system already investigated and applied by the authors for aeronautical components (Ciminello *et al.*, 2010; Ameduri and Ciminello, 2010) is used here to a new particular test case, namely a wiper mechanism for an automotive application. The paper at hand includes a preliminary experimental evaluation of the control of the wiper assembly vibrations supported by some FEA computations. The SSSR design is also described and followed by preliminary experimental results. The authors show possible issues with realistic damping of low amplitude vibrations of the wiper system bracket.

2. Synchronized switch damping (SSD) method

The synchronized switch damping (SSD) method, also called the pulse-switched method, consists of nonlinear processing of the voltage on a piezoelectric actuator. It is implemented with a simple electronic switch synchronously driven with the structural motion.

This switch, which is used to reverse the voltage on the piezoelectric element, allows one to briefly connect a simple electrical network (short circuit, inductor and voltage sources depending on the SSD version) to the piezoelectric element. Due to this process, a voltage magnification is obtained and a phase shift appears on the resulting voltage. The force generated by the resulting voltage is hence opposite to the structural motion, thus creating energy dissipation. The dissipated energy corresponds to the part of the mechanical energy converted into electric energy. Maximizing this energy is equivalent to minimizing mechanical energy in the structure.

Several SSD techniques are reported. The simplest is called SSDS, as shown in Fig. 1, which stands for synchronized switch damping on the short circuit (Clark, 1999).

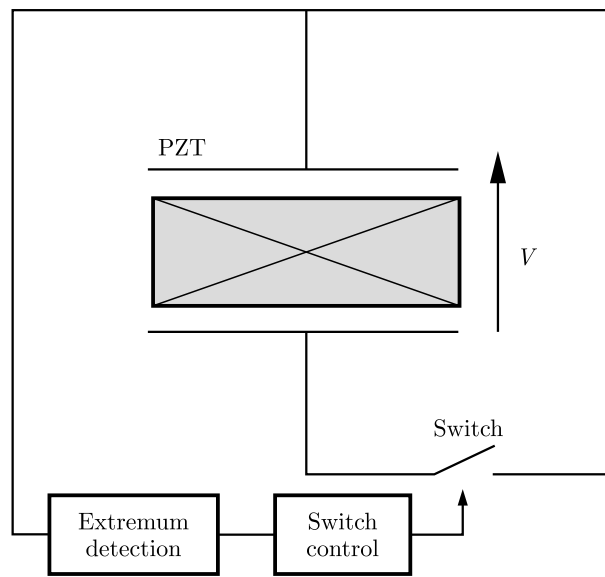


Fig. 1. Principle of the SSDS technique

The SSDS technique consists of a simple switching device in parallel with the piezoelectric patch without other electric devices. The switch is kept open for most of the time during the vibration period and then closed when the voltage reaches the maximum (corresponding to the maximum of the strain on the piezoelectric patch) and left closed for a short period in order to dissipate the stored electric energy.

According to the work of Qiu *et al.* (2009), for the SSDS circuit, the transferred energy E_t in a period is given by

$$E_t = \frac{4\alpha^2}{C_0} u_M^2 \quad (2.1)$$

where α is the piezoelectric coefficient, C_0 is the capacitance of the piezoelectric element and u_M is the amplitude of vibration (Badel *et al.*, 2006).

To further increase the dissipated energy, the SSDI technique (synchronized switch damping on the inductor) shown in Fig. 2, has been developed by Richard *et al.* (1998), Guyomar *et al.* (2001) and Petit *et al.* (2004).

In the SSDI approach, the inductor is connected in series with the switch. Because the piezoelectric patch and the inductor constitute an L-C resonance circuit, fast inversion of the

voltage on the piezoelectric patch is achieved by appropriately controlling the closing time and duration of the switch.

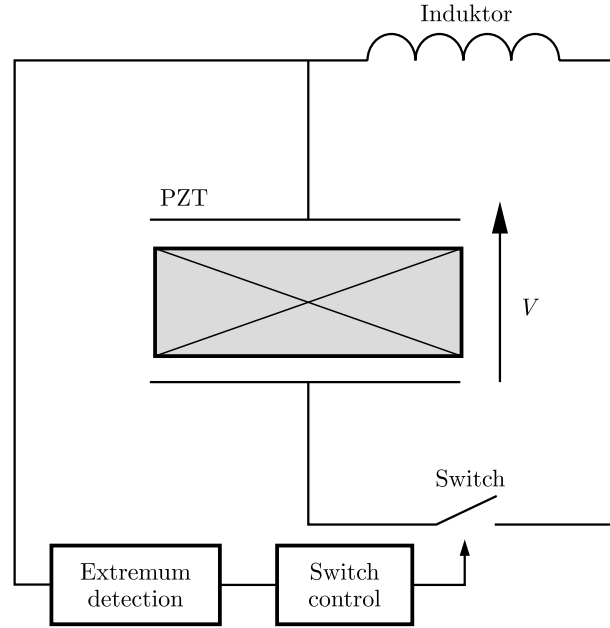


Fig. 2. Principle of the SSDI technique

The switch is closed at the displacement extremes, and the duration of the closed state lasts half of the period. This leads to an artificial increase of the dissipated energy. The period of the L-C circuit is chosen to be much smaller than that of the mechanical vibration.

In the SSDI technique, the dissipated energy E_t during the period is given by

$$E_t = \frac{4\alpha^2}{C_0} \frac{1+\gamma}{1-\gamma} u_M^2 \quad (2.2)$$

where $\gamma \in [0, 1]$ is the voltage inversion coefficient. Comparing equations (2.1) and (2.22), the transferred energy is magnified by means of $(1+\gamma)/(1-\gamma)$ factor (Badel *et al.* (2006)).

Although most semi-active studies have been devoted so far to single-mode control, the switching laws can be also used for multi-mode control. In the method proposed by Makihara *et al.* (2007a,c), switch actions are automatically generated by the control law applicable to multi-modal control of a structure with multiple piezoelectric transducers.

In the method proposed by Ciminello *et al.* (2010), a similar technology was tested to verify its experimental performance on a 2D structure over a broadband frequency range. The selected test specimen was a 220 mm×280 mm, 7 mm thick, 10-ply fiberglass laminate plate. The system was made of several actuator/sensor piezoelectric ceramic pairs linked to a 4-channel control circuit. Active elements were embedded into the structure at different locations to produce effects over a large number of modes. The placement resulted from an optimization study performed to maximize their action over the frequency bandwidth of interest. The equivalent induced damping was estimated for seven out of eight bending modes present in the investigated interval. Amplitude reductions up to 16 dB were attained. The experimental results were found to be in good accordance with the numerical predictions.

Through about 10 years of research, several electronic switching circuits and switch control laws have been developed. However, more improvements must still to be provided for practical applications. Due to the energy loss during voltage inversion, these switching laws are not always optimal as demonstrated by experimental results (Makihara *et al.*, 2007b; Viscardi and Leo, 2016). More efficient control laws and higher robustness of the control system are required.

3. Problem formulation

The target of the activity at hand is the vibration control of the mechanical wiper system of a hatchback passenger car. The system is linked to the chassis of the vehicle in three points (red circles in Fig. 3).

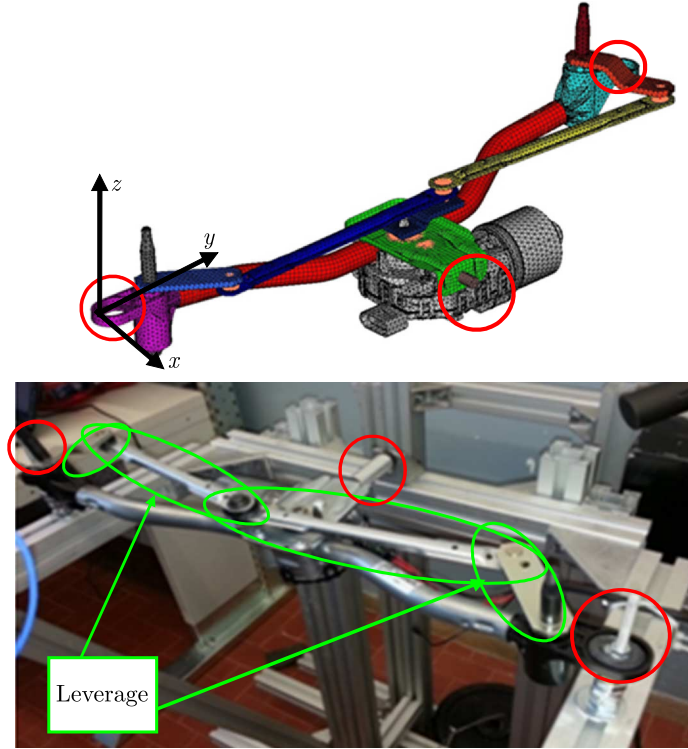


Fig. 3. Digital and physical mock-up of the wiper system

It has been identified that the electric motor of the wiper system presents an imbalance transmitting vibrations to the main body via the support bracket (part in red colour in Fig. 4).

According to this problem and to the specifications (that is the reduction of vibrations in the frequency range 600-850 Hz, which is the range of interest as provided by the experimental measures on the car and as said in the subsequent lines), a feasibility study on the vibration suppression provided by a semi-active synchronized switch shunt resonator (SSSR) is investigated.

Specific analysis with the wiper system of the car used as the test case is addressed to measure the force transmitted to the chassis of the car through the constraint points of the wiper generated by the electrical motor in operating conditions. Figure 5 shows the force spectrogram transmitted in the Z direction according to the reference system in Fig. 3. The force is measured on the right lateral constraint and shows a maximum peak in the 600-850 Hz frequency range. The red curve is the measured force with the wiper blades mounted, and the blue curve refers to the wiper blades dismissed.

The design and manufacturing of the dedicated control system has been developed through the next steps:

- Measurements of the acoustic performance for the original wiper system (without system control) in the real hatchback passenger car cabin.
- Dynamic characterization of the support bracket in the wiper system.
- Numerical simulation of the dynamic behaviour of the support bracket in the wiper system.
- Design of the basic layout of the control system.

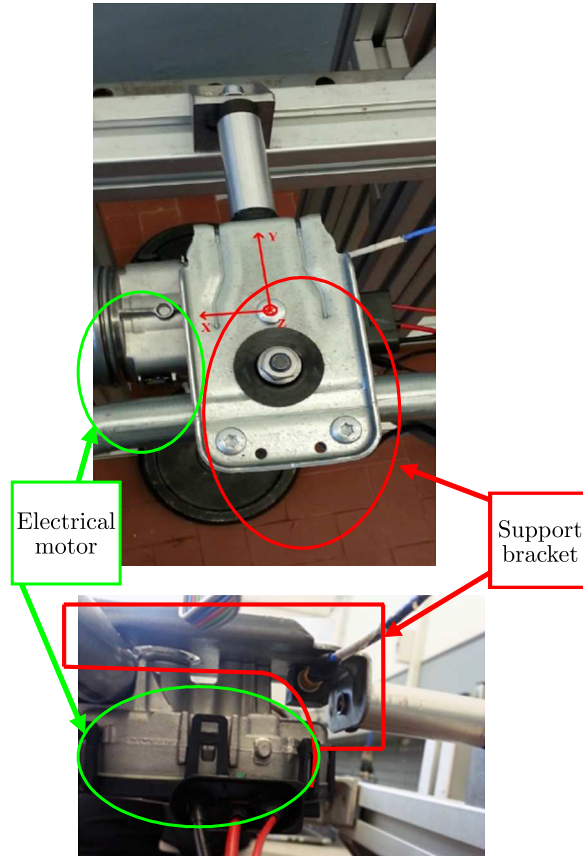


Fig. 4. Assembly bracket with an electrical motor. The upper and lateral view

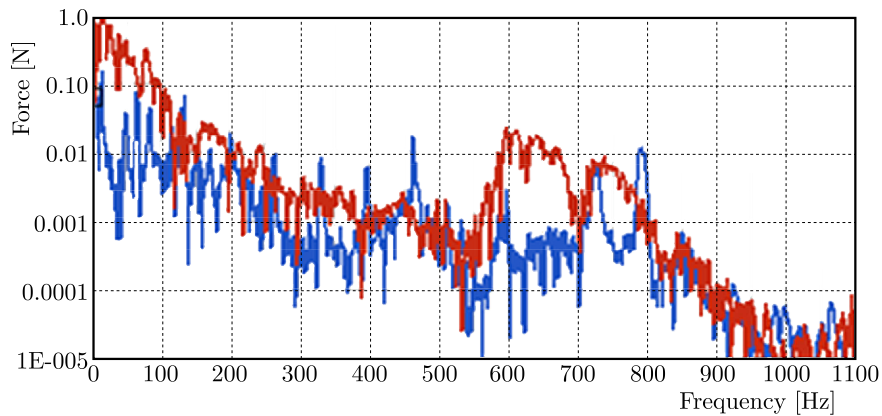


Fig. 5. Force wiper system-chassis in the Z direction on the right lateral constraint

4. Acoustic performance of the wiper in the vehicle cab

The acoustic performance of the mechanical wiper has been measured. Measurements were performed by the authors in different operative speeds of the wiper system and with thermodynamic engine in the “off” and “on” state.

The experimental set-up was composed by two Roga MI-17 Icp microphones which were installed on both sides of the head of the driver at the ear level. An additional Roga MI-17 Icp microphone was installed outside the vehicle in front to the bonnet at a distance of one meter.

Besides, an accelerometer was installed on the bottom face of the support bracket to measure the vibrating level produced by the electrical motor in real operative conditions. Another one

was positioned on the interior surface of the windshield to measure acceleration transmitted by the wiper to have an idea about the most important transmission path between the windshield and the chassis.

For data acquisition, an LMS Scadas Mobile 5 with eight channels and TestLab software were used.

The first data logging was done for the accelerometers in two different conditions. The first one was characterized by the thermodynamic engine “on” at different rotational speeds (idle, 1500, 2000 rpm) while keeping the wiper system “off”. The second data logging was characterized by the thermodynamic engine “off” while keeping the wiper system “on”. For every measure the car was left with the gearbox in neutral position.

Figure 6 shows that the acceleration of the support bracket produced by the excitation of the wiper electrical motor is higher than the one produced by the stand alone thermal engine. Therefore, the effect of the wiper on the vibrating energy, transmitted by the support bracket to the chassis is not negligible.

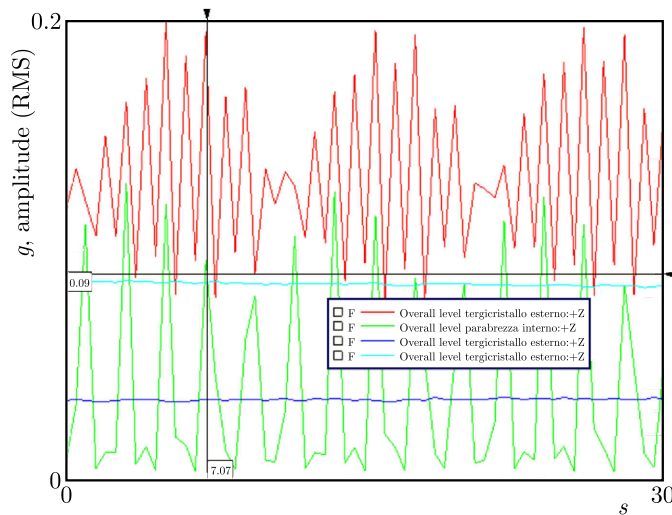


Fig. 6. Acceleration of the support bracket for the thermal engine “on” and the wiper “off” (blue curve – idle, cyan – 1500 rpm); acceleration of the support bracket (red curve) and the windshield (green curve) for the thermal engine “off” and the wiper “on”

Besides, the amplitude of acceleration of the support bracket, expressed in “g” units, is higher than the windshield one.

In the next figures, the background noise of the environment inside and outside the car are reported (the thermal motor and the wiper system in “off” condition) and besides the internal and external noise in the cases of three different wiper speeds (Vel1, Vel2 and Vel3).

Inside and outside the passenger compartment, the background noise is almost the same, even if at low frequencies is smaller inside due to attenuation generated by the windscreen of the car.

It can be noted that the noise with the wiper electrical motor “on” is higher than the background noise. The external noise is approximately the same for three different speeds of the wiper (Fig. 8), although the internal noise increases with the increasing of the speed (Fig. 9).

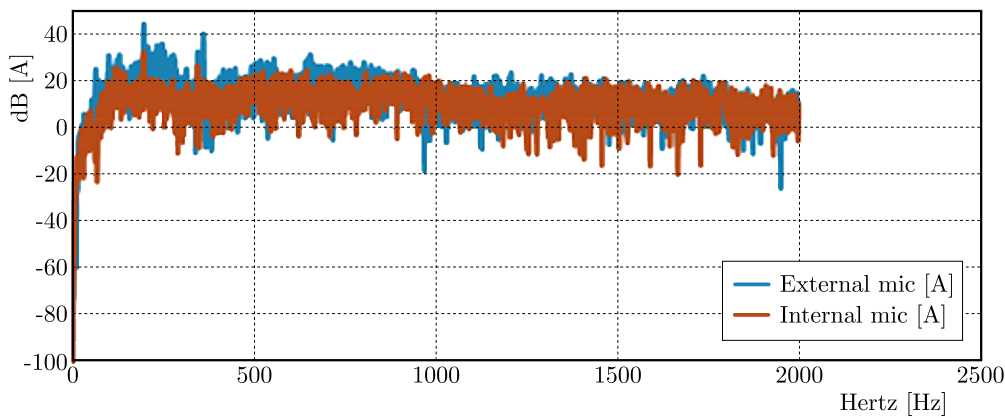


Fig. 7. Internal and external background noise diagrams [dB(A)]

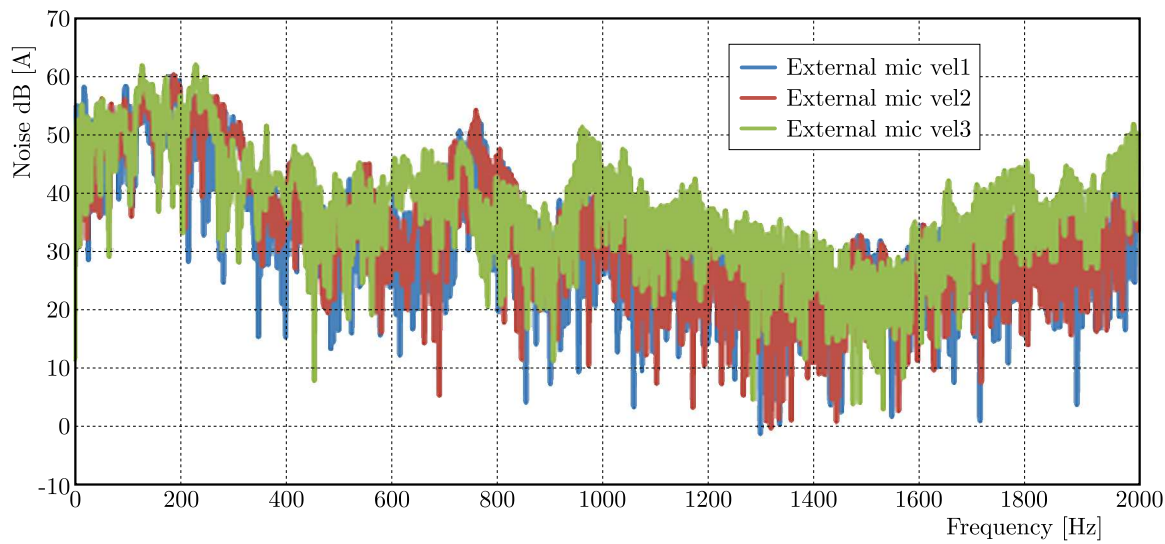


Fig. 8. External noise vs. variation of the wiper speed

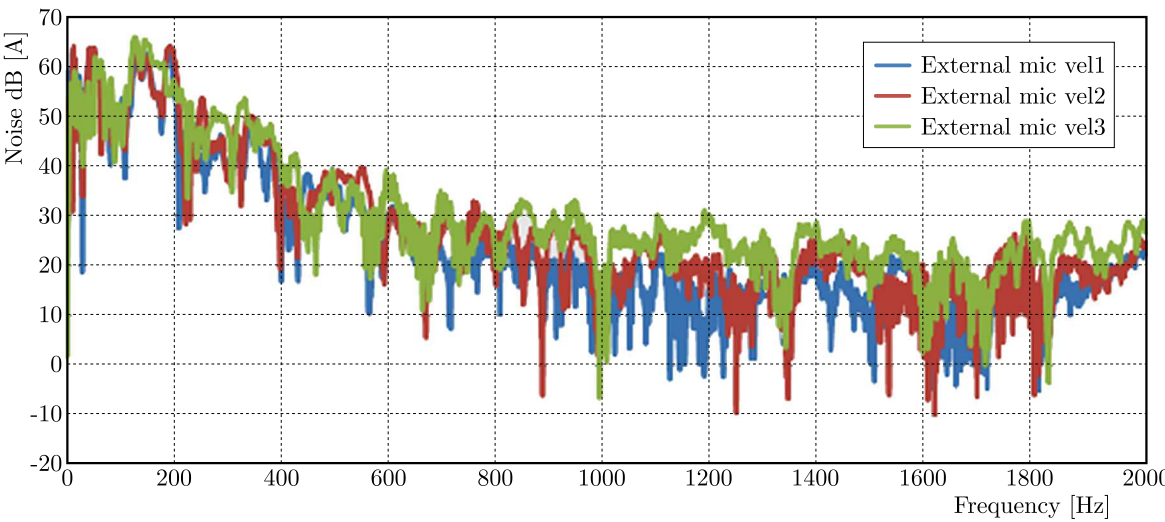


Fig. 9. Internal noise vs. variation of the wiper speed

Besides, it is evident that the perceived noise outside the vehicle is always greater than 1 dB compared to that received inside. This is due to the windscreen that acts as a soundproof.

The tests performed with accelerometers and microphones confirm that there are high peaks of acceleration and pressure in the frequency range between 600 Hz and 850 Hz (blue circle in Fig. 10) validating the preliminary numerical FE analysis.

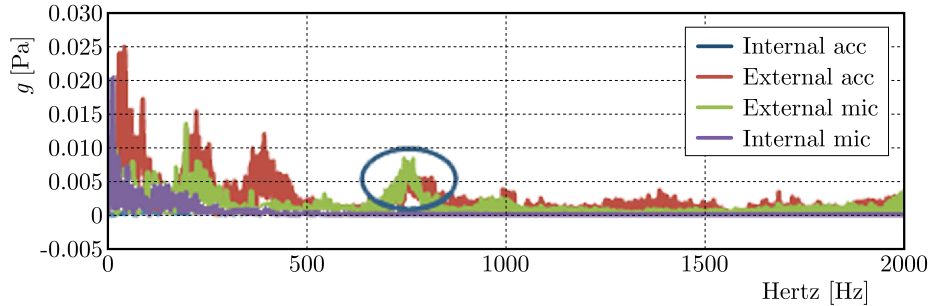


Fig. 10. Summary diagram of tests performed on the wiper at Vel2

5. Experimental set-up and dynamic characterization

In order to reproduce the same constraints with the chassis in the bonnet compartment of the car, an aluminum frame has been built carrying three clamping points. The wiper was installed on this frame (Fig. 3) in order to perform the test campaign.

At first, a dynamic characterization test was performed through the vibrations measured by a triaxial piezoelectric accelerometer placed on the bottom face of the support bracket (Fig. 4). The tests were carried out at two different electric motor velocities: Vel1 and Vel2. Moreover, the tests were conducted both with and without leverage (see Fig. 3) in order to left the support bracket free from the rotating kinematic system and to make vibrometer laser analysis (Fig. 11).

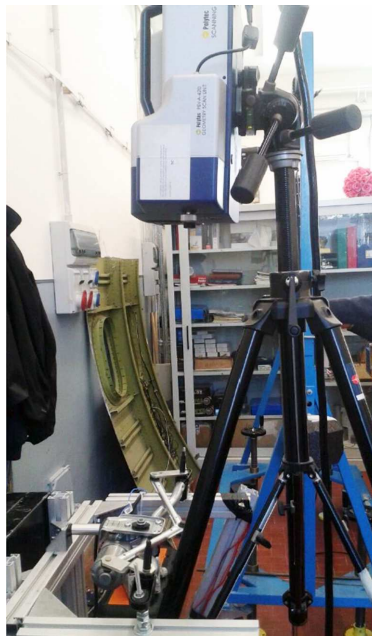


Fig. 11. Mechanical wiper system installed in the laboratory set-up with Polytec PSV-400 Scanning Vibrometer

Following graphs shows that the peak of acceleration has a light shift in the case of absence of leverage for both speeds of the wiper motor (from a value of 494 Hz to 540 Hz for Vel1 and from 760 Hz to 830 Hz for Vel2).

Besides, from the data analysis it results that acceleration values measured without leverage are generally greater than those measured with the leverage; the only exception is the acceleration referred to the y axis, which presents higher values when the leverage is present.

It is however clear that there is an influence of the presence of the leverage on the global dynamic behaviour of the wiper.

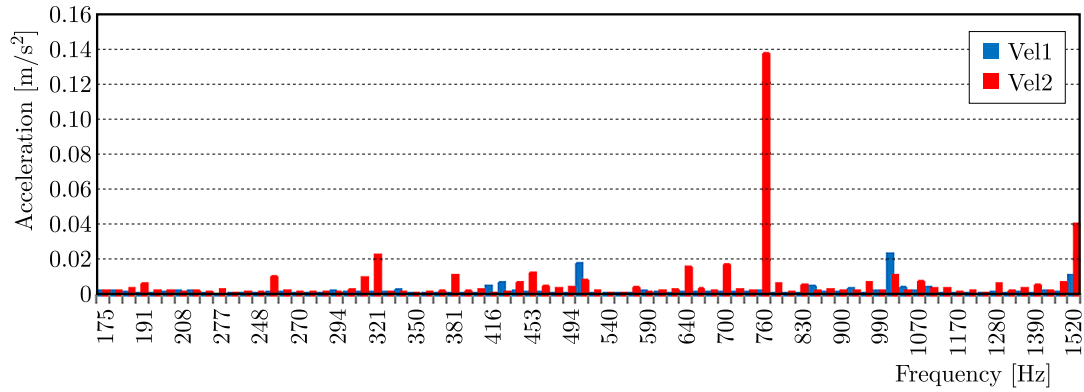


Fig. 12. Frequency spectrum (X axis) 1/24 octave with leverage

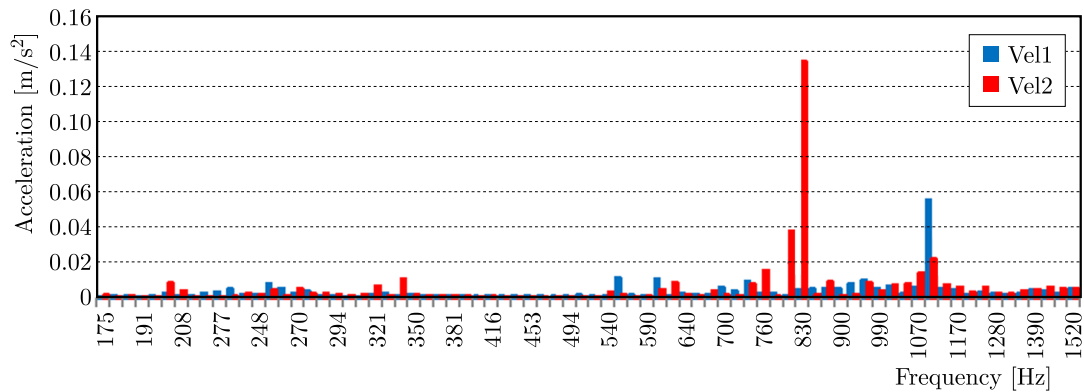


Fig. 13. Frequency spectrum (X axis) 1/24 octave without leverage

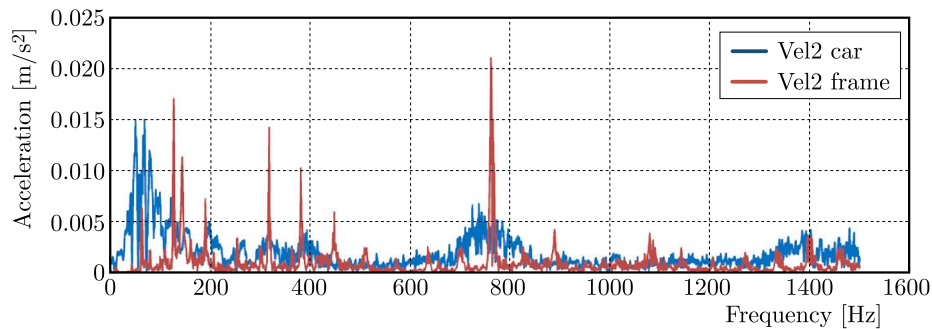


Fig. 14. Acceleration in the time domain (X axis) for tests on the car and on the set-up

There are some differences in the system behaviour depending on the typology of the main support (car chassis or frame structure).

In particular, the wiper blades provide a considerable amount of friction on the glass, which is an important noise source. To characterize the structural vibration of the support bracket, a Polytec PSV-400 scanning vibrometer was used. The laser was positioned at 550 mm from the surface of the bracket. In order to properly acquire displacements, velocities and accelerations of the brackets, all the following tests were carried out without leverage of the kinematic system because of their interference with the track of the laser beam.

The measurements have been conducted tracing a scanning grid composed of 176 dots on the support bracket surface and detecting, through the scanning vibrometer, the velocity of each point. The test has been performed both at Vel1 and Vel2 in order to identify eventual differential behaviour, focusing on modal shapes and frequency resonances in the range between 500 Hz and 850 Hz.

The following images (Figs. 15 and 16) have been achieved considering the Vel1 electric motor velocity.

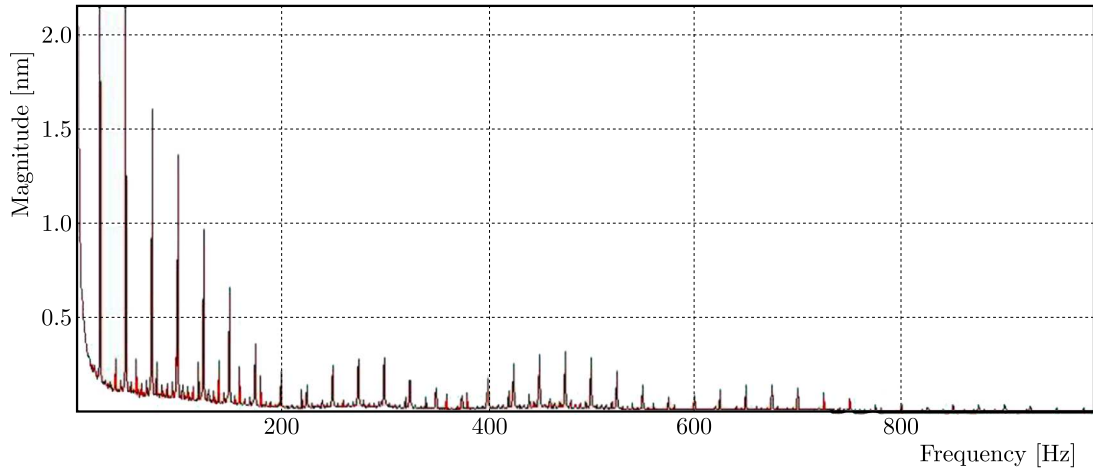


Fig. 15. FRF displacement vs frequency at Vel1 for the point of maximum displacement

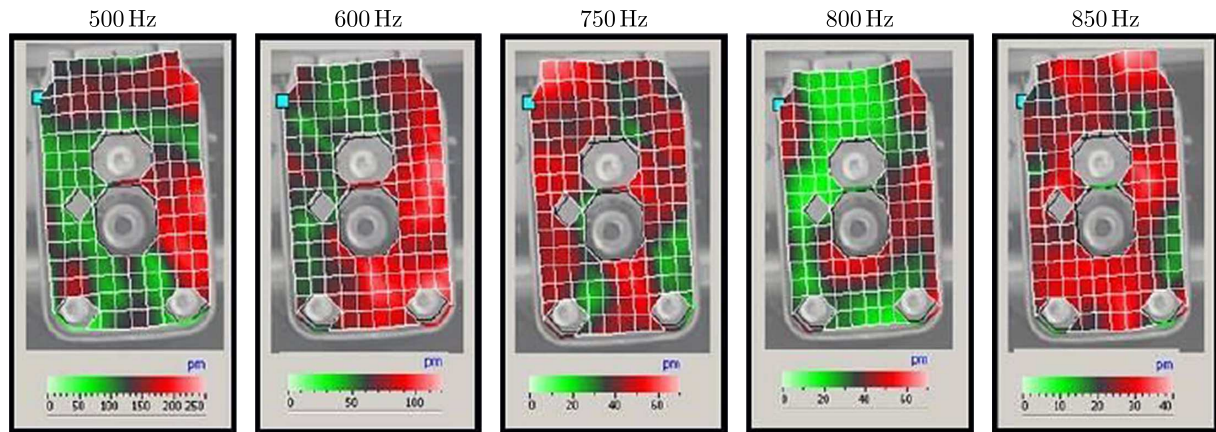


Fig. 16. Modes of vibrations images computed by PSV-400 scanning vibrometer at Vel1

It is clear that this curve is characterised by periodic behaviour with three repeated distinctive groups of peaks. According to this spectrogram, 500 Hz, 600 Hz, 750 Hz, 800 Hz and 850 Hz have been analysed in detail.

Modal shapes and strain distribution are required to optimize strain energy transmission from the SSSR to the bracket. It is in fact necessary to know the locations of the plate presenting the highest deformations in the frequency range during the test finalized to a good positioning of the piezo patch. The piezo devices must maximize the energy extracted from the mechanical part and convert it into the electrical energy for the control supply.

The map of displacements reported in Fig. 16 is used to compute the associated deformations by applying the following expression which comes from the definition of the discrete form of the second derivative linked to the strain by a half of the thickness t for a small displacement

$$\varepsilon = \frac{t}{2} \frac{w_{i-1} - 2w_i + w_{i+1}}{\Delta x^2} \quad (5.1)$$

where w is the transverse displacement measured by the vibrometer laser, and x is the coordinate in the plane.

In reference to the transversal displacements of the plate for the support bracket at 750 Hz, the maximum deformation is $4.4 \cdot 10^{-4} \mu\epsilon$.

6. Numerical analysis

The Nastran SOL111, has been used to verify the map of displacements at 750 Hz. In particular, the analysis shows that the modal shape for this frequency is characterized by a torsional deformation of the bracket around the axis of the central rivet connection (Fig. 17), thus highlighting the region with highest deformations and in accordance with the experimental data (blue circle in Fig. 16).

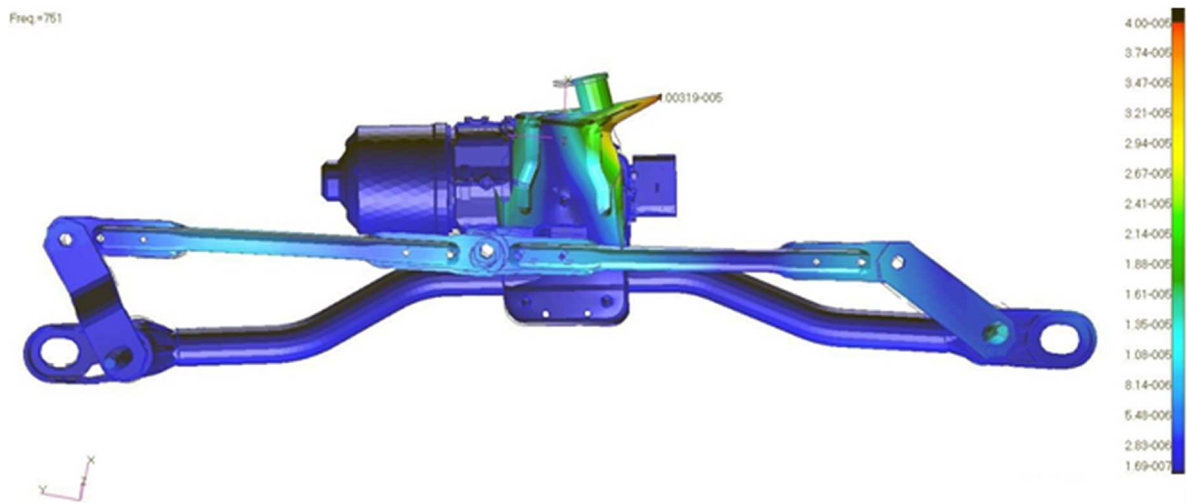


Fig. 17. Modes of vibration at 750 Hz by FEM analysis

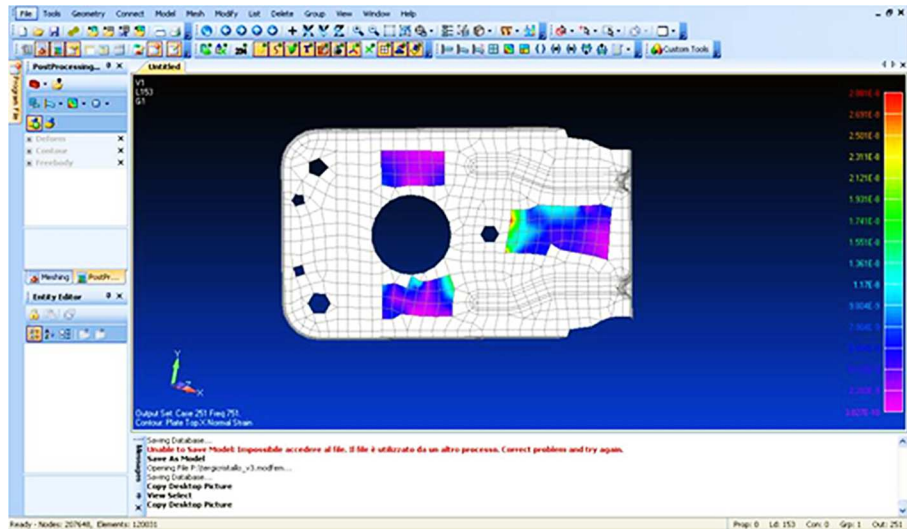


Fig. 18. In plane strain map

The strain energy map is also plotted, which shows that in the plane of the bracket the areas of most energy are around the central rivet and holes, as expected (Fig. 18). This analysis highlighted the areas of interest for deformation energy congruent with the experimental data.

In addition, this area is a unique suitable area, flat enough to bond the piezoelectric patch. In the same region, the finite element analysis shows deformation of the order of magnitude of $5 \cdot 10^{-4} \mu\epsilon$ in accordance with the experimental valuation.

7. Conclusion and future developments

An original study of a windshield wiper mechanical system has been herein reported. Theoretical analysis highlighted a mechanical imbalance transmitting vibrations to the wiper main body via the support bracket. This problem can be of high interest for future electrical cars design, in which motor noise Siano *et al.* (2016) will be negligible with respect to other mechanical subsystems causing annoyance to passengers.

The paper reports a preliminary feasibility study of a well established control technology on a new automotive application. A semi-passive shunt control technique opportunely designed for the vibrations reduction within the required frequency band has been here used to a new particular test case, namely a wiper mechanism for an automotive application. The paper at hand includes a preliminary experimental evaluation of the wiper assembly for vibrations control, supported by some FEA computations. The SSSR design is also described, followed by preliminary experimental results. The authors show possible issues with realistic damping of low amplitude vibrations of the wiper system bracket. However this technique seems to more adequately face this type of application in respect to other ANC and AVC approaches (Magliacano *et al.*, 2016a,b).

A real windshield wiper mechanical system has been then installed on a steel truss support. The constraint has been reproduced according to the car schematics, the engine has been powered and the transmitted vibrations have been detected via vibrometer laser instrumentation.

Due to complex geometry of the wiper characterized by sharp curvatures and local stiffeners, only short areas have been available for secondary bonding of sensors. Strain gauges and pzt have been installed and the energy strain level has been correlated and compared to the vibrometer output.

The results were in good agreement, thus showing the robustness of the predicted numerical evaluations and applied methodologies. Nevertheless, the results showed very low deformations. The implementation of a semi-passive shunt control could be applied with some restrictions. A Synchronized Switch Shunt Resonator proved to be the most promising technical solution, according to the mechanical specifications, but requiring a very sensitive transducer device on the same time.

Acknowledgments

The present work has been part of the Low Noise project, co-financed by the Italian University and Research Industry. The authors of the present work address an acknowledgement to all partners involved in the project but special thanks are addressed to Gaetano Arena for his strong, enthusiastic and effective support in the development of the experimental activity in the laboratory of Aerospace Section of the Industrial Engineering Department of the University Federico II in Naples.

References

1. AMEDURI S., CIMINELLO M., 2010, Fourier expansion solution for a Switched Shunt Control applied to a duct, *Journal of Theoretical and Applied Mechanics*, **48**, 2
2. BADEL A., SEBALD G., GUYOMAR D., LALLART M., LEFEUVRE E., RICHARD C., 2006, Piezo-electric vibration control by synchronized switching on adaptive voltage sources: Towards wideband semi-active damping, *Journal of Acoustics Society American*, **119**, 5, 2815-2825

3. CIMINELLO M., CALABRÒ A., AMEDURI S., CONCILIO S., 2008, Synchronized Switched Shunt Control technique applied on a cantilevered beam: experimental investigations, *Journal of Intelligent Material Systems and Structures*, **19**, 9, 1089-1100
4. CIMINELLO M., LECCE L., AMEDURI S., CALABRÒ A., CONCILIO S., 2010, Multi-tone Switching Shunt Control by a PZT network embedded into a fiberglass panel: design, manufacture, and test, *Journal of Intelligent Material Systems and Structures*, **21**, 437-451
5. CLARK W.W., 1999, Semi-active vibration control with piezoelectric materials as variable stiffness actuators, *AIAA/ASME/ASCE/AHS/ASC Structures, Structural Dynamics, and Materials Conference and Exhibit*, Part 4
6. GUYOMAR D., RICHARD C., PETIT L., 2001, Non-linear system for vibration damping, *142th Meeting of Acoustical Society of America*, Fort Lauderdale, USA
7. HOLLKAMP J.J., 1994, Multimodal passive vibration suppression with piezoelectric materials and resonant shunts, *Journal of Intelligent Material Systems and Structures*, **5**, 49-56
8. MAGLIACANO D., VISCARDI M., CIMINELLO M., DIMINO I., CONCILIO A., 2016a, Feasibility study for a tonal vibration control system of a mounting bracket for automotive gearboxes, *International Journal of Mechanics*, **10**, 403-410
9. MAGLIACANO D., VISCARDI M., DIMINO I., CONCILIO A., 2016b, Active vibration control by piezoceramic actuators of a car floor panel, *23rd International Congress on Sound and Vibration, ICSV*
10. MAKIHARA K., ONODA J., MINESUGI K., 2005, Low-energy-consumption hybrid vibration suppression based on an energy-recycling approach, *AIAA Journal*, **43**, 8, 1706-1715
11. MAKIHARA K., ONODA J., MINESUGI K., 2007a, A self-sensing method for switching vibration suppression with a piezoelectric actuator, *Smart Materials and Structures*, **162**, 2, 455-461
12. MAKIHARA K., ONODA J., MINESUGI K., 2007b, Comprehensive assessment of semi-active vibration suppression including energy analysis, *Journal of Vibration and Acoustics*, **129**, 84-93
13. MAKIHARA K., ONODA J., MINESUGI K., 2007c, Using tuned electrical resonance to enhance bang-bang vibration control, *AIAA Journal*, **45**, 2, 497-504
14. ONODA J., MAKIHARA K., MINESUGI K., 2003, Energy-recycling semi-active method for vibration suppression with piezoelectric transducers, *AIAA Journal*, **41**, 4, 711-719
15. PETIT L., LEFEUVRE E., RICHARD C., GUYOMAR D., 2004, A broadband semipassive piezoelectric technique for structural damping, *SPIE International Symposium on Smart Structures and Materials: Damping and Isolation*, San Diego, CA, USA
16. QIU J., JI H., ZU K., 2009, Semi-active vibration control using piezoelectric actuators in smart structures, *Frontiers of Mechanical Engineering in China*, **4**, 3, 242-251
17. RICHARD C., GUYOMAR D., AUDIGIER D., CHING G., 1998, Semi-passive damping using continuous switching of a piezoelectric device, *SPIE Smart Structures and Materials Conference: Passive Damping and Isolation*, San Diego
18. SIANO D., VISCARDI M., PANZA M.A., 2016, Automotive Materials: An Experimental Investigation of an Engine Bay Acoustic Performances, *Energy Procedia*, **101**, 598-605
19. VISCARDI M., DI LEO R., 2016, Implementation of an electronic circuit for SSSA control approach of a plate type element and experimental match with a feed-forward approach, *Archive of Mechanical Engineering*, **LXIII**, 4, 665-677

OPTIMUM DESIGN OF FIBER ANGLE AND HOLE ORIENTATION OF AN ORTHOTROPIC PLATE

XIAOLI ZHANG, AIZHONG LU, SHAOJIE WANG, NING ZHANG

North China Electric Power University, Institute of Hydroelectric and Geotechnical Engineering, Beijing, China
e-mail: zning1125@ncepu.edu.cn (N. Zhang)

With the goal of decreasing the stress concentration along the hole boundary in an orthotropic plate under inequi-biaxial loadings, an optimum design of the fiber angle and hole orientation is presented. The maximum absolute tangential stress along the hole boundary is taken as the objective function, and the fiber orientation angle and the hole orientation angle are considered as design variables. The conformal transformation method of a complex function and the Differential Evolution (DE) algorithm are used. Two non-circular shapes, ellipse and hexagon are taken as examples to analyze the problem. Based on the results, we can conclude that the major axis of elliptical holes should be designed in the direction of the maximum external loading for a perforated structure in an orthotropic plate. However, the principal direction that has the larger Young's modulus should be inclined to the direction of the minimum loading, especially for a significantly orthotropic plate.

Keywords: orthotropic plate, fiber orientation angle, hole orientation angle, conformal transformation method, differential evolution algorithm

1. Introduction

Natural materials, such as wood and rock, and composite materials, such as fiberboard, epoxy resin bonded fiber and fiber reinforced polymer, all display anisotropic properties. Specifically, orthotropic plates with different holes have found widespread applications in various fields such as aerospace, marine, automobile and mechanics because of high specific stiffness and specific strength as well as the designability of the properties (Jain, 2009; Romeo, 2001; Li and Zheng, 2007). The stress concentration along the boundary of the hole becomes an important research problem for this structure (Toubal *et al.*, 2005; Sharma, 2011; Engels *et al.*, 2001). Generally, tangential stresses at different points along the hole boundary in orthotropic plates are different and, usually, it is the maximum value that depends the stability on the plate (Savin, 1961). Thus, it is important to decrease the tangential stress concentration along the hole boundary in the design of orthotropic plates.

Some researchers have studied the shape optimization of holes in isotropic plates based on different optimization criteria or methods. Bjorkman and Richards (1976, 1979) proposed the concept of a harmonic hole and obtained the optimal shape of the hole under different loads. Taking the minimum integration of the square of tangential stress as the objective, Dhira (1981) solved a series of shape optimization problems by the complex variables function, the same method as Bjorkman. Aiming at minimizing the maximum value of the tangential stress along the hole boundary, Lu *et al.* (2014a,b) obtained the optimum shape of the support section of a tunnel at great depths using the complex variables function method. The hole-shape optimization problem has also been solved using the Evolutionary Structural Optimization (ESO) procedure (Ren *et al.*, 2005) and the Simulated Annealing (SA) procedure (Sobótka *et al.*, 2013).

So far, the existing studies have mainly focused on the shape optimization of hole in isotropic plates to decrease stress concentration. For many practical applications, however, the shape

of the hole is always determined by some specific demands. Hence, the optimization results sometimes cannot meet the actual requirement. Furthermore, many plates in actual applications are orthotropic. For orthotropic plates, however, the determination of stress distribution is more complex than that for isotropic plates. Lekhnitskii (1968, 1981) used the complex function method, developed by Muskhelishvili (1963), to determine the stress in an anisotropic plate, and gave an accurate solution of stress around an elliptic hole under in-plane loading at infinity. Some researchers have obtained analytical solutions for other non-elliptic holes (Romeo, 2001; Rao *et al.*, 2010; Daoust and Hoa, 1991; Ukadgaonker and Kakhandki, 2005; Rezaeepazhand and Jafari, 2008). Lu *et al.* (2015) found an accurate analytic solution of stress for plates with an arbitrarily shaped hole using the power-series method.

It can be seen from the stress analysis of an orthotropic plate that the stress distribution along the hole boundary mainly depends on the fiber orientation angle and the hole orientation angle for certain loadings and hole shapes. Therefore, how to decide the two angles of an orthotropic plate in minimization of the stress concentration is important. Sharma *et al.* (2014) researched the optimization of fiber orientation angle for single lamina of composite materials (graphite/epoxy and glass/epoxy) with circular and elliptical holes; however, the hole orientation angle was not taken into consideration. In this paper, not only the fiber orientation angle but also the hole orientation angle are taken into consideration, and other more complicated shapes of holes are considered, in which the maximum absolute value of the tangential stress reaches its minimum value.

Herein, the Differential Evolution (DE) algorithm (Storn and Price, 1997) is used, and the following assumptions are made: the orthotropic plate is infinite and elastic under the in-plane loading at infinity (see Fig. 1); the problem can be treated as a plane stress problem.

2. Fundamental theories

Although the optimization of fiber orientation angle and hole orientation of an orthotropic plate is an inverse problem, the process of obtaining the optimal results requires solving a series of forward problems. In every optimization process, the solution for the tangential stress along the hole boundary should be based on the material properties, external loads, shapes and orientation angles of the hole. In this paper, the conformal transformation method of the complex function is adopted to first map the outer regions of the hole in the physical plane to the outer regions of the unit circle in the image plane. Then, the analytical solution of stress along the hole boundary can be obtained using the power-series method.

2.1. Transformation of the mapping function under different coordinates

Figure 1 illustrates an orthotropic plate with an arbitrarily shaped hole under an in-plane loading. xoy is the global Cartesian coordinate system, where x and y are along the directions of σ_x^∞ and σ_y^∞ , respectively. x_1oy_1 and $x'oy'$ are two local Cartesian coordinates. x_1 is the symmetric axis of the hole, and the angle α between the positive direction of the x -axis and x_1 -axis denotes the hole orientation. x' and y' are along the principal direction of the elastic materials, and the angle φ denotes the fiber orientation. The outer region of the hole in the local coordinates x_1oy_1 (z -plane) is mapped to the outer region of the unit circle (ζ -plane) using the following mapping function

$$z_* = x_1 + iy_1 = R_1 \left(\zeta + \sum_{k=1}^n C_k \zeta^{-k} \right) \quad (2.1)$$

where $i = \sqrt{-1}$, and R_1 is a real constant and C_k are complex constants denoting the size and shape of the hole, respectively. $\zeta = \rho e^{i\theta}$ (θ is the polar angle in the ζ -plane, $\rho = 1$ on the hole

boundary). When n is large enough, Eq. (2.1) can describe a variety of shapes of the hole. The mapping function in the global coordinates should be obtained using the following method due to the change of the hole orientation angle.

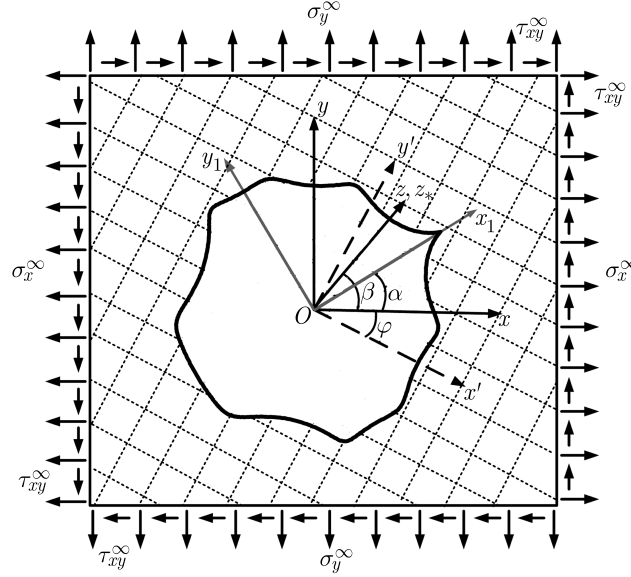


Fig. 1. Orthotropic plate with an arbitrarily shaped hole under an in-plane loading

As shown in Fig. 1, the local coordinates x_1oy_1 overlap the global coordinates xoy after rotating α degrees clockwise. The vector z ($z = x + iy$) with a length of r in the coordinates xoy makes an angle β with the x -axis.

In the global coordinates xoy

$$z = re^{i\beta} \quad (2.2)$$

In the local coordinates x_1oy_1

$$z_* = re^{i(\beta-\alpha)} \quad (2.3)$$

Then, Eq. (2.4) can be obtained because Eqs. (2.2) and (2.3) share the same vector z

$$z_* = re^{i(\beta-\alpha)} = e^{-i\alpha} re^{i\beta} = e^{-i\alpha} z \quad (2.4)$$

Then

$$z = \omega(\zeta) = e^{i\alpha} z_* = e^{i\alpha} R_1 \left(\zeta + \sum_{k=1}^n C_k \zeta^{-k} \right) = R \left(\zeta + \sum_{k=1}^n C_k \zeta^{-k} \right) \quad (2.5)$$

It can be seen that the mapping function in the coordinates xoy can be easily determined by Eq. (2.5) as long as the corresponding mapping function in the coordinates x_1oy_1 is given even if the hole orientation angle α changes. Changing the real constant R_1 in Eq. (2.1) to a complex constant R ($R = R_1 e^{i\alpha}$) is what we need to do.

2.2. The affine transformation and mapping

The three complex variables involved in solving the anisotropic plane problems are z , z_1 and z_2 , and the affine mathematical relationships between the three complex variables are

$$\begin{aligned} z_1 &= x + \mu_1 y = \gamma_1 z + \delta_1 \bar{z} \\ z_2 &= x + \mu_2 y = \gamma_2 z + \delta_2 \bar{z} \end{aligned} \quad (2.6)$$

where $\gamma_1 = (1 - i\mu_1)/2$, $\gamma_2 = (1 - i\mu_2)/2$, $\delta_1 = (1 + i\mu_1)/2$, $\delta_2 = (1 + i\mu_2)/2$, $\mu_1 = \alpha_1 + i\beta_1$, $\mu_2 = \alpha_2 + i\beta_2$, α_k and β_k ($k = 1, 2$) are real constants related to the material properties.

If three polar coordinates are introduced, and by transforming the outer regions of the hole in the z -, z_1 -, and z_2 -planes into the outer regions of the unit circle in the ζ -, ζ_1 -, and ζ_2 -planes, respectively, the three mapping functions which satisfy Eqs. (2.6) can then be obtained. The three mapping functions are expressed by $z = \omega(\zeta)$, $z_1 = \omega_1(\zeta_1)$ and $z_2 = \omega_2(\zeta_2)$, respectively (Lu *et al.*, 2015)

$$\begin{aligned} z_1 = \omega_1(\zeta_1) &= \gamma_1 R \left(\zeta_1 + \sum_{k=1}^n C_k \zeta_1^{-k} \right) + \delta_1 \bar{R} \left(\frac{1}{\zeta_1} + \sum_{k=1}^n \bar{C}_k \zeta_1^k \right) \\ z_2 = \omega_2(\zeta_2) &= \gamma_2 R \left(\zeta_2 + \sum_{k=1}^n C_k \zeta_2^{-k} \right) + \delta_2 \bar{R} \left(\frac{1}{\zeta_2} + \sum_{k=1}^n \bar{C}_k \zeta_2^k \right) \end{aligned} \quad (2.7)$$

where $\zeta_1 = \rho_1 e^{i\theta_1}$ and $\zeta_2 = \rho_2 e^{i\theta_2}$. The angles θ_1 and θ_2 are the polar angles in the ζ_1 - and ζ_2 -planes, respectively. $\rho_1 = \rho_2 = 1$ on the hole boundary.

Assuming that $\zeta_1 = \zeta_2 = \zeta = \sigma = e^{i\theta}$ along the unit circle, the relationships between ζ , ζ_1 and ζ_2 can also be established

$$\begin{aligned} \gamma_1 R \left(\zeta_1 + \sum_{k=1}^n C_k \zeta_1^{-k} \right) + \delta_1 \bar{R} \left(\frac{1}{\zeta_1} + \sum_{k=1}^n \bar{C}_k \zeta_1^k \right) &= \gamma_1 R \left(\zeta + \sum_{k=1}^n C_k \zeta^{-k} \right) + \delta_1 \bar{R} \left(\bar{\zeta} + \sum_{k=1}^n \bar{C}_k \bar{\zeta}^{-k} \right) \\ \gamma_2 R \left(\zeta_2 + \sum_{k=1}^n C_k \zeta_2^{-k} \right) + \delta_2 \bar{R} \left(\frac{1}{\zeta_2} + \sum_{k=1}^n \bar{C}_k \zeta_2^k \right) &= \gamma_2 R \left(\zeta + \sum_{k=1}^n C_k \zeta^{-k} \right) + \delta_2 \bar{R} \left(\bar{\zeta} + \sum_{k=1}^n \bar{C}_k \bar{\zeta}^{-k} \right) \end{aligned} \quad (2.8)$$

Equations (2.8) are suitable for any point in the region $|\zeta| \geq 1$. Given a point ζ , then points ζ_1 and ζ_2 can be determined by Eqs. (2.8). z , z_1 , and z_2 can be calculated by Eqs. (2.5) and (2.7), respectively.

2.3. Calculation of the analytical solution of stress

For the plane stress problem of an orthotropic plane, when the body forces are not taken into consideration, the compatibility equation for Airy's stress function $F = F(x', y')$ in the local coordinates $x'oy'$ can be given as (Lekhnitskii, 1968, 1981)

$$a'_{22} \frac{\partial^4 F}{\partial x'^4} - 2a'_{26} \frac{\partial^4 F}{\partial x'^3 \partial y'} + (2a'_{12} + a'_{66}) \frac{\partial^4 F}{\partial x'^2 \partial y'^2} - 2a'_{16} \frac{\partial^4 F}{\partial x' \partial y'^3} + a'_{11} \frac{\partial^4 F}{\partial y'^4} = 0 \quad (2.9)$$

where a'_{ij} are constants related to the material properties. The solution to Eq. (2.9) is related to the roots of the following characteristic equation

$$a'_{11} \mu'^4 - 2a'_{16} \mu'^3 + (2a'_{12} + a'_{66}) \mu'^2 - 2a'_{26} \mu' + a'_{22} = 0 \quad (2.10)$$

The four conjugate complex roots in Eq. (2.10) are $\mu'_1, \bar{\mu}'_1, \mu'_2$ and $\bar{\mu}'_2$, which can be calculated by the principal elastic constants. However, the complex roots in the global coordinates xoy should be calculated due to the change of the fiber orientation. When the local coordinates $x'oy'$ overlap the global coordinates xoy after rotating φ degrees counter clockwise, μ_1 and μ_2 in the global coordinates can be given as (Lekhnitskii, 1968)

$$\mu_1 = \frac{\mu'_1 \cos \varphi - \sin \varphi}{\cos \varphi + \mu'_1 \sin \varphi} \quad \mu_2 = \frac{\mu'_2 \cos \varphi - \sin \varphi}{\cos \varphi + \mu'_2 \sin \varphi} \quad (2.11)$$

In this paper, only the situation of $\mu_1 \neq \mu_2$ is discussed. The solution to Eq. (2.9) can be expressed by the two analytical functions $F_1(z_1)$ and $F_2(z_2)$ as

$$F = 2\text{Re}[F_1(z_1) + F_2(z_2)] \quad (2.12)$$

where z_1 and z_2 are exactly the same as given in the previous Sections.

Let $\Phi_1(z_1) = dF_1(z_1)/dz_1$ and $\Phi_2(z_2) = dF_2(z_2)/dz_2$, respectively. The stress boundary conditions on the edge of the hole expressed by $\Phi_1(z_1)$ and $\Phi_2(z_2)$ can be given as

$$\begin{aligned} 2\text{Re}[\Phi_1(z_1) + \Phi_2(z_2)] &= f_1 \\ 2\text{Re}[\mu_1\Phi_1(z_1) + \mu_2\Phi_2(z_2)] &= f_2 \end{aligned} \quad (2.13)$$

where z_1 and z_2 are two points on the boundary.

The problem discussed here is an infinite field with holes, and no loads exist along the edge of the hole. Therefore, $f_1 = f_2 = 0$, and $\Phi_1(z_1)$ and $\Phi_2(z_2)$ can be given in the following form

$$\Phi_1(z_1) = B^*z_1 + \Phi_1^0(z_1) \quad \Phi_2(z_2) = (B'^* + iC'^*)z_2 + \Phi_2^0(z_2) \quad (2.14)$$

where B^* , B'^* , and C'^* can be determined according to the stress components acting at infinity (i.e., σ_x^∞ , σ_y^∞ and τ_{xy}^∞) as

$$\begin{aligned} B^* &= \frac{\sigma_x^\infty + (\alpha_2^2 + \beta_2^2)\sigma_y^\infty + 2\alpha_2\tau_{xy}^\infty}{2[(\alpha_2 - \alpha_1)^2 + (\beta_2^2 - \beta_1^2)]} \\ B'^* &= \frac{(\alpha_1^2 - \beta_1^2 - 2\alpha_1\alpha_2)\sigma_y^\infty - \sigma_x^\infty - 2\alpha_2\tau_{xy}^\infty}{2[(\alpha_2 - \alpha_1)^2 + (\beta_2^2 - \beta_1^2)]} \\ C'^* &= \frac{(\alpha_1 - \alpha_2)\sigma_x^\infty + [\alpha_2(\alpha_1^2 - \beta_1^2) - \alpha_1(\alpha_2^2 - \beta_2^2)]\sigma_y^\infty + [(\alpha_1^2 - \beta_1^2) - (\alpha_2^2 - \beta_2^2)]\tau_{xy}^\infty}{2\beta_2[(\alpha_2 - \alpha_1)^2 + (\beta_2^2 - \beta_1^2)]} \end{aligned}$$

Here, $\Phi_1^0(z_1)$ and $\Phi_2^0(z_2)$ in Eqs. (2.14) should have the following form after substituting $z_1 = \omega_1(\zeta_1)$ and $z_2 = \omega_2(\zeta_2)$ into them

$$\Phi_1^0(z_1) = \Phi_1^0[\omega_1(\zeta_1)] = \sum_{k=0}^{\infty} a_k \zeta_1^{-k} \quad \Phi_2^0(z_2) = \Phi_2^0[\omega_2(\zeta_2)] = \sum_{k=0}^{\infty} b_k \zeta_2^{-k} \quad (2.15)$$

where $a_k = a_{1k} + ia_{2k}$, $b_k = b_{1k} + ib_{2k}$, a_{1k} , a_{2k} , b_{1k} and b_{2k} are undetermined real constants ($k = 0, \dots, \infty$).

Along the edge of the hole, $\zeta_1 = \sigma = e^{i\theta}$ and $\zeta_2 = \sigma = e^{i\theta}$. The undetermined coefficients a_k and b_k can be determined from Eqs. (2.13)-(2.15) by using the power-series method. Then, the stress components σ_x , σ_y and τ_{xy} in the Cartesian coordinates can be determined by the following equations (Lu *et al.*, 2015)

$$\begin{aligned} \sigma_x &= 2\text{Re}[\mu_1^2\Phi_1'(z_1) + \mu_2^2\Phi_2'(z_2)] & \sigma_y &= 2\text{Re}[\Phi_1'(z_1) + \Phi_2'(z_2)] \\ \tau_{xy} &= -2\text{Re}[\mu_1\Phi_1'(z_1) + \mu_2\Phi_2'(z_2)] \end{aligned} \quad (2.16)$$

where

$$\begin{aligned} \Phi_1'(z_1) &= B^* - \sum_{k=1}^n k a_k \zeta_1^{-k-1} / \left[\gamma_1 R \left(1 - \sum_{k=1}^n k C_k \zeta_1^{-k-1} \right) + \delta_1 \overline{R} \left(-\frac{1}{\zeta_1^2} + \sum_{k=1}^n k \overline{C}_k \zeta_1^{k-1} \right) \right] \\ \Phi_2'(z_2) &= B'^* + iC'^* - \sum_{k=1}^n k b_k \zeta_2^{-k-1} / \left[\gamma_2 R \left(1 - \sum_{k=1}^n k C_k \zeta_2^{-k-1} \right) + \delta_2 \overline{R} \left(-\frac{1}{\zeta_2^2} + \sum_{k=1}^n k \overline{C}_k \zeta_2^{k-1} \right) \right] \end{aligned} \quad (2.17)$$

The stress components σ_ρ , σ_θ and $\tau_{\rho\theta}$ in orthogonal curvilinear coordinates can be determined by the following equations

$$\sigma_\rho + \sigma_\theta = \sigma_x + \sigma_y \quad \sigma_\theta - \sigma_\rho + 2i\tau_{\rho\theta} = \frac{\zeta^2 \omega'(\zeta)}{\rho^2 \overline{\omega'(\zeta)}} (\sigma_y - \sigma_x + 2i\tau_{xy}) \quad (2.18)$$

Along the hole boundary where $\zeta_1 = \zeta_2 = \zeta = \sigma = e^{i\theta}$ and $\rho = 1$, the analytical solution of stress can be solved easily by Eqs. (2.16)-(2.18). In this way, when the mapping functions are known and the material parameters and external loads are given, no matter how the fiber orientation angle and hole orientation angle change, the analytical solution of the stress along and near the hole boundary can be calculated. In addition, this analytical solution of the stress is suitable for an arbitrarily shaped hole.

2.4. Optimization

Tangential stress concentration along the boundary of the hole will cause damage if its magnitude exceeds the material strength. Consequently, the optimization criterion we take is that the absolute maximum value of the tangential stress along the hole boundary should be kept at the minimum. In the optimization, the fiber orientation angle φ and the hole orientation angle α are the unknown variables. A set of the initial values of φ and α are given; then, the tangential stress with the maximum absolute value $\max|\sigma_\theta|$ could be obtained through the complex variable method. By revising the values of design variables φ and α , the final values of $\hat{\varphi}$ and $\hat{\alpha}$ that lead to the minimal value of $\max|\sigma_\theta|$ should be the optimized results. The mathematical model could be expressed as follows

$$\begin{aligned} F(X) &= \max_{\theta \in [0, 2\pi]} |\sigma_\theta| \\ \min F(X) \quad & X \in D = \{\varphi, \alpha\} \\ \text{s.t.} \quad & 0 \leq \varphi \leq 2\pi \quad 0 \leq \alpha \leq 2\pi \end{aligned} \quad (2.19)$$

The original DE algorithm (Storn and Price, 1997) is used in the computations. It can be written as DE/rand/1/bin. As defined by Storn and Price, the DE algorithm is characterized by three main parameters NP , F and CR as

$$\begin{aligned} x_{i,G} \quad & i = 1, 2, \dots, NP \\ v_{i,G+1} &= x_{r1,G} + F(x_{r2,G} - x_{r3,G}) \\ u_{ji,G+1} &= \begin{cases} v_{ji,G+1} & \text{if } (randb(j) \leq CR) \quad \vee \quad j = rnbr(i) \\ x_{ji,G} & \text{if } (randb(j) > CR) \quad \wedge \quad j \neq rnbr(i) \end{cases} \quad j = 1, 2, \dots, D \end{aligned} \quad (2.20)$$

In this paper, the number of population vectors NP equals 200. The real and constant factor F equals 0.8, and the crossover constant CR is equal to 0.5.

3. Examples

As shown in Fig. 1, the external loads are chosen as $\sigma_x^\infty : \sigma_y^\infty = 2 : 7$ and $\tau_{xy}^\infty = 0$. Sign convention is defined as positive for tension and negative for compression. It can be seen from the results of the following examples that all of the maximum tangential stresses are tensile stresses. The values of the independent principal elastic constants in the local coordinates $x'oy'$ are: $E_1 = 1.4 \cdot 10^5$ Pa, $\nu_{12} = 0.46$ and $G_{12} = 1.2 \cdot 10^4$ Pa, where the subscripts 1 and 2 represent the directions along the x' - and y' -axis, respectively. To analyze the effect of Young's modulus on the optimization results, we take different values of E_2/E_1 , i.e., 0.2, 0.5, 2.0 and 5.0. The

material coefficients in Eq. (2.9) can be obtained by the three elastic constants as $a'_{11} = 1/E_1$, $a'_{22} = 1/E_2$, $a'_{16} = a'_{26} = 0$, $a'_{12} = -\nu_{12}/E_1$, and $a'_{66} = 1/G_{12}$ (Lekhnitskii, 1968; Chen, 1994).

The hexagonal hole and the elliptical hole are selected as examples. The size of the hole has no influence on the calculation of the stress field, because the domain occupied by the plate is infinite. In order not to lose the generality, take $R_1 = 1.0$. The mapping function of Eq. (2.5) can be described as

$$z = \omega(\zeta) = 1.0e^{i\alpha} \left(\zeta + \sum_{k=1}^n C_k \zeta^{-k} \right) \quad (3.1)$$

The imaginary part of the coefficient C_k is equal to zero, because the hole shapes of the examples are all symmetric about the x_1 -axis.

For the elliptical hole: $a/b = 1.5$, $n = 1$, $C_1 = (a - b)/(a + b) = 0.2$.

For the hexagonal hole: $n = 29$, $C_5 = 0.0667$, $C_{11} = 0.0101$, $C_{17} = 0.0036$, $C_{23} = 0.0018$ and $C_{29} = 0.0010$ (Savin, 1961). The other C_k are all equal to zero.

3.1. Optimization of the fiber orientation angle φ

In this Section, only the fiber orientation angle φ is taken as the design variable, while the external loads and hole orientation angle α are given. The hole orientation angle α shown in Fig. 1 is set to 0° (see Fig. 2), meaning that the coordinates x_1oy_1 coincide with xoy . The local coordinates $x'oy'$ still follow the fiber orientation, coinciding with xoy after rotation by φ degrees counterclockwise. The scope of the optimized variable is $\varphi \in 0^\circ\text{--}90^\circ$ because of the symmetry of the external loads and the hole shape.

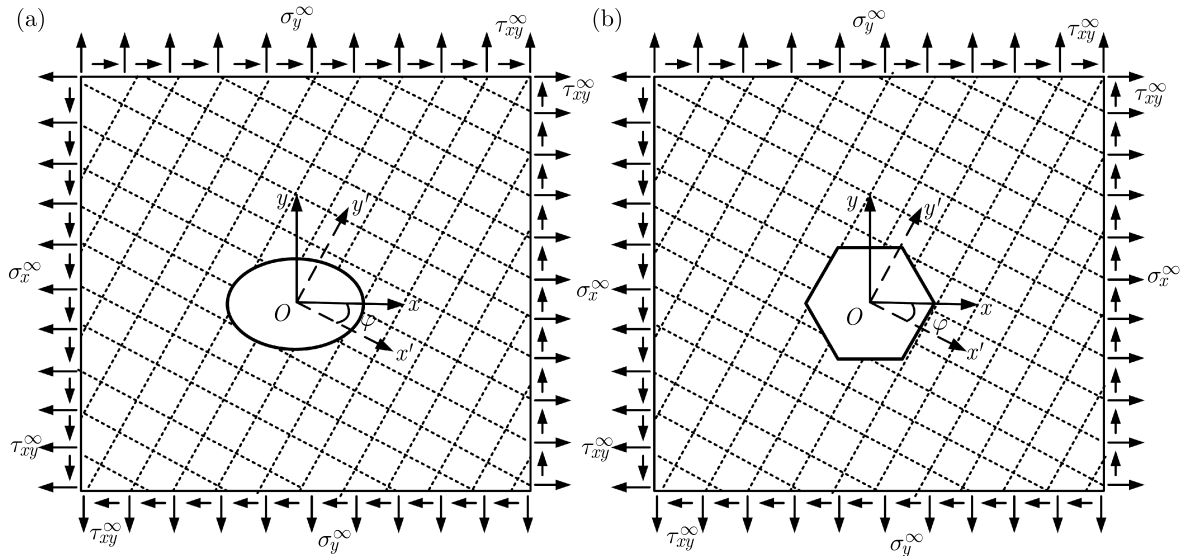


Fig. 2. The location of holes with two coordinates: (a) elliptical hole, (b) hexagonal hole

3.1.1. Elliptical hole

The optimal fiber orientation and its corresponding tangential stress along the boundary of the elliptical hole are illustrated in Figs. 3 and 4, respectively. The optimized fiber orientation angles and the maximum tangential stresses are listed in Table 1. The global coordinates xoy in Fig. 3 are in accordance with that in Fig. 2a, and the oblique lines in Fig. 3 represent the fiber directions in the x' -axis (Fig. 2a) for different values of E_2/E_1 . It should be noted that the

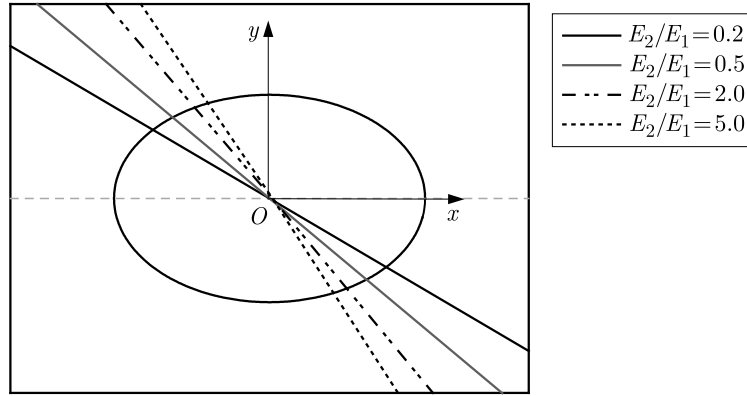


Fig. 3. The optimal fiber orientation of the orthotropic plate with the elliptical hole

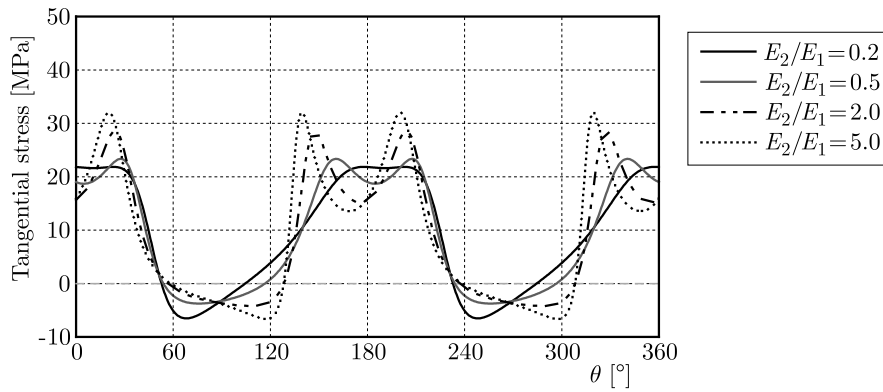


Fig. 4. Tangential stresses along the boundary of the elliptical hole at the optimal fiber orientation

Table 1. The optimal fiber orientation angles and the $\max |\sigma_\theta|$ of an orthotropic plate with the elliptical hole

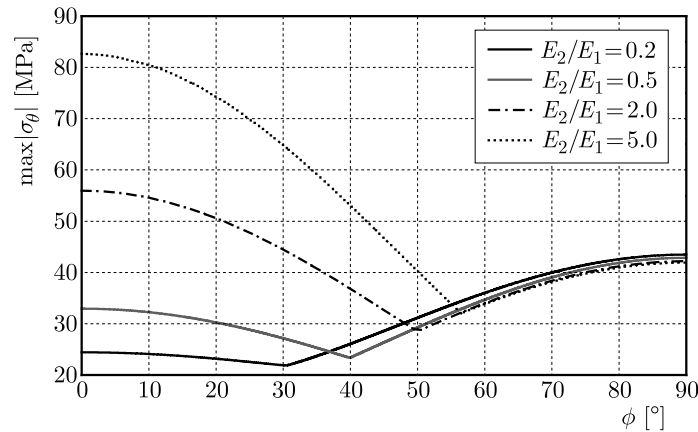
	E_2/E_1			
	0.2	0.5	2.0	5.0
φ [°]	30.46	39.89	49.96	56.49
$\max \sigma_\theta $ [MPa]	21.84	23.34	28.50	32.04

angle θ in Fig. 4 is the polar angle in the ζ -plane and $\theta = 0^\circ$ corresponds to the intersection of the positive x -axis and the excavation boundary.

It can be seen from Figs. 3 and 4 and Table 1 that both the optimal fiber orientation angle φ and the maximum tangential stress increase with the increasing value of E_2/E_1 . The maximum tangential stress concentration is evident in approximately 30° , 150° , 210° and 330° , not similar to the isotropic plate, where the maximum tangential stress usually occurs at 0° and 180° . Under the given loading condition, the compressive stress can be found around the intersection of the y -axis and the hole boundary with a smaller magnitude than the tensile stress.

Considering that there is only one variable in this case, the optimal fiber orientation angle φ can be obtained without any optimization algorithm. Figure 5 illustrates the maximum absolute tangential stress $\max |\sigma_\theta|$ for different fiber orientation angles, showing that the minimum value of $\max |\sigma_\theta|$ and the corresponding fiber orientation angles are identical with the results listed in Table 1, which verifies the results obtained by the DE algorithm.

For an elliptical hole, the stresses have also been analyzed by Ukadgaonker and Rao (2000). To verify the fundamental theories of Section 2, we compared the normalized stresses of σ_x , σ_y and τ_{xy} along the hole boundary with the results obtained by Ukadgaonker and Rao (2000,

Fig. 5. The $\max|\sigma_\theta|$ for different fiber orientation angles**Table 2.** Normalized stresses of σ_x , σ_y and τ_{xy} for equi-biaxial tension on a graphite/epoxy plate, 60° fibers containing an elliptical hole ($a/b = 2$)

θ [deg]	Ukadgaonker and Rao (2000)			Zhang <i>et al.</i>		
	σ_x	σ_y	τ_{xy}	σ_x	σ_y	τ_{xy}
0	0	3.44	0	0	3.4393	0
20	0.82	1.54	-1.12	0.8172	1.5421	-1.1226
40	1.46	0.52	-0.87	1.4589	0.518	-0.8693
60	1.54	0.13	-0.45	1.5423	0.1285	-0.4452
80	1.41	0.01	-0.12	1.4076	0.0109	-0.1241
90	1.3	0	0	1.3033	0	0
100	1.18	0.01	0.1	1.1812	0.0092	0.1041
120	0.89	0.07	0.26	0.8867	0.0739	0.256
140	0.57	0.2	0.34	0.5651	0.2007	0.3367
160	1.23	2.32	1.69	1.2272	2.316	1.6859
180	0	3.44	0	0	3.4393	0

page 348, Table 3) in Table 2. Taking the same values of material parameters and external loadings, Table 2 shows that the results obtained by the two papers are in a very close agreement.

3.1.2. Hexagonal hole

The optimized fiber orientation angles and their corresponding tangential stresses along the boundary of the hexagonal hole are illustrated in Figs. 6 and 7, respectively. The maximum tangential stress occurs at the points marked with an asterisk. When the ratios of the elastic moduli are $E_2/E_1 = 0.2, 0.5, 2.0$ and 5.0 , the corresponding optimal fiber orientation angles are $\varphi = 32.15^\circ, 40.47^\circ, 42.74^\circ$ and 57.90° , respectively (shown in Fig. 6), which shows a great difference for the different ratios of E_2/E_1 . Figure 7 illustrates that the tangential stress reaches the corresponding extreme values in/near the corner points. The maximum tangential stresses for different E_2/E_1 are found in different positions but are still around the corner points, and the values of the maximum tangential stress range from 42.89 MPa ($E_2/E_1 = 0.5$) to 70.77 MPa ($E_2/E_1 = 5.0$), meaning that the location and magnitude of the maximum tangential stress are highly dependent on Young's modulus for a given hole shape and loading condition. We can also see that the tangential stresses along the boundary are mainly tensile stresses with the exception of the two sides BC and EF, which are parallel to the direction of the minimum loading. Moreover, the magnitude of the compressive stress is much smaller than that of the tensile stress.

Comparing with the results in Fig. 4, the stress concentration along the boundary of the hexagonal hole is much larger than that along the boundary of the elliptical hole because there are sharp corners on the hexagonal hole.

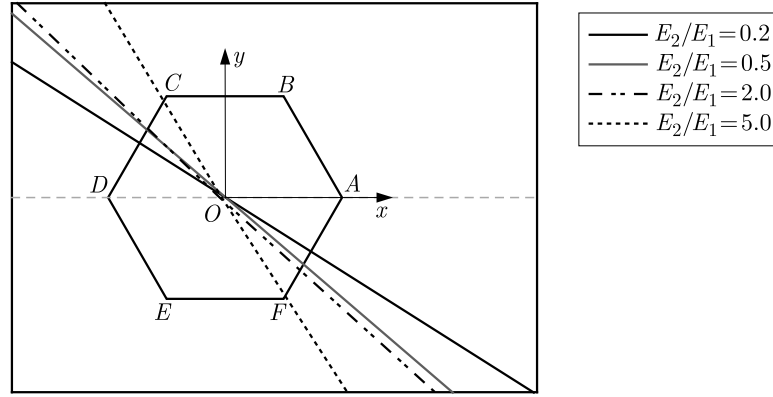


Fig. 6. The optimal fiber orientation of the orthotropic plate with the hexagonal hole

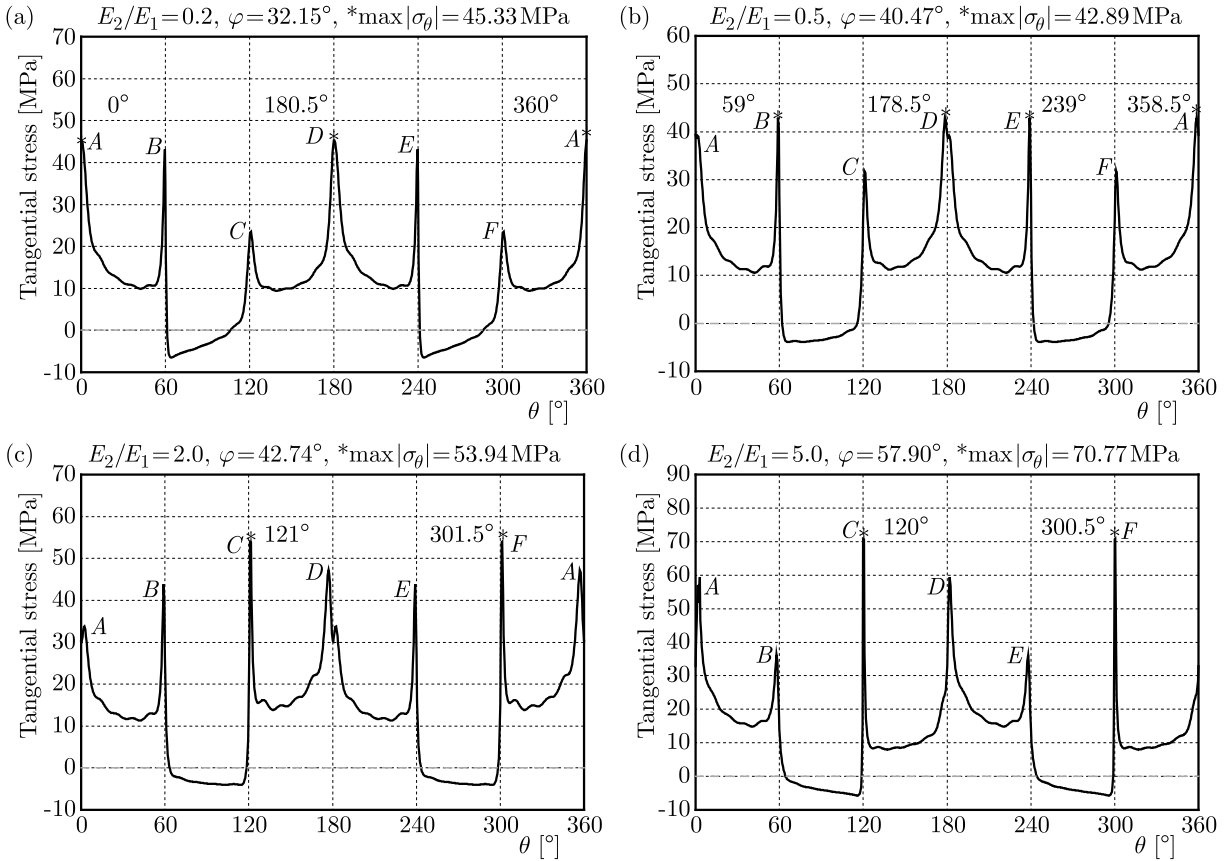


Fig. 7. Tangential stresses along the boundary of the hexagonal hole at the optimal fiber orientation

3.2. Optimization of the fiber and hole orientation angles

Considering that the hole orientation angle also influences the tangential stress along the boundary of the hole, both the fiber orientation angle and the hole orientation angle are chosen as the design variables in this Section with the external loads given (refer Fig. 1).

3.2.1. Elliptical hole

Because of the symmetry of the external loads and the elliptical hole, the scopes of optimized variables are given as $\alpha \in 0^\circ\text{--}180^\circ$ and $\varphi \in 0^\circ\text{--}90^\circ$. The optimal fiber and hole orientation angles and the corresponding tangential stress along the boundary of the hole are illustrated in Figs. 8 and 9, and Table 3, respectively.

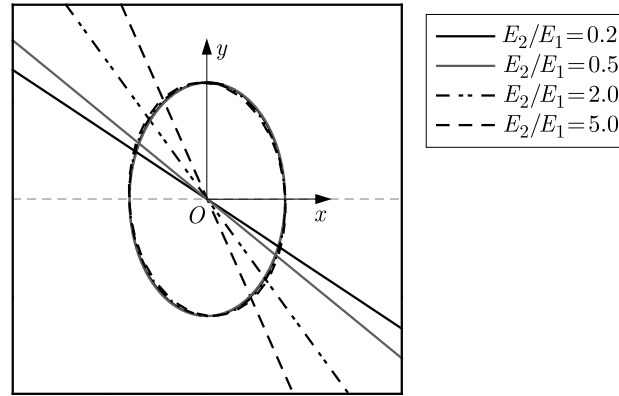


Fig. 8. The optimal fiber and hole orientation angles of the orthotropic plate with the elliptical hole

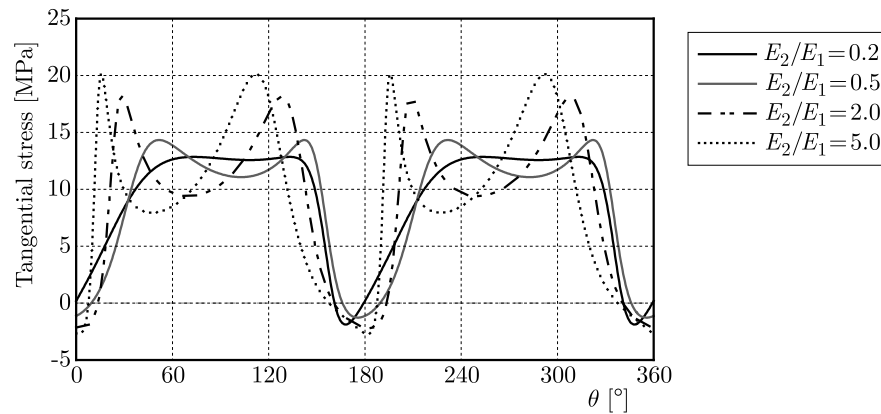


Fig. 9. Tangential stresses along the boundary of the elliptical hole at the optimal fiber and hole orientation

Table 3. The optimal fiber and hole orientation and the $\max|\sigma_\theta|$ of the orthotropic plate with the elliptical hole

	E_2/E_1			
	0.2	0.5	2.0	5.0
φ [°]	33.64	39.25	53.98	66.13
α [°]	90.95	89.29	92.43	94.84
$\max \sigma_\theta $ [MPa]	12.85	14.33	18.12	20.11

It can be seen from Fig. 8 and Table 3 that the optimal fiber orientation angle increases greatly with an increase in the ratio of E_1/E_2 . Nevertheless, the hole orientation angles are all near the same degree of 90° , that is to say, the major axis of the elliptical hole should be set in the direction of the maximum external load. It can also be verified by comparing Figs. 4 and 9. Under the given loadings, vertical elliptical holes (Fig. 9) always produce smaller tangential stress concentration compared to the horizontal ones (Fig. 4). In addition, the similar laws of the two cases are that the maximum tangential stress increases with the ratio of E_2/E_1 and compressive stress is found in Fig. 9 as well.

3.2.2. Hexagonal hole

Because a hexagonal hole has more symmetry axes, the scopes of the optimized variables are reduced to $\alpha \in 0^\circ\text{--}60^\circ$ and $\varphi \in 0^\circ\text{--}90^\circ$. Figures 10-13 show the optimal placements of the fiber and hole orientation angles and the corresponding tangential stress along the hole boundary. It should be noted that the angle $\theta = 0^\circ$ corresponds to the intersection of the positive x_1 -axis and the hole in this case.

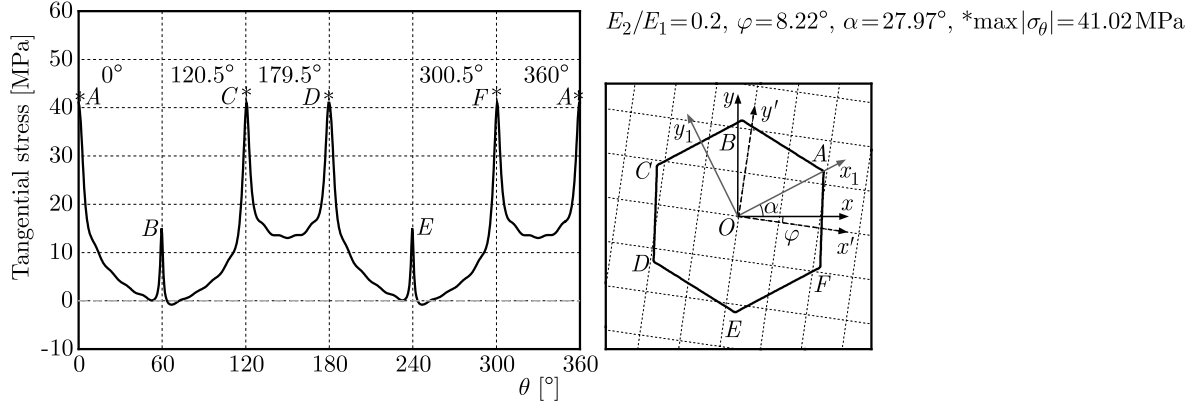


Fig. 10. The optimal placement of fiber and hole orientation angles of orthotropic plates and the tangential stresses along the boundary of the hexagonal hole when $E_2/E_1 = 0.2$

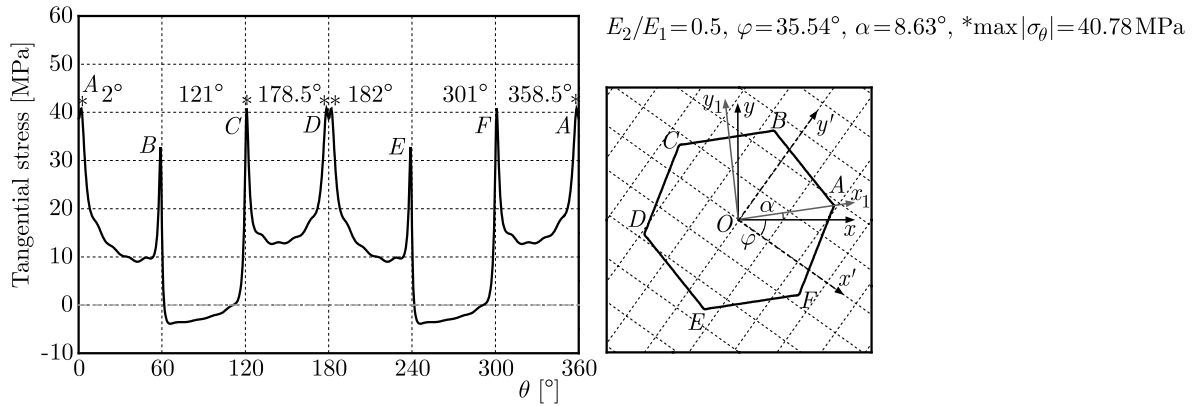


Fig. 11. The optimal placement of fiber and hole orientation angles of orthotropic plates and the tangential stresses along the boundary of the hexagonal hole when $E_2/E_1 = 0.5$

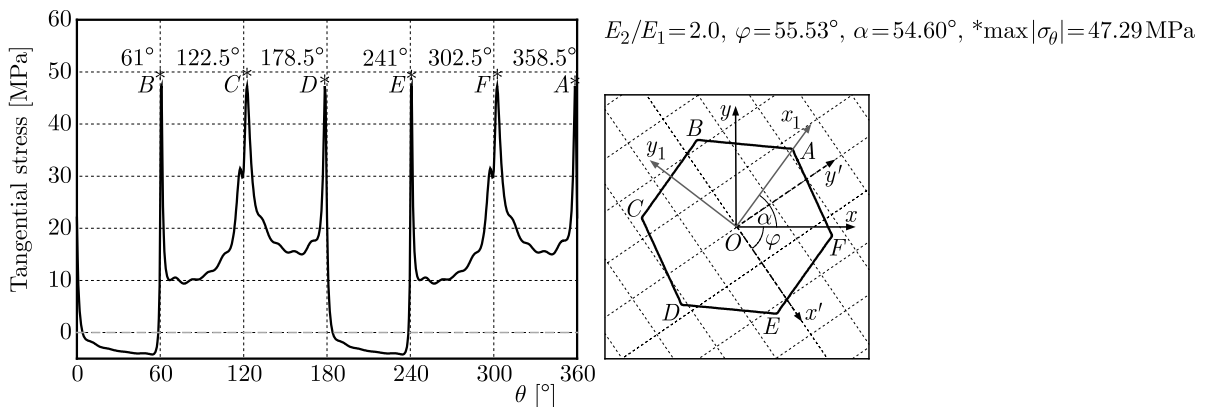


Fig. 12. The optimal placement of fiber and hole orientation angles of orthotropic plates and the tangential stresses along the boundary of the hexagonal hole when $E_2/E_1 = 2.0$

It can be seen from Figs. 10-13 that both the optimized fiber orientation angle and the hole orientation angle are apparently different for different ratios of E_2/E_1 . Under the given inequi-

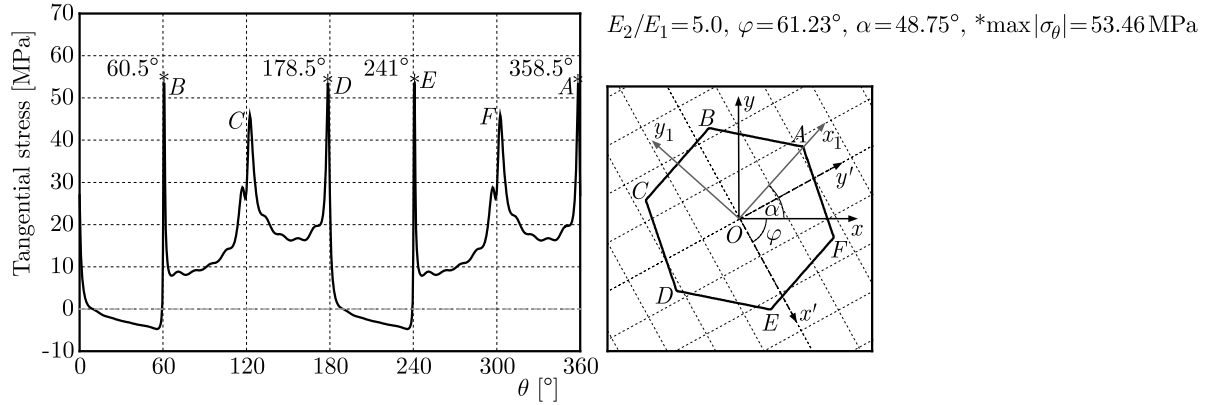


Fig. 13. The optimal placement of fiber and hole orientation angles of orthotropic plates and the tangential stresses along the boundary of the hexagonal hole when $E_2/E_1 = 5.0$

-biaxial tensile loading, compressive tangential stress may occur and is more likely to be found in the sides that are parallel (BC and EF in Figs. 6 and 7), or inclined (BC and EF in Figs. 11, AB and DE in Figs. 12 and 13) to the direction of the minimum external loading.

Combining with the above example on the hexagonal hole (see Section 3.1.2), we find that for holes with sharp corners, the tangential stress concentration is more likely to occur around the corner points but not always exactly in the corner points. The point D in Fig. 11 gives the most obvious evidence. In addition, the tangential stress concentration is smaller when both the fiber and hole orientation angles are optimized compared to the case in Section 3.1. Thus, when we design a perforated structure in an orthotropic plate, the two parameters should be considered jointly to decrease the tangential stress concentration along the boundary of the hole. From all of the examples given in Sections 3.1 and 3.2, we obtain that for a significantly orthotropic plate ($E_2/E_1 = 0.2$ or 5.0) with a central hole, setting the principal direction that has the larger Young's modulus inclined to the direction of the minimum loading may decrease the tangential stress concentration along the hole boundary.

3.2.3. Optimality verification of fiber and hole orientation angles

The optimality verification should be carried out to guarantee that the optimized fiber and hole orientation angles, φ and α , are the global optimal solutions. Taking the hexagonal hole as an example, only one condition is analyzed when the ratio of the elastic modulus is given as $E_2/E_1 = 2.0$. The external loads and other parameters are the same as in the previous examples. The variation of the maximum tangential stress $\max |\sigma_\theta|$ with respect to φ , α and the contour map is illustrated in Fig. 14. The degree intervals of φ and α are all set as 0.01° . It can be seen from Fig. 14 that the value of $\max |\sigma_\theta|$ differs for different φ and α . According to the calculation results, $\max |\sigma_\theta|$ reaches the minimum value of 47.30 MPa only when $\varphi = 55.53^\circ$ and $\alpha = 54.60^\circ$, which verifies the results shown in Fig. 12.

4. Conclusions

To decrease the tangential stress concentration around an arbitrarily shaped hole in an orthotropic plate, the optimization design on the fiber orientation angle and the hole orientation angle are conducted. The tangential stress distributions around non-circular shapes are given. The results show that the tangential stress concentration around a hole with corner points in an orthotropic plate under an inequi-biaxial loading is more likely to occur in/near the corner points. Furthermore, the tangential stress concentration around a hole with corner points is found to

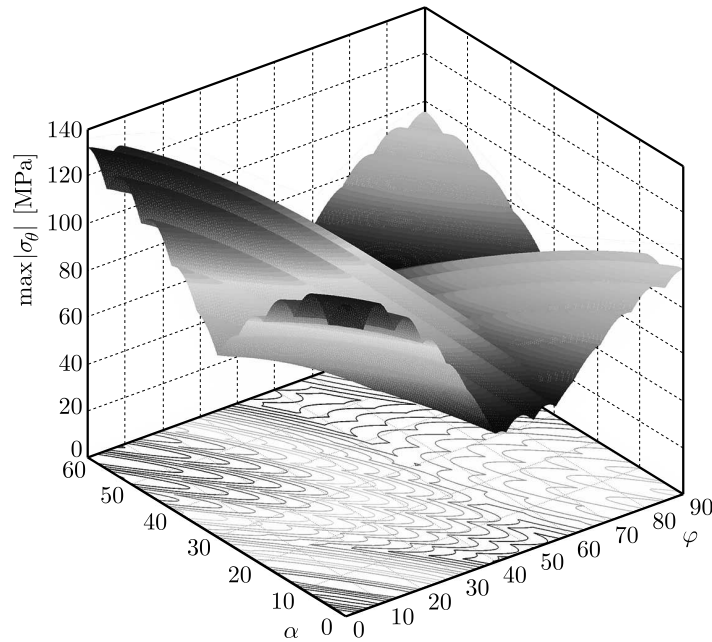


Fig. 14. The three-dimensional map and contour map of $\max |\sigma_\theta|$ for all possible placements of the fiber and hole orientation angles

be more significant compared to that around a smooth convex hole. Under an inequi-biaxial loading, compressive stress can usually be found and is mainly located at the sides that are parallel or inclined to the direction of the minimum external loading.

Based on the results, the following several treatments can be referred in the designing of orthotropic plates in order to decrease the tangential stress concentration: (1) avoid holes with corner points and choose smooth convex holes instead, such as an ellipse hole; (2) set the major axis of an ellipse in the direction of the maximum external loading and (3) set the principal direction that has the larger Young's modulus inclined to the direction of the minimum loading, especially for a significantly orthotropic plate.

Funding

This research work was supported by the Natural Science Foundation of China (Grant No. 11572126, 51704117) and the Fundamental Research Funds for the Central Universities (NCEPU2016XS55).

References

1. BJORKMAN G.S., RICHARDS R., 1976, Harmonic holes – an inverse problem in elasticity, *Journal of Applied Mechanics*, **43**, 3, 414-418
2. BJORKMAN G.S., RICHARDS R., 1979, Harmonic holes for nonconstant fields, *Journal of Applied Mechanics*, **46**, 3, 573-576
3. CHEN Z.Y., 1994, *Analytical Method of Rock Mechanics Analysis*, China Coal Industry Publishing House, Beijing
4. DAOUST J., HOA S.V., 1991, An analytical solution for anisotropic plates containing triangular holes, *Composite Structures*, **19**, 2, 107-130
5. DHIR S.K., 1981, Optimization in a class of hole shapes in plate structures, *Journal of Applied Mechanics*, **48**, 4, 905-908
6. ENGELS H., ZAKHAROV D., BECKER W., 2001, The plane problem of an elliptically reinforced circular hole in an anisotropic plate or laminate, *Archive of Applied Mechanics*, **71**, 9, 601-612

7. JAIN N.K., 2009, Analysis of stress concentration and deflection in isotropic and orthotropic rectangular plates with central circular hole under transverse static loading, *World Academy of Science Engineering and Technology*, **3**, 12, 1513-1519
8. LEKHNITSKII S.G., 1968, *Anisotropic Plates*, Gordon and Breach, New York
9. LEKHNITSKII S.G., 1981, *Theory of Elasticity of an Anisotropic Body*, Mir Publishers, Moscow
10. LI C., ZHENG Y.P., 2007, Influence of different orifice figure on hole-edge stress of composite material plate with hole (in Chinese), *Engineering Mechanics*, **24**, 10, 19-24
11. LU A.Z., CHEN H.Y., QIN Y., ZHANG N., 2014a, Shape optimisation of the support section of a tunnel at great depths, *Computers and Geotechnics*, **61**, 3, 190-197
12. LU A.Z., CHEN H.Y., QIN Y., ZHANG N., 2014b, Shape optimization of tunnel support section under contact condition of pure slip, *Chinese Journal of Rock Mechanics and Engineering*, **33**, 8, 1563-1571
13. LU A.Z., ZHANG N., ZHANG X.L., LU D.H., LI W.S., 2015, Analytic method of stress analysis for an orthotropic rock mass with an arbitrary-shaped tunnel, *International Journal of Geomechanics*, **15**, 4, 04014068
14. MUSKHELISHVILI N.I., 1963, *Some Basic Problems of the Mathematical Theory of Elasticity*, Noordhoff, Groningen
15. RAO D.K.N., BABU M.R., REDDY K.R.N., SUNIL D., 2010, Stress around square and rectangular cutouts in symmetric laminates, *Composite Structures*, **92**, 12, 2845-2859
16. REN G., SMITH J.V., TANG J.W., XIE Y.M., 2005, Underground excavation shape optimization using an evolutionary procedure, *Computers and Geotechnics*, **32**, 2, 122-132
17. REZAEPAZHAND J., JAFARI M., 2008, Stress analysis of composite plates with non-circular cutout, *Key Engineering Materials*, **385-387**, 365-368
18. ROMEO G., 2001, Analytical and experimental behavior of laminated panels with rectangular opening under biaxial tension, compression and shear loads, *Journal of Composite Materials*, **35**, 8, 639-664
19. SAVIN G.N., 1961, *Stress Concentration Around Holes*, Pergamon Press, New York
20. SHARMA D.S., 2011, Stress concentration around circular/elliptical/triangular cutouts in infinite composite plate, *Proceedings of the World Congress on Engineering*, **3**, 2626-2631
21. SHARMA D.S., PATEL N.P., TRIVEDI R.R., 2014, Optimum design of laminates containing an elliptical hole, *International Journal of Mechanical Sciences*, **85**, 8, 76-87
22. SOBÓTKA M., ŁYDŹBA D., RÓŹAŃSKI A., 2013, Shape optimization of underground excavation by simulated annealing, *Studia Geotechnica et Mechanica*, **35**, 1, 209-218
23. STORN R., PRICE K., 1997, Differential evolution – a simple and efficient heuristic for global optimization over continuous spaces, *Journal of Global Optimization*, **11**, 4, 341-359
24. TOUBAL L., KARAMA M., LORRAIN B., 2005, Stress concentration in a circular hole in composite plate, *Composite Structures*, **68**, 1, 31-36
25. UKADGAONKER V.G., KAKHANDKI V., 2005, Stress analysis for an orthotropic plate with an irregular shaped hole for different in-plane loading conditions – Part 1, *Composite Structures*, **70**, 3, 255-274
26. UKADGAONKER V.G., RAO D.K.N., 2000, A general solution for stresses around holes in symmetric laminates under in plane loading, *Composite Structures*, **49**, 3, 339-354

SELECTED EXAMPLES OF REFERRING THE EXAMINED STOCHASTIC TECHNICAL STABILITY TO THE ISO STANDARDS

JERZY KISIŁOWSKI

*Kazimierz Pulaski University of Technology and Humanities in Radom, Faculty of Transport and Electrical Engineering,
Radom, Poland; e-mail: jkisolow@kisolowscy.waw.pl*

JAROSŁAW ZALEWSKI

*Warsaw University of Technology, Faculty of Administration and Social Sciences, Warsaw, Poland
e-mail: j.zalewski@ans.pw.edu.pl*

In this paper, certain examples of comparison between the selected definition of the stochastic technical stability (for motor vehicle models) and the ISO definitions (developed for real vehicles) have been discussed. Being able to refer the examined stability of a mathematical model to the real object may result in verifying the properties of the latter on the basis of model tests, instead of the field trials. Such an attempt has been presented previously, but in a more general approach. The aim of this paper is to present a certain attempt to compare the results obtained for a simulated vehicle model in virtual environment with the specific definitions of stability dedicated to the real motor vehicles. The background of this considerations lies in the examination of the stochastic technical stability, which allows any mechanical system undergo external random disturbances, such as road irregularities.

Keywords: motor vehicle stability, ISO norm, comparisons

1. Introduction

In the analysis of stability it seems important to choose an appropriate definition which, depending on the ease of interpretation and nature of disturbances, allows analysis of the tested object. The ability to refer the obtained results to real-world objects (e.g. motor vehicle) seems to be important, for which stability criteria are determined according to the ISO standards.

Stability of a nonlinear mathematical model of a motor vehicle, with additional external disturbances, is considered. Disturbances stemming from road irregularities are assumed as a stochastic process, stationary in broader sense as well as globally ergodic, which enabled analysis based on a single trajectory representing motion of the vehicle (Kisilowski and Zalewski, 2008).

For motor vehicles, the stability is adopted in accordance with ISO 8855:1991 which, in comparison to the stochastic technical stability, gives an opportunity to examine the motor vehicle stability on the basis of an exemplary model (described with the use of differential equations) and refer the results to the real one, in real maneuver.

The term “stochastic” has been previously connected to the aspects of stability, e.g. in (Khasminskii, 2012; Kisilowski and Zalewski, 2016), however not related to the ISO standards. Stability was also examined for motor vehicles, e.g. in (Karnopp, 2004), however not combining both the use of the stochastic technical stability and the ability to relate the results to real vehicles.

Certain aspects of vehicle stability were considered previously. For example, in (Chung and Yi, 2006) motor vehicle stability control based on the side slip angle was proposed, as well as the evaluation of certain control schemes on a virtual test track. In (Doumiati *et al.*, 2013) the investigation on the coordination of active front steering and rear braking for a driver-assist

system in yaw control of a motor vehicle was proposed. In (Güvenç *et al.*, 2009) asymmetrical load in a vehicle, combined with μ -split braking forces caused by side wind or unilateral tire pressure loss was examined. As a result, unexpected yaw disturbances were observed, which required yaw stabilisation provided either by a driver or by an automatic driver-assist system.

Stability was also examined in relation to control systems. In (Segawa *et al.*, 2001) the so-called D^* control system was proposed, which, according to the authors, could offer mainly high steering response and reduced driving effort, whereas in (Zheng *et al.*, 2006) the use of the vehicle yaw moment and wheel slip control were used in the dynamic control system, mainly for tracking the desired vehicle behaviour.

Taking the above into consideration, it is fair to say that research on the vehicle stability has two major directions: vehicle dynamics with the use of mechanical dependencies and control with the use of systems basing on the obtained data. It seems however important that the mechanical reliances could be connected with simulation results and normalized descriptions (ISO).

Analysis of the possibility to compare results obtained in a simulation with the ISO standards was presented in (Kisilowski and Zalewski, 2015). However, it was not previously discussed on specific examples.

In this paper, the motor vehicle model, considered as well in (Kisilowski and Zalewski, 2016), is used as an example. It seems questionable when, under what circumstances, a vehicle after accident and repair is roadworthy. In order to provide the realism of the analysed problem, the stochastic technical stability definition is taken into consideration, as it provides random disturbances acting on the mechanical system (here the vehicle). One of the discussed examples was previously created in (Kisilowski and Zalewski, 2016).

2. Stability of a motor vehicle

The concept of stability in terms of motor vehicle motion is presented in ISO 8855: 1991. To so called steady-state of the vehicle is described as a condition in which the sum of all external and inertial forces and moments forms a constant. Other conditions have been described as other states (non-steady). Hence, definitions of stability, quoted in the paper (Kisilowski and Zalewski, 2016), are as follows:

- non-periodic stability – stability characteristic at a prescribed steady-state equilibrium if, following any small and temporary disturbance or control input, the vehicle will return to the steady-state equilibrium without oscillation;
- neutral stability – stability characteristics at a prescribed steady state equilibrium if, for any small and temporary disturbance or control input, the vehicle motion remains close to the motion defined by the steady-state equilibrium, but does not return to it;
- oscillatory stability – oscillatory vehicle response of a decreasing amplitude and a return to the original steady-state equilibrium;
- non-periodic instability – ever-increasing response without oscillation;
- oscillatory instability – oscillatory response of an increasing amplitude about the initial steady-state equilibrium.

3. Stochastic technical stability

Stochastic technical stability is defined according to, e.g. (Bogusz, 1972), where a system of stochastic equations is assumed

$$\frac{dx}{dt} = f(x, t, \xi(t)) \quad (3.1)$$

where $x = (x_1, \dots, x_n)$ and $f(x, t, y) = (f_1, \dots, f_n)$ and $\xi(t) = (\xi_1, \dots, \xi_n)$ are vectors and $\xi(t)$ for $t \geq 0$ is a stochastic process which describes random disturbances. Any set of equations can be represented by such a system (Kisilowski and Zalewski, 2016).

The function $f(x, t, y)$ is assumed to be determined for each $x \in E_n$, $y \in E_n$ and $t \geq 0$. Absolute integrability is assumed for a stochastic process $f(0, t, \xi(t))$

$$P\left\{\int_0^T |f(0, t, \xi(t))| dt < \infty\right\} = 1 \quad \text{for each } T > 0 \quad (3.2)$$

as well as the existence of another stochastic process $f(X, t, \xi(t))$, which fulfills the Lipschitz criterion in $[0, T]$ interval for another process $\eta(t)$, also absolutely integrable in that given interval. This assumption is described as follows

$$|f(x_2, t, \xi(t)) - f(x_1, t, \xi(t))| \leq \eta(t)|x_2 - x_1| \quad (3.3)$$

As a result of the above assumptions, there exists only one solution of the set of equations (3.1), being an absolutely continuous stochastic process with the probability 1 for $t \geq t_0$, with the initial conditions $t = t_0$ and $x(t_0) = x_0$.

It is also assumed that there exist two areas in the Euclidean space E_n : ω – limited and open and Ω – limited and closed, where $\omega \subset \Omega$. There is as well a positive number ε , where $0 < \varepsilon < 1$ and the stochastic process $X(t)$ specified for $t \geq t_0$.

Initial conditions for each solution are $t = t_0$, $x(t_0) = x_0$ and the solution itself is presented as (t, t_0, x_0) .

Definition of the stochastic technical stability reads: if every solution of equation (3.1), with its initial conditions belonging to ω , remains in the Ω area with the probability $1 - \varepsilon$, then system (3.1) is stochastically technically stable towards ω , Ω and the process $\xi(t)$ with the probability $1 - \varepsilon$ (Fig. 1).

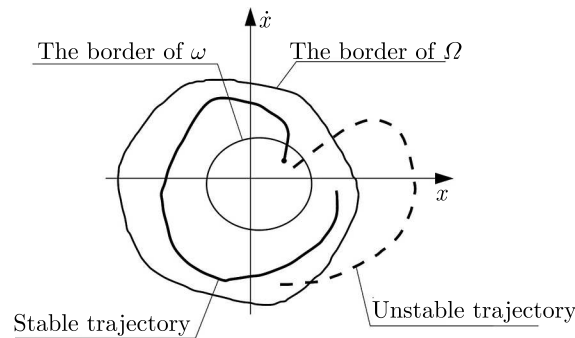


Fig. 1. Graphic interpretation of the stochastic technical stability. Source: Bogusz (1972)

It can also be described by the formula

$$P\{(t, t_0, x_0) \in \Omega\} > 1 - \varepsilon \quad \text{for } \bar{x}_0 \in \omega \quad (3.4)$$

The above definitions of the motor vehicle stability according to ISO standards can be compared with the stability defined for mathematical models, according to certain assumptions and criteria which concern not only the vehicle but the disturbances coming from road irregularities as well. It was previously theoretically discussed in (Kisilowski and Zalewski, 2015) but with no specific examples. As a result, the following conclusions were made in relation to the stochastic technical stability versus the ISO standards. All comparisons are possible if trajectories of the vehicle are taken into account.

The definition of non-periodic stability can be compared with the stochastic technical stability provided that the accepted disturbances will generate a relatively small deviation from the assumed stable motion, because the return to this state should seem fluent without oscillations. In the presented case, random disturbances could, for example, originate from transverse irregularities of the road as well as a strong blow of wind whose resultant force would be perpendicular to the plane of symmetry of the vehicle. This may cause transverse drift of the vehicle.

The neutral stability (motion close to the steady-state, but without oscillations) can as well be compared to the stochastic technical stability, because of the assumption that the solution remains in the acceptable area around the steady-state.

The comparison seems also be possible between the oscillatory stability and the stochastic technical stability, since both definitions provide return of a representative point of the vehicle to the steady-state. Also implementing stochastic disturbances that cause oscillations seems important when considering the vehicle response. Oscillatory stability does not have to mean a periodic decrease of the trajectory amplitude.

Both periodic and non-periodic instabilities characterised by the strengthening of the vehicle response with or without oscillation, respectively, can be compared to the stochastic technical stability depending, among others, on which the model is analysed (linear or non-linear) and what type of disturbances are taken into account (constant or random).

4. Comparison of the methods

The above conclusions show that stability of technical objects presented as mathematical models with the use of differential equations (in this case motor vehicles) seems to be a valuable tool for analysis of the correctness of their functioning. Moreover, significant seems the fact of the possibility of experimental verification of tested models by analysing motion of their real counterparts.

In this Section, certain examples of comparison between the stochastic technical stability and selected ISO standards are shown. Three presented examples show simulation results for a sports two seater (in MSC Adams/Car environment), differently laden and moving in different road conditions. Description of this model was presented, among others, in (Zalewski, 2014a,b). In each given case the FTIRE (flexible tire ring) tire model was used instead of the PAC89 originally attached to the vehicle model, because of random irregularities in the road surface. Typical tire models do not allow running simulations on two-dimensional stochastic uneven road profiles, where the wavelength of a single irregularity is less than the wheel radius (Zalewski, 2014a,b).

Nominal parameters of the considered model of the motor vehicle in MSC Adams/Car have been adopted as in (Zalewski, 2014a,b):

- mass of the unladen vehicle: $m_{UB} = 995$ kg;
- location of the “origo” point in relation to the front edge center of the unladen vehicle: $x_c = 0.9$ m, $y_c = 0$ m, $z_c = 0.48$ m;
- nominal location of the center of mass in relation to the “origo” (Kisilowski and Zalewski, 2016) in the unladen vehicle: $x_c = 1.5$ m, $y_c = 0$, $z_c = 0.45$ m;
- nominal values of the inertia moments for the unladen vehicle relative to the axes which intersect the “origo” point: $I_x = 401$ kg·m², $I_y = 2940$ kg·m², $I_z = 2838$ kg·m²;
- nominal values of the deviation moments of inertia of the unladen vehicle relative to the same intersecting “origo”: $I_{xy} = 0$, $I_{xz} = 671$ kg·m², $I_{yz} = 0$.

Example I

As the first example, results from the work (Zalewski, 2014) are presented, where a single lane change maneuver has been simulated using the model described previously as well in the MSC Adams/Car component.

Assumptions for the vehicle load and the course of maneuver have been taken as follows:

- mass of the vehicle was increased by the baggage ($m_B = 60$ kg), driver ($m_1 = 75$ kg) and passenger ($m_2 = 110$ kg);
- initial speed of the vehicle moving at the fifth gear was 100 km/h;
- coordinates of the center of mass in the laden vehicle with respect to “origo”: $x_{cL} = 1.472$ m, $y_{cL} = 0.085$ m, $z_{cL} = 0.454$ m;
- inertia and deviation moments of inertia with regard to “origo”: $I_{xL} = 464$ kg·m², $I_{yL} = 3442$ kg·m², $I_{zL} = 3295$ kg·m², $I_{xyL} = 155$ kg·m², $I_{xzL} = 828$ kg·m², $I_{yzL} = 47.8$ kg·m².

The above mentioned “origo” point is the origin of the coordinate system located underneath the vehicle model (on the ground level) but moving along with the model during simulation. It is presented in Fig. 2.

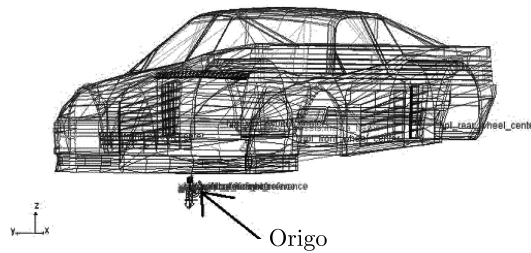


Fig. 2. Location of the “origo” point. Source: MSC Adams/Car

The vehicle model used here had non-linear elastic – damping elements. In Fig. 3, the spring deflection, whereas in Fig. 4 – the damping force versus velocity of the acting damper are presented. A MacPherson column based suspension is used in the model.

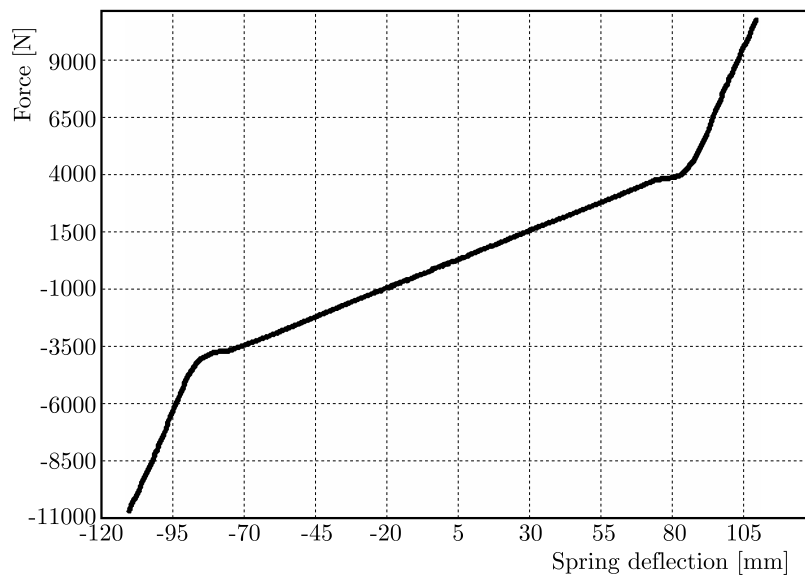


Fig. 3. The force – spring deflection characteristics in the vehicle suspension. Source: Zalewski (2014a)

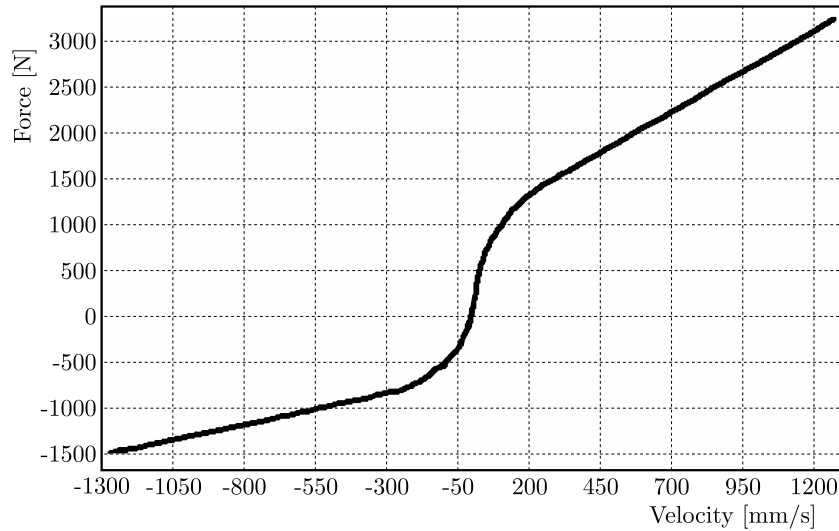


Fig. 4. The damping force – damper velocity characteristics in the vehicle suspension.
Source: Zalewski (2014a)

A single lane change maneuver simulation has been carried out for the following configurations:

- a) vehicle laden as shown above, riding on a flat and icy road ($\mu = 0.3$);
- b) vehicle laden as shown above and riding on an icy and randomly uneven road.

The maneuver has been realised on a 480 m long road section at a constant speed of 100 km/h. Random disturbances acting on the vehicle as road irregularities were described among others in (Zalewski, 2014a). The discussed maneuver has been carried out for extreme icy road conditions.

As a result, two trajectories were obtained, each for one of the above described configurations. The thin curve marks the vehicle trajectory on a flat surface, whereas the bold curve – the trajectory obtained for the uneven road (Fig. 5).

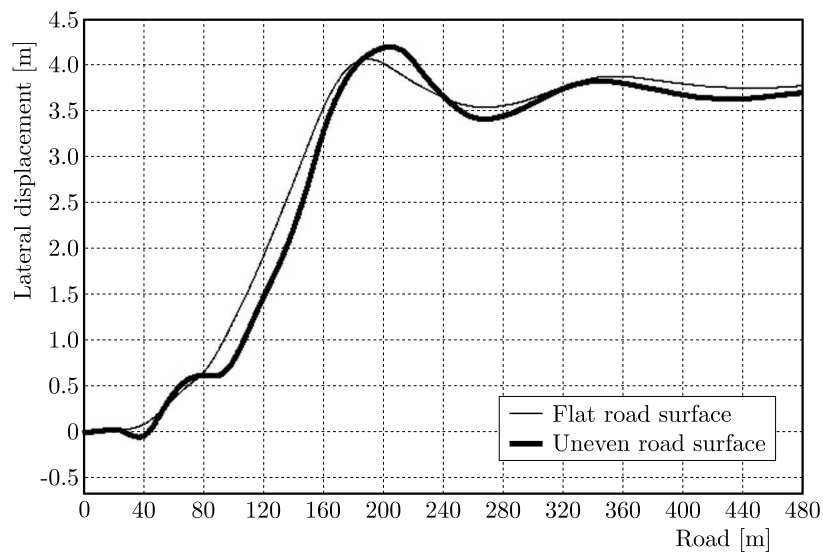


Fig. 5. Lateral displacement versus covered distance. Source: Zalewski (2014a)

Example II

Another example is based on the results obtained from (Zalewski, 2014). By adding mass of the driver ($m_1 = 75$ kg), passenger ($m_2 = 105$ kg) and baggage ($m_B = 50$ kg), the entire mass of the vehicle model increased (Figs. 6 and 7), so that new parameters of mass – inertia in the vehicle body were determined:

- disturbed location of the mass center with regard to the “origo”: $x_{cL} = 1.481$ m, $y_{cL} = 0.081$ m, $z_{cL} = 0.454$ m;
- inertia moments of the vehicle with regard to the axes intersecting the “origo”: $I_{xL} = 461$ kg·m², $I_{yL} = 3441$ kg·m², $I_{zL} = 3297$ kg·m²;
- deviation moments of the vehicle with regard to the axes intersecting the “origo”: $I_{xyL} = 148$ kg·m², $I_{xzL} = 824$ kg·m², $I_{yzL} = 45.5$ kg·m².

Simulation of the impulse steer maneuver described in (Zalewski, 2014a) was carried, among others, for the icy even and icy, uneven road surface with randomly occurring irregularities. The vehicle moved at the speed of 70 km/h, and its course was disturbed by implementing an impulse turn of the steering wheel about 90° counterclockwise.

The spring – damping elements were non-linear, similarly as in the first example, so the results depended on initial conditions and concerned only such cases as discussed in this paper.

Two vehicle configurations were selected for analysis: the laden vehicle on an icy flat road surface and the laden vehicle on an icy road surface with randomly appearing irregularities.

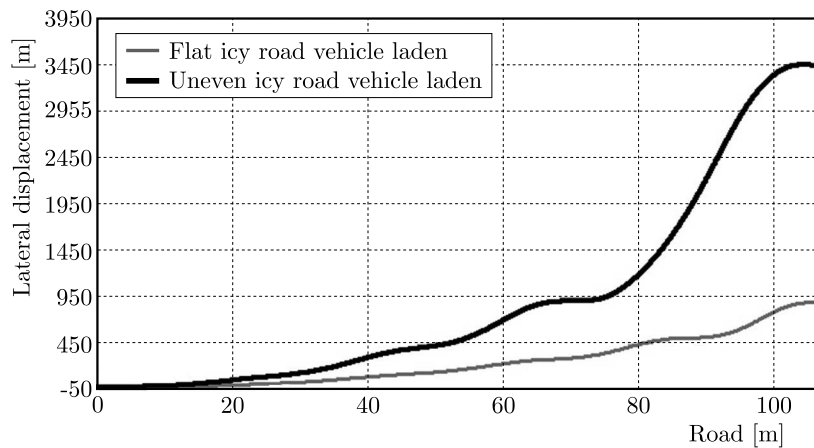


Fig. 6. The Ω area of the feasible solutions containing parts of the obtained trajectories.

Source: Zalewski (2014a)

The simulation took place on a 107 m length section of a straight road. Two trajectories for the described motion conditions were selected for further analysis – both representing the above discussed configurations, respectively (Fig. 6).

Example III

According to the work (Kisilowski and Zalewski, 2016), the following configuration of disturbances has been assumed:

- the vehicle was laden with the driver ($m_d = 74$ kg), passenger ($m_p = 105$ kg) and baggage ($m_b = 45$ kg).

As in the previous examples, new coordinates of the center of mass have been determined:

- location of the center of mass for the laden vehicle in regard to the “origo”: $x_{cL} = 1.562$ m, $y_{cL} = 0.016$ m, $z_{cL} = 0.471$ m;

- inertia moments of the laden body with regard to the axes intersecting the “origo”:
 $I_{xL} = 460 \text{ kg}\cdot\text{m}^2$, $I_{yL} = 3624 \text{ kg}\cdot\text{m}^2$, $I_{zL} = 3464 \text{ kg}\cdot\text{m}^2$;
- deviation moments of the laden body with regard to the axes intersecting the “origo”:
 $I_{xyL} = 29 \text{ kg}\cdot\text{m}^2$, $I_{xzL} = 863 \text{ kg}\cdot\text{m}^2$, $I_{yzL} = 8.8 \text{ kg}\cdot\text{m}^2$.

An incomplete double lane change maneuver has been simulated. After the maneuver was finished, the vehicle remained in the middle of width of a single-lane road. The vehicle drove at the speed of 120 km/h, reflecting the necessity of an emergency response to an emerging obstacle. The simulation was carried out in MSC Adams/Car component as well in two configurations:

- laden vehicle moving on a dry and flat road;
- laden vehicle on an icy and randomly uneven road.

The resulting two trajectories for the described case are shown in Fig. 7.

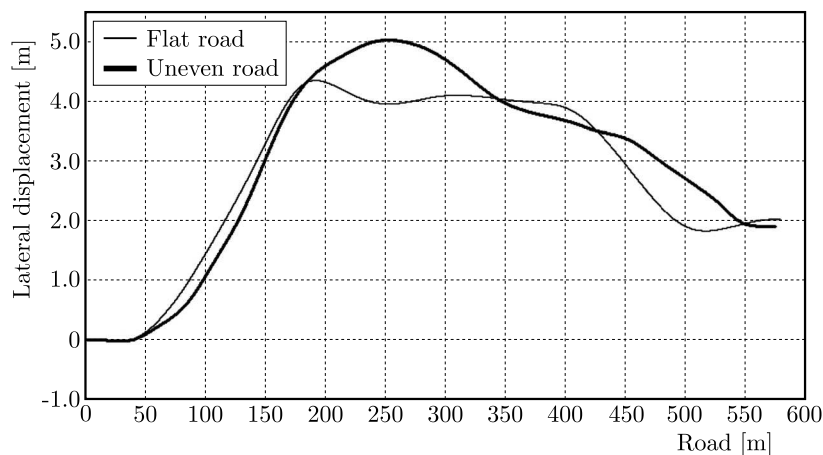


Fig. 7. Lateral displacement of the vehicle model versus the distance covered, for the laden vehicle body and both road surface conditions. Source: Kisilowski and Zalewski (2016)

Basing on the obtained simulation results for three different maneuvers in different road conditions, certain conclusions can be made. Provided that such analysis can be conducted on the basis of the obtained trajectories, it seems possible to compare the stochastic technical stability with the stability according to ISO standards, both for the motor vehicle in virtual and real world, respectively.

As in Example I, it can be seen that both trajectories in Fig. 5, after performing the single lane change, remain close to each other. If the thin line was assumed to be the steady state motion, than the thick line could be regarded as neutrally stable, according to the ISO definitions. It seems that the qualitative assesment of both obtained trajectories is sufficient in the given case.

In Example II, however, it seems that the vehicle realising motion along the thick line is non-periodically unstable versus the thin line, assumed to be the steady state motion. For the first 100 m of the covered distance, the difference between the lateral displacement of both trajectories for the horizontal axis (distance [m], Fig. 6) increased without oscillation, as according to the ISO standards.

Finally, for the trajectories obtained in Example III (Fig. 7), it seems not easy to justify whether the thick line is oscillatory or neutrally stable versus the thin line. However, none of the given examples proved to be oscillatory unstable or non-periodic stable (none of them returned to the assumed steady state).

5. Conclusions

Basing on the presented results, certain conclusions can be made. It seems that comparison between stability of vehicles examined in virtual reality with the use of the given mathematical definition, and stability as a feature of real vehicles as mechanical objects described according to the specified norm, is possible. Moreover, the presented method seems versatile enough to be used in other examples, i.e. different vehicle models and different maneuvers.

Correctness of the final results in this case seems to depend on the accuracy of the vehicle model as well as simulation of its motion. However, vehicle stability, considered as a certain feature of each vehicle in the period of its maintenance, does not seem to require vehicle models being as accurate as the real vehicles. The ability to specify the mass – inertia parameters of the modeled vehicle seems to be the most important.

References

1. BOGUSZ W., 1972, *Technical Stability* (in Polish), PWN, Warszawa
2. CHUNG T., YI K., 2006, Design and evaluation of side slip angle-based vehicle stability control scheme on a virtual test track, *IEEE Transactions on Control Systems Technology*, **14**, 2
3. DOUMIATI M., SENAME O., DUGARD L., MARTINEZ-MOLINA J.J., GASPARD P., SZABO Z., 2013, Integrated vehicle dynamics control via coordination of active front steering and rear braking, *European Journal of Control*, **19**
4. GÜVENÇ B.A., GÜVENÇ L., KARAMAN S., 2009, Robust yaw stability controller design and hardware-in-the-loop testing for a road vehicle, *IEEE Transactions on Vehicular Technology*, **58**, 2
5. KARNOPP D., 2004, *Vehicle Stability*, CRC Press
6. KHASHMINSKII R., 2012, *Stability of Stochastic Differential Equations*, 2nd Edition, Springer-Verlag, Berlin, Heidelberg
7. KISIŁOWSKI J., ZALEWSKI J., 2008, Chosen problems of examination of car stability, *Archives of Transportation Systems Telematics*, **1**, 1
8. KISIŁOWSKI J., ZALEWSKI J., 2015, Stability of road vehicle mathematical models and the real objects (the ISO norm) (in Polish), *Logistyka*, **4**
9. KISIŁOWSKI J., ZALEWSKI J., 2016, Analysis of the stochastic technical stability of engineering structures on example of moving car, *Journal of Theoretical and Applied Mechanics*, **54**, 4
10. SEGAWA M., NAKANO S., NISHIRARA O., KUMAMOTO H., 2001, Vehicle stability control strategy for steer by wire system, *JSAE Review*, **22**
11. ZALEWSKI J., 2014a, The influence of road conditions on the stability of a laden vehicle mathematical model, realising a single lane change maneuver, *Telematics – Support for Transport, Communications in Computer and Information Science*, **471**
12. ZALEWSKI J., 2014b, Effect of disturbing the center of gravity on stability of a vehicle subject to impulse distortion of the straightforward motion (in Polish), *Zeszyty Naukowe Polskiego Stowarzyszenia Zarządzania Wiedzą*, **70**
13. ZHENG S., TANG H., HAN Z., ZHANG Y., 2006, Controller design for vehicle stability enhancement, *Control Engineering Practice*, **14**

MODIFIED SPLIT HOPKINSON PRESSURE BAR FOR INVESTIGATIONS OF DYNAMIC BEHAVIOUR OF MAGNETORHEOLOGICAL MATERIALS

LESZEK J. FRAŚ, RYSZARD B. PEŁCHERSKI

Institute of Fundamental Technological Research of the Polish Academy of Science, Warsaw, Poland

e-mail: lfras@ippt.pan.pl

The magnetorheological fluid is a functional material that is changing its rheological properties and finally solidifies in a magnetic field. The dynamic behaviour, tested with the use of the Split Hopkinson Pressure Bar is an important issue for description of this material, which is commonly used in different kinds of shock absorbers. This note presents a new idea how to modify the known SHPB set up in order to investigate dynamic properties of magnetorheological materials.

Keywords: Split Hopkinson Pressure Bar (SHPB), Magnetorheological Fluid (MRF), dynamic behaviour, solidification in magnetic field, ferroelements

1. Introduction

The magnetorheological fluid (MRF) is a material which is composed of microsized (less than $10\text{ }\mu\text{m}$ diameter) magnetoactive carbonyl iron particles immersed in a carrier fluid, e.g. oil. The influence of the magnetic field changes properties of the MRF. The ferroelements are joined together and form characteristic shapes – braids, which are created along the magnetic field lines. The braids are concentrating in the process of sticking together. The applied magnetic field is changing the state of the material leading to solidification. Then the yield shear strength appears the important material parameter, the value of which is dependent on strength of the magnetic field. The aim of the paper is to present the idea how to investigate the behaviour of the solidified magnetorheological fluid under high strain rates. The experimental tests are carried out with application of the own construction of a laboratory test stand – the modified Split Hopkinson Pressure Bar (SHPB).

The Hopkinson Pressure bar was not only used to test metallic materials or brittle solids at high strain rates. Kenner (1980) adopted the split Hopkinson pressure bar to test pressure pulses in different kinds of fluids – ethyl alcohol, distilled water, glycerin and two kinds of oil. The experimental results help one to evaluate the one dimensional representation of pulse transmission and reflection at a solid-fluid interface. The results of experimental investigations make a basis for creation of a mathematical expression describing the pressure pulse distributed in the fluid. Another attempt to use the SHPB to test fluids was presented by Lim *et al.* (2009). The authors tested Cannon N4000 and N5100 fluids consisting 100% polybutene. The experimental part was prepared with use of the SHPB furnished with aluminum bars and the fluid container was specially prepared. This part was machined of soft and flexible rubber and was tested with respect to fluid expansion in the radial direction. The dynamical tests of the polymer materials were considered by Siviour and Jordan (2016) where the behaviour of the rearrangement of microstructure of amorphous polymers was reviewed. The preliminary information about testing magnetorehological fluid under high strain rates was announced by Fraś (2015). There was presented a proposal of the laboratory set-up and an attempt to use the Perzyna viscoplasticity

model to describe the behavior of magnetorheological fluids. Another attempt of testing magnetically controlled materials was presented by Wang (2016). The authors tested a self-prepared material with content of 75% carbonyl iron particles in several magnetic fields – from 95 to 382 kA/m. During those experiments, stress values from 5 to almost 16 MPa (for maximal magnetic field value) were obtained. Another attempt to use the Split Hopkinson Pressure Bar with magnetically controlled materials to test magnetorheological elastomers was presented by Liao *et al.* (2013). The authors used for several magnetic field strengths – maximally 320 kA/m and received in a dynamic compression test maximal stress values about 6 MPa with velocity of the striker about 30 m/s. The micro-sized ferroelements in the magnetic field created the structure of viscoplastic solids. The structural rearrangements controlled by the magnetic field in the course of deformation can be investigated experimentally due to the recent developments of MEMS devices designed by Jarząbek *et al.* (2015).

2. Magnetorheological fluid

The magnetorheological fluid contains micro-sized ferroelements. The particles are spherically shaped and their diameter is less than $10\text{ }\mu\text{m}$. The magnetoactive ferroelements are coated with a silicon shield and immersed in the carrying fluid, e.g. mineral oil. The silicon coating prevents from aggregation of particles which are made of a carbonyl iron material. The influence of the magnetic field forces the ferroelements to connect together into characteristic linear shapes – the braids. The linearly-shaped elements made of ferroelements are sticking together and create the solid structure of the material.

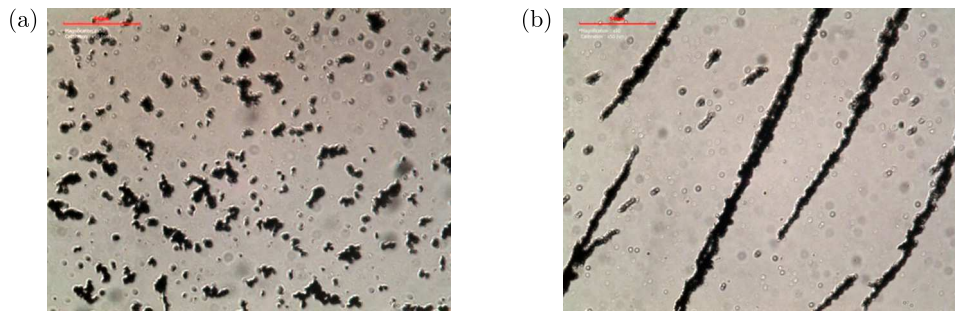


Fig. 1. The ferroelements in neutral state (a) and under the influence of a magnetic field (b)

The ferroelements can freely move in the carrying fluid. Figure 1b shows the influence of the magnetic field on the way how the ferroelements are connected. The magnetoactive particles are sticking together creating characteristic braids parallel to the line of the magnetic field. The whole rearrangement of the structure during the deformation process can be described by tearing off a single ferroelement from the braid. The structure is deformed in the course of taking off from the sequence of separate braids.

The rearrangement of ferroelements under the external force tends to swap the neighboring element. The particle is shifted and this produces a shear angle. The interaction energy of two particles is given as follows (Jolly *et al.*, 1996)

$$E_{12} = \frac{|m^2|(1 - 3\cos^2\theta)}{4\pi\mu_1\mu_0r^3} \quad (2.1)$$

where m is mass of the particle, θ corresponds to the angle of shear, r denotes the distance between particles and μ_1 is the relative permeability, μ_0 is vacuum permeability. The shift of a

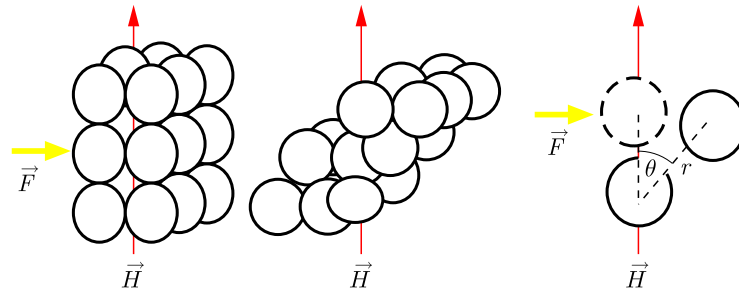


Fig. 2. The rearrangement of the structure, F – external force, H – magnetic flux

single ferroelement produces migration of the braid. The refreshable features of the magnetorheological fluid allow one to use them as an energy absorption material. The shifting of a single ferroelement by some external force causes reorganization of the skeleton structure.

3. The laboratory test stand

The testing stand is made on the basis of the Split Hopkinson Pressure Bar with 7075 alloy aluminum bars. Their length is 1000 mm and diameter 20 mm. The strain gauges are cemented in the middle – four on the each bar, and they are working as a quarter bridge sub system with the signal amplifier. The main idea is to modify the present laboratory device and prepare it to test the magnetorheological fluid – LORD MRF-140CG in a magnetic field at high strain rates by using the prepared coil – the resistivity of used copper 0.7 mm wire is 180 Ohm. It generates a 120 kA/m magnetic flux with a 360 V and 2 A direct current power supply. The coil with inner diameter 30 mm and length 50 mm has 80 turns of the wire. The power line is realized by EA-PS 8360-30 and the maximum voltage is 360 V while the current is 50 A. The laboratory device to investigate magnetorheological materials is subjected to modification. The idea of the proposed modification is presented in Fig. 3.

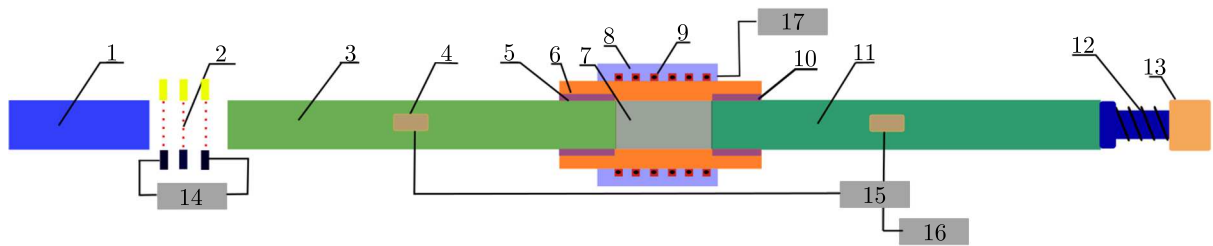


Fig. 3. 1 – striker, 2 – laser sensor to measure velocity, 3 – incident bar, 4 – strain gauges, 5 – glue, 6 – deformable hose, 7 – MR fluid, 8 – coil cover, 9 – coil, 10 – glue, 11 – transmitter bar, 12 – spring, 13 – momentum trap, 14 – velocity measure system, 15 – signal amplifier, 16 – oscilloscope, 17 – power supply for coils

The novelty of the proposed laboratory test stand is the application of coils for the sleeves shown in Fig. 3 to induce a constant magnetic field. Also a new shear testing device is designed. Due to this, the dynamic axial compression and shear tests of the solidified magnetorheological material is possible. The theory of measurement of the axial strain and determination of the axial stress with the use of the SHPB was presented by Klepaczko (2007). The striker accelerated by the gas gun achieves velocity V_0 which is measured by a matrix of diodes and photodiodes. In the case of impact by the striker against an incident bar shock wave is triggered. It has length $\varphi = 2L$, where L is length of the striker. The time period of this wave is $T = 2L/C_0$, where C_0 is the velocity of the sound wave inside the bar.

4. Results

During the experiment, the MR fluid solidified under the magnetic field responds to the stress waves. The effect of the compressive longitudinal incident pulse and the reflected pulse can be observed in Fig. 4b.

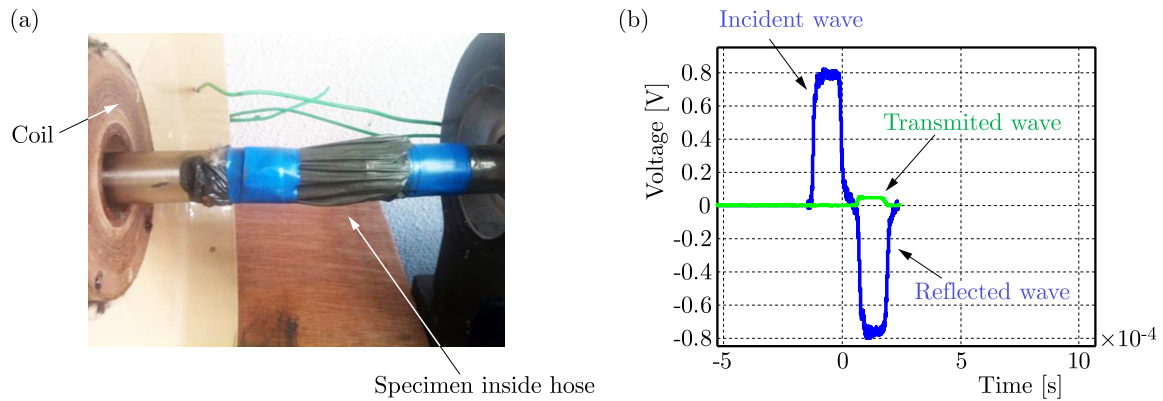


Fig. 4. (a) The deformable hose with the MR fluid before the test, (b) the observed wave forms of the tested material

The MR specimen is closed in a deformable hose made of latex with carefully prepared dimensions – 10 mm long and 20 mm in the external diameter of the bars, which allows one to keep about 3.2 ml of the fluid injected with a syringe – Fig. 4a. It provides free deformation of the solidified MR fluid. The specially designed coil is generating a 120 kA/m magnetic flux and is responsible for sticking the ferroelements together. The generated field is parallel to the axis of incident – the transmitted bars what keeps the solidified ferroelements between the bars. The magnetoactive particles are arranged along the lines of the magnetic field. The deformable hose presented in Fig. 4 a with the MR fluid inside allows free deformation during the dynamical tests. The influence of the thin rubber hose on the longitudinal stress waves can be neglected. The results of experimental investigation are presented below.

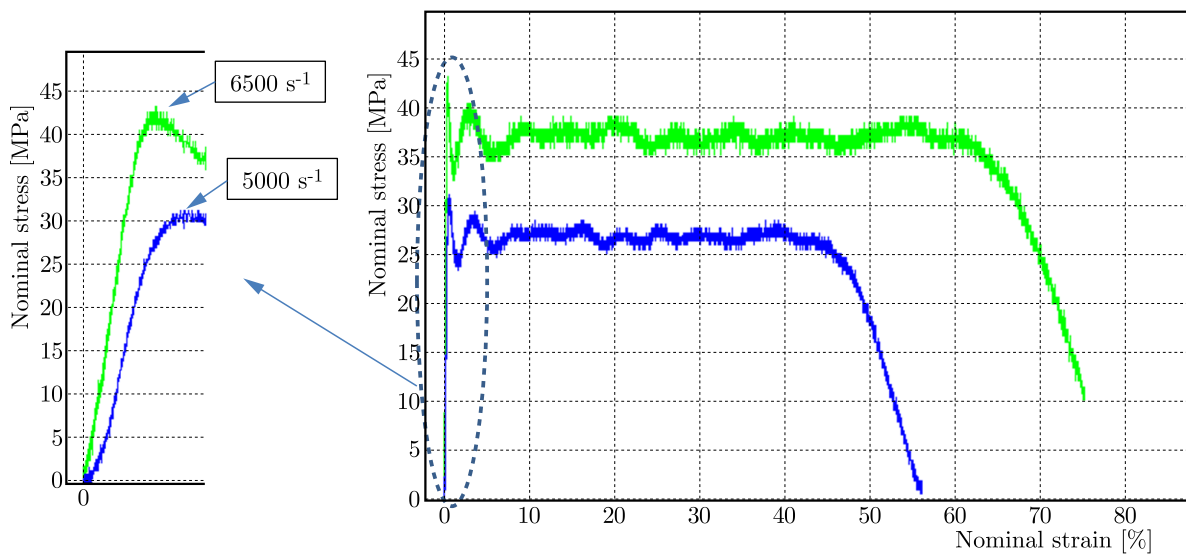


Fig. 5. The results of the experiment, the nominal stress-strain curve

The results presented in Fig. 5 are obtained during experimental investigation. The material has been tested with a 300 mm long striker and with two velocities 18 m/s and $10 \text{ m/s} \pm 0.1 \text{ m/s}$.

During the experiment aluminum bars without the shaper placed between the striker and the incident bar were used. The measured values were multiplied 200 times by the signal amplifier. For this reason, the obtained transmitted wave had an amplitude about 0.08 V with the velocity of the striker about 18 m/s and about 0.035 V for ~ 10 m/s.

5. Conclusions

The Split Hopkinson Pressure Bar has been adopted to test the magnetorheological fluid at high strain rates. The material was tested for two velocities of the striker to test and evaluate the laboratory set-up. The obtained results can be compared with the results of Wang *et al.* (2016) who tested similar materials but with a lower content of iron particles 74% versus 84% in our case. Wang *et al.* (2016) obtained for 200 mT (159 kA/m) and the strain rate 6000 s^{-1} the stress values in the range of 10-17 MPa. The material structure of Wang *et al.* (2016) was completely different (74% of carbonyl irons and several another additions closed into the gel structure) but the order of magnitude was similar to tested LORD MRF-140CG (84% of carbonyl irons). The effect of dispersion can play an essential role in the interpretation of the experimental data. The dispersion effect in the aluminium bars is not significant due to the large ratio of wavelength to the bar diameter, however, it has not been analysed yet and requires further studies. The comparison of our preliminary results confirms the validity of the concept of the proposed laboratory set-up and gives a promising perspective for a more detailed investigation aiming at the identification of Perzyna model.

Acknowledgment

This work was supported by the NCN (National Science Centre Poland) Research Project: 2015/17/N/ST8/02018.

References

1. FRAŚ L.J., 2015, The Perzyna viscoplastic model in dynamic behaviour of magnetorheological fluid under high strain rates, *Engineering Transactions (Rozprawy Inżynierskie)*, ISSN: 0867-888X, **63**, 2, 233-243
2. JARZĄBEK D.M., CHMIELEWSKI M., WOJCIECHOWSKI T., 2015, The measurement of the adhesion force between ceramic particles and metal matrix in ceramic reinforced-metal matrix composites, *Composites Part A – Applied Science and Manufacturing*, **76**, 124-130
3. JOLLY M.R., CARLSON J.D., MUNOZ B.C., 1996, A model of the behaviour of magnetorheological materials, *Smart Materials and Structures*, **5**, 607-614
4. KENNER V.H., 1980, The fluid Hopkinson bar, *Experimental Mechanics*, **20**, 7, 226-232
5. KLEPACZKO J.R., 2007, *Introduction to Experimental Techniques for Materials Testing at High Strain Rates*, Institute of Aviation, Warsaw
6. LIAO G., GONG X., XUAN S., 2013, Magnetic field-induced compressive property of magnetorheological elastomer under high strain rate, *Industrial and Engineering Chemistry Research*, **52**, 25, 8445-8453
7. LIM A.S., LOPATNIKOV S.L., GILLESPIE JR. J.W., 2009, Phenomenological modelling of the response of a dense colloidal suspension under dynamic squeezing flow, *Polymer Testing*, **28**, 891-900

8. SIVIOUR C.R., JORDAN J.L., 2016, High strain rate mechanics of polymers: a review, *Dynamic Behavior of Materials*, **2**, 15-32
9. WANG Y., WANG S., XU C., XUAN S., JIANG W., GONG X., 2016, Dynamic behavior of magnetically responsive shear-stiffening gel under high strain rate, *Composites Science and Technology*, **127**, 169-176

Manuscript received August 24, 2017; accepted for print November 3, 2017

ENHANCED ENERGY CONVERSION AS A RESULT OF FLUID-SOLID INTERACTION IN MICRO- AND NANOSCALE

JANUSZ BADUR, PAWEŁ ZIÓŁKOWSKI, SEBASTIAN KORNET, TOMASZ KOWALCZYK,
KAMIL BANAŚ, MATEUSZ BRYK

Institute of Fluid Flow Machinery, Energy Conversion Department, Polish Academy of Sciences, Gdańsk, Poland

PIOTR JÓZEF ZIÓŁKOWSKI

Institute of Fluid Flow Machinery, Energy Conversion Department, Polish Academy of Sciences, Gdańsk, Poland

Gdańsk University of Technology, Faculty of Civil and Environmental Engineering, Gdańsk, Poland

e-mail: pziolkowski@imp.gda.pl

MICHAŁ STAJNKE

Institute of Fluid Flow Machinery, Energy Conversion Department, Polish Academy of Sciences, Gdańsk, Poland

It is known that nano- and micromechanics require new approaches to right describing of surface-like phenomena which lead to an enhanced energy conversion. In this work, a general form of surface forces that consist of a contribution from both the friction and mobility components has been extended to collect the effects of bulk and surface motion of a fluid. Quite similar impact can be observed for a solid-fluid mixture, where the principle of effective stress for this new type of approach should be considered from the very beginning. The second motivation of our work is to present the multiscale domain of fluid-solid interaction which describes some “emergence effects” for materials with especially high volumetric surface densities.

Keywords: enhanced energy conversion, micro- and nanomechanics, fluid-solid interaction, pressure and thermally driven flow

1. Introduction

Though the classical continuous mechanics theory is enormously useful, it does not take into account all the phenomena that occur in the fluid-solid interface at the micro- and nanoscale. Thus, new approaches in continuum thermodynamics with slip velocity, thermal transpiration and a variety of different “jump” phenomena on the surface like: temperature, concentration, pressure, electric potential, order parameter, etc., are developed with comparison to experimental results (Badur *et al.*, 2011, 2015; Henry and Minier, 2014; Kowalewski *et al.*, 2016; Lewandowski *et al.*, 2011; Nakielski *et al.*, 2015; Nitoń *et al.*, 2013; O’Hare *et al.*, 2007; Thomson and Trojan, 1997; Ziółkowski and Badur, 2014). Moreover, these surface processes, in general, lead to some enhancement of energy conversion in comparison to the bulk classical transport model (Badur *et al.*, 2015; Lemański and Karcz, 2008; Morini *et al.*, 2011; Nakielski *et al.*, 2015). A similar impact can be observed for porous saturated solids, when the Terzaghi principle of effective stress leads to a new situation in which the exchange of momentum and thermal energy in such continua undergo in a more complex manner (Badur *et al.*, 2011, 2015; Lemański and Karcz, 2008; Thomson and Trojan, 1997; Ziółkowski and Badur, 2014). The enhanced conversion of energy is observed in new micro- and nanodevices as outside devices which work in power plants.

Practically, we should use the surface phenomena to improve the exchange of mass, momentum and energy (Kucaba-Piętal *et al.*, 2009; Lemański and Karcz, 2008; Lewandowski *et al.*,

2011; Morini *et al.*, 2011; O'Hare *et al.*, 2007; Reese *et al.*, 2003; Thomson and Trojan, 1997; Ziółkowski and Badur, 2014). Also quite new challenges for accurate prediction and assessment of the material effort (the risk of fracture) are developed for these processes (Banaszkiewicz, 2015; Banaszkiewicz and Rehmus-Forc, 2015; Pęcherski *et al.*, 2011; Vadillo *et al.*, 2011). A schematic presentation of these emerging aspects of the modelling of fluid-solid interactions in the multiscale domain is highlighted in Fig. 1.

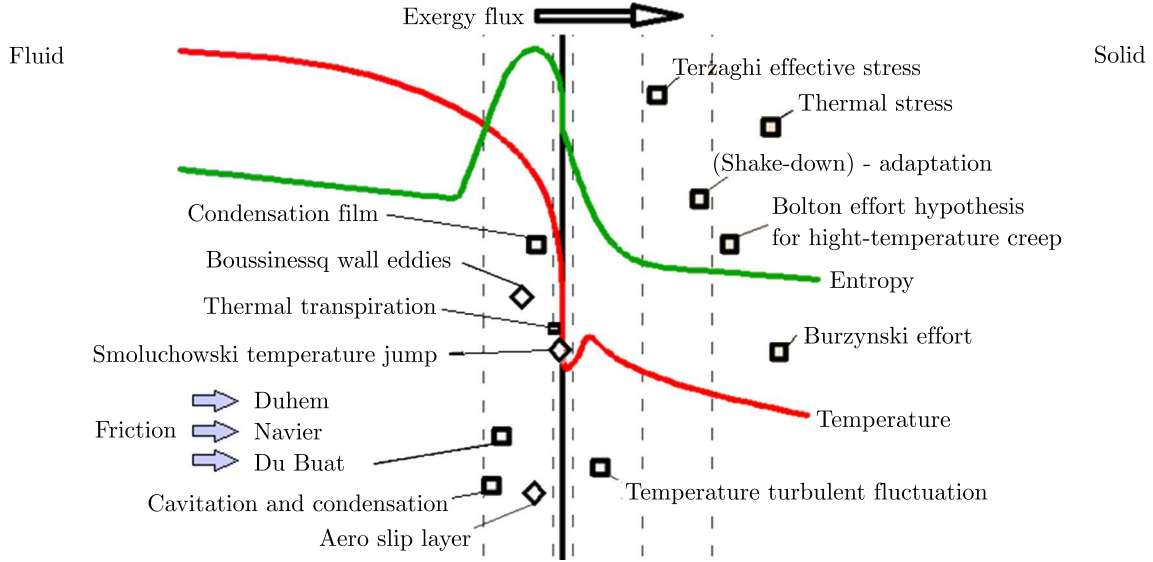


Fig. 1. Schematic presentation of emerging aspects of mathematical modelling that takes into account fluid-solid interaction in the multiscale domain

2. Collected effects of fluid-solid interaction in porous flow

One example of applicability of this method to improve flow in porous media is a model of thermal transpiration described mainly via a mobility force. Beside the classical “bulk” behavior, wall stresses should also incline us to introduce new quantities such as surface friction force, surface mobility, etc. In the presented reasoning, it has been postulated that the general surface “vis impressa” can be additively split into friction and mobility parts. Here, the mobility forces are defined as an ability of a fluid (gas or liquid) to flow along the wall without the assistance of, or even in opposition to, bulk (volume) forces. A whole description of this phenomenon is presented in (Badur *et al.*, 2011, 2015). In this short communication, let us mention only reexamination of the Poiseuille-Knudsen-Reynolds equation in terms of a sum of three contributions: the bulk pressure driven flow and two mobility surface forces, mainly: the Knudsen surface slip driven flow and the Reynolds surface thermally driven flow.

A peculiar difficulty of the modeling of flow in porous media arises often when there is a need of applying some extension of Darcy equation, like for instance, the Brinkmann-Darcy-Forchheimer equation (Hooman, 2008). Treating that a laboratory nanopipe is fully equivalent to a single porous channel and looking for common effects of the bulk and surface motion, one may consider the following momentum flux integral in any cross section of a porous medium oriented by the tangential component of the unit vector \mathbf{n}_{tan}

$$\iint_{\text{bulk section}} (\rho \mathbf{v} \otimes \mathbf{v} + \mathbf{p}) \mathbf{n}_{\text{tan}} + \oint_C (\rho_s \mathbf{v}_s \otimes \mathbf{v}_s + \mathbf{p}_s + \mathbf{n}_{\text{nor}} \mathbf{p} + \mathbf{f}_{\partial V}) \mathbf{n}_{\text{tan}} dC = 0 \quad (2.1)$$

In the above, $\rho \mathbf{v}$ and $\rho_s \mathbf{v}_s$ are the bulk and the surface momentum density vectors, ρ and ρ_s are the gas density in the bulk and on the boundary. Next, $\mathbf{p} = p_{ij} \mathbf{e}_i \otimes \mathbf{e}_j = \mathbf{p}^T$ and $\mathbf{p}_s = \mathbf{p}_s^T$ are the bulk and the surface flux momentum. The boundary force can be separated into surface friction and surface mobility, thus: $\mathbf{f}_{\partial V} = \mathbf{f}_r + \mathbf{f}_m$ (Badur *et al.*, 2011, 2015). The total momentum influx will be

$$\mathcal{M} = \iint_{\text{bulk section}} \rho \mathbf{v} v_{\tan} dA + \oint_{\mathcal{C}} \rho_s \mathbf{v}_s v_{s \tan} d\mathcal{C} \quad \mathcal{M} = \dot{m} \mathbf{v}_r \quad (2.2)$$

where $\iint_{\text{bulk section}} \rho \mathbf{v} v_{\tan} dA$ – contribution from the bulk velocity and $\oint_{\mathcal{C}} \rho_s \mathbf{v}_s v_{s \tan} d\mathcal{C}$ – contribution from the slip velocity $v_{s \tan} = \mathbf{v}_s \mathbf{n}_{\tan}$. Using some arguments from technique of homogenization, we can postulate the existence of a resultant velocity \mathbf{v}_r which is parallel to the vector of total momentum (2.2)₂. This vector is located somewhere in a geometrical center of the velocity profile. In many cases, independently of the shape of the cross section, the bulk profile of velocity is nearly flat and ending with the value of $v_{s \tan} \approx |\mathbf{v}_s|$ – the magnitude of slip velocity. In the above, according with the traditional Reynolds notation, \dot{m} denotes the resultant mass flow rate. Taking into account that $\mathbf{f}_{\partial V} = \mathbf{f}_r + \mathbf{f}_m = \nu \mathbf{v}_s - c_{m\theta} \text{grad}_s \theta_s$, integral (2.1) can be reorganized, expressing explicitly the thermal mobility part $c_{m\theta} \text{grad}_s \theta_s$ with the thermomobility coefficient $c_{m\theta}$ and the slip friction part $\nu \mathbf{v}_s$, where ν is the Navier surface friction coefficient

$$\dot{m} \mathbf{v}_r = \iint_{\text{Poiseuille}} (p \mathbf{I} - 2\mu \mathbf{d}) \mathbf{n} dA - \oint_{\text{Darcy}} \nu \mathbf{v}_s \mathbf{I}_s d\mathcal{C} - \oint_{\text{Reynolds}} c_{m\theta} \text{grad}_s(\theta_s) \mathbf{I}_s d\mathcal{C} \quad (2.3)$$

Since the porosity in any cross section of porous media is quite arbitrary, then the known procedure of homogenization can be applied, thus Eq. (2.3) leads finally to a 3D resultant equation (Vignoles *et al.*, 2008)

$$\mathbf{v}_r = -\left(\frac{P}{\mu} \mathbf{B} + \mathbf{D}_K\right) \frac{\text{grad } P}{P} + \mathbf{D} \frac{\text{grad } T}{T} \quad (2.4)$$

where \mathbf{v}_r is the resultant filtration velocity, μ – gas viscosity, \mathbf{B} – permeability tensor, \mathbf{D}_K – Knudsen accommodation diffusion tensor and \mathbf{D} – thermal transpiration coefficient tensor. Here, the single surface pressure tensor \mathbf{p}_s does not appear, slip velocity \mathbf{v}_s or surface temperature θ_s either, since after homogenization their role retakes the capillarity pressure P and the capillarity temperature T . Also, the two-dimensional surface gradient $\text{grad}_s(\cdot)$, due to homogenization, turns into the three-dimensional gradient $\text{grad}(\cdot)$. This phenomenological model is based on the already averaged equations for the bulk flow resistance and the surface mobility forces, which means that some local coefficients, like the Navier slip and Reynolds transpiration can be used to a direct definition of \mathbf{B} , \mathbf{D}_K and \mathbf{D} , respectively.

References

1. BADUR J., KARCZ M., LEMAŃSKI M., 2011, On the mass and momentum transport in the Navier-Stokes slip layer, *Microfluidics and Nanofluidics*, **11**, 439-449
2. BADUR J., ZIÓŁKOWSKI P.J., ZIÓŁKOWSKI P., 2015, On the angular velocity slip in nano flows, *Microfluidics and Nanofluidics*, **19**, 191-198
3. BANASZKIEWICZ M., 2015, Multilevel approach to lifetime assessment of steam turbines, *International Journal of Fatigue*, **73**, 39-47
4. BANASZKIEWICZ M., REHMUS-FORC A., 2015, Stress corrosion cracking of a 60 MW steam turbine rotor, *Engineering Failure Analysis*, **51**, 55-68

5. HENRY C., MINIER J.-P., 2014, Progress in particle resuspension from rough surfaces by turbulent flows, *Progress in Energy and Combustion Science*, **45**, 1-53
6. HOOMAN K., 2008, Heat and fluid flow in a rectangular microchannel filled with a porous medium, *International Journal of Heat and Fluid Flow*, **51**, 5804-5810
7. KOWALEWSKI T.A., NAKIELSKI P., PIERINI F., ZEMBRZYCKI K., PAWŁOWSKA S., 2016, Micro and nano fluid mechanics, [In:] *Advances in Mechanics: Theoretical, Computational and Interdisciplinary Issues*, M. Kleiber et al. (Eds.), 27-34
8. KUCABA-PIĘTAL A., WALENTA Z., PERADZYŃSKI Z., 2009, Molecular dynamics computer simulation of water flows in nanochannels, *Bulletin of the Polish Academy of Sciences Technical Sciences*, **57**, 55-61
9. LEMAŃSKI M., KARCZ M., 2008, Performance of lignite-syngas operated tubular Solid Oxide Fuel Cell, *Chemical and Process Engineering*, **29**, 233-248
10. LEWANDOWSKI T., OCHRYMIUK T., CZERWIŃSKA J., 2011, Modeling of heat transfer in micro-channel gas flow, *ASME Journal of Heat Transfer*, **133**, 022401-1
11. MORINI G.L., YANG Y., CHALABI H., LORENZINI M., 2011, A critical review of the measurement techniques for the analysis of gas microflow through microchannels, *Experimental Thermal and Fluid Science*, **35**, 849-893
12. NAKIELSKI P., PAWŁOWSKA S., PIERINI F., LIWIŃSKA W., HEJDUK P., ZEMBRZYCKI K., ZABOST E., KOWALEWSKI T., 2015, Hydrogel nanofilaments via core-shell electrospinning, *PLoS ONE*, **10**, 6, e0129816, DOI: 10.1371/journal.pone.0129816
13. NITOŃ P., ŻYWOCIŃSKI A., FIAŁKOWSKI M., HOLYST R., 2013, A “nano-windmill” driven by a flux of water vapour: a comparison to the rotating ATPase, *Nanoscale*, **5**, 9732-9738
14. O'HARE L., LOCKERBY D.A., REESE J.M., EMERSON D.R., 2007, Near-wall effects in rarefied gas micro-flows: some modern hydrodynamic approaches, *International Journal of Heat and Fluid Flow*, **28**, 37-43
15. PĘCHERSKI R.B., SZEPTYŃSKI P., NOWAK M., 2011, An extension of Burzyński hypothesis of material effort accounting for the third invariant of stress tensor, *Archives of Metallurgy and Materials*, **56**, 2, 503-508
16. REESE M., GALLIS M.A., LOCKERBY D.A., 2003, New directions in fluid dynamics: non-equilibrium aerodynamic and microsystem flows, *Philosophical Transactions A: Mathematical, Physical and Engineering Sciences*, **361**, 2967-2988
17. THOMSON P.A., TROJAN S.M., 1997, A general boundary condition for liquid flow at solid surface, *Nature*, **389**, 360-362
18. VADILLO G., FERNANDEZ-SAEZ J., PĘCHERSKI R.B., 2011, Some applications of Burzynski yield condition in metal plasticity, *Materials and Design*, **32**, 628-635
19. VIGNOLES G.L., CHARRIER P., PREUX C., DUBROCA B., 2008, Rarefied pure gas transport in non-isothermal porous media: effective transport properties from homogenization of the kinetic equation, *Transport in Porous Media*, **73**, 2, 211-232
20. ZIÓŁKOWSKI P., BADUR J., 2014, Navier number and transition to turbulence, *Journal of Physics: Conference Series*, **530**, 012035, DOI: 10.1088/1742-6596/530/1/012035

INFORMATION FOR AUTHORS

Journal of Theoretical and Applied Mechanics (JTAM) is devoted to all aspects of solid mechanics, fluid mechanics, thermodynamics and applied problems of structural mechanics, mechatronics, biomechanics and robotics. Both theoretical and experimental papers as well as survey papers can be proposed.

We accept articles in English only. The text of a *JTAM* paper should not exceed **12 pages of standard format A4** (11-point type size, including abstract, figures, tables and references), short communications – **4 pages**.

The material for publication should be sent to the Editorial Office via electronic journal system: <http://www.ptmts.org.pl/jtam/index.php/jtam>

Papers are accepted for publication after the review process. Blind review model is applied, which means that the reviewers' names are kept confidential to the authors. The final decision on paper acceptance belongs to the Editorial Board.

After qualifying your paper for publication we will require L^AT_EX or T_EX or Word document file and figures.

The best preferred form of figures are files obtained by making use of editorial environments employing vector graphics:

- generated in CorelDraw (*.cdr), AutoCad and ArchiCad (*.dwg) and Adobe Illustrator (*.ai). We require original files saved in the standard format of the given program.
- generated by calculation software (e.g. Mathematica) – we need files saved in *.eps or *.pdf formats.
- made in other programs based on vector graphics – we ask for *.eps, *.wmf, *.svg, *.psfiles.

Any figures created without application of vector graphics (scans, photos, bitmaps) are strongly encouraged to be supplied in *.jpg, *.tif, *.png formats with resolution of at least 300 dpi.

Requirements for paper preparation

Contents of the manuscripts should appear in the following order:

- Title of the paper
- Authors' full name, affiliation and e-mail
- Short abstract (**maximum 100 words**) and 3-5 key words (**1 line**)
- Article text (equations should be numbered separately in each section; each reference should be cited in the text by the last name(s) of the author(s) and the publication year)
- References in alphabetical order. See the following:
 1. Achen S.C., 1989, A new boundary integral equation formulation, *Journal of Applied Mechanics*, **56**, 2, 297-303
 2. Boley B.A., Weiner J.H., 1960, *Theory of Thermal Stresses*, Wiley, New York
 3. Canon W., 1955, Vibrations of heated beams, Ph.D. Thesis, Columbia University, New York
 4. Deresiewicz H., 1958, Solution of the equations of thermoelasticity, *Proceedings of Third U.S. National Congress of Applied Mechanics*, 287-305
- Titles of references originally published not in English, should be translated into English and formulated as follows:
 5. Huber M.T., 1904, Specific work of strain as a measure of material effort (in Polish), *Czasopismo Techniczne*, **XXII**, 3, 80-81

All the data should be reported in **SI units**.

Contents

Kazemi M. — Hygrothermoelastic buckling response of composite laminates by using modified shear deformation theory	3
Zenkour A.M. — A generalized thermoelastic dual-phase-lagging response of thick beams subjected to harmonically varying heat and pressure	15
Wang D., Hao Z., Chen Y., Zhang Y. — Dynamic and resonance response analysis for a turbine blade with varying rotating speed	31
Buśkiewicz J. — Reduced number of design parameters in optimum path synthesis with timing of four-bar linkage	43
Ustrzycka A., Szuwalski K. — Annular rotating disks optimal with respect to mixed creep rupture	57
Peyyala P.K., Subba Rao V.V. — An analytical study on buckling behavior of CNT/polymer composite plates using the first order shear deformation theory	71
Akbarzadeh P. — A locally modified single-phase model for analyzing magnetohydrodynamic boundary layer flow and heat transfer of nanofluids over a nonlinearly stretching sheet with chemical reaction	81
Jemielita G.E. — Bending analysis of plates by superposing cylindrical deflections	95
Meshkini M., Firoozbakhsh K., Jabbari M., SelkGhafari A. — An analytical investigation of a 2D-PPMs hollow infinite cylinder under Thermo-Electro-Mechanical (TEM) loadings	107
Chiter A., Zegadi R., El'Hadi Bekka R., Felkaoui A. — A new method for automatic defects detection and diagnosis in rolling element bearings using Wald test	123
Jayalekshmi S., Gireesh Kumar P. — Modified model for shear stress distribution using TRI-1 lunar soil simulant	137
Perkowski D.M., Kulchytsky-Zhyhailo R., Kołodziejczyk W. — On axisymmetric heat conduction problem for multilayer graded coated half-space	147
Zhang D., Gao S., Niu S., Liu H. — A prediction method for load distribution in threaded connections	157
Nikolov N., Sinapov P. — Determination of the internal resistance of a hammer drill chisel	169
Haryadi G.D., Tungga Dewa R., Ekaputra I.M.W. — Fatigue crack growth and probability assessment for transverse TIG welded Aluminum alloy 6013-T4	179
Kluger K., Łagoda T. — Modification of the algorithm for calculating fatigue life for the criteria based on the concept of the critical plane	191
Rogowski H., Hansen M.O.L., Maroński R. — Steady and unsteady analysis of NACA 0018 airfoil in vertical-axis wind turbine	203
Augustyniak M. — Old materials – new capabilities: lattice materials in structural mechanics	213
Ambroziak A., Kłosowski P. — Polyester sail technical woven fabric behaviour under uniaxial and biaxial tensile tests	227
Grzelczyk D., Biesiacki P., Mrozowski J., Awrejcewicz J. — Dynamic simulation of a novel “broomstick” human forward fall model and finite element analysis of the radius under the impact force during fall	239
Navarro H.A., Cveticanin L. — Extension of the Hamiltonian approach with general initial conditions	255
Uzny S., Sokół K. — On bifurcation load of a three-member slender system with an internal crack subjected to Euler's load	269
Viscardi M., Di Leo R., Ciminello M., Brandizzi M. — Preliminary experimental/numerical study of the vibration annoyance control of a windshield wiper mechanical system through a Synchronized Switch Shunt Resonator (SSSR) technology	283
Zhang X., Lu A., Wang S., Zhang N. — Optimum design of fiber angle and hole orientation of an orthotropic plate	297
Kisilowski J., Zalewski J. — Selected examples of referring the examined stochastic technical stability to the ISO standards	313
<u>Short Research Communication</u>	
Frąś L.J., Pęcherski R.B. — Modified Split Hopkinson Pressure Bar for investigations of dynamic behaviour of magnetorheological materials	323
Badur J., Ziółkowski P., Kornet S., Kowalczyk T., Banaś K., Bryk M., Ziółkowski P.J., Stajnke M. — Enhanced energy conversion as a result of fluid-solid interaction in micro- and nanoscale	329